

Exploring Chemical Complexity in Group IV Reticular Solids



VNIVERSITATIS VALÈNCIA

Instituto de Ciencia Molecular (ICMol)

Thesis submitted by Belén Lerma Berlanga
for the degree of Doctor in Chemistry

Supervised by
Dr. Carlos Martí Gastado
and
Dr. Natalia Muñoz Padial

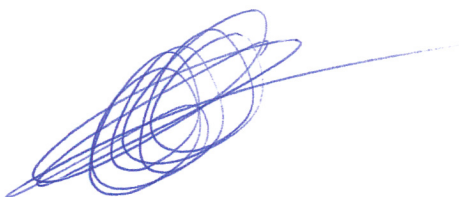
May 2022

El Prof. Carlos Martí Gastaldo, investigador ERC y post Ramón y Cajal en el Instituto de Ciencia Molecular (ICMol), de la Universitat de València y la Dr. Natalia Muñoz Padial, investigadora “La Caixa Junior Leader Retaining” en el Instituto de Ciencia Molecular (ICMol), de la Universitat de València.

CERTIFICAN:

Que Belén Lerma Berlanga ha realizado la presente Tesis Doctoral, titulada “*Exploiting Chemical Complexity in Group IV Reticular Solids*” bajo su dirección en el Instituto de Ciencia Molecular (ICMol), autorizando mediante este escrito la presentación de la misma para optar al grado de Doctor en Química por la Universitat de València.

En Paterna, a 5 de mayo de 2022.



Dr. Carlos Martí Gastaldo
Co-Director y tutor



Dr. Natalia Muñoz Padial
Co-Directora

Abbreviations

1D	One-dimensional
2,2'-bpy	2,2'-bipyridine
2D	Two-dimensional
2-MeIm	2-methylimidazole
3D	Three-dimensional
4,4'-bpy	4,4'-bipyridine
A	Adenine
AAS	Atomic Absorption Spectroscopy
AFM	Atomic Force Microscopy
ATR-IR	Attenuated total reflection Infrared
BCPBD	1,4-bis-p-carboxyphenylbuta-1,3-diene
BET	Brunauer-Emmer-Teller
BLC	Burkholderia cepacian
C ₆₀	Fullerene
cdc	Cubane-1,4-dicarboxylate
CD-MOFs	Cyclodextrin MOFs
cMUV	cage-type Material of Universitat de València
COF	Covalent-Organic Framework
CP MAS-NMR	Cross Polarization Magic Angle Spinning Nuclear Magnetic Resonance
Cp*	Pentamethyl-cyclopentadienyl
CPM	Crystalline Porous Material
CSD	Cambridge Structural Database
DBBs	Domain building blocks
DFT	Density Functional Theory
DIFP	Diisopropyl-fluorophosphate
DMNP	Dimethyl-4-nitrophenyl phosphate
DNA	Deoxyribonucleic acid
DOT	2,5-Dioxidoterephthalate

DUT	Dresden University of Technology
EDTA	Ethylenediaminetetraacetic acid
EDX	Energy-Dispersive X-ray
EPR	Electron Paramagnetic Resonance
Et ₃ N	triethylamine
EXAFS	Extended X-ray Absorption Fine Structure
FDM	Fudan material
FJU	Fujian Jiangxia University
H ₂ BBDC	5-boronobenzene-1,3-dicarboxylic acid
H ₂ BDC	1,4-benzenedicarboxylic acid (terephthalic acid)
H ₂ BPDC	4,4'-biphenyldicarboxylic acid
H ₂ BpyDC	[2,2'-bipyridine]-5,5'-dicarboxylic acid
H ₂ FDC	2,4-furandicarboxylic acid
H ₂ Me ₄ BPDC	3,3',5,5'-tetramethyl-4,4'-biphenyldicarboxylate
H ₂ NDC	1,4-naphthalenedicarboxylate
H ₂ PyC	4-pyrazolecarboxylate
H ₂ PyDC	1 <i>H</i> -3,5-pyrazoledicarboxylic acid
H ₂ PZDC	4,4'-(pyridazine-3,6-diyl)dibenzoic acid
H ₂ TDC	2,5-thiophenedicarboxylic acid
H ₂ TPDC	(1,1':4',1''-terphenyl)-4,4''-dicarboxylic acid
H ₂ TPDC'	9,10-bis(triisopropylsilyloxy)phenanthrene-2,7-dicarboxylate
H ₂ TPY	4'-(4-carboxyphenyl)[2,2':6',2''-terpyridine]-5,5''-dicarboxylate
H ₂ TZDC	4,4'-(1,2,4,5-tetrazine-3,6-diyl)dibenzoic acid
H ₃ BTB	4,4',4''-Benzene-1,3,5-triyl-tris(benzoic acid)
H ₃ BTC	1,3,5-benzene-tricarboxylic acid
H ₃ BTCTB	4,4',4''-[benzene-1,3,5-triyltris(carbonylimino)] trisbenzoic acid
H ₃ hmtt	5,5',10,10',15,15'-hexamethyltruxene-2,7,12-tricarboxylic acid
H ₄ TCPP	tetrakis(4-carboxyphenyl)porphyrin

H ₄ TCPPM	tetrakis (4-carboxyphenyl) porphyrin metalate
HBC	Hexabenzocoronene
HIAM	Hoffmann Institute of Advanced Material
HKUST	Hong Kong University of Science and Technology
Hodip	5,5'-oxydiisophthalic acid
HPB	Hexaphenylbenzene
HSAB	Hard-Soft-Acid-Base
Htz	<i>1H</i> -1,2,3-triazole
IAST	Ideal Adsorbed Solution Theory
ICP-AES	Inductively Coupled Plasma- Atomic Emission Spectroscopy
ICP-MS	Inductively Coupled Plasma-Mass Spectroscopy
iEDDA	Electron-Demand Diels-Alder
INA	Isonicotinic acid
Ipa	Isophthalate
IR	Infrared Spectroscopy
IRMOF	Isorecticular MOFs
IVCT	Intravalence charge transfer
JNU	Jawaharlal Nehru University
LIFM	Lehn Institute of Functional Materials
LMCT	Ligand to Metal Charge Transfer
LSK	German acronym of the Laboratory for Catalysis and Sustainable Chemistry at the Paul Scherrer Institute
MAS-NMR	Magic Angle Spinning Nuclear Magnetic Resonance
MAS-SS-NMR	Magic Angle Spinning-Solid State- Nuclear Magnetic Resonance
MIL	Materials Institute Lavoisier
MLCT	Metal-to-Ligand Charge-Transfer
MMCT	Metal-to-Metal Charge-Transfer
MOF	Metal-Organic Framework
MOP	Metal-Organic Polyhedra
MOPF	Metal–Organic Polyhedra Frameworks

MTV	Multivariate
MUF	Massey University Framework
MUV	Material of Universitat de València
NacNac	β -diketiminat
NbU	Ningbo University
NGA	Negative Gas Adsorption
NMR	Nuclear Magnetic Resonance
NPD	Neutron Powder Diffraction
NPF	Nebraska Porous Framework
NPs	Nanoparticles
OHC-Im	Imidazole-2-carboxaldehyde
PBU	Primary Building Unit
PCN	Porous Coordination Network
PDF	Pair Distribution Function
PPh ₂	Diphenylphosphine
PSE	Post-Synthetic Exchange
PSM	Post-Synthetic Methodologies
PSME	Post Synthetic Metal Exchange
PSP	Pore Space Partition
PTE	Phosphotriesterase
PTIR	Photo Thermal Induced Resonance
PXRD	Powder X-ray Diffraction
Q _{st}	isosteric heat of adsorption
RBS	Rutherford Backscattering Spectrometry
RCSR	Reticular Chemistry Structure Resource
REDOR	Rotational- Echo Double- Resonance
RNA	Ribonucleic acid
SALE	Solvent Assisted Linker Exchange
SALEM	Solvent-Assisted Linker-Exchanged Material

Salen	refers to a tetradentate C ₂ -symmetric ligand synthesized from salicylaldehyde and ethylenediamine
SBU	Secondary Building Units
SCXRD	Single-Crystal X-Ray Diffraction
SEM	Scanning Electron Microscope
SERS	Surface-Enhanced Raman Spectroscopy
sMOF	stratified MOF
SRO	Short-Range Order
SS-NMR	Solid State- Nuclear Magnetic Resonance
TEM	Transmission Electron Microscopy
TGA	Thermogravimetric Analysis
TIPS	Bis(triisopropylsilyloxy)phenanthrene groups
TPMOF	Trigonal-Prism-derived MOF
UiO	Universitet i Oslo
UMCM	University of Michigan Crystalline Material
UMOP	UNIST metal–organic polyhedra
UPC	China University of Petroleum
XANES	X-ray Absorption Near Edge Structure
XAS	X-ray Absorption
XPS	X-ray Photoelectron Spectroscopy
XRD	X-ray Diffraction
XRF	X-Ray Fluorescence
ZIF	Zeolitic Imidazolate Framework

Abstract

This thesis tackles the challenge of expanding synthetic tools to increase the chemical complexity of reticular materials based on group IV metals. Two approaches have been taken: *i)* incorporating chemical variance in the organic component (Chapters 2 - 4) and *ii)* in the inorganic component (Chapter 5). In order to address this, two families of reticular solids, metal-organic polyhedra (MOPs) and metal-organic frameworks (MOFs), based on Ti(IV) and Zr(IV) metals are been used as platforms.

Chapter 1 provides an overview of the rise of chemical complexity in reticular solids, especially in Metal-Organic Frameworks (MOFs). In the first part, the concept of *reticular chemistry*, *topology* and *isoreticular expansion*, as well as the necessary tools to design and prepare porous periodic structures are introduced. Then, the porous networks are presented by increasing order of complexity. The classification starts with the study of *binary* networks, continuing with the presentation of the networks of intermediate complexity, such as *multivariate* and *multicomponent* frameworks. And finally, it advances in complexity up to *hybrid multicomponent* frameworks. The discussion also includes the presentation of the characterization techniques used for deciphering the organic and inorganic variance. Moreover, it highlights the importance of the structural richness and intrinsic properties of complex MOFs to extend their applications in relevant research fields.

On the following chapters, the experimental results are also presented in increasing order of chemical complexity. Chapter 2 shows the preparation of multivariate MOPs by the combination of functionalized organic linkers in different ratios. Chapters 3 and 4 are focused on the tetrazine-based MOF, UiO-68-TZDC. Firstly, we demonstrate how precise control of post-synthetic linker exchange conditions permits controlling the spatial distribution of pristine and photoactive linkers across multivariate crystals which enables to encode photocatalytic properties. Then, we introduce the use of tetrazine tags as a versatile tool for post-synthetic covalent modification of frameworks to access a broad variety of pore environments of multiple chemistries. Finally, in Chapter 5, we present an unprecedented methodology to introduce metal variance in the inorganic nodes of heterometallic titanium-organic frameworks in which the metal cluster can be transformed by transmetalation reactions to induce changes in connectivity and points of extension of the SBU getting new topologies.

Chapter 2 proposes to extend the chemical diversity of Metal-Organic Polyhedra (MOPs) by combining the use of hydroxamic group as metal binders in the organic linker with titanium. Our approach enables the synthesis of the first example of a porous Titanium-Organic Polyhedra, cMUV-11 (cMUV = *cage-type Material of Universitat de València*), which displays permanent porosity with a value close from the highest reported so far. cMUV-11 crystallizes as discrete neutral cubes where packing in the solid state is controlled by a H-bond network of N-H...O H-bonds involving complementary hydroxamic groups from adjacent cages. This new robust

MOP is compatible with the combination of functionalized linkers that determines pore chemistry and tune the structural response to solvent evacuation.

Chapter 3 reports the synthesis of single crystals of UiO-68 and its photoactive-derivate UiO-68-TZDC, which contains tetrazine moieties in the organic linker. The analysis of single-phase frameworks reveals the necessity of combining both linkers in the same structure for obtaining a robust platform for catalytic applications. UiO-68 crystals are amenable to post-synthetic linker exchange reactions which result in the combination of TPDC and TZDC linker in multivariate UiO-68-TZDC%. The fine selection of synthetic conditions allows the control of linker spatial distribution over the crystal. The careful analysis of resultant microstructures (*core-shell* and *homogeneous distributions*) facilitates the understanding of the catalytic behaviour of solids.

Chapter 4 explores the use of tetrazine moiety as a tag for general framework post-functionalization in one-step. The compatibility of tetrazine with inverse Electron-Demand Diels-Alder (iEDDA) reactivity assist the covalent modification of UiO-68-TZDC. The selected mild conditions guarantee quantitative transformations respecting the intrinsic structure and porosity of the original framework. Our protocol enables the introduction of a broad scope of dienophiles leading multiple pore environments with diverse chemical functionalities, such as hydroxyl, phenyl, succinimide, terminal carboxylic groups, aliphatic chains, chiral centers and even fullerenes, in the resultant pyridazine and dihydropyridazine frameworks. The effect of tetrazine reticulation on iEDDA reactivity is also analysed.

Finally, **Chapter 5** introduces a pioneer methodology for the synthesis of heterometallic titanium frameworks by metal-exchange reaction in MUV-10 crystals (MUV = *Material of Universitat de València*). MUV-10 presents Ti_2Ca_2 metal-oxo clusters which combine hard Ti^{4+} ions and soft Ca^{2+} centres more prone to metal exchange. The soaking of the MUV-10 crystals in different methanolic salt solutions ($M = Fe^{2+}, Co^{2+}, Ni^{2+}, Cu^{2+},$ and Zn^{2+}) in controllable times drives a topological transformation into MUV-101 (Co, Fe, Ni, Zn) which is isostructural to MIL-100 and MUV-102 (Cu), an heterometallic analogue of HKUST. This methodology constitutes a complementary route for the introduction of variance in metal nodes for increasing the level of complexity in mixed-metal MOFs. Thus, enables the formation of heterometallic titanium frameworks, that are not accessible under solvothermal conditions, and opens the door to the synthesis of additional titanium heterometallic phases following the principles of reticular chemistry.

Publications

The following works were published during the course of this PhD:

[1] C. T. Stoppiello; H. Isla; M. Martínez-Abadía; M. W. Fay; C. D. Parmenter; M. J. Roe; B. Lerma-Berlanga; C. Martí-Gastaldo; A. Mateo-Alonso; A. N. Khlobystov. “Three-dimensional nanoscale analysis reveals aperiodic mesopores in a covalent organic framework and conjugated microporous polymer”. *Nanoscale*, **2019**, *11*, 2848-2854.

[2] J. Navarro-Sánchez; N. Almora-Barrios; B. Lerma-Berlanga; J. J. Ruiz-Pernía; V. A. Lorenz-Fonfria; I. Tuñón; C. Martí-Gastaldo. “Translocation of enzymes into a mesoporous MOF for enhanced catalytic activity under extreme conditions”. *Chem. Sci.*, **2019**, *10*, 4082-4088.

[3] M. Martínez-Abadía, C. T. Stoppiello, K. Strutynski, B. Lerma-Berlanga, C. Martí-Gastaldo, A. Saeki, M. Melle-Franco, A. N. Khlobystov, A. Mateo-Alonso. “A Wavy Two-Dimensional Covalent Organic Framework from Core-Twisted Polycyclic Aromatic Hydrocarbons”. *J. Am. Chem. Soc.* **2019**, *141*, 36, 14403–14410.

[4] N. M. Padial †, B. Lerma-Berlanga †, N. Almora-Barrios, J. Castells-Gil, I. da Silva, M. de la Mata, S. I. M. Jesús Hernández-Saz, A. E. Platero-Prats, S. Tatay, C. Martí-Gastaldo. “Heterometallic titanium-organic frameworks by metal-induced dynamic topological transformations”. *J. Am. Chem. Soc.* **2020**, *142*, 14, 6638–6648.

[5] B. Lerma-Berlanga, C. R. Ganivet, N. Almora-Barrios, S. Tatay, Y. Peng, J. Albero, O. Fabelo, J. González-Platas, H. García, N. M. Padial, C. Martí-Gastaldo. “Effect of Linker Distribution in the Photocatalytic Activity of Multivariate Mesoporous Crystals”. *J. Am. Chem. Soc.* **2021**, *143*, 4, 1798–1806.

[6] M. Martínez-Abadía, K. Strutyński, C. T. Stoppiello, B. Lerma Berlanga, C. Martí-Gastaldo, A. N. Khlobystov, A. Saeki, Manuel Melle-Franco, A. Mateo-Alonso. “Understanding charge transport in wavy 2D covalent organic frameworks”. *Nanoscale*, **2021**, *13*, 6829-6833.

[7] B. Lerma-Berlanga, J. Castells-Gil, Carolina R. Ganivet, N. Almora-Barrios, J. González-Platas, O. Fabelo, N. M. Padial, C. Martí-Gastaldo. “Permanent porosity in hydroxamate titanium-organic polyhedra”. *J. Am. Chem. Soc.* **2021**, *143*, 50, 21195–21199.

[8] A. Riaño, K. Strutyński, Meng Liu, C. T. Stoppiello, B. Lerma-Berlanga, A. Saeki, C. Martí-Gastaldo, A. N. Khlobystov, G. Valenti, F. Paolucci, M. Melle-Franco, A. Mateo-Alonso. “An Expanded 2D Fused Aromatic Network with 90-Ring Hexagons”. *Angew. Chem. Int. Ed.*, **2022**, *61*, 2.

Table of contents

Chapter 1: Chemical Complexity in Metal-Organic Frameworks	1
1. Reticular chemistry and design principles.....	3
2. Increased chemical complexity: From binary to multicomponent MOF	8
2.1. Multivariance in binary frameworks	10
2.1.1. Organic approach.....	10
2.1.2. Inorganic approach.....	13
2.1.3. Multivariance and control of the distribution of organic and inorganic components.....	19
2.2. Multicomponent frameworks	29
2.2.1. Organic diversity in multicomponent nets.....	29
2.2.2. Inorganic diversity in multicomponent nets.....	32
2.2.3. Diversity in organic and inorganic hybrid multicomponent nets.....	40
2.3. Multivariance in multicomponent frameworks	37
3. Deciphering chemical complexity.....	39
3.1. Multivariance in the organic connector	40
3.1.1. Evaluating multiple-linkers presence.....	40
3.1.2. Evaluating relative ratio and quantification of linkers.....	43
3.1.3. Evaluating linker spatial distribution.....	46
3.2. Multivariance in the inorganic connector.....	53
3.2.1. Evaluating multiple-metal presence.....	53
3.2.2. Evaluating relative ratio and concentration of metals	56
3.2.3. Evaluating metal coordination environment and oxidation state.....	56
3.2.4. Evaluating metal spatial distribution	61
4. Heterogeneity and complexity yield enhanced MOF properties.....	65
4.1. Gas storage and separation	65
4.2. Heterogeneous catalyst	69
4.3. Environmental applications.....	72
4.4. Luminescence and sensing.....	75
5. References	79

Chapter 2: Permanent Porosity in Hydroxamate Titanium-Organic Polyhedra	107
1. Motivation.....	109
2. Summary of key results.....	110
3. References.....	115
Publication 1: Permanent Porosity in Hydroxamate Titanium-Organic Polyhedra	119
Chapter 3: Effect of Linker Distribution in the Photocatalytic Activity of Multivariate Zr-MOFs	167
1. Motivation.....	169
2. Summary of key results.....	170
3. References.....	175
Publication 2: Effect of Linker Distribution in the Photocatalytic Activity of Multivariate Mesoporous Crystals	179
Chapter 4: Exploiting tetrazine tag to enrich pore complexity: from pyridazine networks to fulleretic materials	251
1. Motivation.....	253
2. Summary of key results.....	254
3. References.....	260
Publication 3: Tetrazine linkers as plug-and-play tags for general framework functionalization and C₆₀ conjugation	265
Chapter 5: Metal-Induced Dynamic Topological Transformations in Heterometallic Ti-MOFs	319
1. Motivation.....	321
2. Summary of key results.....	321
3. References.....	326
Publication 4: Heterometallic Titanium-Organic Frameworks by Metal-Induced Dynamic Topological Transformations	329
Chapter 6: Conclusions	441
Resumen de la tesis doctoral	449
Resum de la tesi doctoral	457

Chapter 1:
***Chemical Complexity in
Metal-Organic Framework***

1. Reticular chemistry and design principles

Reticular chemistry is understood as the linking of well-defined molecular building blocks by strong bonds into pre-designed crystalline periodic structures. Before the general implementation of this concept in the field of materials, crystallizing porous frameworks through strong directional bonds was considered a challenge. In this direction, reticular chemistry emerged as a result of precise merging of covalent organic and inorganic coordination chemistry. The combination of the ability of the rational use of covalent bond formation, applied in the synthesis of complex organic natural products, with the formation of thermodynamic controlled extended architectures by single step reactions, has resulted in an unprecedented control over the design of porous extended materials. During the last two decades, the discovery of new inorganic clusters and their combination with a vast myriad of organic linkers have made of these materials the most diverse class of extended crystals nowadays.¹⁻³ This is exemplified by the three different prominent types of reticular porous materials:⁴ metal-organic frameworks (MOFs), covalent organic frameworks (COFs) and metal-organic polyhedral (MOPs).

Reticular chemistry provides the concepts to design and construct a targeted molecular framework from interlinking organic and inorganic components. For that, it is essential to understand the shape and connectivity of their constituents, namely, building blocks and identify the geometry of the units that determine the net's topology. There are three main aspects to consider for reticular design: *building blocks*, *topology* and *isoreticular expansion* (Figure 1.1.). Although these concepts are extrapolated to all families of porous crystalline materials, our discussion will be mainly focused on the aspects related to MOF chemistry.

Building blocks

The diversity of building blocks provides countless opportunities for the practice of reticular chemistry. Building blocks are divided in two broad categories: *i*) molecular and supermolecular building blocks, also called linkers or connectors, which represent the organic part of the material; and *ii*) inorganic building blocks which can be single-metal-ions, metal clusters or one-dimensional infinite rods. The understanding of the structural features of building blocks is essential to control their internal geometry and topology of the resulting frameworks.

In MOFs and MOPs synthesis, most linkers selected are high symmetry and their points of extension ranging from 2 to 8. Commonly, connectors based on rigid polyaromatic linkers yield frameworks with better chemical and mechanically stability. As metal connectors, carboxylates,⁵ azolates,⁶ phosphates,⁷ and catecholates⁸ functional groups are usually employed due to the strong metal coordination. Regarding the inorganic building blocks, their structure and number of metal ions in the cluster as well as their connectivity are also very diverse, ranging from single-metal nodes to polynuclear metal clusters. Polynuclear clusters can

display a different number of metals, from bimetallic up to nonanuclear clusters. These are typically formed by lanthanoids and highly charged transition metals metals, such as Al^{3+} , Cr^{3+} , Zr^{4+} , Hf^{4+} , and Ti^{4+} , which can, in turn, also form infinite rods of metal-oxo chains depending on the reaction conditions used. It is important to note that the choice of organic connector, i.e., carboxylate, azolates, catecholates, etc. can have a direct effect on the type of the inorganic building block obtained

On the contrary, COFs are exclusively based on the interlinking of organic molecular building units.⁹ These materials are based on (poly)aromatic core and extending units similar to the linkers used in MOFs but generally limited to a smaller number of points of extension due to the typical valences of organic molecules. COFs present their own linkage groups that are based on covalent bonds and can be overall classified in two general types: *i*) B-O linkages based on boronate ester, boroxine, borosilicate and spiroborate; and *ii*) Schiff-base linkages including imines, hydrazones, squaraines, β -ketoenamines, benzoxazoles and phenazines.

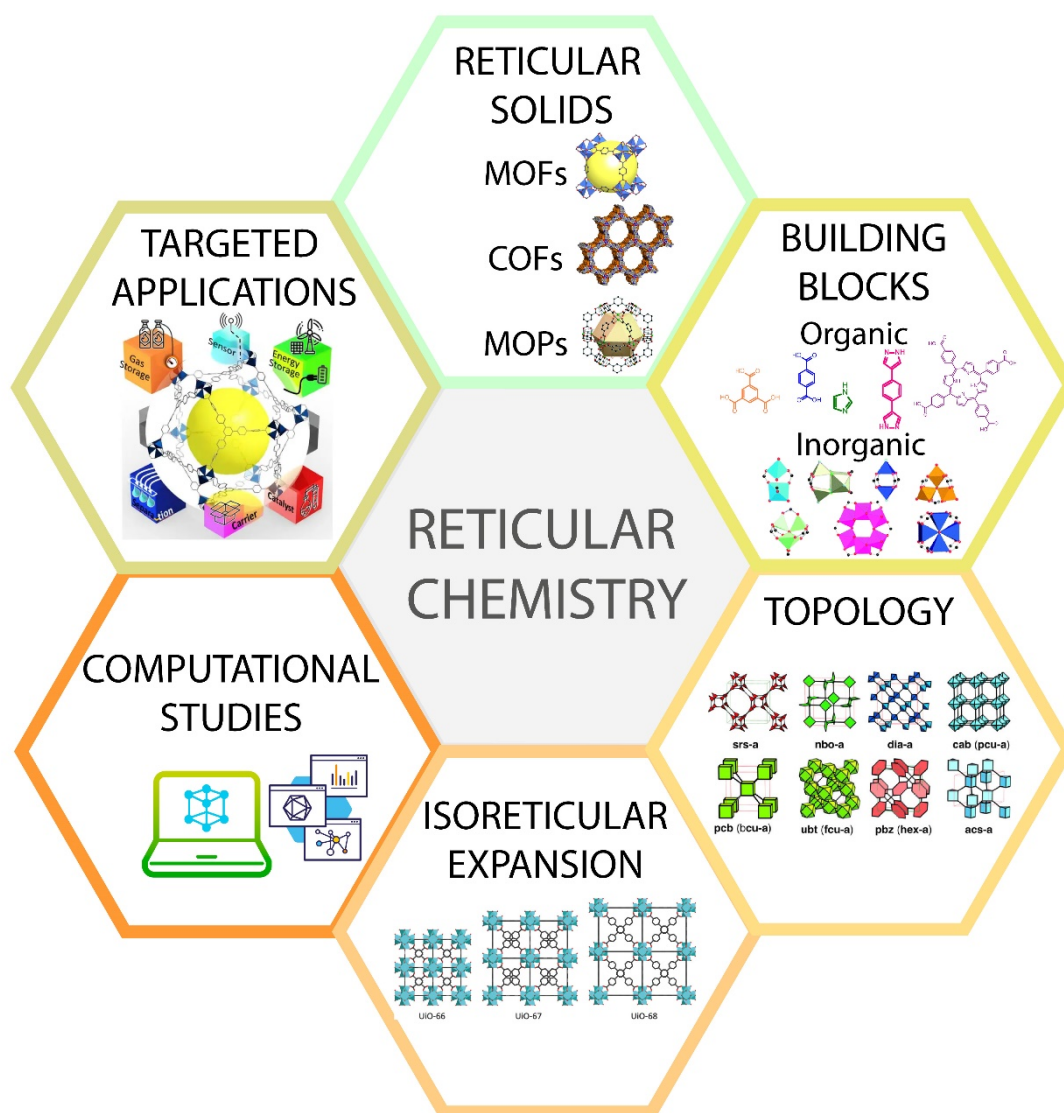


Figure 1.1. Scheme showing the main aspects of Reticular Chemistry.

Topology

The development of reticular chemistry has demonstrated to be an excellent tool for translating the complexity of molecular systems to infinite 2D and 3D porous structures. The rich diversity of MOFs, MOPs and COFs are fuelled by the variety of connectivity imparted by their building units. This connectivity of building units in reticular frameworks is also known as *valency*. In case of MOFs, the valency of metal entities ranges from 3 to 24 for discrete units and infinity for 1D rods, that can in turn be combined with organic connectors of varying connectivity points and internal geometries for a vast chemical space with more than 2000 reported topologies.^{10,11} In this regard, the simplification of the networks according to reticular principles becomes essential to facilitate their systematic study. The underlying net topology of any periodic structure can be analysed by a hierarchical simplification approach that uses spheres and sticks for simplifying nodes (vertices) and linkers (edges), respectively. In this formalism, metal ions (or metal clusters) and ligands usually serve as secondary building units (SBUs) or tertiary building units.¹²⁻¹⁵ The coordination of the simplified nodes defines the underlying net of the structure. The categorizing of the different structures into common nets or graphs simplifies their analysis and provides a guideline of pre-selected platforms for materials design and construction in reticular chemistry.¹⁶ This concept was beautifully illustrated by Yaghi and co-workers who gathered in a table all possible binary frameworks accessible to reticular chemistry¹⁰ (*Figure 1.2.*). We refer the newcomer to the field to that work for a clear introduction to these concepts. By contrast, COFs are made by connecting preformed trigonal-planar, square-planar, and tetrahedral organic building units with linkages of low valency, principally owing to the heavy reliance of organic chemistry on sp^2 and sp^3 hybridization. In this regard, Yaghi's group have invested a great effort in introducing new topologies which are highly desired to broaden the structural diversity and application of COF materials. In 2015, two different C_6 -symmetric vertices blocks were employed in combination with C_2 -symmetric benzene linkers to prepare HPB-COF and HBC-COF.¹⁷ More recently, in 2020, Yaghi and his team reported a strategy for making COFs with valency 8 (cubes) and rods based on the design of the linker which combined boron and phosphorus groups.¹⁸ However, the scope of COF chemistry is still limited compared to MOFs, which is evidenced by only 18 different topologies reported.¹⁹ A similar trend is also observed in MOPs,²⁰ which also represent a growing family of materials amenable to the design principles of Reticular Chemistry.

On the other hand, the high chemical diversity of MOFs is reflected in a close to one hundred thousand of MOF structures reported in the [Cambridge Structural Database](#) (CSD) since 1995²¹. The importance of the field is denoted by specific subsets of structures as [Reticular Chemistry Structure Resource](#) (RCSR)²² for accelerate search of periodic materials. In 2008, O'Keeffe *et al.* launched the RCSR database with the purpose of providing a universal system of nomenclature,

classification, identification, and retrieval of these topological structures in face of the explosive growth in this area.

Building unit 1 \ Building unit 2	— 2-c Linear	 3-c Triangle	 4-c Square	 4-c tet	 6-c Hexagon	 6-c oct
 3-c Triangle	 srs	 bwt, pyo , srs-b, ths-b	 fjh, fmj, gee, iab, yac, yao	 asn, ept , ofp	 cys, dnf*	 anh, ant , apo, brk, cep*, cml, czz, eea, qom, rti, tsx, zzz
 4-c Square	 nbo, lt, rhr	 pto, tbo	 cev, cdl, cdm, cdm, cds, cdz, mot , muo, qdl, qzd, ssc, sse, ssf, sst	 pts	 nts	 myd, ybh
 4-c tet	 dia, lcs, qtz, sod	 bor, ctn	 fgl, mog, pds, pth, pli, ptr, ptt	 bni, byl, cag, cbt, coe, crb, fel, icm, kea, lon, pcl, qtz-b, sca, tpd, ucn	—	 alw, bix, cor, ing, spl, toc
 6-c Hexagon	 hxg	 cys, dnf	 she	—	 hxg-b	—
 6-c oct	 pcu, bcs, crs, reo	 pyr, spn	 soc	 gar, iac, ibd, toc	—	 pcu-b, bcs-b
 6-c trp	 lcy, acs	 ceq, dag, fmz, hwx, moo, sab, sit, ydq	 stp	 fsi, hea, tpt	 htp	 nia
 8-c cub	 bcu	 the	 scu, csq, sqc	 flu	—	 ocu
 12-c cuo	 fcu	 sky	 ftw	 edc	—	—
 12-c ico	—	—	—	 ith	—	—
 12-c hpr	—	 aea	 shp	—	—	—
 12-c tte	—	 ttt	—	—	 mgc	—
 24-c tro	—	—	—	 twf	—	—

Figure 1.2. Table of possible bipartite nets made by reticular chemistry. All topologies are shown as their corresponding augmented net. If more than one net exists, then the identifier of the indicated net is shown in bold. Extracted from ref 10.

Isorecticular expansion

The concept of isorecticular chemistry has become a core principle in Reticular Chemistry. Isorecticular design summarises all strategies used to generate a series of compounds with the same preferred topology but differing only in the nature and size of the building blocks. Isorecticular expansion is the strategy used for increasing pore size and surface areas, and/or tuning pore surface functionality for MOFs by propagating the structure of a prototypical MOF structure. This method takes advantage of experimental conditions of the original MOF to synthesize new isorecticular frameworks with tailored features. The concept of “pore size expansion”, which was inherited from the porous metal salts,²³ was introduced by Yaghi *et al.* in 2002.²⁴ Since that moment, predesigned building blocks have been purposefully incorporated into extended networks with targeted specific features. The first examples focused on the applicability of this method to afford an isorecticular series of archetype structures as MOF-5,²⁴ HKUST²⁵, UiO-66,²⁶ and MOF-74²⁷ structures. Sometimes the linker elongation does not have the expected impact on pore dimensions which is indicative of the growth of interwoven or interpenetrate nets.^{24,25} The mathematical rules which govern the reticular expansion or contraction has been successfully rationalized for specific materials as is the case of sph-MOFs,²⁸ unfortunately, it has not been possible to generalise these guidelines to other MOF topologies. Several synthetic alternatives are known to attempt to reduce interpenetration, such as using more dilute conditions,^{24,29} modulating reaction time,³⁰ controlling π -stacking interactions³¹ or incorporating bulky substituents³² or template-controlling during the synthesis. Nonetheless, the interpenetration might be beneficial for some applications²⁸ such as gas storage,^{33,34} gas separation³⁵ or catalysis.³⁶⁻³⁸

The reticular expansion approach has also been applied in the opposite direction to reduce pore aperture. In some specific applications such as gas separation, MOFs with relatively small pore sizes are capable of acting as molecular sieves enabling selective molecular exclusion and maximizing the guest-host interactions.³⁹

The application of the principles of reticular chemistry provides the design tools required to navigate an immense chemical space, where countless possible structures remain yet to be discovered experimentally. In this direction, the computational chemistry is a powerful tool to model and simulate the reticular frameworks addressing the experimental limitations.⁴⁰⁻⁴⁴ Mathematical models can reproduce unaffordable framework structures replacing the building blocks and estimate the physicochemical properties, interactions and dynamics of the resultant nets based on physical principles and empirical chemical knowledge. Progressive digitization of reticular chemistry workflow is arguably the way forward to tackle more complex problems.

2. Increased chemical complexity: From binary to multicomponent MOF

Reviewing the reticular chemistry progress, the first reticular materials ever reported were binary MOFs, composed by two components: the organic linker and a metal acting as inorganic building unit. Here, the different components are defined as structural building units with well-defined extension points. For example, we consider UiO-66 as a binary structure, in which the two components are the hexanuclear zirconium cluster and the BDC linker.²⁶ The rapid development of the reticular chemistry has expanded the scope of variability of structure giving rise to different accessible complexity levels (*Figure 1.3.*). A range of organic and inorganic building blocks can be combined to obtain pre-design bipartite net which represent the primary level of complexity. Furthermore, these building blocks can be modified to incorporate new desired properties or modified the existing ones giving rise to multivariance in each component. Thus, multivariate (MTV) approach introduces multiple types of functional groups or metal atoms into a binary net leading to *multivariance* networks. The orientation, number, relative position, and ratio of the building blocks units can be controlled unaltering the connectivity of the frame. These new arrays of new functionalities provide properties beyond the simply linear sums of those of the pure components.⁴⁵ The next level of complexity is achieved by the incorporation of multiple kind of building blocks in the same backbone accessing to a wide range of topologies. This level is represented by *multicomponent* frameworks. In this direction, the next complexity challenge is combining multivariance in multicomponent frameworks which results in *hybrid multicomponent* frameworks. This increased of complexity is somewhat reminiscent of biological systems (e.g. peptides, RNA, DNA...) in which the introduction of complexity onto an ordered backbone is crucial for the sophistication of their function.⁴⁶

For clarity, during this discussion, frameworks have been presented by order of increasing complexity. In addition, each level has been divided into organic and inorganic approach.

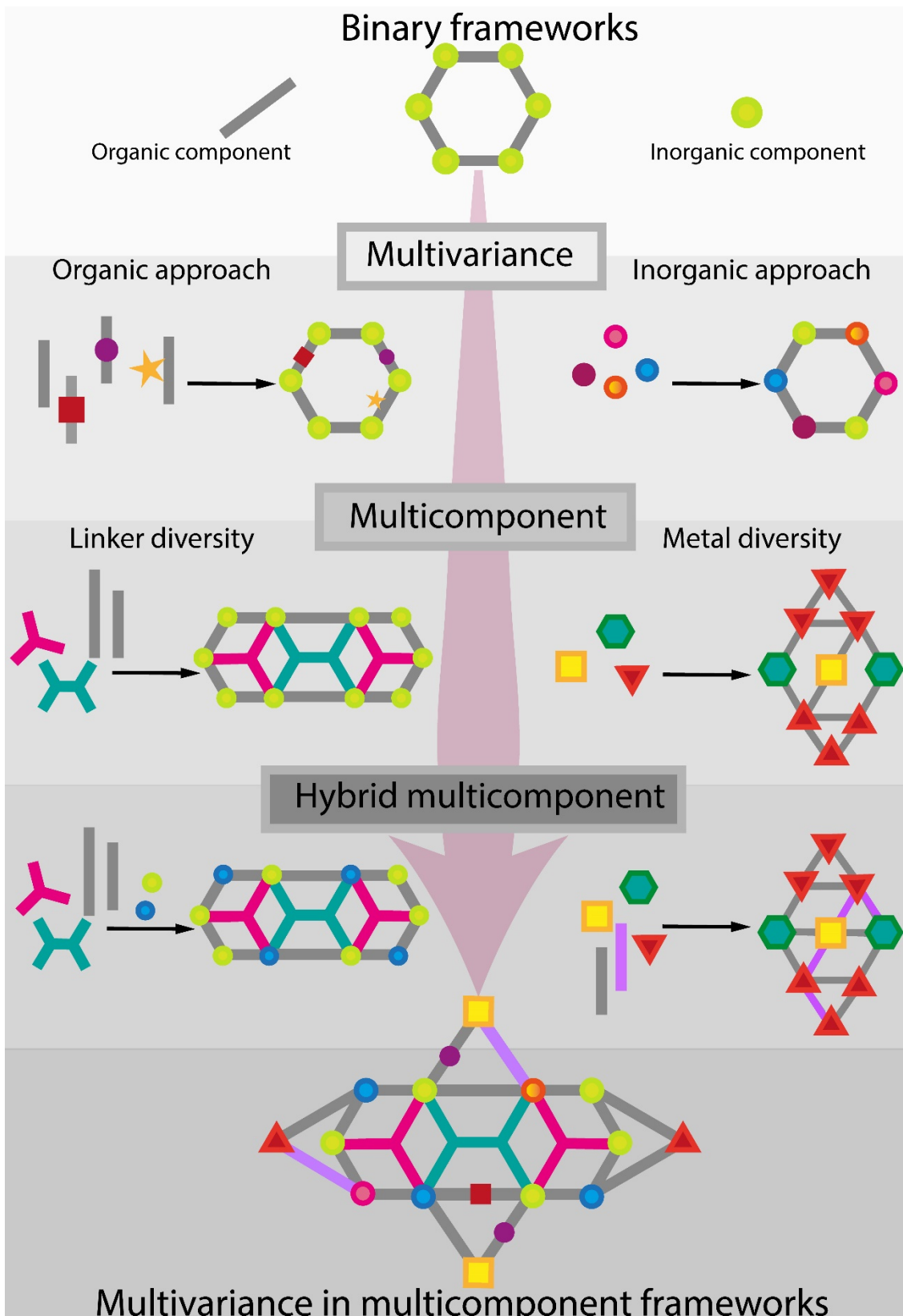


Figure 1.3. Overview of increased complexity in MOFs.

2.1. Multivariance in binary frameworks

In multivariate MOFs (MTV-MOFs), the complexity is incorporated by using organic linkers with identical backbones -meaning same size, geometry, and connectivity- but different substituents, and varying SBUs metal content without altering their linkage across the backbone. This incorporation of heterogeneous functionalities leads to anisotropy, without disturbing the entire topology of MOF and maintaining the long-range order (crystallinity). This anisotropy is originated from the ratio and spatial arrangement of components along specific directions of the crystal. This well-defined manner to introduce variance was instituted by Yaghi and co-workers in 2010⁴⁵ and was then denoted by the term “heterogeneity within order”.⁴⁶ In the following section, we introduce different routes to introduce variance from the functionalization of the organic and inorganic components of the network.

2.1.1. Organic approach

Probably, an early example which provided the basis for multi-linker MTV-MOF was reported in 2010 by Yaghi,⁴⁵ where up to eight functional groups [-NH₂, -Br, -(Cl)₂, -NO₂, -(CH₃)₂, -C₄H₄, -(OC₃H₅)₂ and -(OC₇H₇)₂] were incorporated by direct synthesis within one pure phase of MOF-5 giving rise to 18 different MTV MOF-5. In the backbone, ZnO₄ and phenylene units were distributed along specific crystallographic positions, but the distribution of functional groups was disordered, leading to a heterogeneous arrangement of appended functional groups throughout the ordered backbone of the framework (*Figure 1.4.*). That heterogeneity was the responsible of the upgraded properties of resulting MTV-MOF-5. For instance, a member of that series, MTV-MOF-5-EHI, displayed up to 400 % better selectivity for CO₂ over CO compared with its same-linker counterparts. That work represented the first clear evidence of how heterogeneity and complexity of MTV-MOFs lead to properties that were not simply linear sums of those of the pure components. Even more interestingly, that also supported the idea that the sequence of functionalities within MTV-MOF could be useful as code for the enhancement of a specific property or achieving a new one. After that finding, the generality of such synergistic effects was also confirmed for MTV MOF-177.⁴⁷ In 2014, again Yaghi’s group extended their strategy to MOF-177 which was composed of ZnO₄ and benzenetribenzoate (BTB) units. In that study, 14 MTV-MOF-177 structures were prepared incorporating different functional groups, by one-pot synthesis, on the triangular BTB linker, having one or more functionalities. MTV-MOF-177 platform not only allowed the incorporation of specific functionalities, as -NO₂, hard accessible by direct synthesis; but also, demonstrated that the presence of more than one kind of functionality (-NH₂ and -OCH₃) in MOFs led to enhancement of 25 % in volumetric H₂ uptake.

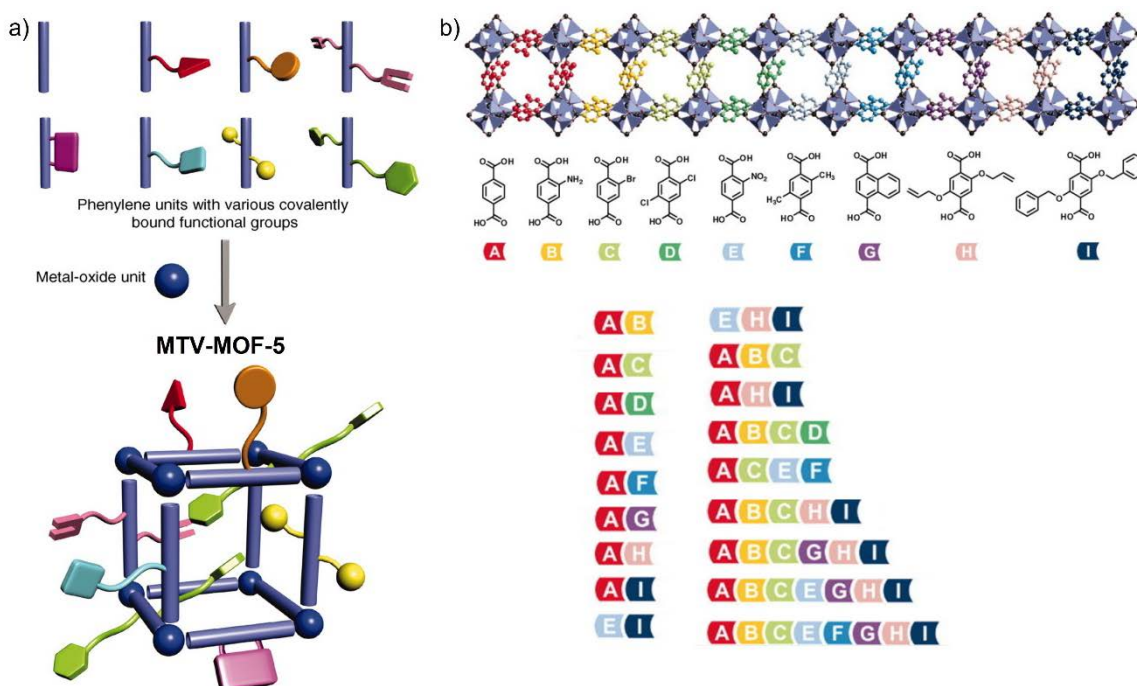


Figure 1.4. a) Schematic representation of the MTV-MOF-5 structure showing the multivariate arrangements of the different functional groups. b) Different combinations of the functional groups yield the 18 different combinations of MTV-MOFs. Adapted from ref 45.

The capability of tuning the host-guest interaction by pore decoration with multiple functional groups was also exploited in MTV-MIL-101 derivatives. Specially for MIL-101(Fe)-(C₄H₄)_x(NH₂)_{1-x} (X = 0 - 100),⁴⁸ where the interactions between the framework and the guest molecules (ibuprofen, rhodamine B and doxorubicin) was tuned. That was reflected in the precisely control of release rates which was not obtained in the physical mixture of the single component MOF counterparts. Later on, the flexibility response, which is responsible of selective gas adsorption, was modulated through MTV-MUF-15 derivatives.^{49,50} The parent MUF-15 material, [Co₆(μ₃-OH)₂(ipa)₅(H₂O)₂], was built up from hexanuclear cobalt (II) clusters and isophthalate (ipa) linkers. The pore environment was easily tailored introducing 5-substituted ipa linkers (-F, -OH, -Br, -NO₂, -CH₃ and -OCH₃). In terms of flexibility, non-functionalized MUF-15 did not exhibit any flexibility, whereas the dynamic behaviour of MUF-15-OCH₃ was completely different, showing flexibility upon C₂H₆, C₂H₄, C₂H₂, and CO₂ at a range of temperatures. The flexibility of MUF-15-OCH₃ could be tuned by doping with different percentage of ipa linkers, which their inclusion increased the gate opening pressure by counteracting the framework flexing.⁵²

The organic multivariate approach has also been extended to the field of porous metal organic polyhedra. Recently, Nam *et al.* described a family of MTV-Zr-based MOPs.⁵¹ UMOP-1-R ([Cp₃Zr₃O(OH)₃]₄(BDC-R)₆]Cl₆[(CH₃)₂NH₂]₂, Cp = η⁵-C₅H₅, H₂BDC = benzene-1,4-dicarboxylic acid, R = CH₃, OH, and Br) derivatives combined different functionalities in relatively random positions over the framework in a one-pot method. The authors studied the photophysical properties of MTV and physical

mixture samples by a qualitative analysis of the solvatochromism in different solvents. They observed different emission's properties between MTV-UMOP-1 and physical mixture samples, possibly attributable to distinct distribution of functional groups and radiative decay kinetics. Later that year, our group reported the first multivariate porous titanium metal-organic polyhedra, denoted by cMUV-11-X%⁵² (see **Chapter 2**). The original cage, which was assembled of benzene-1,4-dihydroxamic acid (*p*-H₄bdha) and titanium single nodes octahedrally coordinated. cMUV-11 crystallized as discrete neutral cubes which packing in the solid state is controlled by a H-bond network of N-H...O H-bonds involving complementary hydroxamic groups from adjacent cages. Multivariate approach enabled to prepare multi-linker cages by the binary combination of original linker (*p*-H₄bdha) with 2-aminobenzene-1,4-dihydroxamic acid (*p*-H₄bdha-NH₂) or 2-methoxybenzene-1,4-dihydroxamic acid (*p*-H₄bdha-OCH₃). The controlled introduction of new hydrogen-bond donor (D) or acceptor (A) groups tuned the cage arrangement in solid state and overcame the structural collapse. The presence of -OCH₃ group had beneficial effects on porosity values, achieving higher BET surface areas than those of original cMUV-11. That suggested the value of organic connector variance for controlling inter-cage interactions for modulating the permanent porosity in that family.

Although all the previously described examples were prepared by direct synthesis in one-pot reaction by mixing differently functionalized linkers; post-synthetic methodologies (PSM) have been also successfully applied to afford MTV-MOFs.⁵³⁻⁵⁵ In first examples of PSM in MOFs the main goal was to achieve the highest degree of modification which was often associated with covalent modification of the ligand struts.⁵⁶⁻⁶² Some years later, in 2011 the concept of *Post-Synthetic Exchange* (PSE) was introduced by Choe and collaborators, who reported the replacement from bridging-linker by dipyriddy linker in extended 2D and 3D MOFs.⁶³ Nonetheless, it was not until 2012 when Cohen *et al.* employed this methodology to introduce simultaneously different functional groups into the same backbone.⁶⁴ That work demonstrated the successfully linker's substitution in two robust, topologically distinct MOFs, MIL- 53(Al) and MIL-68(In), under relatively mild conditions. The authors highlighted the detrimental role of the kinetic inertness of the Cr(III) ion in MIL-101(Cr) exchange. At the same time, Farha and Hupp introduced a new terminology to refer the post-synthetic ligand exchange such as *Solvent-Assisted Linker Exchange*, coining SALE acronym.⁶⁵ Their work was the first example of SALE in ZIFs, in which authors were able to obtain a previously reported ZIF CdIF-9 in high yield, as well as synthesize a new ZIF, SALEM-1, by exposing the parent ZIF CdIF-4 to excess solutions of 2-nitroimidazole and 2-methylimidazole under solvothermal conditions. Experimental results confirmed that SALE occurred via single crystal-to-single crystal transformation rather than via dissolution and recrystallization.

2.1.2. Inorganic approach

Whereas variance in organic component usually involves linkers with similar size, the heterogeneity in inorganic component may implicate metal or metal ions of different sizes, coordination geometry and strength. However, it is often necessary to reach a compromise between the amounts of each metal component. For instance, physical mixtures of crystals with different compositions may be formed when the difference between any of these parameters is too high to be tolerated by the crystal lattice. Here, we can distinguish four scenarios by which metal variance can be incorporated in MTV- MOF:

- 1) Variation of metals in SBUs.
- 2) Different metals inserted into linkers through coordination (*Metalloligands*).
- 3) Extraneous metals or metal clusters attached to the original SBUs.
- 4) Altering SBU connectivity by metal-induced topological transformations.

Compared to strategies 1, 3 and 4, that involve the chemical modification of the SBU, 2 is reliant on an exogenous modification in which metal multivariance is incorporated to the linker. The approaches 1 to 3 are respectful with the original connectivity of the cluster whereas 4 proceed by a metal-induced transformations that modifies the connectivity and points of extension of the SBU and thus the resulting framework topology (*Figure 1.5.*).

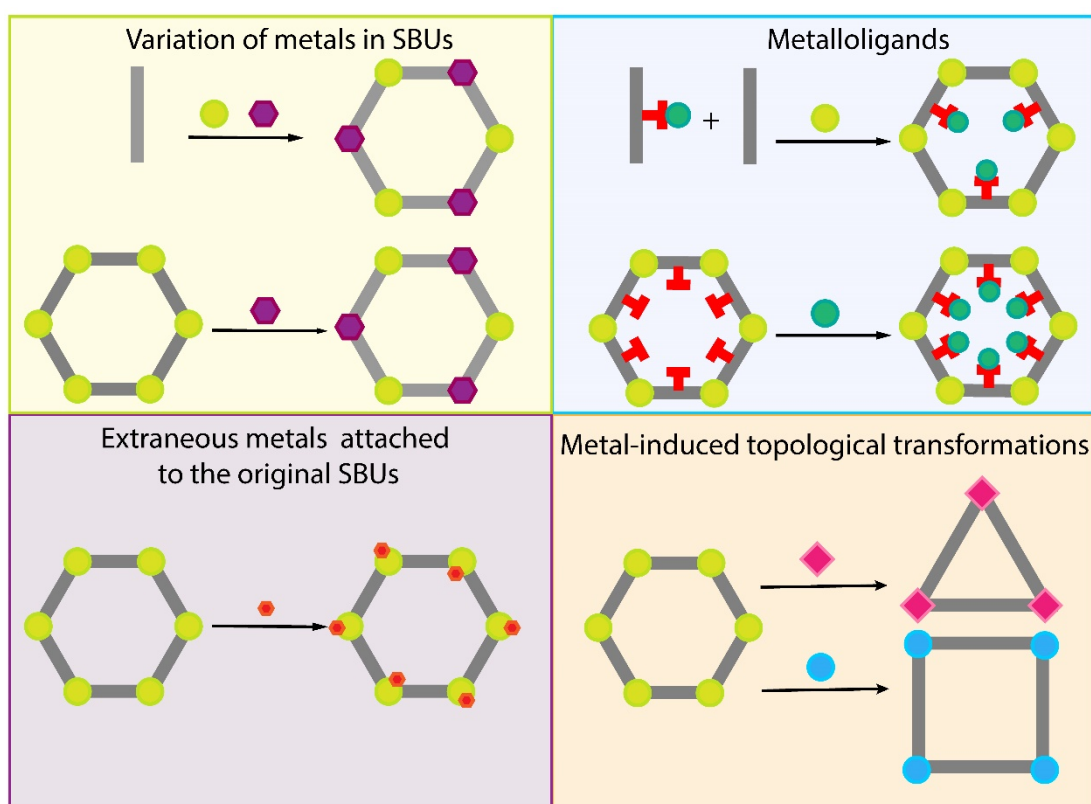


Figure 1.5. Scheme of the four scenarios for introducing metal variance MTV-MOFs.

The incorporation of metal variance through SBU metal content variation can be performed by different approaches. One-pot synthesis using mixtures of different metal precursors is the main attractive route due to the reduced number of steps. The success of this methodology relies in the use of metal ions with the same charge, ionic radius, and similar chemical behaviour to rule out the phase segregation and enhance the homogeneous incorporation. However, this approach shows some issues, such as the lack of control over the final metal distribution. Sometimes only one of the metals is really incorporated at the nodes, while the second one is present in satellite nodal positions or in a different phase as small (hydroxy)oxide cluster.

One of the direct-synthesis multi-metal MTV-MOF reference example was reported by Yaghi's group, where up to 10 metals were incorporated into a pure single-phase structure of MTV-MOF-74.⁶⁶ In that study, one-pot reaction was used to make isostructural MTV-MOF-74 [$M_2(\text{DOT})$; DOT = dioxidoterephthalate] with 2 (Mg and Co), 4 (Mg, Co, Ni, and Zn), 6 (Mg, Sr, Mn, Co, Ni, and Zn), 8 (Mg, Ca, Sr, Mn, Fe, Co, Ni, and Zn), and 10 (Mg, Ca, Sr, Ba, Mn, Fe, Co, Ni, Zn, and Cd) different kinds of divalent metals. The authors emphasized the good reproducibility and the capability of incorporating metal ions (i.e., Ca, Sr, Ba, and Cd) from which the parent MOF structure had been remained unknown. Energy-Dispersive X-ray (EDX) spectra confirmed the presence of all expected metal ions and their heterogeneous distribution within each of the crystalline particles.

Another well established strategy is the replacement of some SBU metal ion by post-synthetic routes.⁶⁷⁻⁷¹ Generally, the metal exchange is usually carried out by stirring the homometallic parent MOF with the complementary metal ion of choice in a liquid solution. The synthetic parameters such as concentration, reaction time and exchange temperature are fine controlled to tune the metal incorporation. Dinca and co-workers demonstrated for the first time the substitution of redox-active di- and trivalent first row transition metals by post-synthetic methods into MOF-5 to give materials that were inaccessible by direct synthetic pathways.⁷² In particular, $[M\text{Zn}_3\text{O}(\text{O}_2\text{C})_6]$ clusters from MOF-5, $[\text{Zn}_4\text{O}(\text{BDC})_3]$, could serve as hosts for Ti^{3+} , $\text{V}^{2+/3+}$, $\text{Cr}^{2+/3+}$, Mn^{2+} , and Fe^{2+} ions (*Figure 1.6. a*). EDX spectra and optical microscope images suggested a homogeneous ions substitution throughout the entire crystal which occurred in a crystal-to-crystal fashion rather than a dissolution-recrystallization mechanism (*Figure 1.6. b*).

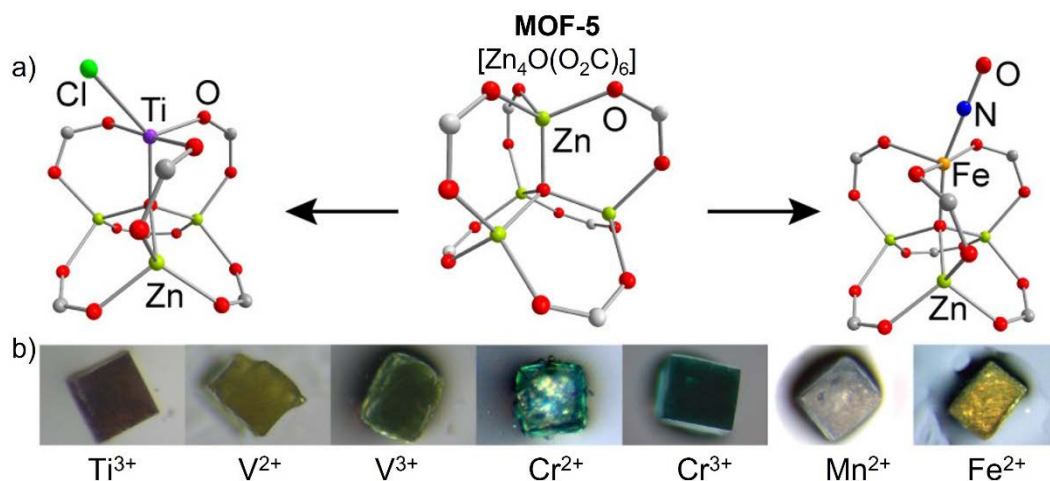


Figure 1.6. a) MOF-5 cluster acts as a unique tripodal chelating ligand for pseudotetrahedral V²⁺, Cr²⁺, Mn²⁺, Fe²⁺, Co²⁺, and Ni²⁺ and pseudotrigonal bipyramidal Ti³⁺, V³⁺, and Cr³⁺ with terminal chloride moieties. These molecular structures depict substitution of a single Zn atom. b) Single crystal to single crystal transformation. Extracted from ref 72.

Complementary metals can be also inserted into the framework through some specific linkers denoted as *metallo ligands* which are mainly constituted by N-donor atoms,⁷³ such as bipyridines,^{74–83} terpyridines,^{84,85} imines,⁸⁶ salicylaldehyde^{87,88} or even diketimines,⁸⁹ commonly called NacNac. These specific linkers may be incorporated via direct-synthesis or by post-synthetic methods. This last methodology was employed by Lin and co-workers to report the successful incorporation of an Ir(III) photo-redox catalyst and a Ni(II) cross-coupling catalyst into a stable Zr₁₂-MOF.⁹⁰ Resultant Zr₁₂-Ir-Ni MOF displayed an efficiently catalyze C-S bond formation between various aryl iodides and thiols. Zr₁₂-Ir-Ni synthesis implicated two-steps route. Initially, Zr₁₂-Ir was prepared by direct synthesis combining zirconium metal salt with bipyridine-based ligand and Ir-photosensitizer ligand, previously prepared. Then, MOF was metalated with Ni²⁺ salt afforded Zr₁₂-Ir-Ni. Its further characterization confirmed the presence of both complexes in the resulting framework and confirmed the complete metalation of bipyridine units.

Post-synthetic methods, especially linker exchange methods have recently proven to be a powerful tool to fabricate single-site MOF catalysts, due to their limited accessibility via direct solvothermal synthesis. Cui group prepared a series of asymmetric metallosalen-UiO-68 MOFs⁸⁸ through SALE strategy incorporating single and mixed M(salen) linkers (H₂L^M, M = Cu, Cr, Mn, Fe, V, Mn-Cr or Mn-V) into UiO-68-Me crystals. Firstly, H₂L^M ligands with similar length and same connectivity of parent H₂TPDC-Me linker were prepared. Afterward, one- or two-step ligand exchange reaction produced single and mixed M(salen), respectively (*Figure 1.7. a*). The successful ligand exchanges were confirmed by dramatic changes in the colours of the crystals, which were consistent with the colours reported for the molecular metallosalen analogues (*Figure 1.7. b*). The incorporation of (*R,R*)-1,2-cyclohexanediamino-*N,N'*-bis(3-*tert*-butyl-salicyliene) unit in H₂L^M provided

chirality to the framework; thus the resulting MTV-UiO-68 displayed a remarkable catalysis activity in a wide range of asymmetric organic reactions.

An alternative route involves the building of the metallocomplex as a linker in a two-step procedure. Firstly, the single metal MOF with the corresponding bifunctional ligand is assembled. Then, the formation of a complex with a second metal ion via a post-metalation process results in the multi-metal MOF. This approach is chosen when the performed complex would not survive to the conditions required for MOF formation, so it is considered more general. One of the earliest examples was the binding of Pd²⁺ and Cu²⁺ ions into the open 2,2'-bipyridine (2,2'-bpy) sites of MOF-253.⁷⁵ That MOF was prepared by solvothermal methods using Al³⁺ salt and bipyridine-based ligands. The accessibility of the chelating 2,2'-bpy units within the framework was confirmed by soaking the solid in acetonitrile solutions of Pd²⁺ and Cu²⁺ ions. That result demonstrated the ability of mixed donor ligands to select for hard metal cations (Al³⁺) during framework assembly, resulting in the first bpy-lined microporous material available to insert a wide variety of metal centres.

Lin's group might be considered an excellent representant of that kind of reticular chemistry. In 2016, that group presented the sequential synthesis of β -diketiminato metallocomplex in UiO-type MOF.⁸⁹ Using the amino-functionalized Zr-MOF as platform, the resultant NacNac-MOF was ready after two sequential reactions. Metalation of the NacNac-MOF with metal salts afforded the desired MOF-supported NacNac-M complexes (M = Fe, Cu, and Co). The catalytic properties of resultant metalated-materials were studied under C-H amination and hydrogenation reactions. One of their most recent works reported the design of bifunctional metal-organic layers (MOL) for tandem catalytic transformations using molecular oxygen and carbon dioxide.⁸⁵ Hf-TPY MOL consisting on Hf₆ SBUs and TPY ligand (TPY = 4'-(4-carboxyphenyl)[2,2':6',2''-terpyridine]-5,5''-dicarboxylate) as the coordinative metal site. Subsequent metallization with FeBr₂ and MnCl₂ and capping with OTf groups afforded HfOTf-Fe and HfOTf-Mn, respectively. HfOTf-Fe converted hydrocarbons into cyanohydrins via tandem reactions: oxidation with O₂ and silylcyanation; whereas HfOTf-Mn transformed styrenes into styrene carbonates via tandem epoxidation and CO₂ insertion. In both cases, metallic cluster and adjacent active sites combined actions.

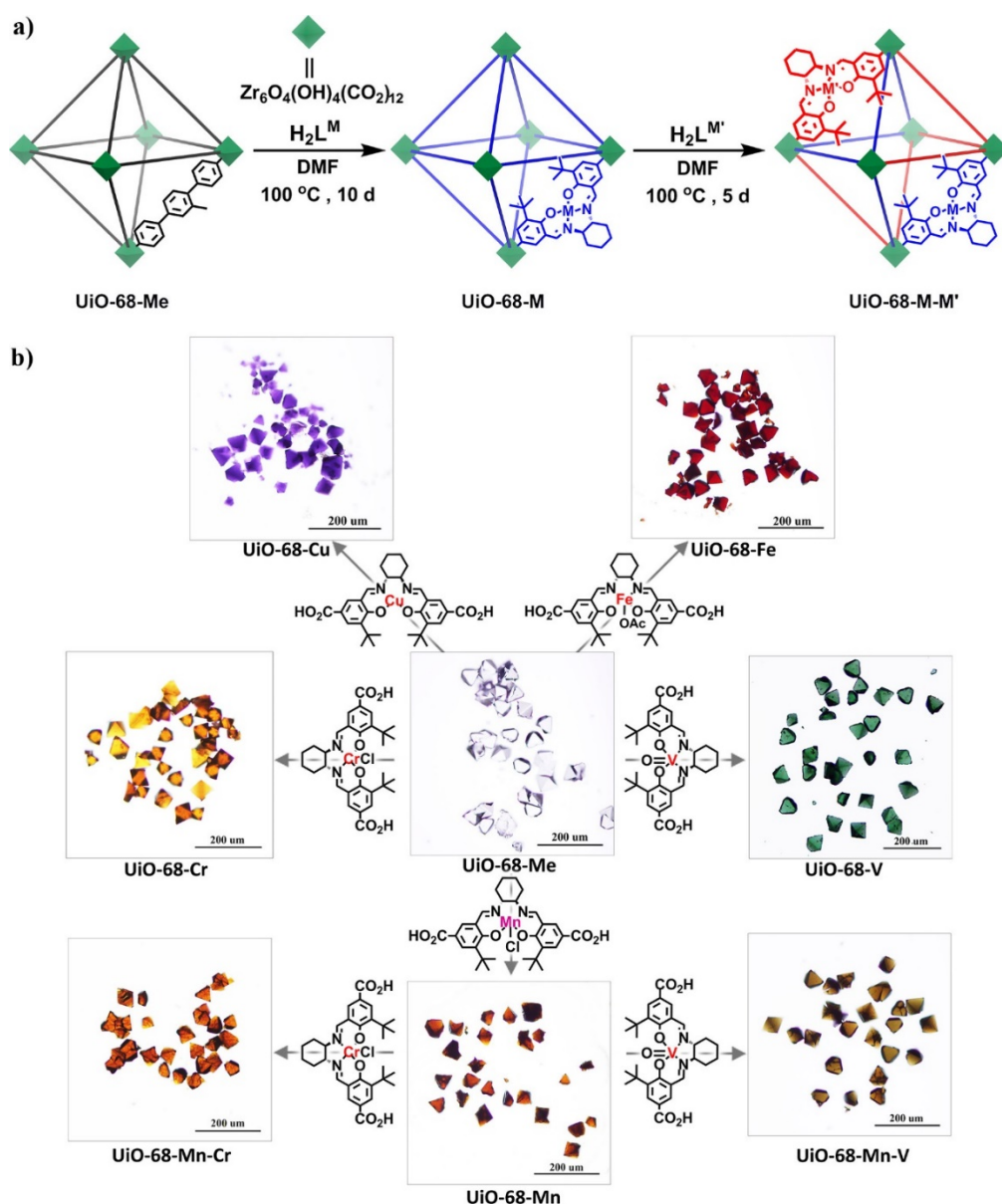


Figure 1.7. a) Schematic representation of the preparation of metallosalen-UiO-68 MOFs. b) Microscope Images of the MOFs after post-synthetic metalation. Extracted from ref 88.

In addition to introduce metal variance in SBUs or by metalloligands, a third type of metal variance is represented by the attachment of extraneous metals or metal clusters to the original SBU which are incorporated by post-synthetic modifications. One of the most widely modified cluster belongs to Zr-based MOF might be due to its chemical robustness and versatility. Different metal ions among which are V^{5+} , In^{3+} , Al^{3+} , Mg^{2+} , Zn^{2+} , Co^{2+} , Cu^+ , Cd^{2+} , Fe^{2+} , Ga^{3+} , Mn^{2+} , Ni^{2+} , Mo, Sn, W and Li^+ and Ti^{4+} or even iridium complexes had been attached to Zr_6 cluster by coordinating with one or more oxygen atoms (Figure 1.8. a) via solution-based post-synthetic modification⁹¹⁻¹⁰⁰ or atomic layer deposition (ALD).¹⁰¹⁻¹⁰⁵

Although to a lesser extent, this strategy has also been applied to introduce metal variance in other clusters, for instance in Ti_8 cluster of MIL-125^{106,107} to incorporate

Ni²⁺-hydride by sequential reactions (Figure 1.8. b); or more recently, in aluminium-based DUT-5 to combine Co^{II} and Al^{III} centers in DUT-5-CoH.¹⁰⁸

The post-synthetic procedures for incorporating metal single-sites are mainly dominated by two approaches. In the first one, the MOF is either activated heating at low pressures to remove H₂O coordinated molecules to generate vacancies, or it is mixed with a weak base (e. g., Et₃N₃) to help deprotonate -H₂O/OH groups. Subsequently, the MOF is incubated in a solution of the corresponding metal salt at mild temperature during a fixed time. The alternative procedure consists of several sequential reactions. Firstly, the μ_2 -OH groups of the cluster are first treated with Li-based compound (e. g., LiCH₂SiMe₃ or *n*-BuLi) to form the μ_2 -OLi intermediate groups. Then the metal salt is added. In the cases of M-hydrides, the sample is hydrogenated by H₂ bubbling or by NaEt₃BH reaction (Figure 1.8. b).

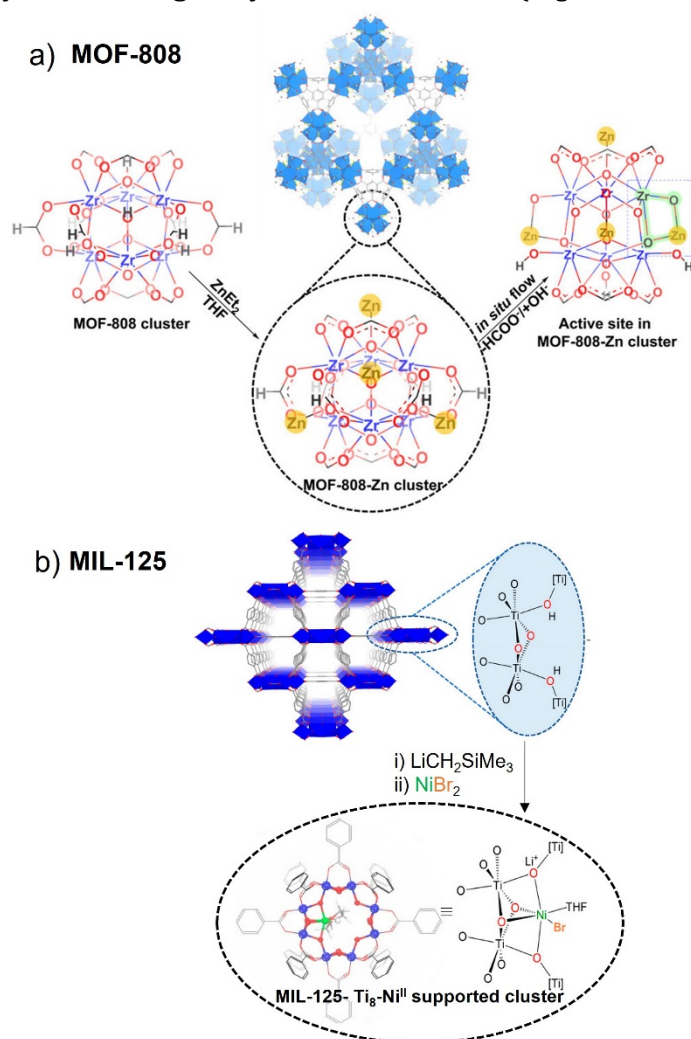


Figure 1.8. a) Scheme of synthesis of MOF-808-Zn and the active site of Zr⁴⁺-O-Zn²⁺. b) Structure of Ti₈-BDC and its sequential metalation with NiBr₂ to form Ti₈-BDC-Ni. Modified from ref 100,106, respectively.

In 2020, Martí-Gastaldo and collaborators reported an unprecedented methodology for the synthesis of heterometallic titanium frameworks amenable to the principles of reticular chemistry¹⁰⁹ (see **Chapter 5**). The substitution of the selective metal ions in the cluster generated changes in the coordination geometry leading to a metastable state that evolves into the formation of SBUs of decreased nuclearity and dependent on the metal incorporated. The structural information encoded in the newly formed SBUs drives the formation of bipartite nets compatible with the connectivity of the organic linker originally present in the crystal. The use of MUV-10(Ca), $[\text{Ti}_2\text{Ca}_2(\text{O})_2(\text{H}_2\text{O})_4(\text{CO}_2)_8]$,¹¹⁰ a 8,3-connected **the** net, as reagent was fundamental to achieving those results. That MOF combined hard (titanium) and soft (calcium) metals in heterometallic nodes which enabled to control metal exchange in soft positions for the generation of new heterometallic SBUs. The post-synthetic metal exchange (PSME) process was studied for the first-row transition metals (Fe^{2+} , Co^{2+} , Ni^{2+} , Cu^{2+} and Zn^{2+}). Reaction with Co, Fe, Ni and Zn induced the formation of a heterometallic MOF containing Ti^{4+} and M^{2+} ions in a 1:2 ratio. Resultant MUV-101(M) was isostructural to the MIL-100 family with **mtn** topology and 6,3-connectivity. MUV-101(M) displayed analogous heterometallic trinuclear SBUs with formula $[\text{Ti}^{\text{IV}}\text{M}^{\text{II}}_2(\mu_3\text{-O})(\text{O}_2\text{C})_6(\text{H}_2\text{O})_3]$. DFT calculations showed that the preference for the octahedral coordination geometry of M^{2+} is responsible for the gradual transformation of the Ti_2Ca_2 SBU into the trimeric TiM_2 SBU upon metal exchange. On the other hand, the exchange with Cu^{2+} , which prefers a square planar geometry, led to the transformation of MUV-10 to produce MUV-102(Cu) which was isostructural to HKUST-1.¹¹¹ The heterometallic analogue featured heterometallic 4-c paddlewheel units with formula $[\text{Ti}^{\text{IV}}\text{Cu}^{\text{II}}(\text{O}_2\text{C})_4(\text{O})(\text{H}_2\text{O})]$. The changes in SBU geometry induced the formation of a **tbo** topology for a 4,3-connected net. That versatile approach provides the incorporation of different transition metals (M = Fe, Co, Ni, Zn, and Cu) to obtain heterometallic phases, some of them not affordable by direct synthesis. Moreover, in contrast to direct methods, the controlled transformation allows access to specific transformation stages and gain control over the formation of hierarchical micro/mesopore structures.

2.1.3. Multivariance and control of the distribution of organic and inorganic components

Increased complexity provided by multivariate MOFs enables incorporate multiple metals and/or linker functionalities within same backbone. This heterogeneity can result in different structural arrangements which may dictate the material features. For a specific composition, the components distribution is expected to change the interactions with guests, which in turn have a huge impact on their applications. In this way, detailed characterization is required to allow to gain a better understanding of the resulting microarrangement and of the possible synergistic effects that may arise.

Structural arrangements are strongly dependent on the synthesis methods and the reaction conditions. Unfortunately, in the greater number of the cases, exact

prediction of the outcome is difficult due to the complexity of MOF formation process. Therefore, most of the works do not focus their attention on describing the type of structural arrangements generated, so the arising products are not classified. Here, we present a categorization of the structural arrangements in four different types: random, core-shell, domains, and specific lattice positions. All these possible structural arrangements are common for multivariance in organic and inorganic component (*Figure 1.9.*), so both have been discussed altogether.

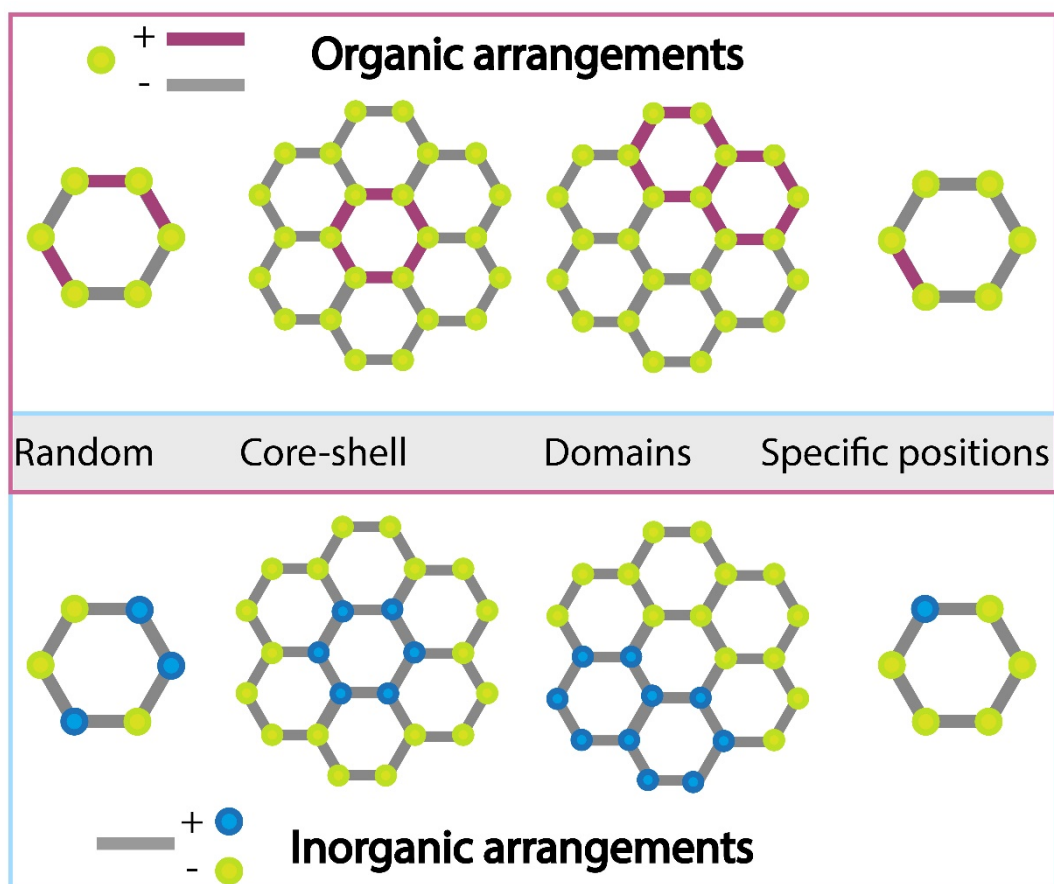


Figure 1.9. Overview of different structural arrangements for MTV-MOFs.

Random

In many of the reported MOFs, in which the type of the ordering is not specified, it is assumed that a random distribution of components is dominant across the solid. Generally, a random distribution involves linkers or metal centres distributed statistically over the framework on equivalent lattice positions resulting in a material with homogeneous properties throughout the whole framework, because all components incorporated are completely intermixed. This type of arrangement provides a high thermal stability and good accessibility to the pores, and it is recommended when the close vicinity of different functionalities is required.

The easiest synthetic route is the direct synthesis mixing the precursors using conventional heating at ambient pressure, solvothermal or by microwave-assisted

procedures. Generally, random distribution is the targeted arrangement when using direct synthesis, but only few reports presented clear evidence for the random incorporation of both components. Regarding mixed-linker MOFs, a nice example of homogeneous linker distribution was reported by Baiker group. Multivariate-linker MIL-53(Al),¹¹² [Al(OH)BDC] were prepared by mixing in one-pot two ligands: [benzene-1,4-dicarboxylate (BDC) and 2-aminobenzene-1,4-dicarboxylate (NH₂-BDC)] (Figure 1.10. a). The influence of the random incorporation on the thermal stability of the multivariate frameworks was analysed. Later, Farrusseng and co-workers confirmed that homogeneity based on the flexible behaviour. For that, the adsorption/desorption isotherms and thermo-diffraction studies on flexible structures were carried out.¹¹³ The linear relationship between the CO₂ breathing pressure and the amine content in the MIL-53(Al) structure illustrated the homogeneity of the crystallite composition (Figure 1.10. b and c).

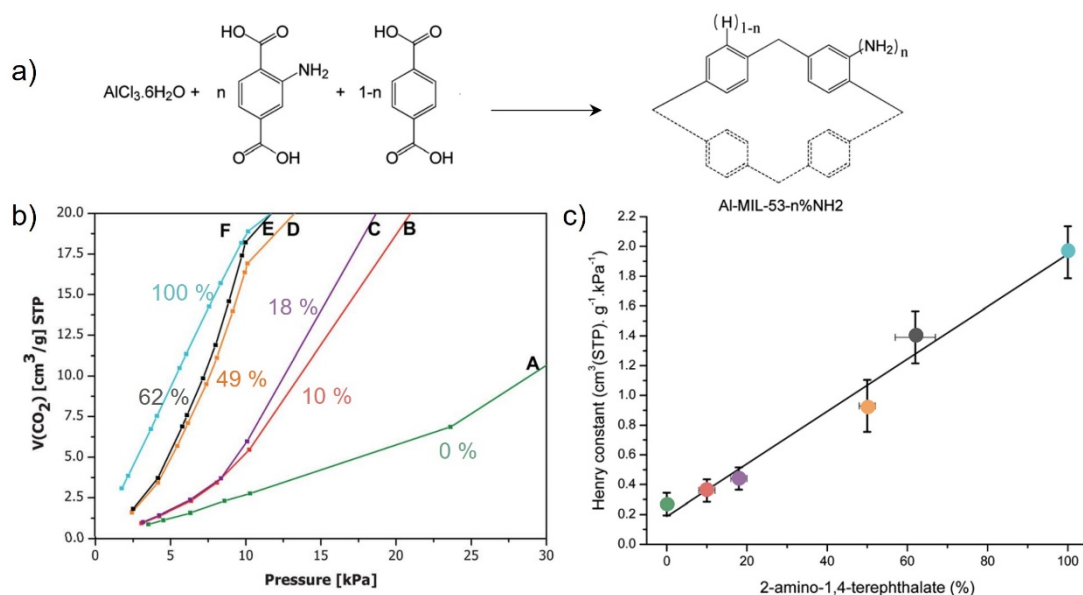


Figure 1.10. a) Scheme of synthesis of MTV-MIL-53(Al)-n%NH₂. b) CO₂ physisorption isotherms of MTV-MIL-53(Al)-n%NH₂ samples. c) Linear evolution of the Henry constant for CO₂ adsorption as a function of the NH₂-BDC linker content. Adapted from ref 113.

Deng and collaborators provided an illustrative example for random distributed multi-metal MOFs. In that work, 36 multi-metal porphyrin-based MOFs with composition of [(M₃O)₂(TCPP)₃] (TCPPM = tetrakis (4-carboxyphenyl) porphyrin) were prepared by direct-synthesis,¹¹⁴ in which the metal content was controlled through varying the stoichiometry of the starting materials (Figure 1.11. a). EDX, XPS, XANES, Mössbauer and EPR analysis were performed to rule out the possibility of heterogeneous physical mixture of MOF and distinguish between two possible scenarios for the spatial arrangements of metals: a) where two different SBUs, each of which is composed of three metal atoms of the same kind, were mixed to form domains in the MOF structure, or b) where there were two kind of metals in the same SBU and those mixed metal SBUs were present throughout the entire MOF crystal giving rise a random distribution. Whereas (Mn_{1.45}Fe_{1.55}O)₂(TCPP-Ni)₃

sample fitted into first scenario (*Figure 1.11. b*); in $(\text{Ni}_{2.07}\text{Fe}_{0.93}\text{O})_2(\text{TCPP-Co})_3$ Fe and Ni metals were randomly distributed in the same SBU (*Figure 1.11. c*). Authors attributed those differences to the ionic radius of the metals and their coordination affinity with oxygen.

Post-synthetic modifications may be considered as an alternative strategy to produce a random distribution.¹¹⁵ For that, the fine control of synthetic conditions such as reaction rate of the exchange process, metal concentration and flexibility of the linkers are crucial; otherwise core-shell particles might be formed preferentially.

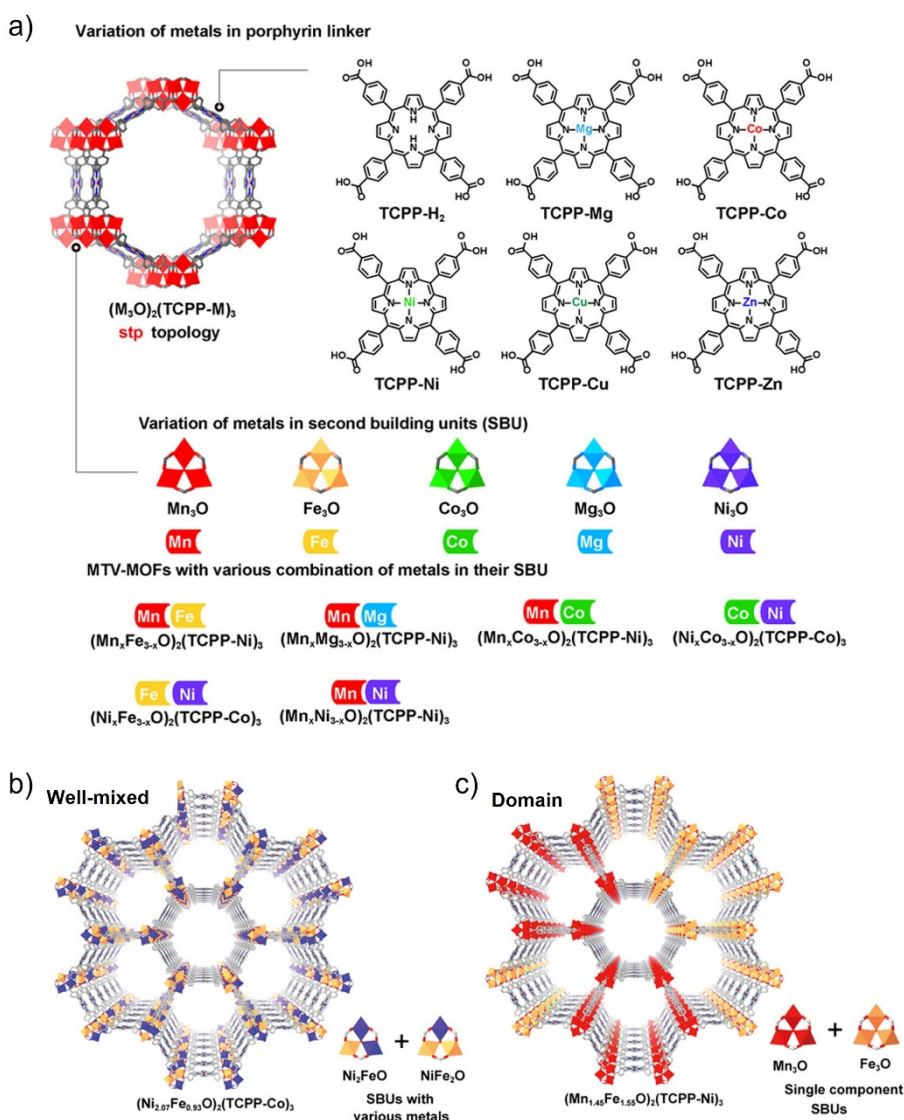


Figure 1.11. a) Multi-metal porphyrin-based MOFs with composition of $[(\text{M}_3\text{O})_2(\text{TCPPM})_3]$ in which the metal variance was introduced by metal in porphyrin linker as well as in SBU. Two metal spatial arrangements in multi-metal MOFs: b) $(\text{Ni}_{2.07}\text{Fe}_{0.93}\text{O})_2(\text{TCPP-Co})_3$ presented random distribution with SBUs with various metals; c) $(\text{Mn}_{1.45}\text{Fe}_{1.55}\text{O})_2(\text{TCPP-Ni})_3$ exhibited domains in which single component SBUs were present. Adapted from ref 114.

Domains

The second type of component distribution represents a transition between a random distribution of linkers and an ordered core-shell structure. The framework components are neither distributed statistically nor well organized but grouped in ordered domains which can be either defined areas like channels or pores or undefined areas within the lattice. This arrangement usually occurs as an unwanted arrangement during the development of mixed MOFs,^{114,116,117} so it is characterized by their lack of reproducibility and reliable characterization.

Microstructural domains are present when one type of linker molecules is preferably incorporated next to a linker of the same kind due to strong interactions with each other. The logical selection of mixed-linkers should be based on similarities the geometrical length,¹¹⁶ flexibility,¹¹⁸ denticity,¹¹⁹ and functional groups modifications, etc. A domain-based linker spatial distribution was found to be critical for creating hierarchical pores inside MTV-MOFs. This strategy is based on preparing mixed-linker MOFs incorporating linkers susceptible to undergo hydrolysis, thermolysis¹²⁰⁻¹²³ or ozonolysis reactions.^{82,124} The specific clustering of these ligands into domains is the key to achieving larger pores after a bond cleavage process via any of the aforementioned treatments. Recently, Zhou's group has spreaded this concept to photosensitive linkers,¹²⁵ where a tetracarboxylate porphyrin linker, TCPP [TCPP = tetrakis(4-carboxyphenyl)porphyrin], was incorporated into UiO-66, serving as the photolabile linker. The stepwise synthesis UiO-66-TCPP in which was comprised of two stages: nucleation and growth. BDC-bonded Zr-oxo clusters and UiO-66 nanoparticles were the dominant constituents at the nucleation stage. The TCPP linker can be further attached to the nuclei by linker exchange. The photolysis performed under homemade laser system equipped with a continuous 405 nm laser promoted the selective removal of TCPP linkers. While the robustness of BDC linkers kept them unaltered, thus creating defective domain in the material. That effect was accentuated by the incorporation of a second labile ligand such as NH₂-BDC (*Figure 1.12.*).

Similarly, in case of metal-mixed MOF, large differences in the electronegativity, ionic radius of the metals and coordination environment may prevent those cations to be present in the same SBU, thus metal-domains were present. As was illustrated by (Mn_{1.45}Fe_{1.55}O)₂(TCPP-Ni)₃ sample of Deng's work¹¹⁴ (*Figure 1.11. c*).

In 2019, Rosi and co-workers introduced a new strategy to generate domains into frameworks using a modular code.¹²⁶ They introduced "domain building blocks" (DBBs) into the MOF lexicon and define them as distinct structural or compositional regions within a MOF. Authors applied this approach to the construction of a rich library of UiO-67 stratified MOF (sMOF) particles consisting of multiple concentric DBBs.

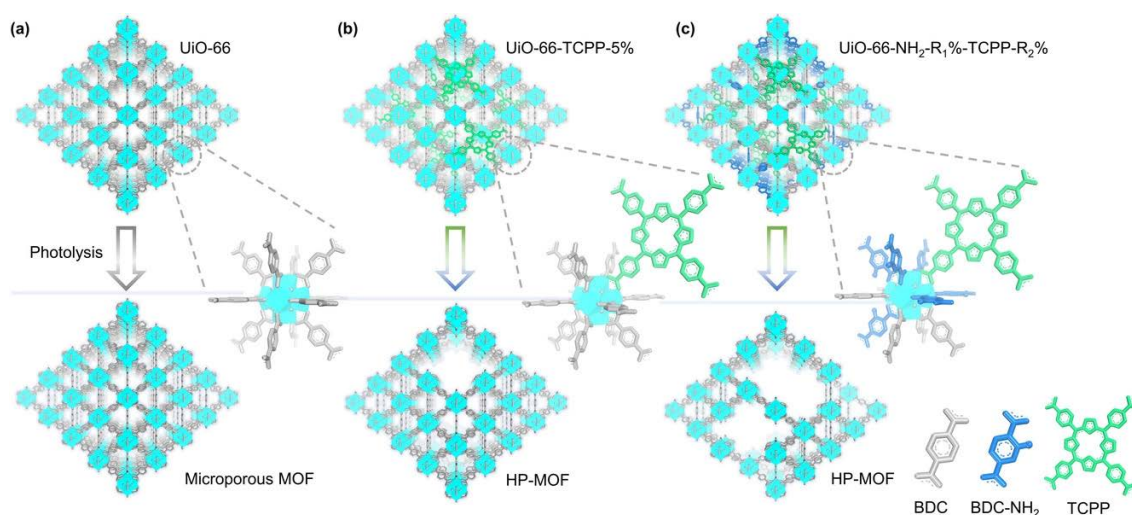


Figure 1.12. a) Microporosity and integrity of UiO-66 are preserved after photolysis. b) Photolysis on UiO-66-TCPP-5% can generate mesopores through eliminating the photolabile linker TCPP. c) Introducing a secondary labile linker $\text{NH}_2\text{-BDC-NH}_2$ increased the ratio of mesopores to micropores after photolysis. Modified from ref 125.

Core-shell

In this third kind of distribution, the components are ordered in a core-shell fashion within the framework. This arrangement combines merits of both the core and shell materials, as well as complements the deficiencies of each other. Therefore, it represents a preferred general strategy for creating novel functional materials.¹²⁷⁻¹²⁹

Originally, core-shell structured MOFs were mainly constructed by epitaxial growth of one type of MOF on the seed of another type of MOF (SURMOFs),¹³⁰⁻¹³² which represented a two-dimensional borderline case. Currently, new approaches for constructing core-shell structured MOFs have been explored as post-synthetic exchange process in a 3-D porous framework.¹³²⁻¹³⁸ Core-shell arrangement results when the diffusion is very low or the exchange is much faster at the edges of the crystal and it is given by thermodynamic drive forces, especially in cases where ligand size effects disfavour substitution within the material. In this case, the outcome is more likely to involve preferential reaction on the outer surface because of the high enthalpic penalty associated with disrupting the lattice structure in the bulk. The size and functionality of the core and the shell can be independently tune adjusting reaction parameters as time, temperature, and concentration. Thus, core-shell microstructure ensures a controllable synthesis of spatially separated functionalities for a wide range of applications. Although there are already some systematic studies on the influences of these parameters, further detailed studies are necessary to facilitate a more precise prediction of the products. In 2012, Song *et al.* clearly showed the time dependence of the core-shell development process during post-synthetic metal exchange in $[\text{M}_6(\text{BTB})_4(4,4'\text{-bpy})_3]$ ($\text{M} = \text{Zn}^{2+}, \text{Co}^{2+}, \text{Cu}^{2+}$ or Ni^{2+} , BTB = 1,3,5-benzenetribenzoate, and BP = 4,4'-bipyridine).¹³³ Due to

different colours of the applied metals, the extent of the exchange process and, thus, the size of the core and the shell could easily be followed using optical microscopy. Shell's size increased progressively with incubation time until one day when a complete metal exchange was reached.

Later, in 2017 Nair and co-workers paid great attention to study the factors that determine the formation of different microstructures of mixed-linker ZIFs,¹³⁹ constructed from similarly sized linkers: 2-methylimidazole (2-MeIm) of ZIF-8 and imidazole-2-carboxaldehyde (OHC-Im) of ZIF-90. The resultant arrangement of mixed-linker ZIFs prepared by SALE and *de novo routes* were completely different. Under appropriate reaction conditions, SALE processes appeared to be capable of generating controlled core-shell ZIF structures of good morphological quality that complement the well-mixed structures obtained by *de novo* methods (*Figure 1.3.*). The authors also studied in detail the effects of crystal size, temperature and time and proposed a generalizable mechanism for SALE processes. They concluded that core-shell structures were formed at mild temperatures and short reaction time, whereas harder conditions led to morphological defects such as pits and holes in the crystals.

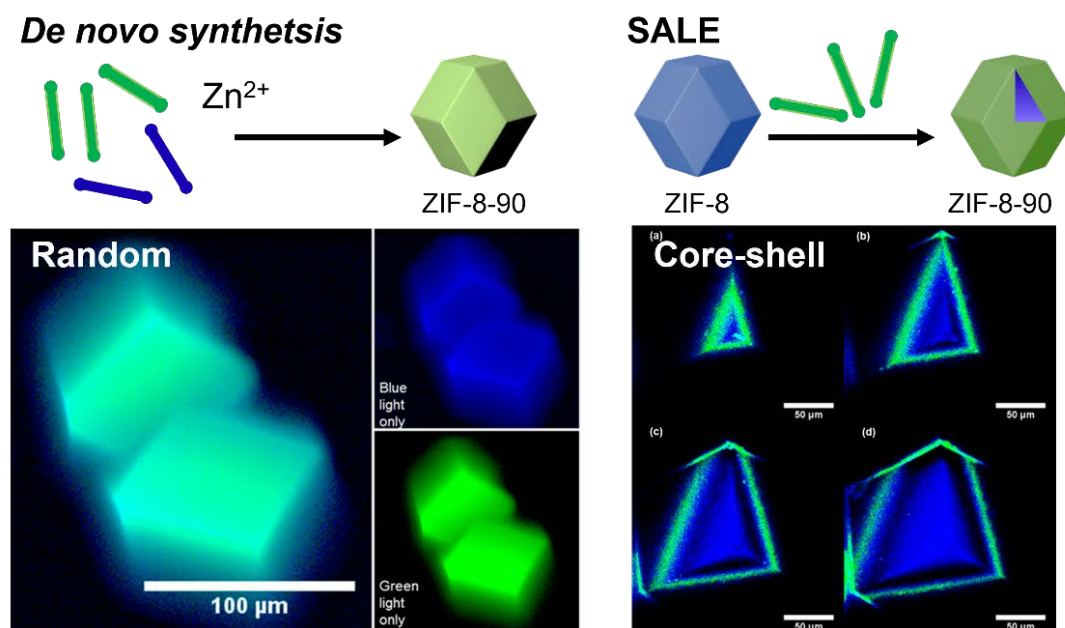


Figure 1.13. The resultant arrangement of mixed-linker ZIFs was controlled by synthetic approach. Adapted from ref 139.

During the same year, Matzger and co-workers studied in detail the diffusion linker exchange process in in MOF-5, UMCM-8, and UiO-66.¹⁴⁰ Authors selected deuterated-BDC (H_2BDC-d_4) as ligand to be incorporated due to it is structurally and chemically identical to parent H_2BDC . Furthermore, the differences in the stretching and bending frequencies of the C-H and C-D bonds allowed to analyse the spatial arrangement by confocal Raman microscopy. The diffusion studies demonstrated that the limited diffusion, possibly originating from the hydrogen bonding of the

linker to the metal cluster, might be responsible for the core-shell structure formation. Thus, it was demonstrated that the combination of the diffusion and exchange relative rates dictate the microstructure of the exchanged material. Later, the same research group explored the effect of solvent choice in MOF-5→MOF-5-d₄ linker exchange process.¹⁴¹ For that, 30 solvents and several binary mixtures were tested, and the resulting microstructures were deeply analysed. The study showed how the thickness of the shell and the extent of exchange (% of H₂BDC-d₄) within that were modulated by the solvent properties.

Recently, Martí-Gastaldo's group has prepared a set of MTV-UiO-68-TZDC% [TZDC = 4,4'-(1,2,4,5-tetrazine-3,6-diyl)dibenzoic acid] samples using UiO-68 crystals as seed.¹⁴² The fine tuning of post-synthetic reaction variables was crucial to control the resultant microarrangements (see **Chapter 3**). Firstly, the role of linker exchange (TZDC) concentration was evaluated. For that, UiO-68 crystals were soaked in different solutions varying TZDC concentration for 3 hours. The results showed the formation of core-shell distributions for low TZDC equivalents (< 5) becoming more homogeneous for higher loadings. At the same time, UiO-68 crystals were exchanged fixing the TZDC equivalents to 2 and prolonging the exchange time to 24 hours. The increase of the reaction time resulted in a random distribution. Those results confirmed the kinetical control upon asymmetric distribution formation.

Also recently, M. Soo Lah and co-workers reported the linker spatial distribution modulation across a 3D-MOF based on pillared 2D-sheets via PSE.¹⁴³ The modulation was achieved by controlling the reaction temperature in accordance with the different temperature sensitivities of the diffusion coefficients and exchange rate constants of the linkers. Concentric core-shell microstructures were obtained at higher temperatures when the exchange of the building blocks was faster than diffusion. On the other hand, at lower temperatures, the kinetics-controlled pillar exchange produced uniform microstructured MOF crystals.

Although the post-synthetic route is the most developed, some alternative had been explored like direct synthesis^{144,145} or encapsulation of different guest molecules into the frameworks. Recently, cyclodextrin MOFs (CD-MOFs) have been chosen as the host to encapsulate organic dyes (7-hydroxicumarina, fluorescein, and rhodamine B) for light-emitting applications.¹⁴⁶ The three sequentially formed and adjustable layers of different dyes generated a core-shell crystal with white-light emission via spectrum superposition.

It is worth noting that core-shell arrangement has been widely used to prepare heterostructures, especially in the development of NPs@MOF and MOF@MOF. These strategies are not covered in detail in this discussion, so it is recommended to consult more specialized works.¹⁴⁷

Specific lattice positions

Specific lattice positions are found in these materials which contain closely related linker molecules or metal cations incorporated at specific lattice sites giving rise a nearly isostructural framework. It is the most significant arrangement usually found in multi-metal MOF with extraneous metals or metal clusters attached to the original SBUs. This arrangement is useful for the investigation of metal-metal interactions and the resulting influence on the properties of the materials, especially in catalysis (*see Section 4.2*).

As it was described for the previous arrangements, specific lattice positions can be reached by different synthetic routes. Some strategies have been reported for introduce a second linker in a selected position, such as careful design of linker to promote a slight distortion of the framework favouring one of the linkers in special positions¹⁴⁸⁻¹⁵² or incorporate new bulky functionalities in the linker to prevent the inclusion of another linker in certain positions. Last approach was illustrated incorporating a voluminous phosphine (PPh₂) groups to the linker in multi-linker LSK-3 structure which was firstly employed in organocatalysis.¹⁵³ The large space requirements of the PPh₂ side group prevented the incorporation of functionalized linker molecules next to each other, and consequently, the PPh₂ groups were located only in a specific plane within the framework. Authors mentioned the potential of a framework steric hindrance to impose selectivity on a catalytic reaction mimicking the pocket observed in the active site of enzymes.

A smart, but rarely used route, proposes a two steps post-synthetic method.^{149,150,154} In the first step, a defect framework with “missing” linker molecules is synthesized which is achieved via treatment of weak linkages (thermolysis, photolysis, hydrolysis or ozonolysis) or capping agents. Then, in the second step, those voids are filled by a different linker. When the defect sites, created in the first step, are ordered, the incorporation of the second linker occurs in a site-specific fashion. Nice example was described by Tu *et al.* in which eight new frameworks were created thanks to the creation of ordered metal and linker vacancies in a cubic Zn-MOF, [Zn₄O(4-pyrazolecarboxylate)₃] (*Figure 1.14*).¹⁵⁴ The immersion of pristine material, which was constructed from Zn₄O(COO)₆ and Zn₄ON₁₂ units linked by PyC linkers, in water at room temperature for 24 hours led to remove a quarter of the metal ions, which represented one Zn atom per each SBU, and half of the linkers; giving rise to new crystalline phase. Then, the immersion of the material in the corresponding solution resulted in filling the ordered vacancies with new cations (Li⁺, Co²⁺, Cd²⁺, and La³⁺) and new functionalized linkers (CH₃-PyC and NH₂-PyC). The shape and the number of crystals monitored during the reactions ruled out the dissolution-recrystallization mechanism and confirmed the single crystal-to single crystal transformation.

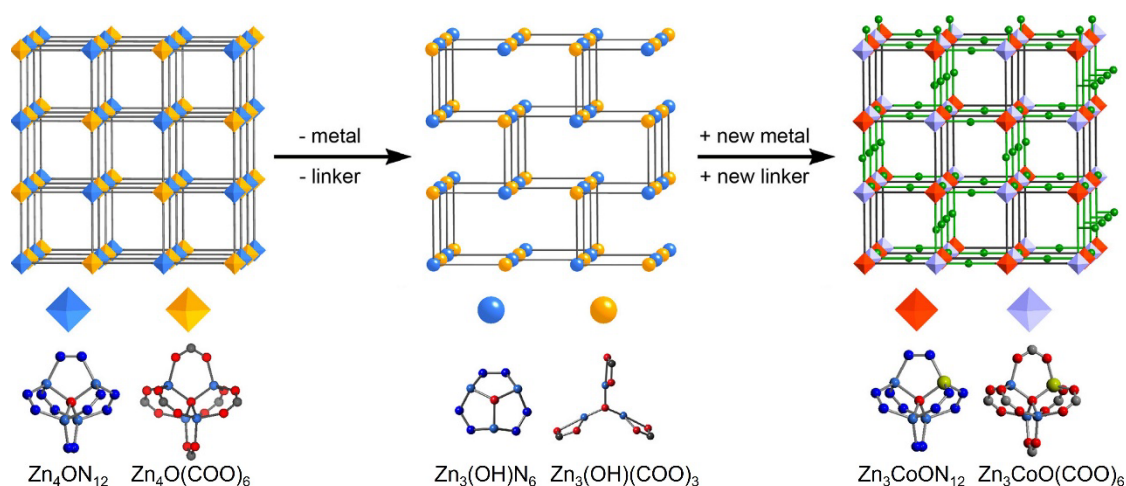


Figure 1.14. Schematic illustration of Zn-MOF undergoing metal and linker elimination reactions and new metal and new linker addition reactions in single-crystal form. A cubic structure (left) containing two types of octahedral SBUs. New structure after water immersion (middle) with two types of triangular SBUs and ordered metal and linker vacancies. That structure could process a second-step transformation by filling the vacancies with new metals and new linkers (right) resulting in a framework with two types of heterometallic octahedral SBUs. Modified from ref 154.

Direct-synthetic methodologies has been also deployed for incorporating a second metal in the metal clusters. For instance, Feng *et al.* who presented a general method for synthesizing heterometallic Fe-MOFs using preformed inorganic building blocks.¹⁵⁵ $[Fe_2M(\mu^3-O)(CH_3COO)_6]$ ($M = Fe^{2/3+}, Co^{2+}, Ni^{2+}, Mn^{2+}, Zn^{2+}, Cr^{3+}$ and Ni^{2+}) performed clusters displayed high versatility to be incorporated as SBU in MOF's building. Their use enabled to prepare more than 34 different structures by combination with thirty different ligands and mixed ligands by rationally tuning the synthetic conditions.

2.2. Multicomponent frameworks

Multicomponent MOFs are well-ordered systems with periodic pore architectures constructed from multiple kinds of building blocks. The incorporation of multiple types of linkers produces different nodes and/or edges in the underlying networks which give rise new specific topologies.

2.2.1. Organic diversity in multicomponent nets

A straightforward and effective strategy to construct multicomponent MOFs is to incorporate multiple linkers with distinct coordination geometries (in terms of length and connectivity) into one network.

Typically, in multicomponent MOF synthesis, linkers with same coordinating functionalities are combined ensuring the coordination of the same metal under one uniform reaction. Nevertheless, in the synthesis in which are involved two or even more types of linkers, a careful control over the synthetic conditions is crucial to hinder the formation of the thermodynamically favoured, competing single-component phase, especially when solvothermal synthetic methods are employed. An instructive example was the synthesis of UMCM-1 by Matzger and co-workers in 2008.¹⁵⁶ UMCM-1, $[(Zn_4O)_3(BDC)_3(BTB)_4]$, was built from two organic linkers of different topologies (BDC was ditopic and BTB was tritopic linker) and octahedral $[Zn_4O(COO)_6]$ SBUs originated during the solvothermal synthesis. Under identical synthetic conditions, using H₂BDC as organic linker combined with Zn²⁺ yielded MOF-5 with *pcu-a* topology; whereas the use of H₃BTB linkers afforded MOF-177 with *qom* topology, so minor changes in the linker ratio conditions led the formation of binary phases or even mixtures (*Figure 1.15.*). The controlled combination of both linkers in the same structure resulted in new network UMCM-1 with *muo* topology, where two types of pores, one microporous cage and one hexagonal mesoporous channel, were responsible of the high BET surface area of 4160 m²·g⁻¹ achieved, higher than for binary MOF-5 framework.

More recently, this same approach was used by Kaskel and collaborators to prepare a family of mesoporous frameworks, among which are DUT-6 $[(Zn_4O)_3(NDC)_3(BTB)_4]$,¹⁵⁷ DUT-32 $[(Zn_4O)_3(BPDC)_3(BTCTB)_4]$ ¹⁵⁸ or DUT-60 $[(Zn_4O)_3(BCPBD)_3(BTPB)_4]$ ¹⁵⁹. All of them with a general framework composition of $[Zn_4O(L)]_3(B)_4$ (L = bridging ditopic linker; B = tritopic linker). The use two types of linkers to interconnect large pores with smaller ones avoids interpenetration and structural collapse by increasing the number of anchoring points. Special mention goes to DUT-60, the MOF with the highest surface area reported to date. That material was conceptually designed in silico using $[Zn_4O_6^+]$ nodes, ditopic and tritopic expanded linkers, targeting *ith-d* topology isorecticular to the previous DUT-6. The synthesis of DUT-60 represented an alternative strategy to obtain large pore size and BET surface area values (7839 m²·g⁻¹) without compromising structural robustness.

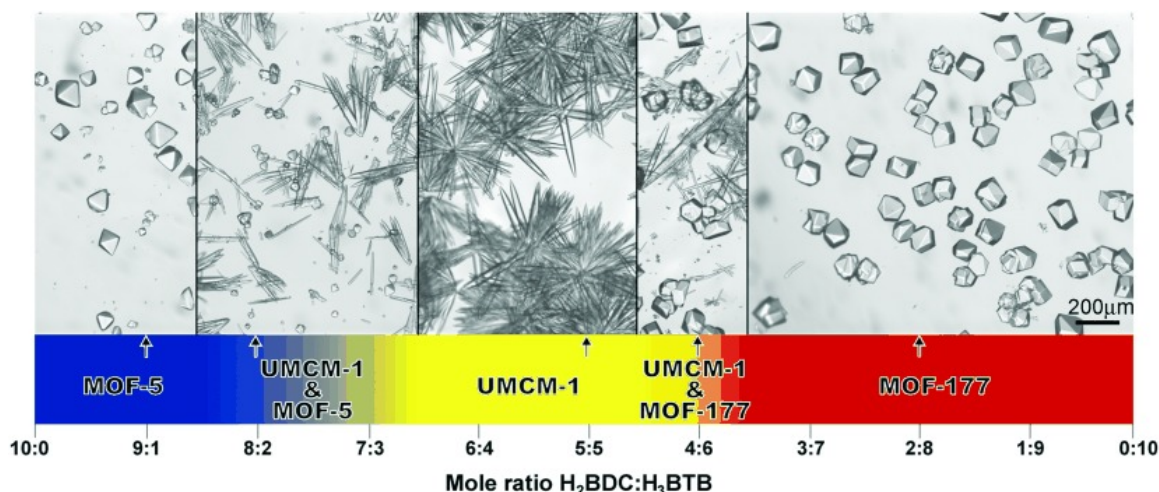


Figure 1.15. Small variations in the synthetic conditions result in the formation of different phases which was evidenced by the morphology of the crystals. Needle-shaped crystals revealed the formation of desired UMCM-1, whereas octahedral geometry was attributed to single-linker phases. Extracted from ref 156.

Although the octahedral $[\text{Zn}_4\text{O}(\text{COO})_6]$ represents one of the most observed units for the inorganic nodes in multicomponent MOFs assembling, as we have described above. SBUs with other geometries, such as trigonal prismatic $[\text{Fe}_3(\mu_3\text{-O})(\text{COO})_6]$ ^{160,161} and 10-, 12-connected Zr-based clusters,^{28,150} were also investigated.

The recent advances in the MOF research area have allowed to increase the chemical complexity of this frameworks assembling quaternary and quinary MOFs with three and four distinct linkers, respectively. The first quaternary MOF belongs to MUF-7 family¹⁶² and was reported in 2013 by Telfer and co-workers. MUF-7a, $[(\text{Zn}_4\text{O})_6(\text{BTB})_8(\text{BDC})_3(\text{BPDC})_3]$, incorporated three topologically distinct linkers (dicarboxylate BDC and BPDC linkers with different lengths, as well as tricarboxylate BTB linkers) with only one kind of $[\text{Zn}_4\text{O}]$ unit. In MUF-7a each metal cluster was linked with four equatorial BTB linkers, one axial BDC linker and one axial BPDC linker, forming an *ith-d* topology. Later, in 2015, the same group replaced the BTB linker of MUF-7a with a more rigid truxene-based linker (H_3HMTT) producing MUF-77, $[(\text{Zn}_4\text{O})_6(\text{HMTT})_8(\text{BPDC})_3(\text{BDC})_3]$.¹⁶³ That derivate showed a notable resilience to water vapor and aqueous environments thanks to the high hydrophobicity of the truxene moiety. More recently, following the same strategy a cubane-1,4-dicarboxylate (cdc) was introduced in the pool of ditopic linkers to get new MUF-7 derivatives,¹⁶⁴ namely CUB-MOFs (Figure 1.16.). Their potential in low-pressure liquid organic hydrogen carrier separations were explored.

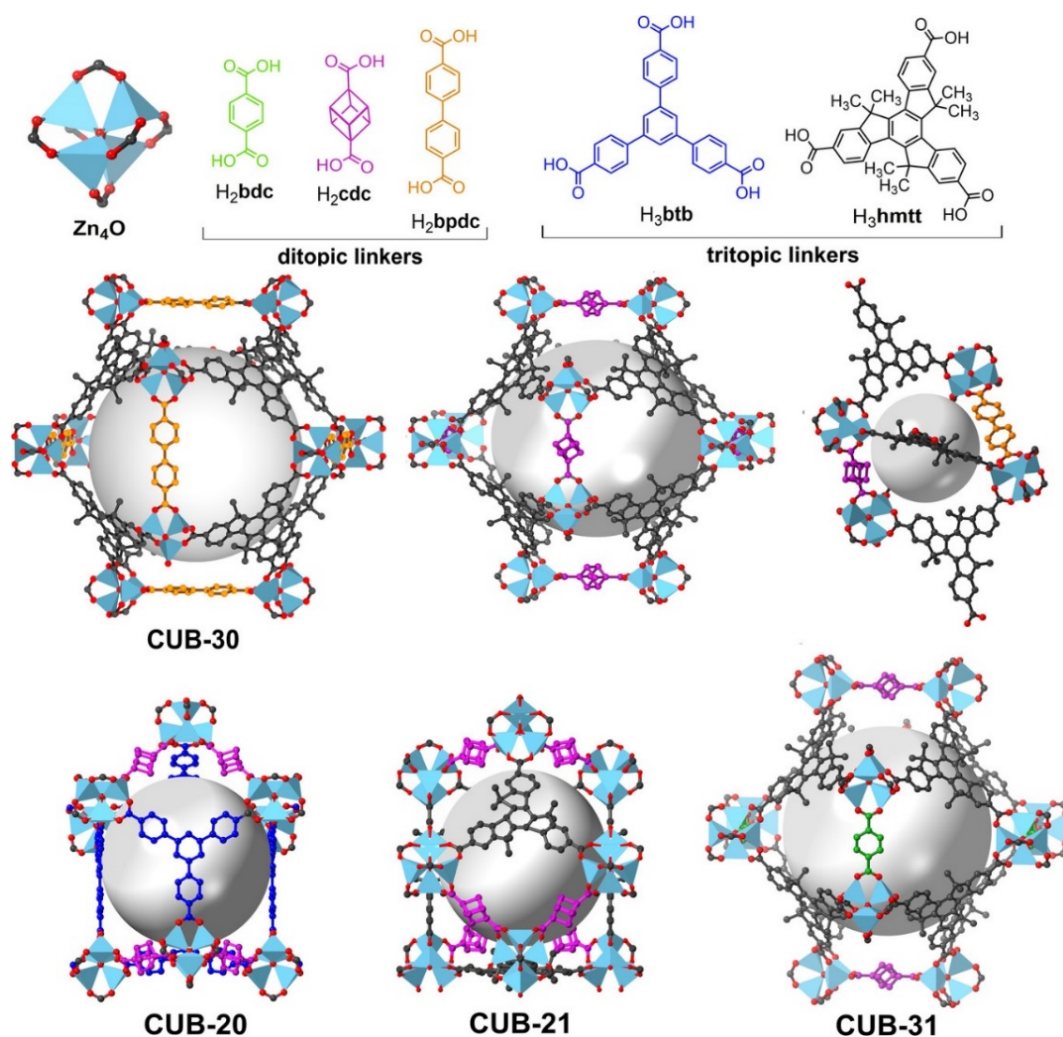


Figure 1.16. Above: Zn-cluster and linkers used for the synthesis of cubane-multicomponent MOFs. Below: crystal structure views of large dodecahedral cavity of CUB-30; smaller dodecahedral cavity of CUB-30; tetrahedral cavity of CUB-30; microporous cavity of CUB-20; microporous cavity of CUB-21; dodecahedral cavity of CUB-31. Extracted from ref 164.

More recently, some examples of quinary MOFs with one metal and four organic linkers were reported by Zhang and Zhou research's groups. Those works have in common the sequential installation of three distinctive linkers into Zr-based MOFs (NPF-300¹⁶⁵ and PCN-606,¹⁴⁸ respectively) by post-synthetic method creating a multivariate pore environment with unprecedented complexity. NPF-300 which was constituted by a planar tetratopic linker and 8-connected Zr_6 cluster,¹⁶⁵ was employed as platform to prepare multinary nets. The in-plane and out-of-plane bending flexibility of the primary linker enabled the stepwise insertion of up to three linkers with different length (NPF-300-3). Authors pointed out that the size-matching and the framework strain were two important factors that dictate the interplay between the thermodynamics and kinetics of the linker insertion and dissociation. Zhou work is discussed later in **Section 2.3**, as it represented a higher degree of chemical complexity in which multivariate chemistry was merged with multicomponent networks.¹⁴⁸

The multicomponent MOFs also resulted from the combination of different types of linkage such as carboxylate, azolate or pyridyl. TPMOF-n family was a nice example of sophisticated topological design of MOFs for heterogeneous biomimetic catalyst.¹⁶⁶ TPMOF-n were built from a complex SBU constituted by $[\text{Zn}_4(\text{tz})_3]$ units, which was further bridged by three TDC_2^- fragments to generate a trigonal prismatic node, $[\text{Zn}_8(\text{tz})_6(\text{TDC})_3]$ ($\text{Htz} = 1H\text{-}1,2,3\text{-triazole}$ and $\text{H}_2\text{TDC} = 2,5\text{-thiophene dicarboxylic acid}$). That triply bound triangular frusta SBU was connected with ditopic ($n = 1\text{-}4$ with *lon* topology), tritopic ($n = 5$ and 6 showed *jea* topology), or tetratopic (a *xai* net, called TPMOF-7) organic ligands to yield three types of nets (Figure 1.17.).

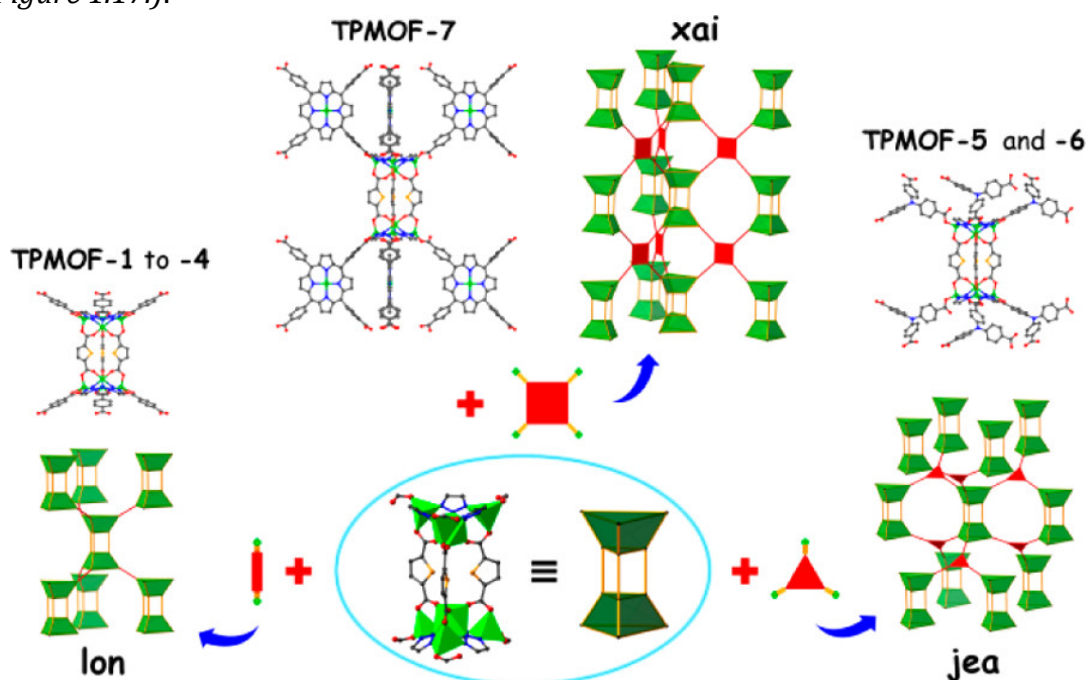


Figure 1.17. Reticular synthesis of a TPMOF-n family based on the triply bound triangular frusta SBU $[\text{Zn}_8(\text{tz})_6(\text{TDC})_3]$ connected with ditopic, tritopic, or tetratopic organic ligands to yield three types of decorated nets. Extracted from ref 166.

2.2.2. Inorganic diversity in multicomponent nets

Regarding metal building blocks, multicomponent MOFs can also be constructed by incorporating multiple inorganic clusters (or SBUs) into one framework. This route has been less investigated compared with organic functionalization due to the sensitivity of SBU formation. Nevertheless, controlling the coordinating affinities between organic linkers and different metals in the reaction, makes possible to generate two kinds of SBUs simultaneously. For that, Hard-Soft-Acid-Base (HSAB) theory is usually employed. Bifunctional organic ligands bearing two types of coordination sites (e.g., pyridyl *N*- and carboxylate *O*-donor) facilitate the integration of two different SBUs into one unique framework through a ligand-oriented assembly process.

Triangular copper pyrazolate building blocks have also been widespread in ternary MOF construction. The in-situ ubiquitous formation of $[\text{Cu}_3(\mu^3\text{-O})(\text{PyC})_3]$ motif

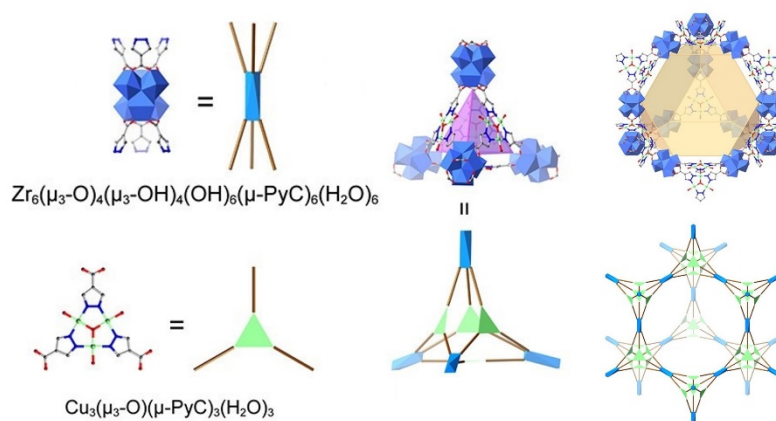
provides a rational strategy to incorporate multiplicity in heterometallic MOFs as was demonstrated in mesoporous FDM-3-7 derivatives.¹⁶⁷ For example, FDM-4 combined octahedral Zn-based SBUs with that triangular copper pyrazolate complex. As it was reported for multicopper sites in natural enzymes such as oxidases and oxygenases, the triangular copper units can undergo modulated redox reactions between $[\text{Cu}^{\text{I}}_3(\text{PyC})_3]$ and $[\text{Cu}^{\text{II}}_3(\mu\text{-OH})(\text{PyC})_3(\text{OH})_3]$ without changing the underlying geometries of the moieties. The catalytic performances of those redox-active multicomponent MOFs were confirmed by catalytic oxidation of CO and aromatic alcohols and the decomposition of H_2O_2 .

More recently, the same approach was followed by Deng and co-workers to report the synthesis of MOF-818 and MOF-919 which resulted from combining $[\text{Cu}_3(\mu^3\text{-O})(\text{PyC})_3]$ SBU with $[[\text{Zr}_6(\mu^3\text{-O})_4(\mu^3\text{-OH})_4(\text{OH})_6(\text{H}_2\text{O})_6]$ or $[\text{M}_3(\mu^3\text{-O})]$ ($\text{M} = \text{Sc}, \text{Al},$ and Fe), respectively.¹⁶⁸ In those structures, the ditopic H_2PyC linker functioned as the edge, while two types of metal-containing SBUs acted as the vertices given rise to three new mesoporous cages which form the superstructure. That work was the first example in which the relation between the connectivity of the vertices in the polyhedral and the size of the cage was systematically studied (*Figure 1.18*).

Besides this pyrazolate building blocks, the molecular building block strategy has also introduced several heterometallic cluster-based MOFs. The work of Zaworotko *et al.* presented a two-step method in which Cr_3 -oxo carboxylate clusters terminating in pyridyl groups were synthesized and subsequently combined with various different metals and organic linkers.¹⁶⁹ It allowed an independent control over the coordination of different metals without complications arising from three or more molecular building blocks in one-pot reactions. This approach was illustrated by *tp-PMBB-5-acs-1* which was sustained by $[\text{Cr}_3(\mu^3\text{-O})(\text{RCO}_2)_6]$ and $[\text{Cu}_3(\mu^3\text{-Cl})(\text{RNH}_2)_6\text{Cl}_6]$ metallic building blocks and represented the first use of the latter cluster in a metal-organic materials.

The high level of chemical complexity involved in incorporating three different SBUs in the same structure is supported by the low number of quaternary MOFs structures reported. One of the first examples was reported in 2012 by Bu and collaborators.¹⁷⁰ The simultaneous formation of zeolite frameworks and covalent attachment of transition- and non-transition-metal clusters in a single step led the formation of CPM-15. CPM-15-Co incorporated tetrahedral $[\text{In}(\text{COO})_4]$, trigonal prismatic $[\text{In}_2\text{Co}(\mu^3\text{-O})]$, and triangular $[\text{Co}_3(\mu_3\text{-OH})]$ units. In that structure, the tetrahedral mononuclear $[\text{In}(\text{COO})_4]$ nodes assembled into a zeolite-type framework, and the other two SBUs were anchored inside the sodalite cages.

MOF- 818



MOF- 919

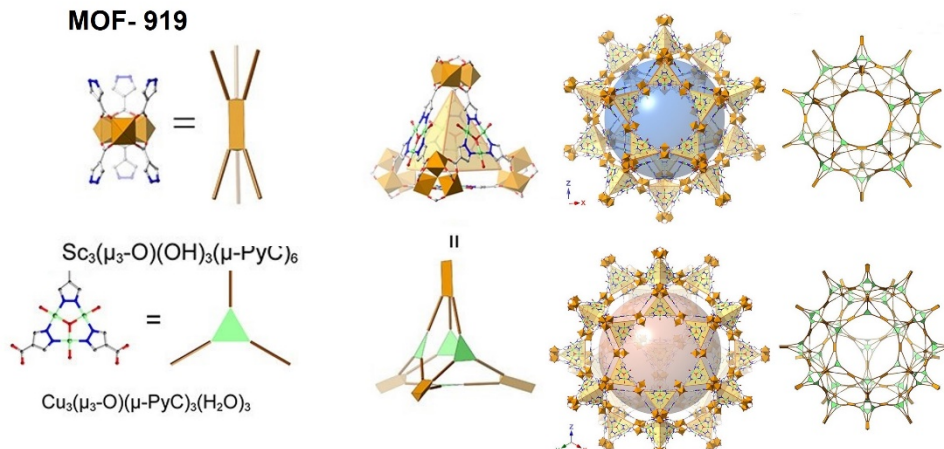


Figure 1.18. Left, structures of MOF-818, including the structure of Zr-SBU and Cu-SBU used to construct mesoporous cages which build the structure. Right, structures of MOF-919, including the structure of Sc-SBU and Cu-SBU used to construct two types of mesoporous cages which build the structure. Modified from ref 168.

Rosi and co-workers used HSAB approach to extend the variability of metal nodes in the same network.¹⁷¹ The combination a bifunctional linker, isonicotinic acid (INA), and its derivatives with one oxophilic, hard-acid metal ion (Zr^{4+} , Hf^{4+} , Dy^{3+}) and a second softer metal ion (Co^{2+} , Cu^{n+} , Ni^{2+} , Fe^{3+} , Cd^{2+}) resulted in MOF-121X (X = 0, 1 and 2) family. In those structures, the isonicotinate carboxylate groups were exclusively coordinated to the hard metal and the nitrogen to the soft one. For instance, MOF-1210 (Zr/Cu) combined the Zr_6 -oxo cluster of UiO-MOF series, $[Zr_6(\mu_3-O)_4(\mu_3-OH)_4(COO)_{12}]$, with geometrically different mononuclear copper nodes (tetrahedral Cu(I) ion and square planar Cu(II) ion) (Figure 1.19).

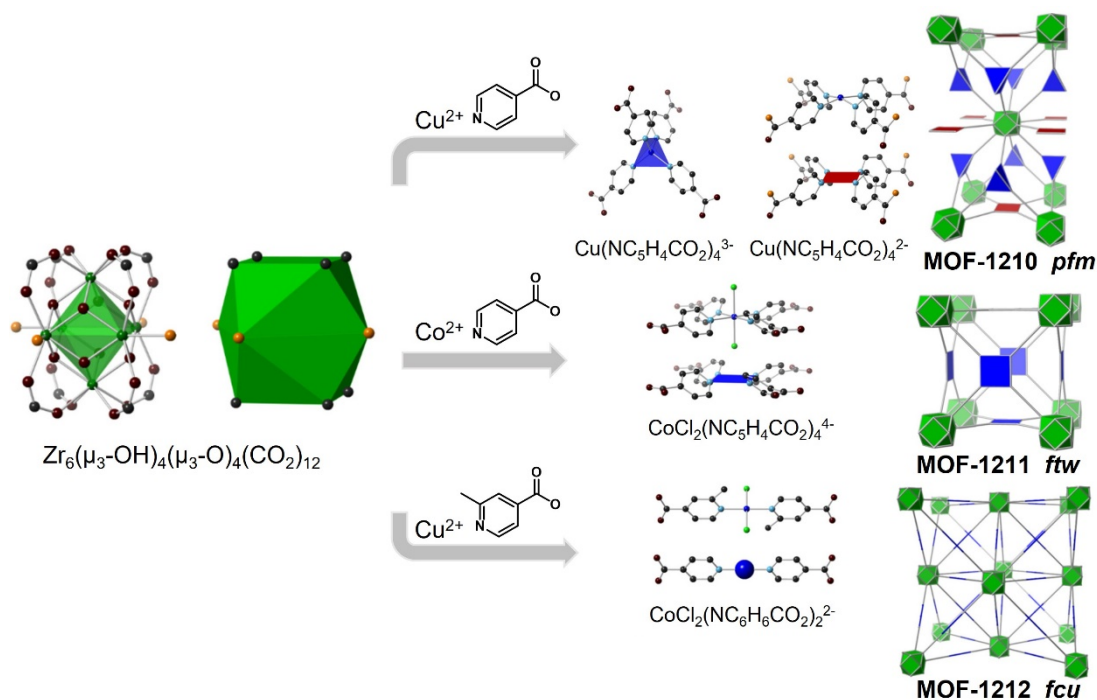


Figure 1.19. The bifunctional isonicotinate linker and its derivatives coordinated distinguish between early and late transition metals. The control of metal-pyridyl complexes' geometry allowed to direct the overall topology to produce new heterometallic MOFs with *p_{mf}*, *f_{tw}* and *f_{cu}*. Modified from ref 171.

2.2.3. Diversity in organic and inorganic hybrid multicomponent nets

The combination of both multiple metal clusters and multiple organic linkers in the same network results in the formation of at least hybrid quaternary MOFs. The synthetic challenge is evidenced by the discrete number of examples available in the literature. Pore space partition (PSP) approach may be useful to prepare hybrid quaternary MOFs, as exemplified by CPM-30 derivatives.¹⁷² CPM-30 consisted of ditopic BPDC linker and trigonal prismatic $[\text{In}_3(\mu^3\text{-O})]$ clusters with open metal sites which pointed toward the centres of the channels at the same height along the channels. Such an alignment of open metal sites hinted at the possibility of introducing extended anchorage points for trapping of metal ions and clusters. Thus, Bu *et al.* introduced secondary metal ions, Zn^{2+} or Co^{2+} , and the auxiliary ligand (isonicotinate, INT^-) into the one-step solvothermal synthesis. The linear INT ligands were successfully anchored onto the open metal sites through their N ends, while their carboxyl ends grabbed metal ions/clusters. The result were CPM-31 $[\text{In}_3(\mu^3\text{-O})(\text{BPDC})_3(\text{INA})_3][\text{Zn}(\text{H}_2\text{O})]$ and CPM-32 $[\text{In}_3(\mu^3\text{-O})(\text{BPDC})_3(\text{INA})_3][\text{Co}_2(\mu^2\text{-OH})(\text{H}_2\text{O})_2]$ structures.

Cage-in-cage strategy has also been an alternative to prepare quaternary MOFs. CPM-24 reported by Bu group was considered an early example.¹⁷³ That nested 3D-3D MOPF@MOPF framework was constructed from two kinds of organic linkers (H_3BTC_3 and INA) and two kinds of cobalt dimeric SBUs (paddlewheel $[\text{Co}_2(\text{CO}_2)_4]$ and hydroxy-bridged $[\text{Co}_2(\text{OH})]^{3+}$) giving rise to cage-in-cage structure. The

cuboctahedral small cage, $\{Co_{24}(BTC)_{24}\}$, was encapsulated in a rhombicuboctahedral large cage $\{Co_{48}(IN)_{48}\}$. More recently, a similar approach was used to isolate JNU-2,¹⁷⁴ a multicomponent microporous MOF. The network combined $[Cu_4(A)_4]$ and $[Zn_2(N-N-PyC)_2(\eta^1-COO)_2(\eta^1-A)_2]$ clusters as SBUs linked by PyC and adenine (A) ligands (Figure 1.20.). JNU-2 structure possessed three cage-like cavities interconnected by small apertures in which channel diameter was close to the domain of the kinetic diameter of C_2H_4 and C_2H_6 molecules. As result, JNU-2 showed an exceptional C_2H_6 selectivity over C_2H_4 under real humidity conditions.

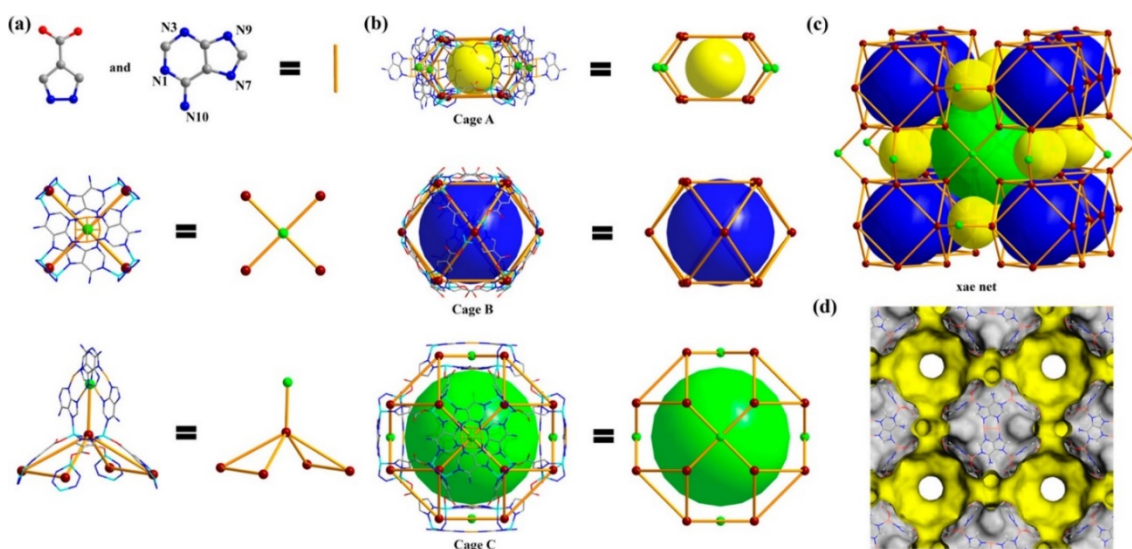


Figure 1.20. a) PyC and Ad ligand serving as a 2-c linker (yellow rod), and $Cu_4(Ad)_4$ and $Zn_2(N-N-PyC)_2(\eta^1-COO)_2(\eta^1-Ad)_2$ SBUs serving as 4-c (green ball) and 5-c (brown ball) nodes, respectively. b, c) Three different cages in JNU-2 arranged in a *xae* topology. d) Connolly surface representation of JNU-2 (yellow/grey curved surface). Extracted from ref 174.

More recently, Li group reported FDM-8¹⁷⁵ which may be considered the sophisticated version of FDM-6 and -7 derivatives.¹⁶⁷ FDM-8 structure comprised three distinct organic linkers (carboxylate-(BDC and NDC) and pyrazolate (PyC)-based) and two kinds of inorganic SBUs, a triangular $[Cu_3-(N-N)_3]$ motifs involving the PyC linkers and octahedral $[Zn_4O(COO)_6]$ clusters entailing all three organic linkers. SXRD analysis revealed two metals and three linkers with ordered spatial arrangements generate two kinds of microporous cages and one kind of mesoporous cage that interconnect in three-dimensional space under *itb-d* topology. FDM-8 showcased the potential of reticular chemistry. A careful design and selection of the coordination geometries allowed to form a unique quinary structure among more than 70 possible structures that can be formed by combining the five constituents presented in solvothermal reaction.

2.3. Multivariance in multicomponent frameworks

High levels of complexity can be reached when the multivariate approach is extended to multinary networks. This strategy involves not only combining different types of ligands and metal clusters in the same network, but also decorating the pore by varying the functionalities of its components. As described in the previous section, a well-defined strategy to achieve a higher degree of functionality of MOFs is to implant different linkers with variable points of extension at precise positions in the crystalline lattice. This is the common route to achieve multivariance in multinary nets. Recently, the Zhou group and the Su group took advantage of that approach by using Zr-based-MOFs.^{148,149,152} In 2016, Zhou and collaborators installed up to three different ligands in missing linker sites of PCN-700 which constituted an ideal platform for systematic modulation of pore volume and pore environment.¹⁵¹ PCN-700 showed a complex functional behaviour by sequential installation of 2,2'-bpy(Cu) and different derivatives of TPDC-R₂ (R = Me, Ph, or Hex). While the 2,2'-bpy(Cu) moiety acted as the catalytic active centre, the TPDC-R₂ with different substituents controlled the window pore size (*Figure 1.21. a*). Therefore, two components within the cavity of PCN-700 worked synergistically as a size selective catalyst for the aerobic alcohol oxidation. The catalytic results showed the role of TPDC substituent on modifying the diffusion rate of substrate and the accessibility of catalytic centres, and consequently controlling the reaction selectivity.

Later, Su and co-workers also used PCN-700 structure to introduce chemical complexity, which, This switchable substitution platform was denoted by the authors as LIFM-28.¹⁵² That MOF displayed two sites available for linker installation: Two sites A formed a space named pocket A that was suitable for insertion of shorter spacers of biphenyldicarboxylate (BPDC) derivatives, while two sites B built a space named pocket B adequate for insertion of longer spacers derived from terphenyldicarboxylate (TPDC) (*Figure 1.21. b*). The combination of those derivatives allowed to prepare up to seventeen functionalized MOFs, LIFM-70-86, with isomorphous structures but variant functional units. Tuning the pore attributes enabled to achieve promising properties such as gas storage and separations as well as catalysis, organic reaction, and luminescence functionalities.

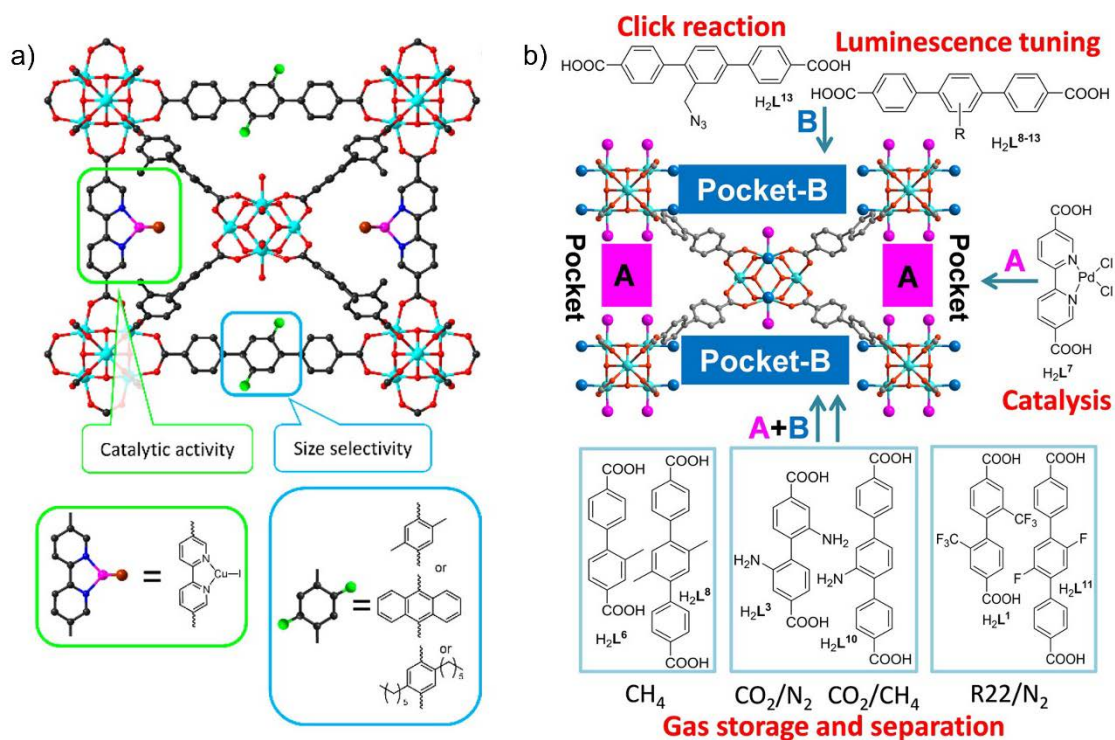


Figure 1.21. a) Size-selective catalytic system for aerobic alcohol oxidation reaction built in PCN-700 through linker installation. Structure of catalytic centre (green box) and size-selective moiety (blue box). Modified from 151. b) Two types of pockets (A and B) for linker installation into LIFM-28 allowed the synthesis of multifunctional LIFM-76-86 available for targeted tasks. Extracted from ref 152.

More recently, the use linkers of low symmetry brought new opportunities to improve the complexity of multicomponent MOFs.¹⁴⁸ For that, two 8-connected Zr₆-MOFs were selected; while PCN-606 presented high symmetric tetratopic linkers, isorecticular PCN-609 introduced low symmetric trapezoidal analogue. The replacement of the rectangular biphenyl groups with a trapezoidal carbazole moiety reduced the symmetry of PCN-609, and consequently, three different pockets were created. The pocket along the c-direction was split in two smaller pores of different size. Meanwhile, the pocket along the a-direction was maintained. Thus, three linkers with different lengths can be incorporated into the network (*Figure 1.22. a*). PCN-609-BDC-BPDC-TPDC provided an ideal platform to place different linkers with specific functionalities. Pocket I accommodated BDC derivatives, whereas pocket II fitted BPDC with different functional groups. Furthermore, the flexible pocket III allowed for a wider range of linkers of variable length to be installed. Thus, up to 447 different MOFs could be achieved (*Figure 1.22. b*).

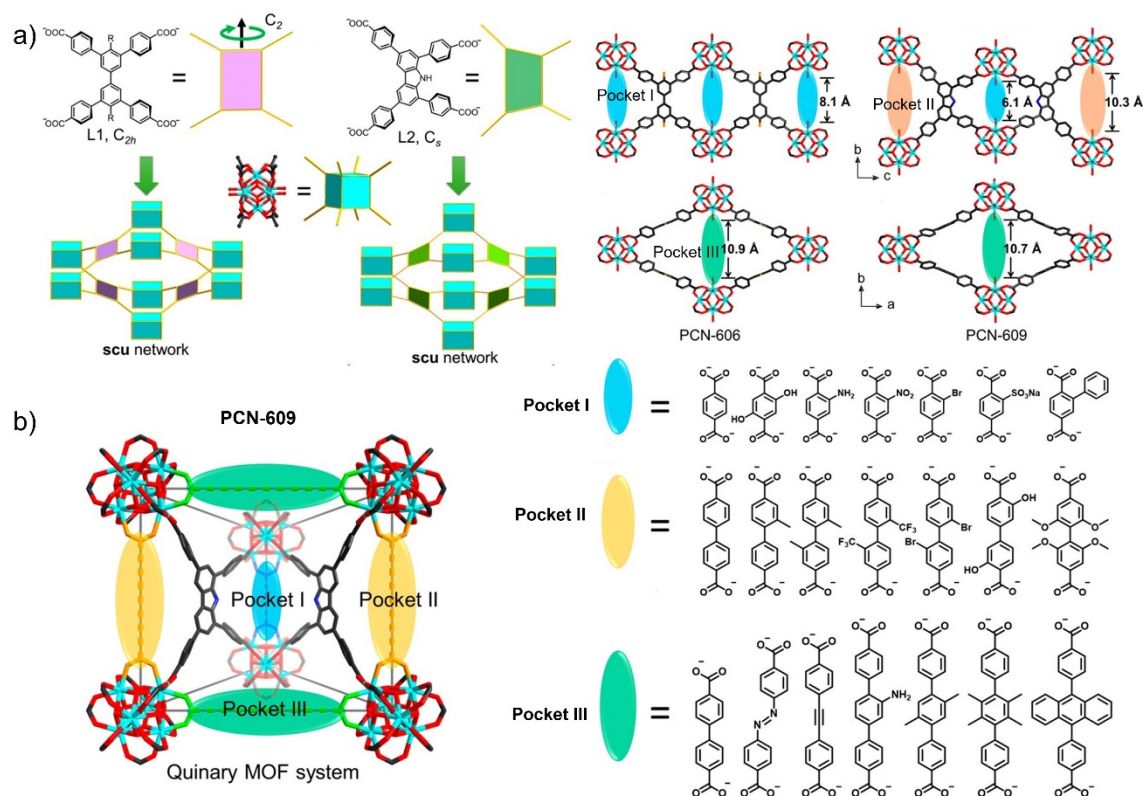


Figure 1.22. a) The decrease in ligand symmetry creates 3 pockets with different lengths resulting in an enhancement of chemical complexity. b) Functionalization of each linker from the quinary MOF system creates multivariate pore environments with unprecedented complexity. Modified from ref 148.

3. Deciphering chemical complexity

Most of the techniques used in the characterization of binary MOFs are common for multinary MOFs, however the analysis of complexity in these materials is challenging and requires greater. A deep characterization of multivariate and multicomponent materials implies, not only the qualitative proof for the incorporation of multiple components in the same product, but even the quantitative ratios of the incorporated molecules. Moreover, understanding the distribution of functionalities throughout the framework (possible arrangements) is essential for a comprehensive study of MOF formation process and the validation of “structure-property-application” relationships.

It is clear that the increase in chemical complexity needs to be accompanied by an improvement in the sophistication of the characterization techniques. Some of these techniques only provide preliminary qualitative information or are focused on studying a single feature. So generally, we need to use different characterization techniques combined with calculations and theoretical models to get a deep understanding of this new generation of materials.

Here, we introduce the main techniques for characterizing the complexity in MOF architectures. They are grouped into two categories based on the study of the organic or inorganic component. Some of these techniques are common to examine both components, others are specific. Within this division, the techniques have been grouped according to the information that they provide (*Figure 1.23.*).

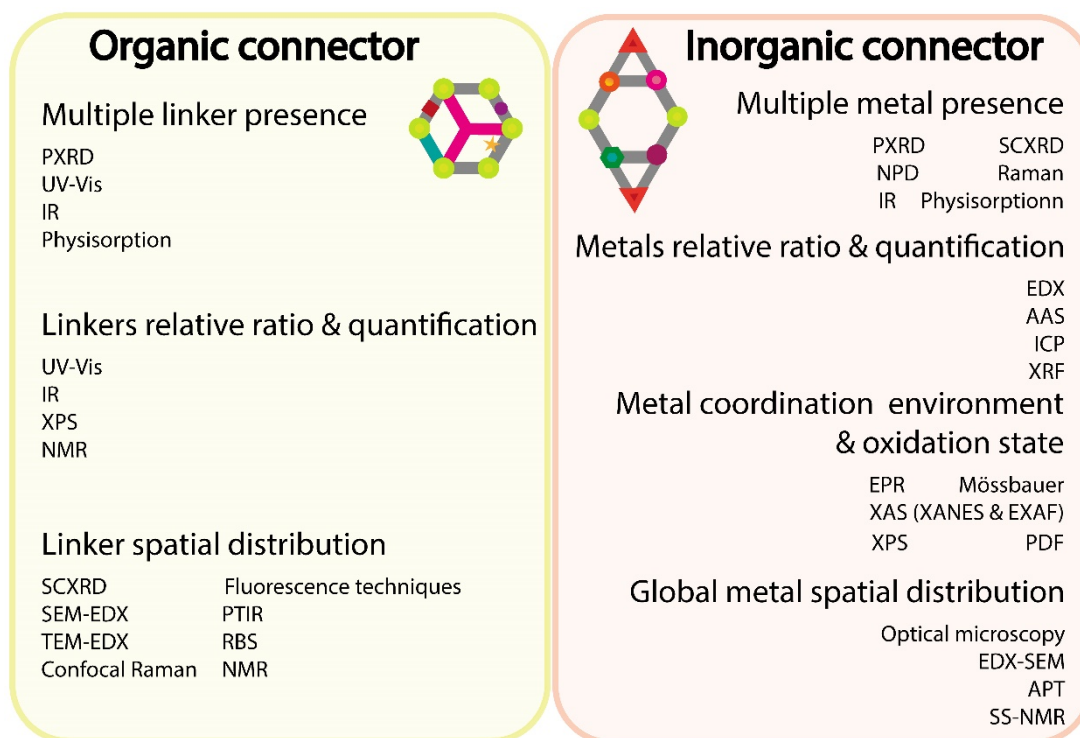


Figure 1.23. MOF complexity characterization techniques divided in two categories based on the type of component.

3.1. Multivariance in the organic connector

To get a full characterization of multi-linker MOFs it is necessary to address the following issues: Knowing the number and the nature of different linkers present in the structure and in what proportion they are found. Also, how they are spatially distributed along the structure.

3.1.1. Evaluating multiple-linkers presence

An initial characterization is based on deciphering the presence of multiple organic functionalities or linkers in the same backbone. For that, we can employ different techniques as Powder X-Ray Diffraction (PXRD). That is one of the most important standard techniques for the characterization of crystalline MOFs. X-ray diffraction analysis (XRD) techniques are used to study the structure of crystalline materials, both single-crystal and powder. XRD works by irradiating a material with incident X-rays, which wavelength is similar to the distance between atoms, and then the measure of scattering of X-rays from atoms according to conditions of Bragg's law produces a diffraction pattern that contains information about the

atomic arrangement in crystal. PXRD allows to identify our crystalline phase, as well as to identify or rule out the possible presence of undesired crystalline impurities. In multiple-linker MOFs, the presence of different linkers in the same backbone results in small differences in unit cell parameters. In an ideal solid solution, the positions of the reflections shift gradually with varying linker ratios according to Vegard's law.^{112,176-182} Although no further formation about the spatial distribution within the framework can be easily obtained, a refinement of the structure via the Rietveld method of high-resolution PXRD measurements may allow for the identification of local incorporation of the second linker within the framework. A good example of this methodology is the work reported by Platero-Prats *et al.* for the rationalisation of the linker distribution of functionalized UiO-67.¹⁸³ The MOF contained the original linker BPDC and the iridium complex derivative Ir-L, where Ir-L = [Cp*Ir(BPDC)(Cl)Cl]²⁻. The authors prepared two different structural models with different spatial distributions of the Ir-L linkers: a cubic model where the Ir-L linkers were randomly distributed over the 12 edges of octahedral cage, and an orthorhombic model with Ir-L linkers distributed over four perpendicular edges of octahedral cage, avoiding occupying adjacent edges separated by < 90°. Rietveld refinements of these structural models against the experimental PXRD data suggested the linker distribution to be like that of the orthorhombic model. This was further rationalised by showing that the bulky nature of the Ir-L linkers favours this arrangement due to the steric hindrance between adjacent linkers.

The spectroscopic techniques as UV-Vis and Infrared (IR) are also helpful for evaluating the presence of multiple linkers. UV-Vis spectroscopy measures the amount of discrete wavelengths of UV or visible light that are absorbed by or transmitted through a sample in comparison to a reference or blank sample. The required amount of energy to promote the electrons to a higher energy state depends on the electronic bonding environments. The absorption is influenced by the sample composition and concentration. So, UV-Vis allows the detection of different functional groups in the material,^{179,184-186} as well as their quantification when reference samples and calibration lines are employed. Furthermore, this technique has been used to monitor the loading of active molecules.¹⁸⁷ Mellot-Draznieks and co-workers reported a non-destructive method to assess and quantify the incorporation of two linkers, BPDC and bpyDC into UiO-67 MOF. That approach combined computational calculations, on a firstly step, with UV/vis spectroscopy and crystallography analysis. The excellent match between DFT calculations and experimental data demonstrated the value of that approach to monitor the exact amount of bpyDC linker incorporated using the relative change in optical band gap values, which was calculated with solid-state UV-Vis absorption.

Unlike UV-Vis spectroscopy, which use larger energy absorbances from electronic transitions, IR spectroscopy relies on the infrared region energy absorbances that occur between various vibrational and rotational states. For different molecular

species the absorption occurs at different frequencies, thus resulting in unique spectral properties. IR is also usually used to get a qualitative incorporation of multiple linkers.^{142,180,188-191} The presence of specific vibrations related with certain functional groups is a proof of the successful incorporation of the functionalized linker molecules into the frameworks. In addition, the observed shift in the vibrational frequency of donor atom-M bonds is used to confirm the metal coordination and rule out the presence of the free linker within the pores. IR technique may also provide quantitative information when reference samples and internal standards are used.

Additionally, gas sorption isotherms also provide indirect information about the presence of different linkers into the backbone. The versatile adsorption experiments can be performed with gases and vapours of different nature (such as N₂, Ar, CO₂, CO, H₂O, ethanol, methanol, dichloromethane...). The response to adsorption may provide information on the chemical environment of the pore, and thus on the functional groups present. Moreover, the functionalization of the linker molecules may modify of the original values of specific surface areas and pore volumes. These qualitative changes can be attributed to different space requirements depending on the bulkiness of the linker or even to the free linker molecules trapped inside the pores during synthetic process. However, quantitative values are not reachable using this characterization technique because synergistic effects often lead to non-linear dependencies on the linker ratios.^{45,192} This phenomena was exemplified by the randomly multivariate MOF-5-derivate presented by Matzger group.¹⁹² In that case, the percentage of the bulky functional group within the framework was determinant to control the level of framework interpenetration and the degree of pore blockage and, consequently, the value of the surface areas. Authors prepared pure TPDC'-MOF-5 (TPDC' = 9,10-bis(triisopropylsilyloxy)phenanthrene-2,7-dicarboxylate), pure Me₄BPDC-MOF-5 (Me₄BPDC = 3,3',5,5'-tetramethyl-4,4'-biphenyldicarboxylate) and multi-linker samples with different TPDC':Me₄BPDC ratios (*Figure 1.24. a*). The adsorption measurements revealed a clear dependence between surface area and composition. The introduction of a small amount of the sterically demanding TPDC' into the interpenetrated framework [Zn₄O(Me₄BPDC)₃] resulted in a reduction of surface area from 1700 to 1580 m²·g⁻¹. As the TPDC' content reached the 40-50 % level of incorporation, the BET surface areas of the products dramatically increased to approximately 3000 m²·g⁻¹. However, when TPDC' concentrations continued to increase, the surface areas, decreased because the TIPS group filled the pores, thus blocking sorption sites, until values close to interpenetrated [Zn₄O(TPDC')₃] structure (1990 m²·g⁻¹) (*Figure 1.24. b*). That nonlinear surface area change was contrasted to linear increase obtained from physical mixtures of pure MOFs.

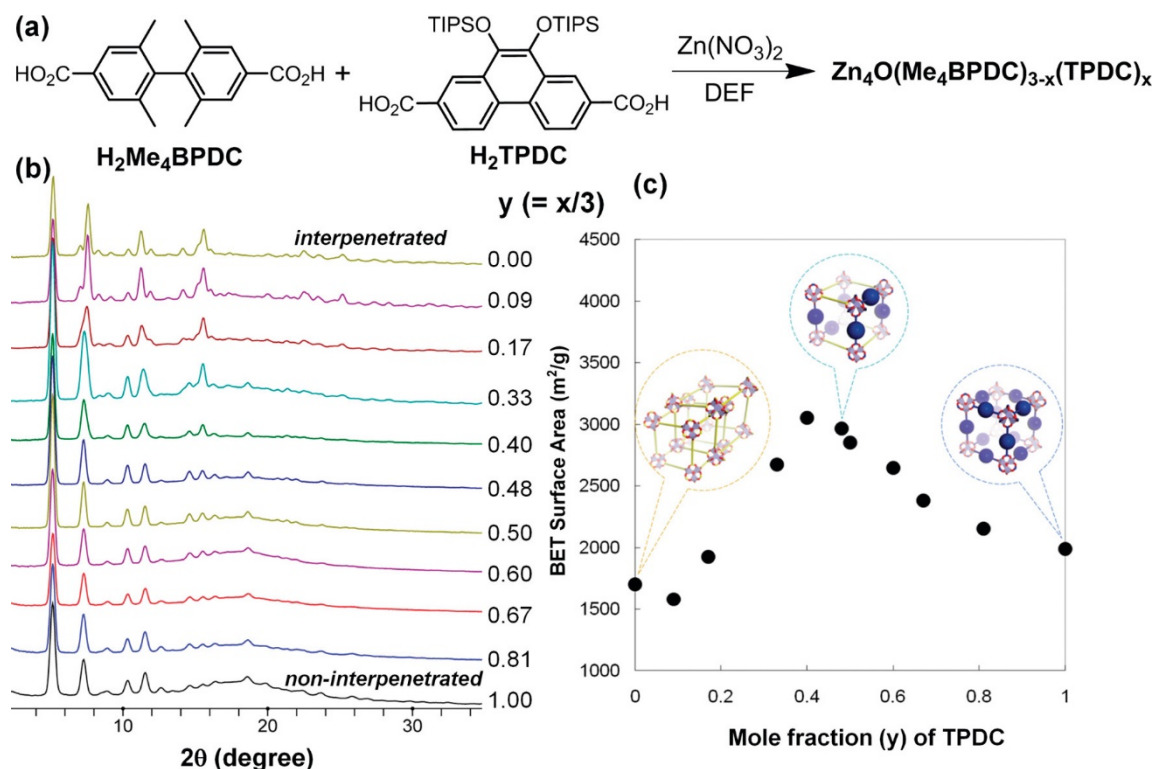


Figure 1.24. a) Synthetic scheme. b) PXRD patterns. c) BET surface areas of MTV-Zn-MOF. Adapted from ref 192.

3.1.2. Evaluating relative ratio and quantification of linkers

When the different ligands present in the structures have distinct contributions to the signal, which can be analysed separately, the relative ratio between the ligands can be obtained. To go further and obtaining quantitative information, in most cases, it is necessary to use internal standards or pre-calibrations. Complementary to UV-Vis and IR spectroscopy, X-ray Photoelectron Spectroscopy (XPS) can be useful to obtain qualitative information about the ligands, without the requirement of large amounts of sample. This technique involves the detection of photoelectrons emitted from a sample as a result of irradiation of the sample by single-energy X-ray photons. XPS is useful for quantitative analysis of surface composition (depth typically of 10 nm) and can detect all elements with the exception of hydrogen and helium through the detection of the binding energies of the photoelectrons. Small variations in binding energies of the photoelectron lines as well as Auger lines satellite peaks, and multiple splitting can be used to identify chemical states. In case of multiple-linker MOFs, XPS provides qualitative information about the presence of new functionalized linker in the network^{193,194} and may confirm the post-synthetic modification of pristine linker.¹⁹⁵ Moreover, XPS allows to quantify relative linkers ratio (%). For instance, the work reported by Zhu *et al.* studied by XPS and ¹¹B-NMR the successful and tuneable incorporation of 5-boronobenzene-1,3-dicarboxylic acid (H_2BBDC) linker into MIL-100 (Cr).¹⁹³ XPS spectra of three MIL-100 (BBDC: BTC feed ratios of 1: 4, 1: 2.3, and 1: 1.5) were collected to verify the integration of boronic acid units. The

intensities of B signal increased with the increase of BBDC: BTC feed ratio. The C1s XPS spectra could provide further information about the introduced boron functional groups, the intensity for C-B signal enhanced corresponding to the higher relative content of BBDC in MOFs, in good agreement with the deduction from boron signals in wide scan XPS profiles (*Figure 1.25. a*).

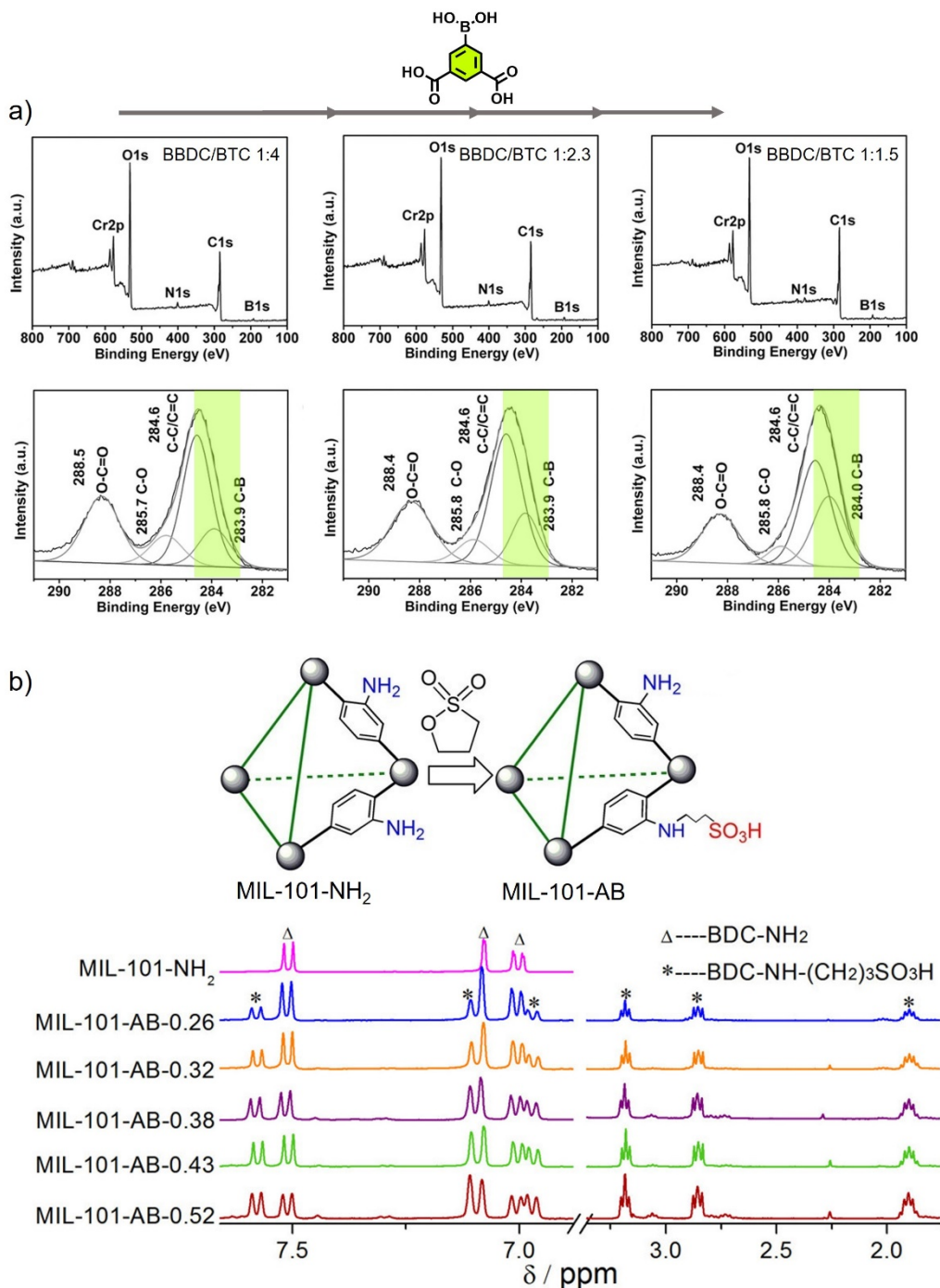


Figure 1.25. a) Wide scan XPS spectra of MIL-100-B synthesized in increased BBDC/BTC feed ratios. The magnified C1s XPS spectra of MTV-MIL-100-B. Modified from ref 193. b) Synthesis of the MTV-MOFs and ¹H NMR spectra of various MOFs after digestion. Extracted from ref 195.

Unlike XPS, which is a surface technique, Nuclear Magnetic Resonance (NMR) techniques provide information about the bulk sample. These techniques are based on the interaction of an externally applied radiofrequency radiation with atomic nuclei. Only atomic nuclei with the quantum number $l \neq 0$ are detectable by NMR spectroscopy (such as ^1H , ^{13}C and ^{15}N , ^{19}F , and ^{31}P). These NMR-active nuclei behave as tiny magnets (magnetic dipoles), capable of aligning with external magnetic fields (a process called magnetization). The magnetic response is dependent on the chemical environment of the nuclei. NMR techniques cover a broad range of possibilities of analysis based on the determination of molecular structure. They provide a qualitative analysis for study the functionalities or quantify ratios of the incorporated linker molecules. The addition of internal standard during the measurement also enables to get quantitative values. NMR methods are even helpful for determining the linker distribution in the nanometre range. The results offered by these techniques are not compromised by the crystallinity of the sample, thus allowing for the analysis of a wider variety of samples.

NMR spectroscopy techniques are divided into two huge blocks, those related to liquid phase and those to solid phase (SS-NMR).¹⁹⁶⁻²⁰¹ In this section, we detail liquid-phase NMR spectroscopy, which is probably one of the most widely used techniques to calculate the relative ratio between ligands in MTV-MOFs,^{45,52,124,142,150,183,191,193,202-204} as well as, to quantify the extent of linkers functionalization with a second desired molecule.^{195,205-207} For instance, MIL-100 was modified through the ring-opening reaction of 1,3-propanesultone with an amino group of the organic linker to combine amino and sulfo groups onto same material for designing of acid-base catalysts.¹⁹⁵ The integration of ^1H -NMR signal was used to calculate the molar fraction of the sulfo-modified linker and quantify the relation of basic and acid sites in the material (*Figure 1.25. b*). Recently, liquid-phase NMR has been used by Martí-Gastado and co-workers to evaluate the degree of functionalization in UiO-68-TZDC, which resulted an ideal candidate to incorporate a range of functionalities by inverse Electron-Demand Diels-Alder (iEDDA) reactivity (see **Chapter 4**). Up to 10 substrates of different nature (fused rings, hydroxy groups, phenyl rings, succinimide, carboxylic terminated groups, aliphatic chains, and C_{60}) were incorporated into the network remaining the crystallinity and intrinsic porosity. Integration of the ^1H NMR signals confirmed that the functionalization proceeded quantitatively, up to near 95%, except for the unstrained alkenes. Furthermore, ^1H NMR was used to follow the evolution of the reaction and to measure the kinetic profiles of the reaction in both the free ligand and the MOF, which showed the positive effects of diene reticulation on reactivity.

For this kind of measurements, the sample should be dissolved. So, it usually involves the digestion of the MOF in a D_2SO_4 : DMSO-d_6 or D_2O : NaOD mixtures to separate the linker from the metal. Hence, no information about the spatial distribution can be obtained because given the fact that the MOF structures are no longer maintained. Therefore, liquid-phase NMR is often combined with specific

techniques that provide spatial information, the most important of which are detailed below. One of the drawbacks of NMR methods is that they are limited to diamagnetic systems that suffer from potentially long relaxation times. The presence of paramagnetic metal ions causes line broadening of all NMR signals from nuclei close to the metal ion, favouring signal overlapping and hindering their analysis and quantification. Moreover, the spatial study becomes difficult in mesoporous MOFs because of low interactions between functional groups due to the enlarged distances.

3.1.3. Evaluating linker spatial distribution

The spatial arrangement of the ligands can be elucidated by different techniques, the choice of one of them depending on the properties of the material. In case of crystalline MOFs, Single-Crystal X-Ray Diffraction (SCXRD) is one, if not the most, of the most powerful techniques to determine the structure, as well as to unequivocally determine the presence of different linkers in the structure. This is especially powerful when the different linkers occupy independent crystallographic positions. For instance, SCXRD data were used to confirm each of the 11 daughter MOFs in the PCN-700 series after linker installation.¹⁴⁹ As well as, SCXRD provided information on the functionalized linker distribution along the edges of cubes in cMUV-11.⁵² However, when 2 or more similar linkers occupy the same crystallographic position, we can only refine the relative occupancy of each linker or functional group without obtaining further information about the spatial distribution of both linkers throughout the crystal. It should also be noted that with this technique we only obtain information of one crystal, which may not be representative of the bulk sample. Nevertheless, although determining the spatial distribution of linker molecules in the structure at the atomic level may become very difficult task, we can use microscopy coupled to spectroscopic techniques that allow us to obtain information about the homogeneity of the linker distribution throughout the crystals.

Energy-Dispersive X-ray spectroscopy (EDS, EDX, or XEDS) is a commonly used technique to study the near-surface composition (micrometres) of a material. Like XPS, the sample is stimulated with a high-energy electron beam that excites an electron in an inner shell, ejecting it from the shell and creating an electron hole. An electron from an outer shell can fill in this hole with the emission of a characteristic X-ray. EDX systems are usually attached to Electron Microscopy instruments (Scanning Electron Microscopy (SEM) or Transmission Electron Microscopy (TEM)) where the imaging capability of the microscope enables to identify the arrangement of the species (compositional maps). This technique allows obtaining relative ratios (%) and studying the distribution of ligands in the crystal,^{137, 208} but requires the presence of high atomic number elements, such as halogenated (Cl, Br or I) substituents, for obtaining reliable data. Matzger and co-workers recently applied this technique to study the role of reagent reactivity and solvent on the spatial

distribution in post-functionalized IRMOF-3.²⁰⁸ For that, a suite of isocyanate reagents with varying reactivity and different solvents were tested. SEM-EDX mapping of IRMOF-3 cross sections after PSM reaction showed differences in the spatial distribution of new substituents: while 2-chloroethyl isocyanate substitution provided a uniform microstructure; a core-shell microstructure was obtained after chloroacetyl isocyanate treatment (*Figure 1.26. a*). The effect of solvent was also plausible, chloroform, a polar solvent, resulted in a slight increase in core-shell character. Furthermore, authors demonstrated the utility of understanding the dynamics of PSM for preparing complex microarrangements that were also analysed by SEM-EDX mapping and line scans (*Figure 1.26. b*).

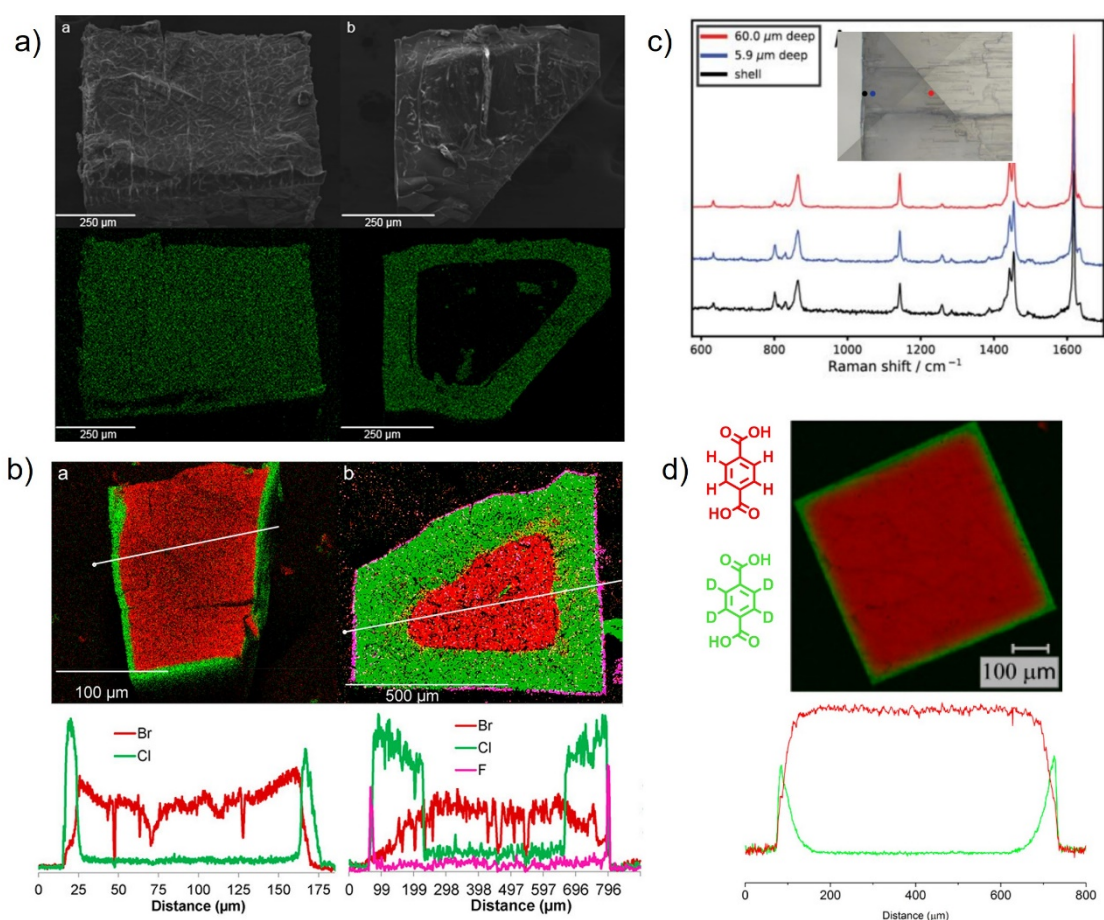


Figure 1.26. a) SEM images and EDS map showing of IRMOF-3 cross sections after PSM with 2-chloroethyl isocyanate (left) and chloroacetyl isocyanate (right). Extracted from 208. b) SEM-EDS maps and line scans of cross sections of IRMOF-3 after PSM showed the complex microarrangements formed. Extracted from 141. c) Raman spectra of cross-sectioned MOF. Spectra taken at different depths of the crystal. d) 2D-Raman maps of MOF-5 showing the core-shell distribution of exchanged linkers (green, BDC-d₄; red, BDC). Line graph from edge to edge showing BDC-d₄ concentrated on the outer edges of the crystal and decreasing toward the centre. Adapted from ref 140.

Confocal microscopy coupled to Raman spectroscopy may be also used to determine the chemical composition along the different points of the crystal providing not only chemical information,¹⁴¹ but also about the resulting microstructure. The

combination of these techniques can yield a mapping of the spatial distribution of linkers with different functional groups throughout the crystal. This feature was developed in a previously mentioned work by Matzger, where resultant core-shell microstructures of MOF-5, UMCM-8 and UiO-66 were analysed via mapping Raman microspectroscopy.¹⁴⁰ For that, the crystals were first embedded in an epoxy resin and sectioned on an ultramicrotome before analysis running. Raman maps of the sliced crystals after PSE reaction showed the formation of a core-shell architecture for the three MOFs. The incorporation of BDC-d₄ occurs at the surface and extends inward toward the centre, so the deuterated linkers signal was highest on the surface and rapidly decreasing toward the centre of the crystal (*Figure 1.26. c, d*). Although this technique does not enable quantification of the different ligands; the size of the shell can still provide an estimation of the degree of exchange. However, the obtention of the Raman spectrum of samples that display fluorescence at the wavelengths used in Raman spectroscopy can be complicated as the Raman signals may be masked by the fluorescence broad band. Also, this technique requires large crystals (> 100 μm), which are not always easily synthesised. To mitigate this drawback, confocal microscopy coupled to Surface-Enhanced Raman Spectroscopy (SERS) has been proposed as alternative.^{209–211}

Although fluorescence was one of the limitations for Raman characterization, this feature is valuable for using fluorescence-based techniques. The native fluorescence of linkers, which is generally, attributed to π - π transitions, is also used to obtain information about spatial microarrangements in MTV-MOFs. Ideally, in a multiple-linker MOF each linker emits in different regions of the spectrum when irradiated by the same wavelength laser. In this way, the fluorescence of each linker can be detected by independent channels and its spatial distribution over the crystal can be analysed. As in Raman spectroscopy, this technique requires crystal size over 100 μm for visual analysis and usually physical slicing of the crystals to obtain cross sections. Therefore, two main limitations can be identified for this method. First is the possible scenario in which the organic components emissions were indistinguishable between them. The second is that such large MOF crystals are often synthetically challenging to obtain and not suitable for all applications, as catalysis.

Nair and collaborators combined native-fluorescence confocal microscopy with NMR techniques to evaluate the resultant arrangement of mixed-linker ZIFs.¹³⁹ That work represented the first direct visual confirmation of the resultant microstructure. ZIF-8 crystals emit blue light (460 nm), and ZIF-90 crystals emit green light (505 nm) when were excited by a 405 nm wavelength laser, due to the different energetic π^* - π^* transitions.^{212,213} The combination of that fluorescence behaviour with confocal microscopy provided information on linker distribution throughout the macrocrystals (*Figure 1.12.*). Thus, the authors obtained a 3D mapping of the linker distribution near the surface as well as the interior of the crystals using true-colour fluorescence imaging, without the necessity of labelling

with dye molecules.^{146,214} Whereas the direct synthesis samples presented uniformly distributed emission at both wavelengths throughout the cross-section, which was characteristic of a hybrid ZIF with the linkers being well-mixed; the SALE ZIF-8-90 hybrid macrocrystals showed a core-shell type of compositional distribution. It was seen that the distribution of ZIF-90 linkers (green colour in *Figure 1.12.*) was limited to the outer edges of the crystals and that the interior of the crystals contain only ZIF-8 linkers (blue colour in *Figure 1.12.*). Although this technique does not provide a quantitative analysis, in the case of working with a cross section, the shell size may give a qualitative estimation of its thickness.

As is detailed in **Chapter 3**, this technique was used in the study of the spatial linker distribution in MTV-UiO-68-TZDC% samples.

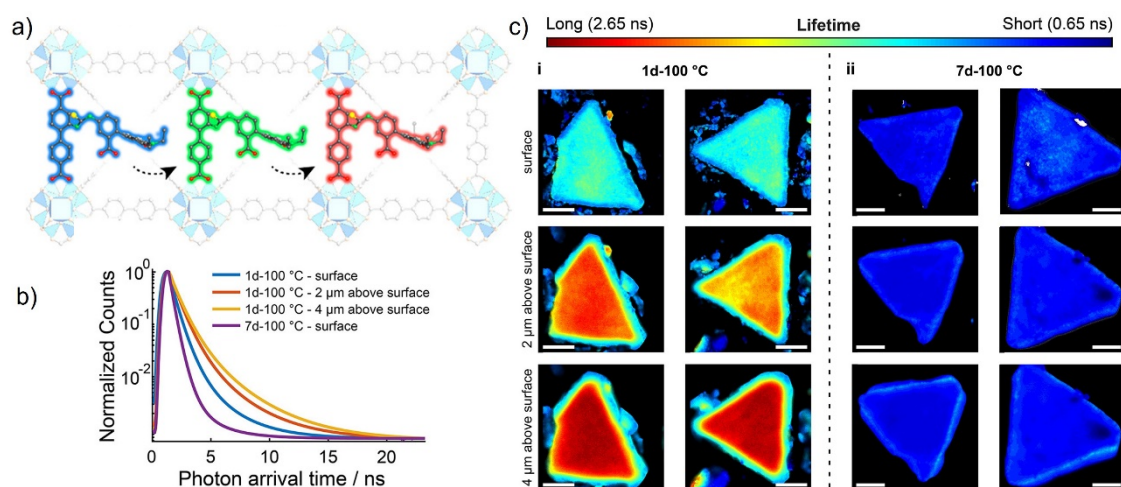


Figure 1.27. a) Scheme of linker exchange process via bulky organic linker migration along the backbone in MOFs. b) Fluorescence lifetime analysis of UiO-67 crystals after PSE. c) FLIM images of UiO-67 crystals. The scale bar is 15 μm. Adapted from ref 215.

Fluorescence Lifetime Imaging (FLIM) studies are based on the fact that the fluorescence lifetime of a fluorophore depends on its molecular environment but not on its concentration.²¹⁶ So, this technique supplies qualitative information about the spatial arrangement of the linkers within the framework.²¹⁷⁻²²⁰ Wuttke and co-workers applied fluorescence imaging combined with fluorescence lifetime analysis to examine the diversity and distribution of defects and functional groups in a UiO-67 framework with fluorescent dye modified linkers. In that work, authors established a correlation between the fluorescence lifetime and local defects in UiO-67: more defects result in shorter lifetime.²²¹ More recently, the same team elucidated the mechanism of linker migration.²¹⁵ The use of fluorescence imaging allowed to monitor the migration of the bulky BPDC-RB linker (biphenyl-4,4'-dicarboxylic acid attached with rhodamine B) across UiO-67 crystals (*Figure 1.27. a*). The heterogeneous distribution of BPDC-RB, which concentrates on the surface and declines toward the crystal interior, revealed that linker diffusion becomes the rate-limiting step of post-synthetic process. PSE samples displayed significant differences in lifetime between the crystal surface and interior (*Figure 1.27. b*). The lifetimes measured at the surface were shorter than those inside the crystals. Such

a gradient in lifetime was analogous to the previously measured fluorescence profile, which exhibits a decay in fluorescence intensity from the outside toward inside of the crystal (*Figure 1.27. c*). In this way, the authors demonstrated that the progression of PSE was accompanied by the generation of missing-linker defects.

Another promising technique is the combination of IR-spectroscopy with lateral resolution of Atomic Force Microscopy (AFM), which results in a novel method called Photo Thermal Induced Resonance (PTIR).²²²⁻²²⁵ This can also provide information about the spatial linker distribution. In the PTIR technique, also known as AFM-IR, the sample is placed on an optical prism and illuminated by total internal reflection with a pulsed tuneable IR laser, while a contact AFM tip extracts the local chemical composition. During the process, the sample is irradiated with a laser pulse resulting in local heating, sample expansion, and excitation of the AFM cantilever motion which is monitored by a four-quadrant photodetector. The local IR spectrum is obtained by plotting the maximum amplitude of the cantilever deflection as a function of the wavelength. While PTIR chemical maps are obtained by illuminating the sample at a fixed wavelength while the AFM tip scans the sample. This technique has been implemented on MOFs to study their linker heterogeneity.²²⁶⁻²²⁸ An early example was developed by Centrone and collaborators to study the structural linker arrangement in In-MIL-68 MixMOFs.²²⁹ For that propose, homolinker samples of In-MIL-68 (BDC linker), In-MIL-68-NH₂ (NH₂-BDC linker) and three multi-linker In-MIL-68 samples (BDC:NH₂-BDC %) were synthesized by different methods (direct and post-synthetic and sequential growth). PTIR spectra were collected in different sections of the crystals. The spectra of direct and post-synthetic growth sample resembled a combination of the spectra for the two homoligand MOFs, showing a homogeneous linker distribution. However, chemical maps of sequential growth sample revealed a lengthwise heterogeneous distribution of ligands. The growth mechanism was also elucidated by PTIR. The crystal's ends maps displayed a stronger intensity of the C-N stretch band from NH₂-BDC, indicating that the material grown on the seed crystals was richer in the aminated ligand as compared to the seed.

Rutherford Backscattering Spectrometry (RBS) is a novel non-invasive method which also provides information about the preferred localization of the introduced linker, as well as enables to quantify the exchange ratio. This enables to stablish the concentration ratios between constituents without any external standard. This information is achieved by detecting the energy of the beam particles after they have been elastically scattered by the Coulomb potential of the sample nuclei (Rutherford scattering). The elastic scattering provides information on the mass of the involved scattering partners which is element specific. In contrast to fluorescence or mapping Raman microspectroscopy, the procedure is rapid and not destructive since the sample does not require preliminary treatment. Moreover, the crystal size limitation is removed due to the smaller depth profiling (ca. 10 μm). RBS method was used for the first time to study PSE in MOFs in 2017 by Ott and collaborators.²³⁰ In that work,

the measurements were limited to monolayers on the substrates, so bulk UiO-66 samples were drop-cast onto silicon wafers. Fortunately, recent studies have extended RBS methods to single crystal.²³¹ The initial optimization work using native UiO-66 crystals yielded a microbeam method which avoided beam damage. The ion beam with a diameter of at most a few micrometres offered unprecedented precision in depth profiling using non-destructive backscattering spectrometry. Authors demonstrated the usefulness of this method on three case studies in single crystals of UiO-type MOF to determine: 1) the distribution of zirconium and hafnium in mixed-metal SBU UiO-66 obtained by solvothermal synthesis, 2) the distribution of linkers before and after post-synthetic introduction into UiO-66, using a heavy element iodine label as a spectrometric marker, and 3) spatial distribution of metal sites after post-synthetic metalation of UiO-67-bpyDC with PtCl₂.

In contrast to liquid-phase NMR, Solid-State Nuclear Magnetic Resonance (SS-NMR) spectroscopy has proven to be an effective tool to characterize the average distances and distributions of linkers or linker domains within MTV-MOFs when it is combined with computational modelling. Recently, some SS-NMR-based methods have been introduced for the analysis of the multiple-linker MOFs. The first method was ¹³C-¹⁵N Rotational- Echo Double- Resonance (REDOR) NMR spectroscopy which could provide information on the average distances among the linkers of two or more different types (or between different functional groups). This method combined with Monte Carlo and molecular dynamics simulations was employed for studying a series of MTV-MOF-5 (*Figure 1.28. a*) reported by Reimer and co-workers in 2013.¹¹⁶ For feasible measurements, linkers had to be isotopically labelled with ¹⁵N. REDOR measurements evaluated the average distances between the ¹³C nuclei of one functional group and ¹⁵N nuclei of another functional group. After the experimental REDOR curves were measured, they were compared to calculated REDOR curves for the different models with different distributions of functional groups (clustered, alternate, and random) (*Figure 1.27. b, c.*). Theoretical prediction of the CO₂ adsorption isotherms compared with the corresponding experimental data further confirmed the spatial arrangement of mixing linkers in MTV-MOFs. That work represented the first studied where linker spatial arrangements were fully comprehended and even more interesting it helped to predict and explain some of the exciting physical properties of synthesized MTV-MOFs.

An alternative method is ¹H spin-diffusion measurements. The advantages of this method are that isotopic labelling is not needed and the fastest compared to the REDOR-based method. However, the main drawback is the notably low resolution of ¹H MAS (magic-angle spinning) NMR spectra. To apply this method, one needs to resolve at least one ¹H NMR signal of one linker from at least one ¹H NMR signal of another linker. If this condition is met, one can measure the rate of ¹H polarization transfer between the two proton sites of two different linkers, and, in a similar way as REDOR method, compare the measured rate (measured spin-diffusion curve) with those calculated for the models with different distributions of the two linkers.

The performance of this second method was combined with density functional theory (DFT) calculation to study the homogeneous linker distribution in DUT-5.²³² More recently, this association was employed to quantitative analysis of the linker composition and spatial arrangement of functional groups and to explore the primary adsorption sites for light alkanes in MTV-UiO-66 samples.²³³ Advanced SS-NMR methods have also developed to improve the ¹H spectral resolution. Combined Rotation and Multiple Pulse Spectroscopy (CRAMPS) method may be considered as the upgrade version of ¹H MAS NMR by including ¹H homonuclear decoupling into the plain ¹H spin-diffusion pulse sequence. This improved resolution in the two-dimensional spectra in combination with computational modelling allowed to elucidate structural arrangements and determine the short-range order (SRO) parameter of mixed-linkers in ZIF-8 and ZIF-90 series.²³⁴ Although, ¹H NMR signals of many linkers employed in MOFs resonates at very similar chemical shifts, the use of ¹³C-detected version of the experiment enhances the applicability of the method, as it is the case of ¹³C-¹H CP MAS-NMR (Cross Polarization Magic Angle Spinning) which was used to study of linker substitution in 3D-Li MOFs.¹⁷⁸ More recently, the study of the acidity of MTV UiO-66-(COOH and SO₃H)²³⁵ and the characterization of mixed-metal DUT-8(Ni) have been carried out using this method.²³⁶

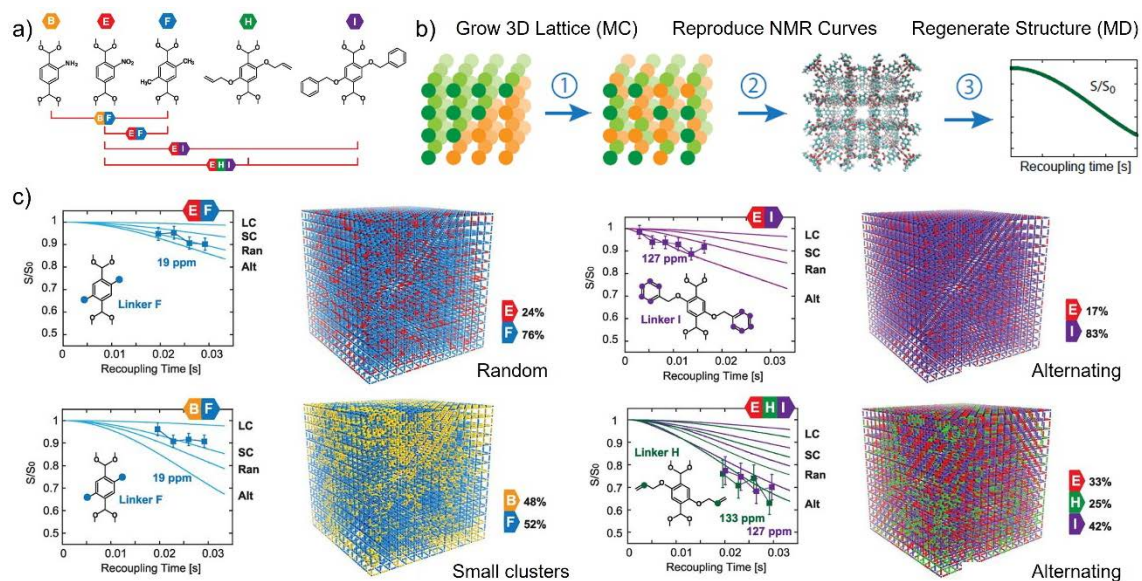


Figure 1.28. a) MTV-MOF-5 linkers. Six linkers are combined with a [Zn₄O] SBU to form MTV-MOF-5. b) Simulation steps used for generating structures and REDOR signal. Step 1 involved lattice Monte Carlo simulation in which different linker apportionments were generated. In step 2, those lattice representation was translated to the corresponding an all-atom model, from which the REDOR curve were computed in step 3. c) Experimental and calculated ¹³C{¹⁵N} REDOR curves with their derived arrangements for the different MTV-MOF-5. Adapted from ref 116.

3.2. Multivariance in the inorganic connector

For a meaningful interpretation of the effects of metal mixing on the properties of MOFs, characterization techniques should cover some relevant points, as the study of the presence and quantification of multiple metal in the structure and their local distribution which may be constituting the nodes, forming part of the organic ligand, inside the pores or even forming part of different phases; as well as, the coordination environment and oxidation state of the metals, and their global distribution into the frameworks.

3.2.1. Evaluating multiple-metal presence

The initial characterization of networks incorporating metal variance is based on confirming the presence of multiple metals. As in the case of the linkers, PXRD might provide a general insight into presence of different metals in the structure. As in the case of multiple-linker MOFs, PXRD can reveal unwanted phase formation and the occurrence of monometallic instead of multiple-metal MOFs. In addition, the gradual evolution of the diffraction peak positions, according to Vegard's law^{237,238} is sometimes regarded as a proof of random metal mixing (*Figure 1.29. a*). Nevertheless, deviations from such linear relation might be interpreted as indications of cluster formation in solid state solutions.²³⁹ However, although X-ray diffraction techniques are very powerful for determining the structure of the material, it should be used with caution when trying to evaluate the relative occupancy of different metals that occupy the same crystallographic site. This is due to the low sensitivity of X-Rays to distinguish between elements of similar atomic number. This makes it necessary to complement X-ray diffraction measurements with other techniques like Neutron powder Diffraction (NPD) measurements to be able to refine the relative occupancy of different metals in the crystal structure of the MOF. For instance, Monge and co-workers had to complement SCXRD with NPD to resolve the occupancy of the metal sites in Zn-Co multi-metal MOFs. NPD study at variable temperatures for different Zn-Co ratios samples evidenced a structural phase transition at low temperatures for which the metal coordination environments were distinct. The multiphase Rietveld refinement confirmed the percentage of each phase based on the ratio of the integrated intensities, previously estimated by ICP. The metal sites in the original phase (exclusively tetrahedral) were refined as zinc atoms, whereas for the transformed phase, the tetrahedral site was refined as fully occupied by zinc, and the octahedral site as fully occupied by cobalt.

In some case, the combination of PXRD and SCXRD has been used to determine the metal composition in greater depth. Nice example was reported by Kim in 2009, in which the analysis of *in situ* SCXRD and PXRD techniques were combined with optical microscopy during the metal exchange reaction to study of the kinetics of post-synthetic metal exchange in Cd-Pb and Cd-Ln MOFs.⁶⁷ During the

transmetalation process samples were soaking during variable times in metal-exchanged solutions. The gradual colour change was followed by optical microscope images of crystals. The *in situ* SXRD study revealed essentially the same framework structure with a gradual decrease of the Cd occupancy (and concomitant increase of the Pb occupancy) with increasing soaking time, in agreement with ICP-AES analysis. Finally, the *in situ* PXRD patterns confirmed the preservation of bulk crystallinity during the process.

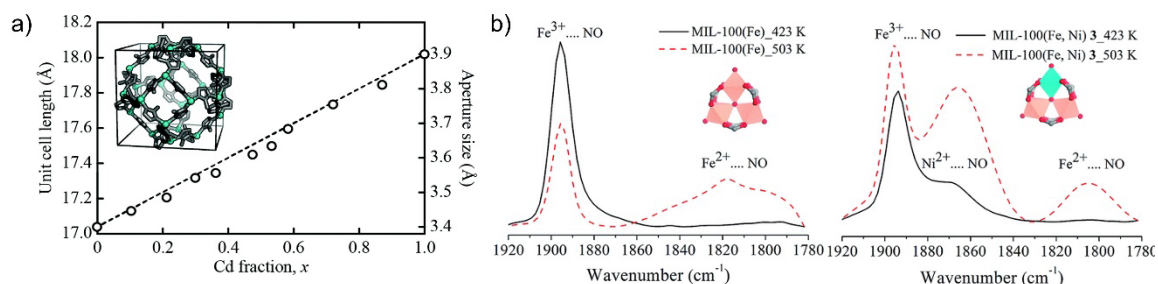


Figure 1.29. a) Compositional dependence of the unit cell length and approximate aperture size in the ZIF-8(Zn-Cd). The dashed line denotes the Vegard's law limit. Extracted from 238. b) IR spectra of MIL-100(Fe-Ni) (left) and monometallic MIL-100(Fe) (right) recorded after introduction of an equilibrium pressure of NO. Spectra after activation of the solid at 423 K are represented with a black line while spectra after activation of the solid at 503 K are represented with a dashed red line. Extracted from ref 240.

The adsorption of small IR-active molecules can be used for the characterization of heterometallic MOFs with coordinatively unsaturated sites.²⁴¹ The comparison of the band positions in heterometallic and the monometallic frameworks can reveal the presence of multiple metals within the framework. As was the case of Serre and collaborators, who confirmed the presence of heterometallic MIL-127(Fe-M) carrying out *in situ* infrared spectroscopy analysis,^{242,243} NO adsorption experiments, monitored by *in situ* IR spectroscopy showed the dependence of $\nu(\text{NO})$ bands of adsorbed nitrosyls on the nature and the oxidation state of the accessible cations. Room temperature NO adsorption on the activated MIL-127(Fe-Ni) at 423 K revealed two $\nu(\text{NO})$ bands (Figure 1.29. b). The high wavenumber band indicated the presence of NO adsorbed on Fe²⁺. After activation at 503 K, new sharp $\nu(\text{NO})$ band was detected, which was not attributable to pure iron-based MOFs. Its wavenumber was close to that reported for NO interaction with the Ni²⁺ cations supported on metal oxides. Thus, that band supported the presence of coordinatively unsaturated Ni²⁺ sites. In certain cases, an intermediate wavenumber might be observed, indicating that two different types of metals are in close vicinity and interacting with each other.

Raman is also widely used to identify different metallic species.²¹⁰ The presence of multiple metals in the cluster may be evidenced by the shift of the bands due to different nuclear charge and ionic radius or even by the splitting of the M-donor atom peaks into two.²⁴⁴ Moreover, Raman allows to detect the presence of new ions

not present in the original structure necessary to compensate the charge of the heterometallic cluster.²⁴⁵

As is the case for multivariance in the organic connector, physisorption measurements permits to identify the presence of the new metal species, either by changes in the adsorption capacity of small organic molecules or by detecting changes in adsorption behaviour, which are sometimes attributed to synergistic effects, due to the proximity of two metals.^{246–254} In many examples, the incorporation of a second metal in the cluster lead to a significant increase in adsorption capacity. For example, Kaur *et al.* prepared a heterometallic Co-Zn-ZIF-8 with varying Co contents.²⁵² CoZn-ZIF-8 showed an enhancement of the surface area by 40% and the pore volume by 33% as compared to monometallic Zn-ZIF-8, probably due to the increase of robustness. At 77 K and 1 bar, Co₇₅Zn₂₅-ZIF-8 showed an enhancement of ~30 % in the CO₂ and 23 % in the H₂ uptakes as compared to Zn analogous. Similar effect was also observed in MOF-74. The increase of Co content in MOF-74(Zn) was denoted by a rise of H₂ adsorption capacity.²⁴⁷ Botas *et al.* found a correlation between the isosteric heat of adsorption (Q_{st}) for H₂ and the band gap energy values of Zn_{1-x}Co_xMOF-74, implying that H₂-metal cluster interactions have a more decisive role in H₂ adsorption.

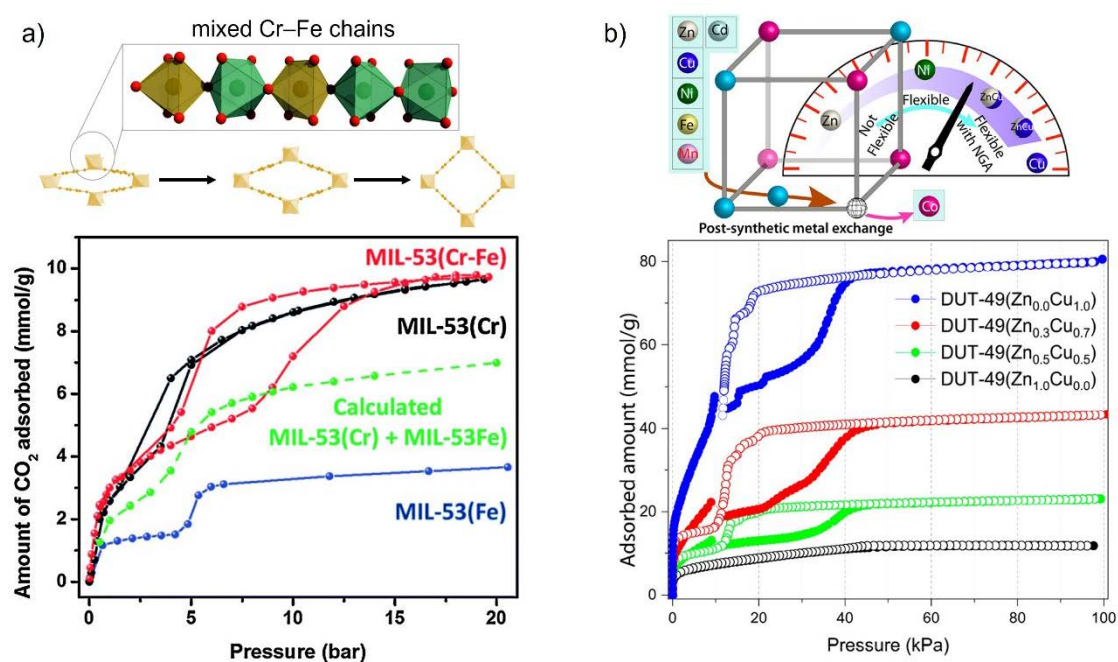


Figure 1.30. a) Tuning the breathing behaviour of MIL-53 by cation mixing. b) Tuning NGA properties of DUT-49 through post-synthetic metal exchange. Adapted from ref 246, 254, respectively.

The degree of SBU substitution in multi-metal MTV-MOFs can also have an impact on network flexibility of flexible MOFs, which can be detected by physisorption measurements as was illustrated by multi-metal-MIL-53.^{248,256} CO₂ sorption tests showed completely different adsorption profiles for MIL-53(Cr-Fe) and homometallic MIL-53(Cr) and MIL-53(Fe) solids.²⁴⁸ Homometallic phases exhibited

stepped sorption isotherms, corresponding to different pore openings. In contrast, MIL-53(Cr-Fe) showed a pronounced effect on the breathing behaviour (*Figure 1.30. a*). Thus, in terms of ease of pore opening, the mixed phase was intermediate between the pure Cr ('easy' to open) and Fe ('hard' to open) solids, demonstrating the effect of the presence of mixed Cr-Fe chains on the flexibility.

More recently, a similar effect was reported by Kaskel and co-workers.²⁵⁵ The metal exchange in paddle wheel centres of DUT-49(M) frameworks (M = Mn, Fe, Ni, Zn, Cd) resulted in a tuneable porosity and the *negative gas adsorption* behaviour (NGA) (*Figure 1.30. b*).²⁵⁷

3.2.2. Evaluating relative ratio and concentration of metals

While in the case of the characterization of multiple-linker MOFs, the EDX technique only provided qualitative information; the high atomic number of the metals allows to assess the global metal concentrations into the framework.^{109,110} In addition, EDX coupled to TEM or to SEM provides elemental composition with a spatial resolution ranging from the nm to μm , respectively. EDX analysis is limited to depth of the order of nm and single region. Thus, since only small volumes are probed, data obtained for many positions in the sample is averaged for measuring global concentrations. The degree of metal exchange at different stages of topological transformations of MUV-10 was evaluated by EDX-SEM as is detailed in **Chapter 5**.

Additionally, techniques like Atomic Absorption Spectroscopy (AAS),²⁵⁸ Inductively Coupled Plasma-Mass Spectroscopy (ICP-MS)^{259,260} or Inductively Coupled Plasma-Atomic Emission Spectroscopy (ICP-AES)^{204,261} are ideally suited to determine absolute element concentrations precisely. They rely on the detection of optical or mass spectra of atoms or small molecular fragments in the gas state. Hence, their main drawback is that they are destructive. However, X-Ray Fluorescence (XRF) can be used as non-destructive alternative²⁶² but requires careful calibration. These techniques are used as complements to other more sophisticated techniques to get deeper information of metal environment and distribution.

3.2.3. Evaluating metal coordination environment and oxidation state

The influence of the oxidation state and coordination environment of a metal ion on its nuclear and electronic energy levels, as well as on the characteristic vibrational frequencies, are the basis of spectroscopic identification of metal sites and oxidation states in MOFs. Although spectroscopic techniques are highly sensitive to small changes in the cation environment, in multi-metal MOFs, cations may be distributed in a variety of coordination environments. So, the interpretation of spectra is not always unambiguous, and the signal is affected by a high number of factors. Therefore, although spectroscopic techniques are very powerful, for the analysis of metal complexity in MOFs it is often required to combine the spectroscopic information with theoretical models and calculations to be able to

draw meaningful conclusions about the metal environment and oxidation state of the different metallic ions. Some of these spectroscopies as Electron Paramagnetic Resonance (EPR) or Mössbauer are considered specific for some type of metals. In turn, X-ray absorption (XAS) is suitable for a wider range of metals. For none of these techniques its applicability is limited by the crystallinity of the material, thus single crystals, polycrystalline as well as amorphous samples can be analysed.

EPR spectroscopy is a fruitful method to provide information about the chemical environment of paramagnetic metal ions. The basic principles behind this technique are very similar to the NMR, except that EPR focuses on the interaction of an external magnetic field with the unpaired electron(s) in a molecule, rather than the nuclei of individual atoms. EPR may probe the incorporation of additional metal, as well as give the information about the electronic ground state of a paramagnetic species and their coordination symmetry and environment.²⁶³ The metal variance in frameworks where all metal nodes are occupied with paramagnetic ions, such as MIL-47(V),²⁶⁴⁻²⁶⁶ MIL-53(Al),²⁶⁷⁻²⁶⁹ DUT-8 (Ni),²⁷⁰ DUT-5 (Al)²⁶¹ or Cu₃(BTC)₂ (HKUST-1),²⁷¹ are usually characterized by this technique. These materials yield broad and featureless EPR spectra at room temperature. Thus, the insertion of additional metal ion implies a change in the EPR signal. In this regard, EPR has been widely employed to study Cu-based heterometallic MOFs,^{204,272-274} especially for HKUST-1.^{109,275-278} The antiferromagnetic coupling between Cu²⁺ ions in the HKUST paddle wheel shall results in a EPR silent S = 0 ground state at low temperatures. In turn, when that dimer is bimetallic a reasonable EPR signal is accessible. These changes were illustrated in a couple of Pöppl's works in which the presence of mixed Cu-Zn paddle wheel SBUs was evidenced by the broadening of the characteristic lines of homometallic HKUST^{275,276} which was attributed to the increase of dipolar coupling between mixed paddle wheels. A completely different behaviour was exhibited at higher temperatures (> 100 K) when the active S = 1 triplet state was populated and therefore, HKUST displays a broad EPR spectrum. So, in the cases when the measurement was at room temperature, the formation of heterometallic paddle wheel was evidenced by the emerging of new sharp signal, as was reflected for HKUST(Cu-Rh)²⁷⁷ (*Figure 1.31*). That behaviour was also observed in the heterometallic version of HKUST(Cu-Ti), MUV-102¹⁰⁹ (see **Chapter 5**). The incorporation of diamagnetic Ti(IV) ions in heterometallic Ti⁴⁺-Cu²⁺ paddle wheel units left uncompensated S = ½ spins that could be detected with EPR at room temperature. The appearing of new signal in EPR spectrum confirmed the presence of paramagnetic Cu²⁺ units indicative of the formation of the heterometallic TiCu cluster compared to the minimum contribution of that signal in the spectrum of HKUST-1.

In some studies, *in situ* EPR has also been performed to study the changes elicited by guest molecules, such as gases, in the cluster.^{236,279}

Mössbauer spectroscopy offers similar structural information to EPR, however, this technique is focused on specific ions, since it is necessary to have a convenient

source of gamma ray which usually consists of a radioactive parent that decays to the desired isotope. In the practice of MOF research, Mössbauer spectroscopy has so far been restricted to studies of ^{57}Fe .²⁸⁰⁻²⁸² Nice examples of the use of this technique were published by Serre where bimetallic MIL-100(Ni-Fe)²⁴³ and, more recently, 101(Cr-Fe)²⁸³ were synthesized and characterized for their catalytic application.

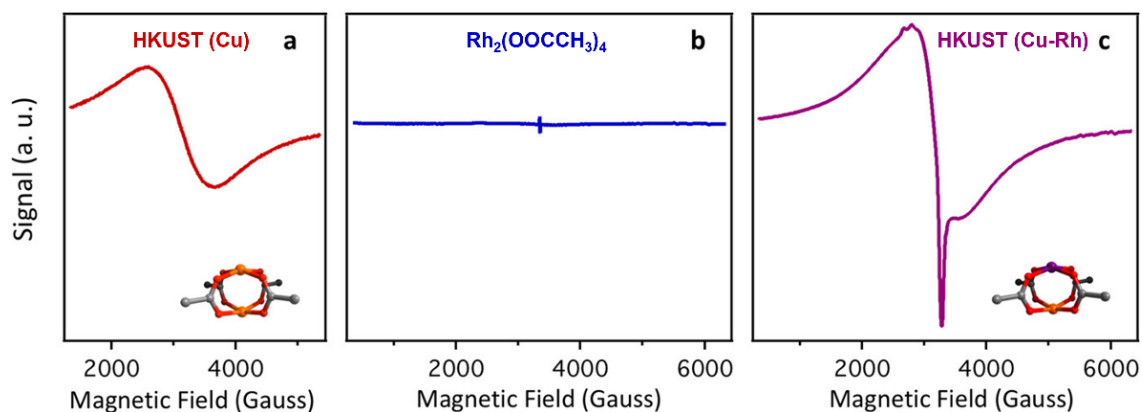


Figure 1.31. EPR spectra at room temperature of a) monometallic HKUST-1 (Cu), b) Rhodium(II) acetate, and c) heterometallic HKUST-1 (Cu-Rh). Modified from ref 277.

XAS is a powerful technique to investigate the short-range order around selected atomic species. So, it is probably the most efficient and generally applicable for the determination of oxidation state and coordination environment of multi-metal-MOFs characterization.²⁸⁴ The sharp edges at the photo-ionization energies of atomic core levels are unique for each atom species and thus provides chemical composition information. Furthermore, the edge energy positions are slightly shifted by the oxidation state of the metal and by its chemical binding state. Unfortunately, the main restrictions of the method are based on the experimental limitations. Generally, to carry out this type of experiment, X-ray synchrotron radiation facilities are required.

The XAS spectrum can be divided into two energy regions whose analysis provides different information and gives rise to two different techniques: the near edge region of this spectrum is associated to X-ray Absorption Near Edge Structure (XANES) technique and the high energy range extending to Extended X-ray Absorption Fine Structure (EXAFS) technique. Concerning XANES, the spectra not only provide oxidation and binding state information from the position of the edge, but also reveals information about the metal coordination geometry.^{75,80} For absolute determination this requires a calibration with compounds for which the oxidation state is known and the chemical environment of the metal ion is comparable to analysed compound. XANES seems very effective to elucidate the oxidation state of the metals coordinated to metalloligands.^{75,78,79,82,85,87} This technique has been widely employed by the Lin group, who have employed XANES to determine the oxidation states of the Ir,⁷⁹ Fe-Cu²⁸⁵ or Co⁷⁸ centres in functionalized Zr-based MOF, the Pd species in Al-MOF^{82s} as well as Fe-Mn centres in Hf-MOFs.⁸⁵

The quantitative fitting of EXAFS data yields information on the distance of neighbouring atoms, their number of neighbours and chemical identity in the first coordination shell, providing a clear proof of metal substitution in the metal-inorganic nodes. The presence of a second metal species in close vicinity, usually in the same SBU, have a significant influence in the spectrum. In some cases, where the disorder in the nearest metal ion shells is not detrimental and the different contributions to that spectrum can be assigned, the identification of nearest metal shell is also possible. Recently, Peng *et al.* introduced EDTA into Zr₆ cluster of MOF-808 to enhance the capture of heavy metal ions²⁸⁶ (Figure 1.31. a). XANES was used to identify the local coordination environments of EDTA in MOF-808-EDTA. The position of the Zr K edge and the corresponding shape were almost the same for both the samples, indicating similarities in the Zr⁴⁺ coordination environment (Figure 1.31. b). A very slight shift of absorption edge indicated that Zr⁴⁺ got electron when formate groups were replaced by EDTA in MOF-808. To get more detailed structural information about the local Zr⁴⁺ environment, EXAFS data were collected and subsequently the Fourier-transformed EXAFS spectra were obtained (Figure 1.31. c). The changes in the coordination number of O around Zr⁴⁺ suggested the EDTA was coordinated with Zr₆ cluster by single -COOH group of EDTA. Therefore, the remained five binding sites of EDTA can be used as a working group for metal ion capture. As in the below example, in most recent works both techniques are combined to extract more complete information from the entire XAS spectrum.^{79,89,92,204,274,287-294}

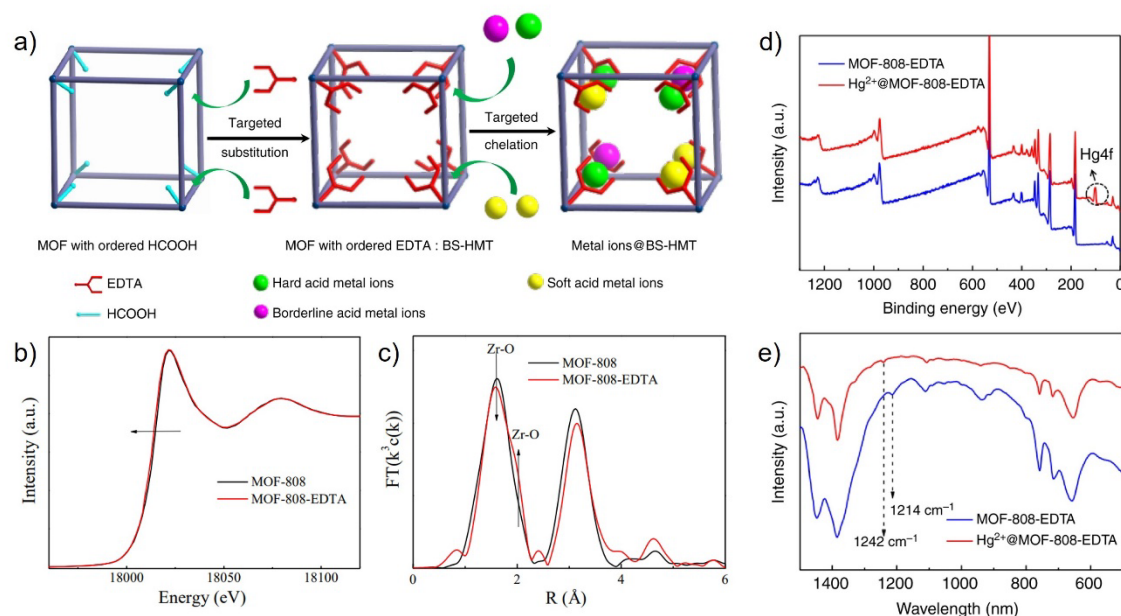


Figure 1.31. a) Schematic illustration of post-synthetic modification in MOF-808 to obtain MOF-808-EDTA as broad-spectrum heavy metal ion trap. b) XANES spectra and c) Zr K-edge EXAFS spectra for Zr₆ cluster in MOF-808 and MOF-808-EDTA. d) Strong chelation between Hg²⁺ and EDTA in MOF-808-EDTA were verified by d) XPS and e) FT-IR. Modified from ref 286.

More recently, the combination of EXAFS analysis with Pair Distribution Function (PDF)²⁹⁵ and simulations has been used to analyse in detail the local structure of decorated clusters^{296,297} or the metal-complex distribution within the multi-metal framework.²⁹⁸ The PDF technique is based on total scattering experiments, typically using a high-energy X-ray synchrotron source or neutrons. It analyses both Bragg and diffuse scattering signals simultaneously, providing powerful information at the local- and intermediate-range scales. In contrast to EXAFS spectroscopy, PDF is not an element sensitive technique and provides “in one shot” the entire structural information of a given material. The experimental data can be correlated with computational and structural models. For example, this combination was employed to study the local structure of a nickel-ALD-modified NU-1000.²⁹⁷ Chapman and co-workers proved the attachment of the Ni₄O_xH nanoclusters to the Zr₆ clusters of the MOF by comparing the PDF data from the pristine NU-1000 and the functionalized structure. The presence of an additional signal linked to the Ni···Zr distances was decisive. By combining those results with modelling and EXAFS analyses results, the authors hypothesized that the local structure and the orientation of the ALD-deposited Ni₄O_xH clusters within the NU-1000 material. The results demonstrated that the added nickel-oxo species are located within the small pores, by bridging the Zr₆-clusters, resulting in the formation of heterobimetallic Ni–Zr–O nanowires in the MOF (*Figure 1.32.*).

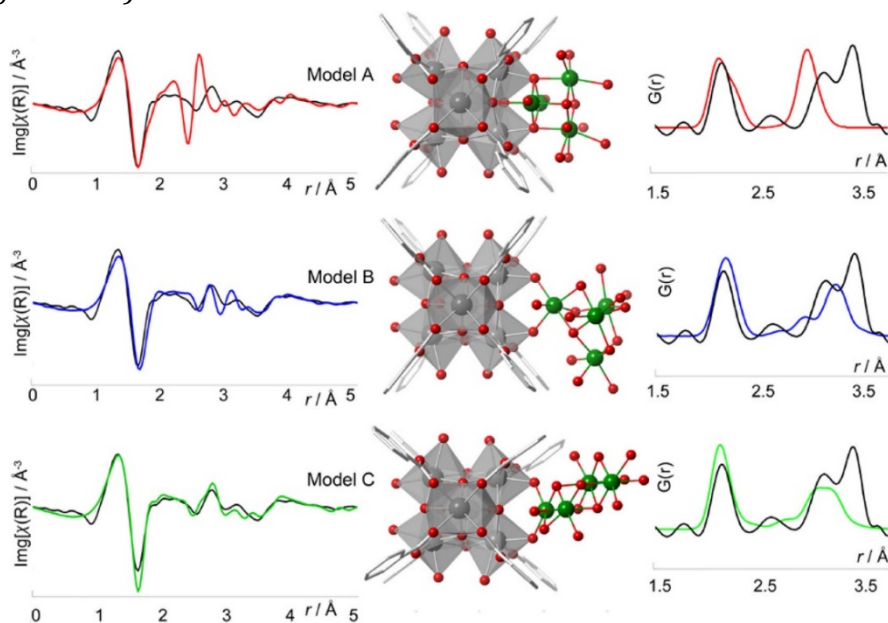


Figure 1.32. Multiple models of a Ni₄ cluster attached to a MOF Zr₆-oxo cluster and a comparison of the corresponding simulated Ni K-edge EXAFS (left) and PDFs (right, Ni–Ni, Ni–O and O–O correlations) with the experimental data (black). Model C in green provides the best match to the experimental data, for both EXAFS and PDF. Extracted from ref 297.

Sometimes, the XAS analysis of multi-metal MOF is combined with XPS. Whereas XPS supply qualitative information about linkers within the frameworks; in case of metals it can be also used to confirm their oxidation expected states^{96,286,290,299–303} (*Figure 1.31. d*). Just like XANES, XPS provides information about relative

abundance^{292,304,305} of the different metal species and their coordination environment. Deng and collaborators reported an approach to bind a range of metal ions into Zr₆ nodes of PCN-MOFs and release them in presence of cysteine derivatives. The quantitative binding and dissociation of metals were evidenced by XPS.³⁰⁶ The mixed-linker PCN-MOFs were prepared by a pair of amino-based tritopic linker and a carboxylate-base monotopic linker which choice determined the size of metal-binding site. Specially, the binding of Cu²⁺ quenched the fluorescence of the crystal and functioned as a switch-on sensor to precisely detect the concentration of biomarkers, such as *L*-cysteine (Cys) in urine. XPS spectra revealed a shift in the binding energy of N in linker and Cu²⁺ when the Cu²⁺ was coordinated. After Cys removal treatment the binding energies returned to the original position indicating the complete dissociation.

3.2.4. Evaluating metal spatial distribution

When it comes to obtaining the distribution of metals in the network, the availability of crystals of sufficient size facilitates the task and may determine the choice of the characterization technique. For multi-metal MOFs samples in which the crystal size is larger than 100 μm and the metal ions exhibit well distinguishable colours, optical microscopy is a good candidate to assess the metal distribution.^{145,307,308} This was illustrated by Song *et al.*, who visually tracked the post-synthetic transmetalation process in Co-MOF deep purple crystals (~ 300 μm) when were soaked in Zn(NO₃)₂ DMF solution at an ambient temperature for different times.¹³³ The optical images of single crystals clearly revealed that the metal exchange proceeded from the outer surface of the crystal towards the centre. The samples from 4 to 12 hours presented a well-defined core-shell arrangement with deep purple core and colourless vertices (*Figure 1.33.*).

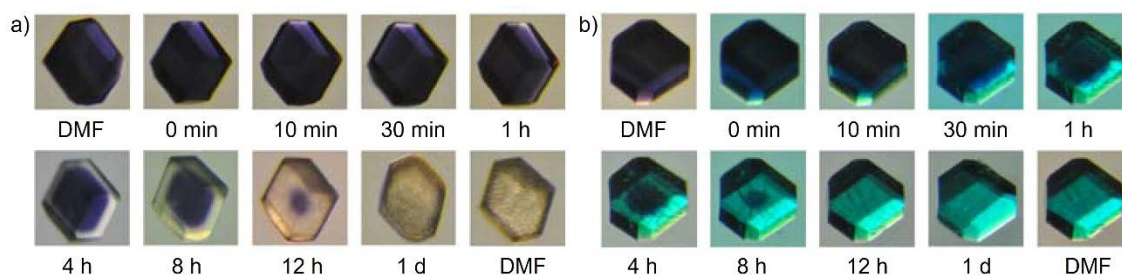


Figure 1.33. Post-synthetic metal exchange leading to visible core-shell particles in reaction time (from 1 to 12 hours) and to a complete metal exchange with reaction time larger than one day. Co-MOF was submerged in a) 0.1 M Zn(NO₃)₂ and b) Cu(NO₃)₂ DMF solution at an ambient temperature. Extracted from ref 133.

When crystals display smaller dimensions, electron microscopy becomes necessary and are the characteristic X-rays emitted by atoms that get ionized by the incident electron beam which are used for element analysis (EDX). The resolution of EDX elemental mapping coupled to SEM largely depends on the interaction volume of the incident electrons with the sample and can go up to several millimetres. In many

studies, EDX metal compositions closely resemble the bulk compositions and mapping images suggest a homogeneous distribution over the sample due to the lack of detailed analysis. A notable exception was Yaghi's work in which extensive SEM-EDX analysis of MTV-MOF-74 revealed remarkable inhomogeneity in the metal distribution,⁶⁶ even for the binary samples. In addition to concentration differences between diverse crystallites, authors also reported variations within same crystal (*Figure 1.34. left*). Those findings were latter supported by Jiao *et al.* work.³⁰⁹ Sometimes, the combination of EDX-SEM with XRF elemental mapping can be useful to determine spatial metal distribution, such as the work reported by Chin *et al.*²⁶⁰ where that combination was used to confirm the presence and location of Zn²⁺ and Co²⁺ on ZIF-8/ZIF-67 Janus particles (*Figure 1.34. middle*).

Whenever higher resolution and selectivity is required, EDX can be detected with higher electron energy beams for very thin samples, coupled to STEM.^{132,134,262,310} Thus, STEM-EDX mapping studies are indispensable for revealing the metal distribution in μm and sub- μm sized multi-metal MOF. This was illustrated by Van Der Voort and collaborators who exploited that approach to reveal the effect of the synthesis conditions on the dispersion of metals ions in Cr/V-MIL-53.²⁶² TEM-EDX measurements were recorded at the edge and in the centre of the crystal, giving an indication of the variation in metal concentration. Whereas the solvothermal crystals clearly showed a uniform dispersion of metal ions in the lattice with no variation of the metal ratio. The micro-wave synthesis led to core-shell compounds with a mixed core and a homogeneous shell (*Figure 1.34. right*).

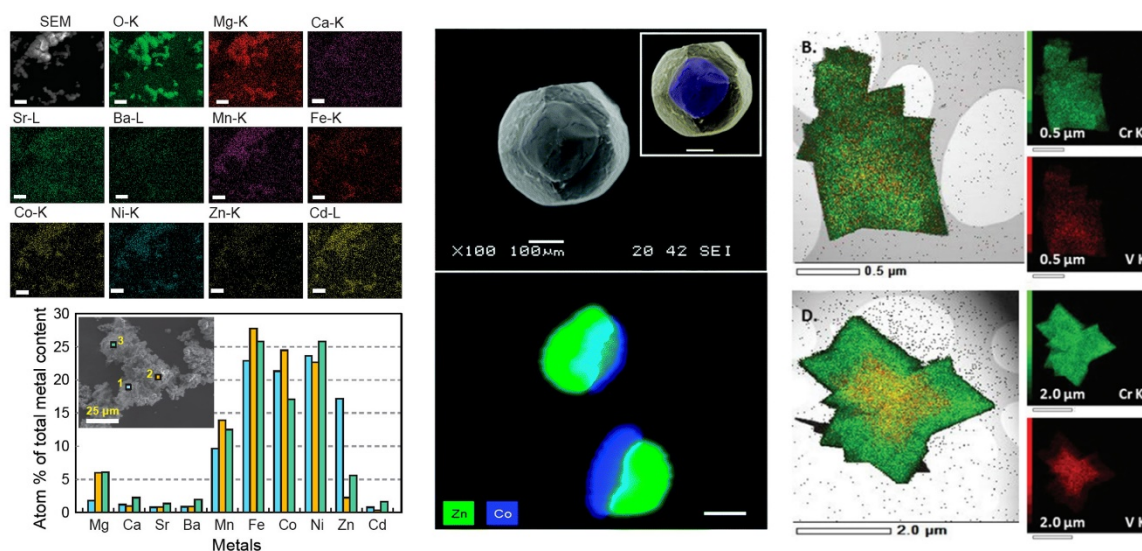


Figure 1.34. Left. EDX mapping shows the metal distribution. SEM-EDX analysis revealed remarkable inhomogeneity in the metal distribution in MTV-MOF-74 samples. Extracted from ref 66. Middle. SEM-EDX mapping showed ZIF-8/ZIF-67 Janus particles. Extracted from ref 260. Right. STEM-EDX mapping demonstrated the effect of reaction conditions on spatial metal distribution. Extracted from ref 262.

As we have shown in **Section 3.2.3.**, techniques such as FT-IR, XPS or Mössbauer may be very sensitive to the nearest coordination environment of the metals, so these techniques may provide insight about metal distribution. Deng and collaborators based their spectroscopic assessment of cation mixing in the SBUs mainly on XPS results.¹¹⁴ The analysis of the spectra allowed to difference between two possible spatial arrangements of metals. For instance, while $(\text{Mn}_{1.45}\text{Fe}_{1.55}\text{O})_2(\text{TCPP-Ni})_3$ formed domains with mixed monometallic SBUs, $(\text{Ni}_{2.07}\text{Fe}_{0.93}\text{O})_2(\text{TCPP-Co})_3$ displayed Fe and Ni metals were randomly distributed in the same SBU (*Figure 1.11.*). In the case of Fe and Mn, the observed binding energy was like monometallic frameworks. In contrast, shifts of the binding energies were observed for the mixed-metal frameworks containing Fe and Ni, which clearly indicated the close vicinity of those metals within the SBU.

The mindful analysis of FT-IR spectra can be helpful to determine metal arrangements. Serre and collaborators found that the frequency of the FT-IR active bending mode of the bridging OH in MIL-53(Fe/Cr) was very sensitive to the nearest metal environment.²⁴⁸ The mixed MIL-53(Fe/Cr) spectrum showed three $\delta(\text{OH})$ vibrational modes with comparable intensities. Two of them appear at the same frequencies as for the pure MIL-53(Cr) and MIL-53(Fe) compounds and were therefore attributed to $\text{Cr}(\mu^2\text{-OH})\text{Cr}$ and $\text{Fe}(\mu^2\text{-OH})\text{Fe}$ vibrations. The third band appearing at the intermediate position was thus specific to the mixed cation solid and is attributed to $\text{Cr}(\mu^2\text{-OH})\text{Fe}$ moieties, univocally proving the presence of mixed Cr-Fe chains within the solid. From the intensities of each type of structural $\mu^2\text{-OH}$ group, authors concluded that those moieties occurred in concentrations as expected for random occupation of the metal nodes by the two metals.

Recently, Yaghi and co-workers used Atom Probe Tomography (APT) to reveal the MOF sequences in real space and at the atomic scale.³¹¹ In this technique, the sample is exposed under laser pulsing, thus atoms are evaporated from the surface of the sample and projected onto a position-sensitive detector. The information from the position-sensitive detector is obtained layer-by layer so that a series of two-dimensional maps are obtained, which are then integrated into a 3D map. In the case of multi-metal MOFs, MOF-74 crystals were synthesized by varying the metal combination (Co/Cd, Co/Pb, and Co/Mn) and synthesis temperature (120 and 85 °C). APT detection efficiency allowed them to identify four types of metal sequences depending on synthetic conditions. Random sequences, short duplicates of two to four metals and more than four as well as sequences of insertions of a single metal into duplicates of another metal were found (*Figure 1.35.*). That report represented the first solid evidence of sequencing of metals in MTV-MOFs, and even more interestingly, it may help to predict what particular sequence encompasses a unique function of a MOF to guide *sequence-to-function* selections.

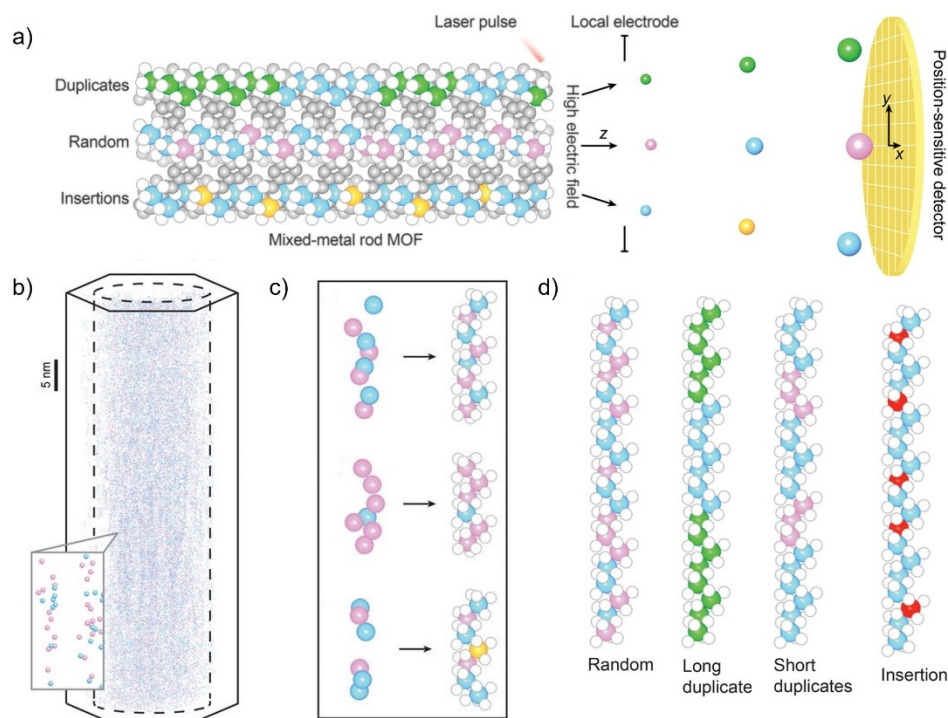


Figure 1.35. a) APT experimental approach. b) 3D-APT reconstruction shows all the metals detected (56.605 in total) from a single crystal of MOF-74-(Co-Cd) in a 3D space. c) Metal chains extracted from the raw data were reconstituted into metal-oxide rod SBUs. d) The structure models of metal-oxide rod SBUs. Adapted from ref 311.

MAS-SS-NMR can be also a profitable probe for local clustering. Based on the chemical shift of the corresponding signal, the local environment can be analysed and eventually other metal species in close vicinity could be detected. By using ^{13}C CPMAS and ^{89}Y MAS NMR experiments the random metal distribution was confirmed on a series of lanthanide-based MOF with various yttrium and lanthanum contents.³¹² ^{17}O MAS-NMR supported by ^{27}Al NMR experiments were used by Ashbrook and collaborators to determine the distribution of Al and Ga in mixed-metal MIL-53 materials.³¹³ The analysis of the signals originating from the metal bridging hydroxyl groups showed only a small proportion of $\text{Al}(\mu_2\text{-OH})\text{Ga}$ moieties, while most of the hydroxyl groups bridged Al/Al or Ga/Ga pairs revealing a not completely random metal distribution. Later, Mali *et al.* demonstrated the random incorporation of Al and Fe in mixed-MIL-100 combining ^{27}Al NMR experiments with spectroscopic techniques.²⁸² Unlike the above example, the decomposition of the ^{27}Al NMR spectrum of MIL-100(Al/Fe) into three contributions showed that their relative intensities were consistent with the random incorporation of Fe and Al into the trimers.

4. Heterogeneity and complexity yield enhanced MOF properties

The increase of complexity in MOFs can also result in the modulation of their properties. Individualized pore programming creates multiple functions that can act sequentially or in parallel which can in turn lead to the appearance of synergistic effects. Thus, multiple-component MOFs may be considered as suitable candidates for transferring the complexity observed in biological systems in homogeneous phase into solid materials; thereby broadening their range of applications for addressing real-world concerns.

In the following subsection we present some of the most recent advances in different research fields, that share the use of complex MOFs to render an improved function compared to their single component counterpart.

4.1. Gas storage and separation

Some of the earliest efforts to obtain multiple-component systems were related to improve the gas adsorption and separations properties of MOFs, as was evidenced by the earliest examples of Yaghi multivariance-MOFs.⁴⁵ MTV-MOF-5-EHI displayed up to 400 % better selectivity for CO₂ over CO compared with pristine MOF-5 (*Figure 1.4.*). In addition, the presence of -NH₂ or -OCH₃ in MTV-MOF-177 resulted in an enhancement of hydrogen uptake of 25 % respect the parent unfunctionalized structure.⁴⁷ Those works demonstrated that the combination of different functional groups modifies the adsorption properties, achieving in some cases a substantial enhancement, which was much larger than expected compared to the simple combination of their constituents.^{233,314} More recently, Dan Zhao and his team employed MTV strategy to prepare fluorine-functionalized-MIL-160 membranes.³¹⁵ The multivariate material exhibited a 11 % increase in selectivity for CO₂/CH₄ separation and a 31 % increase in CO₂ permeance compared to those of the MIL-160 membrane. Also in 2021, Martí-Gastaldo group reported the enhancement on N₂ adsorption due to the controllable incorporation of -OCH₃ functionalized linker in MTV-hydroxamate titanium-organic polyhedral, denoted as cMUV-11 (see **Chapter 2**). Low loading of -OCH₃ group resulted in an increase of the BET surface area value of 20 % with respect those value of the non-functionalized cage.

Mixed-linker multicomponent MOFs also present benefits in their gas adsorption properties.^{28,148,152,163,165,174,175,316,317} Such as FDM-8, a quinary framework where the existing hierarchical pores enabled to obtain a high working capacity what qualifies FDM-8 to be among the best materials known for high-pressure methane storage.¹⁷⁵ In addition, CUB-30, a quaternary framework from CUB-MOFs family¹⁶⁴ (*Figure 1.16.*), stood out for presenting an unprecedented high preference for cyclohexane adsorption over benzene at low partial pressures. The cubane-based linker provides an appropriate pore environment with smaller dodecahedral pore with substantially more van der Waals interaction sites for interaction.

Recently, Li and co-workers have reported a ternary microporous framework incorporating both primary and secondary building units for splitting alkane isomers.³¹⁸ HIAM-302 was made of V-shaped, trapezoidal tetracarboxylate linkers, 8-connected hexanuclear $Y_6(OH)_8(COO)_2$ SBU and a mononuclear $Y(COO)_4$ primary building unit (PBU), featuring an unprecedented 3D **lyu** net with 1D channels. The experimental results showed linear and monobranched hexanes adsorption but fully exclusion of their dibranched isomer, thus HIAM-302 acted as a molecular sieve for splitting monobranched and dibranched alkanes. Meanwhile, DFT calculations were performed to study the interaction of hexane isomers with the framework and to assess their transport within the channels. The theoretical data were in good agreement with the experimental adsorption. n-hexane displayed the lowest energy barrier suggesting its rapid loading into the channels of HIAM-302 without notable limitations. Monobranched hexane showed slightly higher energy barrier which could still be overcome at room temperature, whereas dibranched compound had a prohibiting energy for entering the pore.

Pore space partition (PSP) strategy³¹⁹⁻³²² which is commonly used to build up multicomponent MOF with organic diversity, divides the large cage or channel space into smaller segments with the aim to increase the density of binding sites and tune host-guest interactions. Thus, this tool is gaining interest owing to its fruitful effect on gas sorption.^{172,323-335} Recent example showed the enhance of C_2H_2/CO_2 separation under ambient conditions through mixed-linker FJU-90.³³⁴ The PSP through the immobilization of a C_3 -symmetric regulated ligand in mother FJU-88 MOF³³⁶ converted its large one-dimensional pores into smaller partialized ones. The resulting activated FJU-90a took up a very large amount of C_2H_2 but much less CO_2 at 298 K and 1 bar. Molecular modelling studies and simulated and experimental breakthroughs confirmed the ability of that material for being the best for C_2H_2/CO_2 separations (*Figure 1.36*). The collaborative role among optimized pore size and hydrogen bonding interactions between pore surface and acetylene were the responsible for that outstanding performance.

When PSP is combined with open metal sites the action turns into cooperative, thus it becomes even more versatile and powerful. As reflected in NbU-12,³³⁷ a 3D bio-MOF which its hexagonal channel of MIL-88D split into two small rectangular channels by adenine connection. Due to the presence of open metal sites from MIL-88D and introduced a Watson-Crick face to the pore surface, NbU-12 exhibited an excellent selectivity performance toward C_2H_6/C_2H_4 and C_2H_6/CH_4 , which was proven by ideal adsorbed solution theory calculation and breakthrough experiments.

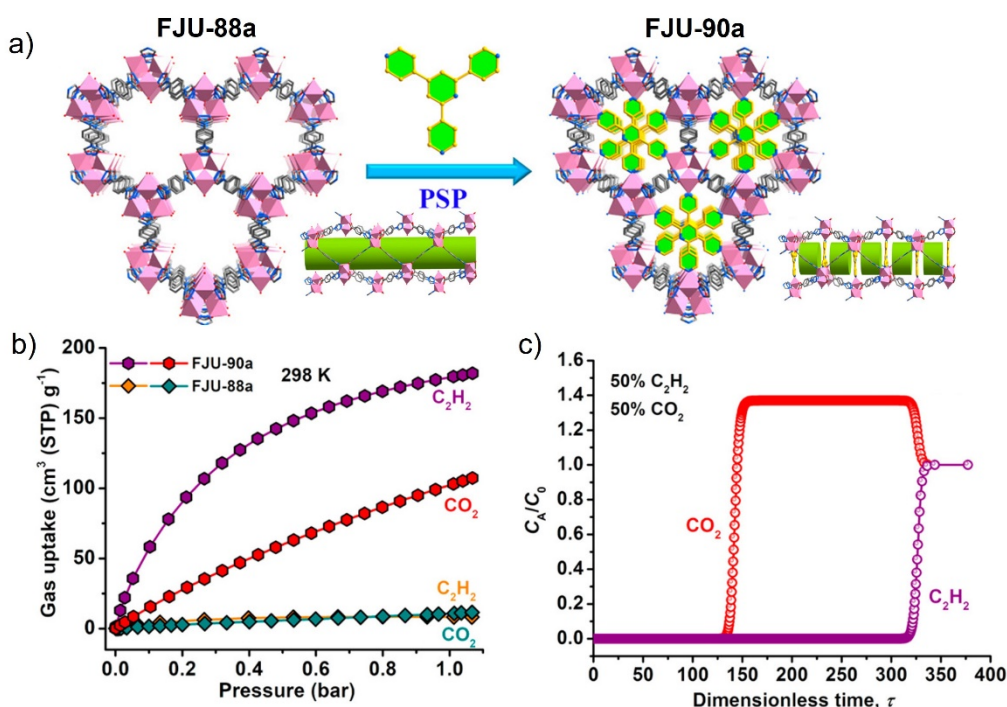


Figure 1.36. PSP strategy in FJU-derivates. b) C₂H₂ and CO₂ single-component adsorption isotherms of FJU-88a and FJU-90a at 298 K. c) Breakthrough simulations for the separation of equimolar C₂H₂/CO₂ mixtures using FJU-90a. Adapted from ref 334.

Likewise, the applications for multi-metal MOFs in gas adsorption are also very diverse. Not only in terms of CO₂^{248,250,252,262,269,338–346} or CH₄^{342,344,346} adsorption but also in H₂^{246,247,252,347} storage and in different kind of separations like CO₂/N₂, CO₂/CH₄, CH₃OH/CH₃CN,³⁴⁸ Xe/Kr²⁹³ or alkane isomers.³¹⁸ The combinations of metal ions in the cluster have a significant impact on adsorption properties. As was early illustrated by MOF-5 where the partial exchange of Zn²⁺ ions with Co²⁺ ions promoted a higher CO₂ adsorption capacity than in the pure MOF-5(Zn).³⁴² Although the substitution of Co²⁺ ions in the Zn₄O cluster was limited and could not exceed 25 %, the proportionally increased in CO₂ adsorption was denoted by the content of Co²⁺ ions which were incorporated into unexposed metal sites that were less accessible to gas molecules. The same trend was observed for bimetallic ZIF-8.²⁵² Kaur *et al.* prepared CoZn-ZIF-8 frameworks by tuning the content of Co and Zn precursors. Co₇₅Zn₂₅-ZIF-8 not only displayed large surface and pore volume (enhanced by 40 % and 33 %, respectively, compared to Zn-ZIF-8) but also showed a remarkable enhancement of around 30 % in the CO₂ and 23 % in the H₂ uptake. That behaviour was also confirmed through heterometallic multivariate CPM-200.²⁵⁰ The highly dissimilar metals combination (e.g., Mg/Ga, Mg/Fe, Mg/V, Mg/Sc) in trimeric [M^{II}₂M^{III}(μ₃-OH)(CO₂)₆] clusters enhanced the CO₂/N₂ selectivity. Feng and co-workers observed that the CO₂ uptake rate follows the sequence: Fe³⁺/Mg²⁺ > In³⁺/Mg²⁺ > V³⁺/Mg²⁺ > Ga³⁺/Mg²⁺ > Sc³⁺/Mg²⁺, demonstrating for the first time the strong correlation between isosteric heat for CO₂ and the charge-to-radius ratio (z/r) of metal ions in MOFs. Moreover, CPM-200-Fe/Mg displayed CO₂ uptake capacity close to the all-time record set by MOF-74-Mg.

Recently, the Zhou research team systematically investigated the effects of metals, terminal ligands, and functional groups on the adsorption energy of C_2H_2 and CO_2 to optimize an adsorbent for C_2H_2/CO_2 separations.³⁴⁹ UPC-200 series were selected as a highly tuneable platform for the design of adsorbents. The optimized material UPC-200(Al)-F-BIM, constructed from Al^{3+} clusters, fluorine-functionalized organic linkers, and benzimidazole terminal ligands, demonstrated the highest separation efficiency and highest C_2H_2 productivity among UPC-200 systems (*Figure 1.37.*). The experimental and computational studies attributed those values to the small pore size and polar functional groups.

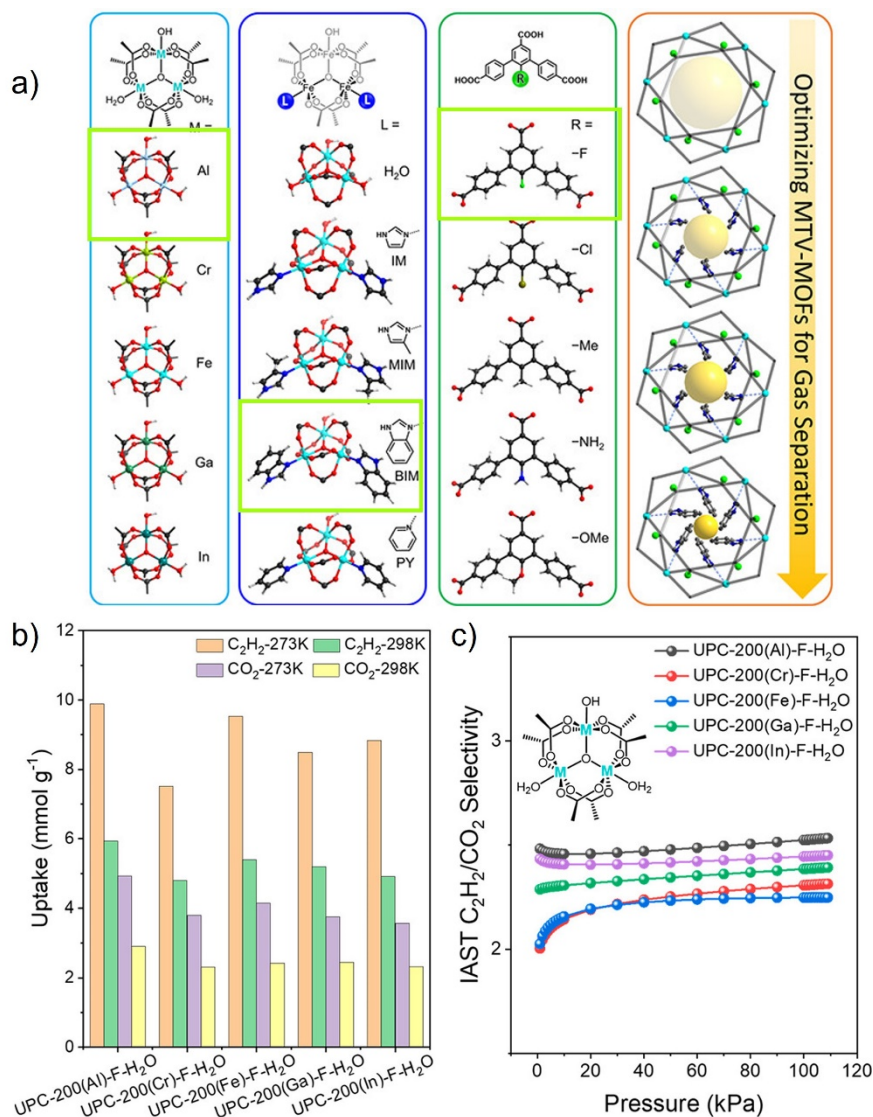


Figure 1.37. a) Inorganic SBUs, terminal, and functionalized organic linkers tested in MTV-UPC-200 synthesis. b) C_2H_2 and CO_2 uptake at 273 K and 298 K. c) IAST calculations for C_2H_2/CO_2 (50/50) mixtures on the UPC-200(M)-F-H₂O. Modified from ref 349.

4.2. Heterogeneous catalyst

Multiple-component MOFs provide a versatile chemical platform for modifiable spatial environments around the active sites, which makes them ideal to design heterogeneous catalysts.^{350,351} The presence of different functional groups can have positive effects on catalytic performance as they can improve the selectivity towards the substrate or modulate the reactivity of the network thanks to the incorporation of bulky or well-defined stereochemistry groups.³⁵² This was exemplified by Su and collaborators with the installation of different ligands with different catalytic centres into predefined positions of multi-linker-LIFM-28.³⁵³ That dynamic installation and uninstallation of functional secondary and ternary ligands into the primitive framework was also combined by chelation and covalent post-synthetic modification processes (*Figure 1.38.*). As a result, multi-linker LIFM-28 was defined as a multiuse and economic platform to construct heterogeneous catalysts which were suitable for single, sequential, and stepwise reactions. A range of single Cu(I)-redox, amine-base, or sulfuric-acid catalytic sites as well as bifunctional catalysts possessing Cu(I)-redox + amine-base or Cu(I)-redox + sulfuric-acid cooperative catalytic sites were implemented into the coordination interspace with precise and quantitative control. Both the single-step reactions, including alcohol-oxidation, Knoevenagel-condensation, click, acetal, and Baylis-Hillman reactions, and the sequential or stepwise catalysis among those elementary reactions were achieved under relatively mild conditions depending on the functionalization.

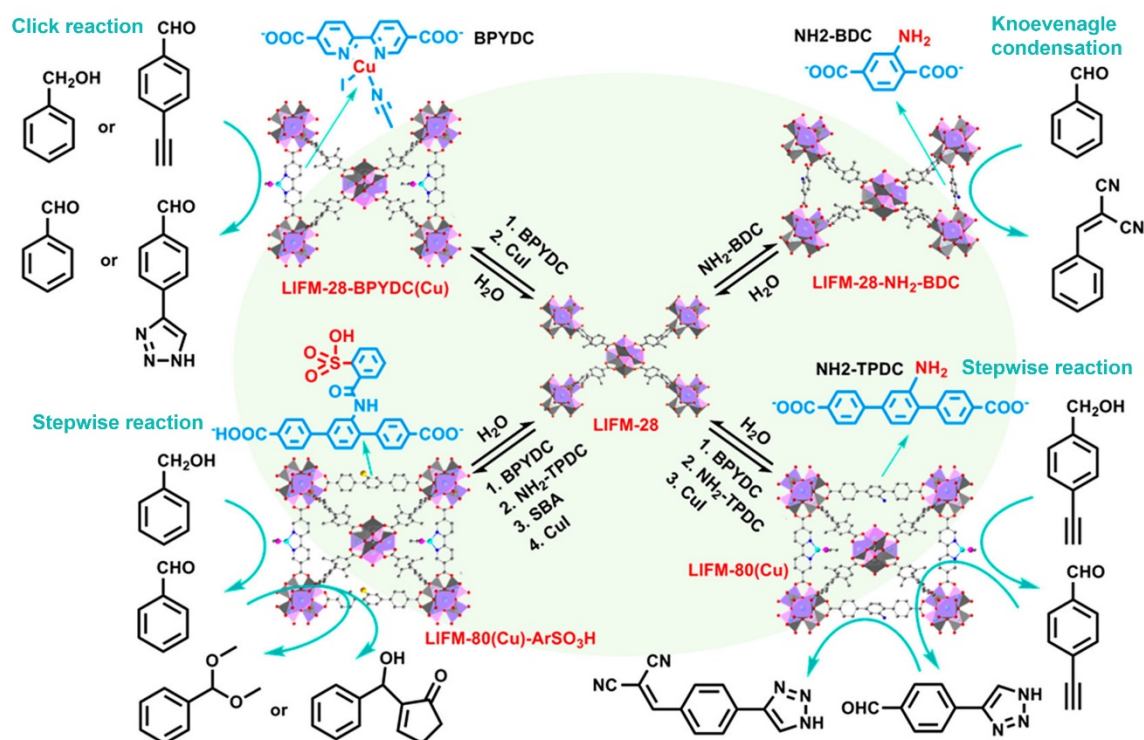


Figure 1.38. Generation of multicomponent MOF catalysts via the dynamic spacer installation approach from LIFM-28 showing their interconversion toward different catalytic purposes. Adapted from ref 353.

Moreover, multiple-linker MOFs can easily introduce chiral moieties, which biomimetic enzyme's catalytic sites,^{80,354–357} to make them become active for asymmetric and enzymatic catalysis reactions,³⁵⁸ very valuable in the pharmaceutical industry. Sometimes this chirality can be acquired through cheap small molecules such as amino acids.^{204,205,359} Recently, Manna and his group reported a strategy to develop heterogeneous single-site enantioselective catalysts based on amino acids (*aa*) and iron for eco-friendly asymmetric catalysis.³⁵⁹ The resultant *aa*-UiO-68-Fe MOF were prepared by tandem route. The *aa* was grafted to the amino-functionalized MOF, followed by Fe metalation. The *aa*-UiO-68-Fe MOF experiments displayed much higher activity and enantioselectivity than its homogeneous control *aa*-Fe complex. The site isolation of the chiral active species confined within the MOF-pores prevented from any intermolecular catalyst deactivation pathways. Hence, *aa*-UiO-Fe MOF showed high turnover numbers of up to 10000 and 15 times of recyclability without diminishing the enantioselectivity.

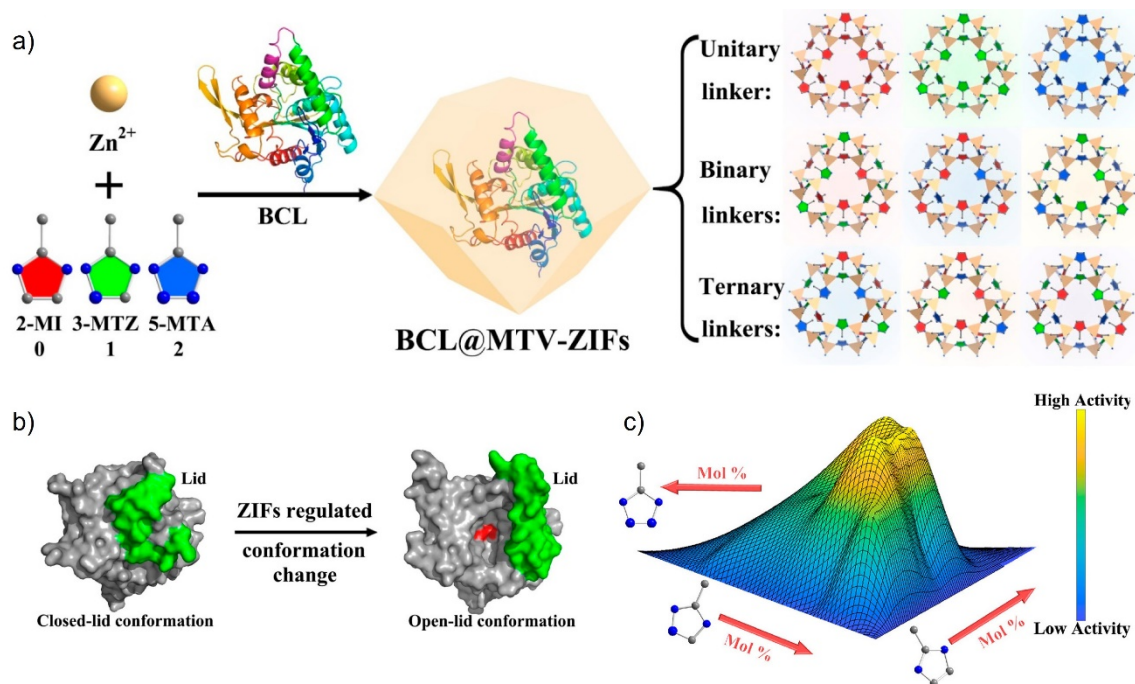


Figure 1.39. a) Scheme of active BCL encapsulation in MTV-ZIFs. b) MTV-ZIF composition regulates protein conformation. c) 3D diagram of different linkers' (2-MI, 3-MTZ, and 5-MTA) ratios of BCL@ZIFs and the catalytic activities, in which the highest activities in every series of ZIFs were connected by the red line. Extracted from ref 365.

Regarding enzymatic catalysis, MOF are excellent candidates to immobilize enzymes,^{360–364} MTV-MOFs provide a platform to modify a MOF's pore and inner-surface with functionality variations to optimize the interior environment to enhance the activity of the encapsulated enzyme. Cheng and co-workers altered the functionality and ratio of linkers in ZIFs to optimize the activity of the *Burkholderia*

cepacian (BLC), encapsulated enzyme, by continuously tuning the framework-enzyme interaction through the hydrophilicity change in the pores' microenvironment (*Figure 1.39.*)³⁶⁵ The spatial arrangement of functional groups along the three-dimensional space across the ZIF-8 crystal was responsible of enzyme conformation and also of the catalytic reactivity.

Recently, Martí-Gastado and co-workers focused their efforts on demonstrating the effect of linker distribution in the photoactivity of mesoporous framework, in particular in UiO-68¹⁴² (see **Chapter 3**). The control of post-synthetic exchange variables allowed to prepare a set of samples with variable percentage of photo-active linker, a tetrazine-based ligand (TZDC), and controllable spatial arrangements. In this way, it was possible to directly compare the catalytic performance of the homolinker-UiO-68-TZDC, core-shell UiO-68-TZDC and random UiO-68-TZDC, both with the same quantity of photo-active linker. The H₂ evolution experiments showed a high boosting on catalytic activity for core-shell sample, whereas for homogeneous distribution sample the photoactivity was comparable to the pristine MOF. The stability test after catalytic reaction revealed a complex scenario in which the catalytic performance was a fine balance between photoactive linker surface concentration and chemical stability of the material both of which were related to linker exchanged distribution inside the crystal.

Probably, one of the most studied catalytic reactions is chemical warfare agent simulant degradation.³⁶⁶⁻³⁷⁷ Thus, multiple-linker MOFs has also been carried out the hydrolysis of these organophosphorus compounds. The encapsulation of imidazole and its derivative into the pores of MOF-808 achieved rapid degradation of dimethyl-4-nitrophenyl phosphate (DMNP) in pure water as well as in a humid environment without liquid base.³⁷⁸ The spatial configuration of active groups generated an active metal site comparable to native phosphotriesterase (PTE) enzyme, in which binuclear Zn centres and the surrounding ligands work cooperatively, enabling the extraordinary catalytic activities. A multivariate strategy has also been used to prepare MTV-UiO-66 including simultaneously up to four functionalities (-NH₂, -OH, -NO₂ and -Br) for catalytic degradation of DMNP.³⁷⁹ The catalytic results showed the importance of -NH₂ group and the synergistic effects of multiple ligand functional groups. As evidenced by seven of the top eight MTV-UiO-66 MOFs contain the NH₂-linker, while the homoligand UiO-66-NH₂ was one of the poorest performing MOFs. That result indicated that there was a synergistic ligand effect occurring when multiple functional groups were incorporated into a single MOF. The synergistic effects were verified preparing physical mixtures using single-linker MOFs in the same ratios as those present in the MTV-UiO-66. The high performance's MTV-sample displayed 3-fold increased degradation activity when compared to the physical mixtures.

Multi-metal MOF have also shown such synergistic effects to degrade nerve agents' simulants in non-buffered solution. MUV-101(Ti,Fe) reported by Martí-Gastado and co-workers degraded efficiently diisopropyl-fluorophosphate (DIFP) thanks to a

dual-metal synergetic mechanism reminiscent of bimetallic enzymes. The combination of Ti(IV) Lewis acid and Fe(III)-OH Brönsted base sites in same cluster led to a lower energy barrier for more efficient degradation.²⁸¹ Just one year later, the cobalt derivate of MUV-101(Ti,Co) was described as an excellent photocatalyst for H₂ production.³⁸⁰

The examples shown above illustrate the positive synergistic effects on catalysis due to the presence of two metals in the same SBU, the inclusion of single metal ions in the cluster^{92,96-99,102,103,105,285,381-383} or the use of metalloligands^{73,74,76,77,79,80,82,85,88-90,384,385} represent alternative routes to progress in the field of heterogeneous catalysis.

4.3. Environmental applications

Environmental applications are focused to address issues like water contamination, as well as its scarcity in particular regions of the planet, or the high levels of CO₂ emissions and their conversion to value-added compounds. Regarding water remediation, the intrinsic heterogeneity and complexity of multicomponent MOFs introduce multiple recognition sites, makes them more selective toward specific molecules. These materials have been employed to capture different types of contaminants such as heavy^{301,386,387} and radioactive metal ions,³⁸⁸ inorganic acids and oxyanions/cations or organic pollutants which includes organic dyes,³⁸⁹⁻³⁹² pharmaceutical and personal care products,³⁹³ as well as herbicides and pesticides.³⁹⁴ Recently, Pardo's group focused its studies on water remediation through amino acid-based MTV-MOFs. They reported new water-stable MTV-MOFs combining two different oxamide-based metalloligands derived from the natural amino acids *L*-serine and *L*-methionine.³⁹⁵ Their hexagonal channels decorated with two types of flexible and functional -CH₂OH and -CH₂CH₂SCH₃ chains enabled, synergistically, the simultaneous and efficient removal of both inorganic heavy metals such as Hg²⁺, Pb²⁺, and Tl⁺, and organic dyes like Pyronin Y, Auramine O, Brilliant green, and Methylene blue. The simultaneously removal experiments with both types of contaminants of different nature revealed a slightly improvement with respect to the single capture experiments. These synergetic effects were demonstrated by SCXRD analysis. The crystallographic analysis revealed the interactions between HgCl₂ and the thioether residues of methionine and the hydrogen-bonds between the Methylene blue and the hydroxyl groups from serine, as well as the interactions within the confined space of MTV-MOF pores between both types of contaminants. The results concluded that multivariate frameworks improved its performance, in terms of kinetics and amount removed, respect the related binary nets with only serine-derived linkers.³⁹⁶ More lately, the replacement of those linkers with *L*-methionine and *L*-methylcysteine amino acid-derived allowed to prepare new family of isorecticular MTV-MOFs with functional channels decorated with both -CH₂SCH₃ and -CH₂CH₂SCH₃ thioalkyl chains.³⁹⁷ Those materials exhibited notable removal efficiencies, being capable to capture 100 % of

neonicotinoid insecticides in a single capture step under dynamic solid-phase extraction conditions. As in the previous example, SCXRD experiments proved the synergistic host-guest interaction, between the two types of thioether groups from the MTV-MOF and the functional groups from the guest contaminants.

In 2017, Yaghi and collaborators demonstrated the potential of MOFs to extract atmospheric water in desert areas to produce potable water.^{398–402} That discovery has attracted a lot of interest among the scientific community, as it may be a promising alternative to address the global water shortage crisis. More recently, Yaghi and his team tried to leverage the potential of MTV-MOFs for water harvesting.⁴⁰³ The use of multivariate-linker MOFs enabled to control the relative humidity (RH) levels at which MOFs extract water from arid air, as well as heat of adsorption, desorption temperature and water productivity, without compromising the pore size, shape, or hydrolytic stability of the materials. Authors sought to modify the water adsorption isotherm shape to improve the working capacity in MOF-303 [Al(OH)(PyDC)], state-of-the-art water-harvesting MOF, by understanding the water uptake process through location of the adsorption sites and the mechanism with which they are populated (*Figure 1.40.*). The extensive studies of SCXRD measurements and DFT calculations allowed to determinate the molecular water uptake mechanism. The detrimental step in which water harvesting was reduced was governed by water interactions with two neighbouring pyrazole functionalities. In this way, authors decided to control the H-bonding in the pocket by substituting PyDC²⁻ with another linker that was less hydrophilic, as 2,4-furandicarboxylic acid (H₂FDC). The controllable substitution of PyDC²⁻ with increasing amounts of FDC²⁻ continuously shifted the water isotherm adsorption step toward higher vapor pressures extending the working range to more arid conditions.

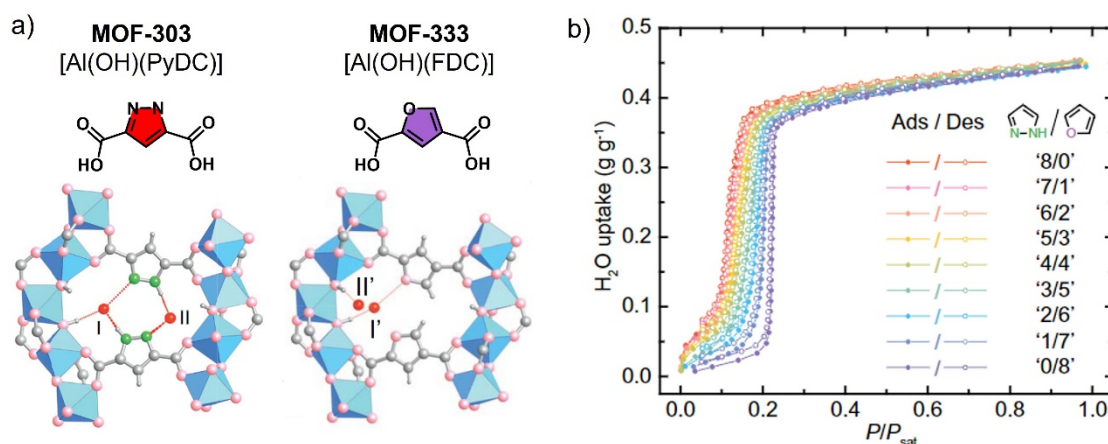


Figure 1.40. a) Scheme of linkers of MOF-303 and MOF-333 and its pockets of the first two water adsorption sites; b) Water sorption isotherms amounts showed a continuously shift toward higher vapor pressures when FDC amount increases. Modified from ref 403.

Besides the capture and storage of CO₂, another appealing strategy is the conversion of CO₂ into fuels or chemical stocks. This is an ideal way to alleviate the environmental problems as this will not only reduce the atmospheric CO₂ levels but also decrease the fossil fuel consumption. Multicomponent MOF can be also used to selectively reduce CO₂ into the production of valuable chemicals such as carbon monoxide (CO), formic acid (HCOOH) and formaldehyde (HCHO).⁴⁰⁴ The mixed-metal MOFs which are dominant in this context,^{100,405–408} especially those cases in which the metal variance is inserted into the MOF by metalloligands.^{84,94,292,409–411} These present an ideal platform for introducing site-isolated light-absorbing entities and single-site CO₂ reduction catalysts. The selectivity of the CO₂ reduction process can be tuned by altering the nature of coordination environment of the catalytic centre. This was recently demonstrated in Zhang and collaborators. They synthesised a stable Eu-MOF as a molecular platform to integrate a Ru(2,2'-bpy)₃ to act as a photosensitizer and as a monometallic catalysts [2,2'-bpy-Cu/ClX] (X = Cl or adenine).⁴¹¹ That material demonstrated high selective photoreduction of CO₂ to formate (99.7 %). However, replacing X with pyridine molecules significantly reduced formate production while increasing the CO yield. Systematic investigations provided a molecularly precise structural model to provide mechanistic insights for selectivity control of CO₂ photoreduction. The experimental and theoretical data revealed that the catalytic process was mediated by the H-bond between the group X and CO₂⁻ derived species, showing that the selectivity of HCOO⁻ may be controlled by simply replacing the coordination ligands.

Embedding nanoparticles within MOFs is a potential strategy for both carbon capture and carbon utilization^{292,412–415} which allows an efficient manage of CO₂ emissions in the atmosphere. More recently, Amal and collaborators have studied the use of NiMg-MOF-74 as a template to disperse small Ni nanoclusters throughout the parent MOF.²⁵⁴ By exploiting the difference in thermal stability of Ni-O and Mg-O coordination bonds in NiMg-MOF-74, thermal treatment at 350 °C resulted in a gradual Ni²⁺ reduction to form highly dispersed Ni nanoclusters within parent MOF pore, while Mg²⁺ remains coordinated in the framework. The Ni:Mg ratio in the pristine NiMg-MOF-74 regulated the Ni nanoparticle formation, MOF structural stability and catalytic activity/selectivity. The authors found that even though Ni was known to favour methane formation for the CO₂ hydrogenation reaction, the selectivity could be altered to produce CO once Ni was engulfed with graphitic carbon.

4.4. Luminescence and sensing

The luminescence properties of molecular materials can be customized by selecting proper linkers which absorb in a broad region of electromagnetic spectrum or mixing different metals which show various colours owing to d-d transitions, MLCT/LMCT/MMCT or intravalence charge transfer (IVCT). The heterogeneity presents in multicomponent MOFs offers novel opportunities, which could not be easily achieved using single-component MOFs.⁴¹⁶

The integration of various π -conjugated organic moieties within the same organic backbone enables to control the distribution multiple functionalities (fluorophore and acceptor) in close arrangement favouring energy transfer reactions.^{219,220,417-421} In the cases when this luminescence is modified by exogenous molecules, MOFs can act as sensors^{151,422,423}. This behaviour was reflected in the recent work reported by Zhou where was assembled a turn-on fluorescence sensor by combining a fluorophore and a recognition moiety within a complex cavity of a multicomponent PCN-700.¹⁵¹ That example showed the emergent synergistic effects of the precise placement of multiple cooperative functional groups within a framework. An anthracene-based fluorophore and a hemicyanine-based CN^- responsive moiety were post-synthetic sequentially installed within a MOF scaffold (*Figure 1.41. a*). Efficient energy transfer between the fluorophore and the recognition moiety could be accomplished through the proximity of the two components within a periodic lattice. The presence of CN^- anions inhibited the energy transfer between the two moieties, resulting in a fluorescence turn-on effect. The high tunability of the MOF platform enabled to fine-tune the ratio between both moieties to maximize the sensitivity of the overall framework. Moreover, the nanosized particles enhanced the cell permeability allowing for in vitro CN^- detection (*Figure 1.41. b*). The confocal fluorescence image of HeLa cells with/without MOF probes showed almost no fluorescence whereas upon incubation with NaCN a strong turn-on fluorescence signal was observed (*Figure 1.41. c*).

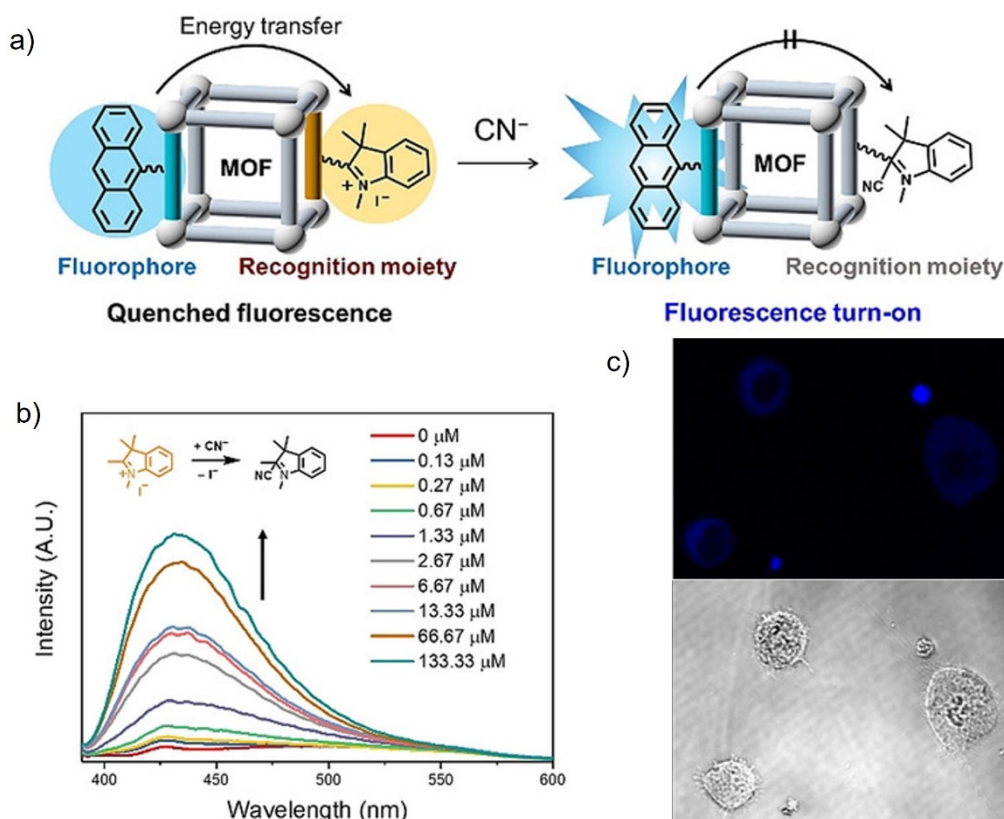


Figure 1.41. a) Schematic representation for the design of a turn-on fluorescence sensor in multicomponent MOFs by integrating a fluorophore and a recognition moiety. b) Fluorescence spectra of modified PCN-700 in the presence of various concentrations of CN^- in water. c) Confocal fluorescence images of HeLa cells. Adapted from ref 151.

Photo-switchable linker-based UiO-68 showed the effect of the location of the photoactive moiety in governing the material properties. Hecht and co-workers demonstrated the potential application as a container with a light-responsive gate of a two-component core-shell UiO-68 type MOF.¹³⁷ The MOF was prepared post-synthetically stirring the starting core-UiO-68 in a solution of linker L^{azo} which featured two tetra-ortho-fluorinated azobenzene moieties and showed a quantitative $\text{E} \rightarrow \text{Z}$ photoisomerization under green light irradiation and reversible pathway upon blue light. The resultant core-shell microarrangement was confirmed by EDX-mapping. For molecular uptake and release experiments core-shell MOF crystals were irradiated with green light to facilitate the dye loading, then irradiated back to the E-rich sample using blue light to enclose the molecule. The release was induced by green light irradiation. The different uptake for the E-rich than for the Z-rich shell confirmed that the azo-benzene ligand shell acts as a photo-responsive kinetic barrier for the diffusion in (and out) of the MOF interior.

Regarding multi-metal-MOFs, mixed-lanthanide MOFs are probably the most studied family which are known to show broad scale luminescence phenomenon in the visible range of spectrum. These compounds offer a wide range of applications including luminescent thermometers,^{424–429} white light emitting compounds,^{430,431} optical sensors^{432–436} and barcoded luminescent materials.⁴³⁷ As happened in other

properties, the spatial distribution of the metals within a mixed-lanthanide MOF affects the fluorescence behaviour. Generally, mixed-lanthanide MOFs have a random distribution of the lanthanide centres throughout the structure. This randomisation can lead to quenching of the colour emissions through energy transfer between emitter centres, making colour control difficult to achieve. Cadman *et al.* employed a method to overcome this quenching by preparing ordered, heterogeneous structures in which the different emitters were located within specific regions of the structure.⁴³⁸ Using a 1:1:1 mixture of europium, gadolinium and terbium nitrates a series of core-shell multi-metal MOF with of the general formula $[\text{Ln}(\text{Hodip})(\text{H}_2\text{O})] \cdot n\text{H}_2\text{O}$ general formula were prepared. The emission spectra proved the effect of metal space arrangement on fluorescence behaviour. While the fluorescence emission spectrum of a sample with random metal distribution was dominated by europium emission bands reflecting the higher proportion of Eu^{3+} centres and quenching of the terbium fluorescence by metal-to-metal energy transfer. In contrast, the emission spectra for core-shell materials with Gd@Tb@Eu and Tb@Eu@Gd were dominated by terbium emissions, suggesting that physical separation from europium suppresses quenching.

Furthermore, the combination of d^{10} ions (for instance Cd^{2+} or Zn^{2+}) in metal centres with π -conjugated organic linkers lead to the formation of luminescent multi-metal-MOFs, which have great potential as chemical sensors.^{253,439–441} The hybrid zinc(II) and copper(II) bimetallic frameworks obtained via metal-ion metathesis by Sun and collaborators showed not only enhanced adsorption but also photoluminescence properties.²⁵³ Whereas the Cu-pure MOF did not display luminescence, the multi-metal MOF had intense emission demonstrating that the post-synthetic method can be used to make materials with improved fluorescence.

Taking advantage of luminescence properties, multicomponent MOFs have been able to extend their applicability to sophisticated fields such as biomedicine acting as biosensors,^{306,442–448} as illustrated by a previously mentioned example of switch-on sensor based on Zr_6 PCN-MOFs.³⁰⁶ The development of test paper composed of metalated nano-MV-PCN-521 showed fluorescence in contact with the biomarkers. The intensity of the fluorescence was directly related to the concentration of the corresponding biomarker (*Figure 1.42.*). The reported sensors were able to detect biomarker concentration as low as 22.5 nM and 46.4 nM, for l-cysteine and glutathione, respectively. Thus, combining low detection limit, specificity, recyclability, and making it suitable portable material for applications in real-world applications.

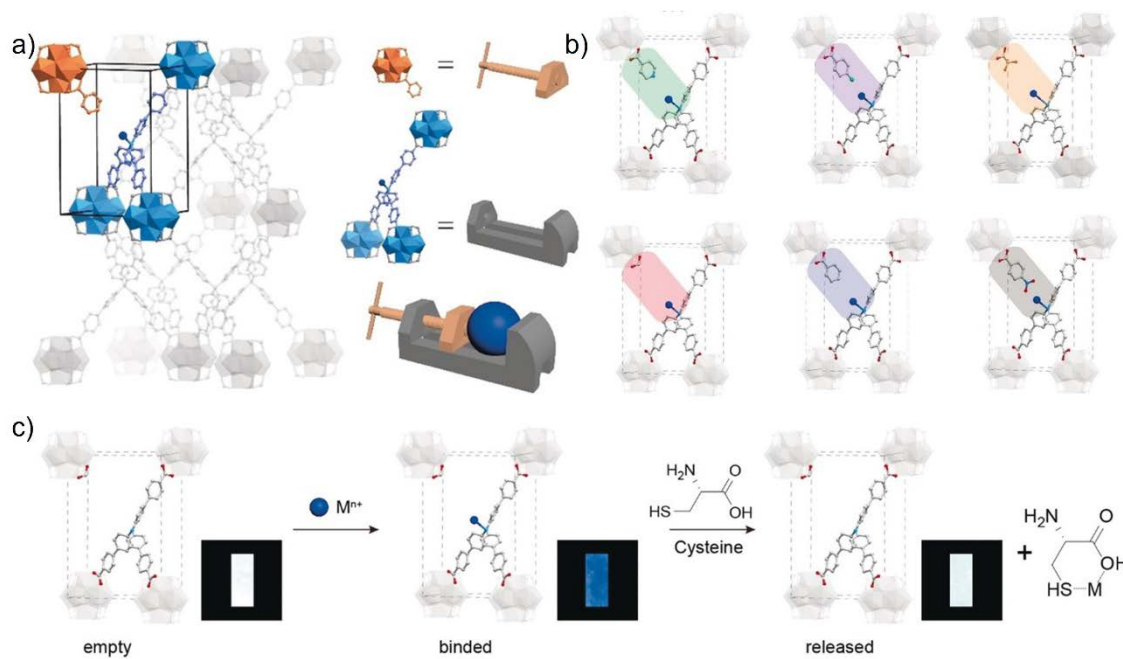


Figure 1.42. a) Illustration of MV-MOF created by molecular vise approach. b) Different metal-binding sites created by various monotopic linkers. c) Association and dissociation of metals in MV-PCN-521-FA, and fluorescence quenching and recovery displayed in test papers composed of nano-MV-PCN-521-FA. Modified from ref 306.

5. References

- (1) Gropp, C.; Canossa, S.; Wuttke, S.; Gándara, F.; Li, Q.; Gagliardi, L.; Yaghi, O. M. Standard Practices of Reticular Chemistry. *ACS Cent. Sci.* **2020**, *6* (8), 1255–1273.
- (2) Freund, R.; Canossa, S.; Cohen, S. M.; Yan, W.; Deng, H.; Guillerm, V.; Eddaoudi, M.; Madden, D. G.; Fairen-Jimenez, D.; Lyu, H.; Macreadie, L. K.; Ji, Z.; Zhang, Y.; Wang, B.; Haase, F.; Wöll, C.; Zaremba, O.; Andreo, J.; Wuttke, S.; Diercks, C. S. 25 Years of Reticular Chemistry. *Angew. Chem. Int. Ed.* **2021**, *60* (45), 23946–23974.
- (3) Slater, A. G.; Cooper, A. I. Function-Led Design of New Porous Materials. *Science* **2015**, *348* (6238).
- (4) Yaghi, O. M. Reticular Chemistry in All Dimensions. *ACS Cent. Sci.* **2019**, *5* (8), 1295–1300.
- (5) Yaghi, O. M.; Li, H.; Eddaoudi, M.; O’Keeffe, M. Design and Synthesis of an Exceptionally Stable and Highly Porous Metal-Organic Framework. *Nature* **1999**, *402* (6759), 276–279.
- (6) Dincâ, M.; Yu, A. F.; Long, J. R. Microporous Metal-Organic Frameworks Incorporating 1,4-Benzeneditetrazolate: Syntheses, Structures, and Hydrogen Storage Properties. *J. Am. Chem. Soc.* **2006**, *128* (27), 8904–8913.
- (7) Gagnon, K. J.; Perry, H. P.; Clearfield, A. Conventional and Unconventional Metal–Organic Frameworks Based on Phosphonate Ligands: MOFs and UMOFs. *Chem. Rev.* **2011**, *112* (2), 1034–1054.
- (8) Hmadeh, M.; Lu, Z.; Liu, Z.; Gándara, F.; Furukawa, H.; Wan, S.; Augustyn, V.; Chang, R.; Liao, L.; Zhou, F.; Perre, E.; Ozolins, V.; Suenaga, K.; Duan, X.; Dunn, B.; Yamamoto, Y.; Terasaki, O.; Yaghi, O. M. New Porous Crystals of Extended Metal-Catecholates. *Chem. Mater.* **2012**, *24* (18), 3511–3513.
- (9) Côté, A.P.; Benin, A. I.; Ockwig, N. W.; O’Keeffe, M.; Matzger, A. J.; Yaghi, O. M. Porous, crystalline, covalent organic frameworks. *Science* **2005** *310* (5751), 1166–1170.
- (10) Kalmutzki, M. J.; Hanikel, N.; Yaghi, O. M. Secondary Building Units as the Turning Point in the Development of the Reticular Chemistry of MOFs. *Sci. Adv.* **2018**, *4* (10).
- (11) Kim, D.; Liu, X.; Lah, M. S. Topology Analysis of Metal-Organic Frameworks Based on Metal-Organic Polyhedra as Secondary or Tertiary Building Units. *Inorg. Chem. Front.* **2015**, *2* (4), 336–360.
- (12) Alexandrov, E. V.; Blatov, V. A.; Kochetkov, A. V.; Proserpio, D. M. Underlying Nets in Three-Periodic Coordination Polymers: Topology, Taxonomy and Prediction from a Computer-Aided Analysis of the Cambridge Structural Database. *CrystEngComm* **2011**, *13* (12), 3947–3958.
- (13) Li, M.; Li, D.; O’Keeffe, M.; Yaghi, O. M. Topological Analysis of Metal-Organic Frameworks with Polytopic Linkers and/or Multiple Building Units and the Minimal Transitivity Principle. *Chem. Rev.* **2014**, *114* (2), 1343–1370.
- (14) O’Keeffe, M.; Yaghi, O. M. Deconstructing the Crystal Structures of Metal-Organic Frameworks and Related Materials into Their Underlying Nets. *Chem. Rev.* **2012**, *112* (2), 675–702.
- (15) Tranchemontagne, D. J.; Tranchemontagne, J. L.; O’Keeffe, M.; Yaghi, O. M. Secondary Building Units, Nets and Bonding in the Chemistry of Metal–Organic Frameworks. *Chem. Soc. Rev.* **2009**, *38* (5), 1257–1283.
- (16) Jiang, H.; Alezi, D.; Eddaoudi, M. A Reticular Chemistry Guide for the Design of Periodic Solids. *Nat. Rev. Mater.* **2021**, *6* (6), 466–487.
- (17) Dalapati, S.; Addicoat, M.; Jin, S.; Sakurai, T.; Gao, J.; Xu, H.; Irle, S.; Seki, S.; Jiang, D. Rational Design of Crystalline Supermicroporous Covalent Organic Frameworks with Triangular Topologies. *Nat. Commun.* **2015**, *6*, 1–8.
- (18) Gropp, C.; Ma, T.; Hanikel, N.; Yaghi, O. M. Design of Higher Valency in Covalent Organic Frameworks. *Science* **2020**, *370* (6515).
- (19) Nguyen, H. L. Reticular Design and Crystal Structure Determination of Covalent Organic Frameworks. *Chem. Sci.* **2021**, *12* (25), 8632–8647.

- (20) Lee, S.; Jeong, H.; Nam, D.; Lah, M. S.; Choe, W. The Rise of Metal-Organic Polyhedra. *Chem. Soc. Rev.* **2021**, *50* (1), 528–555.
- (21) Yaghi, O. M.; Li, G.; Li Hailian. Selective Binding and Removal of Guests in a Imcroporous Metal-Organic Framework. *Nature* **1995**, *378*, 703–706.
- (22) Keeffe, M. O.; Peskov, M. a; Ramsden, S. J.; Yaghi, O. M. The Reticular Chemistry Structure Resource (RCSR) Database of, and Symbols for, Crystal Nets. *Acc. Chem. Res.* **2008**, *41* (12), 1782–1789.
- (23) Kiang, Y. H.; Gardner, G. B.; Lee, S.; Xu, Z.; Lobkovsky, E. B. Variable Pore Size, Variable Chemical Functionality, and an Example of Reactivity within Porous Phenylacetylene Silver Salts. *J. Am. Chem. Soc.* **1999**, *121* (36), 8204–8215.
- (24) Eddaoudi, M.; Kim, J.; Rosi, N.; Vodak, D.; Wachter, J.; O’Keeffe, M.; Yaghi, O. M. Systematic Design of Pore Size and Functionality in Isorecticular MOFs and Their Application in Methane Storage. *Science* **2002**, *295* (5554), 469–472.
- (25) Furukawa, H.; Go, Y. B.; Ko, N.; Park, Y. K.; Uribe-Romo, F. J.; Kim, J.; O’Keeffe, M.; Yaghi, O. M. Isorecticular Expansion of Metal-Organic Frameworks with Triangular and Square Building Units and the Lowest Calculated Density for Porous Crystals. *Inorg. Chem.* **2011**, *50* (18), 9147–9152.
- (26) Cavka, J. H.; Olsbye, U.; Guillou, N.; Bordiga, S.; Lillerud, K. P. A New Zirconium Inorganic Building Brick Forming Metal Organic Frameworks with Exceptional Stability. *J. Am. Chem. Soc.* **2008**, *130* (42), 13850–13851.
- (27) Deng, H.; Grunder S.; Cordova K. E; Valente, C.; Furukawa, H.; Hmadeh, M.; Gándara, F.; Whalley, A. C.; Liu, Z.; Asahina, S.; Kazumori, H.; O’Keeffe, M.; Terasaki, O.; Stoddart, J. F.; Yaghi, O. M. Large-Pore Apertures in a Series of Metal-Organic Frameworks. *Science*. **2012**, *336*, 1018–1023.
- (28) Jiang, H.; Jia, J.; Shkurenko, A.; Chen, Z.; Adil, K.; Belmabkhout, Y.; Weselinski, L. J.; Assen, A. H.; Xue, D. X.; O’Keeffe, M.; Eddaoudi, M. Enriching the Reticular Chemistry Repertoire: Merged Nets Approach for the Rational Design of Intricate Mixed-Linker Metal-Organic Framework Platforms. *J. Am. Chem. Soc.* **2018**, *140* (28), 8858–8867.
- (29) Tan, J.; Tao, Y.; Zhang, X.; Wang, Q.; Zeng, T.; Shi, Z.; Cordova, K. E.; Lee, Y.; Liu, H.; Zhang, Y. B. Control over Interpenetration for Boosting Methane Storage Capacity in Metal-Organic Frameworks. *J. Mater. Chem. A* **2021**, *9* (44), 24857–24862.
- (30) O’Nolan, D.; Madden, D. G.; Kumar, A.; Chen, K. J.; Pham, T.; Forrest, K. A.; Patyk-Kazmierczak, E.; Yang, Q. Y.; Murray, C. A.; Tang, C. C.; Space, B.; Zaworotko, M. J. Impact of Partial Interpenetration in a Hybrid Ultramicroporous Material on C₂H₂/C₂H₄ Separation Performance. *Chem. Commun.* **2018**, *54* (28), 3488–3491.
- (31) Gupta, M.; Vittal, J. J. Control of Interpenetration and Structural Transformations in the Interpenetrated MOFs. *Coord. Chem. Rev.* **2021**, *435*, 213789.
- (32) Deshpande, R. K.; Waterhouse, G. I. N.; Jameson, G. B.; Telfer, S. G. Photolabile Protecting Groups in Metal–Organic Frameworks: Preventing Interpenetration and Masking Functional Groups. *Chem. Commun.* **2012**, *48* (10), 1574–1576.
- (33) Sun, D.; Ma, S.; Ke, Y.; Collins, D. J.; Zhou, H. C. An Interweaving MOF with High Hydrogen Uptake. *J. Am. Chem. Soc.* **2006**, *128* (12), 3896–3897.
- (34) Ma, S.; Sun, D.; Ambrogio, M.; Fillinger, J. A.; Parkin, S.; Zhou, H. C. Framework-Catenation Isomerism in Metal-Organic Frameworks and Its Impact on Hydrogen Uptake. *J. Am. Chem. Soc.* **2007**, *129* (7), 1858–1859.
- (35) Cheon, Y. E.; Suh, M. P. Multifunctional Fourfold Interpenetrating Diamondoid Network: Gas Separation and Fabrication of Palladium Nanoparticles. *Chem. Eur. J.* **2008**, *14* (13), 3961–3967.
- (36) Lin, Z.; Zhang, Z. M.; Chen, Y. S.; Lin, W. Highly Efficient Cooperative Catalysis by Co III (Porphyrin) Pairs in Interpenetrating Metal-Organic Frameworks . *Angew. Chem.* **2016**, *128* (44), 13943–13947.
- (37) López-Maya, E.; Padial, N. M.; Castells-Gil, J.; Ganivet, C. R.; Rubio-Gaspar, A.; Cirujano, F. G.;

- Almora-Barrios, N.; Tatay, S.; Navalón, S.; Martí-Gastaldo, C. Selective Implantation of Diamines for Cooperative Catalysis in Isoreticular Heterometallic Titanium–Organic Frameworks. *Angew. Chem.* **2021**, *133* (21), 11975–11980.
- (38) Song, F.; Wang, C.; Falkowski, J. M.; Ma, L.; Lin, W. Isoreticular Chiral Metal–Organic Frameworks for Asymmetric Alkene Epoxidation: Tuning Catalytic Activity by Controlling Framework Catenation and Varying Open Channel Sizes. *J. Am. Chem. Soc.* **2010**, *132* (43), 15390–15398.
- (39) Xue, D. X.; Belmabkhout, Y.; Shekhah, O.; Jiang, H.; Adil, K.; Cairns, A. J.; Eddaoudi, M. Tunable Rare Earth Fcu-MOF Platform: Access to Adsorption Kinetics Driven Gas/Vapor Separations via Pore Size Contraction. *J. Am. Chem. Soc.* **2015**, *137* (15), 5034–5040.
- (40) Ongari, D.; Talirz, L.; Smit, B. Too Many Materials and Too Many Applications: An Experimental Problem Waiting for a Computational Solution. *ACS Cent. Sci.* **2020**, *6* (11), 1890–1900.
- (41) Lyu, H.; Ji, Z.; Wuttke, S.; Yaghi, O. M. Digital Reticular Chemistry. *Chem* **2020**, *6* (9), 2219–2241.
- (42) Yao, Z.; Sánchez-Lengeling, B.; Bobbitt, N. S.; Bucior, B. J.; Kumar, S. G. H.; Collins, S. P.; Burns, T.; Woo, T. K.; Farha, O. K.; Snurr, R. Q.; Aspuru-Guzik, A. Inverse Design of Nanoporous Crystalline Reticular Materials with Deep Generative Models. *Nat. Mach. Intell.* **2021**, *3* (1), 76–86.
- (43) Rosen, A. S.; Iyer, S. M.; Ray, D.; Yao, Z.; Aspuru-Guzik, A.; Gagliardi, L.; Notestein, J. M.; Snurr, R. Q. Machine Learning the Quantum-Chemical Properties of Metal–Organic Frameworks for Accelerated Materials Discovery. *Matter* **2021**, *4* (5), 1578–1597.
- (44) Pollice, R.; Dos Passos Gomes, G.; Aldeghi, M.; Hickman, R. J.; Krenn, M.; Lavigne, C.; Lindner-D'Addario, M.; Nigam, A.; Ser, C. T.; Yao, Z.; Aspuru-Guzik, A. Data-Driven Strategies for Accelerated Materials Design. *Acc. Chem. Res.* **2021**, *54* (4), 849–860.
- (45) Deng, H.; Doonan, C. J.; Furukawa, H.; Ferreira, R. B.; Towne, J.; Knobler, C. B.; Wang, B.; Yaghi, O. M. Ratios in Metal–Organic Frameworks. *Science* **2010**, *327* (5967), 846–850.
- (46) Furukawa, H.; Müller, U.; Yaghi, O. M. “Heterogeneity within Order” in Metal–Organic Frameworks. *Angew. Chem. Int. Ed.* **2015**, *54* (11), 3417–3430.
- (47) Zhang, Y. B.; Furukawa, H.; Ko, N.; Nie, W.; Park, H. J.; Okajima, S.; Cordova, K. E.; Deng, H.; Kim, J.; Yaghi, O. M. Introduction of Functionality, Selection of Topology, and Enhancement of Gas Adsorption in Multivariate Metal–Organic Framework-177. *J. Am. Chem. Soc.* **2015**, *137* (7), 2641–2650.
- (48) Dong, Z.; Sun, Y.; Chu, J.; Zhang, X.; Deng, H. Multivariate Metal–Organic Frameworks for Dialing-in the Binding and Programming the Release of Drug Molecules. *J. Am. Chem. Soc.* **2017**, *139* (40), 14209–14216.
- (49) Qazvini, O. T.; Macreadie, L. K.; Telfer, S. G. Effect of Ligand Functionalization on the Separation of Small Hydrocarbons and CO₂ by a Series of MUF-15 Analogues. *Chem. Mater.* **2020**, *32* (15), 6744–6752.
- (50) Qazvini, O. T.; Scott, V. J.; Bondorf, L.; Ducamp, M.; Hirscher, M.; Coudert, F. X.; Telfer, S. G. Flexibility of a Metal–Organic Framework Enhances Gas Separation and Enables Quantum Sieving. *Chem. Mater.* **2021**, *33* (22), 8886–8894.
- (51) Nam, D.; Kim, J.; Hwang, E.; Nam, J.; Jeong, H.; Kwon, T. H.; Choe, W. Multivariate Porous Platform Based on Metal–Organic Polyhedra with Controllable Functionality Assembly. *Matter* **2021**, *4* (7), 2460–2473.
- (52) Lerma-Berlanga, B.; Castells-Gil, J.; Ganivet, C. R.; Almora-Barrios, N.; González-Platas, J.; Fabelo, O.; Padial, N. M.; Martí-Gastaldo, C. Permanent Porosity in Hydroxamate Titanium–Organic Polyhedra. *J. Am. Chem. Soc.* **2021**, *143* (50), 21195–21199.
- (53) Cohen, S. M. The Postsynthetic Renaissance in Porous Solids. *J. Am. Chem. Soc.* **2017**, *139* (8), 2855–2863.
- (54) Mandal, S.; Natarajan, S.; Mani, P.; Pankajakshan, A. Post-Synthetic Modification of Metal–Organic Frameworks Toward Applications. *Adv. Funct. Mater.* **2021**, *31* (4), 1–22.

- (55) Kalaj, M.; Cohen, S. M. Postsynthetic Modification: An Enabling Technology for the Advancement of Metal-Organic Frameworks. *ACS Cent. Sci.* **2020**, *6* (7), 1046–1057.
- (56) Wang, Z.; Cohen, S. M. Postsynthetic Covalent Modification of a Neutral Metal-Organic Framework. *J. Am. Chem. Soc.* **2007**, *129* (41), 12368–12369.
- (57) Wang, Z.; Cohen, S. M. Postsynthetic Modification of Metal-Organic Frameworks. *Chem. Soc. Rev.* **2009**, *38* (5), 1315–1329.
- (58) Haneda, T.; Kawano, M.; Kawamichi, T.; Fujita, M. Direct Observation of the Labile Imine Formation through Single-Crystal-to-Single-Crystal Reactions in the Pores of a Porous Coordination Network. *J. Am. Chem. Soc.* **2008**, *130* (5), 1578–1579.
- (59) Doonan, C. J.; Morris, W.; Furukawa, H.; Yaghi, O. M. Isorecticular Metalation of Metal-Organic Frameworks. *J. Am. Chem. Soc.* **2009**, *131* (27), 9492–9493.
- (60) Burrows, A. D.; Frost, C. G.; Mahon, M. F.; Richardson, C. Post-Synthetic Modification of Tagged Metal-Organic Frameworks. *Angew. Chem. Int. Ed.* **2008**, *47* (44), 8482–8486.
- (61) Costa, J. S.; Gamez, P.; Black, C. A.; Roubreau, O.; Teat, S. J.; Reedijk, J. Chemical Modification of a Bridging Ligand inside a Metal-Organic Framework While Maintaining the 3D Structure. *Eur. J. Inorg. Chem.* **2008**, *10*, 1551–1554.
- (62) Morris, W.; Doonan, C. J.; Furukawa, H.; Banerjee, R.; Yaghi, O. M. Crystals as Molecules: Postsynthesis Covalent Functionalization of Zeolitic Imidazolate Frameworks. *J. Am. Chem. Soc.* **2008**, *130* (38), 12626–12627.
- (63) Burnett, B. J.; Barron, P. M.; Hu, C.; Choe, W. Stepwise Synthesis of Metal-Organic Frameworks: Replacement of Structural Organic Linkers. *J. Am. Chem. Soc.* **2011**, *133* (26), 9984–9987.
- (64) Kim, M.; Cahill, J. F.; Fei, H.; Prather, K. A.; Cohen, S. M. Postsynthetic Ligand and Cation Exchange in Robust Metal-Organic Frameworks. *J. Am. Chem. Soc.* **2012**, *134* (43), 18082–18088.
- (65) Karagiari, O.; Bury, W.; Sarjeant, A. A.; Stern, C. L.; Farha, O. K.; Hupp, J. T. Synthesis and Characterization of Isostructural Cadmium Zeolitic Imidazolate Frameworks via Solvent-Assisted Linker Exchange. *Chem. Sci.* **2012**, *3* (11), 3256–3260.
- (66) Wang, L. J.; Deng, H.; Furukawa, H.; Gándara, F.; Cordova, K. E.; Peri, D.; Yaghi, O. M. Synthesis and Characterization of Metal-Organic Framework-74 Containing 2, 4, 6, 8, and 10 Different Metals. *Inorg. Chem.* **2014**, *53* (12), 5881–5883.
- (67) Das, S.; Kim, H.; Kim, O. Metathesis in Single Crystal: Complete and Reversible Exchange of Metal Ions Constituting the Frameworks of Metal-Organic Frameworks. *J. Am. Chem. Soc.* **2009**, *131* (11), 3814–3815.
- (68) Brozek, C. K.; Dinca, M. Lattice-Imposed Geometry in Metal-Organic Frameworks: Lacunary Zn 40 Clusters in MOF-5 Serve as Tripodal Chelating Ligands for Ni 2+. *Chem. Sci.* **2012**, *3* (6), 2110–2113.
- (69) Lalonde, M.; Bury, W.; Karagiari, O.; Brown, Z.; Hupp, J. T.; Farha, O. K. Transmetalation: Routes to Metal Exchange within Metal-Organic Frameworks. *J. Mater. Chem. A* **2013**, *1* (18), 5453–5468.
- (70) Brozek, C. K.; Dinca, M. Cation Exchange at the Secondary Building Units of Metal-Organic Frameworks. *Chem. Soc. Rev.* **2014**, *43* (16), 5456–5467.
- (71) Brozek, C. K.; Dinca, M. Thermodynamic Parameters of Cation Exchange in MOF-5 and MFU-4l. *Chem. Commun.* **2015**, *51* (59), 11780–11782.
- (72) Brozek, C. K.; Dinca, M. Ti³⁺, V^{2+/3+}, Cr^{2+/3+}, Mn²⁺, and Fe²⁺-Substituted MOF-5 and Redox Reactivity in Cr- and Fe-MOF-5. *J. Am. Chem. Soc.* **2013**, *135* (34), 12886–12891.
- (73) Drake, T.; Ji, P.; Lin, W. Site Isolation in Metal-Organic Frameworks Enables Novel Transition Metal Catalysis. *Acc. Chem. Res.* **2018**, *51* (9), 2129–2138.
- (74) Manna, K.; Zhang, T.; Lin, W. Postsynthetic Metalation of Bipyridyl-Containing Metal-Organic Frameworks for Highly Efficient Catalytic Organic Transformations. *J. Am. Chem. Soc.* **2014**, *136* (18), 6566–6569.
- (75) Bloch, E. D.; Britt, D.; Lee, C.; Doonan, C. J.; Uribe-Romo, F. J.; Furukawa, H.; Long, J. R.; Yaghi, O. M. Metal Insertion in a Microporous Metal-Organic Framework Lined with 2,2'-Bipyridine.

- J. Am. Chem. Soc.* **2010**, *132* (41), 14382–14384.
- (76) Manna, K.; Zhang, T.; Greene, F. X.; Lin, W. Bipyridine- and Phenanthroline-Based Metal-Organic Frameworks for Highly Efficient and Tandem Catalytic Organic Transformations via Directed C-H Activation. *J. Am. Chem. Soc.* **2015**, *137* (7), 2665–2673.
- (77) Dau, P. V.; Cohen, S. M. A Bifunctional, Site-Isolated Metal-Organic Framework-Based Tandem Catalyst. *Inorg. Chem.* **2015**, *54* (7), 3134–3138.
- (78) Zhang, T.; Manna, K.; Lin, W. Metal-Organic Frameworks Stabilize Solution-Inaccessible Cobalt Catalysts for Highly Efficient Broad-Scope Organic Transformations. *J. Am. Chem. Soc.* **2016**, *138* (9), 3241–3249.
- (79) Feng, X.; Song, Y.; Li, Z.; Kaufmann, M.; Pi, Y.; Chen, J. S.; Xu, Z.; Li, Z.; Wang, C.; Lin, W. Metal-Organic Framework Stabilizes a Low-Coordinate Iridium Complex for Catalytic Methane Borylation. *J. Am. Chem. Soc.* **2019**, *141* (28), 11196–11203.
- (80) Quan, Y.; Song, Y.; Shi, W.; Xu, Z.; Chen, S.; Jiang, X.; Wang, C.; Lin, W. Metal-Organic Framework with Dual Active Sites in Engineered Mesopores for Bioinspired Synergistic Catalysis. *J. Am. Chem. Soc.* **2020**, *142* (19), 8602–8607.
- (81) Schneemann, A.; Wan, L. F.; Lipton, A. S.; Liu, Y. S.; Snider, J. L.; Baker, A. A.; Sugar, J. D.; Spataru, C. D.; Guo, J.; Autrey, T. S.; Jørgensen, M.; Jensen, T. R.; Wood, B. C.; Allendorf, M. D.; Stavila, V. Nanoconfinement of Molecular Magnesium Borohydride Captured in a Bipyridine-Functionalized Metal-Organic Framework. *ACS Nano* **2020**, *14* (8), 10294–10304.
- (82) Song, Y.; Feng, X.; Chen, J. S.; Brzezinski, C.; Xu, Z.; Lin, W. Multistep Engineering of Synergistic Catalysts in a Metal-Organic Framework for Tandem C-O Bond Cleavage. *J. Am. Chem. Soc.* **2020**, *142* (10), 4872–4882.
- (83) Gao, Z.; Lai, Y.; Tao, Y.; Xiao, L.; Zhang, L.; Luo, F. Constructing Well-Defined and Robust Th-MOF-Supported Single-Site Copper for Production and Storage of Ammonia from Electroreduction of Nitrate. *ACS Cent. Sci.* **2021**, *7* (6), 1066–1072.
- (84) Guo, Y.; Shi, W.; Yang, H.; He, Q.; Zeng, Z.; Ye, J. Y.; He, X.; Huang, R.; Wang, C.; Lin, W. Cooperative Stabilization of the [Pyridinium-CO₂-Co] Adduct on a Metal-Organic Layer Enhances Electrocatalytic CO₂ Reduction. *J. Am. Chem. Soc.* **2019**, *141* (44), 17875–17883.
- (85) Shi, W.; Quan, Y.; Lan, G.; Ni, K.; Song, Y.; Jiang, X.; Wang, C.; Lin, W. Bifunctional Metal-Organic Layers for Tandem Catalytic Transformations Using Molecular Oxygen and Carbon Dioxide. *J. Am. Chem. Soc.* **2021**, *143* (40), 16718–16724.
- (86) Chen, L.; Jiang, Y.; Huo, H.; Liu, J.; Li, Y.; Li, C.; Zhang, N.; Wang, J. Metal-Organic Framework-Based Composite Ni@MOF as Heterogenous Catalyst for Ethylene Trimerization. *Appl. Catal. A Gen.* **2020**, *594*, 117457.
- (87) Manna, K.; Zhang, T.; Carboni, M.; Abney, C. W.; Lin, W. Salicylaldimine-Based Metal - Organic Framework Enabling Highly Active Olefin Hydrogenation with Iron and Cobalt Catalysts. *J. Am. Chem. Soc.* **2014**, *136* (38), 13182–13185.
- (88) Tan, C.; Han, X.; Li, Z.; Liu, Y.; Cui, Y. Controlled Exchange of Achiral Linkers with Chiral Linkers in Zr-Based UiO-68 Metal-Organic Framework. *J. Am. Chem. Soc.* **2018**, *140* (47), 16229–16236.
- (89) Thacker, N. C.; Lin, Z.; Zhang, T.; Gilhula, J. C.; Abney, C. W.; Lin, W. Robust and Porous β -Diketiminato-Functionalized Metal-Organic Frameworks for Earth-Abundant-Metal-Catalyzed C-H Amination and Hydrogenation. *J. Am. Chem. Soc.* **2016**, *138* (10), 3501–3509.
- (90) Zhu, Y.; Lan, G.; Fan, Y.; Veroneau, S. S.; Song, Y.; Micheroni, D.; Lin, W. Merging Photoredox and Organometallic Catalysts in a Metal-Organic Framework Significantly Boosts Photocatalytic Activities. *Angew. Chem.* **2018**, *130* (43), 14286–14290.
- (931) Nguyen, H. G. T.; Schweitzer, N. M.; Chang, C. Y.; Drake, T. L.; So, M. C.; Stair, P. C.; Farha, O. K.; Hupp, J. T.; Nguyen, S. T. Vanadium-Node-Functionalized UiO-66: A Thermally Stable MOF-Supported Catalyst for the Gas-Phase Oxidative Dehydrogenation of Cyclohexene. *ACS Catal.* **2014**, *4* (8), 2496–2500.
- (92) Manna, K.; Ji, P.; Lin, Z.; Greene, F. X.; Urban, A.; Thacker, N. C.; Lin, W. Chemoselective Single-Site Earth-Abundant Metal Catalysts at Metal-Organic Framework Nodes. *Nat. Commun.*

- 2016**, 7, 1–11.
- (93) Ji, P.; Manna, K.; Lin, Z.; Feng, X.; Urban, A.; Song, Y.; Lin, W. Single-Site Cobalt Catalysts at New $Zr_{12}(\mu_3-O)_8(\mu_3-OH)_8(\mu_2-OH)_6$ Metal–Organic Framework Nodes for Highly Active Hydrogenation of Nitroarenes, Nitriles, and Isocyanides. *J. Am. Chem. Soc.* **2017**, *139* (20), 7004–7011.
- (94) An, B.; Zhang, J.; Cheng, K.; Ji, P.; Wang, C.; Lin, W. Confinement of Ultrasmall Cu/ZnOx Nanoparticles in Metal–Organic Frameworks for Selective Methanol Synthesis from Catalytic Hydrogenation of CO₂. *J. Am. Chem. Soc.* **2017**, *139* (10), 3834–3840.
- (95) Manna, K.; Ji, P.; Greene, F. X.; Lin, W. Metal–Organic Framework Nodes Support Single-Site Magnesium–Alkyl Catalysts for Hydroboration and Hydroamination Reactions. *J. Am. Chem. Soc.* **2016**, *138* (24), 7488–7491.
- (96) Otake, K. I.; Cui, Y.; Buru, C. T.; Li, Z.; Hupp, J. T.; Farha, O. K. Single-Atom-Based Vanadium Oxide Catalysts Supported on Metal–Organic Frameworks: Selective Alcohol Oxidation and Structure–Activity Relationship. *J. Am. Chem. Soc.* **2018**, *140* (28), 8652–8656.
- (97) Yuan, S.; Peng, J.; Zhang, Y.; Shao-Horn, Y. Stability Trend of Metal–Organic Frameworks with Heterometal-Modified Hexanuclear Zr Building Units. *J. Phys. Chem. C* **2019**, *123* (46), 28266–28274.
- (98) Syed, Z. H.; Sha, F.; Zhang, X.; Kaphan, D. M.; Delferro, M.; Farha, O. K. Metal–Organic Framework Nodes as a Supporting Platform for Tailoring the Activity of Metal Catalysts. *ACS Catal.* **2020**, *10* (19), 11556–11566.
- (99) Yang, Y.; Zhang, X.; Kanchanakungwankul, S.; Lu, Z.; Noh, H.; Syed, Z. H.; Farha, O. K.; Truhlar, D. G.; Hupp, J. T. Unexpected “Spontaneous” Evolution of Catalytic, MOF-Supported Single Cu(II) Cations to Catalytic, MOF-Supported Cu(0) Nanoparticles. *J. Am. Chem. Soc.* **2020**, *142* (50), 21169–21177.
- (100) Zhang, J.; An, B.; Li, Z.; Cao, Y.; Dai, Y.; Wang, W.; Zeng, L.; Lin, W.; Wang, C. Neighboring Zn–Zr Sites in a Metal–Organic Framework for CO₂ Hydrogenation. *J. Am. Chem. Soc.* **2021**, *143* (23), 8829–8837.
- (101) Kim, I. S.; Borycz, J.; Platero-Prats, A. E.; Tussupbayev, S.; Wang, T. C.; Farha, O. K.; Hupp, J. T.; Gagliardi, L.; Chapman, K. W.; Cramer, C. J.; Martinson, A. B. F. Targeted Single-Site MOF Node Modification: Trivalent Metal Loading via Atomic Layer Deposition. *Chem. Mater.* **2015**, *27* (13), 4772–4778.
- (102) Yang, D.; Odoh, S. O.; Wang, T. C.; Farha, O. K.; Hupp, J. T.; Cramer, C. J.; Gagliardi, L.; Gates, B. C. Metal–Organic Framework Nodes as Nearly Ideal Supports for Molecular Catalysts: NU-1000- and UiO-66-Supported Iridium Complexes. *J. Am. Chem. Soc.* **2015**, *137* (23), 7391–7396.
- (103) Li, Z.; Schweitzer, N. M.; League, A. B.; Bernales, V.; Peters, A. W.; Getsoian, A. B.; Wang, T. C.; Miller, J. T.; Vjunov, A.; Fulton, J. L.; Lercher, J. A.; Cramer, C. J.; Gagliardi, L.; Hupp, J. T.; Farha, O. K. Sintering-Resistant Single-Site Nickel Catalyst Supported by Metal–Organic Framework. *J. Am. Chem. Soc.* **2016**, *138* (6), 1977–1982.
- (104) Li, Z.; Peters, A. W.; Platero-Prats, A. E.; Liu, J.; Kung, C. W.; Noh, H.; DeStefano, M. R.; Schweitzer, N. M.; Chapman, K. W.; Hupp, J. T.; Farha, O. K. Fine-Tuning the Activity of Metal–Organic Framework-Supported Cobalt Catalysts for the Oxidative Dehydrogenation of Propane. *J. Am. Chem. Soc.* **2017**, *139* (42), 15251–15258.
- (105) Hackler, R. A.; Pandharkar, R.; Ferrandon, M. S.; Kim, I. S.; Vermeulen, N. A.; Gallington, L. C.; Chapman, K. W.; Farha, O. K.; Cramer, C. J.; Sauer, J.; Gagliardi, L.; Martinson, A. B. F.; Delferro, M. Isomerization and Selective Hydrogenation of Propyne: Screening of Metal–Organic Frameworks Modified by Atomic Layer Deposition. *J. Am. Chem. Soc.* **2020**, *142* (48), 20380–20389.
- (106) Song, Y.; Li, Z.; Ji, P.; Kaufmann, M.; Feng, X.; Chen, J. S.; Wang, C.; Lin, W. Metal–Organic Framework Nodes Support Single-Site Nickel(II) Hydride Catalysts for the Hydrogenolysis of Aryl Ethers. *ACS Catal.* **2019**, *9* (2), 1578–1583.
- (107) Feng, X.; Song, Y.; Chen, J. S.; Xu, Z.; Dunn, S. J.; Lin, W. Rational Construction of an Artificial

- Binuclear Copper Monooxygenase in a Metal-Organic Framework. *J. Am. Chem. Soc.* **2021**, *143* (2), 1107–1118.
- (108) Antil, N.; Kumar, A.; Akhtar, N.; Newar, R.; Begum, W.; Manna, K. Metal-Organic Framework-Confining Single-Site Base-Metal Catalyst for Chemoselective Hydrodeoxygenation of Carbonyls and Alcohols. *Inorg. Chem.* **2021**, *60* (12), 9029–9039.
- (109) Padial, N. M.; Lerma-Berlanga, B.; Almora-Barrios, N.; Castells-Gil, J.; Da Silva, I.; De La Mata, M.; Molina, S. I.; Hernández-Saz, J.; Platero-Prats, A. E.; Tatay, S.; Martí-Gastaldo, C. Heterometallic Titanium-Organic Frameworks by Metal-Induced Dynamic Topological Transformations. *J. Am. Chem. Soc.* **2020**, *142* (14), 6638–6648.
- (110) Castells-Gil, J.; Padial, N. M.; Almora-Barrios, N.; Albero, J.; Ruiz-Salvador, A. R.; González-Platas, J.; García, H.; Martí-Gastaldo, C. Chemical Engineering of Photoactivity in Heterometallic Titanium-Organic Frameworks by Metal Doping. *Angew. Chem.* **2018**, *130* (28), 8589–8593.
- (111) Chui, S. S. Y.; Lo, S. M. F.; Charmant, J. P. H.; Orpen, A. G.; Williams, I. D. A Chemically Functionalizable Nanoporous Material [Cu₃(TMA)2(H₂O)₃](N). *Science*. **1999**, *283* (5405), 1148–1150.
- (112) Marx, S.; Kleist, W.; Huang, J.; Maclejewski, M.; Baiker, A. Tuning Functional Sites and Thermal Stability of Mixed-Linker MOFs Based on MIL-53(Al). *Dalt. Trans.* **2010**, *39* (16), 3795–3798.
- (113) Lescouet, T.; Kockrick, E.; Bergeret, G.; Pera-Titus, M.; Aguado, S.; Farrusseng, D. Homogeneity of Flexible Metal-Organic Frameworks Containing Mixed Linkers. *J. Mater. Chem.* **2012**, *22* (20), 10287–10293.
- (114) Liu, Q.; Cong, H.; Deng, H. Deciphering the Spatial Arrangement of Metals and Correlation to Reactivity in Multivariate Metal-Organic Frameworks. *J. Am. Chem. Soc.* **2016**, *138* (42), 13822–13825.
- (115) Carson, F.; Martínez-Castro, E.; Marcos, R.; Miera, G. G.; Jansson, K.; Zou, X.; Martín-Matute, B. Effect of the Functionalisation Route on a Zr-MOF with an Ir-NHC Complex for Catalysis. *Chem. Commun.* **2015**, *51* (54), 10864–10867.
- (116) Kong, X.; Deng, H.; Yan, F.; Kim, J.; Swisher, J. A.; Smit, B.; Yaghi, O. M.; Reimer, J. A. Mapping of functional groups in metal-organic frameworks. *Science* **2013**, *341*(6148), 882–885.
- (117) Li, B.; Ma, D.; Li, Y.; Zhang, Y.; Li, G.; Shi, Z.; Feng, S.; Zaworotko, M. J.; Ma, S. Dual Functionalized Cages in Metal-Organic Frameworks via Stepwise Postsynthetic Modification. *Chem. Mater.* **2016**, *28* (13), 4781–4786.
- (118) Liu, S. Y.; Zhou, D. D.; He, C. T.; Liao, P. Q.; Cheng, X. N.; Xu, Y. T.; Ye, J. W.; Zhang, J. P.; Chen, X. M. Flexible, Luminescent Metal-Organic Frameworks Showing Synergistic Solid-Solution Effects on Porosity and Sensitivity. *Angew. Chem.* **2016**, *128* (52), 16255–16259.
- (119) Feng, L.; Yuan, S.; Li, J. L.; Wang, K. Y.; Day, G. S.; Zhang, P.; Wang, Y.; Zhou, H. C. Uncovering Two Principles of Multivariate Hierarchical Metal-Organic Framework Synthesis via Retrosynthetic Design. *ACS Cent. Sci.* **2018**, *4* (12), 1719–1726.
- (120) Feng, L.; Yuan, S.; Zhang, L. L.; Tan, K.; Li, J. L.; Kirchon, A.; Liu, L. M.; Zhang, P.; Han, Y.; Chabal, Y. J.; Zhou, H. C. Creating Hierarchical Pores by Controlled Linker Thermolysis in Multivariate Metal-Organic Frameworks. *J. Am. Chem. Soc.* **2018**, *140* (6), 2363–2372.
- (121) Geary, J.; Wong, A. H.; Xiao, D. J. Thermolabile Cross-Linkers for Templating Precise Multicomponent Metal-Organic Framework Pores. *J. Am. Chem. Soc.* **2021**, *143* (27), 10317–10323.
- (122) Bueken, B.; Van Velthoven, N.; Krajnc, A.; Smolders, S.; Taulelle, F.; Mellot-Draznieks, C.; Mali, G.; Bennett, T. D.; De Vos, D. Tackling the Defect Conundrum in UiO-66: A Mixed-Linker Approach to Engineering Missing Linker Defects. *Chem. Mater.* **2017**, *29* (24), 10478–10486.
- (123) Naghdi, S.; Cherevan, A.; Giesriegl, A.; Guillet-Nicolas, R.; Biswas, S.; Gupta, T.; Wang, J.; Haunold, T.; Bayer, B. C.; Ruppel, G.; Toroker, M. C.; Kleitz, F.; Eder, D. Selective Ligand Removal to Improve Accessibility of Active Sites in Hierarchical MOFs for Heterogeneous Photocatalysis. *Nat. Commun.* **2022**, *13* (1).
- (124) Guillerm, V.; Xu, H.; Albalad, J.; Imaz, I.; Maspoch, D. Postsynthetic Selective Ligand Cleavage

- by Solid-Gas Phase Ozonolysis Fuses Micropores into Mesopores in Metal-Organic Frameworks. *J. Am. Chem. Soc.* **2018**, *140* (44), 15022–15030.
- (125) Wang, K. Y.; Feng, L.; Yan, T. H.; Wu, S.; Joseph, E. A.; Zhou, H. C. Rapid Generation of Hierarchically Porous Metal-Organic Frameworks through Laser Photolysis. *Angew. Chem. Int. Ed.* **2020**, *59* (28), 11349–11354.
- (126) Luo, T. Y.; Liu, C.; Gan, X. Y.; Muldoon, P. F.; Diemler, N. A.; Millstone, J. E.; Rosi, N. L. Multivariate Stratified Metal-Organic Frameworks: Diversification Using Domain Building Blocks. *J. Am. Chem. Soc.* **2019**, *141* (5), 2161–2168.
- (127) Lauhon, L. J.; Gudlksen, M. S.; Wang, D.; Lieber, C. M. Epitaxial Core-Shell and Core-Multishell Nanowire Heterostructures. *Nature* **2002**, *420* (6911), 57–61.
- (128) Ghosh Chaudhuri, R.; Paria, S. Core/Shell Nanoparticles: Classes, Properties, Synthesis Mechanisms, Characterization, and Applications. *Chem. Rev.* **2012**, *112* (4), 2373–2433.
- (129) El-Toni, A. M.; Habila, M. A.; Labis, J. P.; Alothman, Z. A.; Alhoshan, M.; Elzatahry, A. A.; Zhang, F. Design, Synthesis and Applications of Core-Shell, Hollow Core, and Nanorattle Multifunctional Nanostructures. *Nanoscale* **2016**, *8* (5), 2510–2531.
- (130) Yoo, Y.; Jeong, H. K. Heteroepitaxial Growth of Isorecticular Metal-Organic Frameworks and Their Hybrid Films. *Cryst. Growth Des.* **2010**, *10* (3), 1283–1288.
- (131) Shekhah, O.; Hirai, K.; Wang, H.; Uehara, H.; Kondo, M.; Diring, S.; Zacher, D.; Fischer, R. A.; Sakata, O.; Kitagawa, S.; Furukawa, S.; Wöll, C. MOF-on-MOF Heteroepitaxy: Perfectly Oriented [Zn₂(Ndc)₂(Dabco)]_n Grown on [Cu₂(Ndc)₂(Dabco)]_n Thin Films. *Dalt. Trans.* **2011**, *40* (18), 4954–4958.
- (132) Lee, H. J.; Cho, Y. J.; Cho, W.; Oh, M. Controlled Isotropic or Anisotropic Nanoscale Growth of Coordination Polymers: Formation of Hybrid Coordination Polymer Particles. *ACS Nano* **2013**, *7* (1), 491–499.
- (133) Song, X.; Kim, T. K.; Kim, H.; Kim, D.; Jeong, S.; Moon, H. R.; Lah, M. S. Post-Synthetic Modifications of Framework Metal Ions in Isostructural Metal-Organic Frameworks: Core-Shell Heterostructures via Selective Transmetalations. *Chem. Mater.* **2012**, *24* (15), 3065–3073.
- (134) Tang, J.; Salunkhe, R. R.; Liu, J.; Torad, N. L.; Imura, M.; Furukawa, S.; Yamauchi, Y. Thermal Conversion of Core-Shell Metal-Organic Frameworks: A New Method for Selectively Functionalized Nanoporous Hybrid Carbon. *J. Am. Chem. Soc.* **2015**, *137* (4), 1572–1580.
- (135) Lee, W. R.; Ryu, D. W.; Phang, W. J.; Park, J. H.; Hong, C. S. Charge Effect of Foreign Metal Ions and the Crystal Growth Process in Hybridized Metal-Organic Frameworks. *Chem. Commun.* **2012**, *48* (88), 10847–10849.
- (136) Park, H.; Kim, S.; Jung, B.; Park, M. H.; Kim, Y.; Kim, M. Defect Engineering into Metal-Organic Frameworks for the Rapid and Sequential Installation of Functionalities. *Inorg. Chem.* **2018**, *57* (3), 1040–1047.
- (137) Mutruc, D.; Goulet-Hanssens, A.; Fairman, S.; Wahl, S.; Zimathies, A.; Knie, C.; Hecht, S. Modulating Guest Uptake in Core-Shell MOFs with Visible Light. *Angew. Chem. Int. Ed.* **2019**, *58* (37), 12862–12867.
- (138) Kim, S.; Lee, J.; Jeong, S.; Moon, H. R.; Kim, M. Surface-Deactivated Core-Shell Metal-Organic Framework by Simple Ligand Exchange for Enhanced Size Discrimination in Aerobic Oxidation of Alcohols. *Chem. Eur. J.* **2020**, *26* (34), 7568–7572.
- (139) Jayachandrababu, K. C.; Sholl, D. S.; Nair, S. Structural and Mechanistic Differences in Mixed-Linker Zeolitic Imidazolate Framework Synthesis by Solvent Assisted Linker Exchange and de Novo Routes. *J. Am. Chem. Soc.* **2017**, *139* (16), 5906–5915.
- (140) Boissonnault, J. A.; Wong-Foy, A. G.; Matzger, A. J. Core-Shell Structures Arise Naturally during Ligand Exchange in Metal-Organic Frameworks. *J. Am. Chem. Soc.* **2017**, *139* (42), 14841–14844.
- (141) Dodson, R. A.; Kalenak, A. P.; Matzger, A. J. Solvent Choice in Metal-Organic Framework Linker Exchange Permits Microstructural Control. *J. Am. Chem. Soc.* **2020**, *142* (49), 20806–20813.
- (142) Lerma-Berlanga, B.; R. Ganivet, C.; Almora-Barrios, N.; Tatay, S.; Peng, Y.; Albero, J.; Fabelo, O.;

- González-Platas, J.; García, H.; M. Padial, N.; Martí-Gastaldo, C. Effect of Linker Distribution in the Photocatalytic Activity of Multivariate Mesoporous Crystals. *J. Am. Chem. Soc.* **2021**, *143* (4), 1798–1806.
- (143) Jeong, S.; Seong, J.; Moon, S. W.; Lim, J.; Baek, S. Bin; Min, S. K.; Lah, M. S. Spatial Distribution Modulation of Mixed Building Blocks in Metal-Organic Frameworks. *Nat. Commun.* **2022**, *13* 1027.
- (144) Koh, K.; Wong-Foy, A. G.; Matzger, A. J. MOF@MOF: Microporous Core-Shell Architectures. *Chem. Commun.* **2009**, 6162–6164.
- (145) Carson, C. G.; Ward, J.; Liu, X. T.; Schwartz, J.; Gerhardt, R. A.; Tannenbaum, R. Dopant-Controlled Crystallization in Metal-Organic Frameworks: The Role of Copper(II) in Zinc 1,4-Benzenedicarboxylate. *J. Phys. Chem. C* **2012**, *116* (29), 15322–15328.
- (147) Chen, Y.; Yu, B.; Cui, Y.; Xu, S.; Gong, J. Core-Shell Structured Cyclodextrin Metal-Organic Frameworks with Hierarchical Dye Encapsulation for Tunable Light Emission. *Chem. Mater.* **2019**, *31* (4), 1289–1295.
- (147) Dai, S.; Tissot, A.; Serre, C. Recent Progresses in Metal–Organic Frameworks Based Core–Shell Composites. *Adv. Energy Mater.* **2022**, *12* (4), 1–26.
- (148) Pang, J.; Yuan, S.; Qin, J.; Wu, M.; Lollar, C. T.; Li, J.; Huang, N.; Li, B.; Zhang, P.; Zhou, H. C. Enhancing Pore-Environment Complexity Using a Trapezoidal Linker: Toward Stepwise Assembly of Multivariate Quinary Metal-Organic Frameworks. *J. Am. Chem. Soc.* **2018**, *140* (39), 12328–12332.
- (149) Yuan, S.; Chen, Y. P.; Qin, J. S.; Lu, W.; Zou, L.; Zhang, Q.; Wang, X.; Sun, X.; Zhou, H. C. Linker Installation: Engineering Pore Environment with Precisely Placed Functionalities in Zirconium MOFs. *J. Am. Chem. Soc.* **2016**, *138* (28), 8912–8919.
- (150) Yuan, S.; Lu, W.; Chen, Y. P.; Zhang, Q.; Liu, T. F.; Feng, D.; Wang, X.; Qin, J.; Zhou, H. C. Sequential Linker Installation: Precise Placement of Functional Groups in Multivariate Metal-Organic Frameworks. *J. Am. Chem. Soc.* **2015**, *137* (9), 3177–3180.
- (151) Li, J.; Yuan, S.; Qin, J. S.; Pang, J.; Zhang, P.; Zhang, Y.; Huang, Y.; Drake, H. F.; Liu, W. R.; Zhou, H. C. Stepwise Assembly of Turn-on Fluorescence Sensors in Multicomponent Metal–Organic Frameworks for in Vitro Cyanide Detection. *Angew. Chem. Int. Ed.* **2020**, *59* (24), 9319–9323.
- (152) Chen, C. X.; Wei, Z. W.; Jiang, J. J.; Zheng, S. P.; Wang, H. P.; Qiu, Q. F.; Cao, C. C.; Fenske, D.; Su, C. Y. Dynamic Spacer Installation for Multirole Metal-Organic Frameworks: A New Direction toward Multifunctional MOFs Achieving Ultrahigh Methane Storage Working Capacity. *J. Am. Chem. Soc.* **2017**, *139* (17), 6034–6037.
- (153) Xu, X.; Rummelt, S. M.; Morel, F. L.; Ranocchiari, M.; Van Bokhoven, J. A. Selective Catalytic Behavior of a Phosphine-Tagged Metal-Organic Framework Organocatalyst. *Chem. Eur. J.* **2014**, *20* (47), 15467–15472.
- (154) Tu, B.; Pang, Q.; Wu, D.; Song, Y.; Weng, L.; Li, Q. Ordered Vacancies and Their Chemistry in Metal-Organic Frameworks. *J. Am. Chem. Soc.* **2014**, *136* (41), 14465–14471.
- (155) Feng, D.; Wang, K.; Wei, Z.; Chen, Y. P.; Simon, C. M.; Arvapally, R. K.; Martin, R. L.; Bosch, M.; Liu, T. F.; Fordham, S.; Yuan, D.; Omary, M. A.; Haranczyk, M.; Smit, B.; Zhou, H. C. Kinetically Tuned Dimensional Augmentation as a Versatile Synthetic Route towards Robust Metal-Organic Frameworks. *Nat. Commun.* **2014**, *5*, 5723.
- (156) Koh, K.; Wong-Foy, A. G.; Matzger, A. J. A Crystalline Mesoporous Coordination Copolymer with High Microporosity. *Angew. Chem.* **2008**, *120* (4), 689–692.
- (157) Klein, N.; Senkovska, I.; Gedrich, K.; Stoeck, U.; Henschel, A.; Mueller, U.; Kaskel, S. A Mesoporous Metal-Organic Framework. *Angew. Chem. Int. Ed.* **2009**, *48* (52), 9954–9957.
- (158) Grünker, R.; Bon, V.; Müller, P.; Stoeck, U.; Krause, S.; Mueller, U.; Senkovska, I.; Kaskel, S. A New Metal-Organic Framework with Ultra-High Surface Area. *Chem. Commun.* **2014**, *50* (26), 3450–3452.
- (159) Hönicke, I. M.; Senkovska, I.; Bon, V.; Baburin, I. A.; Bönisch, N.; Raschke, S.; Evans, J. D.; Kaskel, S. Balancing Mechanical Stability and Ultrahigh Porosity in Crystalline Framework Materials. *Angew. Chem. Int. Ed.* **2018**, *57* (42), 13780–13783.

- (160) Chevreau, H.; Devic, T.; Salles, F.; Maurin, G.; Stock, N.; Serre, C. Mixed-Linker Hybrid Superpolyhedra for the Production of a Series of Large-Pore Iron(III) Carboxylate Metal-Organic Frameworks. *Angew. Chem. Int. Ed.* **2013**, *52* (19), 5056–5060.
- (161) Virmani, E.; Beyer, O.; Lüning, U.; Ruschewitz, U.; Wuttke, S. Topology-Guided Functional Multiplicity of Iron(II)-Based Metal-Organic Frameworks. *Mater. Chem. Front.* **2017**, *1* (10), 1965–1974.
- (162) Liu, L.; Konstas, K.; Hill, M. R.; Telfer, S. G. Programmed Pore Architectures in Modular Quaternary Metal-Organic Frameworks. *J. Am. Chem. Soc.* **2013**, *135* (47), 17731–17734.
- (163) Liu, L.; Telfer, S. G. Systematic Ligand Modulation Enhances the Moisture Stability and Gas Sorption Characteristics of Quaternary Metal-Organic Frameworks. *J. Am. Chem. Soc.* **2015**, *137* (11), 3901–3909.
- (164) Macreadie, L. K.; Babarao, R.; Setter, C. J.; Lee, S. J.; Qazvini, O. T.; Seeber, A. J.; Tsanaksidis, J.; Telfer, S. G.; Batten, S. R.; Hill, M. R. Enhancing Multicomponent Metal–Organic Frameworks for Low Pressure Liquid Organic Hydrogen Carrier Separations. *Angew. Chem.* **2020**, *132* (15), 6146–6154.
- (165) Zhang, X.; Frey, B. L.; Chen, Y. S.; Zhang, J. Topology-Guided Stepwise Insertion of Three Secondary Linkers in Zirconium Metal-Organic Frameworks. *J. Am. Chem. Soc.* **2018**, *140* (24), 7710–7715.
- (166) Qin, J. S.; Du, D. Y.; Li, M.; Lian, X. Z.; Dong, L. Z.; Bosch, M.; Su, Z. M.; Zhang, Q.; Li, S. L.; Lan, Y. Q.; Yuan, S.; Zhou, H. C. Derivation and Decoration of Nets with Trigonal-Prismatic Nodes: A Unique Route to Reticular Synthesis of Metal-Organic Frameworks. *J. Am. Chem. Soc.* **2016**, *138* (16), 5299–5307.
- (167) Tu, B.; Pang, Q.; Xu, H.; Li, X.; Wang, Y.; Ma, Z.; Weng, L.; Li, Q. Reversible Redox Activity in Multicomponent Metal-Organic Frameworks Constructed from Trinuclear Copper Pyrazolate Building Blocks. *J. Am. Chem. Soc.* **2017**, *139* (23), 7998–8007.
- (168) Wang, C.; Cong, H.; Zhou, Y.; Song, Y.; Liu, Q.; Deng, H.; O’Keeffe, M.; Hu, G.; Wu, J.; Ma, Y. Mesoporous Cages in Chemically Robust MOFs Created by a Large Number of Vertices with Reduced Connectivity. *J. Am. Chem. Soc.* **2018**, *141* (1), 488–496.
- (169) Elsaidi, S. K.; Mohamed, M. H.; Wojtas, L.; Cairns, A. J.; Eddaoudi, M.; Zaworotko, M. J. Two-Step Crystal Engineering of Porous Nets from [Cr₃(M₃-O)(RCO₂)₆] and [Cu₃(M₃-Cl)(RNH₂)₆Cl₆] Molecular Building Blocks. *Chem. Commun.* **2013**, *49* (74), 8154–8156.
- (170) Zheng, S. T.; Wu, T.; Zuo, F.; Chou, C.; Feng, P.; Bu, X. Mimicking Zeolite to Its Core: Porous Sodalite Cages as Hangers for Pendant Trimeric M₃(OH) Clusters (M = Mg, Mn, Co, Ni, Cd). *J. Am. Chem. Soc.* **2012**, *134* (4), 1934–1937.
- (171) Muldoon, P. F.; Liu, C.; Miller, C. C.; Koby, S. B.; Gamble Jarvi, A.; Luo, T. Y.; Saxena, S.; O’Keeffe, M.; Rosi, N. L. Programmable Topology in New Families of Heterobimetallic Metal-Organic Frameworks. *J. Am. Chem. Soc.* **2018**, *140* (20), 6194–6198.
- (172) Zheng, S. T.; Zhao, X.; Lau, S.; Fuhr, A.; Feng, P.; Bu, X. Entrapment of Metal Clusters in Metal-Organic Framework Channels by Extended Hooks Anchored at Open Metal Sites. *J. Am. Chem. Soc.* **2013**, *135* (28), 10270–10273.
- (173) Zheng, S. T.; Wu, T.; Irfanoglu, B.; Zuo, F.; Feng, P.; Bu, X. Multicomponent Self-Assembly of a Nested Co₂₄@Co₄₈ Metal-Organic Polyhedral Framework. *Angew. Chem. Int. Ed.* **2011**, *50* (35), 8034–8037.
- (174) Zeng, H.; Xie, X. J.; Xie, M.; Huang, Y. L.; Luo, D.; Wang, T.; Zhao, Y.; Lu, W.; Li, D. Cage-Interconnected Metal-Organic Framework with Tailored Apertures for Efficient C₂H₆/C₂H₄ Separation under Humid Conditions. *J. Am. Chem. Soc.* **2019**, *141* (51), 20390–20396.
- (175) Tu, B.; Diestel, L.; Shi, Z. L.; Bandara, W. R. L. N.; Chen, Y.; Lin, W.; Zhang, Y. B.; Telfer, S. G.; Li, Q. Harnessing Bottom-Up Self-Assembly To Position Five Distinct Components in an Ordered Porous Framework. *Angew. Chem. Int. Ed.* **2019**, *58* (16), 5348–5353.
- (176) Kleist, W.; Jutz, F.; Maciejewski, M.; Baiker, A. Mixed-Linker Metal-Organic Frameworks as Catalysts for the Synthesis of Propylene Carbonate from Propylene Oxide and CO₂. *Eur. J. Inorg. Chem.* **2009**, *24*, 3552–3561.

- (177) Kleist, W.; Maciejewski, M.; Baiker, A. MOF-5 Based Mixed-Linker Metal-Organic Frameworks: Synthesis, Thermal Stability and Catalytic Application. *Thermochim. Acta* **2010**, *499* (1–2), 71–78.
- (178) Yeung, H. H. M.; Li, W.; Saines, P. J.; Köster, T. K. J.; Grey, C. P.; Cheetham, A. K. Ligand-Directed Control over Crystal Structures of Inorganic-Organic Frameworks and Formation of Solid Solutions. *Angew. Chem. Int. Ed.* **2013**, *52* (21), 5544–5547.
- (179) Hendon, C. H.; Bonnefoy, J.; Quadrelli, E. A.; Canivet, J.; Chambers, M. B.; Rouse, G.; Walsh, A.; Fontecave, M.; Mellot-Draznieks, C. A Simple and Non-Destructive Method for Assessing the Incorporation of Bipyridine Dicarboxylates as Linkers within Metal-Organic Frameworks. *Chem. Eur. J.* **2016**, *22* (11), 3713–3718.
- (180) Taddei, M.; Tiana, D.; Casati, N.; Van Bokhoven, J. A.; Smit, B.; Ranocchiari, M. Mixed-Linker UiO-66: Structure-Property Relationships Revealed by a Combination of High-Resolution Powder X-Ray Diffraction and Density Functional Theory Calculations. *Phys. Chem. Chem. Phys.* **2017**, *19* (2), 1551–1559.
- (181) Xu, W.; Tu, B.; Liu, Q.; Shu, Y.; Liang, C. C.; Diercks, C. S.; Yaghi, O. M.; Zhang, Y. B.; Deng, H.; Li, Q. Anisotropic Reticular Chemistry. *Nat. Rev. Mater.* **2020**, *5* (10), 764–779.
- (182) Yuan, S.; Huang, L.; Huang, Z.; Sun, D.; Qin, J.; Yuan, S.; Huang, L.; Huang, Z.; Sun, D.; Qin, J.; Feng, L.; Li, J. Continuous Variation of Lattice Dimensions and Pore Sizes in Metal – Organic Frameworks. *J. Am. Chem. Soc.* **2020**, *142* (10), 4732–4738.
- (183) Platero-Prats, A. E.; Bermejo Gómez, A.; Chapman, K. W.; Martín-Matute, B.; Zou, X. Functionalising Metal-Organic Frameworks with Metal Complexes: The Role of Structural Dynamics. *CrystEngComm* **2015**, *17* (40), 7632–7635.
- (184) Chen, Q.; Sun, J.; Li, P.; Hod, I.; Moghadam, P. Z.; Kean, Z. S.; Snurr, R. Q.; Hupp, J. T.; Farha, O. K.; Stoddart, J. F. A Redox-Active Bistable Molecular Switch Mounted inside a Metal-Organic Framework. *J. Am. Chem. Soc.* **2016**, *138* (43), 14242–14245.
- (185) Guo, W.; Xia, W.; Cai, K.; Wu, Y.; Qiu, B.; Liang, Z.; Qu, C.; Zou, R. Kinetic-Controlled Formation of Bimetallic Metal–Organic Framework Hybrid Structures. *Small* **2017**, *13* (41), 1–8.
- (186) Han, G.; Wu, S.; Zhou, K.; Xia, H. L.; Liu, X. Y.; Li, J. Full-Color Emission in Multicomponent Metal-Organic Frameworks via Linker Installation. *Inorg. Chem.* **2022**, *61* (8), 3363–3367.
- (187) Saghanejhadtehrani, M.; Schneider, E. K.; Heinke, L. Multi-Component Uptake of Dye Molecules by Films of Nanoporous Metal–Organic Frameworks. *ChemPhysChem* **2017**, *18* (24), 3548–3552.
- (188) Reinsch, H.; Waitschat, S.; Stock, N. Mixed-Linker MOFs with CAU-10 Structure: Synthesis and Gas Sorption Characteristics. *Dalt. Trans.* **2013**, *42* (14), 4840–4847.
- (189) Gotthardt, M. A.; Grosjean, S.; Brunner, T. S.; Kotzel, J.; Gänzler, A. M.; Wolf, S.; Bräse, S.; Kleist, W. Synthesis and Post-Synthetic Modification of Amine-, Alkyne-, Azide- and Nitro-Functionalized Metal-Organic Frameworks Based on DUT-5. *Dalt. Trans.* **2015**, *44* (38), 16802–16809.
- (190) Xu, L.; Luo, Y.; Sun, L.; Pu, S.; Fang, M.; Yuan, R. X.; Du, H. Bin. Tuning the Properties of the Metal-Organic Framework UiO-67-Bpy: Via Post-Synthetic N -Quaternization of Pyridine Sites. *Dalt. Trans.* **2016**, *45* (20), 8614–8621.
- (191) Feng, L.; Wang, K. Y.; Lv, X. L.; Powell, J. A.; Yan, T. H.; Willman, J.; Zhou, H. C. Imprinted Apportionment of Functional Groups in Multivariate Metal-Organic Frameworks. *J. Am. Chem. Soc.* **2019**, *141* (37), 14524–14529.
- (192) Park, T. H.; Koh, K.; Wong-Foy, A. G.; Matzger, A. J. Nonlinear Properties in Coordination Copolymers Derived from Randomly Mixed Ligands. *Cryst. Growth Des.* **2011**, *11* (6), 2059–2063.
- (193) Zhu, X.; Gu, J.; Zhu, J.; Li, Y.; Zhao, L.; Shi, J. Metal-Organic Frameworks with Boronic Acid Suspended and Their Implication for Cis-Diol Moieties Binding. *Adv. Funct. Mater.* **2015**, *25* (25), 3847–3854.
- (194) Zhao, J.; Li, H.; Han, Y.; Li, R.; Ding, X.; Feng, X.; Wang, B. Chirality from Substitution: Enantiomer Separation via a Modified Metal-Organic Framework. *J. Mater. Chem. A* **2015**, *3*

- (23), 12145–12148.
- (195) Liu, H.; Xi, F. G.; Sun, W.; Yang, N. N.; Gao, E. Q. Amino- and Sulfo-Bifunctionalized Metal-Organic Frameworks: One-Pot Tandem Catalysis and the Catalytic Sites. *Inorg. Chem.* **2016**, *55* (12), 5753–5755.
- (196) Hoffmann, H. C.; Debowski, M.; Müller, P.; Paasch, S.; Senkovska, I.; Kaskel, S.; Brunner, E. Solid-State NMR Spectroscopy of Metal-Organic Framework Compounds (MOFs). *Materials (Basel)*. **2012**, *5* (12), 2537–2572.
- (197) Witherspoon, V. J.; Xu, J.; Reimer, J. A. Solid-State NMR Investigations of Carbon Dioxide Gas in Metal-Organic Frameworks: Insights into Molecular Motion and Adsorptive Behavior. *Chem. Rev.* **2018**, *118* (20), 10033–10048.
- (198) Li, S.; Lafon, O.; Wang, W.; Wang, Q.; Wang, X.; Li, Y.; Xu, J.; Deng, F. Recent Advances of Solid-State NMR Spectroscopy for Microporous Materials. *Adv. Mater.* **2020**, *2002879*, 1–22.
- (199) Brunner, E.; Rauche, M. Solid-State NMR Spectroscopy: An Advancing Tool to Analyse the Structure and Properties of Metal-Organic Frameworks. *Chem. Sci.* **2020**, *11* (17), 4297–4304.
- (200) Qi, G.; Wang, Q.; Xu, J.; Deng, F. Solid-State NMR Studies of Internuclear Correlations for Characterizing Catalytic Materials. *Chem. Soc. Rev.* **2021**, *50* (15), 8382–8399.
- (201) Fu, Y.; Guan, H.; Yin, J.; Kong, X. Probing Molecular Motions in Metal-Organic Frameworks with Solid-State NMR. *Coord. Chem. Rev.* **2021**, *427*, 213563.
- (202) Ren, D.; Xia, H.; Zhou, K.; Wu, S.; Liu, X.; Wang, X.; Li, J. Tuning and Directing Energy Transfer in the Whole Visible Spectrum through Linker Installation in Metal–Organic Frameworks. *Angew. Chem.* **2021**, *133* (47), 25252–25258.
- (203) Gotthardt, M. A.; Schoch, R.; Brunner, T. S.; Bauer, M.; Kleist, W. Design of Highly Porous Single-Site Catalysts through Two-Step Postsynthetic Modification of Mixed-Linker MIL-53(Al). *Chempluschem* **2015**, *80* (1), 188–195.
- (204) Baek, J.; Rungtaweivoranit, B.; Pei, X.; Park, M.; Fakra, S. C.; Liu, Y.-S.; Matheu, R.; Alshimri, S. A.; Alshehri, S.; Trickett, C. A.; Somorjai, G. A.; Yaghi, O. M. Bioinspired Metal–Organic Framework Catalysts for Selective Methane Oxidation to Methanol. *J. Am. Chem. Soc.* **2018**, *140* (51), 18208–18216.
- (205) Fracaroli, A. M.; Siman, P.; Nagib, D. A.; Suzuki, M.; Furukawa, H.; Toste, F. D.; Yaghi, O. M. Seven Post-Synthetic Covalent Reactions in Tandem Leading to Enzyme-like Complexity within Metal-Organic Framework Crystals. *J. Am. Chem. Soc.* **2016**, *138* (27), 8352–8355.
- (206) Justin, A.; Esp, J.; Kochetygov, I.; Asgari, M.; Trukhina, O.; Queen, W. L. A Two Step Postsynthetic Modi Fi Cation Strategy: Appending Short Chain Polyamines to Zn-NH₂-BDC MOF for Enhanced CO₂ Adsorption. *Inorg. Chem.* **2021**, *60* (16), 11720–11729.
- (207) Jędrzejowski, D.; Pander, M.; Nitek, W.; Bury, W.; Matoga, D. Turning Flexibility into Rigidity: Stepwise Locking of Interpenetrating Networks in a MOF Crystal through Click Reaction. *Chem. Mater.* **2021**, *33* (18), 7509–7517.
- (208) Du Bois, D. R.; Matzger, A. J. Reagent Reactivity and Solvent Choice Determine Metal-Organic Framework Microstructure during Postsynthetic Modification. *J. Am. Chem. Soc.* **2021**, *143* (2), 671–674.
- (209) Sun, H.; Cong, S.; Zheng, Z.; Wang, Z.; Chen, Z.; Zhao, Z. Metal-Organic Frameworks as Surface Enhanced Raman Scattering Substrates with High Tailorability. *J. Am. Chem. Soc.* **2019**, *141* (2), 870–878.
- (210) Lai, H.; Li, G.; Xu, F.; Zhang, Z. Metal-Organic Frameworks: Opportunities and Challenges for Surface-Enhanced Raman Scattering—a Review. *J. Mater. Chem. C* **2020**, *8* (9), 2952–2963.
- (211) Huang, C.; Li, A.; Chen, X.; Wang, T. Understanding the Role of Metal–Organic Frameworks in Surface-Enhanced Raman Scattering Application. *Small* **2020**, *16* (43), 1–17.
- (212) Song, Y.; Hu, D.; Liu, F.; Chen, S.; Wang, L. Fabrication of Fluorescent SiO₂@zeolitic Imidazolate Framework-8 Nanosensor for Cu²⁺ Detection. *Analyst* **2015**, *140* (2), 623–629.
- (213) Liu, C.; Yan, B. Luminescent Zinc Metal-Organic Framework (ZIF-90) for Sensing Metal Ions, Anions and Small Molecules. *Photochem. Photobiol. Sci.* **2015**, *14* (9), 1644–1650.
- (214) Ma, M.; Gross, A.; Zacher, D.; Pinto, A.; Noei, H.; Wang, Y.; Fischer, R. A.; Metzler-Nolte, N. Use

- of Confocal Fluorescence Microscopy to Compare Different Methods of Modifying Metal-Organic Framework (MOF) Crystals with Dyes. *CrystEngComm* **2011**, *13* (8), 2828–2832.
- (215) Danaf, N. Al; Schrimpf, W.; Hirschle, P.; Lamb, D. C.; Ji, Z.; Wuttke, S. Linker Exchange via Migration along the Backbone in Metal–Organic Frameworks. *J. Am. Chem. Soc.* **2021**, *143* (28), 10541–10546.
- (216) Becker, W. Fluorescence Lifetime Imaging-Techniques and Applications. *J. Microsc.* **2012**, *247* (2), 119–136.
- (217) Schrimpf, W.; Ossato, G.; Hirschle, P.; Wuttke, S.; Lamb, D. C. Investigation of the Co-Dependence of Morphology and Fluorescence Lifetime in a Metal-Organic Framework. *Small* **2016**, 3651–3657.
- (218) Ramachandra, S.; Popovică, Z. D.; Schuermann, K. C.; Cucinotta, F.; Calzaferri, G.; De Cola, L. Förster Resonance Energy Transfer in Quantum Dot-Dye-Loaded Zeolite L Nanoassemblies. *Small* **2011**, *7* (10), 1488–1494.
- (219) Newsome, W. J.; Chakraborty, A.; Ly, R. T.; Pour, G. S.; Fairchild, D. C.; Morris, A. J.; Uribe-Romo, F. J. J-Dimer Emission in Interwoven Metal-Organic Frameworks. *Chem. Sci.* **2020**, *11* (17), 4391–4396.
- (220) Lustig, W. P.; Shen, Z.; Teat, S. J.; Javed, N.; Velasco, E.; O’Carroll, D. M.; Li, J. Rational Design of a High-Efficiency, Multivariate Metal-Organic Framework Phosphor for White Led Bulbs. *Chem. Sci.* **2020**, *11* (7), 1814–1824.
- (221) Schrimpf, W.; Jiang, J.; Ji, Z.; Hirschle, P.; Lamb, D. C.; Yaghi, O. M.; Wuttke, S. Chemical Diversity in a Metal–Organic Framework Revealed by Fluorescence Lifetime Imaging. *Nat. Commun.* **2018**, *9* (1), 1647.
- (222) Lahiri, B.; Holland, G.; Centrone, A. Chemical Imaging beyond the Diffraction Limit: Experimental Validation of the PTIR Technique. *Small* **2013**, *9* (3), 439–445.
- (223) Lahiri, B.; Holland, G.; Aksyuk, V.; Centrone, A. Nanoscale Imaging of Plasmonic Hot Spots and Dark Modes with the Photothermal-Induced Resonance Technique. *Nano Lett.* **2013**, *13* (7), 3218–3224.
- (224) Chae, J.; An, S.; Ramer, G.; Stavila, V.; Holland, G.; Yoon, Y.; Talin, A. A.; Allendorf, M.; Aksyuk, V. A.; Centrone, A. Nanophotonic Atomic Force Microscope Transducers Enable Chemical Composition and Thermal Conductivity Measurements at the Nanoscale. *Nano Lett.* **2017**, *17* (9), 5587–5594.
- (225) dos Santos, A. C. V.D.; Lendl, B.; Ramer, G. Systematic Analysis and Nanoscale Chemical Imaging of Polymers Using Photothermal-Induced Resonance (AFM-IR) Infrared Spectroscopy. *Polym. Test.* **2022**, *106*, 107443.
- (226) Ma, X.; Zhou, X.; Yu, A.; Zhao, W.; Zhang, W.; Zhang, S.; Wei, L.; Cook, D. J.; Roy, A. Functionalized Metal-Organic Framework Nanocomposites for Dispersive Solid Phase Extraction and Enantioselective Capture of Chiral Drug Intermediates. *J. Chromatogr. A* **2018**, *1537*, 1–9.
- (227) Mandemaker, L. D. B.; Rivera-Torrente, M.; Delen, G.; Hofmann, J. P.; Lorenz, M.; Belianinov, A.; Weckhuysen, B. M. Nanoweb Surface-Mounted Metal–Organic Framework Films with Tunable Amounts of Acid Sites as Tailored Catalysts. *Chem. Eur. J.* **2020**, *26* (3), 691–698.
- (228) Han, M.; Zhang, X.; Gao, H.; Chen, S.; Cheng, P.; Wang, P.; Zhao, Z.; Dang, R.; Wang, G. In Situ Semi-Sacrificial Template-Assisted Growth of Ultrathin Metal–Organic Framework Nanosheets for Electrocatalytic Oxygen Evolution. *Chem. Eng. J.* **2021**, *426*, 131348.
- (229) Katzenmeyer, A. M.; Canivet, J.; Holland, G.; Farrusseng, D.; Centrone, A. Assessing Chemical Heterogeneity at the Nanoscale in Mixed-Ligand Metal-Organic Frameworks with the PTIR Technique. *Angew. Chem. Int. Ed.* **2014**, *53* (11), 2852–2856.
- (230) Fluch, U.; Paneta, V.; Primetzhofer, D.; Ott, S. Uniform Distribution of Post-Synthetic Linker Exchange in Metal-Organic Frameworks Revealed by Rutherford Backscattering Spectrometry. *Chem. Commun.* **2017**, *53* (48), 6516–6519.
- (231) McCarthy, B. D.; Liseev, T.; Sortica, M. A.; Paneta, V.; Gschwind, W.; Nagy, G.; Ott, S.; Primetzhofer, D. Elemental Depth Profiling of Intact Metal-Organic Framework Single Crystals by Scanning Nuclear Microprobe. *J. Am. Chem. Soc.* **2021**, *143* (44), 18626–18634.

- (232) Krajnc, A.; Kos, T.; Zabukovec Logar, N.; Mali, G. A Simple NMR-Based Method for Studying the Spatial Distribution of Linkers within Mixed-Linker Metal-Organic Frameworks. *Angew. Chem. Int. Ed.* **2015**, *54* (36), 10535–10538.
- (233) Xiao, Y.; Chu, Y.; Li, S.; Su, Y.; Tang, J.; Xu, J.; Deng, F. Primary Adsorption Sites of Light Alkanes in Multivariate UiO-66 at Room Temperature as Revealed by Solid-State NMR. *J. Phys. Chem. C* **2020**, *124* (6), 3738–3746.
- (234) Jayachandrababu, K. C.; Verploegh, R. J.; Leisen, J.; Nieuwendaal, R. C.; Sholl, D. S.; Nair, S. Structure Elucidation of Mixed-Linker Zeolitic Imidazolate Frameworks by Solid-State ¹H CRAMPS NMR Spectroscopy and Computational Modeling. *J. Am. Chem. Soc.* **2016**, *138* (23), 7325–7336.
- (235) Tang, J.; Li, S.; Chu, Y.; Xiao, Y.; Xu, J.; Deng, F. Solid-State NMR Studies of the Acidity of Functionalized Metal–Organic Framework UiO-66 Materials. *Magn. Reson. Chem.* **2020**, *58* (11), 1091–1098.
- (236) Blahut, J.; Lejeune, A. L.; Ehrling, S.; Senkovska, I.; Kaskel, S.; Wisser, F. M.; Pintacuda, G. Monitoring Dynamics, Structure, and Magnetism of Switchable Metal–Organic Frameworks via ¹H-Detected MAS NMR. *Angew. Chem. Int. Ed.* **2021**, *60* (40), 21778–21783.
- (237) Lammert, M.; Glißmann, C.; Stock, N. Tuning the Stability of Bimetallic Ce(IV)/Zr(IV)-Based MOFs with UiO-66 and MOF-808 Structures. *Dalt. Trans.* **2017**, *46* (8), 2425–2429.
- (238) Sapnik, A. F.; Geddes, H. S.; Reynolds, E. M.; Yeung, H. H. M.; Goodwin, A. L. Compositional Inhomogeneity and Tuneable Thermal Expansion in Mixed-Metal ZIF-8 Analogues. *Chem. Commun.* **2018**, *54* (69), 9651–9654.
- (239) Bruni, G. Solid Solutions. *Chem. Rev.* **1980**, *1* (4), 345–375.
- (240) Wongsakulphasatch, S.; Nouar, F.; Rodriguez, J.; Scott, L.; Guillouzer, C. Le; Devic, T.; Horcajada, P.; Llewellyn, P. L.; Vimont, A.; Clet, G.; Daturi, M.; Serre, C. Direct accessibility of mixed-metal (iii/ii) acid sites through the rational synthesis of porous metal carboxylates. *Chem. Comm.* **2015**, *51*, 10194–10197.
- (241) Hadjiivanov, K. I.; Panayotov, D. A.; Mihaylov, M. Y.; Ivanova, E. Z.; Chakarova, K. K.; Andonova, S. M.; Drenchev, N. L. Power of Infrared and Raman Spectroscopies to Characterize Metal-Organic Frameworks and Investigate Their Interaction with Guest Molecules. *Chem. Rev.* **2021**, *121* (3), 1286–1424.
- (242) Martínez-Camarena, A.; Delgado-Pinar, E.; Soriano, C.; Alarcón, J.; Llinares, J. M.; Tejero, R.; García-España, E. Enhancement of SOD activity in boehmite supported nanoreceptors. *Chem. Comm.* **2018**, *54*, 3871–3874.
- (243) Giménez-Marqués, M.; Santiago-Portillo, A.; Navalón, S.; Álvaro, M.; Briois, V.; Nouar, F.; Garcia, H.; Serre, C. Exploring the Catalytic Performance of a Series of Bimetallic MIL-100(Fe, Ni) MOFs. *J. Mater. Chem. A* **2019**, *7* (35), 20285–20292.
- (244) Nguyen, H. T. T.; Tran, K. N. T.; Van Tan, L.; Tran, V. A.; Doan, V. D.; Lee, T.; Nguyen, T. D. Microwave-Assisted Solvothermal Synthesis of Bimetallic Metal-Organic Framework for Efficient Photodegradation of Organic Dyes. *Mater. Chem. Phys.* **2021**, *272*, 125040.
- (245) Vuong, G. T.; Pham, M. H.; Do, T. O. Direct Synthesis and Mechanism of the Formation of Mixed Metal Fe 2Ni-MIL-88B. *CrystEngComm* **2013**, *15* (45), 9694–9703.
- (246) Dincă, M.; Long, J. R. High-Enthalpy Hydrogen Adsorption in Cation-Exchanged Variants of the Microporous Metal-Organic Framework Mn₃[(Mn₄Cl)₃(BTT)₈(CH₃OH)₁₀]₂. *J. Am. Chem. Soc.* **2007**, *129* (36), 11172–11176.
- (247) Botas, J. A.; Calleja, G.; Sánchez-Sánchez, M.; Orcajo, M. G. Effect of Zn/Co Ratio in MOF-74 Type Materials Containing Exposed Metal Sites on Their Hydrogen Adsorption Behaviour and on Their Band Gap Energy. *Int. J. Hydrogen Energy* **2011**, *36* (17), 10834–10844.
- (248) Nouar, F.; Devic, T.; Chevreau, H.; Guillou, N.; Gibson, E.; Clet, G.; Daturi, M.; Vimont, A.; Marc Grenèche, J.; Breeze, M. I.; Walton, R. I.; Llewellyn, P. L.; Serre, C. Tuning the Breathing Behaviour of MIL-53 by Cation Mixing. *Chem. Commun.* **2012**, *48* (82), 10237–10239.
- (249) Cattaneo, D.; Warrender, S. J.; Duncan, M. J.; Kelsall, C. J.; Doherty, M. K.; Whitfield, P. D.; Megson, I. L.; Morris, R. E. Tuning the Nitric Oxide Release from CPO-27 MOFs. *RSC Adv.* **2016**,

- 6 (17), 14059–14067.
- (250) Zhai, Q. G.; Bu, X.; Mao, C.; Zhao, X.; Feng, P. Systematic and Dramatic Tuning on Gas Sorption Performance in Heterometallic Metal-Organic Frameworks. *J. Am. Chem. Soc.* **2016**, *138* (8), 2524–2527.
- (251) Zhou, Z.; Mei, L.; Ma, C.; Xu, F.; Xiao, J.; Xia, Q.; Li, Z. A Novel Bimetallic MIL-101(Cr, Mg) with High CO₂ Adsorption Capacity and CO₂/N₂ Selectivity. *Chem. Eng. Sci.* **2016**, *147*, 109–117.
- (252) Kaur, G.; Rai, R. K.; Tyagi, D.; Yao, X.; Li, P. Z.; Yang, X. C.; Zhao, Y.; Xu, Q.; Singh, S. K. Room-Temperature Synthesis of Bimetallic Co-Zn Based Zeolitic Imidazolate Frameworks in Water for Enhanced CO₂ and H₂ Uptakes. *J. Mater. Chem. A* **2016**, *4* (39), 14932–14938.
- (253) Cui, P. P.; Zhang, X. Du; Wang, P.; Zhao, Y.; Azam, M.; Al-Resayes, S. I.; Sun, W. Y. Zinc(II) and Copper(II) Hybrid Frameworks via Metal-Ion Metathesis with Enhanced Gas Uptake and Photoluminescence Properties. *Inorg. Chem.* **2017**, *56* (22), 14157–14163.
- (254) Zurrer, T.; Wong, K.; Horlyck, J.; Lovell, E. C.; Wright, J.; Bedford, N. M.; Han, Z.; Liang, K.; Scott, J.; Amal, R. Mixed-Metal MOF-74 Templated Catalysts for Efficient Carbon Dioxide Capture and Methanation. *Adv. Funct. Mater.* **2021**, *31* (9), 1–12.
- (255) Garai, B.; Bon, V.; Krause, S.; Schwotzer, F.; Gerlach, M.; Senkovska, I.; Kaskel, S. Tunable Flexibility and Porosity of the Metal-Organic Framework DUT-49 through Postsynthetic Metal Exchange. *Chem. Mater.* **2020**, *32* (2), 889–896.
- (256) Bitzer, J.; Heck, S. L.; Kleist, W. Tailoring the Breathing Behavior of Functionalized MIL-53(Al,M)-NH₂ Materials by Using the Mixed-Metal Concept. *Microporous Mesoporous Mater.* **2020**, *308*, 110329.
- (257) Krause, S.; Bon, V.; Senkovska, I.; Stoeck, U.; Wallacher, D.; Többsen, D. M.; Zander, S.; Pillai, R. S.; Maurin, G.; Coudert, F. X.; Kaskel, S. A Pressure-Amplifying Framework Material with Negative Gas Adsorption Transitions. *Nature* **2016**, *532* (7599), 348–352.
- (258) Farhana, Haase, J.; Krautscheid, H.; Bertmer, M. Formation of Mixed Metal Cu₃-xZnx(btc)₂ Frameworks with Different Zinc Contents: Incorporation of Zn²⁺ into the Metal-Organic Framework Structure as Studied by Solid-State NMR. *J. Phys. Chem. C* **2012**, *116*, 20866–20873.
- (259) Feng, X.; Ji, P.; Li, Z.; Drake, T.; Oliveres, P.; Chen, E. Y.; Song, Y.; Wang, C.; Lin, W. Aluminum Hydroxide Secondary Building Units in a Metal-Organic Framework Support Earth-Abundant Metal Catalysts for Broad-Scope Organic Transformations. *ACS Catal.* **2019**, *9* (4), 3327–3337.
- (260) Tan, T. T. Y.; Cham, J. T. M.; Reithofer, M. R.; Andy Hor, T. S.; Min Chin, J. Motorized Janus Metal Organic Framework Crystals. *Chem. Commun.* **2014**, *50* (96), 15175–15178.
- (261) Depauw, H.; Nevjestic, I.; Wang, G.; Leus, K.; Callens, F.; De Canck, E.; De Buysser, K.; Vrielinck, H.; Van Der Voort, P. Discovery of a Novel, Large Pore Phase in a Bimetallic Al/V Metal-Organic Framework. *J. Mater. Chem. A* **2017**, *5* (47), 24580–24584.
- (262) Depauw, H.; Nevjestic, I.; De Winne, J.; Wang, G.; Haustraete, K.; Leus, K.; Verberckmoes, A.; Detavernier, C.; Callens, F.; De Canck, E.; Vrielinck, H.; Van Der Voort, P. Microwave Induced “Egg Yolk” Structure in Cr/V-MIL-53. *Chem. Commun.* **2017**, *53* (60), 8478–8481.
- (263) Dalal, N. S.; Murillo, C. A. The Usefulness of EPR Spectroscopy in the Study of Compounds with Metal-Metal Multiple Bonds. *Dalt. Trans.* **2014**, *43* (23), 8565–8576.
- (264) Leus, K.; Vandichel, M.; Liu, Y. Y.; Muylaert, I.; Musschoot, J.; Pyl, S.; Vrielinck, H.; Callens, F.; Marin, G. B.; Detavernier, C.; Wiper, P. V.; Khimyak, Y. Z.; Waroquier, M.; Van Speybroeck, V.; Van Der Voort, P. The Coordinatively Saturated Vanadium MIL-47 as a Low Leaching Heterogeneous Catalyst in the Oxidation of Cyclohexene. *J. Catal.* **2012**, *285* (1), 196–207.
- (265) Leus, K.; Couck, S.; Vandichel, M.; Vanhaelewyn, G.; Liu, Y. Y.; Marin, G. B.; Driessche, I. Van; Depla, D.; Waroquier, M.; Speybroeck, V. Van; Denayer, J. F. M.; Voort, P. Van Der. Synthesis, Characterization and Sorption Properties of NH₂-MIL-47. *Phys. Chem. Chem. Phys.* **2012**, *14* (44), 15562–15570.
- (266) Yang, X.; Qiu, W.; Gao, R.; Wang, Y.; Bai, Y.; Xu, Z.; Bao, S. J. MIL-47(V) Catalytic Conversion of H₂O₂ for Sensitive H₂O₂ Detection and Tumor Cell Inhibition. *Sensors Actuators B Chem.* **2022**, *354*, 131201.

- (267) Mendt, M.; Jee, B.; Stock, N.; Ahnfeldt, T.; Hartmann, M.; Himsl, D.; Pöpl, A. Structural Phase Transitions and Thermal Hysteresis in the Metal-Organic Framework Compound MIL-53 as Studied by Electron Spin Resonance Spectroscopy. *J. Phys. Chem. C* **2010**, *114* (45), 19443–19451.
- (268) Nevjestic, I.; Depauw, H.; Leus, K.; Kalendra, V.; Caretti, I.; Jeschke, G.; Van Doorslaer, S.; Callens, F.; Van Der Voort, P.; Vrielinck, H. Multi-Frequency (S, X, Q and W-Band) EPR and ENDOR Study of Vanadium(IV) Incorporation in the Aluminium Metal-Organic Framework MIL-53. *ChemPhysChem* **2015**, *16* (14), 2968–2973.
- (269) Nevjestic, I.; Depauw, H.; Gast, P.; Tack, P.; Deduytsche, D.; Leus, K.; Van Landeghem, M.; Goovaerts, E.; Vincze, L.; Detavernier, C.; Van Der Voort, P.; Callens, F.; Vrielinck, H. Sensing the Framework State and Guest Molecules in MIL-53(Al) via the Electron Paramagnetic Resonance Spectrum of VIV Dopant Ions. *Phys. Chem. Chem. Phys.* **2017**, *19* (36), 24545–24554.
- (270) Mendt, M.; Ehrling, S.; Senkovska, I.; Kaskel, S.; Pöpl, A. Synthesis and Characterization of Cu-Ni Mixed Metal Paddlewheels Occurring in the Metal-Organic Framework DUT-8(Ni_{0.98}Cu_{0.02}) for Monitoring Open-Closed-Pore Phase Transitions by X-Band Continuous Wave Electron Paramagnetic Resonance Spectroscopy. *Inorg. Chem.* **2019**, *58* (7), 4561–4573.
- (271) Pöpl, A.; Kunz, S.; Himsl, D.; Hartmann, M. CW and Pulsed ESR Spectroscopy of Cupric Ions in the Metal-Organic Framework Compound Cu₃(BTC)₂. *J. Phys. Chem. C* **2008**, *112* (7), 2678–2684.
- (272) Kozachuk, O.; Khaletskaya, K.; Halbherr, M.; Bétard, A.; Meilikhov, M.; Seidel, R. W.; Jee, B.; Pöpl, A.; Fischer, R. A. Microporous Mixed-Metal Layer-Pillared [Zn₁-XCu_x(Bdc)(Dabco)_{0.5}] MOFs: Preparation and Characterization. *Eur. J. Inorg. Chem.* **2012**, No. 10, 1688–1695.
- (273) Poryvaev, A. S.; Sheveleva, A. M.; Demakov, P. A.; Arzumanov, S. S.; Stepanov, A. G.; Dybtsev, D. N.; Fedin, M. V. Pulse EPR Study of Gas Adsorption in Cu²⁺-Doped Metal-Organic Framework [Zn₂(1,4-BDC)₂(DABCO)]. *Appl. Magn. Reson.* **2018**, *49* (3), 255–264.
- (274) Li, J.; Huang, H.; Xue, W.; Sun, K.; Song, X.; Wu, C.; Nie, L.; Li, Y.; Liu, C.; Pan, Y.; Jiang, H. L.; Mei, D.; Zhong, C. Self-Adaptive Dual-Metal-Site Pairs in Metal-Organic Frameworks for Selective CO₂ Photoreduction to CH₄. *Nat. Catal.* **2021**, *4* (8), 719–729.
- (275) Jee, B.; Eisinger, K.; Gul-E-Noor, F.; Bertmer, M.; Hartmann, M.; Himsl, D.; Pöpl, A. Continuous Wave and Pulsed Electron Spin Resonance Spectroscopy of Paramagnetic Framework Cupric Ions in the Zn(II) Doped Porous Coordination Polymer Cu₃-XZnx(Btc)₂. *J. Phys. Chem. C* **2010**, *114* (39), 16630–16639.
- (276) Šimenas, M.; Jee, B.; Hartmann, M.; Banys, J.; Pöpl, A. Adsorption and Desorption of HD on the Metal-Organic Framework Cu_{2.97}Zn_{0.03}(Btc)₂ Studied by Three-Pulse ESEEM Spectroscopy. *J. Phys. Chem. C* **2015**, *119* (51), 28530–28535.
- (277) Metavarayuth, K.; Ejegbavwo, O.; McCarver, G.; Myrick, M. L.; Makris, T. M.; Vogiatzis, K. D.; Senanayake, S. D.; Manley, O. M.; Ebrahim, A. M.; Frenkel, A. I.; Hwang, S.; Rajeshkumar, T.; Jimenez, J. D.; Chen, K.; Shustova, N. B.; Chen, D. A. Direct Identification of Mixed-Metal Centers in Metal-Organic Frameworks: Cu₃(BTC)₂ Transmetalated with Rh²⁺ Ions. *J. Phys. Chem. Lett.* **2020**, *11* (19), 8138–8144.
- (278) Bitzer, J.; Otterbach, S.; Thangavel, K.; Kultraeva, A.; Schmid, R.; Pöpl, A.; Kleist, W. Experimental Evidence for the Incorporation of Two Metals at Equivalent Lattice Positions in Mixed-Metal Metal-Organic Frameworks. *Chem. Eur. J.* **2020**, *26* (25), 5667–5675.
- (279) Mendt, M.; Vervoorts, P.; Schneemann, A.; Fischer, R. A.; Pöpl, A. Probing Local Structural Changes at Cu²⁺ in a Flexible Mixed-Metal Metal-Organic Framework by in Situ Electron Paramagnetic Resonance during CO₂ Ad- and Desorption. *J. Phys. Chem. C* **2019**, *123* (5), 2940–2952.
- (280) Rubio-Giménez, V.; Waerenborgh, J. C.; Clemente-Juan, J. M.; Martí-Gastaldo, C. Spontaneous Magnetization in Heterometallic NiFe-MOF-74 Microporous Magnets by Controlled Iron Doping. *Chem. Mater.* **2017**, *29* (15), 6181–6185.

- (281) Castells-Gil, J.; M. Padial, N.; Almora-Barrios, N.; Gil-San-Millán, R.; Romero-Ángel, M.; Torres, V.; da Silva, I.; Vieira, B. C. J.; Waerenborgh, J. C.; Jagiello, J.; Navarro, J. A. R.; Tatay, S.; Marti-Gastaldo, C. Heterometallic Titanium-Organic Frameworks as Dual-Metal Catalysts for Synergistic Non-Buffered Hydrolysis of Nerve Agent Simulants. *Chem* **2020**, *6* (11), 3118–3131.
- (282) Mali, G.; Mazaj, M.; Arčon, I.; Hanžel, D.; Arčon, D.; Jagličić, Z. Unraveling the Arrangement of Al and Fe within the Framework Explains the Magnetism of Mixed-Metal MIL-100(Al,Fe). *J. Phys. Chem. Lett.* **2019**, *10* (7), 1464–1470.
- (283) Vallés-García, C.; Gkaniatsou, E.; Santiago-Portillo, A.; Giménez-Marqués, M.; Álvaro, M.; Greneche, J. M.; Steunou, N.; Sicard, C.; Navalón, S.; Serre, C.; García, H. Design of Stable Mixed-Metal MIL-101(Cr/Fe) Materials with Enhanced Catalytic Activity for the Prins Reaction. *J. Mater. Chem. A* **2020**, *8* (33), 17002–17011.
- (284) Morel, F. L.; Pin, S.; Huthwelker, T.; Ranocchiari, M.; Van Bokhoven, J. A. Phosphine and Phosphine Oxide Groups in Metal-Organic Frameworks Detected by P K-Edge XAS. *Phys. Chem. Chem. Phys.* **2015**, *17* (5), 3326–3331.
- (285) Pi, Y.; Feng, X.; Song, Y.; Xu, Z.; Li, Z.; Lin, W. Metal-Organic Frameworks Integrate Cu Photosensitizers and Secondary Building Unit-Supported Fe Catalysts for Photocatalytic Hydrogen Evolution. *J. Am. Chem. Soc.* **2020**, *142* (23), 10302–10307.
- (286) Peng, Y.; Huang, H.; Zhang, Y.; Kang, C.; Chen, S.; Song, L.; Liu, D.; Zhong, C. A Versatile MOF-Based Trap for Heavy Metal Ion Capture and Dispersion. *Nat. Commun.* **2018**, *9*.
- (287) Ronda-Lloret, M.; Pellicer-Carreño, I.; Grau-Atienza, A.; Boada, R.; Diaz-Moreno, S.; Narciso-Romero, J.; Serrano-Ruiz, J. C.; Sepúlveda-Escribano, A.; Ramos-Fernandez, E. V. Mixed-Valence Ce/Zr Metal-Organic Frameworks: Controlling the Oxidation State of Cerium in One-Pot Synthesis Approach. *Adv. Funct. Mater.* **2021**, *31* (29), 1–7.
- (288) Ma, X.; Liu, H.; Yang, W.; Mao, G.; Zheng, L.; Jiang, H. L. Modulating Coordination Environment of Single-Atom Catalysts and Their Proximity to Photosensitive Units for Boosting MOF Photocatalysis. *J. Am. Chem. Soc.* **2021**, *143* (31), 12220–12229.
- (289) Antil, N.; Akhtar, N.; Newar, R.; Begum, W.; Kumar, A.; Chauhan, M.; Manna, K. Chiral Iron(II)-Catalysts within Valinol-Grafted Metal-Organic Frameworks for Enantioselective Reduction of Ketones. *ACS Catal.* **2021**, *11* (11), 10450–10459.
- (290) Yuan, S.; Zhang, P.; Zhang, L.; Garcia-Esparza, A. T.; Sokaras, D.; Qin, J. S.; Feng, L.; Day, G. S.; Chen, W.; Drake, H. F.; Elumalai, P.; Madrahimov, S. T.; Sun, D.; Zhou, H. C. Exposed Equatorial Positions of Metal Centers via Sequential Ligand Elimination and Installation in MOFs. *J. Am. Chem. Soc.* **2018**, *140* (34), 10814–10819.
- (291) Lomachenko, K. A.; Jacobsen, J.; Bugaev, A. L.; Atzori, C.; Bonino, F.; Bordiga, S.; Stock, N.; Lamberti, C. Exact Stoichiometry of CexZr6-x Cornerstones in Mixed-Metal UiO-66 Metal-Organic Frameworks Revealed by Extended X-Ray Absorption Fine Structure Spectroscopy. *J. Am. Chem. Soc.* **2018**, *140* (50), 17379–17383.
- (292) Jiao, L.; Yang, W.; Wan, G.; Zhang, R.; Zheng, X.; Zhou, H.; Yu, S.; Jiang, H. Single-Atom Electrocatalysts from Multivariate Metal-Organic Frameworks for Highly Selective Reduction of CO₂ at Low Pressures. *Angew. Chem.* **2020**, *132* (46), 20770–20776.
- (293) Wang, H.; Shi, Z.; Yang, J.; Sun, T.; Rungtaweeworant, B.; Lyu, H.; Zhang, Y. B.; Yaghi, O. M. Docking of CuI and AgI in Metal-Organic Frameworks for Adsorption and Separation of Xenon. *Angew. Chem. Int. Ed.* **2021**, *60* (7), 3417–3421.
- (294) Feng, X.; Jena, H. S.; Krishnaraj, C.; Arenas-Esteban, D.; Leus, K.; Wang, G.; Sun, J.; Rüscher, M.; Timoshenko, J.; Roldan Cuenya, B.; Bals, S.; Voort, P. Van Der. Creation of Exclusive Artificial Cluster Defects by Selective Metal Removal in the (Zn, Zr) Mixed-Metal UiO-66. *J. Am. Chem. Soc.* **2021**, *143* (51), 21511–21518.
- (295) Castillo-Blas, C.; Moreno, J. M.; Romero-Muñiz, I.; Platero-Prats, A. E. Applications of Pair Distribution Function Analyses to the Emerging Field of: Non-Ideal Metal-Organic Framework Materials. *Nanoscale* **2020**, *12* (29), 15577–15587.
- (296) Rangwani, S.; Howarth, A.; DeStefano, M. R.; Malliakas, C. D.; Platero-Prats, A. E.; Chapman, K.

- W.; Farha, O. K. Adsorptive Removal of Sb(V) from Water Using a Mesoporous Zr-Based Metal–Organic Framework. *Polyhedron* **2018**, *151*, 338–343.
- (297) Platero-Prats, A. E.; League, A. B.; Bernales, V.; Ye, J.; Gallington, L. C.; Vjunov, A.; Schweitzer, N. M.; Li, Z.; Zheng, J.; Mehdi, B. L.; Stevens, A. J.; Dohnalkova, A.; Balasubramanian, M.; Farha, O. K.; Hupp, J. T.; Browning, N. D.; Fulton, J. L.; Camaioni, D. M.; Lercher, J. A.; Truhlar, D. G.; Gagliardi, L.; Cramer, C. J.; Chapman, K. W. Bridging Zirconia Nodes within a Metal-Organic Framework via Catalytic Ni-Hydroxo Clusters to Form Heterobimetallic Nanowires. *J. Am. Chem. Soc.* **2017**, *139* (30), 10410–10418.
- (298) González Miera, G.; Bermejo Gómez, A.; Chupas, P. J.; Martín-Matute, B.; Chapman, K. W.; Platero-Prats, A. E. Topological Transformation of a Metal-Organic Framework Triggered by Ligand Exchange. *Inorg. Chem.* **2017**, *56* (8), 4576–4583.
- (299) Li, B.; Zhang, Y.; Shi, Z. Metal-Cation-Directed de Novo Assembly of a Functionalized Guest Molecule in the Nanospace of a Metal–Organic Framework. *J. Am. Chem. Soc.* **2014**, *136* (4), 1202–1205.
- (300) Zhang, W.; Chen, Z.; Al-Naji, M.; Guo, P.; Cwik, S.; Halbherr, O.; Wang, Y.; Muhler, M.; Wilde, N.; Gläser, R.; Fischer, R. A. Simultaneous Introduction of Various Palladium Active Sites into MOF: Via One-Pot Synthesis: Pd at[Cu₃-XPdx(BTC)₂]N. *Dalt. Trans.* **2016**, *45* (38), 14883–14887.
- (301) Wang, X. S.; Chen, C. H.; Ichihara, F.; Oshikiri, M.; Liang, J.; Li, L.; Li, Y.; Song, H.; Wang, S.; Zhang, T.; Huang, Y. B.; Cao, R.; Ye, J. Integration of Adsorption and Photosensitivity Capabilities into a Cationic Multivariate Metal-Organic Framework for Enhanced Visible-Light Photoreduction Reaction. *Appl. Catal. B Environ.* **2019**, *253* (March), 323–330.
- (302) Cheng, Y.; Wen, C.; Sun, Y. Q.; Yu, H.; Yin, X. B. Mixed-Metal MOF-Derived Hollow Porous Nanocomposite for Trimodality Imaging Guided Reactive Oxygen Species-Augmented Synergistic Therapy. *Adv. Funct. Mater.* **2021**, *31* (37), 1–15.
- (303) Liang, J.; Liu, M.; Xu, X.; Liu, Z. A Valuable Strategy to Improve Ferroelectric Performance Significantly via metallic Ion Doping in the Lattice Nodes of Metal-Organic Frameworks. *Chem. Commun.* **2021**, *57* (20), 2515–2518.
- (304) Zhang, W.; Kauer, M.; Halbherr, O.; Epp, K.; Guo, P.; Gonzalez, M. I.; Xiao, D. J.; Wiktor, C.; Llabrés i Xamena, F. X.; Wöll, C.; Wang, Y.; Muhler, M.; Fischer, R. A. Ruthenium Metal–Organic Frameworks with Different Defect Types: Influence on Porosity, Sorption, and Catalytic Properties. *Chem. Eur. J.* **2016**, *22* (40), 14297–14307.
- (305) Wang, X. N.; Zhang, P.; Kirchon, A.; Li, J.; Chen, W. M.; Zhao, Y. M.; Li, B.; Zhou, H. C. Crystallographic Visualization of Post-Synthetic Nickel Clusters into Metal-Organic Framework. *J. Am. Chem. Soc.* **2019**, *141* (34), 13654–13663.
- (306) Wang, Y.; Liu, Q.; Zhang, Q.; Peng, B.; Deng, H. Molecular Vise Approach to Create Metal-Binding Sites in MOFs and Detection of Biomarkers. *Angew. Chem. Int. Ed.* **2018**, *57* (24), 7120–7125.
- (307) Song, X.; Jeong, S.; Kim, D.; Lah, M. S. Transmetalations in Two Metal-Organic Frameworks with Different Framework Flexibilities: Kinetics and Core-Shell Heterostructure. *CrystEngComm* **2012**, *14* (18), 5753–5756.
- (308) Furukawa, S.; Hirai, K.; Nakagawa, K.; Takashima, Y.; Matsuda, R.; Tsuruoka, T.; Kondo, M.; Haruki, R.; Tanaka, D.; Sakamoto, H.; Shimomura, S.; Sakata, O.; Kitagawa, S. Heterogeneously Hybridized Porous Coordination Polymer Crystals: Fabrication of Heterometallic Core-Shell Single Crystals with an in-Plane Rotational Epitaxial Relationship. *Angew. Chem. Int. Ed.* **2009**, *48* (10), 1766–1770.
- (309) Jiao, Y.; Morelock, C. R.; Burtch, N. C.; Mounfield, W. P.; Hungerford, J. T.; Walton, K. S. Tuning the Kinetic Water Stability and Adsorption Interactions of Mg-MOF-74 by Partial Substitution with Co or Ni. *Ind. Eng. Chem. Res.* **2015**, *54* (49), 12408–12414.
- (310) Fukushima, T.; Horike, S.; Kobayashi, H.; Tsujimoto, M.; Isoda, S.; Foo, M. L.; Kubota, Y.; Takata, M.; Kitagawa, S. Modular Design of Domain Assembly in Porous Coordination Polymer Crystals via Reactivity-Directed Crystallization Process. *J. Am. Chem. Soc.* **2012**, *134* (32),

- 13341–13347.
- (311) Ji, Z.; Li, T.; Yaghi, O. M. Sequencing of Metals in Multivariate Metal-Organic Frameworks. *Science* **2020**, *369* (6504), 674–680.
- (312) Haquin, V.; Etienne, M.; Daiguebonne, C.; Freslon, S.; Calvez, G.; Bernot, K.; Le Pollès, L.; Ashbrook, S. E.; Mitchell, M. R.; Bünzli, J. C.; Eliseeva, S. V.; Guillou, O. Color and Brightness Tuning in Heteronuclear Lanthanide Terephthalate Coordination Polymers. *Eur. J. Inorg. Chem.* **2013**, *20*, 3464–3476.
- (313) Bignami, G. P. M.; Davis, Z. H.; Dawson, D. M.; Morris, S. A.; Russell, S. E.; McKay, D.; Parke, R. E.; Iuga, D.; Morris, R. E.; Ashbrook, S. E. Cost-Effective 17O Enrichment and NMR Spectroscopy of Mixed-Metal Terephthalate Metal-Organic Frameworks. *Chem. Sci.* **2018**, *9* (4), 850–859.
- (314) Yu, Q.; Guo, L.; Lai, D.; Zhang, Z.; Yang, Q.; Yang, Y.; Ren, Q.; Bao, Z. A Pore-Engineered Metal-Organic Framework with Mixed Ligands Enabling Highly Efficient Separation of Hexane Isomers for Gasoline Upgrading. *Sep. Purif. Technol.* **2021**, *268*, 118646.
- (315) Fan, W.; Ying, Y.; Peh, S. B.; Yuan, H.; Yang, Z.; Yuan, Y. Di; Shi, D.; Yu, X.; Kang, C.; Zhao, D. Multivariate Polycrystalline Metal-Organic Framework Membranes for CO₂/CH₄ Separation. *J. Am. Chem. Soc.* **2021**, *143* (42), 17716–17723.
- (316) Furukawa, H.; Ko, N.; Go, Y. B.; Aratani, N.; Choi, S. B.; Choi, E.; Yazaydin, A. Ö.; Snurr, R. Q.; O’Keeffe, M.; Kim, J.; Yaghi, O. M. Ultrahigh Porosity in Metal-Organic Frameworks. *Science* **2010**, *329* (5990), 424–428.
- (317) Schulte, Z. M.; Kwon, Y. H.; Han, Y.; Liu, C.; Li, L.; Yang, Y.; Jarvi, A. G.; Saxena, S.; Vesper, G.; Johnson, J. K.; Rosi, N. L. H₂/CO₂ separations in Multicomponent Metal-Adeninate MOFs with Multiple Chemically Distinct Pore Environments. *Chem. Sci.* **2020**, *11* (47), 12807–12815.
- (318) Yu, L.; Ullah, S.; Zhou, K.; Xia, Q.; Wang, H.; Tu, S.; Huang, J.; Xia, H.; Liu, X.; Thonhauser, T.; Li, J. A Microporous Metal–Organic Framework Incorporating Both Primary and Secondary Building Units for Splitting Alkane Isomers. *J. Am. Chem. Soc.* **2022**, *144* (9), 3766–3770.
- (319) Zhao, X.; Bu, X.; Nguyen, E. T.; Zhai, Q. G.; Mao, C.; Feng, P. Multivariable Modular Design of Pore Space Partition. *J. Am. Chem. Soc.* **2016**, *138* (46), 15102–15105.
- (320) Zhai, Q. G.; Bu, X.; Zhao, X.; Li, D. S.; Feng, P. Pore Space Partition in Metal-Organic Frameworks. *Acc. Chem. Res.* **2017**, *50* (2), 407–417.
- (321) Feng, L.; Day, G. S.; Wang, K. Y.; Yuan, S.; Zhou, H. C. Strategies for Pore Engineering in Zirconium Metal-Organic Frameworks. *Chem* **2020**, *6* (11), 2902–2923.
- (322) Lin, R. B.; Xiang, S.; Zhou, W.; Chen, B. Microporous Metal-Organic Framework Materials for Gas Separation. *Chem* **2020**, *6* (2), 337–363.
- (323) Tan, Y. X.; He, Y. P.; Zhang, J. Pore Partition Effect on Gas Sorption Properties of an Anionic Metal-Organic Framework with Exposed Cu²⁺ Coordination Sites. *Chem. Commun.* **2011**, *47* (38), 10647–10649.
- (324) Liu, L.; Yao, Z.; Ye, Y.; Yang, Y.; Lin, Q.; Zhang, Z.; O’Keeffe, M.; Xiang, S. Integrating the Pillared-Layer Strategy and Pore-Space Partition Method to Construct Multicomponent MOFs for C₂H₂/CO₂ Separation. *J. Am. Chem. Soc.* **2020**, *142* (20), 9258–9266.
- (325) Xue, Y. Y.; Bai, X. Y.; Zhang, J.; Wang, Y.; Li, S. N.; Jiang, Y. C.; Hu, M. C.; Zhai, Q. G. Precise Pore Space Partitions Combined with High-Density Hydrogen-Bonding Acceptors within Metal–Organic Frameworks for Highly Efficient Acetylene Storage and Separation. *Angew. Chem. Int. Ed.* **2021**, *60* (18), 10122–10128.
- (326) Hong, Q.; Wang, W.; Chen, S.; Chen, K.; Liu, M.; Zhang, H.; Zhang, J. Host–Guest Pore Space Partition in a Boron Imidazolate Framework for Ethylene Separation. *Chem. Mater.* **2022**, *34* (1), 307–313.
- (327) Feng, P.; Hong, A. N.; Kusumoputro, E.; Wang, Y.; Yang, H.; Chen, Y.; Bu, X. Simultaneous Control of Pore-Space Partition and Charge Distribution in Multi-Modular Metal-Organic Frameworks. *Angew. Chem. Int. Ed.* **2022**, *61* (13).
- (328) Ling, Y.; Deng, M.; Chen, Z.; Xia, B.; Liu, X.; Yang, Y.; Zhou, Y.; Weng, L. Enhancing Co₂ Adsorption of a Zn-Phosphonocarboxylate Framework by Pore Space Partitions. *Chem.*

- Commun.* **2013**, *49* (1), 78–80.
- (329) Zhao, X.; Bu, X.; Zhai, Q. G.; Tran, H.; Feng, P. Pore Space Partition by Symmetry-Matching Regulated Ligand Insertion and Dramatic Tuning on Carbon Dioxide Uptake. *J. Am. Chem. Soc.* **2015**, *137* (4), 1396–1399.
- (330) Wei, Y. S.; Zhang, M.; Liao, P. Q.; Lin, R. B.; Li, T. Y.; Shao, G.; Zhang, J. P.; Chen, X. M. Coordination Templated [2+2+2] Cyclotrimerization in a Porous Coordination Framework. *Nat. Commun.* **2015**, *6*, 8348.
- (331) Zhai, Q. G.; Bu, X.; Mao, C.; Zhao, X.; Daemen, L.; Cheng, Y.; Ramirez-Cuesta, A. J.; Feng, P. An Ultra-Tunable Platform for Molecular Engineering of High-Performance Crystalline Porous Materials. *Nat. Commun.* **2016**, *7*, 13645.
- (332) Chen, K. J.; Madden, D. G.; Pham, T.; Forrest, K. A.; Kumar, A.; Yang, Q. Y.; Xue, W.; Space, B.; Perry, J. J.; Zhang, J. P.; Chen, X. M.; Zaworotko, M. J. Tuning Pore Size in Square-Lattice Coordination Networks for Size-Selective Sieving of CO₂. *Angew. Chem. Int. Ed.* **2016**, *55* (35), 10268–10272.
- (333) Kim, J. Y.; Balderas-Xicohténcatl, R.; Zhang, L.; Kang, S. G.; Hirscher, M.; Oh, H.; Moon, H. R. Exploiting Diffusion Barrier and Chemical Affinity of Metal-Organic Frameworks for Efficient Hydrogen Isotope Separation. *J. Am. Chem. Soc.* **2017**, *139* (42), 15135–15141.
- (334) Ye, Y.; Ma, Z.; Lin, R. B.; Krishna, R.; Zhou, W.; Lin, Q.; Zhang, Z.; Xiang, S.; Chen, B. Pore Space Partition within a Metal-Organic Framework for Highly Efficient C₂H₂/CO₂ Separation. *J. Am. Chem. Soc.* **2019**, *141* (9), 4130–4136.
- (335) Kim, D.; Seong, J.; Han, S.; Baek, S. Bin; Lah, M. S. Pore Space Partition of a Fragile Ag(i)-Carboxylate Framework: Via Post-Synthetic Linker Insertion. *Chem. Commun.* **2020**, *56* (61), 8615–8618.
- (336) Ye, Y.; Chen, S.; Chen, L.; Huang, J.; Ma, Z.; Li, Z.; Yao, Z.; Zhang, J.; Zhang, Z.; Xiang, S. Additive-Induced Supramolecular Isomerism and Enhancement of Robustness in Co(II)-Based MOFs for Efficiently Trapping Acetylene from Acetylene-Containing Mixtures. *ACS Appl. Mater. Interfaces* **2018**, *10* (36), 30912–30918.
- (337) Zhang, Q.; Chen, J.; Zhu, X. C.; Li, J.; Wu, D. 7-Connected FeIII₃-Based Bio-MOF: Pore Space Partition and Gas Separations. *Inorg. Chem.* **2020**, *59* (23), 16829–16832.
- (338) Hong, K.; Bak, W.; Chun, H. Unique Coordination-Based Heterometallic Approach for the Stoichiometric Inclusion of High-Valent Metal Ions in a Porous Metal-Organic Framework. *Inorg. Chem.* **2013**, *52* (10), 5645–5647.
- (339) Hon Lau, C.; Babarao, R.; Hill, M. R. A Route to Drastic Increase of CO₂ Uptake in Zr Metal Organic Framework UiO-66. *Chem. Commun.* **2013**, *49* (35), 3634–3636.
- (340) Kim, D.; Coskun, A. Template-Directed Approach Towards the Realization of Ordered Heterogeneity in Bimetallic Metal–Organic Frameworks. *Angew. Chem. Int. Ed.* **2017**, *56* (18), 5071–5076.
- (341) Yang, J.; Du, B.; Yuan, N.; Jia, X.; Li, J. Vapor-Assisted Preparation of Mn/Fe/Co/Zn-Cu Bimetallic Metal-Organic Frameworks Based on Octahedron Micron Crystals (PCN-6'). *New J. Chem.* **2019**, *43* (17), 6452–6456.
- (342) Botas, J. A.; Calleja, G.; Sánchez-Sánchez, M.; Orcajo, M. G. Cobalt Doping of the MOF-5 Framework and Its Effect on Gas-Adsorption Properties. *Langmuir* **2010**, *26* (8), 5300–5303.
- (343) Zheng, S. T.; Wu, T.; Chou, C.; Fuhr, A.; Feng, P.; Bu, X. Development of Composite Inorganic Building Blocks for MOFs. *J. Am. Chem. Soc.* **2012**, *134* (10), 4517–4520.
- (344) Wang, Z.; Zheng, B.; Liu, H.; Lin, X.; Yu, X.; Yi, P.; Yun, R. High-Capacity Gas Storage by a Microporous Oxalamide-Functionalized NbO-Type Metal-Organic Framework. *Cryst. Growth Des.* **2013**, *13* (11), 5001–5006.
- (345) Song, X.; Oh, M.; Lah, M. S. Hybrid Bimetallic Metal-Organic Frameworks: Modulation of the Framework Stability and Ultralarge CO₂ Uptake Capacity. *Inorg. Chem.* **2013**, *52* (19), 10869–10876.
- (346) Wei, Z.; Lu, W.; Jiang, H. L.; Zhou, H. C. A Route to Metal-Organic Frameworks through Framework Templating. *Inorg. Chem.* **2013**, *52* (3), 1164–1166.

- (347) Naeem, A.; Ting, V. P.; Hintermair, U.; Tian, M.; Telford, R.; Halim, S.; Nowell, H.; Hołyńska, M.; Teat, S. J.; Scowen, I. J.; Nayak, S. Mixed-Linker Approach in Designing Porous Zirconium-Based Metal-Organic Frameworks with High Hydrogen Storage Capacity. *Chem. Commun.* **2016**, 52 (50), 7826–7829.
- (348) Ferrando-Soria, J.; Serra-Crespo, P.; De Lange, M.; Gascon, J.; Kapteijn, F.; Julve, M.; Cano, J.; Lloret, F.; Pasán, J.; Ruiz-Pérez, C.; Journaux, Y.; Pardo, E. Selective Gas and Vapor Sorption and Magnetic Sensing by an Isorecticular Mixed-Metal-Organic Framework. *J. Am. Chem. Soc.* **2012**, 134 (37), 15301–15304.
- (349) Fan, W.; Yuan, S.; Wang, W.; Feng, L.; Liu, X.; Zhang, X.; Wang, X.; Kang, Z.; Dai, F.; Yuan, D.; Sun, D.; Zhou, H. C. Optimizing Multivariate Metal-Organic Frameworks for Efficient C₂H₂/CO₂ Separation. *J. Am. Chem. Soc.* **2020**, 142 (19), 8728–8737.
- (350) Zhao, M.; Yuan, K.; Wang, Y.; Li, G.; Guo, J.; Gu, L.; Hu, W.; Zhao, H.; Tang, Z. Metal-Organic Frameworks as Selectivity Regulators for Hydrogenation Reactions. *Nature* **2016**, 539 (7627), 76–80.
- (351) Guo, J.; Qin, Y.; Zhu, Y.; Zhang, X.; Long, C.; Zhao, M.; Tang, Z. Metal-Organic Frameworks as Catalytic Selectivity Regulators for Organic Transformations. *Chem. Soc. Rev.* **2021**, 50 (9), 5366–5396.
- (352) Liu, L.; Zhou, T. Y.; Telfer, S. G. Modulating the Performance of an Asymmetric Organocatalyst by Tuning Its Spatial Environment in a Metal-Organic Framework. *J. Am. Chem. Soc.* **2017**, 139 (39), 13936–13943.
- (353) Cao, C. C.; Chen, C. X.; Wei, Z. W.; Qiu, Q. F.; Zhu, N. X.; Xiong, Y. Y.; Jiang, J. J.; Wang, D.; Su, C. Y. Catalysis through Dynamic Spacer Installation of Multivariate Functionalities in Metal-Organic Frameworks. *J. Am. Chem. Soc.* **2019**, 141 (6), 2589–2593.
- (354) Zhang, M.; Gu, Z. Y.; Bosch, M.; Perry, Z.; Zhou, H. C. Biomimicry in Metal-Organic Materials. *Coord. Chem. Rev.* **2015**, 293–294, 327–356.
- (355) Nath, I.; Chakraborty, J.; Verpoort, F. Metal Organic Frameworks Mimicking Natural Enzymes: A Structural and Functional Analogy. *Chem. Soc. Rev.* **2016**, 45 (15), 4127–4170.
- (356) Osadchii, D. Y.; Olivos-Suarez, A. I.; Szécsényi, Á.; Li, G.; Nasalevich, M. A.; Dugulan, I. A.; Crespo, P. S.; Hensen, E. J. M.; Veber, S. L.; Fedin, M. V.; Sankar, G.; Pidko, E. A.; Gascon, J. Isolated Fe Sites in Metal Organic Frameworks Catalyze the Direct Conversion of Methane to Methanol. *ACS Catal.* **2018**, 8 (6), 5542–5548.
- (357) Bour, J. R.; Wright, A. M.; He, X.; Dincă, M. Bioinspired Chemistry at MOF Secondary Building Units. *Chem. Sci.* **2020**, 11 (7), 1728–1737.
- (358) Dybtsev, D. N.; Bryliakov, K. P. Asymmetric Catalysis Using Metal-Organic Frameworks. *Coord. Chem. Rev.* **2021**, 437, 213845.
- (359) Newar, R.; Akhtar, N.; Antil, N.; Kumar, A.; Shukla, S.; Begum, W.; Manna, K. Amino Acid-Functionalized Metal-Organic Frameworks for Asymmetric Base-Metal Catalysis. *Angew. Chem.* **2021**, 133 (19), 11059–11065.
- (360) Liang, K.; Coghlan, C. J.; Bell, S. G.; Doonan, C.; Falcaro, P. Enzyme Encapsulation in Zeolitic Imidazolate Frameworks: A Comparison between Controlled Co-Precipitation and Biomimetic Mineralisation. *Chem. Commun.* **2016**, 52 (3), 473–476.
- (361) Shieh, F. K.; Wang, S. C.; Yen, C. I.; Wu, C. C.; Dutta, S.; Chou, L. Y.; Morabito, J. V.; Hu, P.; Hsu, M. H.; Wu, K. C. W.; Tsung, C. K. Imparting Functionality to Biocatalysts via Embedding Enzymes into Nanoporous Materials by a de Novo Approach: Size-Selective Sheltering of Catalase in Metal-Organic Framework Microcrystals. *J. Am. Chem. Soc.* **2015**, 137 (13), 4276–4279.
- (362) Liu, Q.; Song, Y.; Ma, Y.; Zhou, Y.; Cong, H.; Wang, C.; Wu, J.; Hu, G.; O’Keeffe, M.; Deng, H. Mesoporous Cages in Chemically Robust MOFs Created by a Large Number of Vertices with Reduced Connectivity. *J. Am. Chem. Soc.* **2019**, 141 (1), 488–496.
- (363) Liang, W.; Xu, H.; Carraro, F.; Maddigan, N. K.; Li, Q.; Bell, S. G.; Huang, D. M.; Tarzia, A.; Solomon, M. B.; Amenitsch, H.; Vaccari, L.; Sumby, C. J.; Falcaro, P.; Doonan, C. J. Enhanced Activity of Enzymes Encapsulated in Hydrophilic Metal-Organic Frameworks. *J. Am. Chem. Soc.* **2019**, 141 (6), 2348–2355

- (364) Navarro-Sánchez, J.; Almora-Barrios, N.; Lerma-Berlanga, B.; Ruiz-Pernía, J. J.; Lorenz-Fonfria, V. A.; Tuñón, I.; Martí-Gastaldo, C. Translocation of Enzymes into a Mesoporous MOF for Enhanced Catalytic Activity under Extreme Conditions. *Chem. Sci.* **2019**, *10* (14), 4082–4088.
- (365) Li, Y. M.; Yuan, J.; Ren, H.; Ji, C. Y.; Tao, Y.; Wu, Y.; Chou, L. Y.; Zhang, Y. B.; Cheng, L. Fine-Tuning the Micro-Environment to Optimize the Catalytic Activity of Enzymes Immobilized in Multivariate Metal-Organic Frameworks. *J. Am. Chem. Soc.* **2021**, *143* (37), 15378–15390.
- (366) Mondloch, J. E.; Katz, M. J.; Isley, W. C.; Ghosh, P.; Liao, P.; Bury, W.; Wagner, G. W.; Hall, M. G.; Decoste, J. B.; Peterson, G. W.; Snurr, R. Q.; Cramer, C. J.; Hupp, J. T.; Farha, O. K. Destruction of Chemical Warfare Agents Using Metal-Organic Frameworks. *Nat. Mater.* **2015**, *14* (5), 512–516.
- (367) López-Maya, E.; Montoro, C.; Rodríguez-Albelo, L. M.; Aznar Cervantes, S. D.; Lozano-Pérez, A. A.; Cenís, J. L.; Barea, E.; Navarro, J. A. R. Textile/Metal-Organic-Framework Composites as Self-Detoxifying Filters for Chemical-Warfare Agents. *Angew. Chem. Int. Ed.* **2015**, *54* (23), 6790–6794.
- (368) Wang, H.; Mahle, J. J.; Tovar, T. M.; Peterson, G. W.; Hall, M. G.; Decoste, J. B.; Buchanan, J. H.; Karwacki, C. J. Solid-Phase Detoxification of Chemical Warfare Agents Using Zirconium-Based Metal Organic Frameworks and the Moisture Effects: Analyze via Digestion. *ACS Appl. Mater. Interfaces* **2019**, *11* (23), 21109–21116.
- (369) Kirlikovali, K. O.; Chen, Z.; Islamoglu, T.; Hupp, J. T.; Farha, O. K. Zirconium-Based Metal-Organic Frameworks for the Catalytic Hydrolysis of Organophosphorus Nerve Agents. *ACS Appl. Mater. Interfaces* **2020**, *12* (13), 14702–14720.
- (370) Katz, M. J.; Moon, S. Y.; Mondloch, J. E.; Beyzavi, M. H.; Stephenson, C. J.; Hupp, J. T.; Farha, O. K. Exploiting Parameter Space in MOFs: A 20-Fold Enhancement of Phosphate-Ester Hydrolysis with UiO-66-NH₂. *Chem. Sci.* **2015**, *6* (4), 2286–2291.
- (371) Moon, S. Y.; Liu, Y.; Hupp, J. T.; Farha, O. K. Instantaneous Hydrolysis of Nerve-Agent Simulants with a Six-Connected Zirconium-Based Metal-Organic Framework. *Angew. Chem. Int. Ed.* **2015**, *54* (23), 6795–6799.
- (372) Moon, S. Y.; Prousaloglou, E.; Peterson, G. W.; DeCoste, J. B.; Hall, M. G.; Howarth, A. J.; Hupp, J. T.; Farha, O. K. Detoxification of Chemical Warfare Agents Using a Zr₆-Based Metal–Organic Framework/Polymer Mixture. *Chem. Eur. J.* **2016**, *22* (42), 14864–14868.
- (373) De Koning, M. C.; Van Grol, M.; Breijjaert, T. Degradation of Paraoxon and the Chemical Warfare Agents VX, Tabun, and Soman by the Metal-Organic Frameworks UiO-66-NH₂, MOF-808, NU-1000, and PCN-777. *Inorg. Chem.* **2017**, *56* (19), 11804–11809.
- (374) Gil-San-Millan, R.; López-Maya, E.; Hall, M.; Padial, N. M.; Peterson, G. W.; DeCoste, J. B.; Rodríguez-Albelo, L. M.; Oltra, J. E.; Barea, E.; Navarro, J. A. R. Chemical Warfare Agents Detoxification Properties of Zirconium Metal-Organic Frameworks by Synergistic Incorporation of Nucleophilic and Basic Sites. *ACS Appl. Mater. Interfaces* **2017**, *9* (28), 23967–23973.
- (375) Chen, Z.; Ma, K.; Mahle, J. J.; Wang, H.; Syed, Z. H.; Atilgan, A.; Chen, Y.; Xin, J. H.; Islamoglu, T.; Peterson, G. W.; Farha, O. K. Integration of Metal-Organic Frameworks on Protective Layers for Destruction of Nerve Agents under Relevant Conditions. *J. Am. Chem. Soc.* **2019**, *141* (51), 20016–20021.
- (376) Garibay, S. J.; Farha, O. K.; Decoste, J. B. Single-Component Frameworks for Heterogeneous Catalytic Hydrolysis of Organophosphorous Compounds in Pure Water. *Chem. Commun.* **2019**, *55* (49), 7005–7008.
- (377) Gil-San-Millan, R.; López-Maya, E.; Platero-Prats, A. E.; Torres-Pérez, V.; Delgado, P.; Augustyniak, A. W.; Kim, M. K.; Lee, H. W.; Ryu, S. G.; Navarro, J. A. R. Magnesium Exchanged Zirconium Metal-Organic Frameworks with Improved Detoxification Properties of Nerve Agents. *J. Am. Chem. Soc.* **2019**, *141* (30), 11801–11805.
- (378) Luo, H. Bin; Castro, A. J.; Wasson, M. C.; Flores, W.; Farha, O. K.; Liu, Y. Rapid, Biomimetic Degradation of a Nerve Agent Simulant by Incorporating Imidazole Bases into a Metal-Organic Framework. *ACS Catal.* **2021**, *11* (3), 1424–1429.

- (379) Kalaj, M.; Palomba, J. M.; Bentz, K. C.; Cohen, S. M. Multiple Functional Groups in UiO-66 Improve Chemical Warfare Agent Simulant Degradation. *Chem. Commun.* **2019**, *55* (37), 5367–5370.
- (380) Wang, Y.; Lv, H.; Grape, E. S.; Gaggioli, C. A.; Tayal, A.; Dharanipragada, A.; Willhammar, T.; Inge, A. K.; Zou, X.; Liu, B.; Huang, Z. A Tunable Multivariate Metal-Organic Framework as a Platform for Designing Photocatalysts. *J. Am. Chem. Soc.* **2021**, *143* (17), 6333–6338.
- (381) Wei, Y. S.; Zhang, M.; Zou, R.; Xu, Q. Metal-Organic Framework-Based Catalysts with Single Metal Sites. *Chem. Rev.* **2020**, *120* (21), 12089–12174.
- (382) Chen, X.; Lyu, Y.; Wang, Z.; Qiao, X.; Gates, B. C.; Yang, D. Tuning Zr12O22 Node Defects as Catalytic Sites in the Metal-Organic Framework Hcp UiO-66. *ACS Catal.* **2020**, *10* (5), 2906–2914.
- (383) Li, Z.; Peters, A. W.; Bernales, V.; Ortuño, M. A.; Schweitzer, N. M.; Destefano, M. R.; Gallington, L. C.; Platero-Prats, A. E.; Chapman, K. W.; Cramer, C. J.; Gagliardi, L.; Hupp, J. T.; Farha, O. K. Metal-Organic Framework Supported Cobalt Catalysts for the Oxidative Dehydrogenation of Propane at Low Temperature. *ACS Cent. Sci.* **2017**, *3* (1), 31–38.
- (384) Xia, Q.; Li, Z.; Tan, C.; Liu, Y.; Gong, W.; Cui, Y. Multivariate Metal-Organic Frameworks as Multifunctional Heterogeneous Asymmetric Catalysts for Sequential Reactions. *J. Am. Chem. Soc.* **2017**, *139* (24), 8259–8266.
- (385) Wang, Y.; Zhao, L.; Ji, G.; He, C.; Liu, S.; Duan, C. Vanadium(VIV)–Porphyrin-Based Metal-Organic Frameworks for Synergistic Bimetallic Activation of Inert C(Sp³)–H Bonds. *ACS Appl. Mater. Interfaces* **2022**, *14* (2), 2794–2804.
- (386) Yuan, S.; Qin, J. S.; Zou, L.; Chen, Y. P.; Wang, X.; Zhang, Q.; Zhou, H. C. Thermodynamically Guided Synthesis of Mixed-Linker Zr-MOFs with Enhanced Tunability. *J. Am. Chem. Soc.* **2016**, *138* (20), 6636–6642.
- (387) Valverde, A.; Payno, D.; Lezama, L.; Laza, J. M.; Wuttke, S.; Luis, R. F. De. Multivariate Functionalization of UiO-66 for Photocatalytic Water Remediation. **2022**, *2200024*, 1–15.
- (388) Zhang, G.; Tan, K.; Xian, S.; Xing, K.; Sun, H.; Hall, G.; Li, L.; Li, J. Ultrastable Zirconium-Based Cationic Metal-Organic Frameworks for Perrhenate Removal from Wastewater. *Inorg. Chem.* **2021** *60* (16), 11730–11738.
- (389) Hu, J.; Yu, H.; Dai, W.; Yan, X.; Hu, X.; Huang, H. Enhanced Adsorptive Removal of Hazardous Anionic Dye “Congo Red” by a Ni/Cu Mixed-Component Metal-Organic Porous Material. *RSC Adv.* **2014**, *4* (66), 35124–35130.
- (390) Li, T. T.; Liu, Y. M.; Wang, T.; Wu, Y. L.; He, Y. L.; Yang, R.; Zheng, S. R. Regulation of the Surface Area and Surface Charge Property of MOFs by Multivariate Strategy: Synthesis, Characterization, Selective Dye Adsorption and Separation. *Microporous Mesoporous Mater.* **2018**, *272*, 101–108.
- (391) Pang, J.; Yuan, S.; Qin, J. S.; Lollar, C. T.; Huang, N.; Li, J.; Wang, Q.; Wu, M.; Yuan, D.; Hong, M.; Zhou, H. C. Tuning the Ionicity of Stable Metal-Organic Frameworks through Ionic Linker Installation. *J. Am. Chem. Soc.* **2019**, *141* (7), 3129–3136.
- (392) Issa, R.; Ibrahim, F. A.; Al-Ghoul, M.; Hmadeh, M. Controlled Growth and Composition of Multivariate Metal-Organic Frameworks-199 via a Reaction-Diffusion Process. *Nano Res.* **2021**, *14* (2), 423–431.
- (393) Han, L.; Liu, X.; Zhang, X.; Li, M.; Li, D.; Qin, P.; Tian, S.; Lu, M.; Cai, Z. Preparation of Multivariate Zirconia Metal-Organic Frameworks for Highly Efficient Adsorption of Endocrine Disrupting Compounds. *J. Hazard. Mater.* **2022**, *424* (PC), 127559.
- (394) Singha, D. K.; Majee, P.; Mondal, S. K.; Mahata, P. Detection of Pesticide Using the Large Stokes Shift of Luminescence of a Mixed Lanthanide Co-Doped Metal-Organic Framework. *Polyhedron* **2019**, *158*, 277–282.
- (395) Mon, M.; Bruno, R.; Tiburcio, E.; Viciano-Chumillas, M.; Kalinke, L. H. G.; Ferrando-Soria, J.; Armentano, D.; Pardo, E. Multivariate Metal-Organic Frameworks for the Simultaneous Capture of Organic and Inorganic Contaminants from Water. *J. Am. Chem. Soc.* **2019**, *141* (34), 13601–13609.

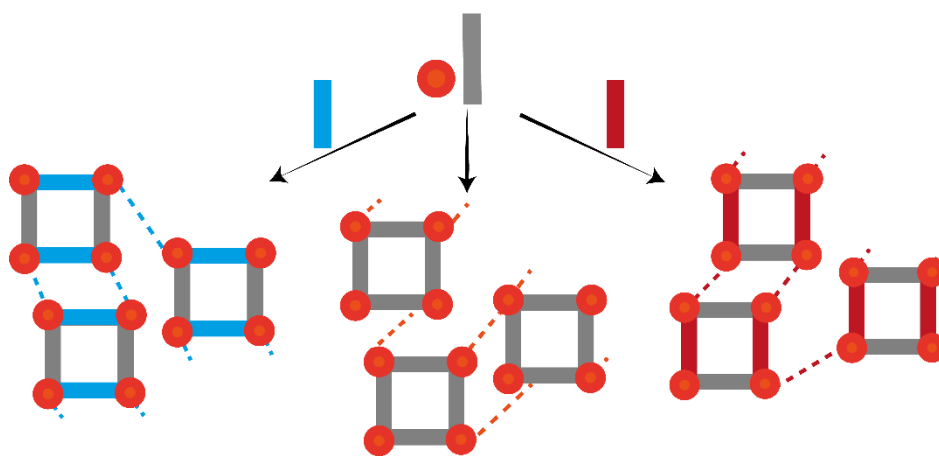
- (396) Mon, M.; Bruno, R.; Tiburcio, E.; Casteran, P. E.; Ferrando-Soria, J.; Armentano, D.; Pardo, E. Efficient Capture of Organic Dyes and Crystallographic Snapshots by a Highly Crystalline Amino-Acid-Derived Metal–Organic Framework. *Chem. Eur. J.* **2018**, *24* (67), 17712–17718.
- (397) Negro, C.; Martínez Pérez-Cejuela, H.; Simó-Alfonso, E. F.; Herrero-Martínez, J. M.; Bruno, R.; Armentano, D.; Ferrando-Soria, J.; Pardo, E. Highly Efficient Removal of Neonicotinoid Insecticides by Thioether-Based (Multivariate) Metal–Organic Frameworks. *ACS Appl. Mater. Interfaces* **2021**, *13* (24), 28424–28432.
- (398) Yang Hyunhongwoo, S.; Rao, S. R.; Narayanan, S.; Kapustin, E. A.; Furukawa, H.; Umans, A. S.; Yaghi, O. M.; Wang, E. N. Powered By Natural Sunlight. *Science* **2017**, *434*, 430–434.
- (399) Kim, H.; Rao, S. R.; Kapustin, E. A.; Zhao, L.; Yang, S.; Yaghi, O. M.; Wang, E. N. Adsorption-Based Atmospheric Water Harvesting Device for Arid Climates. *Nat. Commun.* **2018**, *9* (1), 1–8.
- (400) Fathieh, F.; Kalmutzki, M. J.; Kapustin, E. A.; Waller, P. J.; Yang, J.; Yaghi, O. M. Practical Water Production from Desert Air. *Sci. Adv.* **2018**, *4* (6), 1–10.
- (401) Hanikel, N.; Prévot, M. S.; Fathieh, F.; Kapustin, E. A.; Lyu, H.; Wang, H.; Diercks, N. J.; Glover, T. G.; Yaghi, O. M. Rapid Cycling and Exceptional Yield in a Metal–Organic Framework Water Harvester. *ACS Cent. Sci.* **2019**, *5* (10), 1699–1706.
- (402) Hanikel, N.; Prévot, M. S.; Yaghi, O. M. MOF Water Harvesters. *Nat. Nanotechnol.* **2020**, *15* (5), 348–355.
- (403) Hanikel, N.; Pei, X.; Chheda, S.; Lyu, H.; Jeong, W.; Sauer, J.; Gagliardi, L.; Yaghi, O. M. Water Harvesting. **2021**, *459*, 454–459.
- (404) Wang, X.; Fan, M.; Guan, Y.; Liu, Y.; Liu, M.; Karsili, T. N. V.; Yi, J.; Zhou, X. D.; Zhang, J. MOF-Based Electrocatalysts for High-Efficiency CO₂ conversion: Structure, Performance, and Perspectives. *J. Mater. Chem. A* **2021**, *9* (40), 22710–22728.
- (405) Lee, Y.; Kim, S.; Kang, J. K.; Cohen, S. M. Photocatalytic CO₂ Reduction by a Mixed Metal (Zr/Ti), Mixed Ligand Metal–Organic Framework under Visible Light Irradiation. *Chem. Commun.* **2015**, *51* (26), 5735–5738.
- (406) Zhao, C.; Dai, X.; Yao, T.; Chen, W.; Wang, X.; Wang, J.; Yang, J.; Wei, S.; Wu, Y.; Li, Y. Ionic Exchange of Metal–Organic Frameworks to Access Single Nickel Sites for Efficient Electroreduction of CO₂. *J. Am. Chem. Soc.* **2017**, *139* (24), 8078–8081.
- (407) Stolar, T.; Prašnikar, A.; Martinez, V.; Karadeniz, B.; Bjelić, A.; Mali, G.; Friščić, T.; Likozar, B.; Užarević, K. Scalable Mechanochemical Amorphization of Bimetallic Cu–Zn MOF-74 Catalyst for Selective CO₂ reduction Reaction to Methanol. *ACS Appl. Mater. Interfaces* **2021**, *13* (2), 3070–3077.
- (408) Qu, Q.; Ji, S.; Chen, Y.; Wang, D.; Li, Y. The Atomic-Level Regulation of Single-Atom Site Catalysts for the Electrochemical CO₂ reduction Reaction. *Chem. Sci.* **2021**, *12* (12), 4201–4215.
- (409) Feng, X.; Pi, Y.; Song, Y.; Brzezinski, C.; Xu, Z.; Li, Z.; Lin, W. Metal–Organic Frameworks Significantly Enhance Photocatalytic Hydrogen Evolution and CO₂ Reduction with Earth-Abundant Copper Photosensitizers. *J. Am. Chem. Soc.* **2020**, *142* (2), 690–695.
- (410) Choi, S.; Jung, W. J.; Park, K.; Kim, S. Y.; Baeg, J. O.; Kim, C. H.; Son, H. J.; Pac, C.; Kang, S. O. Rapid Exciton Migration and Amplified Funneling Effects of Multi-Porphyrin Arrays in a Re(I)/Porphyrinic MOF Hybrid for Photocatalytic CO₂ Reduction. *ACS Appl. Mater. Interfaces* **2021**, *13* (2), 2710–2722.
- (411) Zhuo, T. C.; Song, Y.; Zhuang, G. L.; Chang, L. P.; Yao, S.; Zhang, W.; Wang, Y.; Wang, P.; Lin, W.; Lu, T. B.; Zhang, Z. M. H-Bond-Mediated Selectivity Control of Formate versus CO during CO₂ Photoreduction with Two Cooperative Cu/X Sites. *J. Am. Chem. Soc.* **2021**, *143* (16), 6114–6122.
- (412) Lippi, R.; Howard, S. C.; Barron, H.; Easton, C. D.; Madsen, I. C.; Waddington, L. J.; Vogt, C.; Hill, M. R.; Sumbly, C. J.; Doonan, C. J.; Kennedy, D. F. Highly Active Catalyst for CO₂ Methanation Derived from a Metal Organic Framework Template. *J. Mater. Chem. A* **2017**, *5* (25), 12990–12997.
- (413) Nakatsuka, K.; Yoshii, T.; Kuwahara, Y.; Mori, K.; Yamashita, H. Controlled Pyrolysis of Ni–MOF-

- 74 as a Promising Precursor for the Creation of Highly Active Ni Nanocatalysts in Size-Selective Hydrogenation. *Chem. Eur. J.* **2018**, *24* (4), 898–905.
- (414) Zhang, H.; Yang, Y.; Liang, Y.; Li, J.; Zhang, A.; Zheng, H.; Geng, Z.; Li, F.; Zeng, J. Molecular Stabilization of Sub-Nanometer Cu Clusters for Selective CO₂ Electromethanation. *ChemSusChem* **2022**, *15* (1), 1–7.
- (415) Wang, Y.; Zhang, X.; Chang, K.; Zhao, Z.; Huang, J.; Kuang, Q. MOF Encapsulated AuPt Bimetallic Nanoparticles for Improved Plasmonic-induced Photothermal Catalysis of CO₂ Hydrogenation. *Chem. Eur. J.* **2022**, *28* (16).
- (416) Xing, S.; Janiak, C. Design and Properties of Multiple-Emitter Luminescent Metal-Organic Frameworks. *Chem. Commun.* **2020**, *56* (82), 12290–12306.
- (417) Cornelio, J.; Zhou, T. Y.; Alkaş, A.; Telfer, S. G. Systematic Tuning of the Luminescence Output of Multicomponent Metal-Organic Frameworks. *J. Am. Chem. Soc.* **2018**, *140* (45), 15470–15476.
- (418) Chen, C. X.; Qiu, Q. F.; Pan, M.; Cao, C. C.; Zhu, N. X.; Wang, H. P.; Jiang, J. J.; Wei, Z. W.; Su, C. Y. Tunability of Fluorescent Metal-Organic Frameworks through Dynamic Spacer Installation with Multivariate Fluorophores. *Chem. Commun.* **2018**, *54* (97), 13666–13669.
- (419) Newsome, W. J.; Ayad, S.; Cordova, J.; Reinheimer, E. W.; Campiglia, A. D.; Harper, J. K.; Hanson, K.; Uribe-Romo, F. J. Solid State Multicolor Emission in Substitutional Solid Solutions of Metal-Organic Frameworks. *J. Am. Chem. Soc.* **2019**, *141* (28), 11298–11303.
- (420) Jia, J.; Gutiérrez-Arzaluz, L.; Shekhah, O.; Alsadun, N.; Czaban-Jóźwiak, J.; Zhou, S.; Bakr, O. M.; Mohammed, O. F.; Eddaoudi, M. Access to Highly Efficient Energy Transfer in Metal-Organic Frameworks via Mixed Linkers Approach. *J. Am. Chem. Soc.* **2020**, *142* (19), 8580–8584.
- (421) Zhu, D.; Zhang, Y.; Bao, S.; Wang, N.; Yu, S.; Luo, R.; Ma, J.; Ju, H.; Lei, J. Dual Intrareticular Oxidation of Mixed-Ligand Metal-Organic Frameworks for Stepwise Electrochemiluminescence. *J. Am. Chem. Soc.* **2021**, *143* (8), 3049–3053.
- (422) Xu, R.; Wang, Y.; Duan, X.; Lu, K.; Micheroni, D.; Hu, A.; Lin, W. Nanoscale Metal-Organic Frameworks for Ratiometric Oxygen Sensing in Live Cells. *J. Am. Chem. Soc.* **2016**, *138* (7), 2158–2161.
- (423) Gui, B.; Meng, Y.; Xie, Y.; Tian, J. W.; Yu, G.; Zeng, W. X.; Zhang, G. X.; Gong, S. L.; Yang, C. L.; Zhang, D. Q.; Wang, C. Tuning the Photoinduced Electron Transfer in a Zr-MOF: Toward Solid-State Fluorescent Molecular Switch and Turn-on Sensor. *Adv. Mater.* **2018**, *30* (34), 1–6.
- (424) Lian, X.; Zhao, D.; Cui, Y.; Yang, Y.; Qian, G. A near Infrared Luminescent Metal-Organic Framework for Temperature Sensing in the Physiological Range. *Chem. Commun.* **2015**, *51* (100), 17676–17679.
- (425) Wang, Z.; Ananias, D.; Carné-Sánchez, A.; Brites, C. D. S.; Imaz, I.; Maspocho, D.; Rocha, J.; Carlos, L. D. Lanthanide-Organic Framework Nanothermometers Prepared by Spray-Drying. *Adv. Funct. Mater.* **2015**, *25* (19), 2824–2830.
- (426) Cui, Y.; Zhu, F.; Chen, B.; Qian, G. Metal-Organic Frameworks for Luminescence Thermometry. *Chem. Commun.* **2015**, *51* (35), 7420–7431.
- (427) Zhao, D.; Yue, D.; Zhang, L.; Jiang, K.; Qian, G. Cryogenic Luminescent Tb/Eu-MOF Thermometer Based on a Fluorine-Modified Tetracarboxylate Ligand. *Inorg. Chem.* **2018**, *57* (20), 12596–12602.
- (428) Yao, J.; Zhao, Y. W.; Zhang, X. M. Breathing Europium-Terbium Co-Doped Luminescent MOF as a Broad-Range Ratiometric Thermometer with a Contrasting Temperature-Intensity Relationship. *ACS Omega* **2018**, *3* (5), 5754–5760.
- (429) Feng, T.; Ye, Y.; Liu, X.; Cui, H.; Li, Z.; Zhang, Y.; Liang, B.; Li, H.; Chen, B. A Robust Mixed-Lanthanide PolyMOF Membrane for Ratiometric Temperature Sensing. *Angew. Chem.* **2020**, *132* (48), 21936–21941.
- (430) Liu, Y.; Pan, M.; Yang, Q. Y.; Fu, L.; Li, K.; Wei, S. C.; Su, C. Y. Dual-Emission from a Single-Phase Eu-Ag Metal-Organic Framework: An Alternative Way to Get White-Light Phosphor. *Chem. Mater.* **2012**, *24* (10), 1954–1960.
- (431) Li, L.; Cheng, J.; Liu, Z.; Song, L.; You, Y.; Zhou, X.; Huang, W. Ratiometric Luminescent Sensor

- of Picric Acid Based on the Dual-Emission Mixed-Lanthanide Coordination Polymer. *ACS Appl. Mater. Interfaces* **2018**, *10* (50), 44109–44115.
- (432) Singha, D. K.; Bhattacharya, S.; Majee, P.; Mondal, S. K.; Kumar, M.; Mahata, P. Optical Detection of Submicromolar Levels of Nitro Explosives by a Submicron Sized Metal-Organic Phosphor Material. *J. Mater. Chem. A* **2014**, *2* (48), 20908–20915.
- (433) Singha, D. K.; Majee, P.; Mondal, S. K.; Mahata, P. A Eu-Doped Y-Based Luminescent Metal-Organic Framework as a Highly Efficient Sensor for Nitroaromatic Explosives. *Eur. J. Inorg. Chem.* **2015**, *2015* (8), 1390–1397.
- (434) Wang, H.; Zhao, D.; Cui, Y.; Yang, Y.; Qian, G. A Eu/Tb-Mixed MOF for Luminescent High-Temperature Sensing. *J. Solid State Chem.* **2017**, *246*, 341–345.
- (435) Xia, T.; Zhu, F.; Jiang, K.; Cui, Y.; Yang, Y.; Qian, G. A Luminescent Ratiometric PH Sensor Based on a Nanoscale and Biocompatible Eu/Tb-Mixed MOF. *Dalt. Trans.* **2017**, *46* (23), 7549–7555.
- (436) Ye, J. W.; Lin, J. M.; Mo, Z. W.; He, C. T.; Zhou, H. L.; Zhang, J. P.; Chen, X. M. Mixed-Lanthanide Porous Coordination Polymers Showing Range-Tunable Ratiometric Luminescence for O₂ Sensing. *Inorg. Chem.* **2017**, *56* (7), 4238–4243.
- (437) White, K. A.; Chengelis, D. A.; Gogick, K. A.; Stehman, J.; Rosi, N. L.; Petoud, S. Near-Infrared Luminescent Lanthanide MOF Barcodes. *J. Am. Chem. Soc.* **2009**, *131* (50), 18069–18071.
- (438) Cadman, L. K.; Mahon, M. F.; Burrows, A. D. The Effect of Metal Distribution on the Luminescence Properties of Mixed-Lanthanide Metal-Organic Frameworks. *Dalt. Trans.* **2018**, *47* (7), 2360–2367.
- (439) Parmar, B.; Bisht, K. K.; Rachuri, Y.; Suresh, E. Zn(II)/Cd(II) Based Mixed Ligand Coordination Polymers as Fluorosensors for Aqueous Phase Detection of Hazardous Pollutants. *Inorg. Chem. Front.* **2020**, *7* (5), 1082–1107.
- (440) Li, L.; Deng, Z. Y.; Xie, X.; Zou, J. Y.; You, S. Y.; Chen, K. H.; Le, J. F. A Luminescent Zinc(II) Coordination Polymer as a Highly Selective and Sensitive Chemosensor for Fe(III) Cation and Cr(VI) Anions Detection in Aqueous Solution. *Inorganica Chim. Acta* **2020**, *513*, 119940.
- (441) Talha, K.; Alamgir; Ahmed, N.; Xie, L. H.; Zhang, X.; Li, J. R. Construction of a Zeolite A-Type Multivariate Metal-Organic Framework for Selective Sensing of Fe³⁺ and Cr^{2O7}-. *CrystEngComm* **2021**, *23* (28), 4923–4929.
- (442) Zhang, S. Y.; Shi, W.; Cheng, P.; Zaworotko, M. J. A Mixed-Crystal Lanthanide Zeolite-like Metal-Organic Framework as a Fluorescent Indicator for Lysophosphatidic Acid, a Cancer Biomarker. *J. Am. Chem. Soc.* **2015**, *137* (38), 12203–12206.
- (443) Wu, S.; Lin, Y.; Liu, J.; Shi, W.; Yang, G.; Cheng, P. Rapid Detection of the Biomarkers for Carcinoid Tumors by a Water Stable Luminescent Lanthanide Metal-Organic Framework Sensor. *Adv. Funct. Mater.* **2018**, *28* (17), 1–10.
- (444) Wang, X. Z.; Mao, X. Y.; Zhang, Z. Q.; Guo, R.; Zhang, Y. Y.; Zhu, N. J.; Wang, K.; Sun, P. P.; Huo, J. Z.; Wang, X. R.; Ding, B. Solvothermal and Ultrasonic Preparation of Two Unique Cluster-Based Lu and y Coordination Materials: Metal-Organic Framework-Based Ratiometric Fluorescent Biosensor for an Ornidazole and Ronidazole and Sensing Platform for a Biomarker of Amoeba Liver Absc. *Inorg. Chem.* **2020**, *59* (5), 2910–2922.
- (445) Zhao, Y.; Zeng, H.; Zhu, X. W.; Lu, W.; Li, D. Metal-Organic Frameworks as Photoluminescent Biosensing Platforms: Mechanisms and Applications. *Chem. Soc. Rev.* **2021**, *50* (7), 4484–4513.
- (446) Ying, X. D.; Chen, J. X.; Tu, D. Y.; Zhuang, Y. C.; Wu, D.; Shen, L. Tetraphenylpyrazine-Based Luminescent Metal-Organic Framework for Chemical Sensing of Carcinoids Biomarkers. *ACS Appl. Mater. Interfaces* **2021**, *13* (5), 6421–6429.
- (447) Zhou, Y. N.; Liu, L. L.; Liu, Q. W.; Liu, X. X.; Feng, M. Z.; Wang, L.; Sun, Z. G.; Zhu, Y. Y.; Zhang, X.; Jiao, C. Q. Dual-Functional Metal-Organic Framework for Luminescent Detection of Carcinoid Biomarkers and High Proton Conduction. *Inorg. Chem.* **2021**, *60* (22), 17303–17314.
- (448) Yi, K.; Li, H.; Zhang, X.; Zhang, L. Designed Tb(III)-Functionalized MOF-808 as Visible Fluorescent Probes for Monitoring Bilirubin and Identifying Fingerprints. *Inorg. Chem.* **2021**, *60* (5), 3172–3180.

Chapter 2:

Permanent Porosity in Hydroxamate Titanium-Organic Polyhedra



1. Motivation

Metal-organic polyhedra (MOPs) are hybrid molecular complexes assembled by coordination linkages¹. These supramolecular cages can feature intrinsic molecular porosity, which makes them attractive in host-guest recognition,^{2,3} gas separation,^{4,5} gas storage,⁶ and catalysis⁷. Furthermore, their molecular nature may ease their processability for integration into membranes⁸ or synthetic channels.⁹ Nevertheless, these supramolecular cages are relatively unexplored compared with extended porous solids such as MOFs, COFs or zeolites. This is arguably related to the difficulties in achieving permanent porosity in molecular cages. Removing guest molecules and avoiding the reorganization, or even structural collapse of the cages in the solid state, is not trivial. This is evidenced by the small number of BET surface areas measured for MOPs and the highest value of 1321 m²·g⁻¹ reported in 2019¹⁰ which is still far away from the high accessible porosity reported for MOFs.¹¹ MOPs with permanent porosity should present a rigid assembly which could ensure an efficient packing and resistance over structural collapse upon desolvation. Regarding structural robustness, the main efforts are focused on controlling poorly directional weak interactions that direct the assembly, avoiding the formation of more dense nonporous phases which are result of maximizing the number of weak contacts during crystallization. The use of appropriate rigid organic linkers and metal centers enables to control the formation of specific polyhedral topologies and shapes. In terms of stability, generally, chemically-stable MOP systems can be attained by well-defined strategies.¹² Some of them are based on grafting hydrophobic alkyl groups around the surface by direct or post-synthetic methods.¹³ As well as, using N-donor ligands with expensive metals (Pd, Pt)¹⁴ and also metal ions with high charge density, mostly works are focused on Zr⁴⁺ ions and carboxylate ligands.¹⁵ In this regard, the difficulties in designing robust cages have restricted their chemical diversity. Whereas over 100.000 crystal structures have been reported of MOFs with a wide range of topologies, only fourteen types of polyhedra are as a result of MOP assembly.

In this work, we proposed to extend the chemical diversity of robust porous cages introducing the hydroxamic group as connector in the organic linker. Hydroxamic acid groups are part of a group of molecules called *siderophores* and have been long known for their exceptional properties to chelate trivalent ions forming extremely stable complexes, in particular with iron.¹⁶ This approach was early used by Raymond to report an exceptional stable [Fe₄L₆] supramolecular cages.¹⁷ More recently, the ability to form strong bonds with other transition metals ions has been reported,¹⁷ also in our group.¹⁸ That encouraged us to combine benzene-1,4-dihydroxamic acid (*p*-H₄bdha) connectors with highly charged metals as Ti(IV) to obtain chemically stable nodes for the assembly of metal-organic cages. So, the main goal is to expand the toolbox of organic linkers, metals, and node geometries for the synthesis of robust porous polyhedra of interest in applications

as separation or catalysis. Complementary, it is aimed to use that stable MOP as a potential platform for introducing chemical variance.

2. Summary of the key results:

The findings of this work were published in “Lerma-Berlanga, B.; Castell-Gil, J.; R. Ganivet, C.; Almora-Barrios, N.; González-Platas, J.; Fabelo, O.; M. Padial, N. and Martí-Gastaldo, C. *Permanent porosity in hydroxamate titanium-organic polyhedral*. *J. Am. Chem. Soc.* **2021**, *143* (50), 21195-21199”. In this work, we described the use of hydroxamate linkers in the assembly of titanium-organic cages. The reported cMUV-11 (cMUV = *cage-type Material of Universidad de València*) was the first example of permanently porous Ti-MOP. Furthermore, it was demonstrated the value of the multivariate chemistry to combine several organic ligands with different functionalities in cMUV-11 structure for engineering its structural response to solvent evacuation.

cMUV-11 was prepared as deep red octahedral crystals of 100 μm (*Figure 2.1. a*) by direct reaction of titanium (IV) isopropoxide with benzene-1,4-dihydroxamic acid (*p*-H₄bdha) in dry DMF using benzoic acid as a modulator under soft solvothermal conditions. The use of shorter reaction times (18 h) and milder temperatures (100 °C) avoided the formation of the extended MUV-11 framework.¹⁸ cMUV-11 crystallized in the tetragonal space group *I4/m* ($a = 24.06$, $c = 24.70$ Å). Those crystals were measured, in the single crystal x-ray diffractometer by Javier González-Platas and Oscar Fabelo, as well as the reduction data and the structure resolution were carried out by them. The structure of cMUV-11 may be described as discrete neutral cubes with formula [Ti₈(*p*-H₂bdha)₈(*p*-bdha)₄]. The eight vertices were composed by titanium single-nodes with links at an angle of near 105° (η) which were linked by twelve *p*-bdha linkers located in the edges and bent with an angle of 157° (θ). That conformed a distorted cube (*cub*) (*Figure 2.1. b*) that deviates from the ideal 90° dihedral angles of the regular hexahedron. That was imposed by the five-membered chelate ring formed by the hydroxamate group that distorted the internal angles of the TiL₃ octahedra. The single-crystal structure analysis showed a H-bond cage assembly. The two vertices of the cube edges interacted with eight neighbouring cages by N-H...O H-bonds involving complementary hydroxamic groups from adjacent edges (*Figure 2.1. c*). That assisted H-bond packing produced a 3D porous framework with *pcb* topology with microporous cavities intrinsic to the *cub* cages (*Figure 2.1. d*). SEM images and LeBail refinement of the PXRD of bulk sample confirmed the phase purity. TGA and ICP measurements showed high thermal and chemical stability, both comparable to other Ti-MOFs values.¹⁸⁻²⁰ cMUV-11 showed a thermal decomposition profile quite similar to MUV-11, suggesting that thermal stability was not affected by reduction in dimensionality from 2 to 0D. The negligible metal leaching after sample incubation in water during 24 h confirmed the ability of the hydroxamic chelates to form hydrolytic robust bonds.

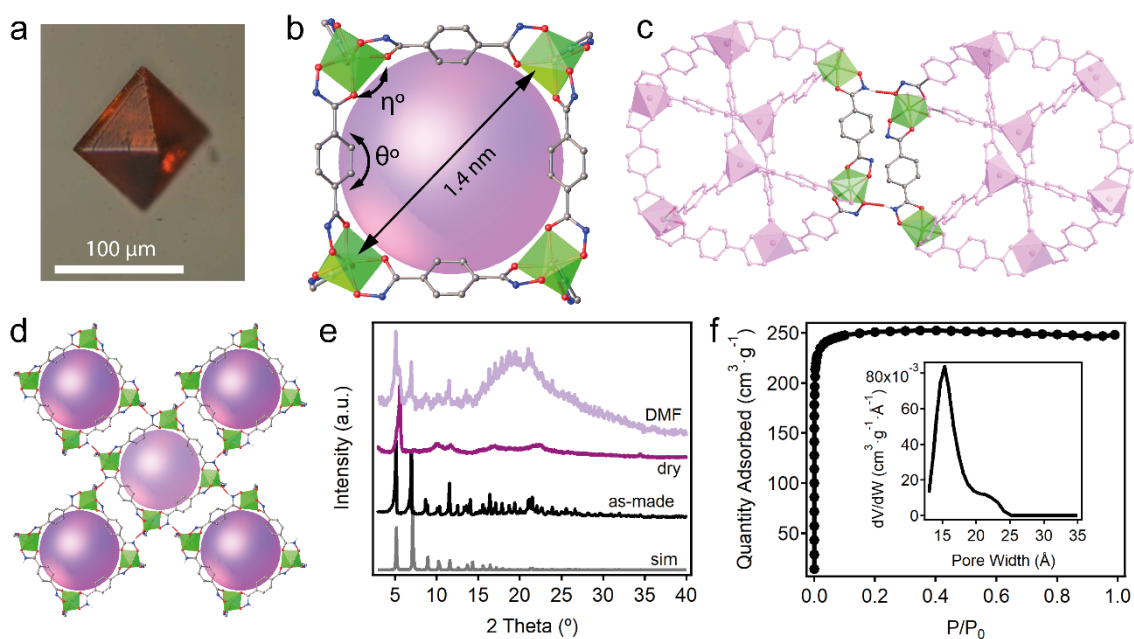


Figure 2.1. a) Crystal of cMUV-11. b) Structure and microporous cavity of the titanium cages featuring a slightly distorted cube geometry and internal cavities of 1.4 nm. c) Hydrogen-bonding interactions between hydroxamate groups from adjacent cages. d) Vertex-to-vertex packing of the cages into a 3D open framework. e) PXRD patterns show the structural response to evacuation and exposure to DMF. f) N₂ isotherm and PSD at 77 K after acetone exchange.

Subsequently, we examined the structural stability of cMUV-11 by evacuating the crystals in vacuum at room temperature. Even though the resultant PXRD showed a drastic broadening of the diffraction lines, indicative of a partial collapse of the structure, the original diffraction pattern was recovered after immersing the crystal in fresh DMF, confirming the flexibility of the H-bonds that control the cage packing (*Figure 2.1. e*). Our preliminary results anticipated the importance of finding an adequate activation protocol to control inter-cage packing which was critical to avoid structural collapse and access permanent porosity. MOPs often require a softer activation treatment than MOFs. In that direction, different volatile solvents (acetone, hexane, and diethyl ether) were tested in the exchange process. The best conditions were reached with acetone exchange, followed by solvent removal and evacuation under vacuum (10^{-3} mbar) at 40 °C for 16 hours. The resultant N₂ adsorption analysis displayed a reversible type-I isotherm with a BET surface area of 1020 m²·g⁻¹ (*Figure 2.1. f*). The analysis of the data by the non-local DFT method (NLDFT) showed a Pore Size Distribution (PSD) centred at 1.5 nm fitting well with the dimensions of the microporous cavity estimated from the crystallographic analysis (*Figure 2.1. b*). A second type of pore around 2.2 nm was related to the extrinsic mesoporosity which suggested a noticeable rearrangement in the cage packing upon activation.

The impact of the activation protocol suggested the crucial role played by inter-cage interactions in controlling the formation of more stable crystalline arrangements, and consequently accessing optimal surface area values. So, we opted for fine tuning the evacuation response by synthesizing mixed-linker versions of cMUV-11-X (X = NH₂ and OCH₃) cages. Our approach allowed us to modulate the external chemical environment of the cages incorporating distanced H-bond capacities groups in controllable ratios by functionalization of *p*-bdha linkers. Amine-functionalization was selected as donor group (D) and methoxy as acceptor (A) (Figure 2.2. a). The resulting cMUV-11-NH₂% and cMUV-11-OCH₃% were prepared by direct synthesis using binary combinations of non-functionalized linker, *p*-H₄bdha, and *p*-H₄bdha-NH₂ (1,4-benzo-2-amine-dihydroxamic acid) or *p*-H₄bdha-OCH₃ (1,4-benzo-2-methoxy-dihydroxamic acid) at variable molar ratios ranging from 10 to 100%. Unfortunately, the single component cages from the functionalized linkers alone could not be prepared, suggesting that the functionalized linkers might destabilize cage assembly compared to *p*-bdha.

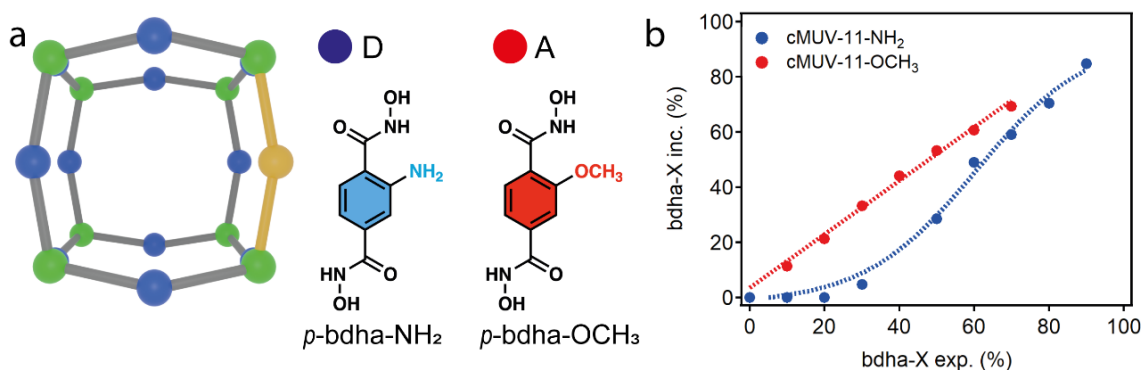


Figure 2.2. a) Mixed-linker cages from combination of *p*-bdha with *p*-bdha-NH₂ or -OCH₃. b) Rate of incorporation of *p*-bdha-X linkers into the crystals as a function of their concentration in solution.

Multivariate cages were isolated as crystals with size, color, and morphology similar to those of the pristine material. The ¹H NMR of the digested solids were used to evaluate the experimental ratio of the linkers in cMUV-11-X% samples. The incorporation trend for each linker suggested a distinct impact of the substituent in the assembling process, possibly due to their different ability to behave as H-bond D or A. Whereas *p*-bdha-NH₂ followed a sigmoidal trend with negligible incorporation at linker percentages below 30% followed by a progressive incorporation at higher ratios up to 90%, requiring higher concentrations of *p*-bdha-NH₂ for achieving notable incorporations. For its part, *p*-bdha-OCH₃ displayed an innocent involvement with linear incorporation up to 70 %, above that value, the impact of -OCH₃ (A) was negative and any solid was formed (Figure 2.2. b). That effect was even more drastic when combining *p*-bdha with 1,4-benzo-2-hydroxi-dihydroxamic acid (*p*-H₄bdha-OH), for which it was not observed the formation of any solid regardless the relative ratio used. Those results proved the effect of linker

functionalization in controlling the formation and composition of multivariate cMUV-11-X cages.

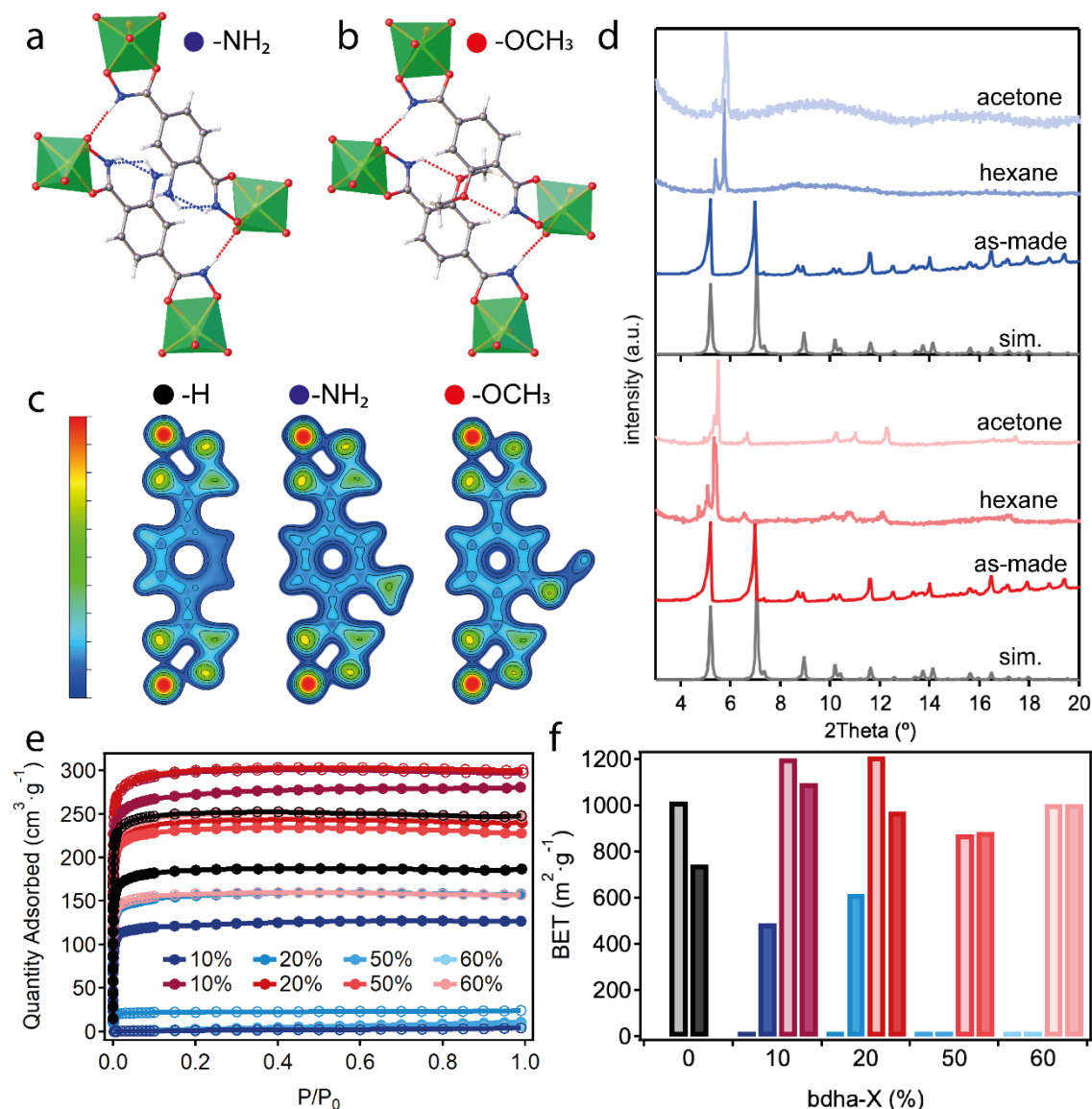


Figure 2.3. Hydrogen-bonding interactions in a) cMUV-11-NH₂-50% and b) -OCH₃-50% crystals. c) DFT calculations showing the charge density changes in the linker for the different substituents. d) Changes in the structural response of both MOPs to solvent evacuation. e) N₂ isotherms at 77 K of cMUV-11-X% (X = 10, 20, 50, 60) cages exchanged with acetone (open symbols) or hexane (solid symbols) and f) corresponding BET surface areas compared with MUV-11 in black.

The phase purity and homogeneity of the samples were evaluated by PXRD and SEM, respectively. The size and quality of the resultant crystals were sufficient to obtain the crystallographic structures of cMUV-11-NH₂-50% and -OCH₃-50% (Figure 2.3. a, b). Crystallographic data permitted a detailed study of the effect of linker functionalization on cage packing. Both structures were isostructural to cMUV-11, without significant alterations of the inter-cage H-bond network. Although, the influence of the substituents was evidenced by the appearance of crystallographic

disorder on *o,m*-positions of the aromatic ring as result of the combination of -H and -NH₂/-OCH3 groups, and the formation of additional intra-cage N-H...N (-NH₂) or N-H...O (-OCH3) interactions. The minor changes in the crystal structures were consistent with the negligible changes in the electronic structure of cMUV-11-X cages (X = H, NH₂ and OCH3). The density functional theory (DFT) calculations performed by Neyvis Almora-Barrios revealed a negligible variation of the charge density around O and N atoms of the hydroxamate group (*Figure 2.3. c*) which resulted in minimum changes to Ti-O bond distances, supported by the minimal variations experimentally observed in the chemical and thermal stability of the three derivatives.

As already observed for cMUV-11, the mixed-linker cages can also undergo a structural reassembly in the solid state that was controlled by the network of H-bonds involving D and A groups. We analysed the response to solvent evacuation of cMUV-11-NH₂-50% and -OCH3-50% after solvent exchange with acetone and hexane, by following the same protocol used with cMUV-11. The PXRD of the solids after evacuation showed clear differences in their structural response (*Figure 2.3. d*). The introduction of NH₂ groups resulted in more drastic structural collapses after solvent removal, compared to methoxy groups, which avoided disruption of the H-bond network maybe because of reduction of solvent interaction due to its non-polar, partly hydrophobic nature. That was consistent with cMUV-11-OCH3 ability to recover back to the H-bond network after being soaked in water.

The impact of the functionalization in the solid-state packing was translated into the porosity values (*Figure 2.3. e, f*). For the analysis, the functionalized cages were exchanged and activated under same protocol as cMUV-11. For the cMUV-11-NH₂-X% series, only the samples exchanged with hexane, and containing low concentrations of amine groups (≤ 20 %) displayed permanent porosity for maximum BET values of 620 m²·g⁻¹. Complete different behaviour was observed for -OCH3 set, samples below 50 % loading yielded higher surface areas than cMUV-11 of near 1200 m²·g⁻¹ after treatment with acetone or hexane. Those results confirmed the effect of inter-cage interactions in modulating the permanent porosity in that family of MOPs.

3. References

- (1) Eddaoudi, M.; Kim, J.; Wachter, J. B.; Chae, H. K.; O'Keeffe, M.; Yaghi, O. M. Porous Metal-Organic Polyhedra: 25 Å Cuboctahedron Constructed from 12 Cu₂(CO₂)₄ Paddle-Wheel Building Blocks. *J. Am. Chem. Soc.* **2001**, *123* (18), 4368–4369.
- (2) Bilbeisi, R. A.; Clegg, J. K.; Hatten, X. De; Devillard, M.; Breiner, B.; Mal, P.; Nitschke, J. R. Subcomponent Self-Assembly and Guest-Binding Properties of Face-Capped Fe₄L₄₈+ Capsules. *J. Am. Chem. Soc.* **2012**, *134*, (11), 5110–5119.
- (3) Xuan, W.; Zhang, M.; Liu, Y.; Chen, Z.; Cui, Y. A Chiral Quadruple-Stranded Helicate Cage for Enantioselective Recognition and Separation. *J. Am. Chem. Soc.* **2012**, *134* (16), 6904–6907.
- (4) Li, J. R.; Yu, J.; Lu, W.; Sun, L. B.; Sculley, J.; Balbuena, P. B.; Zhou, H. C. Porous Materials with Pre-Designed Single-Molecule Traps for CO₂ Selective Adsorption. *Nat. Commun.* **2013**, *4*, 1–8.
- (5) Inokuma, Y.; Kawano, M.; Fujita, M. Crystalline Molecular Flasks. *Nat. Chem.* **2011**, *3* (5), 349–358.
- (6) Rowland, C. A.; Lorzing, G. R.; Gosselin, E. J.; Trump, B. A.; Yap, G. P. A.; Brown, C. M.; Bloch, E. D. Methane Storage in Paddlewheel-Based Porous Coordination Cages. *J. Am. Chem. Soc.* **2018**, *140*, (36), 11153–11157.
- (7) Brown, C. J.; Toste, F. D.; Bergman, R. G.; Raymond, K. N. Supramolecular Catalysis in Metal-Ligand Cluster Hosts. *Chem. Rev.* **2015**, *115* (9), 3012–3035.
- (8) Liu, J.; Duan, W.; Song, J.; Guo, X.; Wang, Z.; Shi, X.; Liang, J.; Wang, J.; Cheng, P.; Chen, Y.; Zaworotko, M. J.; Zhang, Z. Self-Healing Hyper-Cross-Linked Metal-Organic Polyhedra (HCMOPs) Membranes with Antimicrobial Activity and Highly Selective Separation Properties. *J. Am. Chem. Soc.* **2019**, *141* (30), 12064–12070.
- (9) Kawano, R.; Horike, N.; Hijikata, Y.; Kondo, M.; Carné-Sánchez, A.; Larpent, P.; Ikemura, S.; Osaki, T.; Kamiya, K.; Kitagawa, S.; Takeuchi, S.; Furukawa, S. Metal-Organic Cuboctahedra for Synthetic Ion Channels with Multiple Conductance States. *Chem* **2017**, *2* (3), 393–403.
- (10) Lorzing, G. R.; Gosselin, A. J.; Trump, B. A.; York, A. H. P.; Sturluson, A.; Rowland, C. A.; Yap, G. P. A.; Brown, C. M.; Simon, C. M.; Bloch, E. D. Understanding Gas Storage in Cuboctahedral Porous Coordination Cages. *J. Am. Chem. Soc.* **2019**, *141*, (30), 12128–12138.
- (11) Hönicke, I. M.; Senkovska, I.; Bon, V.; Baburin, I. A.; Bönisch, N.; Raschke, S.; Evans, J. D.; Kaskel, S. Balancing Mechanical Stability and Ultrahigh Porosity in Crystalline Framework Materials. *Angew. Chem. Int. Ed.* **2018**, *57*, (42), 13780–13783.
- (12) Mollick, S.; Fajal, S.; Mukherjee, S.; Ghosh, S. K. Stabilizing Metal–Organic Polyhedra (MOP): Issues and Strategies. *Chem. Asian J.* **2019**, *14* (18), 3096–3108.
- (13) Mollick, S.; Mukherjee, S.; Kim, D.; Qiao, Z.; Desai, A. V.; Saha, R.; More, Y. D.; Jiang, J.; Lah, M. S.; Ghosh, S. K. Hydrophobic Shielding of Outer Surface: Enhancing the Chemical Stability of Metal–Organic Polyhedra. *Angew. Chem. Int. Ed.* **2019**, *58* (4), 1041–1045.
- (14) Lu, Z.; Knobler, C. B.; Furukawa, H.; Wang, B.; Liu, G.; Yaghi, O. M. Synthesis and Structure of Chemically Stable Metal-Organic Polyhedra. *J. Am. Chem. Soc.* **2009**, *131* (35), 12532–12533.
- (15) Liu, G.; Di Yuan, Y.; Wang, J.; Cheng, Y.; Peh, S. B.; Wang, Y.; Qian, Y.; Dong, J.; Yuan, D.; Zhao, D. Process-Tracing Study on the Postassembly Modification of Highly Stable Zirconium Metal–Organic Cages. *J. Am. Chem. Soc.* **2018**, *140* (20), 6231–6234.
- (16) Marmion, C. J.; Griffith, D.; Nolan, K. B. Hydroxamic Acids - An Intriguing Family of Enzyme Inhibitors and Biomedical Ligands. *Eur. J. Inorg. Chem.* **2004**, *15*, 3003–3016.
- (17) Beissel, T.; Powers, R. E.; Raymond, K. N. Symmetry-Based Metal Complex Cluster Formation. *Angew. Chem. Int. Ed.* **1996**, *35* (10), 1084–1086.

- (18) Padial, N. M.; Castells-Gil, J.; Almora-Barrios, N.; Romero-Angel, M.; Da Silva, I.; Barawi, M.; García-Sánchez, A.; De La Peña O'Shea, V. A.; Martí-Gastaldo, C. Hydroxamate Titanium-Organic Frameworks and the Effect of Siderophore-Type Linkers over Their Photocatalytic Activity. *J. Am. Chem. Soc.* **2019**, *141* (33), 13124–13133.
- (19) Hendon, C. H.; Tiana, D.; Fontecave, M.; Sanchez, C.; D'Arras, L.; Sassoie, C.; Rozes, L.; Mellot-Draznieks, C.; Walsh, A. Engineering the Optical Response of the Titanium-MIL-125 Metal-Organic Framework through Ligand Functionalization. *J. Am. Chem. Soc.* **2013**, *135* (30), 10942–10945.
- (20) Castells-Gil, J.; M. Padial, N.; Almora-Barrios, N.; Da Silva, I.; Mateo, D.; Albero, J.; García, H.; Martí-Gastaldo, C. De Novo Synthesis of Mesoporous Photoactive Titanium(IV)-Organic Frameworks with MIL-100 Topology. *Chem. Sci.* **2019**, *10* (15), 4313–4321.

Publication 1:

***Permanent Porosity in Hydroxamate
Titanium-Organic Polyhedra***

J. Am. Chem. Soc., **2021**, *143* (50), 21195-
21199

Permanent Porosity in Hydroxamate Titanium–Organic Polyhedra

Belén Lerma-Berlanga, Javier Castells-Gil, Carolina R. Ganivet, Neyvis Almora-Barrios, Javier González-Platas, Oscar Fabelo, Natalia M. Padial, and Carlos Martí-Gastaldo*



Cite This: *J. Am. Chem. Soc.* 2021, 143, 21195–21199



Read Online

ACCESS |



Metrics & More



Article Recommendations



Supporting Information

ABSTRACT: Following the synthesis of hydroxamate titanium–organic frameworks, we now extend these siderophore-type linkers to the assembly of the first titanium–organic polyhedra displaying permanent porosity. Mixed-linker versions of this molecular cage (cMUV-11) are also used to demonstrate the effect of pore chemistry in accessing high surface areas of near 1200 m²·g^{−1}.

Metal–organic polyhedra (MOPs) are hybrid molecular complexes assembled by coordination linkages.¹ These supramolecular cages feature intrinsic molecular porosity, which makes them attractive in host–guest recognition,^{2,3} separation,^{4,5} storage,⁶ and catalysis.⁷ Compared with extended porous solids such as metal–organic frameworks (MOFs), covalent organic frameworks (COFs), and zeolites, MOPs are relatively unexplored and represent a rapidly growing class of porous molecular solids.⁸ Their molecular nature can ease their processability for integration into membranes⁹ or synthetic channels.¹⁰ However, permanent porosity in MOPs is still less common because of the difficulties in designing robust cages that display porosity after guest removal. Even though the assembly of cages with prefabricated porosity can be controlled with the symmetry and directionality of metal–organic nodes,¹¹ the accessible porosity also depends on their packing in the solid state, which is controlled by intermolecular interactions that are much weaker than the directional bonding in extended networks.

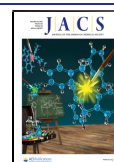
This is evidenced by the small number of surface areas measured for metal–organic cages.⁸ Among the 120 Brunauer–Emmett–Teller (BET) surface areas reported since 2005,¹² only 10 reach the 1000 m²·g^{−1} limit up to the maximum value of 1320 m²·g^{−1} reported in 2019.¹³ Analysis of these examples reveals the predominance of cuboctahedral (*cuo*) and octahedral (*oct*) cages assembled from bent dicarboxylic acid ligands and bimetallic paddlewheel units. Like the case of extended reticular solids, further advancement of the field will be fueled by expanding the toolbox of organic linkers, metals, and node geometries for the assembly of robust porous polyhedra. Close to 90% of the MOPs reported are based on clusters with high nuclearity reminiscent of the secondary building units in MOFs. Even though the design of mononuclear cages is common in supramolecular chemistry, they hardly display permanent porosity. This problem is associated with the use of soft N-donor linkers that render weak metal–linker joints more prone to collapse. The use of higher-p*K*_a imidazolates as connectors has proven to be successful in directing the assembly of porous cages with In³⁺ (MOC-2)¹⁴ and Pd²⁺ (MOP-100).¹⁵ We argued that this same concept could be extended to polycarboxylate linkers by

replacing carboxylic groups with hydroxamic groups. This siderophore-type chelating agent combines coordination modes similar to those for carboxylate with stronger bonds with some transition metal ions. We recently reported the formation of a porous titanium–organic framework by the use of benzene-1,4-dihydroxamic acid (*p*-H₄bdha).¹⁶ MUV-11 displayed excellent chemical stability as result of the formation of octahedral Ti(IV) mononuclear chelates. This same chelate was also used by Tezcan to design a 3D framework built from exceptionally stable [Fe₄(*m*-H₂bdha)₆] nodes,¹⁷ reminiscent of the hydroxamate supramolecular cages first reported by Raymond with Fe(III).¹⁸ Also, the use of highly charged metals such as Zr or Ti(IV) is accepted as an ideal choice for the assembly of chemically stable cages from robust linkages.¹⁹

We investigate the use of hydroxamate in the assembly of titanium–organic cages. cMUV-11 (cMUV = cage-type Material of Universidad de València) is the first example of a titanium MOP displaying permanent porosity. cMUV-11 was synthesized as dark-red octahedral crystals with sizes near 100 μm by the reaction of titanium(IV) isopropoxide and *p*-H₄bdha in *N,N*-dimethylformamide (DMF) with benzoic acid as a modulator (Figure 1a). Compared with the synthesis of MUV-11,¹⁶ the use of shorter reaction times, milder temperatures, and benzoic acid as a modulator are important to avoid the formation of the extended framework. Single-crystal X-ray diffraction analysis revealed that cMUV-11 crystallizes in the tetragonal space group *I4/m* (*a* = 24.06 Å, *c* = 24.70 Å). The structure is based on discrete neutral cubes with formula [Ti₈(*p*-H₂bdha)₈(*p*-bdha)₄] and Ti···Ti diagonals of 18.896 Å (Figure 1b). Like MUV-11, one-third of the hydroxamic –NH groups in the linkers are deprotonated for the assembly of a neutral cage. Eight single-node titanium connection points with links at an angle of near 105° (*η*) sit in the vertices and are linked by 12 *p*-bdha linkers located in the edges and bent

Received: September 1, 2021

Published: December 8, 2021



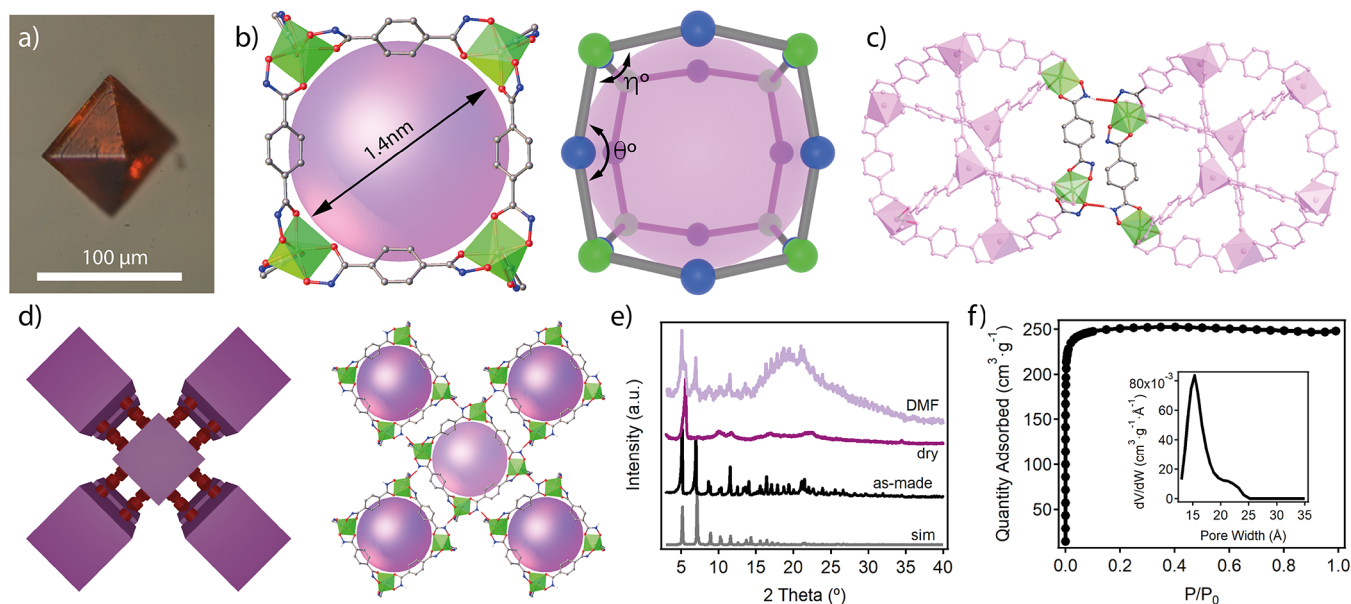


Figure 1. (a) Crystal of cMUV-11. (b) Structure and microporous cavity of the titanium cages featuring a slightly distorted cube geometry and internal cavities of 1.4 nm. (c) Hydrogen-bonding interactions between hydroxamate groups from adjacent cages. (d) Vertex-to-vertex packing of the cages into a 3D open framework. (e) Structural response to evacuation and exposure to DMF. (f) N_2 isotherm and PSD at 77 K after acetone exchange.

with an angle of $\theta = 157^\circ$. This conforms to a distorted cube (*cub*) that deviates from the ideal 90° dihedral angles of the regular hexahedron. This is imposed by the five-membered chelate ring formed by the hydroxamate group that distorts the internal angles of the TiL_3 octahedra. This configuration seems to be key for the assembly of the structure, as it reinforces the rigidity of the nodes and locks the hydroxamate groups in place to enable intermolecular hydrogen bonds. The two vertices of the cube edges interact with eight neighboring cages by following a vertex-to-vertex pattern. All of the $N-H\cdots O$ hydrogen bonds ($d_{N-O} = 2.624 \text{ \AA}$) are symmetry-equivalent and involve complementary hydroxamic groups from adjacent edges that act as donors and acceptors (Figure 1c). As result, the cages pack in a 3D open framework with a *pcb* topology (Figure 1d) and microporous cavities intrinsic to the *cub* cages. The analysis of the crystallographic file reveals pore windows of 0.7 nm and internal cavities of 1.4 nm, giving a solvent-accessible volume of near 70%.

As summarized in Supporting Information (SI) section S4, scanning electron microscopy (SEM) and LeBail refinement of the powder X-ray diffraction (PXRD) data for bulk samples were used to confirm the phase purity. Thermogravimetric analysis (TGA) in air showed well-defined decomposition steps at 200 and 430°C that correspond to the early oxidation of the linker followed by cage decomposition. This thermal stability is identical to that of MUV-11¹⁶ and comparable to those of other Ti^{4+} frameworks,^{20,21} suggesting that the thermal stability is not affected by the reduction in dimensionality. We tested the chemical stability of the cage by soaking freshly made crystals in water for 24 h followed by Inductively Coupled Plasma-Mass Spectrometry (ICP-MS) analysis of the supernatant. Metal leaching was almost negligible ($4 \text{ mg}\cdot\text{L}^{-1}$), confirming the ability of hydroxamate chelates to provide excellent resistance toward hydrolysis. Our preliminary tests suggest that cMUV-11 displays limited solubility in conventional solvents. We next examined the structural stability of cMUV-11 by evacuating the crystals in

vacuum at room temperature. As shown in Figure 1e, this treatment induced a drastic broadening of the diffraction lines indicative of partial collapse of the structure. Still, we were able to identify (110), (220), and (310) diffraction lines from the original structure. The original diffraction pattern was recovered by immersion of the crystal in DMF, confirming the flexibility of the hydrogen bonds that control the cage packing and anticipating the importance of finding an adequate activation protocol to prevent structural collapse. We opted for solvent exchange with acetone followed by evacuation at 10^{-3} mbar at 40°C for 16 h. The crystals displayed a reversible type-I isotherm characteristic of a microporous material, with no signature of hysteretic behavior and a BET surface area of $1020 \text{ m}^2\cdot\text{g}^{-1}$ (Figure 1f). This value is not far from the highest porosity reported for a MOP. All examples displaying porosities above $1000 \text{ m}^2\cdot\text{g}^{-1}$ to date are based on paddlewheel or multinuclear clusters, which are more likely to yield robust cages. In our case, the incorporation of rigid hydroxamate chelates seems to be crucial in controlling the response of cMUV-11 to evacuation and enable permanent porosity in a coordination cage based on mononuclear nodes. The experimental pore size distribution (PSD) calculated using nonlinear Density Functional Theory (DFT) methods shows a narrow peak centered at 1.5 nm, in good agreement with the dimensions of the microporous cavity estimated from the crystallographic analysis. There is also a broader peak at 2.2 nm that accounts for 10% of the porosity. This extrinsic mesoporosity cannot be directly correlated with the structure of cMUV-11 and might be indicative of changes in the cage packing upon evacuation. To better understand this behavior, we explored the use of other volatile solvents such as ether and hexane by following the same evacuation protocol. We observed a reduction in the surface area in both cases, down to a minimum of $750 \text{ m}^2\cdot\text{g}^{-1}$ for hexane. This change is concomitant with a decrease in the contribution of the intrinsic micropores to the global porosity at the expense of an increase in the extrinsic mesoporosity.

Controlling the cage structure and connectivity for more stable crystalline arrangements is certainly essential to optimize the porosity.²² We hypothesized that this might be investigated in our case by using *p*-bdha linkers functionalized with complementary hydrogen-bond donor (D) and acceptor (A) groups that might modify the connectivity pattern fixed by the hydroxamate groups in cMUV-11. We synthesized the mixed-linker cages cMUV-11-NH₂ and -OCH₃ by following the same protocol used for the original cage but using binary combinations of *p*-bdha with 2-aminobenzene-1,4-dihydroxamic acid (*p*-H₄bdha-NH₂) or 2-methoxybenzene-1,4-dihydroxamic acid (*p*-H₄bdha-OCH₃) at variable molar ratios ranging from 10 to 100% (Figure 2a). We used a robotic

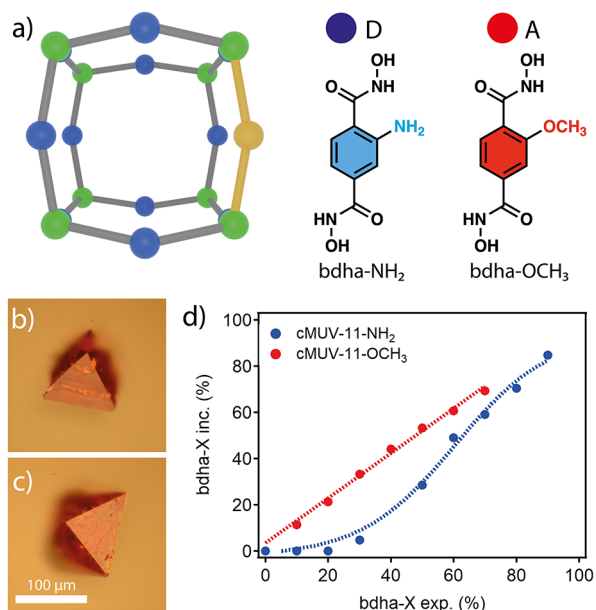


Figure 2. (a) Mixed-linker cages from combination of *p*-bdha with *p*-bdha-NH₂ or -OCH₃. (b, c) Crystals of (b) cMUV-11-NH₂-50% and (c) -OCH₃-50%. (d) Rate of incorporation of *p*-bdha-X linkers into the crystals as a function of their concentration in solution.

platform for the automated dosing of solutions to ensure maximum reproducibility. Multivariate cages were isolated as crystals with size, color, and morphology similar to those of the pristine material (Figure 2b,c). The experimental ratio of the linkers in cMUV-11-X% was analyzed with ¹H NMR (Nuclear Magnetic Resonance) spectroscopy after digestion of the crystals in acid. Figure 2d shows the rates of incorporation of *p*-bdha-X into the crystals as functions of the percentage of linkers in solution. *p*-bdha-OCH₃ follows a linear regime up to a maximum of near 70% from which the MOP cannot be formed. In turn, *p*-bdha-NH₂ follows a sigmoidal trend with negligible incorporation at linker percentages below 30% followed by progressive incorporation at higher ratios up to 90%. This suggests a distinct effect of the linker in controlling the assembly of [Ti₈(*p*-bdha)_{12-y}(*p*-bdha-X)_y] (X = NH₂, OCH₃) cages, possibly due to their different abilities to behave as hydrogen-bond donors or acceptors. The impact of -OCH₃ (A) groups is only detrimental at higher concentrations. In turn, the presence of -NH₂ (D/A) requires higher concentrations for the cage assembly. This effect is even more drastic when *p*-H₄bdha is combined with 2-hydroxybenzene-1,4-dihydroxamic acid (*p*-H₄bdha-OH), for which we do not observe the formation of any solid regardless of the

relative ratio used. Our results highlight the effect of linker functionalization in controlling the formation and composition of multivariate cMUV-11-X cages. Also, single-component cages cannot be prepared from the functionalized linkers alone, suggesting that the functionalized linkers might destabilize cage assembly compared to *p*-bdha (SI section S2).

The phase purity and homogeneity of the samples were evaluated by PXRD and SEM, respectively (SI section S4), confirming the formation of mixed-linker phases isostructural to cMUV-11 in all cases. Single crystals of cMUV-11-NH₂-50% and -OCH₃-50% were measured at low temperature (100 K) to elucidate the effect of linker functionalization on the cage packing (Figure 3a,b). Both structures show local crystallographic disorder affecting the ortho and meta positions of the aromatic ring as result of the combination of -H and -NH₂/-OCH₃ groups, consistent with the ratios calculated by ¹H NMR analysis. The incorporation of these groups prompts the formation of additional intracage N-H...N (-NH₂) or N-H...O (-OCH₃) interactions but does not change the network of intercage hydrogen bonds that control the cage packing and are slightly shortened by 0.01 and 0.03 Å, respectively. Our DFT calculations show that compared to cMUV-11, the effect of both substituents on the charge density around the O and N atoms of the hydroxamate group is negligible (Figure 3c). This is translated into minimum changes in the Ti-O bond distances and corresponding strengths of the linkages for similar thermal stabilities according to TGA. The ICP analysis also confirmed minimum metal leaching after 24 h. We argued that the main differences between the pristine and functionalized cages would be dominated by the changes in pore polarity. We analyzed the responses to solvent evacuation of cMUV-11-NH₂-50% and -OCH₃-50% after solvent exchange with acetone and hexane following the same protocol as used with cMUV-11. The PXRD patterns of the solids after evacuation show clear differences in their structural response. The introduction of polar -NH₂ groups results in more drastic structural collapse after solvent removal, which becomes even more acute for a polar solvent such as acetone (Figure 3d). In turn, nonpolar methoxy groups seem better fitted to minimize solvent interactions and avoid disruption of the hydrogen-bonding network responsible for long-range packing. As result, the MOP retains better crystallinity regardless of the polarity of the solvent used. The effect of *p*-bdha-X is also translated into the accessible porosity of the multivariate cages calculated from N₂ isotherms (Figure 3e). For the cMUV-11-NH₂-X% series, only the samples exchanged with hexane and containing low concentrations of amine groups (≤20%) display permanent porosity with a maximum BET value of 620 m²·g⁻¹ (Figure 3f). This value is below those displayed by cMUV-11 tested under the same conditions and confirms the detrimental effect of these groups in rigidifying the cage assembly toward solvent evacuation. In turn, -OCH₃ functionalization below 50% yields surface areas of nearly 1200 or 1100 m²·g⁻¹ after treatment with acetone or hexane, which are higher than those of cMUV-11, suggesting the effect of intercage interactions in modulating the permanent porosity in this family of MOPs. This is consistent with the irreversible collapse of the -H and -NH₂ cages in water that can be reverted back only in the case of cMUV-11-OCH₃.

cMUV-11 is the first example of a permanently porous titanium-organic cage. This molecular solid is packed from vertex-to-vertex hydrogen-bonded microporous hydroxamate mononuclear cubes that are compatible with linker function-

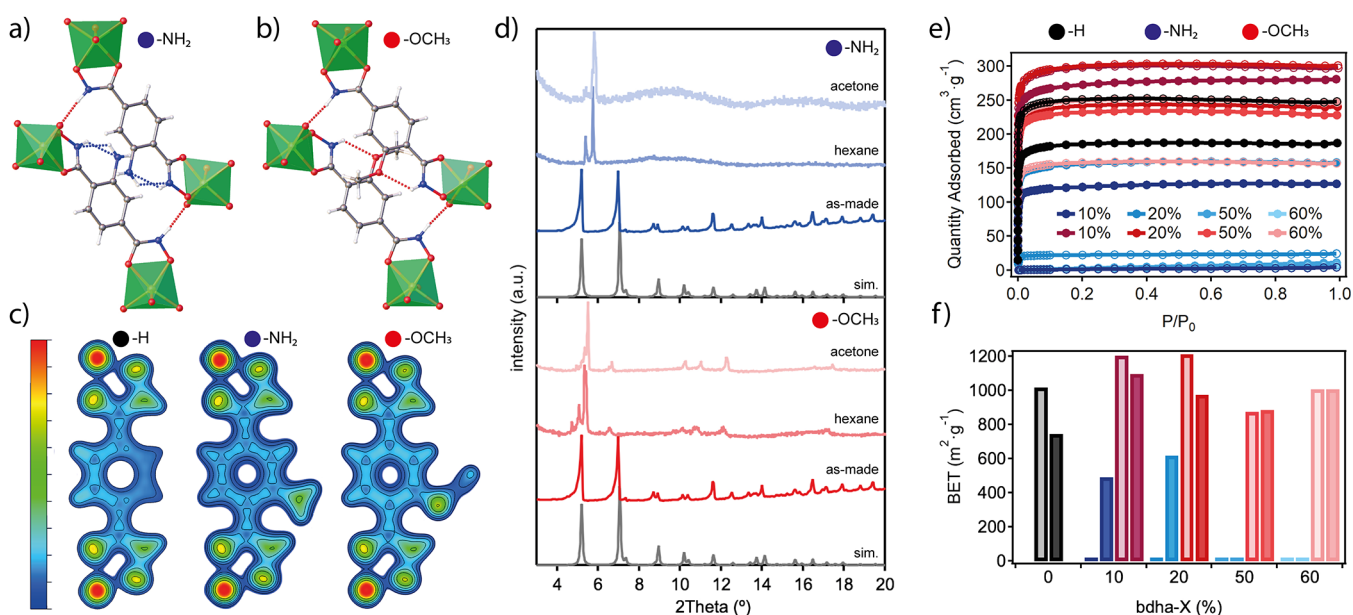


Figure 3. (a, b) Hydrogen-bonding interactions in (a) cMUV-11-NH₂-50% and (b) -OCH₃-50% crystals. (c) DFT calculations showing the charge density changes in the linker for the different substituents. (d) Changes in the structural response of both MOPs to solvent evacuation. (e) N₂ isotherms at 77 K of cMUV-11-X% (X = 10, 20, 50, 60) cages exchanged with acetone (open symbols) or hexane (solid symbols) and (f) corresponding BET surface areas compared with MUV-11 in black.

alization. This synthetic versatility was used to produce mixed-linker cages with tailorable pore chemistry and varying sensitivity to solvent evacuation for permanent porosities above 1000 m²·g⁻¹. Compared with extended titanium MOFs, which are simultaneously treated as semiconductor (TiO₂) or molecular catalysts,²³ we are confident that these titanium MOPs might be an ideal platform to engineer photocatalytic performance in porous solids by using only molecular concepts exclusive of homogeneous catalysis.

■ ASSOCIATED CONTENT

Supporting Information

The Supporting Information is available free of charge at <https://pubs.acs.org/doi/10.1021/jacs.1c09278>.

Synthetic and experimental details, physical characterization, and supporting tables and figures (PDF)

Accession Codes

CCDC 2106822–2106824 contain the supplementary crystallographic data for this paper. These data can be obtained free of charge via www.ccdc.cam.ac.uk/data_request/cif, or by emailing data_request@ccdc.cam.ac.uk, or by contacting The Cambridge Crystallographic Data Centre, 12 Union Road, Cambridge CB2 1EZ, U.K.; fax: +44 1223 336033.

■ AUTHOR INFORMATION

Corresponding Author

Carlos Martí-Gastaldo – *Functional Inorganic Materials Team, Instituto de Ciencia Molecular (ICMol), Universitat de València, 46980 Paterna, València, Spain*; orcid.org/0000-0003-3203-0047; Email: carlos.marti@uv.es

Authors

Belén Lerma-Berlanga – *Functional Inorganic Materials Team, Instituto de Ciencia Molecular (ICMol), Universitat de València, 46980 Paterna, València, Spain*

Javier Castells-Gil – *Functional Inorganic Materials Team, Instituto de Ciencia Molecular (ICMol), Universitat de València, 46980 Paterna, València, Spain*; Present Address: School of Chemistry, University of Birmingham, Edgbaston, Birmingham B15 2TT, United Kingdom; orcid.org/0000-0001-7931-3867

Carolina R. Ganivet – *Functional Inorganic Materials Team, Instituto de Ciencia Molecular (ICMol), Universitat de València, 46980 Paterna, València, Spain*; orcid.org/0000-0002-4738-6460

Neyvis Almora-Barrios – *Functional Inorganic Materials Team, Instituto de Ciencia Molecular (ICMol), Universitat de València, 46980 Paterna, València, Spain*; orcid.org/0000-0001-5269-2705

Javier González-Platas – *Departamento de Física, Instituto Universitario de Estudios Avanzados en Física Atómica, Molecular y Fotónica (IUDEA), MALTA Consolider Team, Universidad de La Laguna, 38204 La Laguna, Tenerife, Spain*; orcid.org/0000-0003-3339-2998

Oscar Fabelo – *Institut Laue Langevin, 38042 Grenoble, France*; orcid.org/0000-0001-6452-8830

Natalia M. Padial – *Functional Inorganic Materials Team, Instituto de Ciencia Molecular (ICMol), Universitat de València, 46980 Paterna, València, Spain*; orcid.org/0000-0001-6067-3360

Complete contact information is available at:

<https://pubs.acs.org/doi/10.1021/jacs.1c09278>

Notes

The authors declare no competing financial interest.

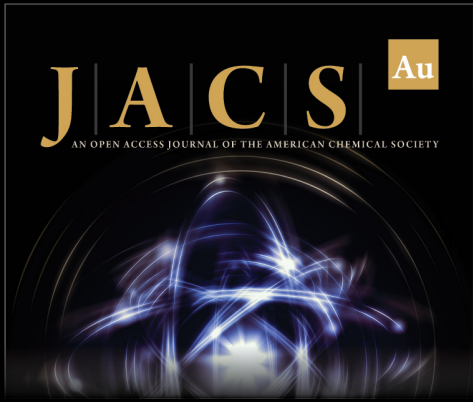
■ ACKNOWLEDGMENTS

This project received funding from the European Union's Horizon 2020 Research and Innovation Programme (ERC Grant Agreement 714122), the EU-FEDER Fund, and the Spanish Government (CEX2019-000919-M, PID2020-

118117RB-I00, and PID2019-106383GB-C44). B.L.-B. thanks the Spanish Government for an FPU (FPU16/04162). N.M.P. thanks la Caixa Foundation for a Postdoctoral Junior Leader–Retaining Fellowship (LCF/BQ/PR20/11770014). We also thank the University of Valencia for research facilities (SCSIE, Tirant, and Nanbiosis).

REFERENCES

- (1) Eddaoudi, M.; Kim, J.; Wachter, J. B.; Chae, H. K.; O’Keeffe, M.; Yaghi, O. M. Porous Metal–Organic Polyhedra: 25 Å Cuboctahedron Constructed from 12 $\text{Cu}_2(\text{CO}_2)_4$ Paddle-Wheel Building Blocks. *J. Am. Chem. Soc.* **2001**, *123*, 4368–4369.
- (2) Bilbeisi, R. A.; Clegg, J. K.; Elgrishi, N.; Hatten, X. de; Devillard, M.; Breiner, B.; Mal, P.; Nitschke, J. R. Subcomponent Self-Assembly and Guest-Binding Properties of Face-Capped $\text{Fe}_4\text{L}_4^{8+}$ Capsules. *J. Am. Chem. Soc.* **2012**, *134*, 5110–5119.
- (3) Xuan, W.; Zhang, M.; Liu, Y.; Chen, Z.; Cui, Y. A Chiral Quadruple-Stranded Helicate Cage for Enantioselective Recognition and Separation. *J. Am. Chem. Soc.* **2012**, *134*, 6904–6907.
- (4) Inokuma, Y.; Kawano, M.; Fujita, M. Crystalline Molecular Flasks. *Nat. Chem.* **2011**, *3*, 349–358.
- (5) Li, J.-R.; Yu, J.; Lu, W.; Sun, L.-B.; Sculley, J.; Balbuena, P. B.; Zhou, H.-C. Porous Materials with Pre-Designed Single-Molecule Traps for CO_2 Selective Adsorption. *Nat. Commun.* **2013**, *4*, 1538.
- (6) Rowland, C. A.; Lorz, G. R.; Gosselin, E. J.; Trump, B. A.; Yap, G. P. A.; Brown, C. M.; Bloch, E. D. Methane Storage in Paddlewheel-Based Porous Coordination Cages. *J. Am. Chem. Soc.* **2018**, *140* (36), 11153–11157.
- (7) Brown, C. J.; Toste, F. D.; Bergman, R. G.; Raymond, K. N. Supramolecular Catalysis in Metal–Ligand Cluster Hosts. *Chem. Rev.* **2015**, *115*, 3012–3035.
- (8) Gosselin, A. J.; Rowland, C. A.; Bloch, E. D. Permanently Microporous Metal–Organic Polyhedra. *Chem. Rev.* **2020**, *120*, 8987–9014.
- (9) Liu, J.; Duan, W.; Song, J.; Guo, X.; Wang, Z.; Shi, X.; Liang, J.; Wang, J.; Cheng, P.; Chen, Y.; Zaworotko, M. J.; Zhang, Z. Self-Healing Hyper-Cross-Linked Metal–Organic Polyhedra (HCMOPs) Membranes with Antimicrobial Activity and Highly Selective Separation Properties. *J. Am. Chem. Soc.* **2019**, *141*, 12064–12070.
- (10) Kawano, R.; Horike, N.; Hijikata, Y.; Kondo, M.; Carné-Sánchez, A.; Larpent, P.; Ikemura, S.; Osaki, T.; Kamiya, K.; Kitagawa, S.; Takeuchi, S.; Furukawa, S. Metal–Organic Cuboctahedra for Synthetic Ion Channels with Multiple Conductance States. *Chem.* **2017**, *2*, 393–403.
- (11) Tranchemontagne, D. J.; Ni, Z.; O’Keeffe, M.; Yaghi, O. M. Reticular Chemistry of Metal–Organic Polyhedra. *Angew. Chem., Int. Ed.* **2008**, *47*, 5136–5147.
- (12) Ni, Z.; Yassar, A.; Antoun, T.; Yaghi, O. M. Porous Metal–Organic Truncated Octahedron Constructed from Paddle-Wheel Squares and Terthiophene Links. *J. Am. Chem. Soc.* **2005**, *127*, 12752–12753.
- (13) Lorz, G. R.; Gosselin, A. J.; Trump, B. A.; York, A. H. P.; Sturluson, A.; Rowland, C. A.; Yap, G. P. A.; Brown, C. M.; Simon, C. M.; Bloch, E. D. Understanding Gas Storage in Cuboctahedral Porous Coordination Cages. *J. Am. Chem. Soc.* **2019**, *141*, 12128–12138.
- (14) Sava, D. F.; Kravtsov, V. C.; Eckert, J.; Eubank, J. F.; Nouar, F.; Eddaoudi, M. Exceptional Stability and High Hydrogen Uptake in Hydrogen-Bonded Metal–Organic Cubes Possessing ACO and AST Zeolite-like Topologies. *J. Am. Chem. Soc.* **2009**, *131*, 10394–10396.
- (15) Lu, Z.; Knobler, C. B.; Furukawa, H.; Wang, B.; Liu, G.; Yaghi, O. M. Synthesis and Structure of Chemically Stable Metal–Organic Polyhedra. *J. Am. Chem. Soc.* **2009**, *131*, 12532–12533.
- (16) Padial, N. M.; Castells-Gil, J.; Almora-Barrios, N.; Romero-Angel, M.; da Silva, I.; Barawi, M.; García-Sánchez, A.; de la Peña O’Shea, V. A.; Martí-Gastaldo, C. Hydroxamate Titanium–Organic Frameworks and the Effect of Siderophore-Type Linkers over Their Photocatalytic Activity. *J. Am. Chem. Soc.* **2019**, *141*, 13124–13133.
- (17) Chiong, J. A.; Zhu, J.; Bailey, J. B.; Kalaj, M.; Subramanian, R. H.; Xu, W.; Cohen, S. M.; Tezcan, F. A. An Exceptionally Stable Metal–Organic Framework Constructed from Chelate-Based Metal–Organic Polyhedra. *J. Am. Chem. Soc.* **2020**, *142*, 6907–6912.
- (18) Beissel, T.; Powers, R. E.; Raymond, K. N. Symmetry-Based Metal Complex Cluster Formation. *Angew. Chem., Int. Ed.* **1996**, *35*, 1084–1086.
- (19) (a) He, Y.-P.; Yuan, L.-B.; Chen, G.-H.; Lin, Q.-P.; Wang, F.; Zhang, L.; Zhang, J. Water-Soluble and Ultrastable Ti_4L_6 Tetrahedron with Coordination Assembly Function. *J. Am. Chem. Soc.* **2017**, *139* (46), 16845–16851. (b) Liu, G.; Di Yuan, Y.; Wang, J.; Cheng, Y.; Peh, S. B.; Wang, Y.; Qian, Y.; Dong, J.; Yuan, D.; Zhao, D. Process-Tracing Study on the Postassembly Modification of Highly Stable Zirconium Metal–Organic Cages. *J. Am. Chem. Soc.* **2018**, *140*, 6231–6234. (c) Lee, S.; Jeong, H.; Nam, D.; Lah, M. S.; Choe, W. The rise of metal–organic polyhedra. *Chem. Soc. Rev.* **2021**, *50*, 528–555.
- (20) Castells-Gil, J.; Padial, N. M.; Almora-Barrios, N.; Albero, J.; Ruiz-Salvador, A. R.; González-Platas, J.; García, H.; Martí-Gastaldo, C. Chemical Engineering of Photoactivity in Heterometallic Titanium–Organic Frameworks by Metal Doping. *Angew. Chem., Int. Ed.* **2018**, *57*, 8453–8457.
- (21) Castells-Gil, J.; Padial, N. M.; Almora-Barrios, N.; da Silva, I.; Mateo, D.; Albero, J.; García, H.; Martí-Gastaldo, C. De Novo Synthesis of Mesoporous Photoactive Titanium(IV)–Organic Frameworks with MIL-100 Topology. *Chem. Sci.* **2019**, *10*, 4313–4321.
- (22) Zhao, C.; Chen, L.; Che, Y.; Pang, Z.; Wu, X.; Lu, Y.; Liu, H.; Day, G. M.; Cooper, A. I. Digital Navigation of Energy-Structure-Function Maps for Hydrogen-Bonded Porous Molecular Crystals. *Nat. Commun.* **2021**, *12*, 817.
- (23) Kolobov, N.; Goesten, M. G.; Gascon, J. Metal–Organic Frameworks: Molecules or Semiconductors in Photocatalysis? *Angew. Chem., Int. Ed.* **2021**, *60*, 26038–26052.



JACS Au
AN OPEN ACCESS JOURNAL OF THE AMERICAN CHEMICAL SOCIETY

Editor-in-Chief
Prof. Christopher W. Jones
Georgia Institute of Technology, USA

Open for Submissions

pubs.acs.org/jacsau ACS Publications
Most-Trust. Most Cited. Most Read.

Supplementary Information

Permanent porosity in hydroxamate titanium-organic polyhedra

Belén Lerma-Berlanga,† Javier Castells-Gil,† Carolina R. Ganivet,† Neyvis Almora-Barrios,† Javier González-Platas,§ Oscar Fabelo,⊥ Natalia M. Padiá† and Carlos Martí-Gastaldo†*

† Functional Inorganic Materials Team, Instituto de Ciencia Molecular (ICMol), Universitat de València, Paterna 46980, València, Spain.

§ Departamento de Física. Instituto Universitario de Estudios Avanzados en Física Atómica, Molecular y Fotónica (IUDEA). MALTA Consolider Team. Universidad de La Laguna, Avda. Astrofísico Fco. Sánchez s/n, La Laguna, Tenerife, E-38204, Spain.

⊥ Institut Laue Langevin, 71 avenue des Martyrs, CS 20156, Grenoble, Cedex 9 38042, France.

Table of content

Supplementary Information	1
S1. General considerations: starting materials and characterization	2
Materials and reagents.....	3
Physical and chemical characterization.....	3
S2. Synthesis of cMUV-11	4
S2.1. Synthesis of organic ligands	4
Preparation of 1,4-benzo-dihydroxamic acid (<i>p</i> -H ₄ bdha).....	4
Preparation of 1,4-benzo-2-amine-dihydroxamic acid (<i>p</i> -H ₄ bdha-NH ₂).....	4
Preparation of 1,4-benzo-2-methoxy-dihydroxamic acid (<i>p</i> -H ₄ bdha-OCH ₃).....	6
Preparation of 1,4-benzo-2-hydroxy-dihydroxamic acid (<i>p</i> -H ₄ bdha-OH).....	9
S2.2. Synthesis of cMUV-11	11
S2.3. Synthesis of cMUV-11-NH₂ & cMUV-11-OCH₃	11
S3. cMUV-11 structures. Single-Crystal X-ray Diffraction Analyses	16
S4. Chemical characterization	20
S4.1. cMUV-11	20
Scanning Electron Microscopy (SEM).....	20
Thermogravimetric Analysis (TGA).....	20
Powder X-Ray Diffraction (PXRD).....	21
S4.2. Solubility test of cMUV-11	22
S4.3. cMUV-11-NH₂ & cMUV-11-OCH₃	25
Scanning Electron Microscopy (SEM).....	25
Thermogravimetric Analysis (TGA).....	26
Elemental analysis (EA).....	26
Powder X-Ray Diffraction (PXRD).....	27
S5. Activation of cMUV-11 cages and N₂ adsorption	28
N ₂ isotherms.....	28
S6. Chemical and Structural Stability	32
ICP-MS measurements.....	32
Powder X-Ray Diffraction (PXRD) after water incubation.....	33
CO ₂ adsorption after water incubation.....	34
Scanning Electron Microscopy (SEM) after water incubation.....	35
S7. Computational calculations	36
References	37

S1. General considerations: starting materials and characterization.

Materials and reagents

Dimethyl 2-aminoterephthalate, dimethyl terephthalate, hydroxylamine hydrochloride ($\text{NH}_2\text{OH}\cdot\text{HCl}$, 99 %), sodium hydroxide (NaOH $\geq 97.0\%$, pellets), iodomethane (CH_3I , $\geq 99.0\%$ (GC)) potassium carbonate ($\geq 99.0\%$) and anhydrous *N,N*-Dimethylformamide (DMF, 99.8 %) were purchased from Sigma-Aldrich. 2-hydroxy-terephthalic acid dimethyl ester was purchased from Fluorochem. Methanol, acetone, hexane, and ether ($\geq 99.9\%$) were purchased from Scharlab. Ultrapure water from Milli-Q equipment was used when required. All reagents and solvents were used without any previous purification unless specified.

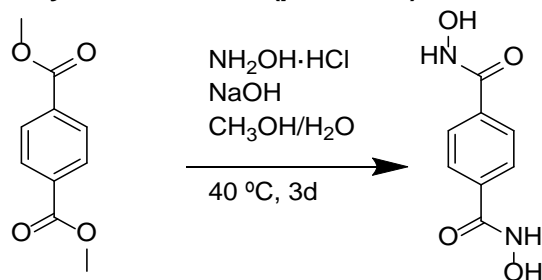
Physical and chemical characterization

- Elemental analysis (EA): Carbon, nitrogen and hydrogen contents were determined by microanalytical procedures using a LECO CHNS.
- Thermogravimetric analysis (TGA) were carried out with a Mettler Toledo TGA/SDTA 851 apparatus between 25 and 600 °C under ambient conditions ($10\text{ }^\circ\text{C}\cdot\text{min}^{-1}$ scan rate and an air flow of $30\text{ mL}\cdot\text{min}^{-1}$).
- Nuclear magnetic resonance (NMR) spectra were recorded on Bruker DRX-500 spectrometer and were calibrated to the residual solvent peak ($\text{DMSO}-d_6$ at 2.50 ppm $^1\text{H-NMR}$). The following abbreviations were used to explain multiplicities: s = singlet, d = doublet, t = triplet, q = quartet, m = multiplet, br = broad.
- Powder X-Ray Diffraction (PXRD) patterns were collected in a PANalytical X'Pert PRO diffractometer using copper radiation ($\text{Cu K}\alpha = 1.5418\text{ \AA}$) with an X'Celerator detector, operating at 40 mA and 45 kV. Profiles were collected in the $2^\circ < 2\theta < 40^\circ$ range with a step size of 0.017° .
- Scanning Electron Microscopy (SEM): particle morphologies and dimensions were studied with a Hitachi S4800 scanning electron microscope at an accelerating voltage of 20 kV, over metalized samples with a mixture of gold and palladium for 90 seconds.
- Inductively coupled plasma mass spectrometry (ICP-MS): the measurements were carried out with an Agilent 7900 apparatus.
- Gas adsorption measurements were recorded on a Micromeritics 3Flex apparatus at relative pressures up to 1 atm. The samples were exchanged with low boiling point solvent and degassed overnight at 40 °C and 10^{-6} Torr prior to analysis. Surface area, pore size and volume values were calculated from N_2 adsorption-desorption isotherms (77 K) Specific surface area was calculated by multi-point Brunauer-Emmett-Teller (BET) method. Total pore volume was taken at $P/P_0=0.96$. Pore size distribution was analysed by using the solid density functional theory (NLDFT) for the adsorption branch by assuming a cylindrical pore model.

S2. Synthesis of cMUV-11

S2.1. Synthesis of organic ligands

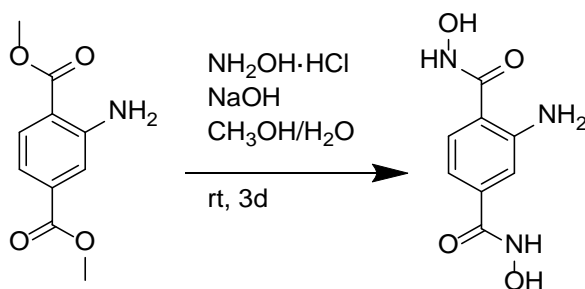
Preparation of 1,4-benzo-dihydroxamic acid (*p*-H₄bdha)



Scheme S1. Synthesis of *p*-H₄bdha ligand.

The synthesis of *p*-H₄bdha was carried out according to the procedure described by Marmion¹ with minor modifications reported by our group.²

Preparation of 1,4-benzo-2-amine-dihydroxamic acid (*p*-H₄bdha-NH₂)



Scheme S2. Synthesis of *p*-H₄bdha-NH₂ ligand.

The synthesis of *p*-H₄bdha-NH₂ was carried out following the procedure for *p*-H₄bdha with slight modifications. Hydroxylamine hydrochloride (1.80 g, 25.9 mmol) was mixed with sodium hydroxide (2.06 g, 51.5 mmol) in deionized water (13 mL). The solution was then added to a suspension of dimethyl 2-aminoterephthalate (1.79 g, 8.6 mmol) in methanol (15 mL). The resulting mixture was stirred for 72 hours at room temperature and subsequently acidified to pH 6 with a solution of 30 % acetic acid. The yellow solid was filtered and washed with deionized H₂O. The desired solid *p*-H₄bdha-NH₂ was dried under reduced pressure overnight (89 % yield). ¹H-NMR (300 MHz, DMSO-*d*₆) δ : 7.34 (d, J = 8.1 Hz, 1H), 7.10 (d, J = 1.5 Hz, 1H), 6.79 (dd, J = 8.1, 1.6 Hz, 1H). ¹³C-NMR (75 MHz, DMSO-*d*₆) δ : 166.0 (C), 149.0 (C), 135.7 (C), 127.6 (CH), 115.0 (CH), 112.6 (CH).

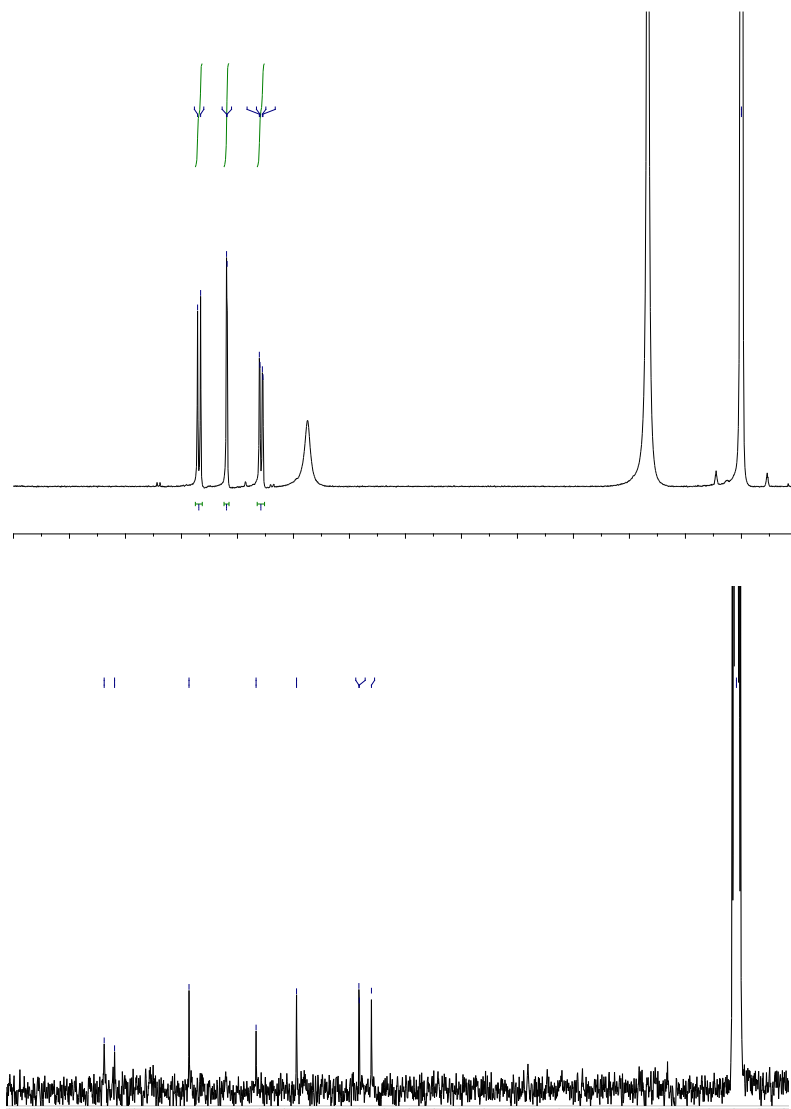
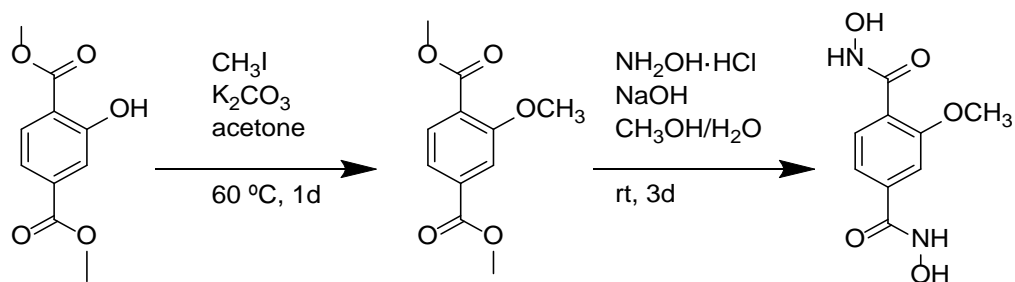


Figure S1. ¹H-NMR spectrum of compound *p*-H₄bdha-NH₂ in DMSO-*d*₆ (top) and ¹³C-NMR spectrum of compound *p*-H₄bdha-NH₂ in DMSO-*d*₆ (bottom).

Preparation of 1,4-benzo-2-methoxy-dihydroxamic acid (*p*-H₄bdha-OCH₃)



Scheme S3. Synthesis of *p*-H₄bdha-OCH₃ ligand.

The first step was the hydroxy group methylation, that was carried out according to the method reported by Min Kim and co-workers.³ 2-Hydroxy-terephthalic acid dimethyl ester (1.65 g, 7.8 mmol), potassium carbonate (11.04 g, 78.4 mmol) and iodomethane (2.44 mL, 39.2 mmol) were charged in 30 mL of acetone. The mixture was stirred and heated at 60 °C for 24 h. After this time, the organic layer was extracted with dichloromethane and H₂O. The organic layer was dried over MgSO₄ and evaporated to obtain the pure product as a white solid (bdMe₂-OCH₃). ¹H-NMR (300 MHz, DMSO-*d*₆) δ: 7.74 (d, J = 8.3 Hz, 1H), 7.61 - 7.57 (m, 2H), 3.89 (s, 6H), 3.81 (s, 3H). ¹³C-NMR (75 MHz, DMSO-*d*₆) δ: 165.7 (C), 165.5 (C), 157.7 (C), 133.7 (C), 130.7 (CH), 124.5 (C), 120.8 (CH), 112.5 (CH), 56.0 (CH₃), 52.5 (CH₃), 52.2 (CH₃).

Then, a solution of hydroxylamine hydrochloride (1.62 g, 23.3 mmol) and sodium hydroxide (1.86 g, 46.5 mmol) in water (19 mL) was added to a suspension of dimethyl 2-methoxyterephthalate (bdMe₂-OCH₃) (1.73 g, 8.6 mmol) in methanol (19 mL). The resulting mixture was stirred for 72 hours at room temperature and subsequently acidified to pH 6 with a solution of 30 % acetic acid. The white solid was filtered and washed with deionized H₂O. The desired solid *p*-H₄bdha-OCH₃ was dried under reduced pressure overnight (90 % yield). ¹H-NMR (300 MHz, DMSO-*d*₆) δ: 11.32 (brs), 10.72 (brs), 9.15 (brs), 7.57 (d, J = 7.8 Hz, 1H), 7.44 – 7.35 (m, 2H), 3.87 (s, 3H). ¹³C-NMR (75 MHz, DMSO-*d*₆) δ: 162.5 (C), 156.4 (C), 135.7 (C), 129.7 (CH), 125.1 (C), 118.8 (CH), 110.1 (CH), 55.8 (CH₃).

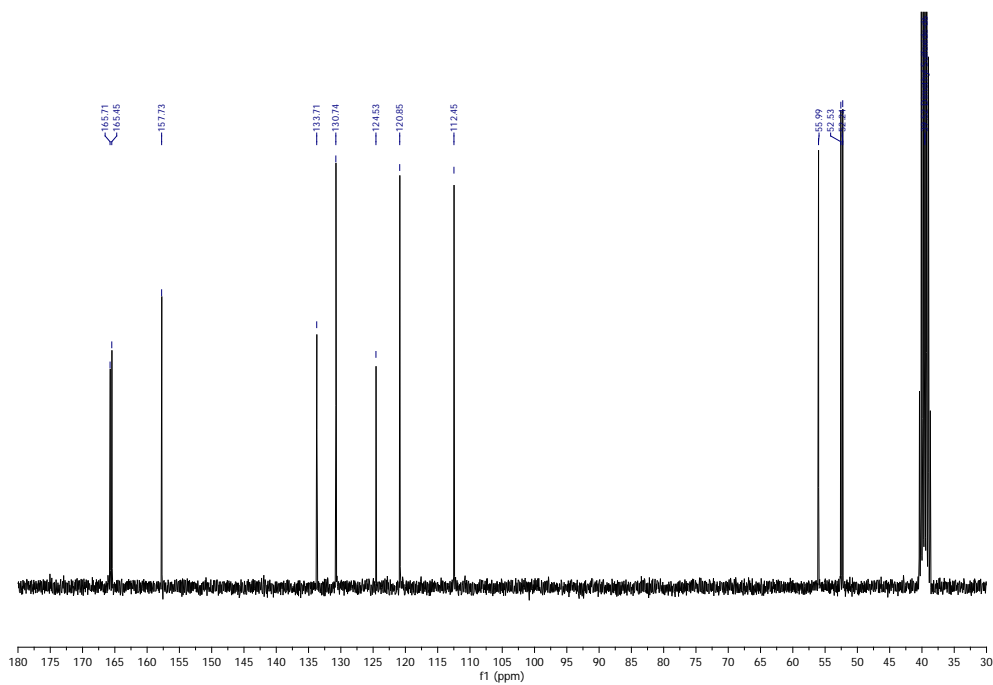
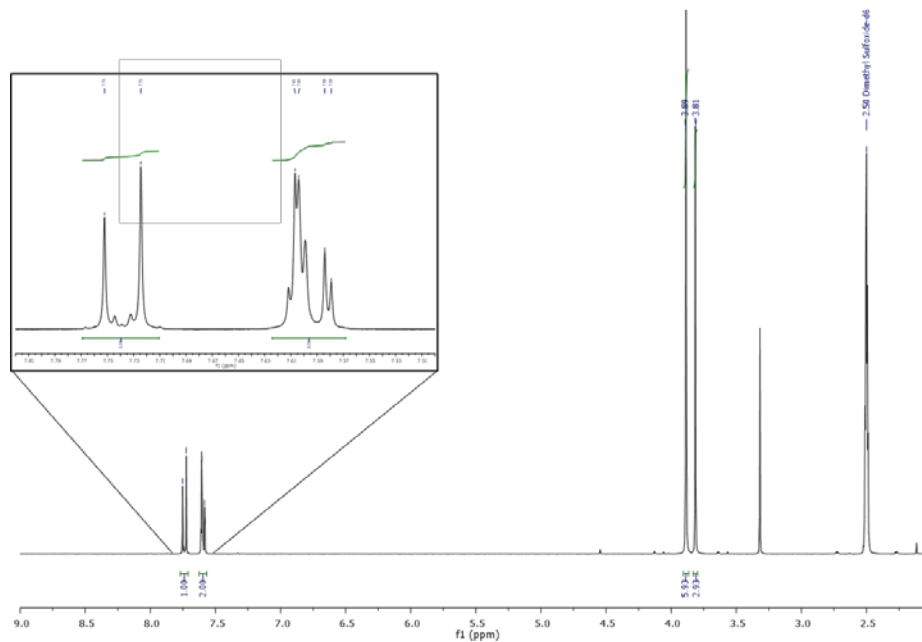


Figure S2. $^1\text{H-NMR}$ spectrum of compound $\text{bdMe}_2\text{-OCH}_3$ in DMSO-d_6 (top) and $^{13}\text{C-NMR}$ spectrum of compound $\text{bdMe}_2\text{-OCH}_3$ in DMSO-d_6 (bottom).

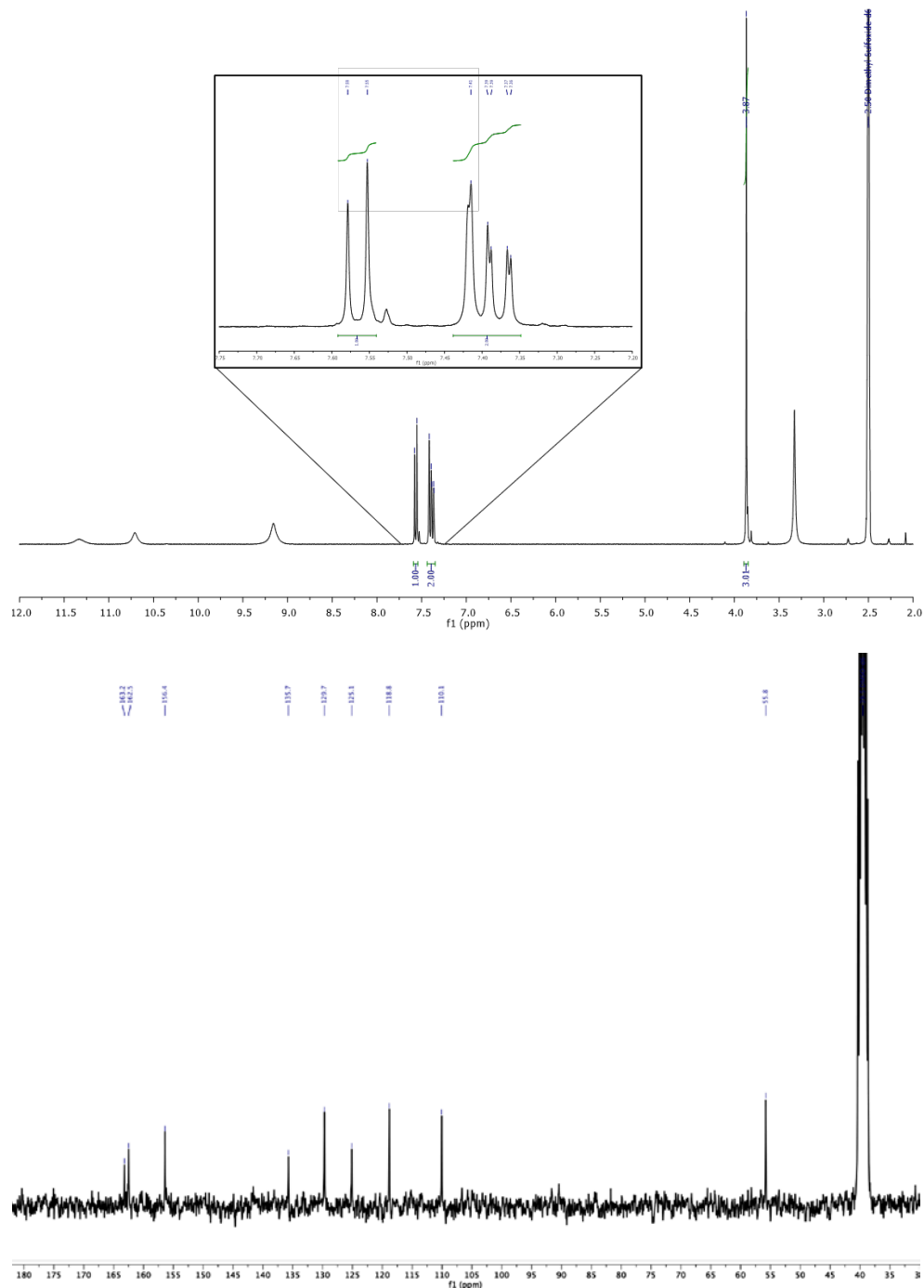
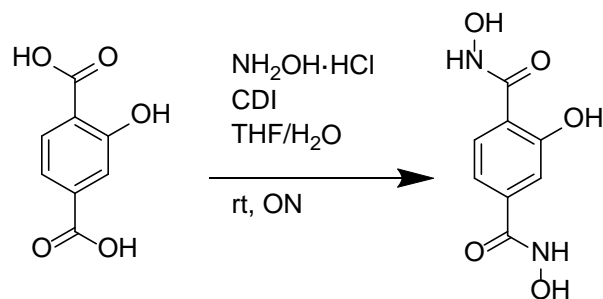


Figure S3. ¹H-NMR spectrum of compound *p*-H₄bdha-OCH₃ in DMSO-*d*₆ (top) and ¹³C-NMR spectrum of compound *p*-H₄bdha-OCH₃ in DMSO-*d*₆ (bottom).

Preparation of 1,4-benzo-2-hydroxy-dihydroxamic acid (*p*-H₄bdha-OH)



Scheme S4. Synthesis of *p*-H₄bdha-OH ligand.

1,1'-Carbonyldiimidazole (CDI) (1.95 g, 12 mmol) was dissolved in 75 mL of tetrahydrofuran (THF). Then, The solution was added to a suspension of 2-hydroxyterephthalic acid (0.73 g, 4 mmol) in methanol (25 mL). Later, a hydroxylamine hydrochloride (1.11 g, 16 mmol) solution (10 mL of deionized water) was added dropwise. The resulting mixture was stirred for 18 hours at room temperature and subsequently acidified to pH 6 with a solution of 30 % acetic acid. The yellow solid was filtered and washed with a mixture of acetone/deionized H₂O (4:1). The desired solid *p*-H₄bdha-NH₂ was dried under reduced pressure overnight (76 % yield). ¹H-NMR (300 MHz, DMSO-*d*₆) δ: 11.01 (brs), δ 8.96 (d, *J* = 18.1 Hz, 2H), 7.33 (d, *J* = 8.1 Hz, 1H), 7.10 (s, 1H), 6.79 (d, *J* = 8.1 Hz, 1H). ¹³C-NMR (75 MHz, DMSO-*d*₆) δ: 164.1 (C), 149.1 (C), 135.7 (C), 127.6 (CH), 115.0 (CH), 112.6 (CH).

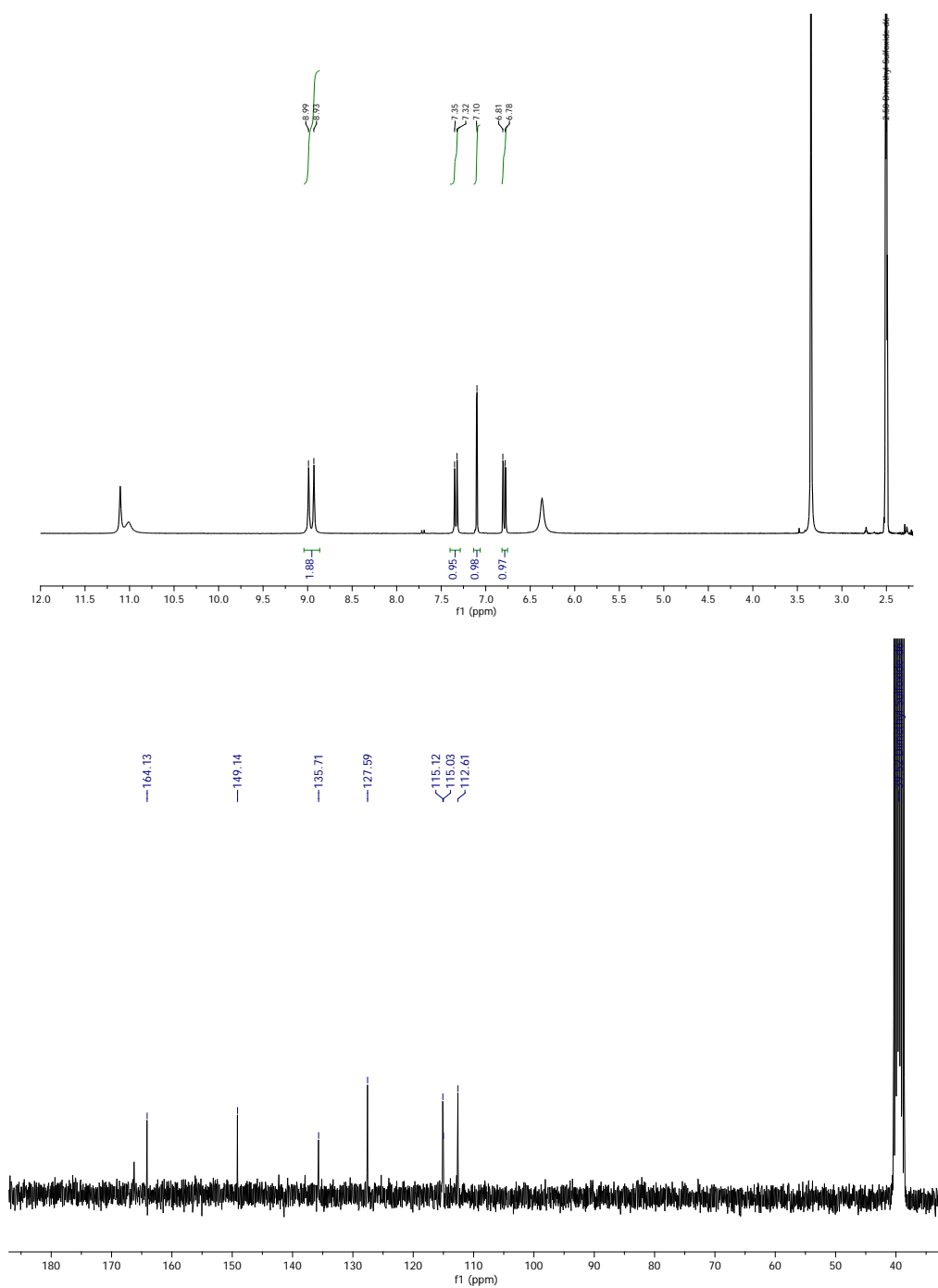


Figure S4. ¹H-NMR spectrum of compound *p*-H₄bdha-OH in DMSO-*d*₆ (top) and ¹³C-NMR spectrum of compound *p*-H₄bdha-OH in DMSO-*d*₆ (bottom).

S2.2. Synthesis of cMUV-11

p-H₄bdha (106 mg; 0.54 mmol) and benzoic acid (165 mg, 1.36 mmol) were suspended in 36 mL of dry *N,N*-dimethylformamide (DMF) in a 50 mL Teflon vial. The mixture was sonicated for 5 minutes. Then, titanium (IV) isopropoxide (55 μ L, 0.18 mmol) was added to the suspension. The vial was sealed and heated in a pre-heat oven at 100 °C for 18 hours.

After natural cooling down to room temperature, this results in the formation of octahedral deep red crystals that were isolated by centrifugation and washed with 60 mL of DMF (3x20 mL). The product was next soaked in fresh aliquots of acetone for 6 days. (Yield ca. 45 % based on Ti). Synthetic yield was calculated by using the molecular formula of desolvated material ($[\text{Ti}_8(\textit{p}\text{-H}_2\text{bdha})_8(\textit{p}\text{-bdha})_4]$). To minimize the presence of solvent in the solid, fresh crystals were washed with DMF and exchanged for 6 days with fresh acetone. Next, sample was heated in a vacuum oven for 24 h at 130 °C. Elemental analysis for $[\text{Ti}_8(\textit{p}\text{-H}_2\text{bdha})_8(\textit{p}\text{-bdha})_4] \cdot (\text{H}_2\text{O})_{6.15} \cdot (\text{C}_3\text{H}_7\text{NO})_{2.6}$: Calc. C (41.48), H (3.71), N (12.4); found: C (41.92), H (3.61), N (11.96).

S2.3. Synthesis of cMUV-11-NH₂ & cMUV-11-OCH₃

By using the synthetic conditions optimized for cMUV-11 as starting point, we ran some reactions with *p*-H₄bdha-NH₂ and *p*-H₄bdha-OCH₃ as linkers to produce functionalized cMUV-11-X cages. These experiments also included systematic variations of the modulator with variable number of equivalents of benzoic acid, acetic acid or trifluoroacetic acid, by using DMF or mixtures of DMF and *N*-methyl-2-pyrrolidone (NMP) as solvent. The reaction time was also varied from 18 to 48 h. These experiments, that involved near to 50 reactions, were unsuccessful and did not allow for the formation of functionalized cMUV-11-X crystalline phases.

Hence, we opted for synthesising mixed-linker cMUV-11-NH₂ and -OCH₃ cages by following the same protocol used for cMUV-11 but using binary combinations of *p*-H₄bdha with *p*-H₄bdha-NH₂ or *p*-H₄bdha-OCH₃ at variable molar ratios ranging from 10 to 100%. We used a FLEX SHAKE high-throughput workstation from Chemspeed® for the automated dosing of solids to ensure maximum reproducibility. The vials were sonicated for 15 minutes to completely solubilize both linkers before placing in a pre-heat oven (100 °C) during 18h. After cooling down to room temperature, the deep red octahedral crystals were isolated by centrifugation and washed with DMF. The resultant crystals were soaked in DMF for further solvent exchange. **Table S1** summarizes the details for the synthesis of cMUV-11-X % cages.

Table S1. Summary of the synthetic conditions for mixed-linker cMUV-11-X% cages.

% <i>p</i> -H ₄ bdha-X molar ratio	<i>p</i> -H ₄ bdha (mmol, mg)	<i>p</i> -H ₄ bdha-NH ₂ (mmol, mg)	<i>p</i> -H ₄ bdha- OCH ₃ (mmol, mg)
10	0.05, 95.4	0.49, 11.5	0.49, 12.2
20	0.43, 84.8	0.11, 23.0	0.11, 24.4
30	0.38, 74.0	0.16, 34.0	0.16, 36.6
40	0.324, 63.6	0.22, 42.0	0.22, 49.0
50	0.27, 53.0	0.27, 57.0	0.27, 61.7
60	0.22, 42.0	0.32, 69.0	0.32, 73.3
70	0.16, 32.0	0.38, 80.0	0.38, 86.0
80	0.11, 21.2	0.43, 91.2	0.43, 98.9
90	0.05, 10.6	0.49, 103.0	0.49, 111.3

It should be noted that in case of cMUV-11-NH₂, the samples prepared for higher *p*-H₄bdha-NH₂ loadings (70-90%) were obtained with remarkable low yields (around 10 %). As result, samples cMUV-11-NH₂ 70, 80 and 90% could not be analysed with gas sorption experiments. In case of cMUV-11-OCH₃, *p*-H₄bdha-OCH₃ loadings over 70 % did not produce any solid. The maximum loading compatible with solid formation was 70%. However, the amount of material isolated was quite small and prevented gas adsorption analysis for cMUV-11-OCH₃ 70%. As in the case of cMUV-11, synthetic yields were calculated by using the molecular formula (proposed by ¹H-NMR analysis) of desolvated materials in all cases, by following the same procedure. Results are summarized in the **Table S2**.

¹H-NMR Analysis. Incorporation ratio.

The percentage of functionalization was evaluated by ¹H-NMR analysis. For that, 10 mg of cMUV-11-X % were suspended in 0.5 mL of DMSO-*d*₆. After that, the sample were digested by addition of two drops of D₂SO₄-*d*₂ (96-98 wt. %). The mixture was stirred for 5 minutes at 80 °C. Then, the resulting clear solution was transferred to an NMR tube and ¹H-NMR was recorded. The ¹H-NMR analysis and peak integration was carried out by using the software MestReNova (version 6.0.2-5475). The characteristic aromatic peaks for each linker were selected by using the 'peak by peak' option followed by integration with 'Autodetect Regions' and 'Peaks' as the calculation method, that does not provide a standard deviation for the corresponding integrals. The ratio of *p*-H₄bdha, *p*-H₄bdha-NH₂ and *p*-H₄bdha-OCH₃ incorporated to the material was calculated from the integration value of the aromatic signal for each ligand following the next equation:

$$\% p - \text{H4bdha} = \frac{\frac{\text{Integral of the } p - \text{H4bdha}}{\text{Number of analyte protons of } p - \text{H4bdha}}}{\frac{\text{Integral of the } p - \text{H4bdha}}{\text{Number of analyte protons of } p - \text{H4bdha}} + \frac{\text{Integral of the } p - \text{H4bdha} - \text{X}}{\text{Number of analyte protons of } p - \text{H4bdha} - \text{X}}} \times 100$$

$$\% \text{ of functionalization} = 100 - \% p - \text{H4bdha}$$

An example of the calculation of the incorporation ratio for cMUV-NH₂ 85% is shown below. The percentage of incorporation is summarized in **Table S2**.

$$\% p - \text{H4bdha} = \frac{\frac{0.72}{4}}{\frac{0.72}{4} + \frac{1}{1}} \times 100 = 15\%$$

$$\% \text{ of functionalization} = 100 - 15 = 85\%$$

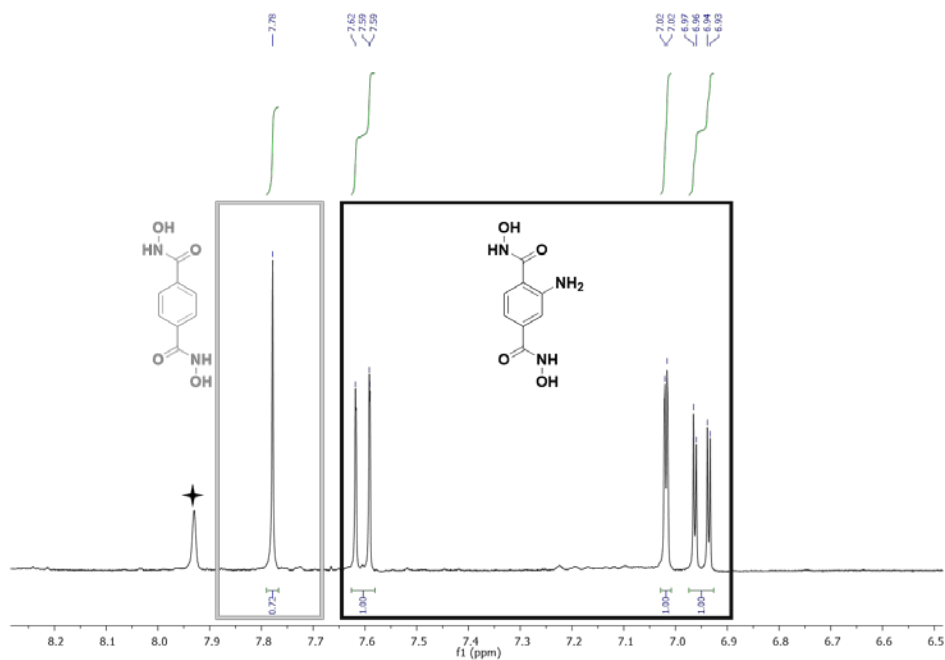
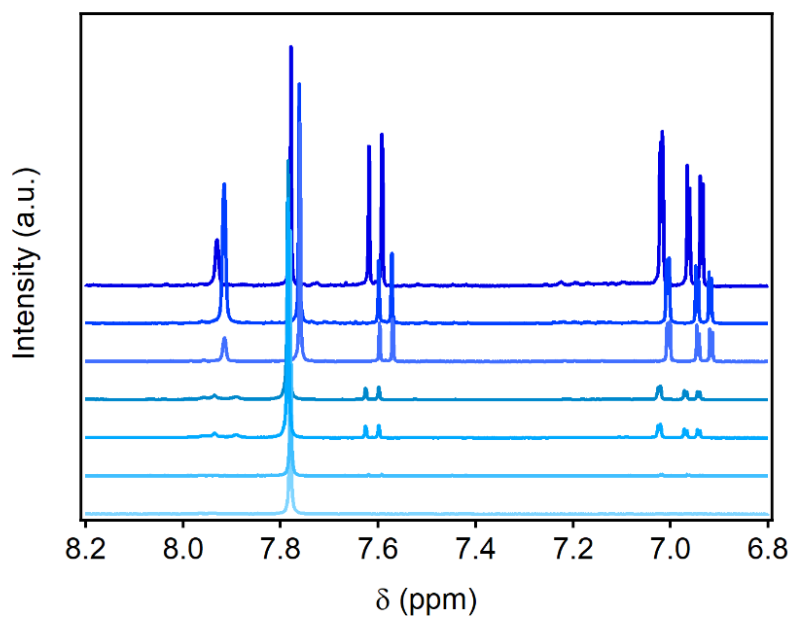


Figure S5. ¹H-NMR of cMUV-NH₂ 85% sample after digestion with D₂SO₄-d₂. The characteristic region of each ligand is framed in grey and black squares. The residual DMF signal is indicated with a black star.

a



b

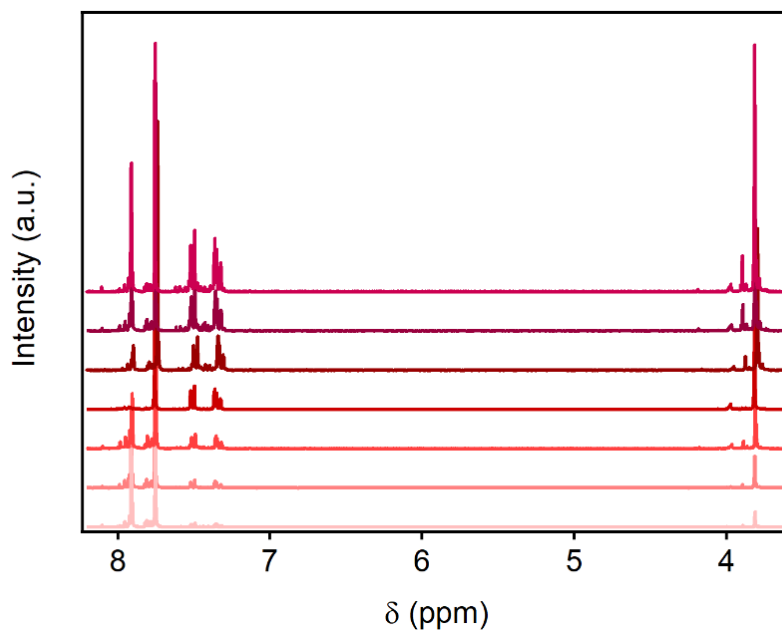


Figure S6. a) ¹H-NMR spectra of digested cMUV-NH₂ % samples. b) ¹H-NMR spectra of digested cMUV-OCH₃ % samples. The slight displacement of the signals is due to the amount of D₂SO₄-d₂ used in the digestion process. The signal at 7.9 ppm corresponds to residual DMF.

Table S2. Summary of the percentage of functionalization (calculated by ¹H-NMR analysis) and yields for cMUV-11-X% cages.

% Functional group added	%-NH₂ incorporated	Yield (%) cMUV-NH₂	% -OCH₃ incorporated	Yield (%) cMUV-OCH₃
10	Negligible	---	11.4	48
20	Negligible	---	21.3	51
30	4.7	45	33.2	53
40	8.1	40	44.1	45
50	28.6	41	53.2	46
60	48.9	33	60.7	42
70	59.0	27	69.3	37
80	70.4	12	No solid formed	---
90	84.6	8	No solid formed	---

S3. cMUV-11 structures. Single-Crystal X-ray Diffraction Analyses

X-ray diffraction data on a single crystal were collected on a Bruker D8 Advance diffractometer with Photon III using CuK α radiation ($\lambda = 1.54184 \text{ \AA}$) at 100(1)K by using APEX3⁴ software. Images were converted to Esperanto format in order to use CrysAlisPro⁵ for data reduction, scaling and absorption correction for cMUV-11 and cMUV-11-NH₂. In the case of cMUV-11-OCH₃, we used APEX3, SAINT-Plus and SADABS⁴. The structure was solved applying the dual-space algorithm implemented in SHELXT program⁶. Fourier recycling and least-squares refinement were used for the model completion with SHELXL-2018⁶. All non-hydrogen atoms have been refined anisotropically, and all hydrogen atoms have been placed in geometrically suitable positions and refined riding with isotropic thermal parameter related to the equivalent isotropic thermal parameter of the parent atom. The geometrical analysis of interactions in the structure was performed with the Olex2 program⁷. The hydrogen atoms were geometrically positioned with C-H = 0.93 \AA and Uiso(H) = 1.2 Ueq(C). Crystal data, collection procedures and refinement results are summarized in **Table S3**. In both cases, the organic linker presents a certain degree of disorder respect to the -NH₂ and -OCH₃ groups linked to the benzene ring. Also, as usual for this type of compounds, the structure contains a large amount of disordered solvent (DMF molecules) in the voids that was impossible to model correctly. Thus, the squeeze procedure was applied at the end of the refinement process in all cases. Crystallographic data for the structures reported in this contribution have been deposited with the Cambridge Crystallographic Data Centre and as supplementary publication files. Copies of the data can be obtained free of charge on application to the CCDC, Cambridge, U.K. (<http://www.ccdc.cam.ac.uk/>) or available as supplementary files.

Table S3. Crystallographic data of cMUV-11 derivatives.

Compound	cMUV-11	cMUV-11-NH ₂	cMUV-11-OCH ₃
Identification code	CCDC2106823	CCDC2106824	CCDC2106822
Empirical Formula	C _{25.5} H _{39.5} N _{7.5} O _{10.5} Ti	C _{19.5} H _{25.65} N _{6.15} O _{8.5} Ti	C _{23.19} H _{33.63} N _{6.5} O _{10.19} Ti
Formula Weight	667.04	530.11	614.41
<i>T</i> /K	100(1)	100(1)	100(1)
Crystal System	Tetragonal	Tetragonal	Tetragonal
Space Group	<i>I</i> 4/ <i>m</i>	<i>I</i> 4/ <i>m</i>	<i>I</i> 4/ <i>m</i>
<i>a</i> /Å	24.0640(4)	24.0023(3)	23.9384(15)
<i>b</i> /Å	24.0640(4)	24.0023(3)	23.9384(15)
<i>c</i> /Å	24.6958(11)	24.7860(14)	24.913(2)
<i>α</i> /°	90	90	90
<i>β</i> /°	90	90	90
<i>γ</i> /°	90	90	90
<i>V</i> /Å ³	14300.7(8)	14279.5(9)	14276(2)
<i>Z</i>	16	16	16
<i>ρ</i> _{calc.} / g cm ⁻³	1.239	0.986	1.143
<i>μ</i> /mm ⁻¹	2.541	2.389	2.491
Crystal size/mm ³	0.10×0.09×0.08	0.11×0.08×0.07	0.10×0.08×0.08
Radiation	Cu K α	Cu K α	Cu K α
<i>2θ</i> range/°	5.128 - 130.174	8.836 - 130.062	5.12 - 118.898
Reflections collected	37676	32576	21207
Independent reflections	6239	6185	4861
Refl's with <i>I</i> > 2(<i>I</i>)	4518	3808	2728
Parameters/ restraints	200/0	218/0	238/8
Largest Peak / hole e ⁻ Å ³	1.23/ -0.46	1.21/ -0.36	0.47/-0.28
Goodness-of-fit on <i>F</i> ²	1.101	1.002	1.039
Final R indexes [<i>I</i> ≥ 2σ (<i>I</i>)]	wR ₂ =0.2635;R ₁ =0.0927	wR ₂ =0.2472;R ₁ =0.0850	wR ₂ =0.2215;R ₁ =0.0800
Final R indexes [all data]	wR ₂ =0.2839;R ₁ =0.1061	wR ₂ =0.2715;R ₁ =0.1051	wR ₂ =0.2530;R ₁ =0.1174

Table S4. Hydrogen bonds⁸ in cMUV-11-X (X = H, NH₂ and OCH₃) cages.**cMUV-11**

Donor-H...Acceptor	d(D-H) (Å)	d(H-A) (Å)	d(D-A) (Å)	D-H-A (°)
N2-H2...O3i	0.88	1.77	2.621(4)	164
N2-H2...N3 ⁱ	0.88	2.51	3.245(5)	142
C4-H4...O6	0.95	2.47	2.796(5)	100
C12-H12...O4	0.95	2.46	2.789(6)	100

(i) 1/2-x, 3/2-y, 3/2-z

cMUV-11-NH₂

Donor-H...Acceptor	d(D-H) (Å)	d(H-A) (Å)	d(D-A) (Å)	D-H-A (°)
N2-H2...O3i	0.88	1.76	2.607(4)	161
N1-H2...N4	0.88	2.11	2.753(15)	129
N2-H2...N3i	0.88	2.49	3.228(5)	142
C3-H3A...O2	0.95	2.44	2.768(5)	100
C12-H12...O4	0.95	2.47	2.798(6)	100

(i) 3/2-x, 3/2-y, 1/2-z

cMUV-11-OCH₃

Donor-H...Acceptor	d(D-H) (Å)	d(H-A) (Å)	d(D-A) (Å)	D-H-A (°)
N2-H2...O6	0.88	1.77	2.600(6)	156
N1-H1...O8	0.88	2.14	2.739(15)	125
C4-H4...O3	0.95	2.44	2.765(7)	100
C12-H12...O5	0.95	2.46	2.787(9)	100

(i) 1/2-x, 1/2-y, 1/2-z

Table S5. Porosity of pristine and functionalized cMUV-11 cages as estimated from Olex2 CalcVoid/CalcSolv analysis with a 0.2 Å resolution.

	Radius largest spherical void [Å]	Structure volume		Cell vol. [Å ³]	Penetration sphere radius [Å]			Solvent accessible	
		Vol. [Å ³]	[%]		a	b	c	Vol. [Å ³]	[%]
cMUV-11	7.0	3586.4	25.1	14300.7	3.6	3.6	3.6	10126.4	70.8
cMUV-11-NH ₂	7.2	3867.6	27.1	14279.5	3.2	3.2	3.8	9720.6	68.1
cMUV-11-OCH ₃	7.2	4107.7	28.8	14276.3	2.6	2.6	3.8	9478.8	66.4

CalcVoid run using `-p -r=0.1` & CalcSolv solvent_radius of 1.80 Å & shrink truncation_radius of 1.80 Å. Van der Waals radii: C, 1.77; H, 1.20; O, 1.52; and Ti, 2.00 Å.

S4. Chemical characterization

S4.1. cMUV-11

Scanning Electron Microscopy (SEM)

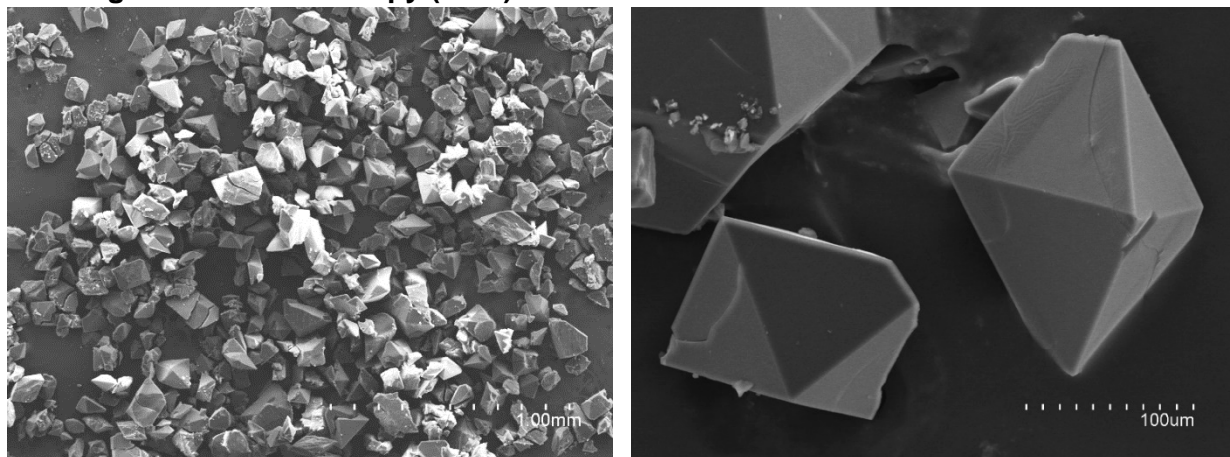


Figure S7. Scanning Electron Microscopy (SEM) images of crystal of cMUV-11. Lower magnification confirms the formation the homogeneity of the sample. Higher magnification shows the particle size is between 50-100 μm .

Thermogravimetric Analysis (TGA)

cMUV-11 shows a first weight loss centred at 210 $^{\circ}\text{C}$ due the early decomposition of the *p*-H₄bdha units. This agrees well with the profile for the thermal decomposition of the free linker (grey line). This decomposition profile is quite similar to the extended framework MUV-11 based on the same connector.² The total decomposition of the MOP takes place above 400 $^{\circ}\text{C}$ to form 21.10 % of TiO₂ (Calc.: 23.62%).

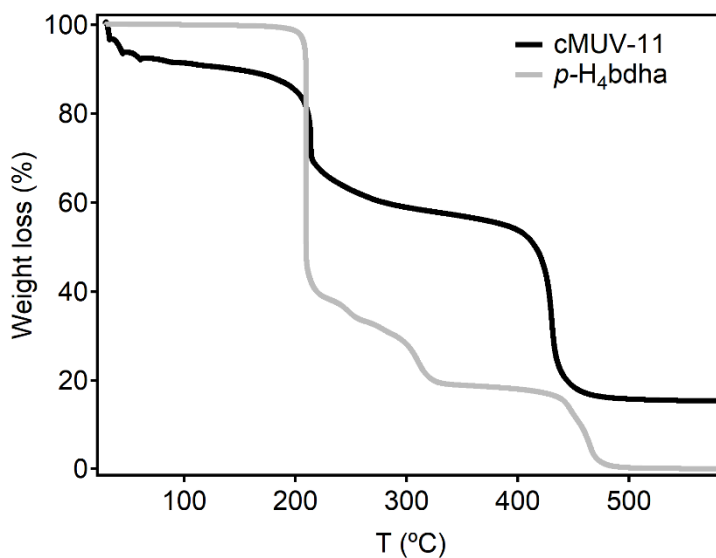


Figure S8. Thermogravimetric analysis of cMUV-11 (black line) and the organic ligand *p*-H₄bdha (grey line).

Powder X-Ray Diffraction (PXRD)

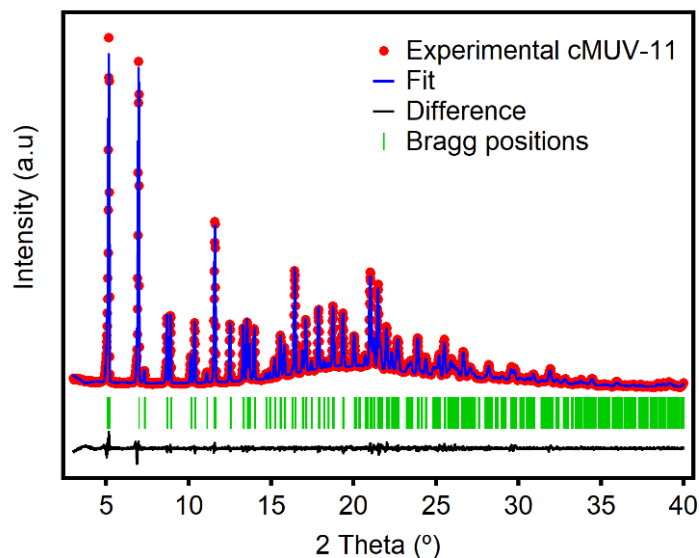


Figure S9. Experimental (red dots), calculated (blue line), difference plot $[(I_{\text{obs}} - I_{\text{calc}})]$ (black line) and Bragg positions (green ticks) for the refinement of the experimental diffraction data of cMUV-11 soaked in DMF collected at room temperature by using the Le Bail method using the single-crystal structural model as starting parameters. Tetragonal, $I 4/m$ (87); $a = b = 24.1052$ $c = 25.3229$ Å; $\alpha = \beta = \gamma = 90^\circ$; $V = 14714$ Å³; $R_e = 2.45$ %, $R_p = 2.99$ %, $R_{wp} = 4.22$ %, $\text{GoF} = 1.72$.

S4.2. Solubility test of cMUV-11

We run a systematic study of the solubility of the as-made crystals in simple and binary combinations of solvents that cover a broad range of polarities and account for the most representative conditions reported for solubilizing MOPs:

Table S6. Representative solvents or mixtures of solvents used for solubilizing MOPs extracted from the literature. In a typical experiment, 2 mg of freshly made crystals of cMUV-11 were dispersed in 5 mL of the corresponding solvent and heated at 60° C for 24 hours in a 10 mL capped vial.

Solvent	Reference	Polarity	Solubility of cMUV-11
Water	9	1	Not soluble
Methanol	9	0.762	Partial solubility(<<0.2 mg·mL ⁻¹)
Dimethylsulfoxide (DMSO)	9	0.444	Partial solubility (0.2 mg·mL ⁻¹)
Dimethylacetamida (DMA)	9,10	0.398	Partial solubility (0.2 mg·mL ⁻¹)
Dimethylformamide (DMF)	9	0.386	Partial solubility (<0.2 mg·mL ⁻¹)
DMF/water (3:1 v/v%)	11	---	Partial solubility
Acetonitrile	9	0.355	Not soluble
Acetone	9	0.355	Not soluble
Tetrahydrofuran (THF)	12	0.207	Not soluble

Dispersion in CH₃OH, DMSO, DMF, DMF/water (3:1), DEF or DMA resulted in the formation of orange/yellowish solutions of variable colour intensity that coexisted with the presence of crystals in suspension. We initially ascribed this to the partial solubilization of the cage in these conditions. For further probe, we attempted to solubilize cMUV-11 in the same conditions by using DMSO-d₆ for analysis of the solution with ¹H-NMR after filtering the suspension. Comparison of the spectra of the free linker and cMUV-11 suggests that the cage is present in solution based on the shift of the aromatic proton signal of the linker from 7.80 to 7.90 ppm likely due to the effect of Ti(IV) coordination. We decided to confirm this point further by MALDI TOF MS of the supernatants. It is worth noting that we could not use to milder ionization conditions as ESI because the quadrupole detector is limited to 1500-2000 m/z and would not be compatible with the m/z ratio of the unfragmented cage. As shown in **Figure S10, bottom**, none of the spectra collected are consistent with the presence of the signals that would correspond to a clean ionization of the [cage]ⁿ⁺ (n=1-8) at m/z values of 2704.9, 1352.4, 901.6, 676.2, 541.0, 450.8, 386.4 or 338.1, and the complex fragmentation patterns observed suggest instead a partial fragmentation in the conditions of the experiment possibly due to the aggressive ionization conditions.

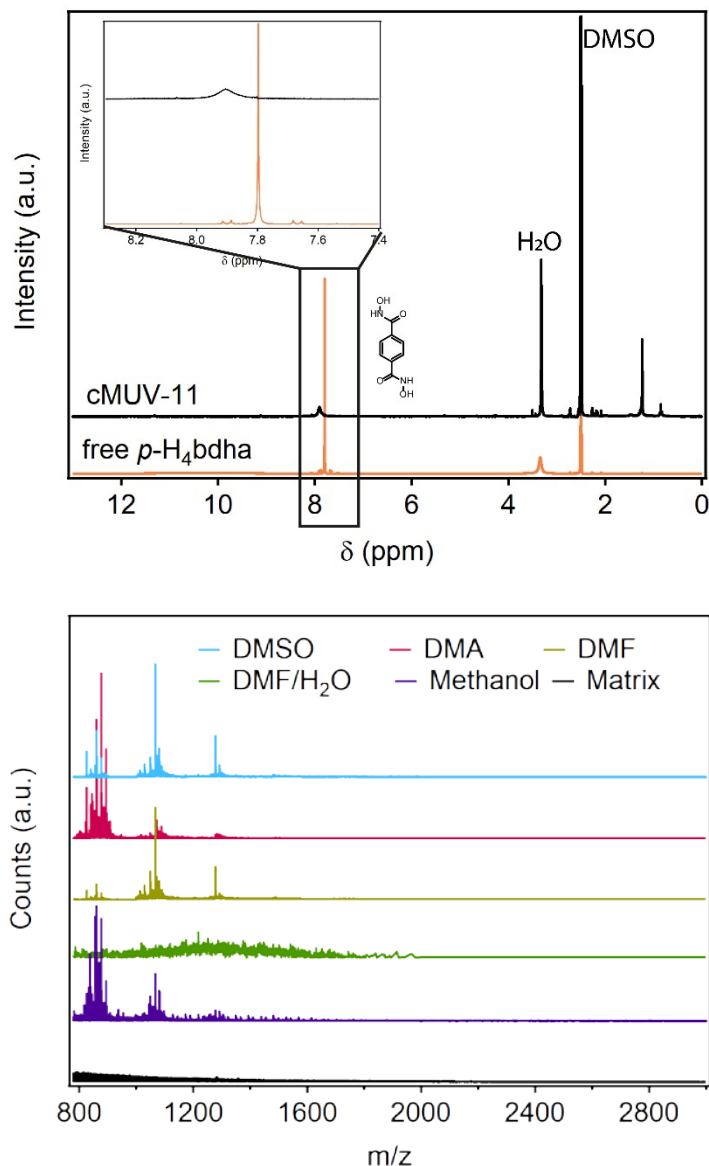


Figure S10. *Top*) $^1\text{H-NMR}$ spectra of the free linker and cMUV-11 in DMSO-d_6 . Residual solvent peak of DMSO-d_6 at 2.50 ppm and of D_2O at 3.33 ppm. *Bottom*) MALDI TOF TOF-MS spectra the orange/yellowish supernatants that result from partial solubilization of cMUV-11 crystals in the different solvents explored.

We have also tested the solubility of the cage in deuterated methanol (CD_3OD) in the same conditions. The $^1\text{H-NMR}$ of the supernatant suggests the presence of intact cages based on the same shift of the aromatic proton compared to the free linker (**Figure S11, top**). The addition of tetrabutylammonium hydroxide (TBA(OH)), for facilitating the deprotonation of the single deprotonated chelates, resulted in the complete dissolution of the crystals for a transparent yellow solution. The NMR spectrum displays two signals that suggest the presence of the cage but also its possible degradation in these conditions. We also collected MALDI TOF TOF-MS spectra for both solutions. As described above, this ionization technique appears to be too aggressive and

results in complex fragmentation patterns that cannot be assigned to cMUV-11 in any of its possible charge states.

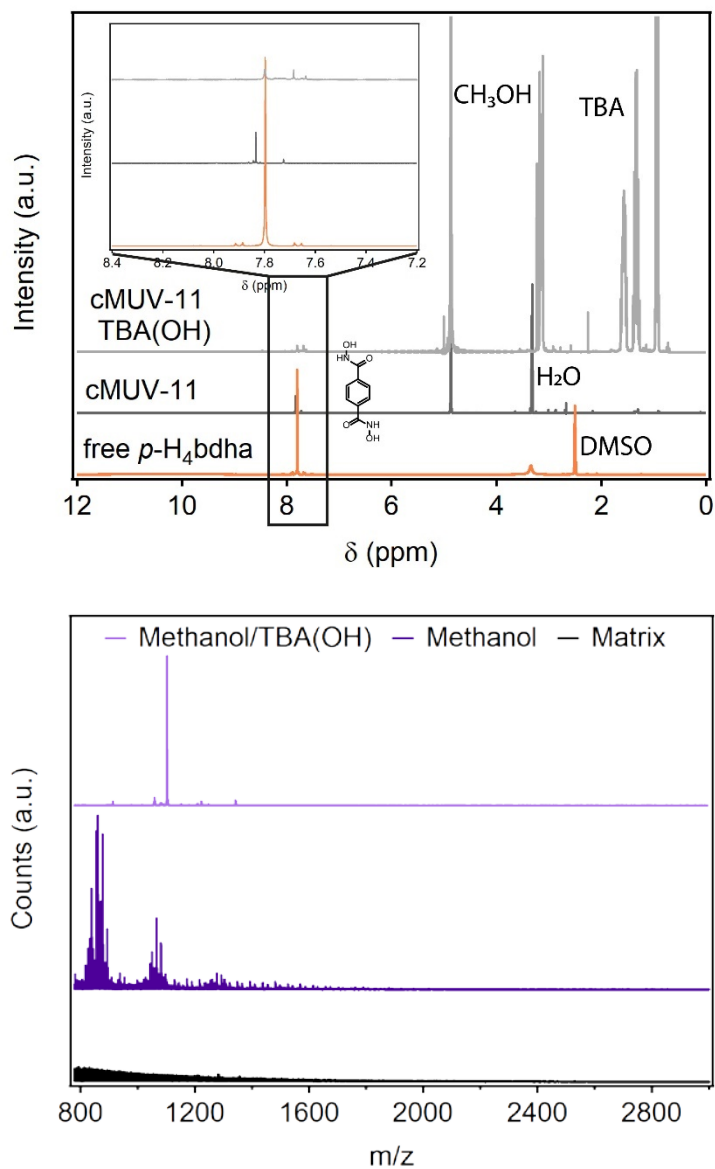


Figure S11. *Top*) ¹H-NMR spectra of the linker (DMSO-d₆), cMUV-11 dissolved in CD₃OD-d₄ and in a mixture of CD₃OD-d₄/TBA(OH) (9:1). Residual solvent peaks of DMSO-d₆ (2.50), CD₃OD-d₄ (4.87) and D₂O (3.33 ppm). *Bottom*) MALDI TOF TOF-MS spectra of the orange/yellowish supernatants that result from partial solubilization of cMUV-11 crystals in different solvents. b) of resultant methanol and methanol/TBA(OH) supernatants.

S4.3. cMUV-11-NH₂ & cMUV-11-OCH₃

Scanning Electron Microscopy (SEM)

cMUV-11-NH₂ 50% and cMUV-11-OCH₃ 50% were selected to confirm the purity of the mixed-linker cages. The appearance of the samples (morphology and crystal size) is not modified either by the functional group or the percentage of loading.

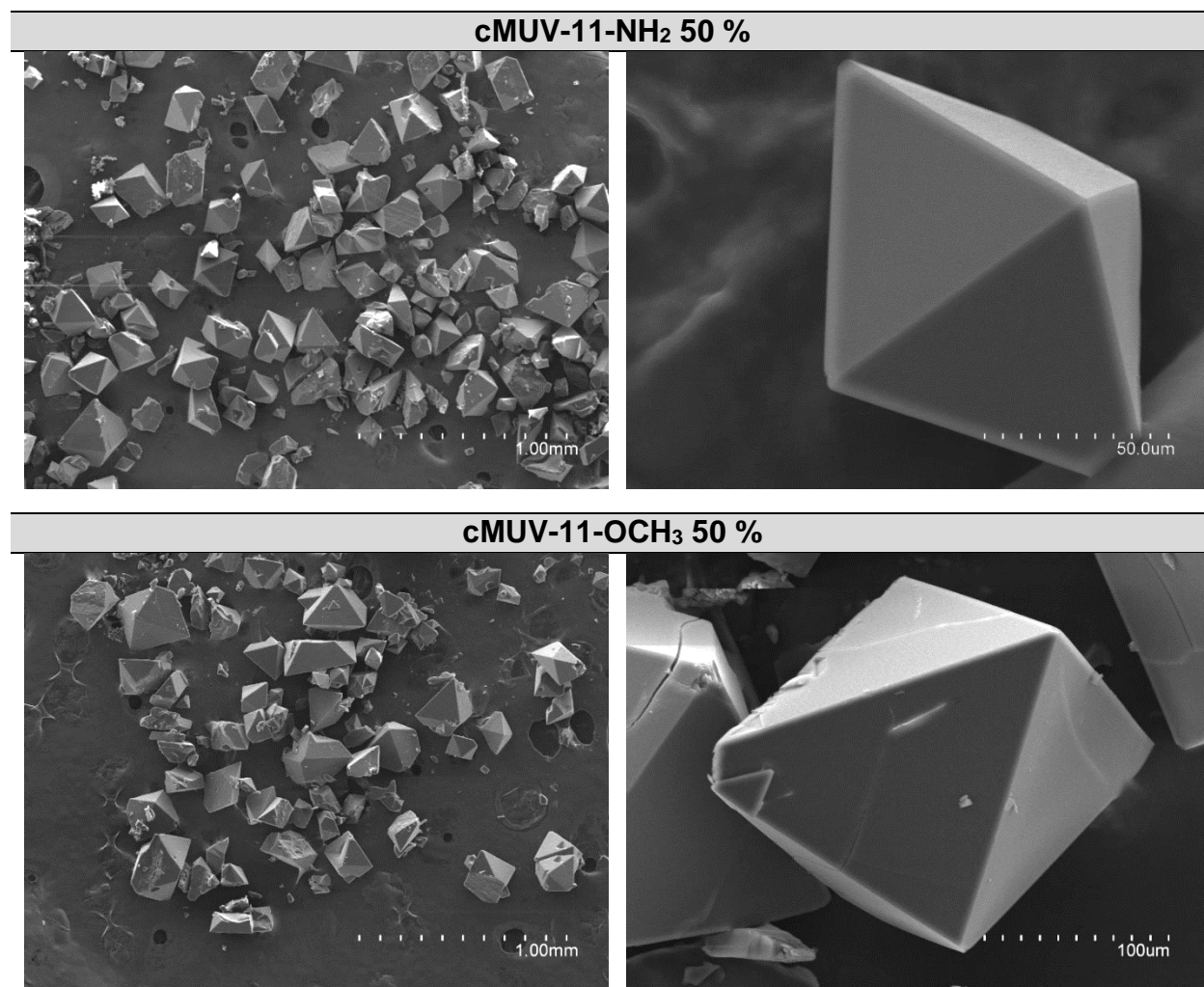


Figure S12. Scanning Electron Microscopy (SEM) images of crystal of cMUV-11-NH₂ (up) and cMUV-11-OCH₃ (down). Lower magnification confirms the formation the homogeneity of the samples. Higher magnification shows the particle size is around 50-100 μm .

Thermogravimetric Analysis (TGA)

The thermal decomposition profiles of the functionalized cages agree well with cMUV-11 and only display a minimum shift in the thermal stability to higher temperatures.

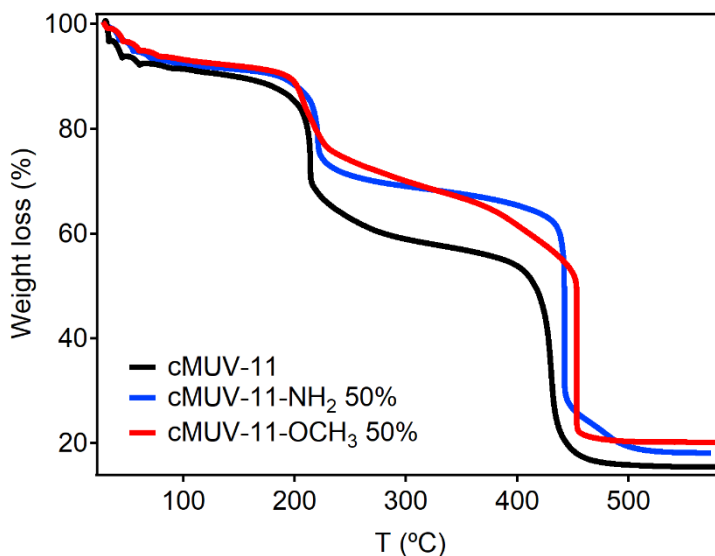


Figure S13. Thermogravimetric analysis of cMUV-11 (black line), cMUV-11-NH₂ 50% (blue line) and cMUV-11-OCH₃ 50% (red line).

Elemental analysis (EA)

cMUV-11-NH₂ 50%: [Ti₈(*p*-H₂bdha)₄(*p*-H₂bdha-NH₂)₄(*p*-bdha)₂(*p*-bdha-NH₂)₂](H₂O)₄·(C₃H₇NO)₄:
Calc. C (39.46), H (3.25), N (14.49); found: C (40.00), H (3.99), N (14.22).

cMUV-11-OCH₃ 50%: [Ti₈(*p*-H₂bdha)₄(*p*-H₂bdha-OCH₃)₄(*p*-bdha)₂(*p*-bdha-OCH₃)₂](H₂O)_{3.75}:
Calc. C (41.19), H (3.57), N (11.19); found: C (41.58), H (3.69), N (10.80).

Powder X-Ray Diffraction (PXRD)

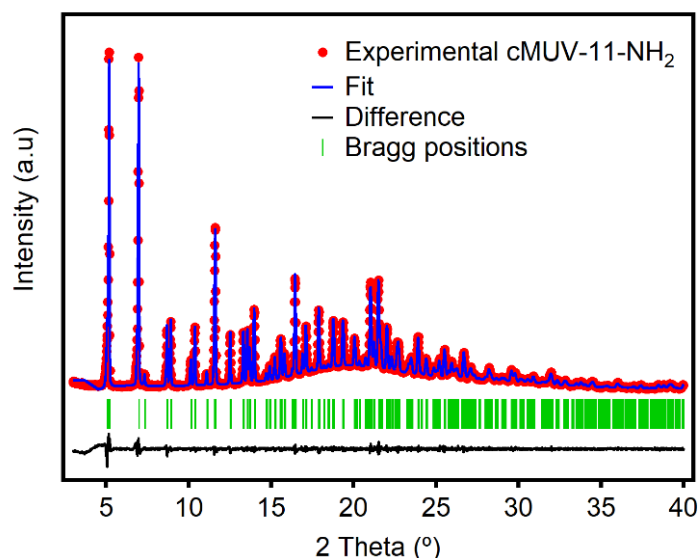


Figure S14. Experimental (red dots), calculated (blue line), difference plot [(l_{obs}-l_{calc})] (black line) and Bragg positions (green ticks) for the refinement of experimental diffraction data of cMUV-11-NH₂ 50% soaked in DMF collected at room temperature by using the Le Bail method using the single-crystal structural model as starting parameters. Tetragonal, I 4/m (87); a = b = 24.081 c = 25.323 Å; α = β = γ = 90°; V = 14684 Å³; Re = 2.43 %, Rp = 3.07 %, Rwp = 4.88 %, GoF = 2.00.

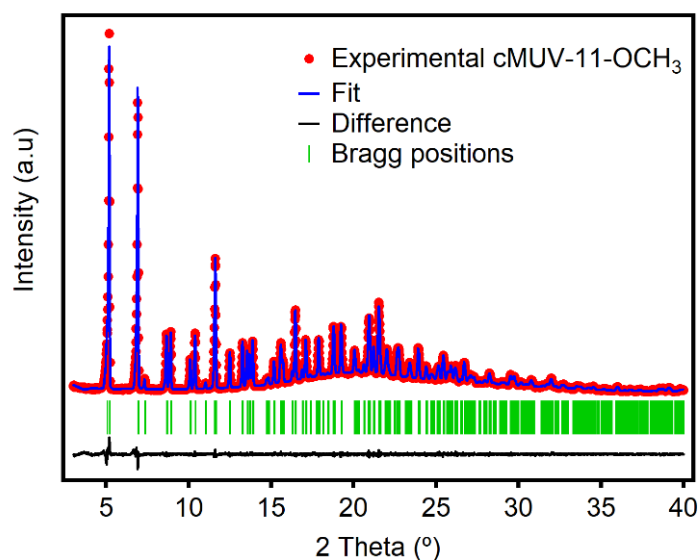


Figure S15. Experimental (red dots), calculated (blue line), difference plot [(l_{obs}-l_{calc})] (black line) and Bragg positions (green ticks) for the refinement of experimental diffraction data of cMUV-11-OCH₃ 50% soaked in DMF collected at room temperature by the LeBail method using the single-crystal structural model as starting parameters. Tetragonal, I 4/m (87); a = b = 24.0544 c = 25.5037 Å; α = β = γ = 90°; V = 14756 Å³; Re = 2.52 %, Rp = 2.57 %, Rwp = 3.55 %, GoF = 1.41.

S5. Activation of cMUV-11 cages and N₂ adsorption

N₂ isotherms

cMUV-11

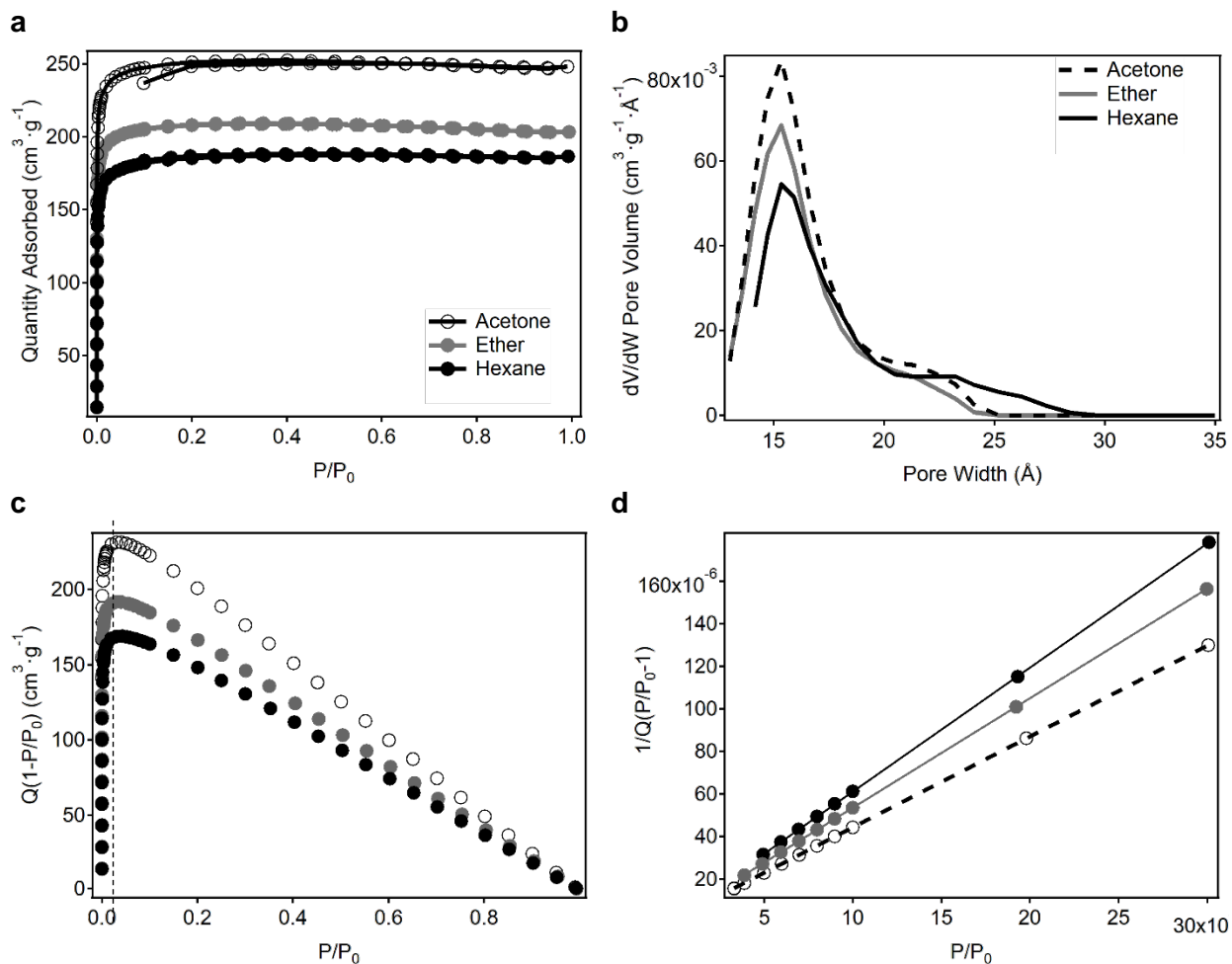


Figure S16. a) N₂ adsorption/desorption isotherms at 77 K. b) Pore size distribution calculated assuming a cylindrical pore model (N₂@77-Carb Cyl Pores, MWNT, NLDFT) of cMUV-11 samples exchanged with different solvents. c) Rouquerol BET, the dashed line represents the limit of the applicability of the BET theory and d) Multi-Point BET analysis.

Table S7. Summary of the adsorption parameters for different solvent exchange for cMUV-11.

Solvent	BET surface area (m ² ·g ⁻¹)	V _p total at P/P ₀ = 0.95 (cm ³ ·g ⁻¹)
Acetone	1020	0.38
Ether	844	0.32
Hexane	747	0.29

Table S8. Summary of the main parameters calculated from the multi-point BET analysis of cMUV-11 exchanged samples.

Solvent	Slope (g·cm ⁻³)	Intercept (g·cm ⁻³)	Range P/P ₀	R ²	C	V _m (cm ³ ·g ⁻¹)	1/(√C+1)	P/P ₀ at V _m
Acetone	0.004266 ± 0.000002	0.000002 ± 0.000000	0.0037-0.037	0.99999	2584.9644	234.3233	0.0193	0.0191
	0.000002							
Ether	0.005153 ± 0.000004	0.000002 ± 0.000000	0.0037-0.037	0.99999	2655.8207	193.9797	0.0190	0.0168
	0.000004							
Hexane	0.005825 ± 0.000004	0.000003 ± 0.000000	0.0037-0.037	0.99999	2013.1356	171.5913	0.0218	0.0203
	0.000004							

cMUV-11-NH₂

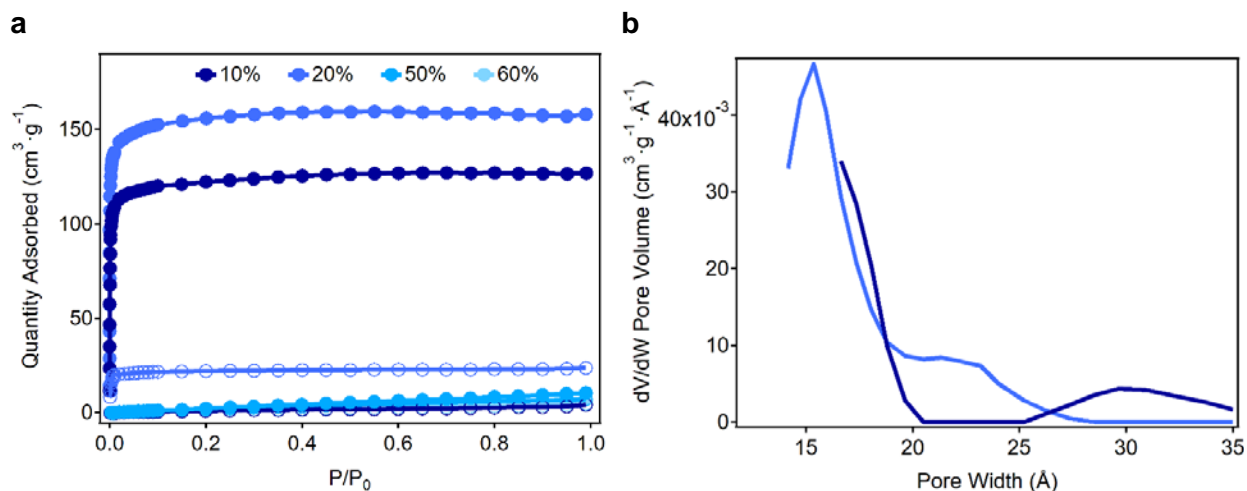


Figure S17. a) N₂ adsorption/desorption isotherm at 77 K and b) Pore size distribution calculated assuming a cylindrical pore model (N₂@77-Carb Cyl Pores, MWNT, NLDFT) of cMUV-11-NH₂ % (X = 10, 20, 50 & 60%) exchanged with acetone (empty symbols) or hexane (filled symbols).

Table S9. Summary of the adsorption parameters for different solvent exchange for cMUV-11-NH₂ samples.

% NH ₂ group	Solvent	BET surface area (m ² ·g ⁻¹)	V _p total at P/P ₀ = 0.95 (cm ³ ·g ⁻¹)
10	Acetone	---	---
10	Hexane	493	0.20
20	Acetone	98	0.04
20	Hexane	620	0.24
50	Acetone	84	0.03
50	Hexane	---	---
60	Acetone	---	---
60	Hexane	---	---

cMUV-11-OCH₃

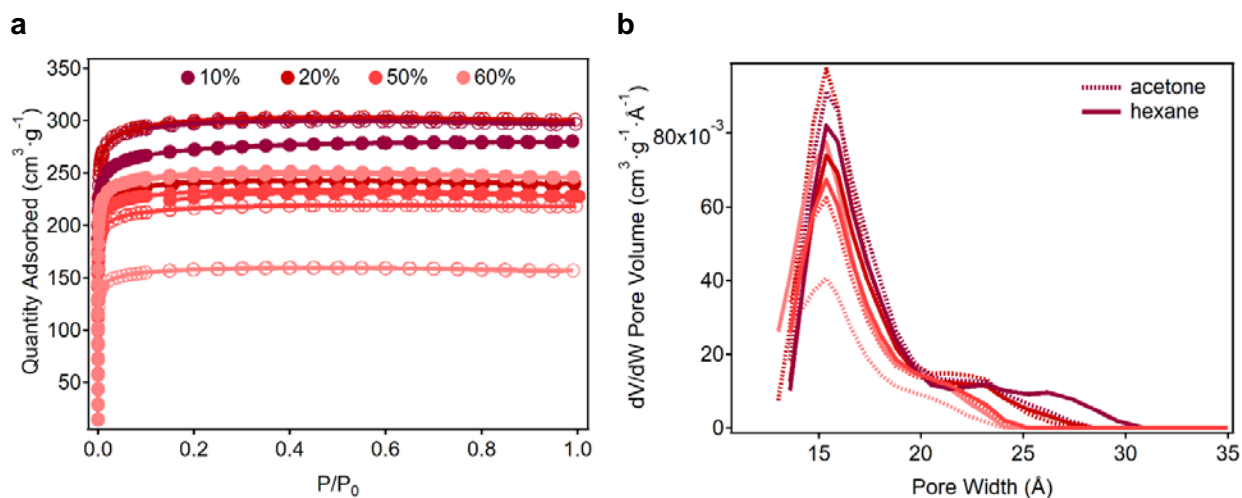


Figure S18. a) N₂ adsorption/desorption isotherm at 77 K of and b) Pore size distribution calculated assuming a cylindrical pore model (N₂@77-Karb Cyl Pores, MWNT, NLDFT) of cMUV-11-OCH₃ % (X = 10, 20, 50 & 60%) exchanged with acetone (empty symbols) or hexane (filled symbols). b) The pore size distribution for exchanged cages is also centred at 15 Å. The dotted-line represents acetone exchange and solid-line hexane exchange.

Table S10. Summary of the adsorption parameters for different solvent exchange for cMUV-11-OCH₃ samples.

% OCH ₃ group	Solvent	BET surface area (m ² ·g ⁻¹)	V _p total at P/P ₀ = 0.95 (cm ³ ·g ⁻¹)
10	Acetone	1206	0.46
10	Hexane	1098	0.43
20	Acetone	1215	0.47
20	Hexane	977	0.37
50	Acetone	875	0.34
50	Hexane	888	0.33
60	Acetone	636	0.24
60	Hexane	1009	0.38

Table S11. Comparison of experimental and theoretical textural properties of the cMUV-11-X family. 50% functionalization is selected as representative of the series.

Sample	SA _{BET} [m ² ·g ⁻¹]		Pore volume [cm ³ ·g ⁻¹]	
	exp ^a	theor	exp ^b	Theor
cMUV-11	1020	3350	0.38	0.96
cMUV-11-NH ₂ -50%	84	3095	0.03	0.83
cMUV-11-OCH ₃ -50%	888	2535	0.33	0.72

^aSpecific surface area (SA) was calculated by multi-point Brunauer-Emmett-Teller (BET) method. ^bTotal pore volume at P/P₀=0.96.

The theoretical accessible surface areas and probe-occupiable volumes of the cage variants (-H, -NH₂, -OCH₃) from their crystallographic structures were calculated by using the software package Zeo++ with a probe size representative of the kinetic diameter of N₂ (chan_radiou=probe_radiou=1.82 and num_samples=100000).¹³ The experimental values are significantly below the theoretical expectations confirming the structural sensitivity of cMUV-11 to solvent evacuation and the importance of retaining the crystalline arrangement for optimum porosity values. This is particularly important for cMUV-11-NH₂, for which the incorporation of polar -NH₂ groups induces more drastic structural changes upon solvent removal. This is consistent with the discussion in the main text and the postulated role of -X cage functions in affecting the structural response of the cage packing to solvent evacuation.

S6. Chemical and Structural Stability

ICP-MS measurements

The hydrolytic stability of the solids was evaluated by incubation in water at different pHs for 24 hours ($10 \text{ mg}\cdot\text{mL}^{-1}$ concentration).

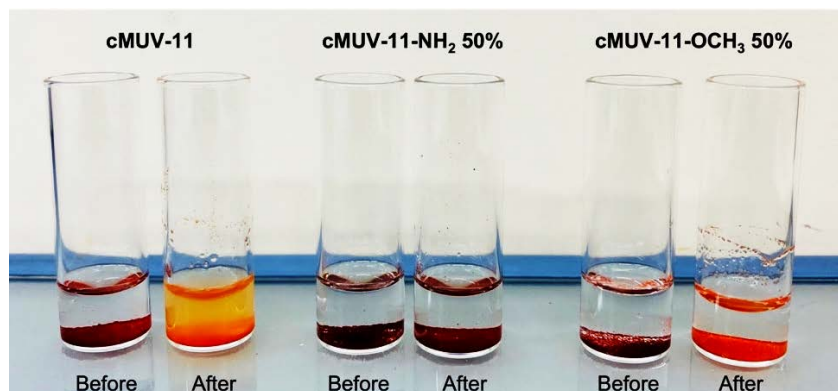


Figure S19. Picture of samples before and after chemical stability test.

Table S12. Values of titanium concentration (ppm) in solution of different standard Ti-MOFs after soaking in water pH = 7 for 24 hours compared with values reported in this work.

Material	Ti ⁴⁺ in solution (ppm)
cMUV-11	4.04 ± 0.05
cMUV-11-NH ₂ 50%	0.29 ± 0.01
cMUV-11-OCH ₃ 50%	2.02 ± 0.04
MUV-11	0.02 ± 0.04
MIL-125 NH ₂	0.83 ± 0.03
MIL-100 (Ti)	0.12 ± 0.01

To complete the hydrolytical stability study, crystals of cMUV-11 variants were incubated in water at pH = 3, 5, 7, 9 and 11 for 24 hours. The resultant supernatants were also analysed by ICP-MS.

As shown in **Figure S20**, the concentration of Ti(IV) in the solutions remains below 8 ppm in all cases. Although the effect of solvent in disrupting the packing of the cages in the solid state has obvious effects in the structure and accessible porosity of these family of materials (**Figure S21 and S22**), our data confirms the value of hydroxamate linkages to enable the formation of robust cages that withstand chemical degradation in a broad range of pH values.

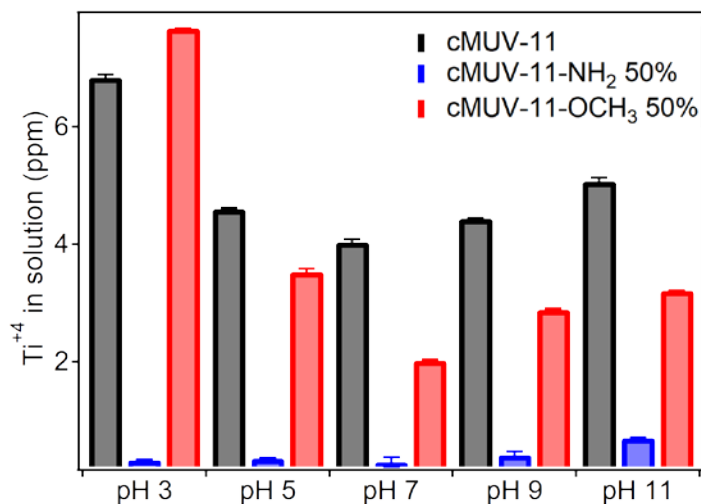


Figure S20. Titanium leaching of cMUV-11 derivatives determined by ICP-MS of the supernatant after incubation in water at variable pH for 24h (black for cMUV-11, blue for -NH₂ and red for -OCH₃).

Powder X-Ray Diffraction (PXRD) after water incubation

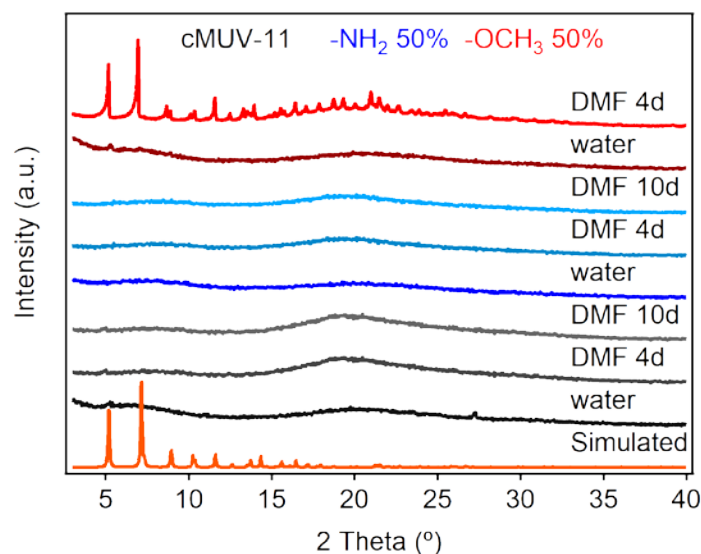


Figure S21. PXRD patterns of cMUV-11 variants (black for -H, blue for -NH₂ and red for -OCH₃) after water incubation for 24 hours and reversibility in DMF for 4 and 10 days.

To investigate the structural stability after water exposure, diffraction measurements of incubated solids were carried out. The PXRD pattern (**Figure S21**) of all cage variations (-H, -NH₂ and -OCH₃) confirm a structural collapse in these conditions. In this regard, we have also investigated the reversibility of this structural collapse in presence of water by soaking the solids in DMF for 4 and 10 days. As shown in **Figure S21**, only cMUV-11-OCH₃ 50% recovered the original structure. We argue reversibility in this case is enabled by the hydrophobicity provided by the OCH₃ groups,

that favours the regeneration of the original structure compared to the irreversibility displayed by -H and -NH₂ variants. This is likely correlated to the smaller impact of solvent evacuation in cMUV-11-OCH₃ that permits accessing higher permanent porosities in comparable conditions of activation.

CO₂ adsorption after water incubation

We have also collected CO₂ isotherms at 298 K to investigate the effect of this structural change on the gas uptake. The cages display the relative trends in CO₂ uptake of the as-made crystals but display a significant reduction in their uptake capacity as result of the structural collapse. These changes are likely provoked by the rupture of the three-dimensional network of H-bonds that direct the packing of the cages in the solid state. The presence of water breaks the original connections and induces a random packing that results in amorphous solids with reduced uptake capacities. Overall, our results confirm the chemical stability of these hydroxamate cages, with strong joints that prevent chemical degradation in water, but the sensitivity of their packing to the presence of water. This behaviour agrees with our original findings that anticipated an important sensitivity of the structure/porosity of the solids to solvent evacuation in presence of polar solvents

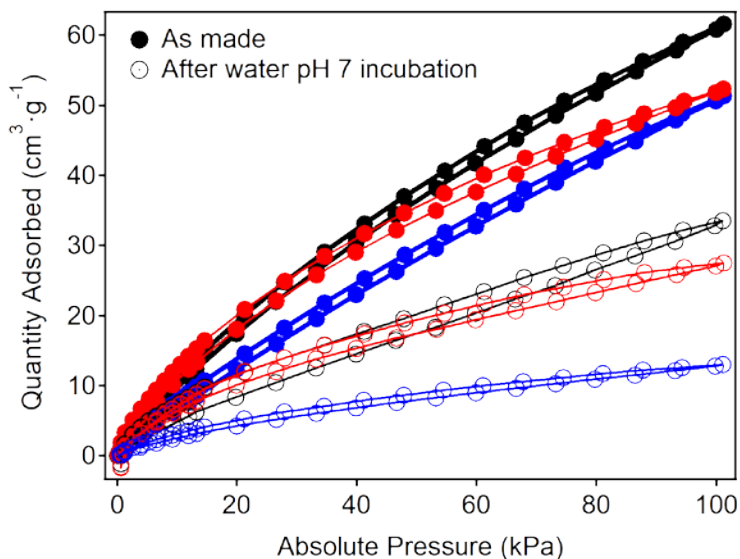


Figure S22. CO₂ adsorption/desorption isotherms of cMUV-11 (black), cMUV-11-NH₂ (blue) and cMUV-11-OCH₃ (red) cages after incubation in water (empty symbols) compared to as made crystals (filled symbols).

Scanning Electron Microscopy (SEM) after water incubation

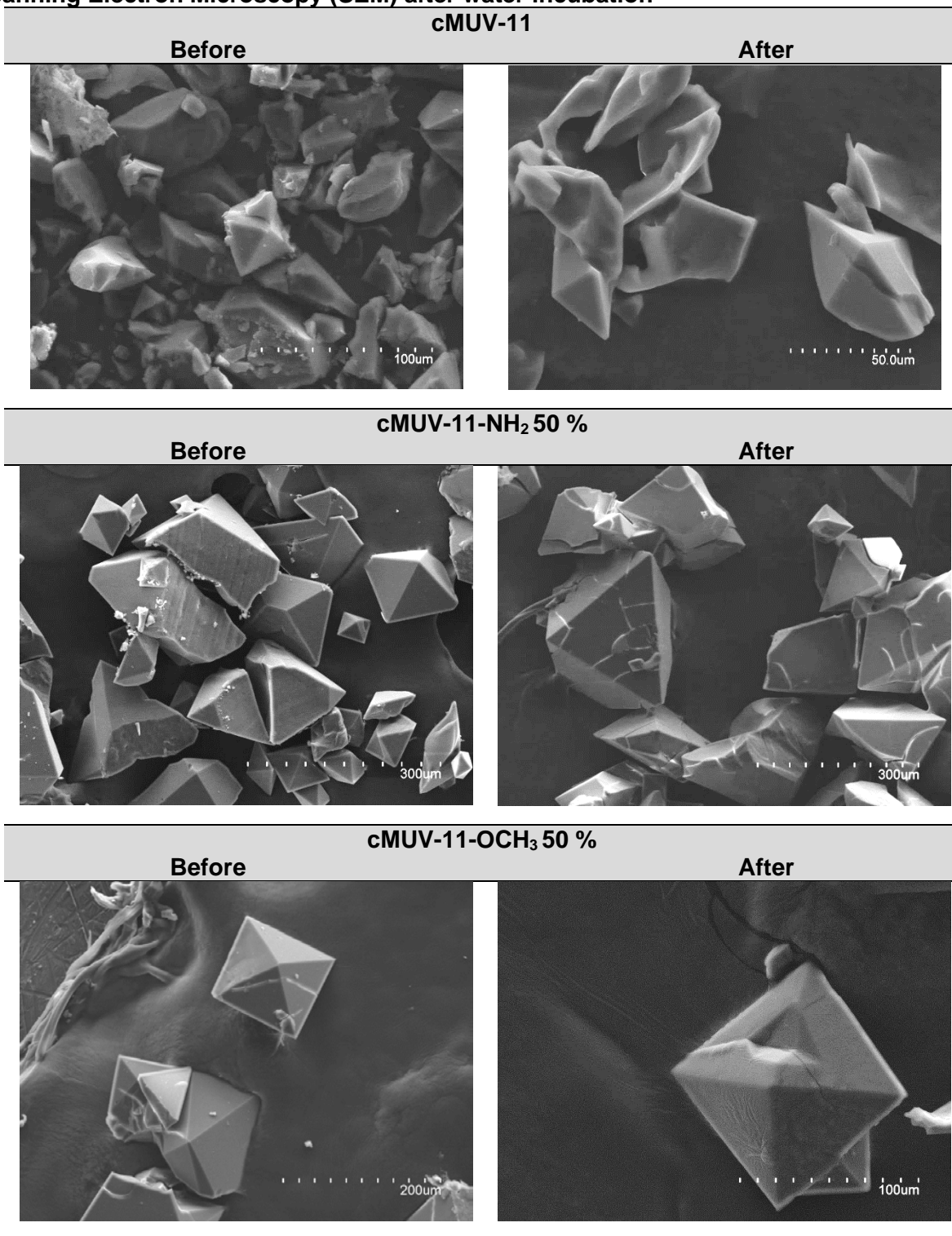


Figure S23. Scanning Electron Microscopy (SEM) images of crystals after water treatment discard significant damage during the process. For a direct comparison, images were taken from the same crystals before and after the treatment.

S7. Computational calculations

All electronic and structural calculations for each structure were calculated using DFT with VASP code^{14,15} employing the screened hybrid functional HSE06^{16,17} and complemented by the Tkatchenko-Scheffer dispersion method^{18,19,20}. The recommended GW PAW pseudopotentials²¹ were used. The kinetic energy cut-off for the plane-wave basis set expansion was chosen as 500 eV, and Γ -points were used for integrations in the reciprocal space, due to the large size of the unit cell of the direct lattice.

Hirshfeld charges for the hydroxamate group with the different substituents generated in a calculation shown in the **Figure S24**. In the interactive Hirshfeld-I method (HI),²² the population of each atom is calculated by assuming that the charge density at each point is shared among the surrounding atoms in direct proportion to their free atom densities at the corresponding distances from the nuclei.

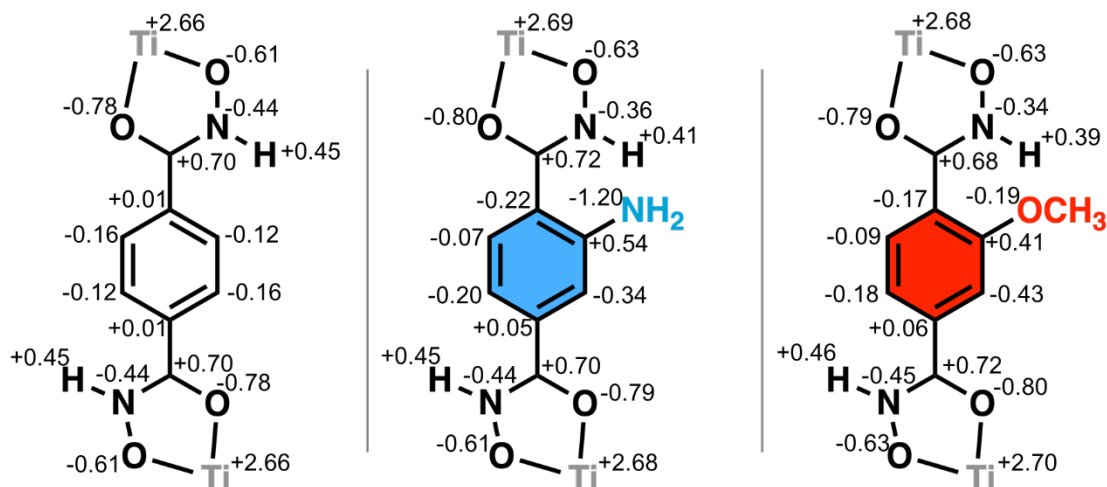


Figure S24. Hirshfeld charges for the hydroxamate group with different substituents ($|\bar{e}|$).

References

- [1] Griffith D.; Krot K.; Comiskey J.; Nolan K. B.; Marmion C. J. *Dalton Trans.*, **2008**, 137–147.
- [2] M. Padial, N.; Castells-Gil, J.; Almora-Barrios, N.; Romero-Angel, M.; Silva, I. da; Barawi, M.; García-Sánchez, A.; O'Shea, V. A. de la P.; Martí-Gastaldo, C. *J. Am. Chem. Soc.* **2019**, *141* (33), 13124–13133.
- [3] Park H.; Kim S.; Jung B.; Park M.H.; Kim Y.; Kim M. *Inorg. Chem.* **2018**, *57*, 1040–1047
- [4] Bruker. APEX3, SAINT-Plus and SADABS. Bruker AXS Inc., Madison, Wisconsin, USA. **2016**
- [5] Rigaku Oxford Diffraction. CrysAlisPro Software system, version 1.171.41.112, Rigaku Corporation, Oxford, UK. **2018**
- [6] Sheldrick, G.M. *Acta Cryst.* **2015**, *A71*, 3-8.
- [7] Dolomanov O.V.; Bourhis L.J.; Gildea R.J.; Howard J.A.K.; Puschmann H. *J. Appl. Cryst.* **2009**, *42*, 339-341.
- [8] Steiner T. C–H–O Hydrogen Bonding in Crystals. *Cryst. Rev.*, **1996**, *6*, 1-57
- [9] Liu, G.; Yuan, Y. D.; Wang, J.; Cheng, Y.; Peh, S. B.; Wang, Y.; Qian, Y.; Dong, J.; Yuan, D.; Zhao, D. *J. Am. Chem. Soc.* **2018**, *140*, 6231-6234.
- [10] Carné-Sánchez, A.; Albalad, J.; Grancha, T.; Imaz, I.; Juanhuix, J.; Larpent, P.; Furukawa, S.; MasPOCH, D. *J. Am. Chem. Soc.* **2019**, *141*, 4094–4102.
- [11] He, Y.-P.; Yuan, L.-B.; Chen, G.-H.; Lin, Q.-P.; Wang, F.; Zhang, L.; Zhang, J. *J. Am. Chem. Soc.* **2017**, *139*, 16845–16851.
- [12] Taggart, G. A.; Antonio, A. M.; Lorzing, G. R.; Yap, G. P. A.; Bloch, E. D. *ACS Appl. Mater. Inter.* **2020**, *12*, 24913–24919.
- [13] Willems, T. F.; Rycroft, C. H.; Kazi, M.; Meza, J. C.; Haranczyk, M. *Microp. Mesop. Mater.* **2012**, *149*, 134-141.
- [14] Kresse G.; Furthmüller J. Efficiency of Ab-Initio Total Energy Calculations for Metals and Semiconductors Using a Plane-Wave Basis Set. *Comput. Mater. Sci.* **1996**, *6*, 15-50.
- [15] Kresse G.; Furthmüller J. Efficient Iterative Schemes for Ab Initio Total-Energy Calculations Using a Plane-Wave Basis Set. *Phys. Rev. B: Condens. Matter Mater. Phys.* **1996**, *54*, 11169-11186.
- [16] Heyd J.; Scuseria G. E.; Ernzerhof M. *J. Chem. Phys.*, **2003**, *118*, 8207-8215.
- [17] Krukau A. V.; Vydrov O. A.; Izmaylov A. F.; Scuseria G. E. *J. Chem. Phys.*, **2006**, *125*, 224106-1.
- [19] Tkatchenko A.; Scheffler M., *Phys. Rev. Lett.*, **2009**, *102*, 073005.
- [19] Bučko T.; Lebègue S.; Hafner J.; Ángyán J. G. *Phys. Rev.*, **2013**, *B 87*, 064110.

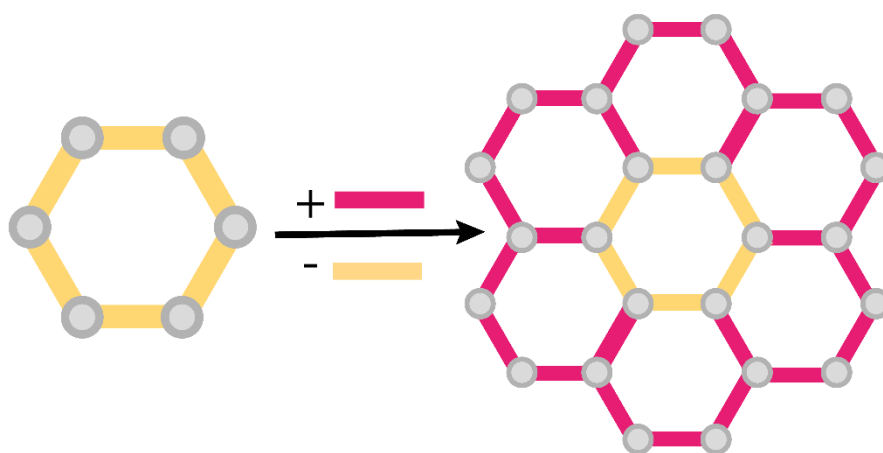
[20] Kerber; Sauer J. *J. Comp. Chem.*, **2008**, 29, 2088.

[21] Lejaeghere K.; Bihlmayer G.; Björkman T.; Blaha P.; Blügel S. Reproducibility in density functional theory calculations of solids. *Science*, **2016**, 351, 1415, aad3000-1.

[22] Bultinck P.; Van Alsenoy C.; Ayers P.W.; Carbó-Dorca R. *J. Chem. Phys.* **2007**, 126, 144111.

Chapter 3:

Effect of Linker Distribution in the Photocatalytic Activity of Multivariate Zr-MOFs



1. Motivation

s-Tetrazines are classic molecules whose first report dates back to the end of the 19th century.¹ It is in the last few decades, when they have become attractive building blocks for the design of functional molecular materials.^{2,3} These molecules can act as visible light antennas, thanks to their deep colour ranging from purple to orange to red because of a weak $n-\pi^*$ transition located in the visible region. Besides, tetrazine derivatives are redox active and can be reversibly reduced due to their electron-deficient character by accepting one electron to give a very stable anion radical. The reduction potential values and the kinetic of the process, as well as the maximum position of the absorption band, can be modulated by chemical substitution (*Figure 3.1*).⁴⁻⁷ As a result, tetrazines are versatile molecular blocks of interest in applications such as light generation⁸, sensors,⁹ solar cells,¹⁰ and electro/photo-active polymers.¹¹ The combination of one-electron reversible reduction behaviour and visible-light sensitization can also be translated to MOFs for generating photoactive frameworks by reticulation of tetrazine derivatives.¹¹⁻¹⁵

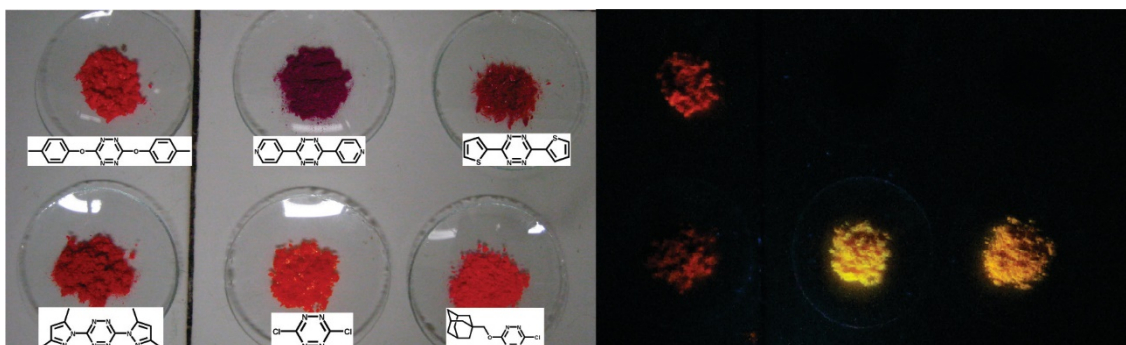


Figure 3.1. Left: photograph under ambient light of selected tetrazines with their corresponding formulas. Right: same samples irradiated at 354 nm showing the variability of the fluorescence of the tetrazines according to their substituents' nature. Extracted from ref 2.

Thus, the combination of a tetrazine derivate as a linker with group IV metals may result in a promising synergy to develop new porous stable heterogeneous photocatalyst. The synthesis of tetrazine-based MOFs can be carried out by direct synthesis in which a tetrazine-derived ligand reacts with selected metal ions, or either taking advantage of post synthetic routes. *Solvent-Assisted Linker Exchange* (SALE), also called *Post-Synthetic Exchange* (PSE), is an efficient synthetic approach for the preparation of improved MOFs through the replacement of linkers in MOFs and is reported as a method to control the spatial distribution of the building blocks. In that way, the controlled exchange of the parent ligand for the tetrazine derivative can lead to the formation of multivariate solids. During that process, the distribution of the ligands is determined by the synthetic conditions and, therefore, uniform and core-shell microstructures can be obtained. The different spatial distributions of mixed building blocks lead to properties that cannot be achieved with mixtures of pure MOFs. Therefore, the spatial distribution modulation is important to improve

the range of application of these materials. In that sense, we propose MTV-tetrazine MOFs as exceptional candidates to study the importance of the linker distribution in their photocatalytic properties. The availability of single crystal facilitates the chemical characterization of resultant microstructures which is particularly important to understand the dynamic exchange reactions often used in SALE processes. Although the isolation of single-crystals from Ti(IV) or Zr(IV)-MOFs are not trivial, we propose the use of High-Throughput (HT) synthetic methodologies to assist the optimization of the synthetic conditions and accelerate the exploration of the chemical space.

2. Summary of the key results:

The results of this chapter were published in “Lerma-Berlanga, B.; R. Ganivet C.; Almora-Barrios N.; Tatay S.; Peng Y.; Albero J.; Fabelo O.; González-Platas J.; García H.; M. Padial N. and Martí-Gastaldo, C. *Effect of Linker Distribution in the Photocatalytic Activity of Multivariate Mesoporous Crystals*. *J. Am. Chem. Soc.* **2021**, *143* (4), 1798–1806”. In this work, we presented the optimization of the synthetic conditions for the preparation of crystals of UiO-68, using H₂TPDC (1,1':4',1''-terphenyl)-4,4''-dicarboxylic acid, and UiO-68-TZDC which was a photoactive analogue based on a tetrazine dicarboxylic derivative, H₂TZDC (1,2,4,5-tetrazine-3,6-diyl)-4,4'-dibenzoic. The study of their chemical properties revealed the requirement to merge both ligands into one structure to prepare a promising hybrid for photocatalysis. MTV-UiO-68-TZDC₀ showed improved properties compared to their counterparts. The deep-analysis of the linker spatial microarrangements resulting from the exchange processes was fundamental to understand the photocatalytic response of the MTV-solids.

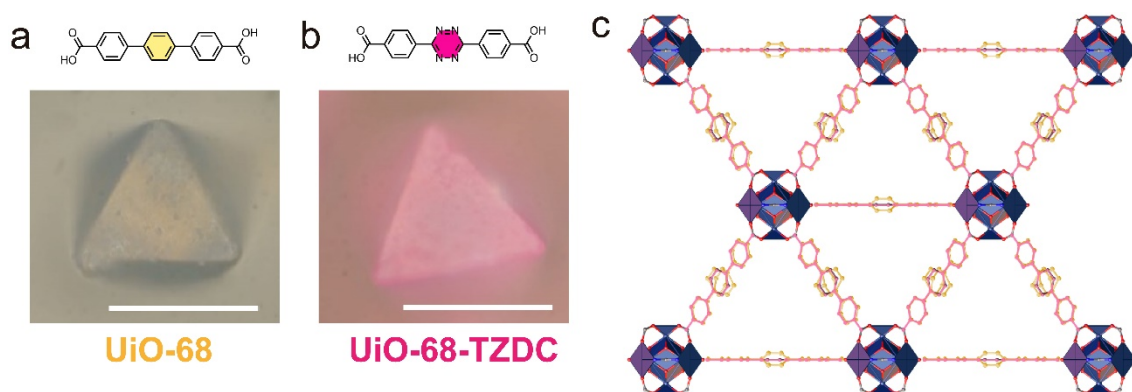


Figure 3.2. Organic linker and crystal of a) UiO-68 and b) photoactive UiO-68-TZDC Scale bars correspond to 50 and 25 μm , respectively. c) Overlay of the two crystallographic-distinct linker structures in (011) showing the slight differences.

UiO-68 and UiO-68-TZDC were prepared by solvothermal methods. Regarding the synthetic conditions, we carried out a systematic study of different reaction parameters as temperature, reaction time, modulator nature, and their respective equivalents. The metal: linker stoichiometry (1:1), zirconium source (ZrCl_4), and

solvent (DMF) were fixed according to the protocols adopted by the MOF community. The implementation of high-throughput methodologies allowed us to achieve a high reproducibility and accelerate the systematic screening of the synthetic parameters which were evaluated based on the crystallinity and PXRD fingerprints of the expected products. Crystals of UiO-68 were isolated as pale-yellow 20 to 50 μm octahedrals (*Figure 3.2. a*) using 40 equivalents of trifluoroacetic (TFA) at 100 $^{\circ}\text{C}$ for 72 h. The conditions optimized for H₂TPDC only required a slight reduction of the modulator equivalents, from 40 to 10, to isolate UiO-68-TZDC as pink octahedral crystals with sizes ranging from 10 to 20 μm (*Figure 3.2. b*). Single-crystals were measured and resolved by Oscar Fabelo and Javier González-Platas. The crystallographic analysis showed that both systems crystallized in the cubic space group *Fm-3m* and displayed an expanded cubic closed-packed structure for the characteristic 12-connected **fcu** topology of the UiO family¹⁷. The impact of the linker replacement in the unit cell parameters was almost negligible ($a = 32.71$ and 32.47 \AA , for TPDC and TZDC respectively) (*Figure 2.2. c*).

Then, we analysed the effect of the linker in the chemical behaviour on the resulted MOFs. Tetrazine core was unfavourable for thermal and chemical stability of the framework. Whereas UiO-68 decomposed in air above 500 $^{\circ}\text{C}$, the thermogravimetric analysis of UiO-68-TZDC showed a gradual decomposition from 250 to 450 $^{\circ}\text{C}$ which was indicative of more prone to oxidation of the tetrazine core at high temperatures. The hydrolytic stability of the solids was evaluated by incubating the solids in water for 24 h. The PXRDs after that treatment suggested that the structure of UiO-68 remained intact whereas UiO-68-TZDC underwent partial amorphization. The negative effect of TZDC was also confirmed by ICP studies that presented a superior Zr⁺⁴ leaching upon incubation. Despite the differences observed for the two networks, the optimization of activation process enabled to us get BET surface areas in excellent agreement with the expected values, 4028 and 4289 $\text{m}^2\cdot\text{g}^{-1}$ for UiO-68 and UiO-68-TZDC, respectively.¹⁷ For its part, CO₂ adsorption analysis revealed stronger gas interactions in UiO-68-TZDC.

Thus, the analysis of the single linker phases revealed the necessity of combining both linkers to produce multivariate frameworks that blend efficient light sensitization, chemical stability, and porosity, all relevant to photocatalytic applications. In that direction, we performed SALE experiments to produce a family of MTV-UiO-68-TZDC% frameworks using UiO-68 crystals as precursors (*Figure 3.3. a*). The reaction time was fixed to 3 h and the TZDC equivalents were varied. The exchanged ratio was evaluated by ¹H NMR and showed a logarithmic incorporation rate of TZDC, as well as a fine control loading from 3 to 50 %. The further analysis by FT-IR, SEM, PXRD, and N₂ adsorption (*Figure 2.3. b*) confirmed phase purity and ruled out any morphological or structural damage during the linker exchange process. Besides respecting the structure and porosity of the pristine solids, the coexistence of TPDC and TZDC in MTV-UiO-68-TZDC% enabled to us reach the chemical stability as it was denoted by PXRD (*Figure 3.3. c*) and ICP measurements.

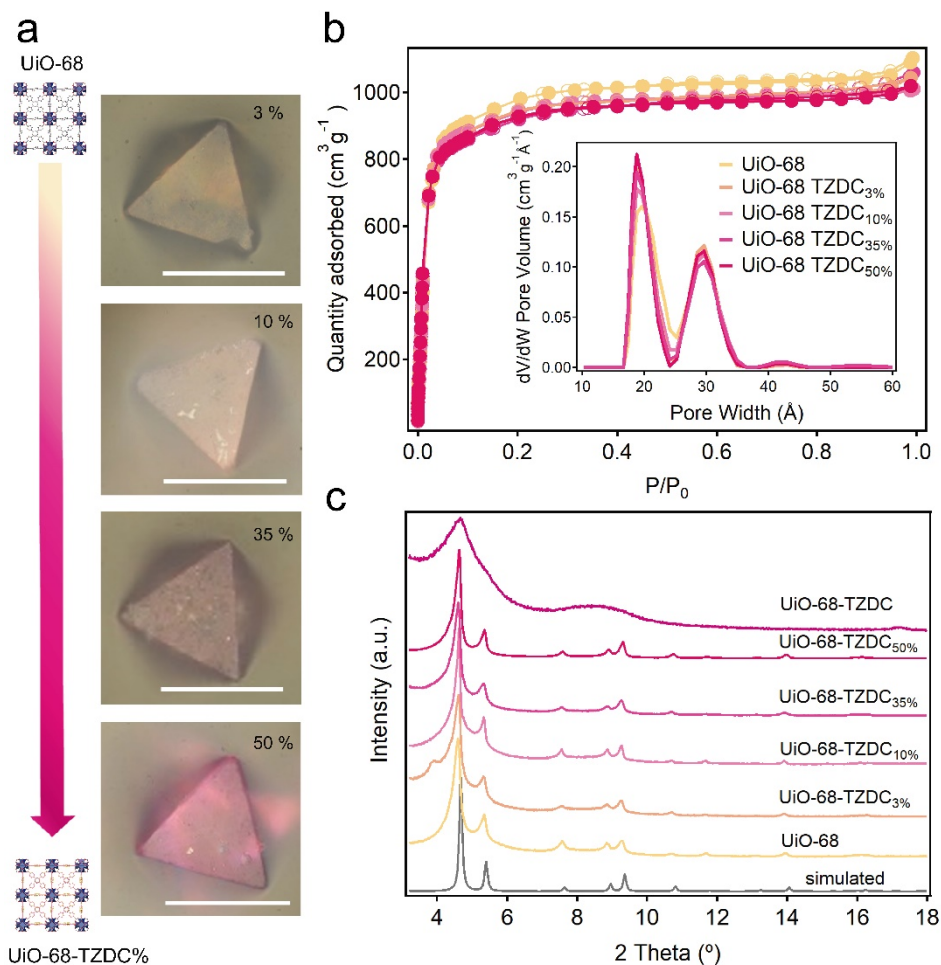


Figure 3.3. a) Optical microscope images of MTV-UiO-68-TZDC_{x%} samples. Scale bars correspond to 50 μm. b) N₂ sorption isotherms at 77 K and PSD for UiO-68-TZDC_{x%} samples. c) PXRD in logarithmic scale of intensity of the solids after soaked in water:methanol (4:1, v/v%) solution for 24 h. Compared to UiO-68-TZDC that becomes amorphous, all solids retained their original structure with negligible changes in their PXRD patterns regardless the TZDC % incorporated.

The impact of tetrazine doping in the electronic structure of the resultant materials was also studied by DFT calculations. Those calculations were carried out by Neyvis Almora-Barrios. The electronic structures of pristine MOFs were dominated by the aromatic 2p orbitals of the linkers, but the presence of the 2p N and C orbitals from the tetrazine ring reduced 1.15 eV its band gap compared to UiO-68 (Figure 3.4. a). Calculations showed that low levels of TZDC exchange were enough to modify the electronic structure and optical properties of the hybrids. The introduction of a single TZDC linker per cell, corresponding to UiO-68-TZDC_{4%}, yielded a lowest unoccupied crystalline orbital (LUCO) dominated by tetrazine orbitals with a band gap's values comparable to pristine UiO-68-TZDC. The additional calculations increasing the level of TZDC doping up to 50% revealed no changes in the LUCO position upon higher levels of doping. That theoretical trend was in good agreement with the experimental optical bandgap values calculated using the Kubelka-Munk function.

Fluorescence confocal microscopy and XPS experiments were useful to examine the chemical complexity of the resultant multivariate frameworks at single crystal level. The confocal images displayed characteristic spatial arrangements of parent (TPDC) and exchanged (TZDC) linker depending on doping levels. The samples between 3 and 20 % exhibited an asymmetric distribution of linkers for the formation of core-shell/TPDC-TZDC architectures with slightly thicker shells for higher doping levels, whereas that distribution becomes more uniform from 35 % onward (*Figure 3.4. b*). In parallel, experiments were carried out to understand the origin of the asymmetric distribution of the linkers. For that, new set of UiO-68-TZDC_{10%} crystals were prepared by prolonging the exchange time to 24 h while fixing the stoichiometric equivalents of TZDC in solution. Compared to the core-shell distribution observed after 3 h, long reaction times seemed to favour the diffusion of TZDC across the crystal forming a more homogeneous distribution not distinguishable with confocal microscopy. Thus, those results pointed out that the distribution of the exchanged linker to form uniform mixtures or core-shell domains was not only controlled by the concentration of TZDC in solution, but also by the exchange time. XPS analysis of the solids also proved the formation of that asymmetric distribution for shorter times, showing an exponential decrease of the superficial concentration of TZDC for longer reaction times.

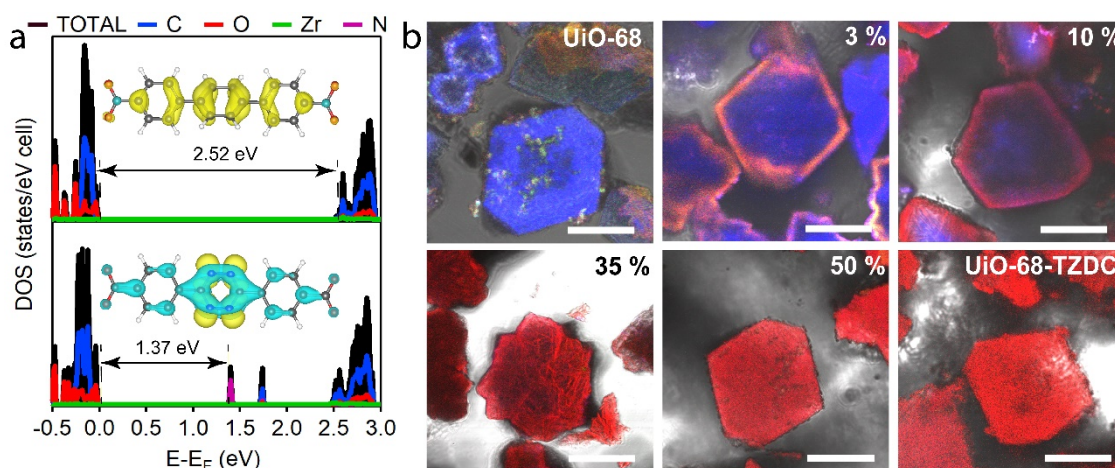


Figure 3.4. a) Total (DOS, black) and projected (PDOS for each atom) density of states for pristine UiO-68 (top) and UiO-68-TZDC_{4%}, (bottom). Inset: orbitals contributing to the HOCO (yellow) and LUCO (cyan) localized on the ligand. b) Fluorescence confocal microscope's images of polish UiO-68 samples reveal the resultant microstructures. Scale bars correspond to 25 and 10 μm for UiO-68 counterparts and pristine UiO-68-TZDC, respectively.

The prepared set of samples, which shared a common electronic structure and optical band gap, constituted a suitable platform for the study of the effect of linker distribution over the photocatalytic activity. The catalytic performance was analysed by toward proton and methyl viologen (MV) reduction. Those experiments were done by the group of Hermenegildo García in Universidad Politécnica de Valencia. Whereas UiO-68-TZDC_{35%} (homogeneous) showed a negligible activity,

UiO-68-TZDC_{10%} (core-shell) displayed an efficient reduction of MV and a linear increase in the H₂ production up to a maximum of $\approx 100 \mu\text{mol}$ (Figure 3.5. a and b), even despite the reduced concentration of TZDC. Analysing those differences, the structural and chemical robustness of samples after photocatalytic experiments were tested. The experimental BET value displayed a clear reduction for 35 % samples indicative of the structure or chemical damage. In order to investigate that effect in detail, we tested and compared the photocatalytic performance of UiO-68, UiO-68-TZDC, and multivariate UiO-68-TZDC_x solids (x = 3, 10, 35, and 50 %). UiO-68-TZDC_{10%} (core-shell) exhibited the best photocatalytic activity in both selected reactions. The accumulated H₂ production after 6.5 h increased with the TZDC % up to a maximum at 10 % from which it went sharply down to negligible values (Figure 3.5. c). That drastic change suggested that the activity was controlled by the density of TZDC in the surface of the crystals which was later confirmed by poor values obtained from UiO-68-TZDC_{10%} (homogeneous). The results pointed out a scenario in which the catalytic performance was a fine balance between photoactive linker surface concentration and stability, both of which were related to linker exchanged distribution inside the crystal.

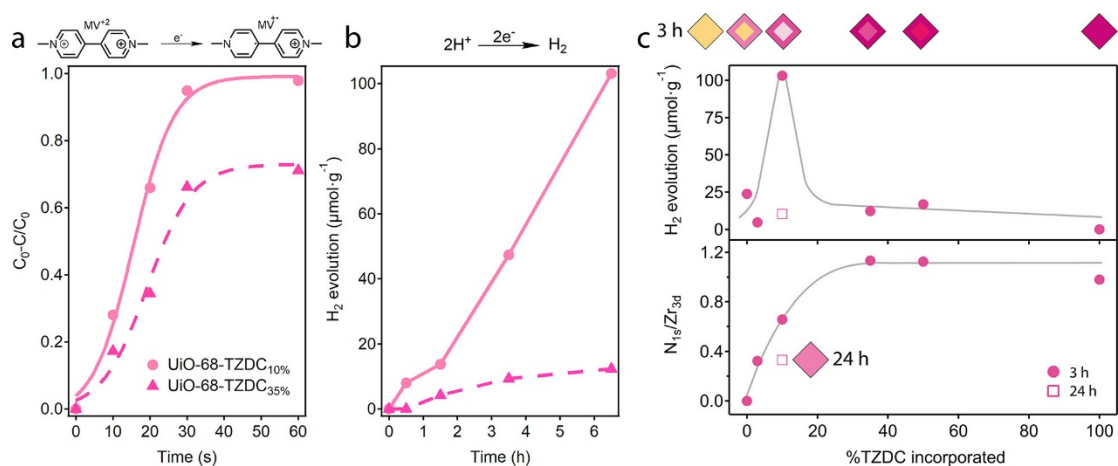


Figure 3.5. a) Photocatalytic methyl viologen reduction yields after 1 min for UiO-68-TZDC_{10%} and UiO-68-TZDC_{35%}. b) Photocatalytic H₂ production after 6.5 h of irradiation for UiO-68-TZDC_{10%} (pink circles) and UiO-68-TZDC_{35%} (deep pink triangles). c) (top) Accumulated H₂ production after 6.5 h of UiO-68, UiO-68-TZDC and MTV-UiO-68-TZDC_x solids prepared at 3 h (filled circles) and 24 h (empty square). (bottom) XPS analysis of the changes in the relative concentration of TZDC units in the surface of the crystals at a penetration depth of 10 nm. Solid lines are only a guide to the eye.

3. References

- (1) Pinner, A. Ueber die Einwirkung von Hydrazin auf Imidoäther. *Ber. Dtsch. Chem. Ges.* **1893**, *26*, 2126-2135.
- (2) Clavier, G.; Audebert, P. S -Tetrazines as Building Blocks for New Functional Molecules and Molecular Materials. *Chem. Rev.* **2010**, *110* (6), 3299–3314.
- (3) Moral, M.; García, G.; Garzón, A.; Granadino-Roldán, J. M.; Fox, M. A.; Yufit, D. S.; Peñas, A.; Melguizo, M.; Fernández-Gómez, M. Electronic Structure and Charge Transport Properties of a Series of 3,6-(Diphenyl)-s-Tetrazine Derivatives: Are They Suitable Candidates for Molecular Electronics? *J. Phys. Chem. C* **2014**, *118* (46), 26427–26439.
- (4) Allain, C.; Piard, J.; Brosseau, A.; Han, M.; Paquier, J.; Marchandier, T.; Lequeux, M.; Boissière, C.; Audebert, P. Fluorescent and Electroactive Low-Viscosity Tetrazine-Based Organic Liquids. *ACS Appl. Mater. Interfaces* **2016**, *8* (31), 19843–19846.
- (5) Guerret-Legras, L.; Maillot, B.; Audibert, J. F.; Dubacheva, G. V.; Galmiche, L.; Lang, P.; Miomandre, F. Electrofluorochromism of Surface-Confined Tetrazines Investigated on the Monolayer Scale. *J. Phys. Chem. C* **2019**, *123* (48), 29255–29261.
- (6) Lee, Y.; Cho, W.; Sung, J.; Kim, E.; Park, S. B. Monochromophoric Design Strategy for Tetrazine-Based Colorful Bioorthogonal Probes with a Single Fluorescent Core Skeleton. *J. Am. Chem. Soc.* **2018**, *140* (3), 974–983.
- (7) Miomandre, F.; Audebert, P. 1,2,4,5-Tetrazines: An Intriguing Heterocycles Family with Outstanding Characteristics in the Field of Luminescence and Electrochemistry. *J. Photochem. Photobiol. C Photochem. Rev.* **2020**, *44*, 100372.
- (8) Malinge, J.; Allain, C.; Galmiche, L.; Miomandre, F.; Audebert, P. Preparation, Photophysical, Electrochemical, and Sensing Properties of Luminescent Tetrazine-Doped Silica Nanoparticles. *Chem. Mater.* **2011**, *23* (20), 4599–4605.
- (9) Nickerl, G.; Senkowska, I.; Kaskel, S. Tetrazine Functionalized Zirconium MOF as an Optical Sensor for Oxidizing Gases. *Chem. Commun.* **2015**, *51* (12), 2280–2282.
- (10) Lédée, F.; Audebert, P.; Trippé-Allard, G.; Galmiche, L.; Garrot, D.; Marrot, J.; Lauret, J. S.; Deleporte, E.; Katan, C.; Even, J.; Quarti, C. Tetrazine Molecules as an Efficient Electronic Diversion Channel in 2D Organic-Inorganic Perovskites. *Mater. Horizons* **2021**, *8* (5), 1547–
- (11) Li, N.; Chang, Z.; Zhong, M.; Fu, Z. X.; Luo, J.; Zhao, Y. F.; Li, G. B.; Bu, X. H. Functionalizing MOF with Redox-Active Tetrazine Moiety for Improving the Performance as Cathode of Li-O₂ Batteries. *CCS Chem.* **2021**, *3* (3), 1297–1305.
- (12) Calahorra, A. J.; Fernández, B.; García-Gallarín, C.; Melguizo, M.; Fairen-Jimenez, D.; Zaragoza, G.; Salinas-Castillo, A.; Gómez-Ruiz, S.; Rodríguez-Diéguez, A. Towards a Potential 4,4'-(1,2,4,5-Tetrazine-3,6-Diyl) Dibenzoic Spacer to Construct Metal-Organic Frameworks. *New J. Chem.* **2015**, *39* (8), 6453–6458.
- (13) Rouschmeyer, P.; Guillou, N.; Serre, C.; Clavier, G.; Martineau, C.; Audebert, P.; Elka, E.; Devic, T.; Soleil, S.; Merisiers, L. O.; Yvette, G. A Flexible Fluorescent Zr Carboxylate Metal – Organic Framework for the Detection of Electron-Rich Molecules in Solution. *Inorg. Chem.* **2017**, *56*, (14), 8423–8429.
- (14) Liang, W.; Bhatt, P. M.; Shkurenko, A.; Adil, K.; Mouchaham, G.; Aggarwal, H.; Mallick, A.; Jamal, A.; Belmabkhout, Y.; Eddaoudi, M. A Tailor-Made Interpenetrated MOF with Exceptional Carbon-Capture Performance from Flue Gas. *Chem* **2019**, *5* (4), 950–963.
- (15) Jędrzejowski, D.; Pander, M.; Nitek, W.; Bury, W.; Matoga, D. Turning Flexibility into Rigidity: Stepwise Locking of Interpenetrating Networks in a MOF Crystal through Click Reaction. *Chem. Mater.* **2021**, *33* (18), 7509–7517.
- (16) Schaate, A.; Roy, P.; Godt, A.; Lippke, J.; Waltz, F.; Wiebcke, M.; Behrens, P. Modulated Synthesis of Zr-Based Metal-Organic Frameworks: From Nano to Single Crystals. *Chem. Eur. J.* **2011**, *17*

- (24), 6643–6651.
- (17) Cavka, J. H.; Olsbye, U.; Guillou, N.; Bordiga, S.; Lillerud, K. P. A New Zirconium Inorganic Building Brick Forming Metal Organic Frameworks with Exceptional Stability. *J. Am. Chem. Soc.* **2008**, *130*, (42), 13850–13851.

Publication 2:

***Effect of Linker Distribution in the
Photocatalytic Activity of
Multivariate Mesoporous Crystals***

J. Am. Chem. Soc., **2021**, *143* (4), 1798-1806

Effect of Linker Distribution in the Photocatalytic Activity of Multivariate Mesoporous Crystals

Belén Lerma-Berlanga, Carolina R. Ganivet, Neyvis Almora-Barrios, Sergio Tatay, Yong Peng, Josep Albero, Oscar Fabelo, Javier González-Platas, Hermenegildo García, Natalia M. Padial,* and Carlos Martí-Gastaldo*



Cite This: *J. Am. Chem. Soc.* 2021, 143, 1798–1806



Read Online

ACCESS |



Metrics & More

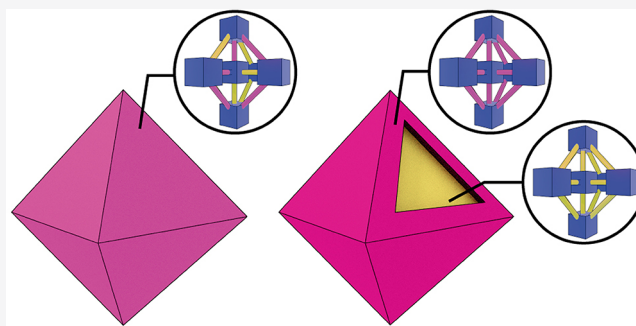


Article Recommendations



Supporting Information

ABSTRACT: The use of Metal–Organic Frameworks as crystalline matrices for the synthesis of multiple component or multivariate solids by the combination of different linkers into a single material has emerged as a versatile route to tailor the properties of single-component phases or even access new functions. This approach is particularly relevant for Zr_6 -MOFs due to the synthetic flexibility of this inorganic node. However, the majority of materials are isolated as polycrystalline solids, which are not ideal to decipher the spatial arrangement of parent and exchanged linkers for the formation of homogeneous structures or heterogeneous domains across the solid. Here we use high-throughput methodologies to optimize the synthesis of single crystals of UiO-68 and UiO-68-TZDC, a photoactive analogue based on a tetrazine dicarboxylic derivative. The analysis of the single linker phases reveals the necessity of combining both linkers to produce multivariate frameworks that combine efficient light sensitization, chemical stability, and porosity, all relevant to photocatalysis. We use solvent-assisted linker exchange reactions to produce a family of UiO-68-TZDC_x binary frameworks, which respect the integrity and morphology of the original crystals. Our results suggest that the concentration of TZDC in solution and the reaction time control the distribution of this linker in the sibling crystals for a uniform mixture or the formation of core–shell domains. We also demonstrate how the possibility of generating an asymmetric distribution of both linkers has a negligible effect on the electronic structure and optical band gap of the solids but controls their performance for drastic changes in the photocatalytic activity toward proton or methyl viologen reduction.



INTRODUCTION

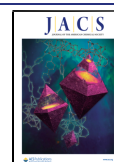
The discovery of the family of Zr(IV) UiO-type Metal–Organic Frameworks (MOFs) by Lillerud and co-workers in 2008 introduced a versatile platform for the design of MOFs with excellent stability.¹ Since then, the use of monocarboxylic acids as modulators² combined with the flexibility of $[Zr_6O_4(OH)_4(CO_2)_{12}]$ clusters acting as inorganic nodes, has enabled us to gain chemical control over the design of isorecticular frameworks with linear dicarboxylic linkers for a huge family of porous materials with tailorable micro/mesoporosity and application in catalysis, gas storage, or separation technologies.^{3,4} Unfortunately, most of these materials can be only synthesized as polycrystalline solids, highlighting the difficulties in isolating single crystals. This problem is even more severe for the mesoporous derivatives, which require the use of elongated linkers with very poor solubility in the organic solvents used in the synthesis. This is possibly why the synthesis of single crystals of UiO-68 using H_2TPDC ($[1,1':4',1''\text{-terphenyl}]-4,4''\text{-dicarboxylic acid}$) linkers still remains elusive, and all crystals available rely on amine,

alcohol, or alkyl derivatives with subsequent changes to the porosity or physical properties of the pristine material.^{5–7}

The availability of single crystals is particularly important in understanding the dynamic exchange reactions often used to produce multivariate frameworks by postsynthetic (PSE)⁸ or solvent-assisted linker exchange (SALE).⁹ The porosity of the framework and the concentration of the exchanged linker control the diffusion of the last. As a result, these variables can impose changes to the microstructure and distribution of exchanged and parent linkers in the framework. Both features might modify the physical properties and performance of the MOF in specific applications. This phenomenon was originally demonstrated for microporous MOF-5, UMCM-8, and UiO-66,¹⁰ but there are no precedents for mesoporous frameworks.

Received: August 26, 2020

Published: January 12, 2021



Built upon our recent experience for the challenging chemistry of titanium,^{11–13} here we use High-Throughput (HT) synthetic methodologies¹⁴ to optimize the conditions required for isolating single crystals of pristine UiO-68 and its photoactive analogue UiO-68-TZDC, based on 4,4'-(1,2,4,5-tetrazine-3,6-diyl)dibenzoic acid (H₂TZDC). The availability of crystals is used to analyze the effect of TZDC concentration in the formation of binary frameworks by SALE. Our results confirm that the crystals evolve from an ordered core–shell microstructure of TZDC/TPDC linkers into a more homogeneous distribution for increasing equivalents of the exchanged linker. By correlating the electronic structure of UiO-68-TZDC_x solids with their photocatalytic activity, we demonstrate the impact of linker distribution over the photocatalytic performance of multivariate mesoporous crystals.

RESULTS AND DISCUSSION

High-Throughput Synthesis of UiO-68 Single Crystals. We designed a first experiment for optimizing the formation of UiO-68 crystals that accounted for systematic variations of temperature (90, 100, or 120 °C), reaction time (48 or 72 h), and equivalents of acid modulator (trifluoroacetic acid (TFA), acetic acid (AcOH), benzoic acid (BA), or formic acid (FA)). The metal/linker stoichiometry, zirconium source, and solvent were fixed according to the protocols adopted by the community to 1:1, ZrCl₄ and *N,N*-dimethylformamide (DMF)¹² for a library of over 80 reactions. We used a FLEX SHAKE HT workstation from Chemspeed for robotic dispensing of solids and liquids combined with a 96-well Powder X-Ray Diffraction (PXRD) plate. This helped in maintaining a high reproducibility and accelerating the systematic screening of reaction parameters based on the crystallinity and PXRD fingerprints of the products. See [Supporting Information, SI, Section S2](#) for more experimental details. As shown in the ternary diagrams in [Figure S4](#), crystals of UiO-68 were only formed by reaction with 40 equiv of TFA at 100 °C over 72 h. The solid was isolated as pale-yellow crystals with octahedral morphology and sizes ranging from 20 to 50 μm ([Figure 1a left](#)). To challenge the versatility of these synthetic conditions we next synthesized H₂TZDC by replacing the central phenyl ring in H₂TPDC with an *s*-tetrazine ring. Tetrazine derivatives are electroactive molecules capable of undergoing reversible transformation into stable anion radicals. As a result, their fluorescence can be electrochemically switched for applications in light generation, sensors, and polymers.^{15,16} These features can also be translated to MOFs for generating photoactive frameworks by reticulation of tetrazine derivatives.¹⁷ Despite the poorer solubility of the tetrazine linker, the conditions optimized for TPDC only required a slight reduction of the modulator equivalents, from 40 to 10, to isolate UiO-68-TZDC as pink octahedral crystals with sizes ranging from 10 to 20 μm ([Figure 1a right](#)). These conditions are substantially different to the reported synthesis of polycrystalline UiO-68-TZDC for particle sizes near 1 μm.¹⁸

UiO-68 and UiO-68-TZDC crystallize in the cubic space group *Fm-3m* ($a = 32.71$ and 32.47 Å, respectively). They display an expanded cubic closed-packed structure for the characteristic 12-connected *fcu* topology of the UiO family.¹ See [SI Section S3](#) for more details. The impact of the linker replacement in the porosity metrics is almost negligible for octahedral and tetrahedral voids of 27.3 and 19.3 Å ([Figure](#)

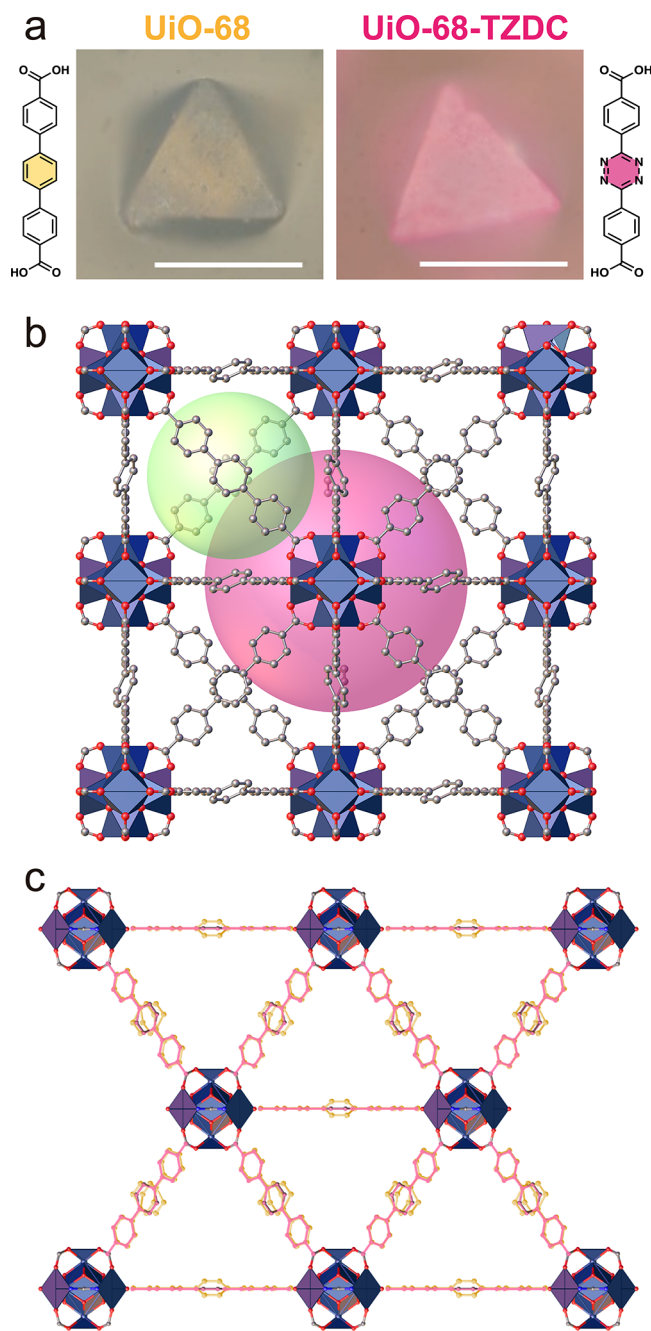


Figure 1. (a) (Left) size and morphology of UiO-68. Scale bars correspond to 50 μm. (Right) size and morphology of photoactive UiO-68-TZDC crystals. Scale bars correspond to 25 μm. (b) Structure of UiO-68 along the *c* axis showing the accessible volume corresponding to octahedral (pink sphere) and tetrahedral voids (green). (c) Overlay of the two crystallographic-distinct linker structures in (011) showing the slight differences that result from the replacement of TPDC with TZDC.

1b,c). As for the internal structure of the linkers, the carboxylate groups remain coplanar in both cases but the central ring presents a certain degree of disorder. We collected crystallographic data at 100 K (UiO-68) and at room temperature (UiO-68-TZDC). The disorder is present in both cases which suggests this is intrinsic to the crystallographic packing of the solids and not thermal in origin.

Porosity and Chemical Stability: Effect of the Linker. The effect of the tetrazine core is more notable in the thermal

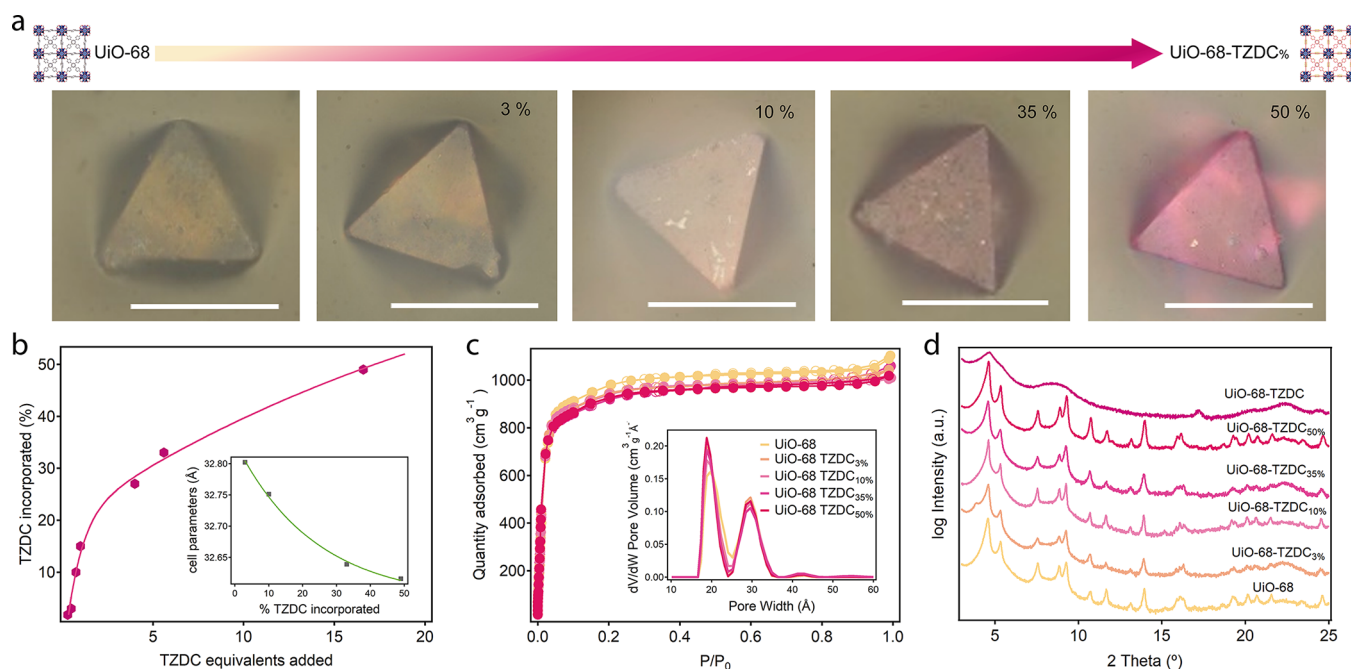


Figure 2. (a) Optical microscope images of UiO-68-TZDC_% samples. Scale bars correspond to 50 μm . (b) TZDC incorporated versus equivalents used in the synthesis. Inset: reduction of cell parameters as result of TZDC incorporation. (c) N_2 sorption isotherms at 77 K and PSD for UiO-68-TZDC_% samples. (Filled marker were used for adsorption and empty marker for desorption). (d) PXRD in logarithmic scale of intensity of the solids after soaked water: methanol (4:1, v/v%) for 24 h.

and chemical stability of the frameworks. Compared to UiO-68 that decomposes in air above 500 $^{\circ}\text{C}$, the thermogravimetric analysis of UiO-68-TZDC shows a gradual decomposition from 250 to 450 $^{\circ}\text{C}$ indicative of the oxidation of the tetrazine core at high temperatures. The hydrolytic stability of the solids was evaluated by incubation in water for 24 h. The PXRDs after this treatment suggest that the structure of UiO-68 remains intact whereas UiO-68-TZDC undergoes partial amorphization (SI Section S4). The negative effect of TZDC on the strength of the framework linkages against hydrolysis is also confirmed by ICP studies, that show a superior leaching ($22.4 \mu\text{g}\cdot\text{L}^{-1}$) of zirconium to solution upon incubation of the solids in water/methanol mixtures (Figure S55). This agrees well with the weakening of the elongated coordination bonds in the last for feebler metal joints more prone to hydrolysis.

We next analyzed the effect of the linker in tuning the structural robustness of the solids for optimizing the process of activation, a critical step to access the expected surface areas.¹⁹ We selected a range of solvents to examine the effect of changes in coordinating ability, polarity, or surface tension in the collapse of porosity (Table S5, Figures S15 and S17).²⁰ Methanol exchange leads to amorphization in both cases likely due to its ability to react with Zr_6 nodes.²¹ In turn, acetone and DMF do not alter the structure of UiO-68 but provoke the collapse of UiO-68-TZDC. This suggests a negative effect of the electron-deficient heterocycle in maximizing the interaction with polar solvents for a framework more susceptible to the capillary-forces generated in the activation process. To confirm this point, we used hexane for minimizing the interaction with the framework due to its low surface tension ($17.9 \text{ mN}\cdot\text{m}^{-1}$ at 25 $^{\circ}\text{C}$) and small dipole moment (0.08 D). Exchange with hexane for 5 days, followed by drying in anhydrous conditions, for avoiding humidity and reducing capillary forces²² is respectful with the structure of both materials. See SI Section S4.6 for more details. Both samples were degassed overnight at

60 $^{\circ}\text{C}$ and 10^{-6} Torr before gas analysis. They display a nonhysteretic, type-I N_2 adsorption isotherms with multipoint BET surface areas in excellent agreement with the expected values, 4028 and 4289 $\text{m}^2\cdot\text{g}^{-1}$ for UiO-68 and UiO-68-TZDC, respectively.¹

The Pore Size Distributions (PSDs) calculated by using Nonlinear Density Functional Theory (NLDFT) models reveal a narrow distribution of two types of mesopores centered at 2.0 and 3.0 nm, consistent with the pore size values calculated from the crystallographic data available (Table S6). Additional measurements collected for samples exchanged with wet hexane or methanol show a significant drop in surface area of 30% and 80% for UiO-68-TZDC, confirming the importance of minimizing solvent-framework interaction to access the expected porosity. Note that this is only critical for the activation step. After that, the solid can be exposed to open air with no impact over its surface area. CO_2 adsorption measurements reveal a modest uptake at 273 K of around 50 $\text{cm}^3\cdot\text{g}^{-1}$. The calculated isosteric heats of adsorption confirm the positive effect of the nitrogenated core in UiO-68-TZDC for stronger interaction with the guest ($Q_{\text{st}} = 31 \text{ kJ}\cdot\text{mol}^{-1}$). The properties of the single-linker phases reveal the necessity of combining both units in the same material to produce a photoactive material without compromising its chemical stability or porosity, both important to photocatalytic applications.

Multivariate Mesoporous Crystals by Solvent-Assisted Linker Exchange. We decided to investigate a HT library of reactions to produce multivariate MOFs²³ by direct combination of TPDC and TZDC with systematic control of ratio, temperature, concentration, and mixture of solvents. All attempts resulted in solids with reduced crystallinity and negligible incorporation of TZDC, suggesting important differences in the reactivity of the linkers with $\text{Zr}(\text{IV})$ (SI Section S5.1). On the basis of their structural similarity, we

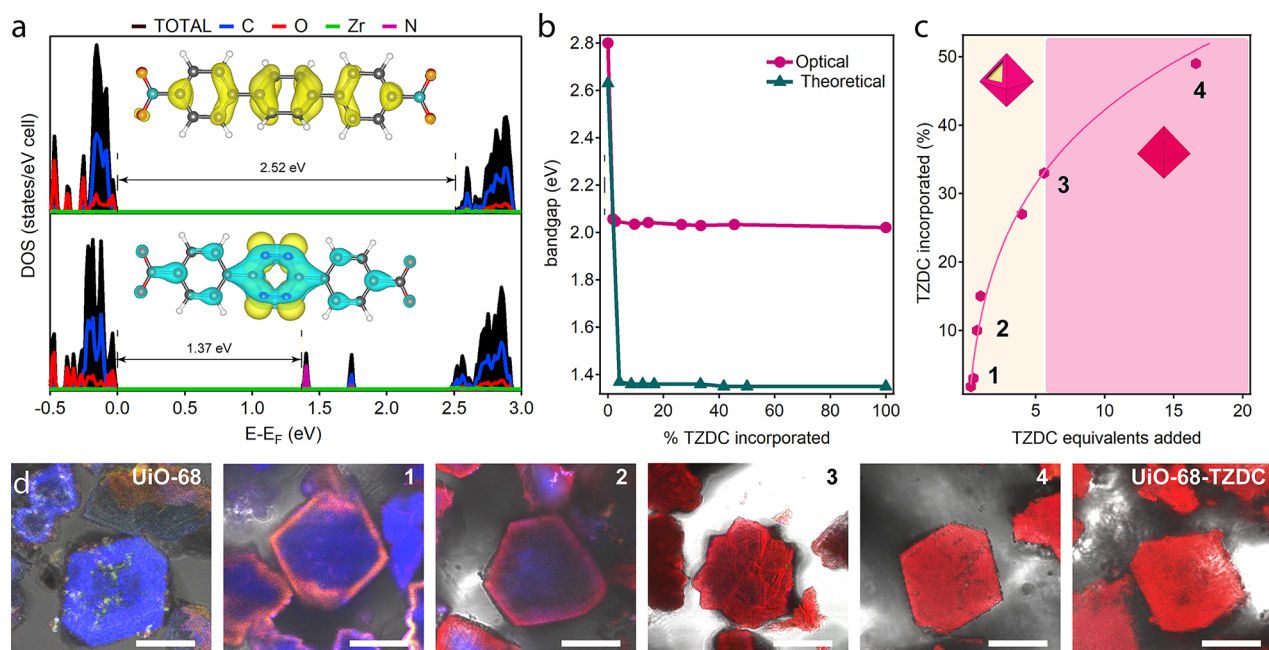


Figure 3. (a) Total (DOS, black) and projected (PDOS for each atoms) density of states for pristine UiO-68 (top) and UiO-68-TZDC_{4%} (bottom) calculated using PBE functional, this is a qualitative approach; the electronic structures could not be computed at the HSE06 level because of the system size. Inset: orbitals contributing to the HOCO (yellow) and LUCO (cyan) localized on the ligand. (b) Experimental and computed band gap values as a function of the TZDC incorporated. (c) Spatial linker arrangement in UiO-68-TZDC_{x%} samples (pale yellow area for core-shell distribution and pink area for a more uniform distribution). (d) Fluorescence confocal microscope's images of polish UiO-68 samples reveal the resultant microstructures. Scale bars correspond to 25 and 10 μm for UiO-68 counterparts and UiO-68-TZDC, respectively.

decided to use postsynthetic linker exchange methods instead. By using UiO-68 crystals as precursors, we prepared a family of UiO-68-TZDC_{x%} multivariate solids by SALE of varying equivalents of the tetrazine linker in DMF at 80 °C for 3 h. We used a base (Et₃N) to deprotonate H₂TZDC and favor the linker exchange (SI Section S5.2).²⁴ UiO-68-TZDC_{x%} crystals were digested and analyzed by ¹H NMR (Nuclear Magnetic Resonance). The integration of the resonances for aromatic protons confirm the presence of both linkers and reveal a fine control over the exchange rate from 3 to 50%, concomitant with the color of the crystals (Figure 2a). The FT-IR spectra of the samples show a shift of 25 cm⁻¹ in the ν_{C=O} vibration compared to the free linker. This rules out the trapping of TZDC in the mesopores of the MOF and confirms that the NMR quantification is representative of the actual incorporation of the linker to the framework. We used these techniques to analyze the maximum exchange ratio possible. Beyond UiO-68 TZDC_{50%}, reactions with more than 20 equiv of TZDC show clear evidence of ineffective linker exchange in the final products. As shown in Figure 2b, UiO-68-TZDC_{3-50%} crystals show the same logarithmic rate of TZDC incorporation with the number of equivalents observed for other Zr-MOFs.²⁵ Phase purity was preliminary evaluated by PXRD Le Bail refinement of all solids. We observe a compression of the unit cell parameters that correlates well with the TZDC% incorporated. All solids display permanent porosity with negligible changes to their surface area and PSD compared to the single-linker phases (Figure 2c). SEM analysis rules out any morphological damage during linker exchange. All crystals retain the octahedral morphology and size of the UiO-68 seed, suggesting that the incorporation of TZDC operates in the crystal and does not involve their dissolution/recrystallization.

Besides respecting the structure and porosity of the pristine solids, the coexistence of TPDC and TZDC in multivariate

UiO-68 crystals allows for reaching a fine balance between chemical stability and photoactivity. We soaked UiO-68-TZDC_{3-50%} crystals in water/methanol mixtures (4:1, v/v%) for 24 h. These methanolic solutions are often used to test the photocatalytic activity of MOFs in hydrogen evolution reactions.¹¹⁻¹³ Compared to UiO-68-TZDC that becomes amorphous, all solids retain their original structure with negligible changes in their PXRD patterns regardless the TZDC% incorporated (Figure 2d). Compared to minimum changes in structural stability, the impact of tetrazine doping on the hydrolytical stability of the multivariate frameworks is more acute. ICP analysis shows an increasing rate of metal leaching upon incorporation of TZDC. Linker sensitization is an efficient way to maximize the photocatalytic activity of MOFs with visible light by taking advantage of their synthetic/structural tunability. This strategy is dominated by porphyrins,²⁶ functionalized organic linkers,^{27,28} or the incorporation of ruthenium or iridium complexes.²⁹ *s*-Tetrazine linkers are also excellent candidates in this regard due to the combination of one-electron reversible reduction behavior and visible-light sensitization.

Impact of Tetrazine Doping in the Electronic Structure of the Framework. To understand the effect of tetrazine doping, we calculated the electronic structure of the hybrid frameworks by using density functional theory (DFT, SI Section S6.1). Figure 3a shows a comparison of the electronic density of states diagram of pristine UiO-68 and UiO-68-TZDC_{4%}, that corresponds to the incorporation of one TZDC linker per unit cell. In UiO-68, the position the highest occupied crystalline orbitals (HOCO) and the lowest unoccupied crystalline orbital (LUCO) is dominated by the aromatic 2p orbitals of TPDC. The introduction of a single TZDC linker per cell yields a LUCO that is also dominated by the linker but shows clear differences. The contribution of the

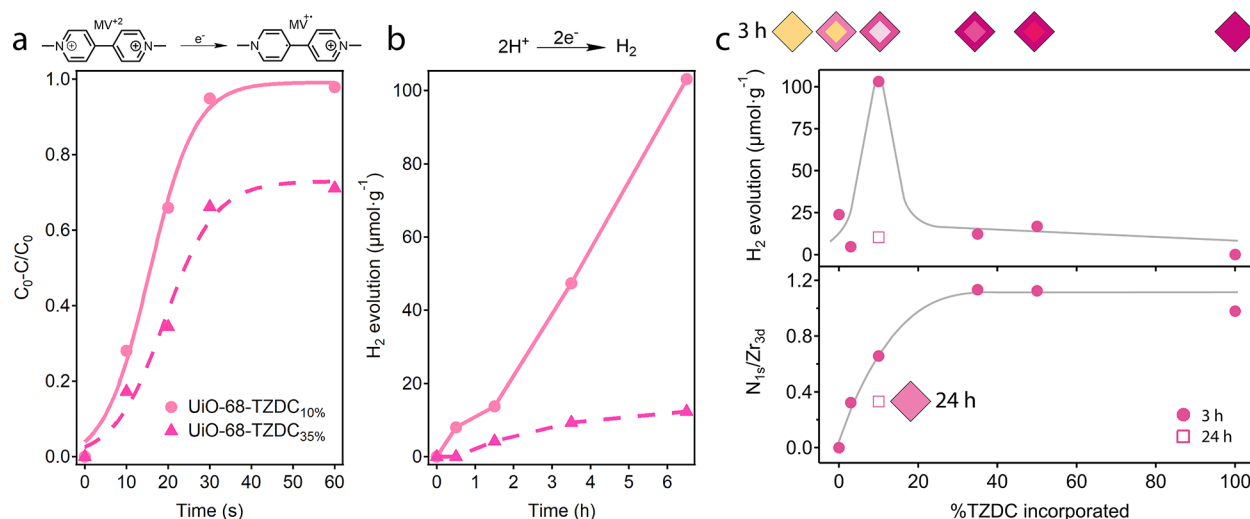


Figure 4. (a) Photocatalytic methyl viologen reduction yields after 1 min for UiO-68-TZDC_{10%} and UiO-68-TZDC_{35%}. (b) Photocatalytic H₂ production after 6.5 h of irradiation for UiO-68-TZDC_{10%} (pink circles) and UiO-68-TZDC_{35%} (deep pink triangles). (c) (top) Accumulated H₂ production after 6.5 h of UiO-68, UiO-68-TZDC and multivariate UiO-68-TZDC_x solids ($x = 3, 10, 35,$ and 50%) prepared at 3 (filled circles) and 24 h (empty square). (bottom) XPS analysis of the changes in relative concentration of TZDC units in the surface of the crystals at a penetration depth of 10 nm. Solid lines are only a guide to the eye.

2p N and C orbitals from the tetrazine ring in UiO-68-TZDC_{4%} reduces the band gap to 1.37 eV compared to the 2.52 eV in UiO-68. We carried out additional calculations by systematically increasing the TZDC content up to 50% (12 linkers per unit cell). As shown in Figure 3a, the position of the LUCO is insensitive to increasing levels of doping and a single linker replacement is sufficient to dominate the electronic structure and optical properties of the hybrids. This effect is very similar to the modification of the band gap with monoaminated terephthalic linkers reported for MIL-125, that also saturates for the replacement of one linker per unit cell.²⁷

To confirm the value of our computational simulations we used UV–vis solid reflectance measurements to estimate the optical band gap of UiO-68-TZDC_{3–50%} by using the Kubelka–Munk function. We observe an excellent match between the trend described by experimental results and computed band gap values, that further confirm the effectiveness of TZDC sensitization at very small doping levels (Figure 3b) (SI Section S6.2).

Chemical complexity in multivariate frameworks can be investigated with different techniques. Diffraction methods cannot account for linker or metal gradients across the crystal, but spectroscopic studies have been quite useful in solving this question. The spatial arrangement of organic crystals at different resolution can be elucidated with microscopic Attenuated Total Reflectance (ATR) infrared spectroscopy,³⁰ Solid-State Nuclear Magnetic Resonance (SS-NMR),³¹ Photo-thermal Induced Resonance (PIR),³² 2D Raman spectroscopy,¹⁰ fluorescence confocal microscopy,³³ or fluorescence lifetime imaging.³⁴ Besides organic linkers, the spatial arrangement of multimetallic Secondary Building Units (SBUs) in multivariate frameworks has been also deciphered by using a combination of X-ray Photoelectron Spectroscopy (XPS) and UV–vis diffuse reflectance spectroscopy,³⁵ Scanning Transmission Electron Microscopy High-Angle Annular Dark Field imaging (STEM-HAADF),^{36,37} or with atomic resolution by using atom probe tomography.³⁸ To analyze the spatial arrangement of parent and exchanged linkers in this case, we

carried out fluorescence studies with a confocal microscope. Images were taken at different heights to account for the three-dimensional distribution of active TZDC and inactive TPDC linkers when excited with a green filter ($\lambda = 559$ nm). Comparison of UiO-68-TZDC at 3 and 35% doping levels suggests a higher concentration of TZCD linkers at the surface of the first based on more intense fluorescence at the edges and vertices of the crystal (SI Section S7 and Movies S1 and S2). For a clearer view of this phenomenon, we used an ultramicrotome to dissect and polish the section of the crystals. This experiment confirms that the crystals show an asymmetric distribution of linkers for the formation of core–shell/TPDC-TZDC architectures between 3 and 20% whereas this distribution becomes more uniform from 35% (Figure 3c,d). A closer analysis of the confocal images of the crystals after 3 and 10% doping also suggests that higher concentrations of TZDC seem to favor the formation of slightly thicker shells. To confirm if this asymmetric distribution of linkers was kinetically controlled, we also synthesized and characterized another set of UiO-68-TZDC_{10%} crystals by prolonging the exchange time to 6, 12, and 24 h while fixing the stoichiometric equivalents of H₂TZDC in solution (SI Section S5.4). Compared to the core–shell distribution present after 3 h, reaction after 24 h seems to favor the diffusion of TZDC across the crystal for a more homogeneous distribution not distinguishable with confocal microscopy. XPS analysis of all samples confirms how longer reaction times induce an exponential decrease of the superficial concentration of TZDC, that seems to be kinetically controlled. Our data reveal how shorter reaction times are more likely to maximize the asymmetric distribution of linkers in multivariate frameworks prepared by linker-exchange reaction.

Overall, this confirms the ability of UiO-type materials to produce chemically diverse arrangements of functionalities after PSE as previously demonstrated with Raman and fluorescence imaging for UiO-66 and -67, respectively.^{10,34} Our results point to a chemically diverse set of crystals with comparable optical band gaps ideal to investigate the effect of linker distribution over their photocatalytic activity. To the

best of our knowledge, this still remains an open question for multivariate MOFs.

Interplay between Linker Distribution and Photocatalytic Activity. To investigate this possibility, we evaluated the photocatalytic performance of UiO-68, UiO-68-TZDC, and multivariate UiO-68-TZDC_x solids ($x = 3, 10, 35,$ and 50%) for the reduction of methyl viologen (MV) and the hydrogen evolution reaction (HER). As shown in Figure 4a, the different distribution of photoactive TZDC and inactive TPDC linkers promotes a much more efficient reduction of MV for UiO-68-TZDC_{10%} despite the reduced concentration of TZDC. This same trend is observed for the HER in a methanolic mixture (Figure 4b). Compared to the negligible activity of UiO-68-TZDC_{35%}, UiO-68-TZDC_{10%} shows a linear increase in the H₂ production up to a maximum of $\sim 100 \mu\text{mol}\cdot\text{g}^{-1}$ after 6.5 h. This boost in performance is concomitant to an increase in the quantum efficiency of close to 15 times higher that might be associated with the formation of core–shell domains. It is worth commenting that related MOF-based photocatalysts, such as UiO-66, have shown negligible H₂ production in the absence of Pt nanoparticles or other cocatalysts, in good agreement with the production observed for UiO-68-TZDC_{35%}.^{39–41} We also observe a clear difference on the experimental BET value of both solids after the tests. Whereas UiO-68-TZDC_{10%} maintains a surface area close to the expected value, the 35% sample displays a clear reduction indicative of partial collapse of the structure or chemical damage (SI Section S8).

To investigate this effect in detail, we tested and compared the photocatalytic performance of UiO-68, UiO-68-TZDC, and multivariate UiO-68-TZDC_x solids ($x = 3, 10, 35,$ and 50%). As shown in Figure 4c, the accumulated H₂ production after 6.5 h increases with the TZCD% up to a maximum at 10% from which it goes sharply down to negligible values. This drastic change suggests that performance is somewhat controlled by the density of TZDC in the surface of the crystals. This was estimated for each case using XPS as the N/Zr ratio calculated from the integrated areas of the N_{1s} and Zr_{3d} survey spectra peaks. The XPS analysis reveals an increase in the nitrogen surface concentration consistent with the progressive replacement of parent TPDC by TZDC units for doping levels equal or below 10%, compared to the complete surface exchange that takes place from 35%. These results suggest a complex scenario in which performance is controlled not only by photoactive linker concentration but also by its distribution inside the crystal. On the basis of the analysis of pristine UiO-68-TZDC (vide supra), complete exchange might compromise the chemical and structural stability of the surface of the crystal at the conditions used in the photocatalytic tests. Compared to 35 and 50% for which complete surface exchange likely induces partial decomposition for an activity drop, the partial exchange at the surface of UiO-68-TZDC_{10%} is more suitable to reach a fine balance between photoactivity and stability. The stability of the frameworks was analyzed by ICP measurements of the solutions in conditions comparable to the photocatalytic tests. The rate of metal leaching remains below $10 \mu\text{g}\cdot\text{L}^{-1}$ for doping levels below 35% but displays an increase from this point with the TZDC% in the crystal, suggesting reduced chemical stability for higher doping levels (SI Section S8). The poor H₂ production displayed by UiO-68-TZDC_{10%} prepared at 24 h also confirms the effect of TZDC surface concentration in the photocatalytic activity of this family of frameworks. Compared to the core–shell architecture formed

after 3 h, the uniform distribution of photoactive linkers attained at longer reaction times is detrimental to overall performance.

CONCLUSIONS

Compared to the synthetic design of multiple component MOFs, which often relies only on the nature and relative percentage of the linkers combined as synthetic variables to tune the properties of the resulting materials, our results demonstrate also the impact of linker distribution as an efficient tool to code their function as previously demonstrated with porosity gradients.⁴² These results confirm the importance of concentration and reaction time in controlling the relative ratio and distribution of mixed components in multivariate frameworks prepared by linker exchange reactions by using single crystals as a template. The reaction time seems to be particularly relevant in our case, as it seems to control linker diffusion to enable the formation of core–shell architectures under kinetic control. We are currently exploring this possibility to maximize the sensitization of multivariate titanium frameworks. Compared to Zr-MOFs for which photostimulated processes are mainly restricted to the linker,⁴³ Ti is more prone to induce ligand to metal charge transfer for higher photocatalytic efficiencies.^{13,28}

EXPERIMENTAL SECTION

Synthesis of UiO-68. H₂TPDC (18 mg; 0.055 mmol) was suspended in a mixture of 3.5 mL of *N,N*-Dimethylformamide (DMF) and 150 μL of Trifluoroacetic Acid (TFA) (40 equiv) in a 5 mL Teflon vial. Subsequently, the ZrCl₄ (12 mg; 0.051 mmol) was added to the suspension. The bottle was sealed and heated in an oven at 100 °C for 72 h. After cooling down to room temperature, this results in the formation of deep yellow octahedral crystals that were isolated by centrifugation and washed with 45 mL of DMF ($3 \times 15 \text{ mL}$) and 45 mL of methanol ($3 \times 15 \text{ mL}$) in the centrifuge tube. The product was soaked in hexane for 3 days, after which it was dried at room temperature.

Synthesis of UiO-68-TZDC. H₂TZDC (18 mg; 0.055 mmol) was suspended in a mixture of 3.5 mL of DMF and 40 μL of TFA (10 equiv) in a 5 mL Teflon vial. Subsequently, the ZrCl₄ (12 mg; 0.051 mmol) was added to the suspension. The bottle was sealed and heated in an oven at 100 °C for 72 h. After cooling down to room temperature, this results in the formation of deep pink octahedral crystals that were isolated by centrifugation and washed with 45 mL of DMF ($3 \times 15 \text{ mL}$) and 45 mL of methanol ($3 \times 15 \text{ mL}$) in the centrifuge tube. The product was soaked in hexane for 7 days, after that it was dried at room temperature.

Synthesis of Multivariate Solids. As-made UiO-68 (140 mg) was immersed in 54 mL of H₂TZDC solution in DMF and 40 μL of trimethylamine (Et₃N) at 80 °C under stirring. Using different equivalents of H₂TZDC (0–17 equiv) for 3 h of reaction produced a controllable UiO-68-TZDC%. After time reaction, the exchanged MOF was thoroughly washed with fresh DMF (40 mL \times 5). The resultant solids were kept in hexane.

DFT Calculations. All structural calculation was performed using dispersion-corrected density functional theory (DFT-D3) with the Vienna Ab initio Simulation Package (VASP),^{44,45} and employing the Perdew–Burke–Ernzerhof (PBE) functional.⁴⁶ The recommended GW PAW pseudopotentials⁴⁷ were used for all geometry and electronic calculations. A plane wave basis set was employed with a kinetic energy cutoff of 500 eV, and a Γ -point grid was used to sample the Brillouin zone. Electronic calculations was moreover performed with a $2 \times 2 \times 2$ Γ -centered grid and PBE functional, although this functional is a qualitative approach, hybrid functional calculations on Zr-MOF have shown PBE to display the correct trends.^{48,49} To investigate the effect of tetrazine doping has on the electronic structure, molecular substitutions were manually installed to the

TPDC linker on experimentally determined unit cell of UiO-68, $[(Zr_6O_4(OH)_4)(TPDC)_{24}]$, and both lattice parameters and atomic positions were further relaxed.

Photocatalytic Methyl Viologen Reduction. Photoinduced electron transfer experiments were carried out using MOF dispersions (0.2 mg/mL) in water/methanol mixtures (4:1, v/v%) containing MV^{2+} (0.15 mM). The MOF dispersions containing MV^{2+} were sonicated, placed in a quartz cuvette capped with rubber septum and Ar purged for 15 min prior irradiation with a 300 W Xe lamp. The UV–vis absorbance of the cuvettes was measured at different irradiation times. The photoinduced electron transfer measurements were followed by the decrease of the MV^{2+} absorption band centered at 260 nm as well as the increase of the $MV^{+•}$ radical cation absorption bands at 395 and 605 nm.

Photocatalytic H₂ Production. A quartz photoreactor equipped with a manometer was loaded with sonicated dispersions of the corresponding MOFs at 1 mg/mL concentration in water/methanol (4:1, v/v) mixture. Prior irradiation the dispersions were purged with Ar for 15 min and pressurized at a final pressure of 1.3 bar. The photoreactor was located under the spot UV–vis light of an optic fiber from a 300 W Xe lamp at 110 mW/cm² for 6.5 h. The H₂ evolution was followed by injecting 250 μ L of the reactor gases in an Agilent 490 MicroGC with a TC detector and Ar as carrier gas (MolSieve 5A column). Quantification of the percentage of each gas was based on prior calibration of the system injecting mixtures of H₂ and Ar with known percentage of gases. Quantum efficiency measurements were carried out measuring the lamp photon flux using a calibrated Si diode and taking into account the produced H₂.

■ ASSOCIATED CONTENT

Supporting Information

The Supporting Information is available free of charge at <https://pubs.acs.org/doi/10.1021/jacs.0c09015>.

Synthetic and experimental details; physical characterization and supporting tables and figures (PDF)

Movie S1, confocal images of UiO-68 TZDC3% showing the evolution of the fluorescence across the crystal (MP4)

Movies S2, confocal images of UiO-68 TZDC35% showing the evolution of the fluorescence across the crystal (MP4)

X-ray crystallographic data for UiO-68 (CIF)

X-ray crystallographic data for UiO-68-TZDC (CIF)

■ AUTHOR INFORMATION

Corresponding Authors

Carlos Martí-Gastaldo – *Functional Inorganic Materials Team, Instituto de Ciencia Molecular (ICMol), Universitat de València, 46980 València, Spain*; orcid.org/0000-0003-3203-0047; Email: carlos.marti@uv.es

Natalia M. Padial – *Functional Inorganic Materials Team, Instituto de Ciencia Molecular (ICMol), Universitat de València, 46980 València, Spain*; orcid.org/0000-0001-6067-3360; Email: nmpadial@ugr.es

Authors

Belén Lerma-Berlenga – *Functional Inorganic Materials Team, Instituto de Ciencia Molecular (ICMol), Universitat de València, 46980 València, Spain*

Carolina R. Ganivet – *Functional Inorganic Materials Team, Instituto de Ciencia Molecular (ICMol), Universitat de València, 46980 València, Spain*

Neyvis Almora-Barrios – *Functional Inorganic Materials Team, Instituto de Ciencia Molecular (ICMol), Universitat*

de València, 46980 València, Spain; orcid.org/0000-0001-5269-2705

Sergio Tatay – *Functional Inorganic Materials Team, Instituto de Ciencia Molecular (ICMol), Universitat de València, 46980 València, Spain*; orcid.org/0000-0003-0785-866X

Yong Peng – *Instituto Universitario de Tecnología Química CSIC-UPV, Universitat Politècnica de València, 46022 València, Spain*

Josep Albero – *Instituto Universitario de Tecnología Química CSIC-UPV, Universitat Politècnica de València, 46022 València, Spain*

Oscar Fabelo – *Institut Laue Langevin, Grenoble, Cedex 9 38042, France*; orcid.org/0000-0001-6452-8830

Javier González-Platas – *Departamento de Física, Instituto Universitario de Estudios Avanzados en Física Atómica, Molecular y Fotónica (IUDEA), MALTA Consolider Team, Universidad de La Laguna, La Laguna, Tenerife E-38204, Spain*; orcid.org/0000-0003-3339-2998

Hermenegildo García – *Instituto Universitario de Tecnología Química CSIC-UPV, Universitat Politècnica de València, 46022 València, Spain*; orcid.org/0000-0002-9664-493X

Complete contact information is available at: <https://pubs.acs.org/10.1021/jacs.0c09015>

Notes

The authors declare no competing financial interest.

■ ACKNOWLEDGMENTS

This work was supported by the EU (ERC Stg Chem-fs-MOF 714122) and Spanish government (CTQ2017-83486-P, RTI2018-098568-A-I00, RYC-2016-1981, CEX2019-000919-M, PID2019-106383GB-C44/AEI/10.13039/501100011033 and RTI2018-098568-A-I00). B.L.-B. thanks the Spanish government for a FPU (FPU16/04162). S.T. thanks the Spanish government for a Ramón y Cajal Fellowship (RYC-2016-60719817). N.M.P. thanks the European Union for a Marie Skłodowska-Curie Global Fellowship (H2020-MSCA-IF-2016-GF-749359-EnanSET). J.G.P. thanks to the SIDIX at Servicios Generales de Apoyo a la Investigación (SEGAI) at La Laguna University. We also thank BSC-RES for computational resources (QS-2020-2-0024) and the University of Valencia for research facilities (Tirant and NANBIOSIS).

■ REFERENCES

- (1) Cavka, J. H.; Jakobsen, S.; Olsbye, U.; Guillou, N.; Lamberti, C.; Bordiga, S.; Lillerud, K. P. A New Zirconium Inorganic Building Brick Forming Metal Organic Frameworks with Exceptional Stability. *J. Am. Chem. Soc.* **2008**, *130*, 13850–13851.
- (2) Schaate, A.; Roy, P.; Godt, A.; Lippke, J.; Waltz, F.; Wiebcke, M.; Behrens, P. Modulated Synthesis of Zr-Based Metal-Organic Frameworks: From Nano to Single Crystals. *Chem. - Eur. J.* **2011**, *17*, 6643–6651.
- (3) Furukawa, H.; Cordova, K. E.; O’Keeffe, M.; Yaghi, O. M. The Chemistry and Applications of Metal-Organic Frameworks. *Science* **2013**, *341*, 1230444.
- (4) Yuan, S.; Feng, L.; Wang, K.; Pang, J.; Bosch, M.; Lollar, C.; Sun, Y.; Qin, J.; Yang, X.; Zhang, P.; Wang, Q.; Zou, L.; Zhang, Y.; Zhang, L.; Fang, Y.; Li, J.; Zhou, H.-C. Stable Metal–Organic Frameworks: Design, Synthesis, and Applications. *Adv. Mater.* **2018**, *30*, 1870277.
- (5) Li, W.-Y.; Yang, S.; Li, Y.-A.; Li, Q.-Y.; Guan, Q.; Dong, Y.-B. Synthesis of an MOF-Based Hg²⁺-Fluorescent Probe: Via Stepwise Post-Synthetic Modification in a Single-Crystal-to-Single-Crystal

Fashion and Its Application in Bioimaging. *Dalton Trans.* **2019**, *48*, 16502–16508.

(6) Tan, C.; Han, X.; Li, Z.; Liu, Y.; Cui, Y. Controlled Exchange of Achiral Linkers with Chiral Linkers in Zr-Based UiO-68 Metal-Organic Framework. *J. Am. Chem. Soc.* **2018**, *140*, 16229–16236.

(7) Gui, B.; Hu, G.; Zhou, T.; Wang, C. Pore Surface Engineering in a Zirconium Metal-Organic Framework via Thiol-Ene Reaction. *J. Solid State Chem.* **2015**, *223*, 79–83.

(8) Kim, M.; Cahill, J. F.; Fei, H.; Prather, K. A.; Cohen, S. M. Postsynthetic Ligand and Cation Exchange in Robust Metal-Organic Frameworks. *J. Am. Chem. Soc.* **2012**, *134*, 18082–18088.

(9) Karagiari, O.; Bury, W.; Sarjeant, A. A.; Stern, C. L.; Farha, O. K.; Hupp, J. T. Synthesis and Characterization of Isostructural Cadmium Zeolitic Imidazolate Frameworks via Solvent-Assisted Linker Exchange. *Chem. Sci.* **2012**, *3*, 3256–3260.

(10) Boissonault, J. A.; Wong-Foy, A. G.; Matzger, A. J. Core-Shell Structures Arise Naturally during Ligand Exchange in Metal-Organic Frameworks. *J. Am. Chem. Soc.* **2017**, *139*, 14841–14844.

(11) Castells-Gil, J.; M. Padial, N.; Almora-Barrios, N.; Albero, J.; Ruiz-Salvador, A. R.; Gonzalez-Platas, J.; Garcia, H.; Marti-Gastaldo, C. Chemical Engineering of Photoactivity in Heterometallic Titanium-Organic Frameworks by Metal Doping. *Angew. Chem. Int. Ed.* **2018**, *130*, 8589–8593.

(12) Castells-Gil, J.; M. Padial, N.; Almora-Barrios, N.; da Silva, I.; Mateo, D.; Albero, J.; Garcia, H.; Marti-Gastaldo, C. De Novo Synthesis of Mesoporous Photoactive Titanium(IV)-Organic Frameworks with MIL-100 Topology. *Chem. Sci.* **2019**, *10*, 4313–4321.

(13) M. Padial, N.; Castells-Gil, J.; Almora-Barrios, N.; Romero-Angel, M.; da Silva, I.; Barawi, M.; Garcia-Sanchez, A.; de la Pena O'Shea, V. A.; Marti-Gastaldo, C. Hydroxamate Titanium-Organic Frameworks and the Effect of Siderophore-Type Linkers over Their Photocatalytic Activity. *J. Am. Chem. Soc.* **2019**, *141*, 13124–13133.

(14) Banerjee, R.; Phan, A.; Wang, B.; Knobler, C.; Furukawa, H.; O'Keeffe, M.; Yaghi, O. M. High-Throughput Synthesis of Zeolitic Imidazolate Frameworks and Application to CO₂ Capture. *Science* **2008**, *319*, 939–943.

(15) Clavier, G.; Audebert, P. S-Tetrazines as Building Blocks for New Functional Molecules and Molecular Materials. *Chem. Rev.* **2010**, *110*, 3299–3314.

(16) Jang, H. S.; Jana, S.; Blizzard, R. J.; Meeuwse, J. C.; Mehl, R. A. Access to Faster Eukaryotic Cell Labeling with Encoded Tetrazine Amino Acids. *J. Am. Chem. Soc.* **2020**, *142*, 7245–7249.

(17) Feng, L.; Lo, S.; Wang, S.; Tan, K.; Li, H.; Yuan, S.; Lin, Y.; Lin, C.; Wang, S.; Lu, K.; Zhou, H.-C. An Encapsulation-Rearrangement Strategy to Integrate Superhydrophobicity into Mesoporous Metal-Organic Frameworks. *Matter* **2020**, *2*, 988–999.

(18) Vinu, M.; Sivasankar, K.; Prabu, S.; Han, J.; Lin, C.; Yang, C.; Demel, J. Tetrazine-Based Metal-Organic Frameworks as Scaffolds for Post-Synthetic Modification by the Click Reaction. *Eur. J. Inorg. Chem.* **2020**, *5*, 461–466.

(19) Dodson, R. A.; Wong-Foy, A. G.; Matzger, A. J. The Metal-Organic Framework Collapse Continuum: Insights from Two-Dimensional Powder X-Ray Diffraction. *Chem. Mater.* **2018**, *30*, 6559–6565.

(20) Ayoub, G.; Islamoglu, T.; Goswami, S.; Friščić, T.; Farha, O. K. Torsion Angle Effect on the Activation of UiO Metal-Organic Frameworks. *ACS Appl. Mater. Interfaces* **2019**, *11*, 15788–15794.

(21) Yang, D.; Bernales, V.; Islamoglu, T.; Farha, O. K.; Hupp, J. T.; Cramer, C. J.; Gagliardi, L.; Gates, B. C. Tuning the Surface Chemistry of Metal Organic Framework Nodes: Proton Topology of the Metal-Oxide-Like Zr₆ Nodes of UiO-66 and NU-1000. *J. Am. Chem. Soc.* **2016**, *138*, 15189–15196.

(22) Mondloch, J. E.; Katz, M. J.; Planas, N.; Semrouni, D.; Gagliardi, L.; Hupp, J. T.; Farha, O. K. Are Zr₆-Based MOFs Water Stable? Linker Hydrolysis vs. Capillary-Force-Driven Channel Collapse. *Chem. Commun.* **2014**, *50*, 8944–8946.

(23) Deng, H.; Doonan, C. J.; Furukawa, H.; Ferreira, R. B.; Towne, J.; Knobler, C. B.; Wang, B.; Yaghi, O. M. Multiple Functional Groups

of Varying Ratios in Metal-Organic Frameworks. *Science* **2010**, *327*, 846–850.

(24) Nickerl, G.; Senkovska, I.; Kaskel, S. Tetrazine Functionalized Zirconium MOF as an Optical Sensor for Oxidizing Gases. *Chem. Commun.* **2015**, *51*, 2280–2282.

(25) Marreiros, J.; Caratelli, C.; Hajek, J.; Krajnc, A.; Fleury, G.; Bueken, B.; De Vos, D. E.; Mali, G.; Roeffaers, M. B. J.; Van Speybroeck, V.; Ameloot, R. Active Role of Methanol in Post-Synthetic Linker Exchange in the Metal-Organic Framework UiO-66. *Chem. Mater.* **2019**, *31*, 1359–1369.

(26) Fateeva, A.; Chater, P. A.; Ireland, C. P.; Tahir, A. A.; Khimyak, Y. Z.; Wiper, P. V.; Darwent, J. R.; Rosseinsky, M. J. A Water-Stable Porphyrin-Based Metal-Organic Framework Active for Visible-Light Photocatalysis. *Angew. Chem. Int. Ed.* **2012**, *51*, 7440–7444.

(27) Hendon, C. H.; Tiana, D.; Fontecave, M.; Sanchez, C.; D'Arras, L.; Sasso, C.; Rozes, L.; Mellot-Draznieks, C.; Walsh, A. Engineering the Optical Response of the Titanium-MIL-125 Metal-Organic Framework through Ligand Functionalization. *J. Am. Chem. Soc.* **2013**, *135*, 10942–10945.

(28) Chambers, M. B.; Wang, X.; Ellezam, L.; Ersen, O.; Fontecave, M.; Sanchez, C.; Rozes, L.; Mellot-Draznieks, C. Maximizing the Photocatalytic Activity of Metal-Organic Frameworks with Aminated-Functionalized Linkers: Substoichiometric Effects in MIL-125-NH₂. *J. Am. Chem. Soc.* **2017**, *139*, 8222–8228.

(29) Elcheikh Mahmoud, M.; Audi, H.; Assoud, A.; Ghaddar, T. H.; Hmadeh, M. Metal-Organic Framework Photocatalyst Incorporating Bis(4'-(4-Carboxyphenyl)-Terpyridine)Ruthenium(II) for Visible-Light-Driven Carbon Dioxide Reduction. *J. Am. Chem. Soc.* **2019**, *141*, 7115–7121.

(30) Furukawa, S.; Hirai, K.; Takashima, Y.; Nakagawa, K.; Kondo, M.; Tsuruoka, T.; Sakata, O.; Kitagawa, S. A Block PCP Crystal: Anisotropic Hybridization of Porous Coordination Polymers by Face-Selective Epitaxial Growth. *Chem. Commun.* **2009**, 5097–5099.

(31) Kong, X.; Deng, H.; Yan, F.; Kim, J.; Swisher, J. A.; Smit, B.; Yaghi, O. M.; Reimer, J. A. Mapping of Functional Groups in Metal-Organic Frameworks. *Science* **2013**, *341*, 882–885.

(32) Katzenmeyer, A. M.; Canivet, J.; Holland, G.; Farrusseng, D.; Centrone, A. Assessing Chemical Heterogeneity at the Nanoscale in Mixed-Ligand Metal-Organic Frameworks with the FTIR Technique. *Angew. Chem. Int. Ed.* **2014**, *53*, 2852–2856.

(33) Jayachandrababu, K. C.; Sholl, D. S.; Nair, S. Structural and Mechanistic Differences in Mixed-Linker Zeolitic Imidazolate Framework Synthesis by Solvent Assisted Linker Exchange and de Novo Routes. *J. Am. Chem. Soc.* **2017**, *139*, 5906–5915.

(34) Schrimpf, W.; Jiang, J.; Ji, Z.; Hirschle, P.; Lamb, D. C.; Yaghi, O. M.; Wuttke, S. Chemical Diversity in a Metal-Organic Framework Revealed by Fluorescence Lifetime Imaging. *Nat. Commun.* **2018**, *9*, 1647.

(35) Liu, Q.; Cong, H.; Deng, H. Deciphering the Spatial Arrangement of Metals and Correlation to Reactivity in Multivariate Metal-Organic Frameworks. *J. Am. Chem. Soc.* **2016**, *138*, 13822–13825.

(36) Luo, T.-Y.; Liu, C.; Gan, X. Y.; Muldoon, P. F.; Diemler, N. A.; Millstone, J. E.; Rosi, N. L. Multivariate Stratified Metal-Organic Frameworks: Diversification Using Domain Building Blocks. *J. Am. Chem. Soc.* **2019**, *141*, 2161–2168.

(37) M. Padial, N.; Lerma-Berlanga, B.; Almora-Barrios, N.; Castells-Gil, J.; da Silva, I.; de la Mata, M.; Molina, S. I.; Hernandez-Saz, J.; Platero-Prats, A. E.; Tatay, S.; Mart-Gastaldo, C. Heterometallic Titanium-Organic Frameworks by Metal-Induced Dynamic Topological Transformations. *J. Am. Chem. Soc.* **2020**, *142*, 6638–6648.

(38) Ji, Z.; Li, T.; Yaghi, O. M. Sequencing of Metals in Multivariate Metal-Organic Frameworks. *Science* **2020**, *369* (6504), 674–680.

(39) Gomes Silva, C.; Luz, I.; Llabres i Xamena, F. X.; Corma, A.; Garcia, H. Water Stable Zr-Benzenedicarboxylate Metal-Organic Frameworks as Photocatalysts for Hydrogen Generation. *Chem. - Eur. J.* **2010**, *16*, 11133–11138.

(40) Lin, R.; Shen, L.; Ren, Z.; Wu, W.; Tan, Y.; Fu, H.; Zhang, J.; Wu, L. Enhanced Photocatalytic Hydrogen Production Activity via

Dual Modification of MOF and Reduced Graphene Oxide on CdS. *Chem. Commun.* **2014**, *50*, 8533–8535.

(41) Wang, R.; Gu, L.; Zhou, J.; Liu, X.; Teng, F.; Li, C.; Shen, Y.; Yuan, Y. Quasi-Polymeric Metal-Organic Framework UiO-66/g-C₃N₄ Heterojunctions for Enhanced Photocatalytic Hydrogen Evolution under Visible Light Irradiation. *Adv. Mater. Interfaces* **2015**, *2*, 1500037.

(42) Liu, C.; Zeng, C.; Luo, T.-Y.; Merg, A. D.; Jin, R.; Rosi, N. L. Establishing Porosity Gradients within Metal–Organic Frameworks Using Partial Postsynthetic Ligand Exchange. *J. Am. Chem. Soc.* **2016**, *138*, 12045–12048.

(43) Nasalevich, M. A.; Hendon, C. H.; Santaclara, J. G.; Svane, K.; van der Linden, B.; Veber, S. L.; Fedin, M. V.; Houtepen, A. J.; van der Veen, M. A.; Kapteijn, F.; Walsh, A.; Gascon, J. Electronic Origins of Photocatalytic Activity in d0Metal Organic Frameworks. *Sci. Rep.* **2016**, *6*, 23676.

(44) Kresse, G.; Furthmüller, J. Efficiency of Ab-Initio Total Energy Calculations for Metals and Semiconductors Using a Plane-Wave Basis Set. *Comput. Mater. Sci.* **1996**, *6*, 15–50.

(45) Kresse, G.; Furthmüller, J. Efficient Iterative Schemes for Ab Initio Total-Energy Calculations Using a Plane-Wave Basis Set. *Phys. Rev. B: Condens. Matter Mater. Phys.* **1996**, *54*, 11169–11186.

(46) Perdew, J. P.; Burke, K.; Ernzerhof, M. Generalized Gradient Approximation Made Simple. *Phys. Rev. Lett.* **1996**, *77*, 3865–3868.

(47) Lejaeghere, K.; Bihlmayer, G.; Björkman, T.; Blaha, P.; Blügel, S.; Blum, V.; Caliste, D.; Castelli, I. E.; Clark, S. J.; Dal Corso, A.; de Gironcoli, S.; Deutsch, T.; Dewhurst, J. K.; Di Marco, I.; Draxl, C.; Dulak, M.; Eriksson, O.; Flores-Livas, J. A.; Garrity, K. F.; Genovese, L.; Giannozzi, P.; Giantomassi, M.; Goedecker, S.; Gonze, X.; Grånäs, O.; Gross, E. K.; Gulans, A.; Gygi, F.; Hamann, D. R.; Hasnip, P. J.; Holzwarth, N. A.; Iuşan, D.; Jochym, D. B.; Jollet, F.; Jones, D.; Kresse, G.; Koepnick, K.; Küçükbenli, E.; Kvashnin, Y. O.; Loch, I. L.; Lubeck, S.; Marsman, M.; Marzari, N.; Nitzsche, U.; Nordström, L.; Ozaki, T.; Paulatto, L.; Pickard, C. J.; Poelmans, W.; Probert, M. I.; Refson, K.; Richter, M.; Rignanese, G. M.; Saha, S.; Scheffler, M.; Schlipf, M.; Schwarz, K.; Sharma, S.; Tavazza, F.; Thunström, P.; Tkatchenko, A.; Torrent, M.; Vanderbilt, D.; van Setten, M. J.; Van Speybroeck, V.; Wills, J. M.; Yates, J. R.; Zhang, G. X.; Cottenier, S. Reproducibility in density functional theory calculations of solids. *Science* **2016**, *351*, 1415.

(48) De Vos, A.; Hendrickx, K.; Van Der Voort, P.; Van Speybroeck, V.; Lejaeghere, K. Missing Linkers: An Alternative Pathway to UiO-66 Electronic Structure Engineering. *Chem. Mater.* **2017**, *29*, 3006–3019.

(49) Hendrickx, K.; Vanpoucke, D. E. P.; Leus, K.; Lejaeghere, K.; Van Yperen-De Deyne, A.; Van Speybroeck, V.; Van Der Voort, P.; Hemelsoet, K. Understanding Intrinsic Light Absorption Properties of UiO-66 Frameworks: A Combined Theoretical and Experimental Study. *Inorg. Chem.* **2015**, *54*, 10701–10710.

Supplementary Information

Effect of linker distribution in the photocatalytic activity of multivariate mesoporous crystals

Belén Lerma-Berlanga, Carolina R. Ganivet, Neyvis Almora-Barrios, Sergio Tatay, Yong Peng, Josep Albero, Oscar Fabelo, Javier González-Platas, Hermenegildo García, Natalia M. Padial and Carlos Martí-Gastaldo

Table of contents

Supplementary Information	1
S1. General considerations: starting materials and characterization	4
Materials and reagents.....	4
Physical and chemical characterization.....	4
S2. Synthesis of UiO-68 single crystal by HT exploration	6
S2.1. Synthesis of organic ligands	6
Preparation of [1,1':4',1''-terphenyl]-4,4''-dicarboxylic acid (H ₂ TPDC)	6
Preparation of 4,4'-(1,2,4,5-tetrazine-3,6-diyl)dibenzoic acid (H ₂ TZDC).....	8
S2.2. Synthesis of the materials	9
Optimization of synthetic conditions for the formation of UiO-68 MOFs	9
Synthesis of UiO-68.....	11
Synthesis of UiO-68-TZDC.....	12
S3. Structural characterization of UiO-68 and UiO-68-TZDC	13
S4. Chemical Characterization	16
S4.1. Scanning Electron Microscopy (SEM-EDX)	16
S4.2. Fourier Transformed Infrared Spectroscopy (FT-IR)	18
S4.3. Powder X-Ray Diffraction (PXRD)	19
S4.4. Thermogravimetric Analysis (TG-SDTA)	20
S.4.5. Chemical Stability	20
S4.6. Adsorption isotherms	21
Study of activation process	21
Analysis of N ₂ adsorption/desorption isotherms at 77 K	23
Analysis of CO ₂ adsorption/desorption isotherms.....	25
S5. Multivariate UiO-68: compromise between photoactivity and chemical stability ...	26
S5.1. Characterization of multivariate approach samples (MV_{TZDC:TPDC})	26
Powder X-Ray Diffraction (PXRD) and Fourier Transformed Infrared Spectroscopy (FT-IR).	26
Scanning Electron Microscopy (SEM-EDX).....	28
S5.2. Characterization of UiO-68 TZDC% samples	29
Synthesis of UiO-68-TZDC%	29
¹ H NMR analysis of SALE samples (UiO-68-TZDC%).....	29
Optical images	31
Fourier Transformed Infrared Spectroscopy (FT-IR).....	32
Powder X-Ray Diffraction (PXRD).....	33
Scanning Electron Microscopy (SEM-EDX).....	36
Analysis of N ₂ adsorption/desorption isotherms at 77 K	37

Chemical stability	38
S5.3. Checking the maximum exchanged ratio by 1H NMR and FT-IR.....	39
S5.4. Study of the kinetic's origen of UiO-68-TZDC10%.....	40
Synthesis of UiO-68-TZDC _{10%} (6, 12 24 h)	40
Kinetic change of TZDC content in bulk and on surface as exchange time.....	40
Fourier Transformed Infrared Spectroscopy (FT-IR).....	41
Powder X-Ray Diffraction (PXRD).....	42
Scanning Electron Microscopy (SEM-EDX).....	42
Analysis of N ₂ adsorption/desorption isotherms at 77 K	43
S6. Interplay between linker-controlled sensitization and photocatalytic properties ..	44
S6.1. DFT calculations	44
S6.2. UV-Vis experiments	45
Experimental Optical Band-Gap Calculation.....	45
S7. Spatial arrangement of linkers in the crystal	47
S7.1. Fluorescence microscopy studies	47
S7.2. Confocal microscopy studies	47
External crystal surface analysis	47
Comprehensive analysis of the resultant microstructure in polished crystals	49
S8. Photocatalytic experiments	57
Methyl viologen reduction.....	57
H ₂ production	57
ICP-MS experiments	59
XPS experiments	59
References	60

S1. General considerations: starting materials and characterization

Materials and reagents

Hydrazine monohydrate ($\text{NH}_2\text{NH}_2 \cdot \text{H}_2\text{O}$, >98.0 %), 4-cyanobenzoic acid (>98.0%), *N*-acetyl-L-cysteine (>98%), and *p*-terphenyl (>99.0%) were purchased from TCI Europe. Oxalyl chloride ($\text{C}_2\text{O}_2\text{Cl}_2$, 2.0M solution in dichloromethane), and aluminium chloride (AlCl_3 , anhydrous powder, 98.5%) were purchased from Acros. Zirconium (IV) chloride (ZrCl_4 , anhydrous, 99.99 %), sodium nitrite (NaNO_2 , >99.0%), and carbon disulfide (CS_2 , anhydrous, >99.0) were purchased from Sigma-Aldrich, and used as received. *N,N*-Dimethylformamide (DMF, $\geq 99.8\%$), acetic acid (CH_3COOH), acetone, hexane and methanol ($\geq 99.9\%$) were purchased from Scharlab. Ultrapure water from Milli-Q equipment was used when required. All reagents and solvents were used without any previous purification unless specified.

Physical and chemical characterization

- Elemental analysis (EA): Carbon, nitrogen and hydrogen contents were determined by microanalytical procedures using a LECO CHNS.
- Infrared spectra (IR) were collected in the range $4000\text{--}650\text{ cm}^{-1}$ with an Agilent Cary 630 FTIR Spectrometer equipped with an ATR module.
- Thermogravimetric analysis (TGA) were carried out with a Mettler Toledo TGA/SDTA 851 apparatus between 25 and 600 °C under ambient conditions ($10\text{ °C}\cdot\text{min}^{-1}$ scan rate and an air flow of $30\text{ mL}\cdot\text{min}^{-1}$).
- NMR spectra were recorded on Bruker DRX-500 spectrometer and were calibrated using residual undeuterated solvent ($\text{DMSO-}d_6$ at 2.50 ppm $^1\text{H-NMR}$). The following abbreviations were used to explain multiplicities: s = singlet, d = doublet, t = triplet, q = quartet, m = multiplet, br = broad.
- Solid state MAS-NMRs data were recorded on a Bruker Avance III 400 WB spectrometer with ultrashielded widemouth magnet (89 mm), 400 MHz (9.4 T).
- X-Ray Diffraction (XRD) patterns were collected in a PANalytical X'Pert PRO diffractometer using copper radiation ($\text{Cu K}\alpha = 1.5418\text{ \AA}$) with an X'Celerator detector, operating at 40 mA and 45 kV. Profiles were collected in the $2^\circ < 2\theta < 40^\circ$ range with a step size of 0.017° .
- Power X-Ray Diffraction (PXRD) patterns for refinement were collected for polycrystalline samples using a 0.5 mm glass capillary mounted and aligned in a PANalytical Empyrean diffractometer (Bragg-Brentano geometry) using copper radiation ($\text{Cu K}\alpha = 1.5418\text{ \AA}$) with an PIXcel detector, operating at 40 mA and 45 kV. Profiles were collected by using a Soller Slit of 0.02° and a divergence slit of $\frac{1}{4}$ at room temperature in the angular range $3^\circ < 2\theta < 40^\circ$ with a step size of 0.017° . LeBail refinements were carried out with the FULLPROF software package.
- Optical images were acquired with a NIKON Eclipse LV-100 optical microscope.
- Scanning Electron Microscopy (SEM): particle morphologies and dimensions were studied with a Hitachi S4800 scanning electron microscope at an accelerating voltage of 20 kV, over metalized samples with a mixture of gold and palladium for 90 seconds.
- Confocal microscope: the incorporation of the fluorescent linker (H_2TZDC) on UiO-68 TZDC% samples were analysed by confocal microscope Olympus FV1000 mounted on a motorized inverted IX81. The 40x objective was used and the excitation line were 405 and 559 nm.
- The emission and excitation spectrums were collected by a spectrofluorometer Fluoromax Horiba-MTB.

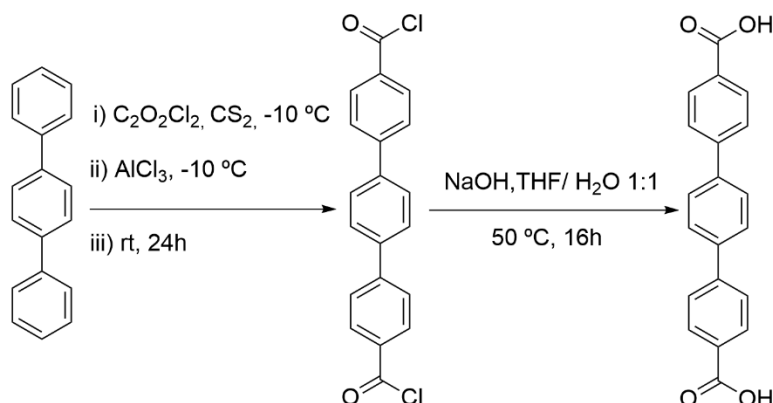
- UV-Vis diffuse reflectance spectroscopy (DRS) was performed on a Jasco V-670 spectrophotometer using an integrated Labsphere in the range 200-800 nm.
- The Raman studies were done using a Raman emission spectrometer Horiba-MTB Xplora. Using a confocal microscopy to guide the spotlight. The excitation line was 785 nm and the diffraction net X lines/mm. The detector was a CCD cooling by Peltier effect.
- Gas adsorption measurements were recorded on a Micromeritics 3Flex apparatus at relative pressures up to 1 atm. As N₂ adsorption, the 5 days hexane dried sample was degassed overnight at 60 °C and 10⁻⁶ Torr prior to analysis. A Micromeritics' ISO Controller was used to keep the temperature constant for the CO₂ adsorption measurements at 273, 283 and 293 K. The isosteric heats of adsorption were determined by means of the Clausius-Clapeyron equation as implemented in the MicroActive Analysis Software using the CO₂ isotherms recorded at 273, 283 and 293 K.
- Survey X-Ray Photoelectron Spectroscopy (XPS) was performed on a thermo scientific K alpha X-ray photoelectron spectrometer, using a type of radiation: monochromatized Al K-alpha radiation (1486.6 eV) at 4*10⁻⁹ mBar. XPS was used to determine the quantitative concentration of the linkers at the surface of the crystals. The nitrogen present can associate with TZDC quantity. We used the integrated areas of N_{1s} and Zr_{3d} to obtain the ratio N/Zr in each case. To analyze the surface of a single crystal the spot size used was 50 μm. The number of scans was adjusted depending on the element and sample.

S2. Synthesis of UiO-68 single crystal by HT exploration

S2.1. Synthesis of organic ligands

Preparation of [1,1':4',1''-terphenyl]-4,4''-dicarboxylic acid (H_2TPDC)

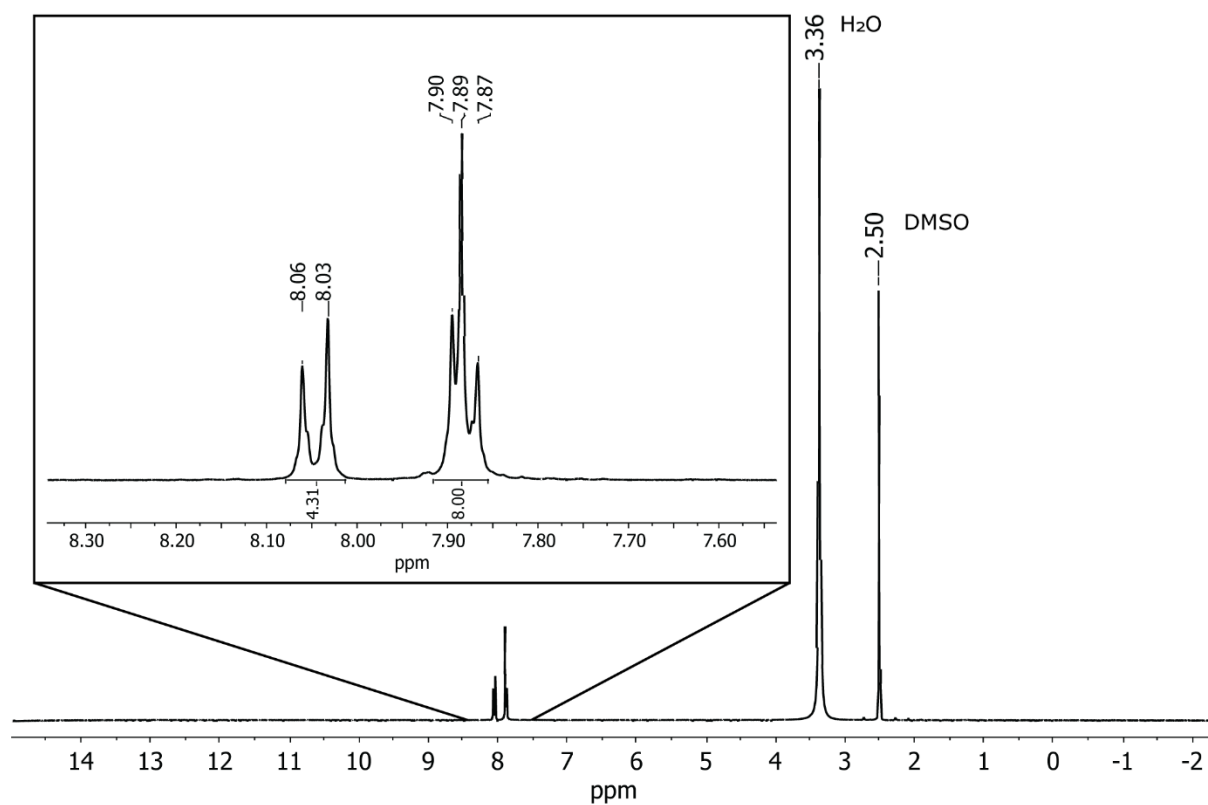
The ligand was isolated following the synthesis previously described by Wöll,¹ shown in the next scheme.



Scheme S1. Synthesis of H_2TPDC ligand.

A 2M solution of oxalyl chloride (6.0 equiv., 52.10 mmol, 26.05 mL) was added to a solution of *p*-terphenyl (1.0 equiv., 8.68 mmol, 2.00 g) in anhydrous CS_2 (30 mL) at $-10\text{ }^\circ C$ (ethylene glycol/ $CO_2(s)$ bath). Then, anhydrous $AlCl_3$ (1.7 equiv., 14.75 mmol, 1.97 g), and after 1h of stirring, additional anh. $AlCl_3$ (1.0 equiv., 8.68 mmol, 1.16 g) was added. Subsequently, the cooling bath was removed, and the reaction mixture was stirred for 24h at room temperature. After that, the mixture was poured into crushed ice and stirred until the dark-brown mixture turned to yellow. Organic solvents were removed under reduced pressure, and the resulting aqueous suspension was filtered and washed with water (3x40 mL), dried and used in the next step without any further purification. Next, the crude was added to a 150 mL of NaOH solution (7.0 equiv., 60.76 mmol, 2.43 g) in THF/ H_2O (1:1 vol/vol.) at room temperature. The mixture was stirred vigorously at $50\text{ }^\circ C$ during 16h. Then, the solution was cooled down to room temperature, THF was removed under reduce pressure and a pale-yellow solid was formed. The aqueous suspension was stirred and carefully acidified until $pH < 2$ by dropwise addition of concentrated HCl. The resulting precipitate was collected by filtration, washed with water until neutral pH and dried under vacuum during 12h at $60\text{ }^\circ C$. A pale yellow solid with a yield of 96% (8.33 mmol, 2.65g), was obtained. 1H NMR (300 MHz, $DMSO-d_6$) δ : 7.98 (d, $J = 8.4$ Hz, 4H), 7.81 (s, 4H), 7.73 (d, $J = 8.5$ Hz, 4H), ^{13}C NMR (75 MHz, $DMSO-d_6$) δ : 167.1, 143.5, 138.8, 130.0, 129.8, 127.6, 126.8.

^1H NMR



^{13}C NMR

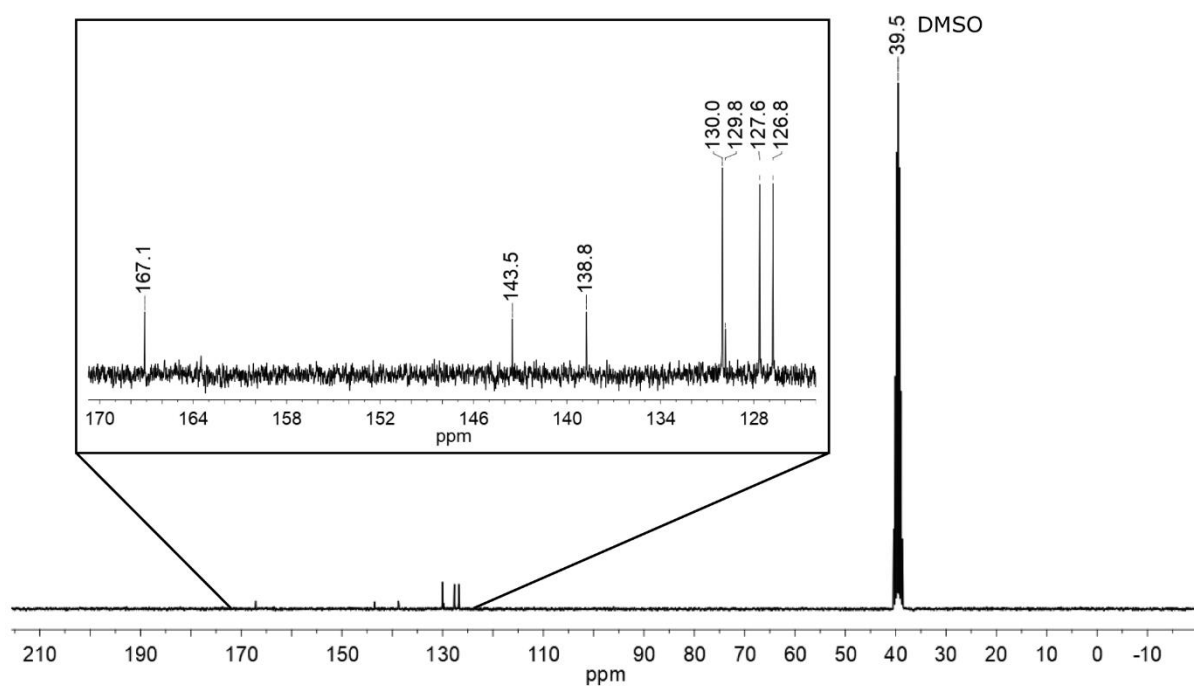
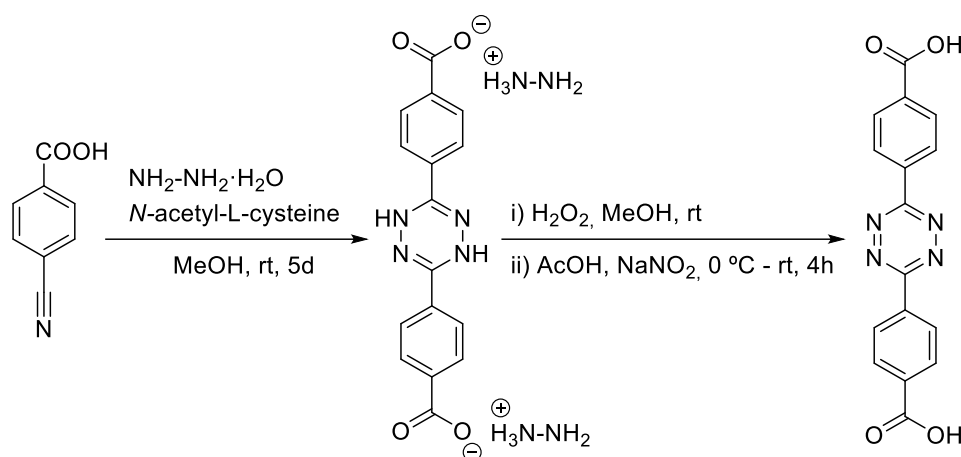


Figure S1. ^1H NMR spectrum of compound H_2TPDC in $\text{DMSO-}d_6$ (top) and ^{13}C NMR spectrum of compound H_2TPDC in $\text{DMSO-}d_6$ (bottom).

Preparation of 4,4'-(1,2,4,5-tetrazine-3,6-diyl)dibenzoic acid (H₂TZDC)

Synthesis of H₂TZDC linker, as depicted below, was carried out following the procedure reported by Rodriguez-Diequez² with some modifications.



Scheme S2. Synthesis of H₂TZDC.

Hydrazine monohydrate (4.0 equiv., 27.2 mmol, 1.32 mL) was added dropwise to a solution of 4-cyanobenzoic acid (1.0 equiv., 6.8 mmol, 1.0 g) and N-acetyl-L-cysteine (1.0 equiv., 6.8 mmol, 1.12 g) in MeOH (12.5 mL) at room temperature under Ar atmosphere. The resulting mixture was stirred at room temperature for 5 days. Then, the yellowish solid formed was collected by filtration, washed with methanol (3x30 mL) and dried under vacuum to afford 1.10 g of the dihydrotetrazine derivative. After that, the solid was re-suspended in MeOH (35 mL) and a H₂O₂ solution (20 mL) was added dropwise at rt. After 1 day of stirring at this temperature, the purple solid formed was collected by filtration and washed with methanol (50 mL). Then, the solid was suspended in acetic acid (20 mL) and completely oxidized after the addition of an aqueous solution of NaNO₂ (3.0 equiv., 20.4 mmol, 1.41 g in 30 mL) at 0 °C (ice/salt bath). Once the evolution of brown nitric oxide gas was finished (approx. 4h of stirring at room temperature), the deep purple solid in the suspension was filtered off, washed with water (2x20 mL) and finally dried to afford 0.99 g (yield: 90% based on 4-cyanobenzoic acid) of ligand H₂TZDC. ¹³C NMR (100 MHz, solid state CP-MAS) δ pm: 173.6, 163.5, 153.8, 131.5-128.3. The values are according to the reported ones.

^{13}C NMR

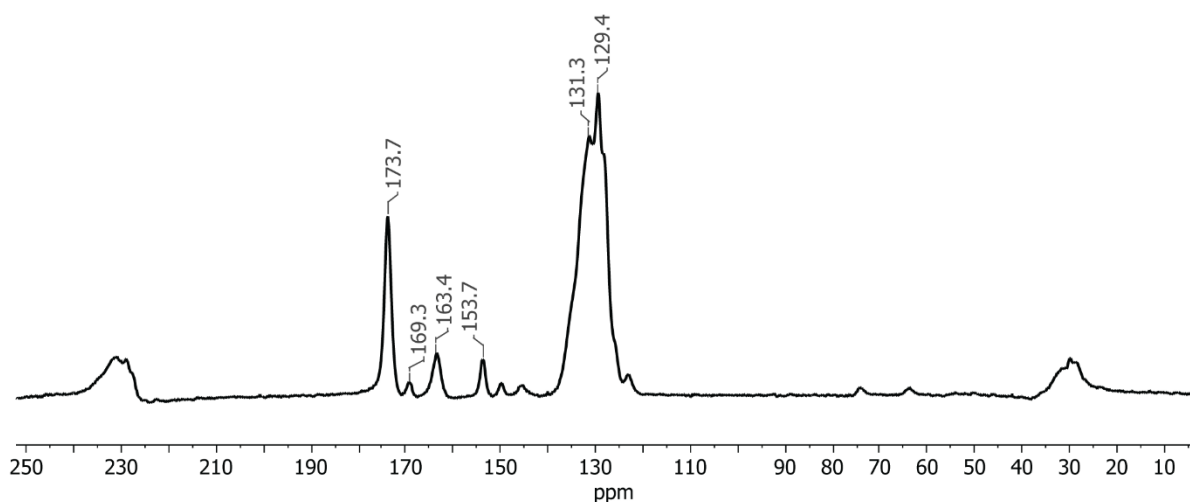


Figure S2. ^{13}C CP/MAS NMR spectrum of compound H_2TZDC in solid state.

S2.2. Synthesis of the materials

Optimization of synthetic conditions for the formation of UiO-68 MOFs

For the optimization of the reaction conditions, we made use of a FLEX SHAKE high-throughput workstation from Chemspeed© for robotic dispensing of solids and liquids. The optimization was carried out by screening different reaction parameters such as temperature, solvent, modulator nature, amount of modulator, concentration, and reaction time. The explored variables were reflected in the table below.

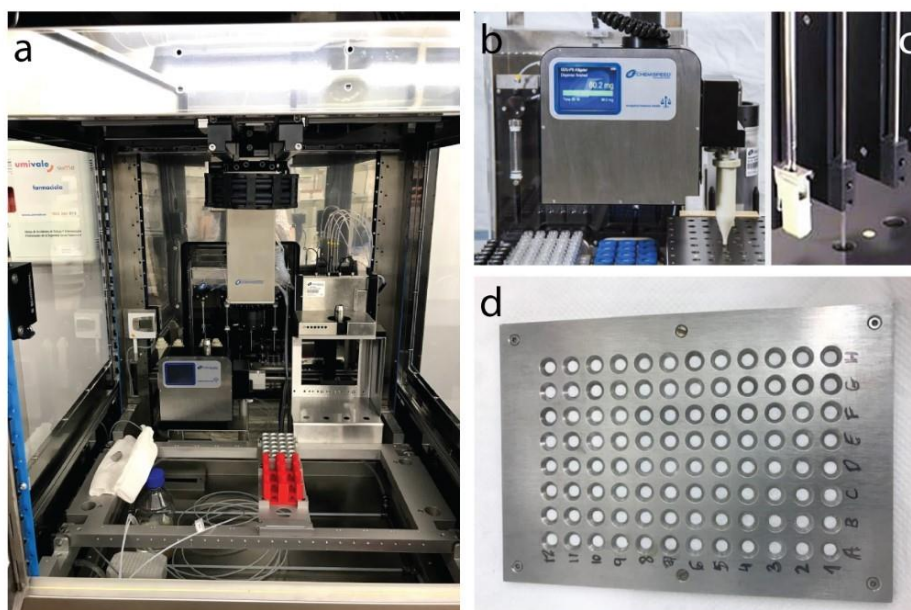


Figure S3. (a) FLEX SHAKE high-throughput workstation from Chemspeed© equipped with complements for the automated dispensing of (b) solids and (c) liquids. (d) 96 multi-well diffraction plate used for accelerating PXRD data collection.

Table S1. Summary of the synthetic conditions explored with automated HT synthesis to identify crystal forming conditions. The optimum conditions for UiO-68 are highlighter in yellow and for UiO-68-TZDC in pink.

Mod's nature	Mod (eq)	T ^a (°C)	Time (h)
TFA	0	120	48
TFA	3	120	48
TFA	5	120	48
TFA	10	120	48
TFA	30	120	48
TFA	48	120	48
TFA	77	120	48
TFA	100	120	48
TFA	117	120	48
TFA	165	120	48
TFA	203	120	48
TFA	242	120	48
TFA	170	120	48
TFA	210	120	48
TFA	250	120	48
TFA	0	100	48
TFA	5	100	48
TFA	10	100	48
TFA	30	100	48
TFA	35	100	48
TFA	60	100	48
TFA	80	100	48
TFA	5	100	48
TFA	20	100	48
TFA	40	100	48
FA	17	100	48
FA	20	100	48
FA	22	100	48
FA	26	100	48
FA	40	100	48
BA	3	100	48
BA	8	100	48
BA	13	100	48
BA	23	100	48
BA	33	100	48
BA	53	100	48
AcOH	3	100	48
AcOH	8	100	48
AcOH	13	100	48
AcOH	23	100	48

Mod's nature	Mod (eq)	T ^a (°C)	Time (h)
TFA	0	100	72
TFA	5	100	72
TFA	10	100	72
TFA	17	100	72
TFA	20	100	72
TFA	30	100	72
TFA	40	100	72
TFA	50	100	72
TFA	80	100	72
TFA	100	100	72
TFA	120	100	72
TFA	150	100	72
TFA	170	100	72
TFA	210	100	72
TFA	250	100	72
AcOH	5	100	72
AcOH	7	100	72
AcOH	15	100	72
AcOH	20	100	72
AcOH	28	100	72
AcOH	37	100	72
AcOH	42	100	72
AcOH	78	100	72
BA	3	100	72
BA	8	100	72
BA	13	100	72
BA	23	100	72
BA	33	100	72

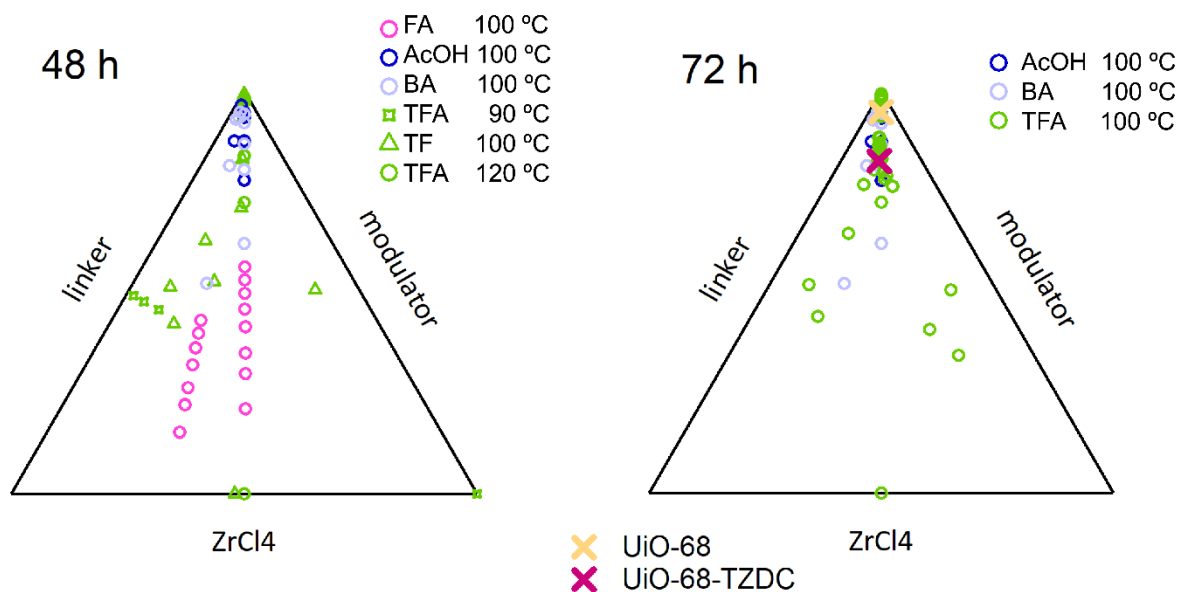


Figure S4. Tri-plots of the explored conditions of UiO-68 and UiO-68-TZDC for 48 h and 72 h. Each condition is marked with different coloured shaped. FA = formic acid, AcOH = acetic acid, BA = benzoic acid, TFA = trifluoroacetic acid. The optimum conditions for the synthesis of UiO-68 crystals are marked with a yellow cross and for UiO-68-TZDC with a pink one.

Synthesis of UiO-68

H₂TPDC (18 mg; 0.055 mmol) was suspended in a mixture of 3.5 mL of *N,N*-dimethylformamide and 150 μ L of TFA (40 equiv.) in a 5 mL Teflon vial. Subsequently, the ZrCl₄ (12 mg; 0.051 mmol) was added to the suspension. The bottle was sealed and heated in an oven at 100 $^{\circ}$ C for 72 hours. After cooling down to room temperature, this results in the formation of deep yellow octahedral crystals that were isolated by centrifugation and washed with 45 mL of DMF (3x15 mL) and 45 mL of methanol (3x15 mL) in the centrifuge tube. The product was soaked in hexane for 3 days, after that it was dried at room temperature. Elemental analysis for [Zr₆O₄(OH)₄(C₂₀H₁₂O₄)₆]: Calc. %: C (55.93), H (2.97), N (0); found %: C (52.96), H (3.25), N (0.87).

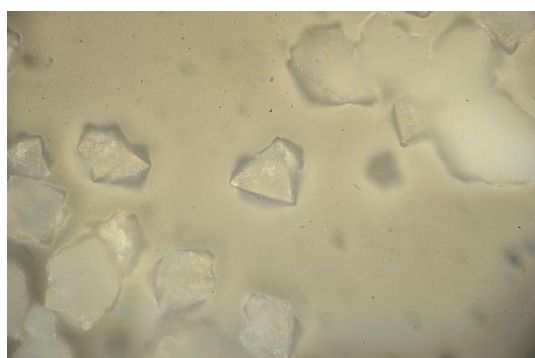


Figure S5. Picture of as-made crystals of UiO-68 acquired with an optical microscope. Picture displays their hexagonal morphology and micrometric size (close to 50 μ m).

Synthesis of UiO-68-TZDC

H₂TZDC (18 mg; 0.055 mmol) was suspended in a mixture of 3.5 mL of *N,N*-dimethylformamide and 40 μL of TFA (10 equiv.) in a 5 mL Teflon vial. Subsequently, the ZrCl₄ (12 mg; 0.051 mmol) was added to the suspension. The bottle was sealed and heated in an oven at 100 °C for 72 hours. After cooling down to room temperature, this results in the formation of deep pink octahedral crystals that were isolated by centrifugation and washed with 45 mL of DMF (3x15 mL) and 45 mL of methanol (3x15 mL) in the centrifuge tube. The product was soaked in hexane for 7 days, after that it was dried at room temperature. Elemental analysis for [Zr₆O₄(OH)₄(C₁₆H₈N₄O₄)₆]: Calc. %: C (44.33), H (2.02), N (12.92); found %: C (45.68), H (2.47), N (11.16).

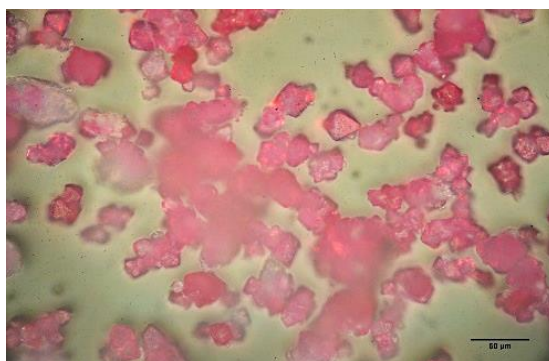


Figure S6. Picture of as-made crystals of UiO-68-TZDC acquired with an optical microscope. Pictures displays their hexagonal morphology and micrometric size (close to 20 μm).

S3. Structural characterization of UiO-68 and UiO-68-TZDC

A single light-yellow rhombohedral crystal (UiO-68) with dimensions 0.08 × 0.05 × 0.04 mm³ was selected and mounted on a Bruker D8 Advance diffractometer with Photon III as detector and Cu K_α radiation (λ=1.54184 Å) and collecting data at 100(1) K using APEX3 software for collecting data. Images were converted to Esperanto format in order to be used for CrysAlis Pro for data reduction, scale and absorption correction. A pink crystal of compound UiO68 TZDC with dimensions 0.05 × 0.03 × 0.03 mm³ was measured in a Rigaku SuperNova diffractometer equipped with Atlas CCD detector using Cu K_α radiation (λ=1.54184 Å) at room temperature. CrysAlisPro software was used to collect, index, scale and apply Numerical absorption correction based on Gaussian integration over a multifaceted crystal model.

The structures were solved with the **ShelXT** 2018/2 (Sheldrick, 2018) solution program using dual methods and by using **Olex2** (Dolomanov et al., 2009) as the graphical interface. The model was refined with **ShelXL** 2018/3 (Sheldrick, 2015) using full matrix least squares minimisation on R^2 . Hydrogen atoms have been placed in geometrically suitable positions and refined riding with isotropic thermal parameter related to the equivalent isotropic thermal parameter of the parent atom. In both cases, the organic linker presents a certain degree of disorder, mainly in the central ring. Any attempt to model this disorder has been unsuccessful. Crystallographic data for structures reported in this contribution have been deposited with the Cambridge Crystallographic Data Centre as supplementary publication CCDC 2023345-2023346.

Table S2. Crystallographic data of UiO-68 and UiO-68-TZDC

Compound	UiO-68	UiO-68-TZDC
Identification code	CCDC_2023346	CCDC_2023345
Empirical Formula	C ₆₀ H ₃₆ O ₁₆ Zr ₃	C ₄₈ H ₂₄ N ₁₂ O ₁₆ Zr ₃
Formula Weight	1286.55	1298.45
<i>T</i> /K	100(1)	293(2)
Crystal System	cubic	cubic
Space Group	<i>Fm-3m</i>	<i>Fm-3m</i>
<i>a</i> /Å	32.70790 (10)	32.4741 (5)
<i>b</i> /Å	32.70790 (10)	32.4741 (5)
<i>c</i> /Å	32.70790 (10)	32.4741 (5)
α /°	90	90
β /°	90	90
γ /°	90	90
<i>V</i> /Å ³	34991.1 (3)	34246.1 (16)
<i>Z</i>	8	8
$\rho_{calc.}$ / g cm ⁻³	0.488	0.504
μ /mm ⁻¹	1.627	1.686
Crystal size/mm ³	0.08×0.05×0.04	0.05×0.03×0.03
Radiation	Cu K _α (λ=1.54184)	Cu K _α (λ = 1.54184)
<i>Q</i> range/ °	4.484 to 66.945	4.516 to 58.864
Reflections collected	24057	4825
Independent reflections	1582 <i>R</i> _{int} = 0.0666	1269 <i>R</i> _{int} = 0.0442
Refl's with <i>I</i> > 2(<i>I</i>)	1416	1039
Parameters/ restraints	47/ 35	48/ 36
Largest Peak / hole e·Å ⁻³	1.46/ -1.32	0.56/ -0.66
Goodness-of-fit on <i>F</i> ²	1.188	1.151
Final <i>R</i> indexes [<i>I</i> ≥ 2σ (<i>I</i>)]	<i>R</i> ₁ =0.0880, <i>wR</i> ₂ =0.2485	<i>R</i> ₁ =0.0469, <i>wR</i> ₂ =0.1286
Final <i>R</i> indexes [all data]	<i>R</i> ₁ =0.0925, <i>wR</i> ₂ =0.2592	<i>R</i> ₁ =0.0621, <i>wR</i> ₂ =0.1386

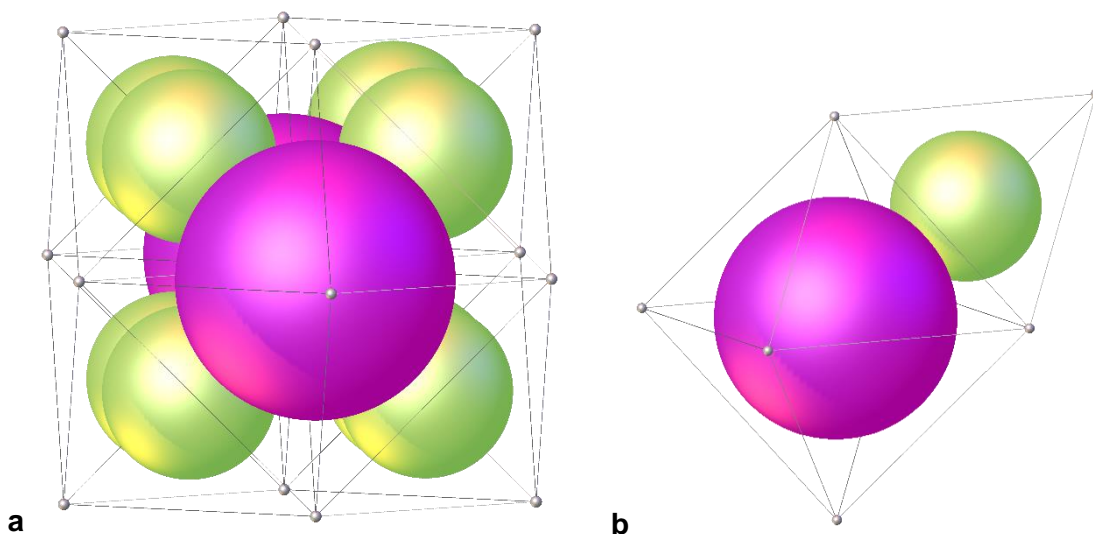


Figure S7. a) Fcu network topology constructed from cuboctahedral 12-c Zr_6O_8 -core SBU (grey dots) and linear ditopic linkers (grey lines). b) Octahedral pores (deep yellow sphere) is surrounded by eight tetrahedral ones (pink sphere) in a face-sharing manner.

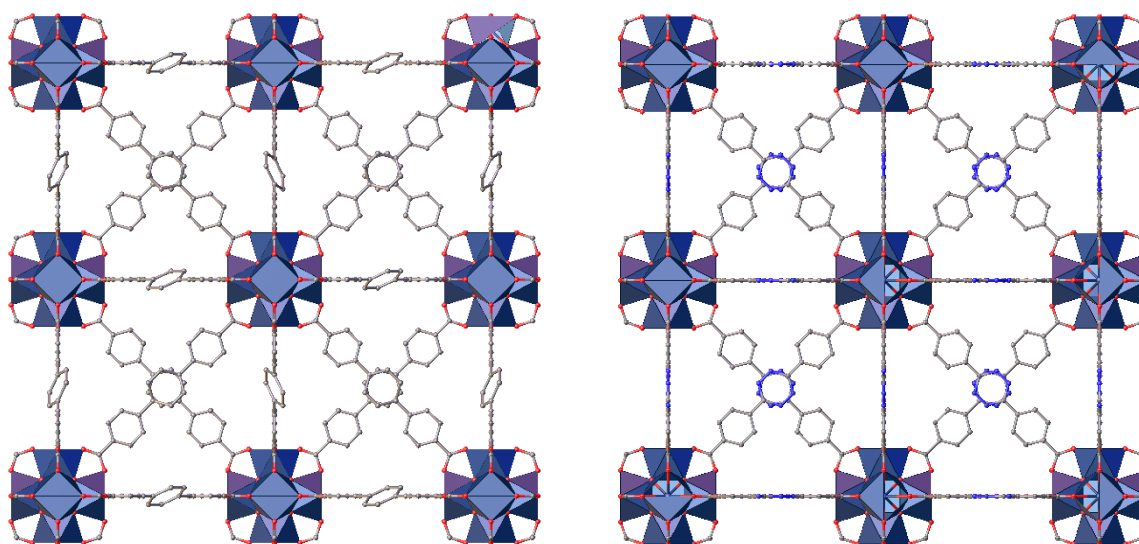


Figure S8. a) View (001) of the structure of UiO-68 (left) and b) View (001) of the structure UiO-68-TZDC (right). Colour code: C (grey), O (red), N(blue), Zr (dark blue). H atoms are omitted for clarity.

Table S3. Summary of the significant distances for chemical stability comprehension.

	UiO-68	UiO-68-TZDC
Zr-O_{oxo} (Å)	2.135 (3)	2.143 (3)
Zr-O_{carboxylate} (Å)	2.199 (4)	2.226 (3)
C-O_{carboxylate} (Å)	1.271 (6)	1.278 (4)

S4. Chemical Characterization

S4.1. Scanning Electron Microscopy (SEM-EDX)

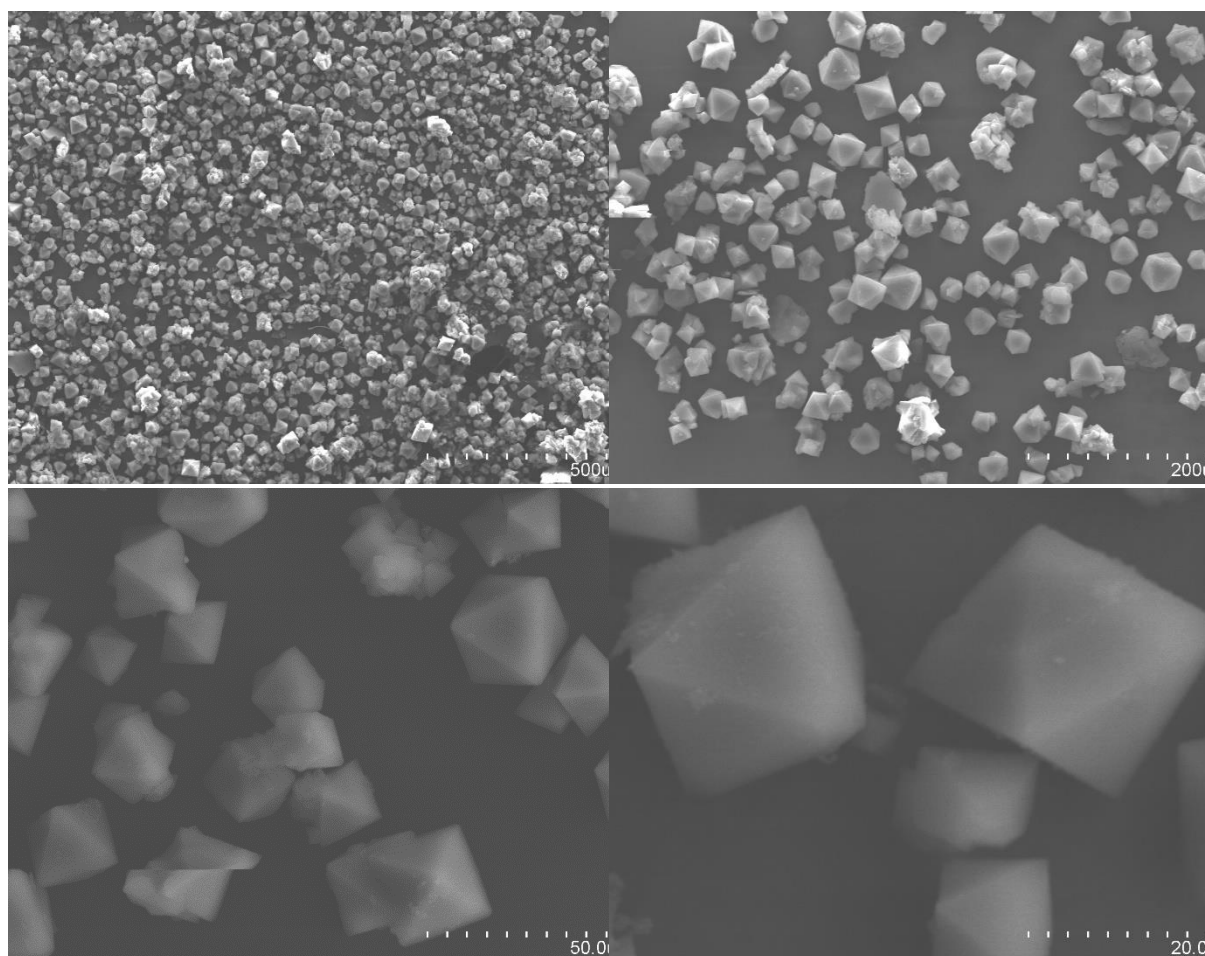


Figure S9. Scanning Electron Microscopy (SEM) images of octahedral crystals of UiO-68 confirm the particle size is around 50 μm .

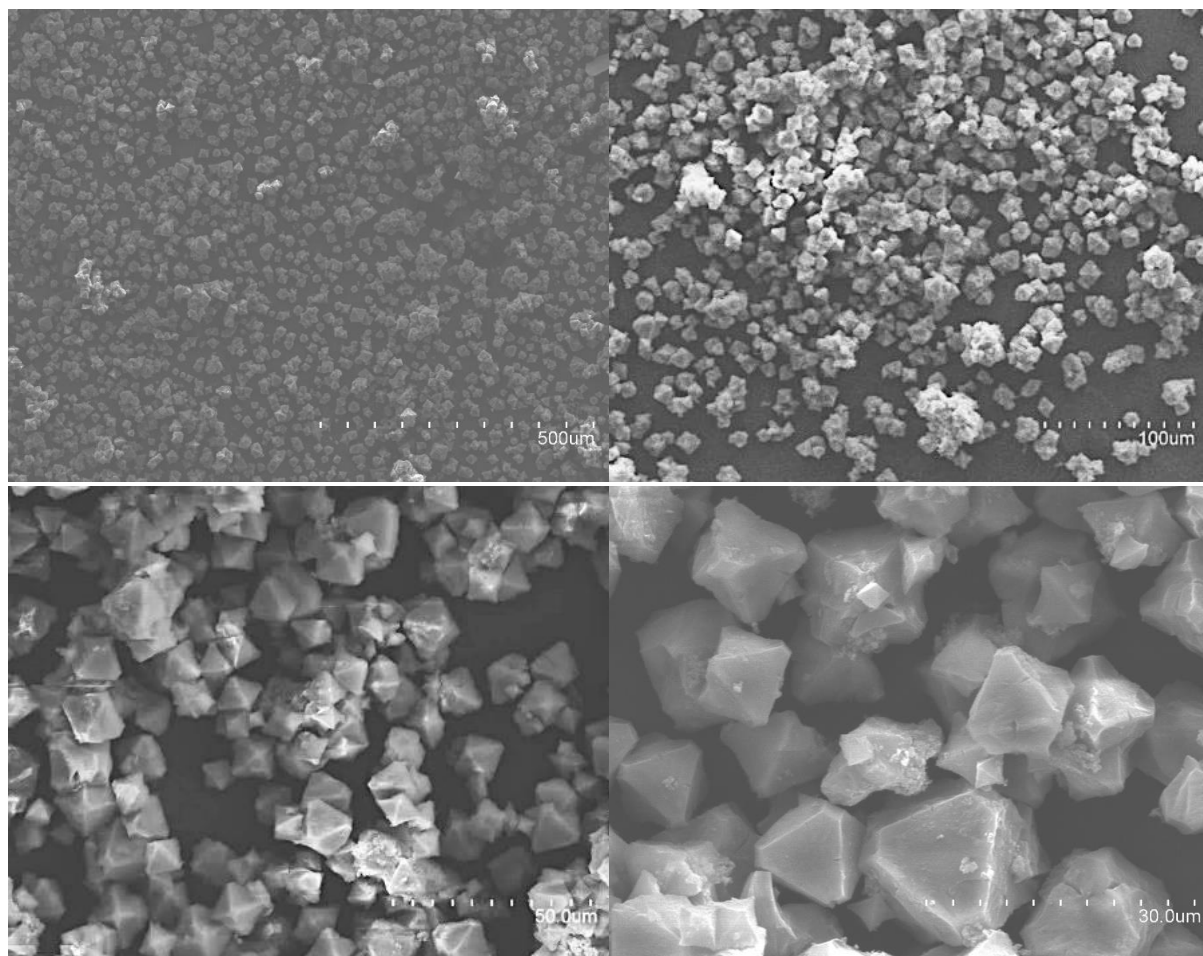


Figure S10. Scanning Electron Microscopy (SEM) images of octahedral crystals of UiO-68-TZDC. Lower magnification confirms the formation the homogeneity of the sample. Higher magnification confirms the particle size is around 20 μm .

S4.2. Fourier Transformed Infrared Spectroscopy (FT-IR)

FT-IR spectra of MOFs after hexane exchanged (UiO-68 and UiO-68 TZDC) and free linkers were collected in the range 4000-650 cm^{-1} . Compared to the free linkers, the IR spectrums of UiO-68 show a shift to lower frequencies of the C=O stretching (1675 cm^{-1}) confirming their coordination in the framework.

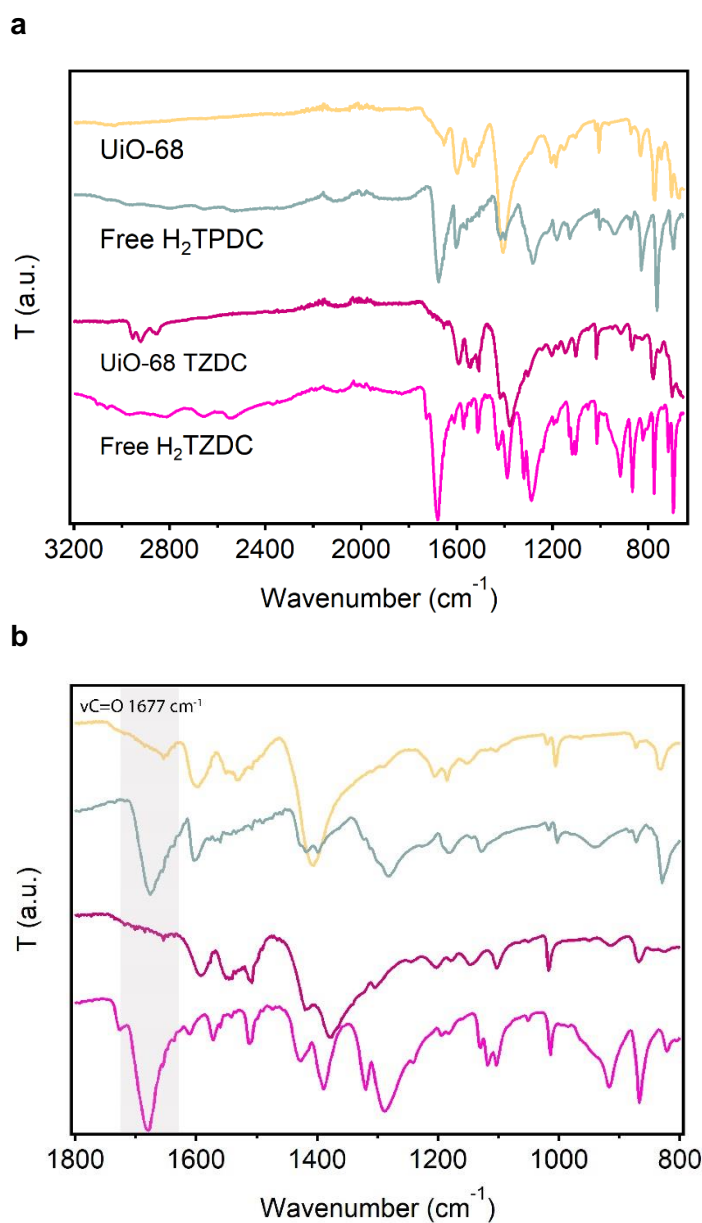


Figure S11. a) Full FT-IR spectra of UiO-68 MOF after hexane exchange and free linkers, UiO-68 (pale yellow), UiO-68-TZDC (deep pink), free H₂TPDC (grey) and free H₂TZDC (purple). b) Magnification of the shift on C=O stretching band from 1677 cm^{-1} for the free linkers to 1655 cm^{-1} for the MOF, rule the presence of unreacted linker out (semi-transparent box).

S4.3. Powder X-Ray Diffraction (PXRD)

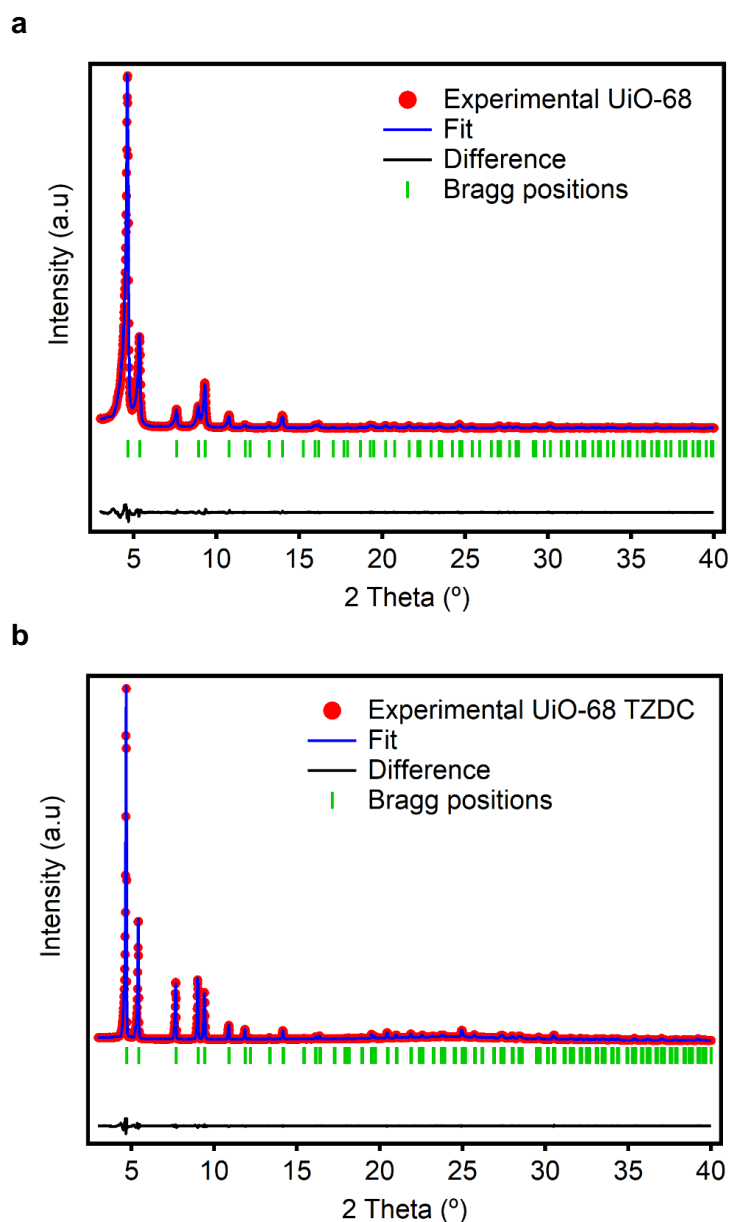


Figure S12. Experimental (red dots), calculated (blue line), difference plot [(I_{obs}–I_{calc})] (black line, bottom panel) and Bragg positions (green ticks, bottom panel) for the LeBail refinement of experimental diffraction data of UiO-68 (top) and UiO-68-TZDC (bottom) collected at room temperature by using the single crystal data as starting parameters.

Table S4. Summary of the parameters obtained from LeBail refinement.

	a=b=c (Å)	V (Å ³)	R _e (%)	R _p (%)	R _{wp} (%)	gof
UiO-68	32.85635	35470	3.49	4.63	6.35	1.82
UiO-68-TZDC	32.48814	34291	1.77	2.37	3.63	2.05

S4.4. Thermogravimetric Analysis (TG-SDTA)

UiO-68 shows a first weight loss below 160 °C due to the removal of DMF molecules occluded in the pores, which were not exchanged by hexane. The decomposition of the framework takes place above 470 °C to form 30.7% of ZrO₂ (Calc.: 28.5 %). UiO-68 TZDC shows a gradual decomposition begins at 250°C up to 450°C to form 28.7% of ZrO₂ (Calc.:28.4%).

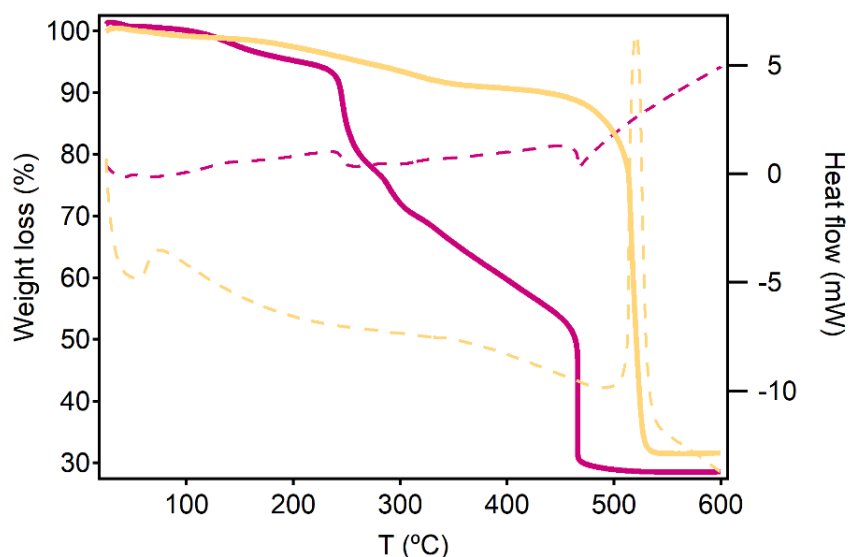


Figure S13. Thermogravimetric analysis (TGA) of hexane exchanged UiO-68 materials.

S.4.5. Chemical Stability

The hydrolytical stability of the solids was evaluated by incubation in water for 24 hours. The PXRDs after this treatment suggest that the structure of UiO-68 remains intact whereas UiO-68-TZDC undergoes partial amorphization.

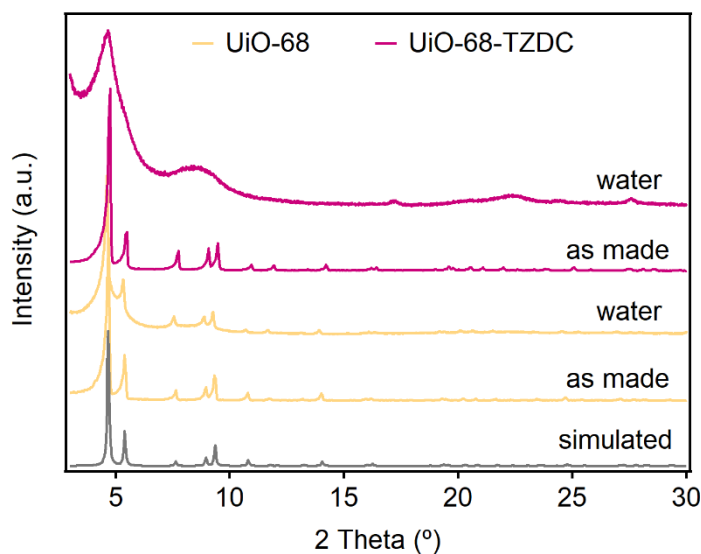


Figure S14. PXRD of the solids as made and after soaked in water for 24 hours.

S4.6. Adsorption isotherms

Study of activation process

To remain porosity of the frameworks the selection of suitable solvent for exchanged as-made sample is crucial. Our first approach was analyzed the samples' sensitivity to solvent exchange. A range of solvents were carefully selected to address a range of properties that could influence MOF stability such as polarity, surface tension or propensity for hydrogen bonding. The solvent's tested were collected in **table S5**, water was used as reference. UiO-68 and UiO-68-TZDC were soaking during 5 days in the solvent. Then, the solvent was removed and PXRD were collected (**Fig. S15a** and **Fig. S15b**).

The role of the humidity in the solvent removal process was evaluated for highest sensitive sample, UiO-68-TZDC. The 5d hexane exchange sample was dried under air and under anhydrous conditions, the PXRD were collected. (**Fig. S15c**). The sample activated under anhydrous conditions revealed high crystallinity. This effect was also shown using MeOH as exchanged solvent.

Table S5. Summary of the parameters of solvents³ used in MOF synthesis and for activation process.

Solvent	Polarity	Dipole moment (D)	Surface tension (mN/m) at 25°C
H₂O	10.2	1.87	72.7
DMF	6.4	3.86	34.4
MeOH	5.1	2.87	22.1
Acetone	5.1	2.69	23.0
Hexane	0.1	0.08	17.9

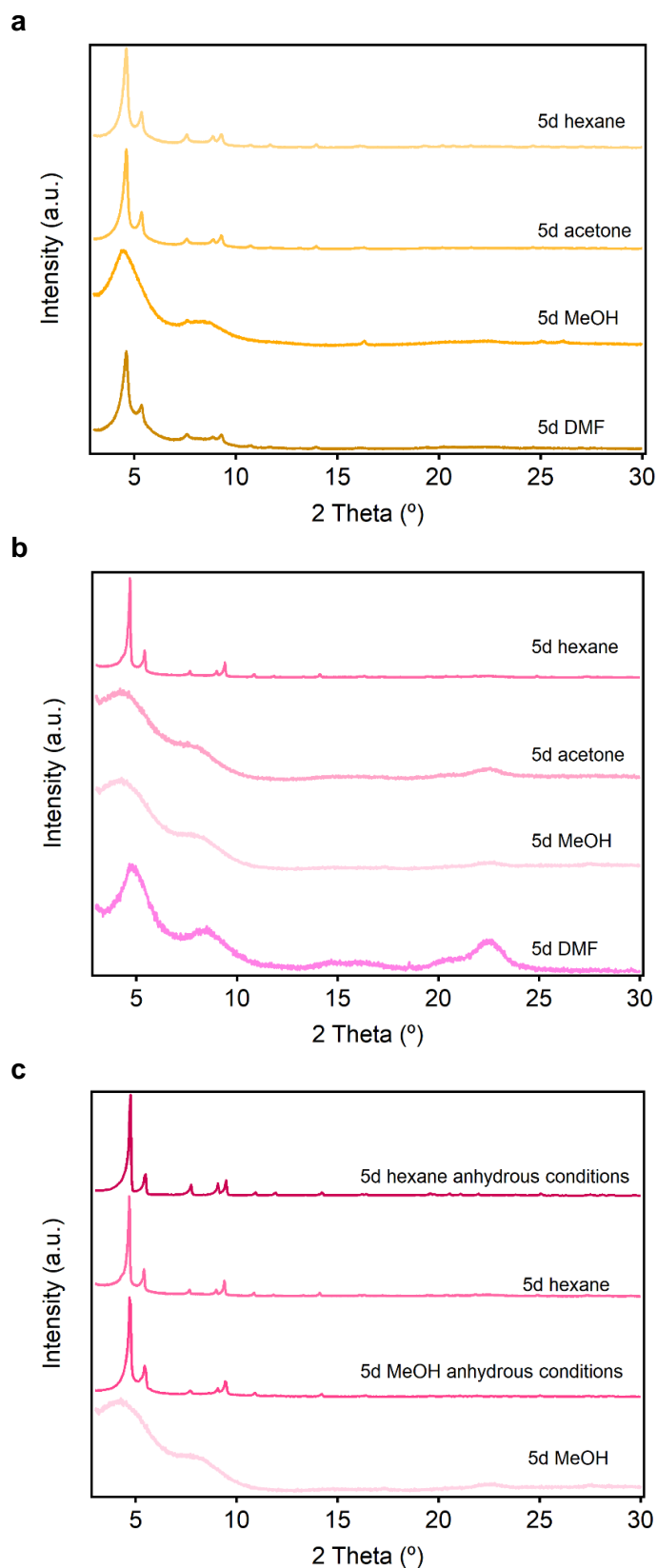


Figure S15. a) XRD patterns of UiO-68 after solvent exchanged process. b) XRD patterns of UiO-68-TZDC after solvent exchanged process. c) XRD patterns of UiO-68-TZDC after solvent exchanged process under anhydrous conditions to study the role of the humidity in the solvent removal process.

Analysis of N₂ adsorption/desorption isotherms at 77 K

Gas adsorption measurements were performed ex situ on exchanged UiO-68 solids. Surface area, pore size and volume values were calculated from nitrogen adsorption-desorption isotherms (77 K) recorded on a Micromeritics 3Flex apparatus. Exchanged samples were degassed overnight at 60 °C and 10⁻⁶ Torr overnight prior to analysis. Brunauer-Emmett-Teller (BET) Surface area analysis was performed as recommended for microporous and mesoporous materials.

Table S6. Summary of the adsorption analysis.

	UiO-68	UiO-68-TZDC
BET surface area (m²·g⁻¹) at P/P₀ = 0.01-0.08	4028	4289
Total pore volume (cm³·g⁻¹) at P/P₀ = 0.96	1.63	1.66
Pore width (Å)	20, 30	21, 29
Theoretical pore size from CIFs (Å)	19.63, 27.77	19.45, 27.50

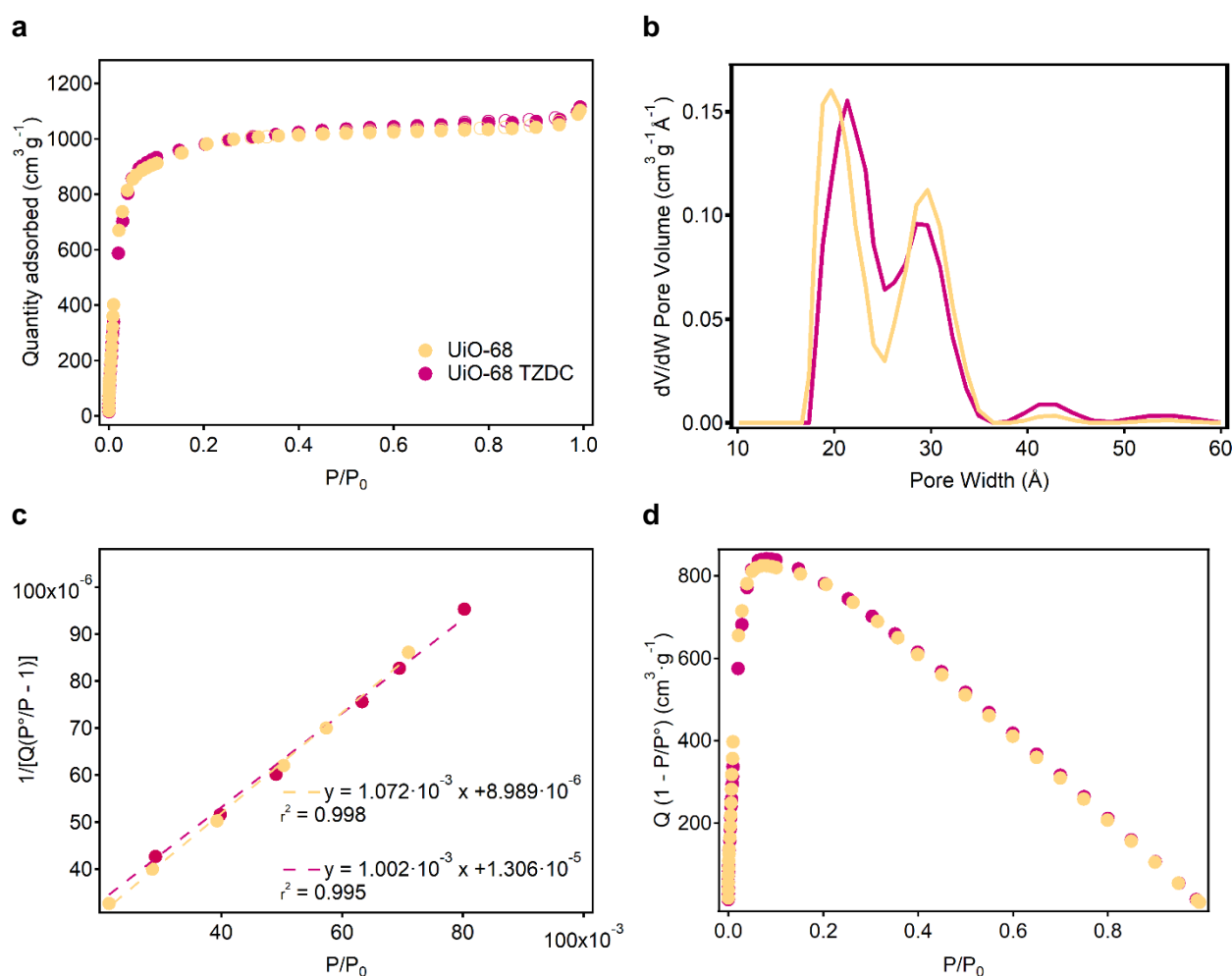


Figure S16. a) Analysis of the N₂ adsorption/desorption isotherm of hexane dried UiO-68s at 77 K. a) b) Pore size distribution. c) Rouquerol BET. d) Multi-Point BET analysis. e) main parameters calculated from the multi-point BET analysis.

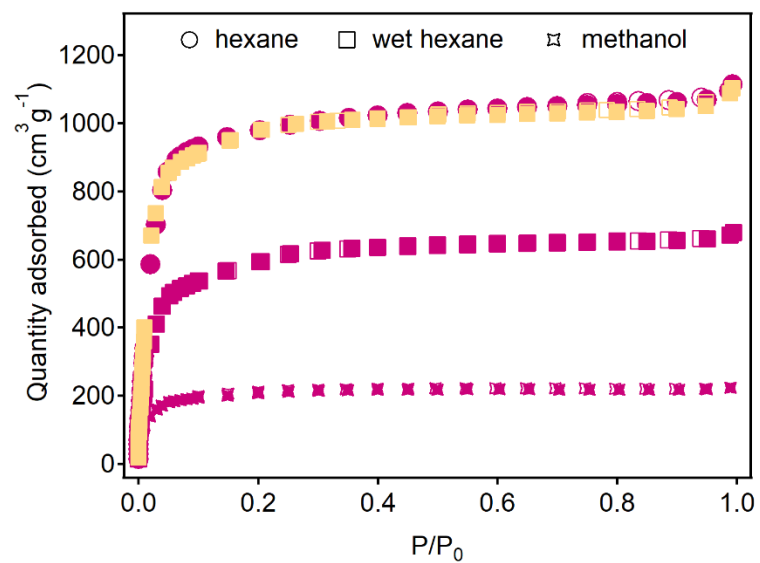


Figure S17. The importance of solvent-framework interactions in UiO-68-TZDC to access the expected porosity.

Analysis of CO₂ adsorption/desorption isotherms

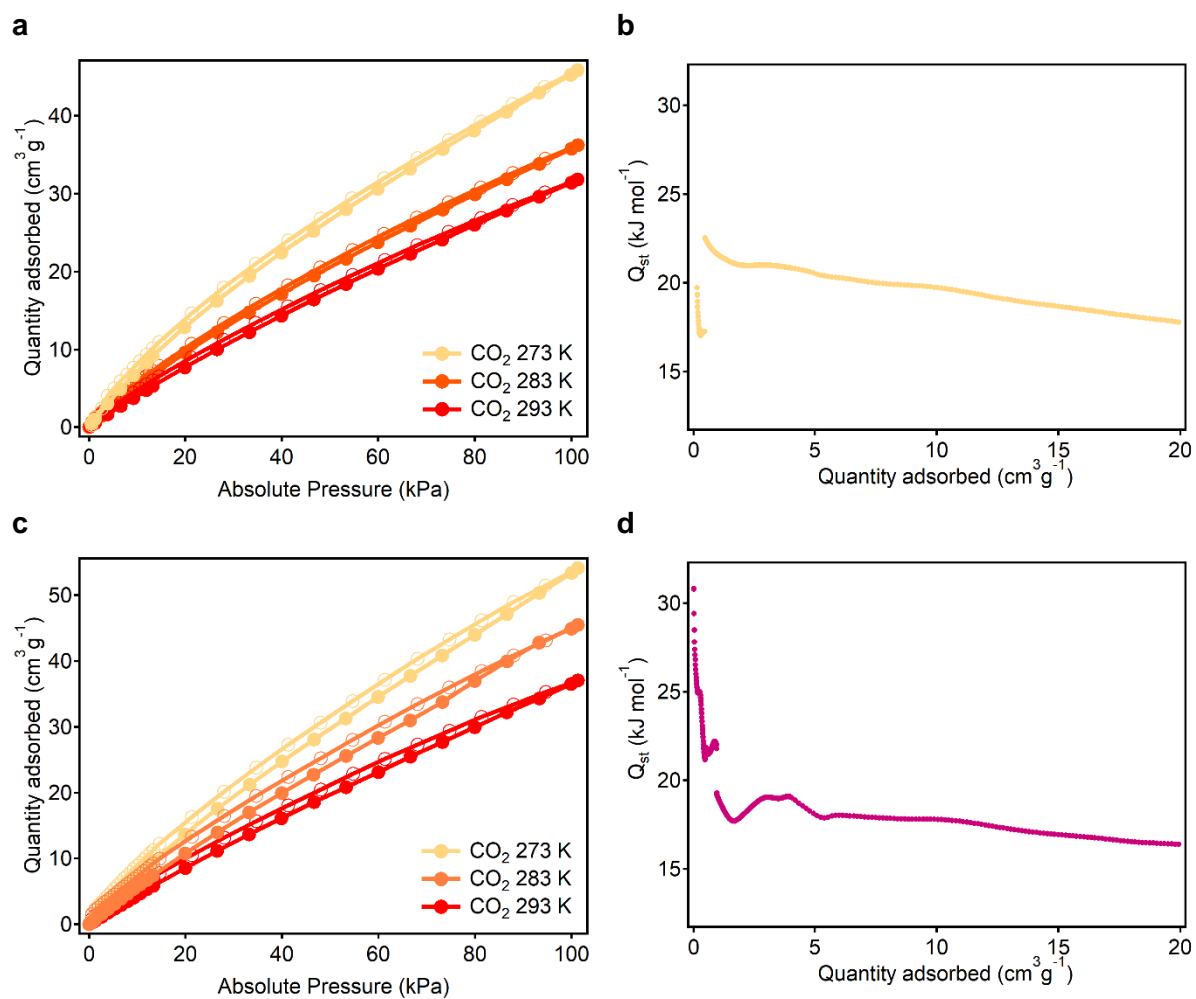


Figure S18. (a) CO₂ adsorption/desorption isotherms of UiO-68 recorded at different temperatures. (b) Isosteric heat of adsorption (Q_{st}) of UiO-68 calculated from the corresponding isotherms. The enthalpy of adsorption at zero loading is 23 kJ·mol⁻¹. (c) CO₂ adsorption/desorption isotherms of UiO-68-TZDC recorded at different temperatures. (d) Isosteric heat of adsorption (Q_{st}) of UiO-68-TZDC. The enthalpy of adsorption at zero loading is 31 kJ·mol⁻¹. Q_{st} was calculated with a virial - type expression.

S5. Multivariate UiO-68: compromise between photoactivity and chemical stability

S5.1. Characterization of multivariate approach samples ($MV_{TZDC:TPDC}$)

Powder X-Ray Diffraction (PXRD) and Fourier Transformed Infrared Spectroscopy (FT-IR).

Taking as starting point the pure phase MOF conditions, we designed the mixed-ligand experiments using HT synthetic methodology. The samples resultants of multivariate synthesis were denoted by $MV_{TZDC:TPDC}$. In this case, the ratio of linkers is the original quantities in the synthesis, not in the resultant solids.

Different ratio of linkers was explored using DMF or mixtures of DMF/NMP as solvent. The reaction time was also scanned from 24 to 72 h. The differences in the linker's solubilities could hinder their co-assembling, so milling solid linkers together or dissolve the linkers individually before getting them in the vial were tested.

Even though many attempts, the most crystalline samples resulting to direct multivariate synthesis ($MV_{TZDC:TPDC}$) were less crystalline than the direct synthesis material (**Fig. S19a**). This effect has been reported in other mixed-linker MOF synthesis.⁴

The selected samples were obtained at 100 °C, 48 h, using 24 to 40 equivalents of TFA.

The carbonyl band of free linker ($\nu_{C=O} = 1675 \text{ cm}^{-1}$) were present in $MV_{TZDC:TPDC}$ samples displaying unreacted linker in the samples (**Fig. S19b**) as it supported by SEM images (**Fig. S20**).

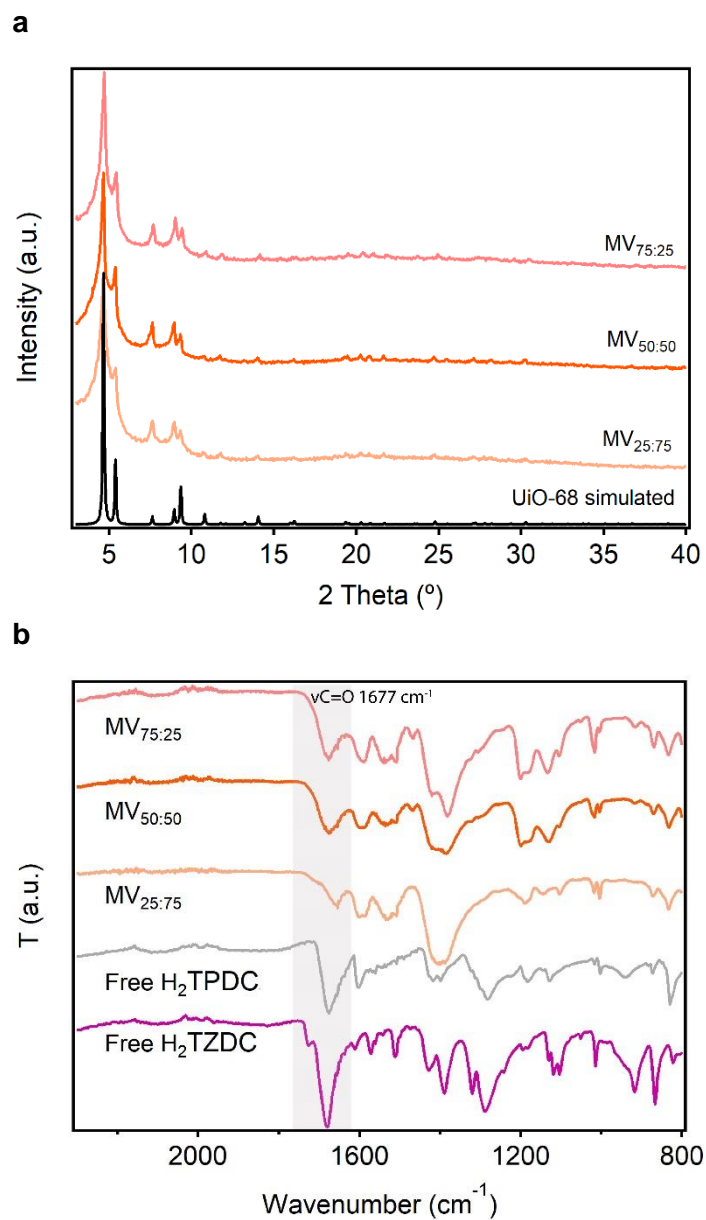


Figure S19. a) PXR D patterns of the multivariate samples. b) FT-IR spectra of solids. All MV-samples show an intense peak of carbonyl stretching at $\nu_{\text{C=O}} = 1677 \text{ cm}^{-1}$ as the free linker vibration, that is meaning the presence of unreacted linker (semi-transparent box).

Scanning Electron Microscopy (SEM-EDX)

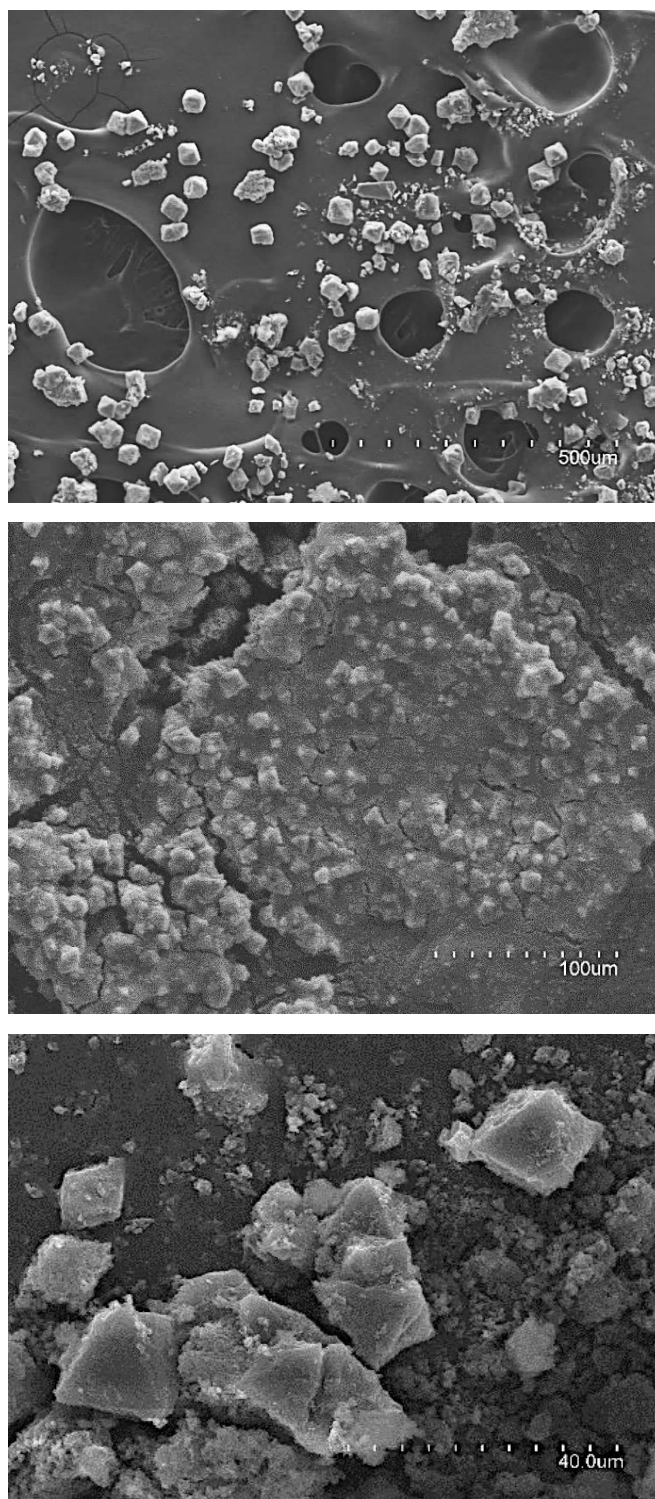


Figure S20. SEM images of multivariate samples show the impurities in the samples.

S5.2. Characterization of UiO-68 TZDC% samples.

Synthesis of UiO-68-TZDC%

As-made UiO-68 (140 mg) was immersed in 54 mL of H₂TZDC solution in DMF and 40 μ L of trimethylamine (Et₃N) at 80 °C under stirring. Using different equivalents of H₂TZDC for 3 hours of reaction produced a controllable UiO-68-TZDC%. (Equivalents of TZDC (regarding UiO-68): 0.3 equiv. for UiO-68-TZDC_{1.8%}, 0.5 equiv. for UiO-68-TZDC_{3%}, 0.75 equiv. for UiO-68-TZDC_{10%}, 1 equiv. for UiO-68-TZDC_{15%}, 4 equiv. for UiO-68-TZDC_{25%}, 6 equiv. for UiO-68-TZDC_{35%} and 17 equiv. for UiO-68-TZDC_{50%}). After time reaction, the exchanged MOF was thoroughly washed with fresh DMF (40 mL \times 5). The resultant solids were kept in hexane. The maximum loading achieved was 50 % of TZDC using 17 equivalents of H₂TZDC.

¹H NMR analysis of SALE samples (UiO-68-TZDC%)

Activated UiO-68 TZDC% samples were digested by addition of 2 drops of D₂SO₄-d₂ solution (96-98 wt. % in D₂O) in 0.5 mL DMSO-d₆ for 5 minutes, then ¹H NMR was collected.

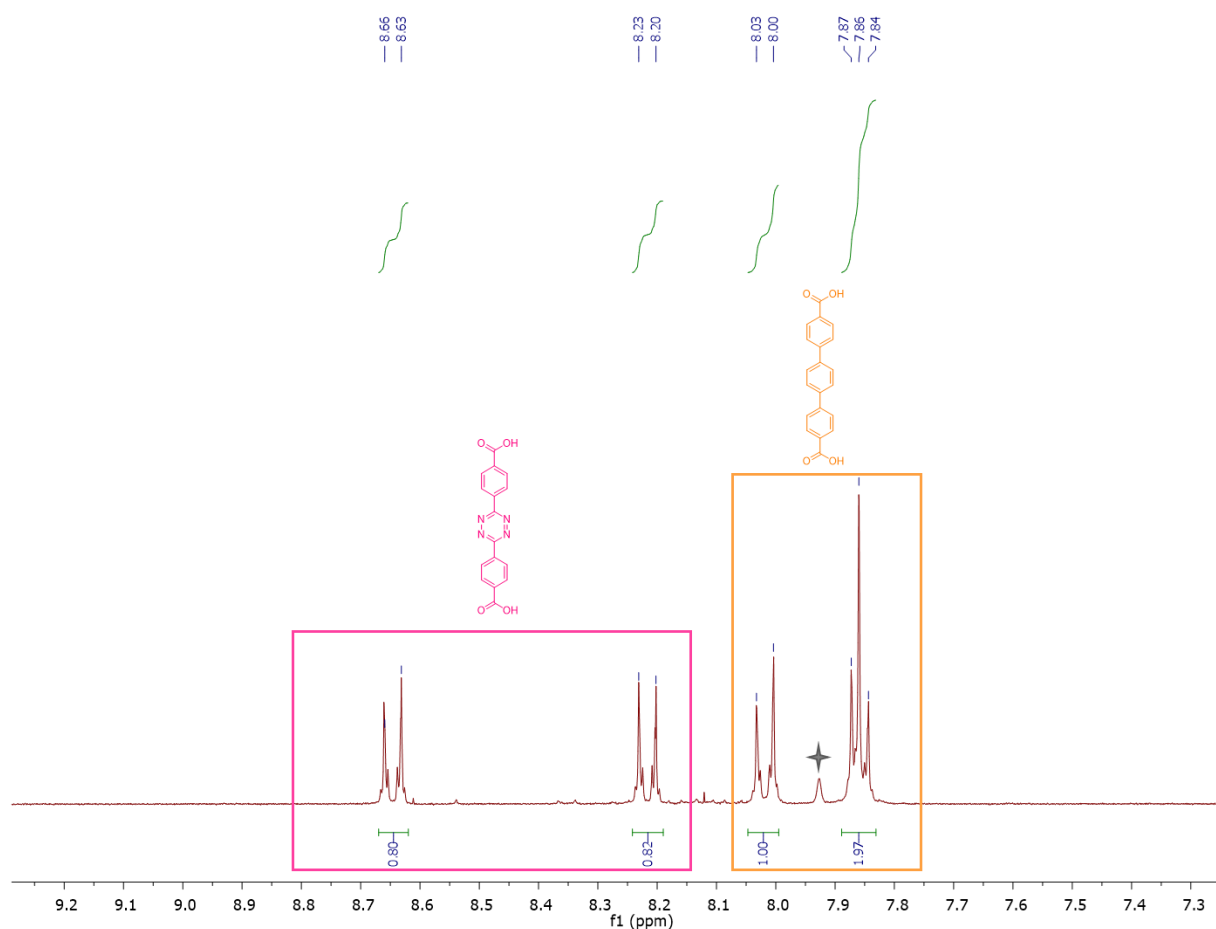


Figure S21. ¹H NMR of UiO-68-TZDC_{50%} after digestion with D₂SO₄-d₂. The residual DMF was indicated with black star. The D₂SO₄-d₂ residual signal was around 11 ppm.

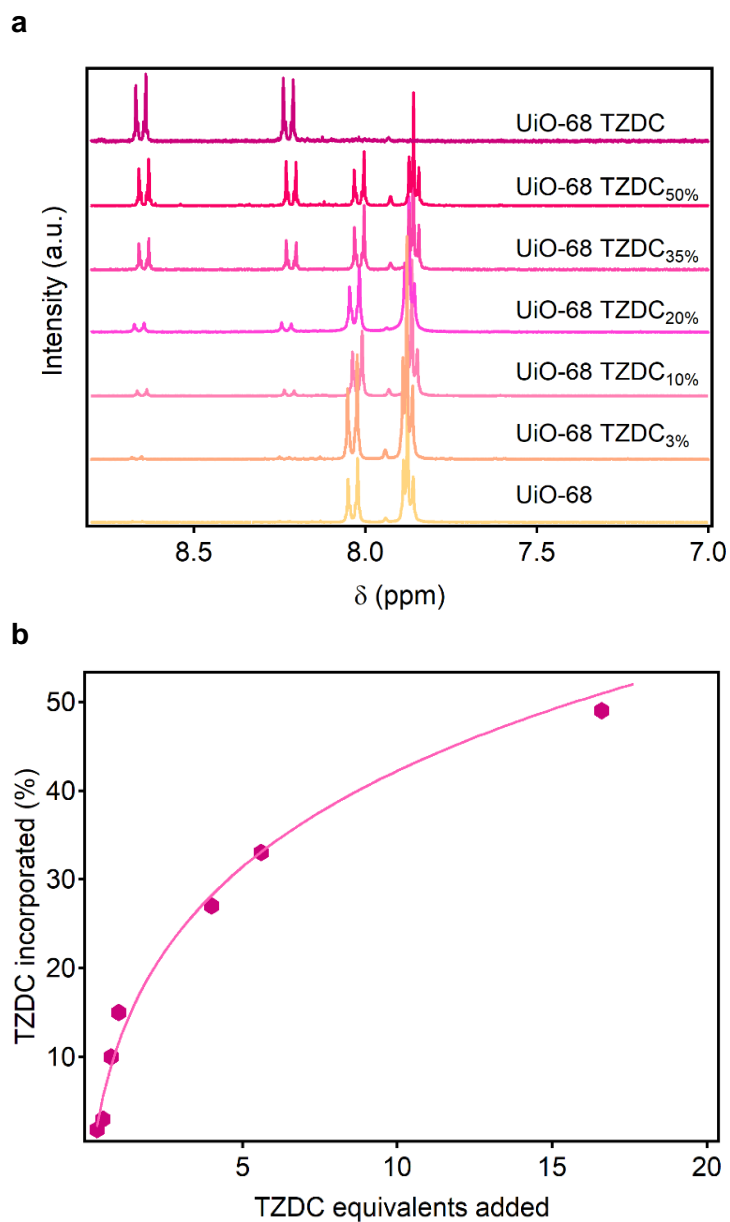


Figure S22. a) ^1H NMR spectra of the digested UiO-68-TZDC% samples with D_2SO_4 at 80°C during 15 minutes. b) Relation between % TZDC incorporated to the material and TZDC equivalents added (regarding UiO-68) to the reaction. The percentage of linker incorporated was calculated by ^1H NMR.

Optical images

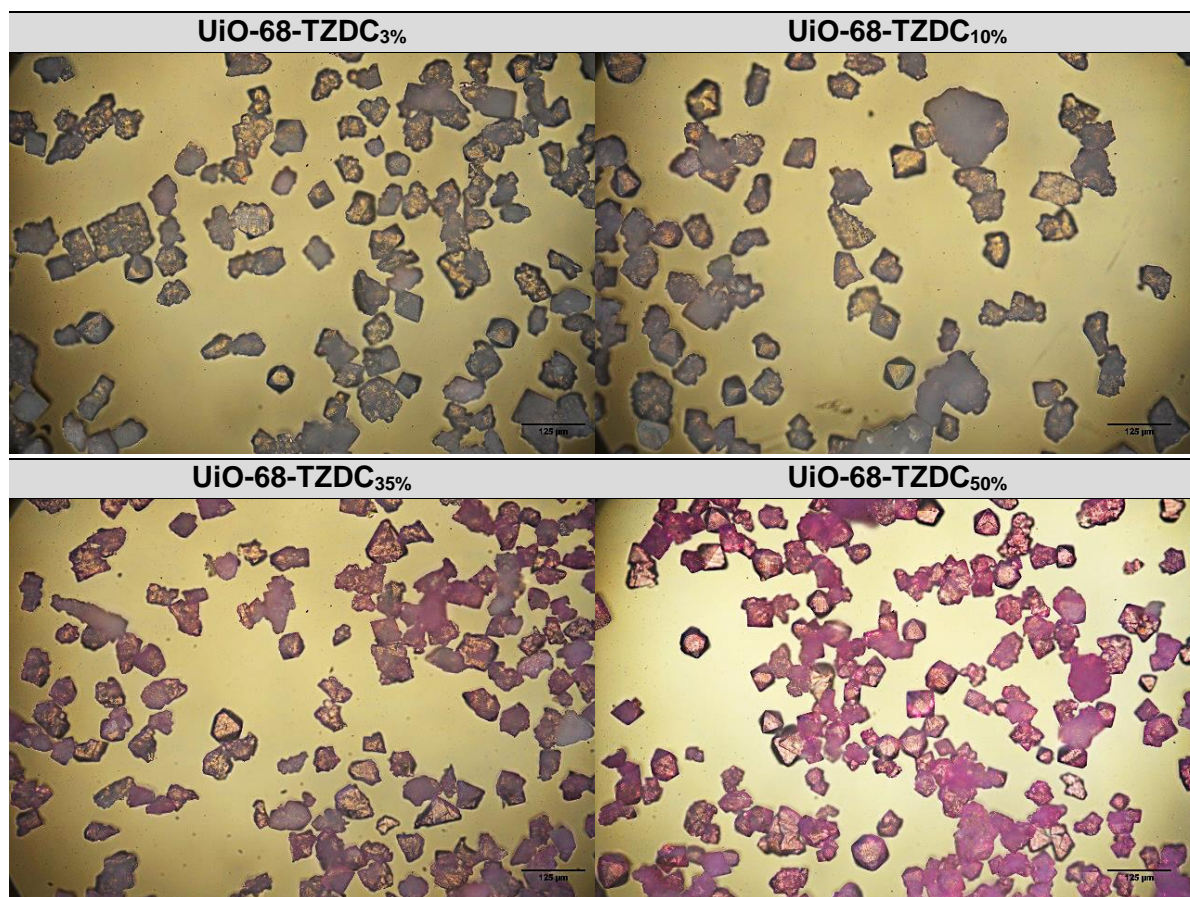


Figure S23. Optical images for UiO-68-TZDC% samples.

Fourier Transformed Infrared Spectroscopy (FT-IR).

IR analysis of resulting washed materials displayed a shift in the carbonyl band ($\nu_{C=O} = 1650 \text{ cm}^{-1}$) according to free linker vibration ($\nu_{C=O} = 1675 \text{ cm}^{-1}$), thus we eliminated the possibility of trapping uncoordinated linker in the cavities during SALE process. A characteristic UiO-68-TZDC band centred around 1378 cm^{-1} is further accentuated in higher loading samples.

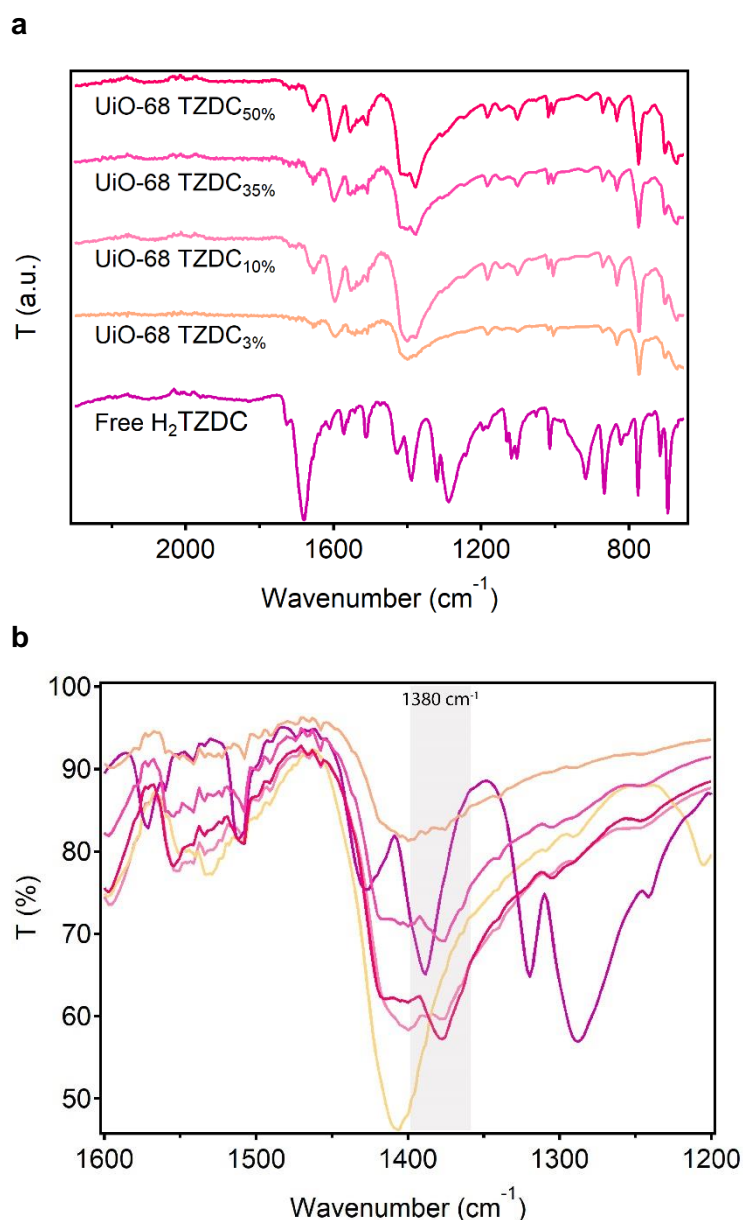
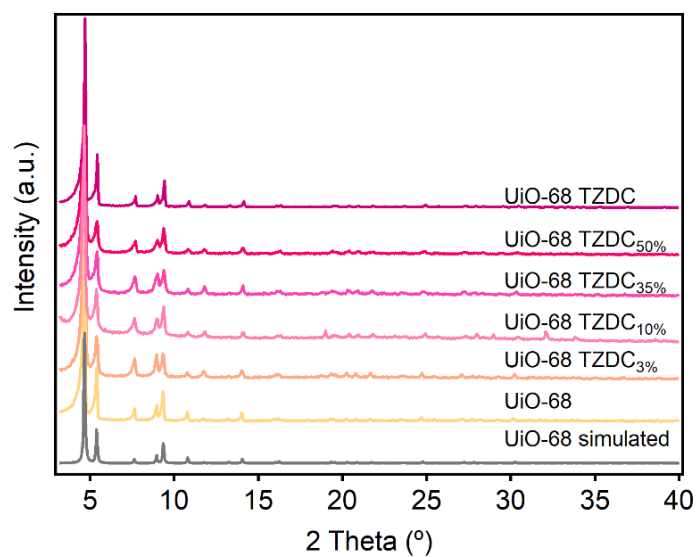


Figure S24. a) General FT-IR spectra of UiO-68-TZDC% samples. b) Characteristic UiO-68 TZDC band centered around 1380 cm^{-1} is further accentuated in higher loading samples (semi-transparent box).

Powder X-Ray Diffraction (PXRD)

a



b

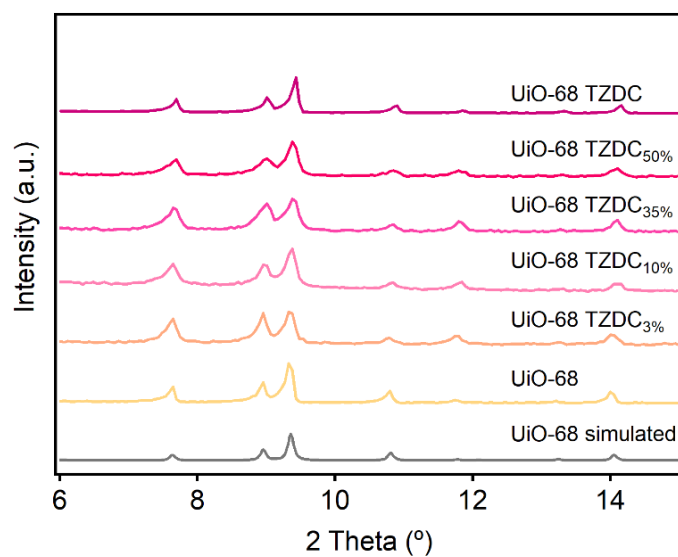


Figure S25. PXRD patterns of the UiO-68-TZDC% samples reveal a progressive shift in 2 theta angular values when the quantity of H₂TZDC added increased.

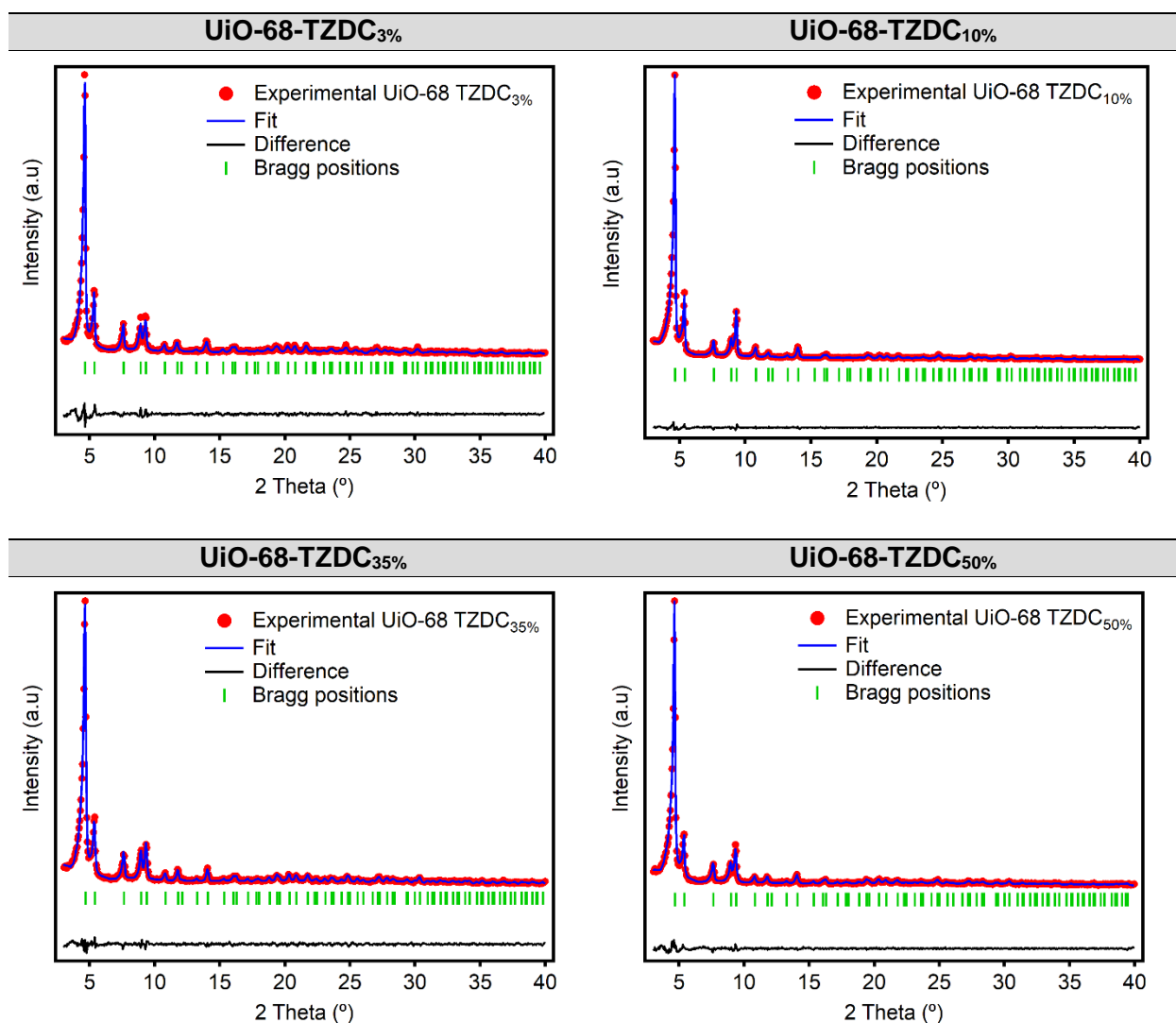


Figure S26. Experimental (red dots), calculated (blue line), difference plot [(I_{obs}–I_{calc})] (black line, bottom panel) and Bragg positions (green ticks, bottom panel) for the LeBail refinement of UiO-68-TZDC_% samples.

Table S7. Summary of the parameters obtained from LeBail refinement.

	a=b=c (Å)	V (Å ³)	R _e (%)	R _p (%)	R _{wp} (%)	gof
UiO-68	32.85635	35470	3.49	4.63	6.35	1.82
UiO-TZDC_{3%}	32.80233	35295	9.47	12.5	8.49	1.48
UiO-TZDC_{10%}	32.75111	35130	3.87	6.05	3.19	1.89
UiO-TZDC_{35%}	32.63905	34771	7.74	11.1	8.48	1.31
UiO-TZDC_{50%}	32.61589	34697	7.19	10.5	7.87	1.34
UiO-68-TZDC	32.48814	34291	1.77	2.37	3.63	2.05

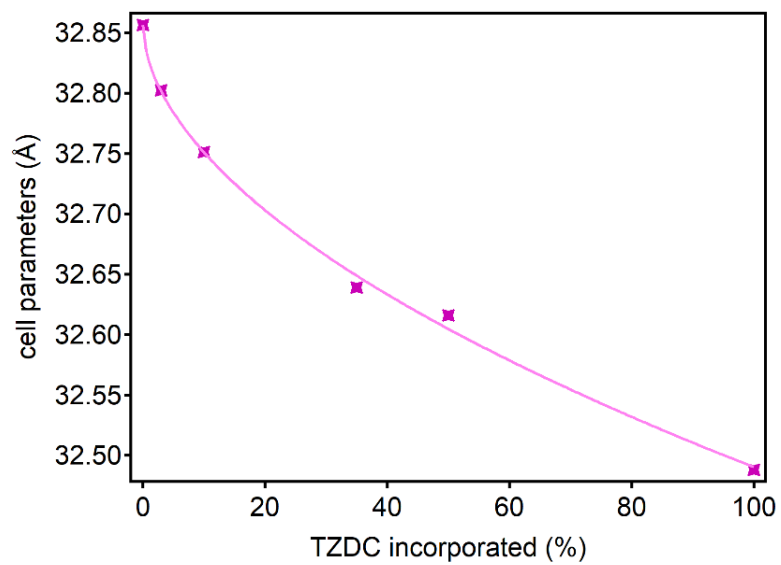


Figure S27. Cell parameters contraction induced by the incorporation of TZDC.

Scanning Electron Microscopy (SEM-EDX)

SEM images of UiO-68 TZDC% samples confirms the size and morphology of UiO-68 crystals is maintained upon linker-exchange reaction.

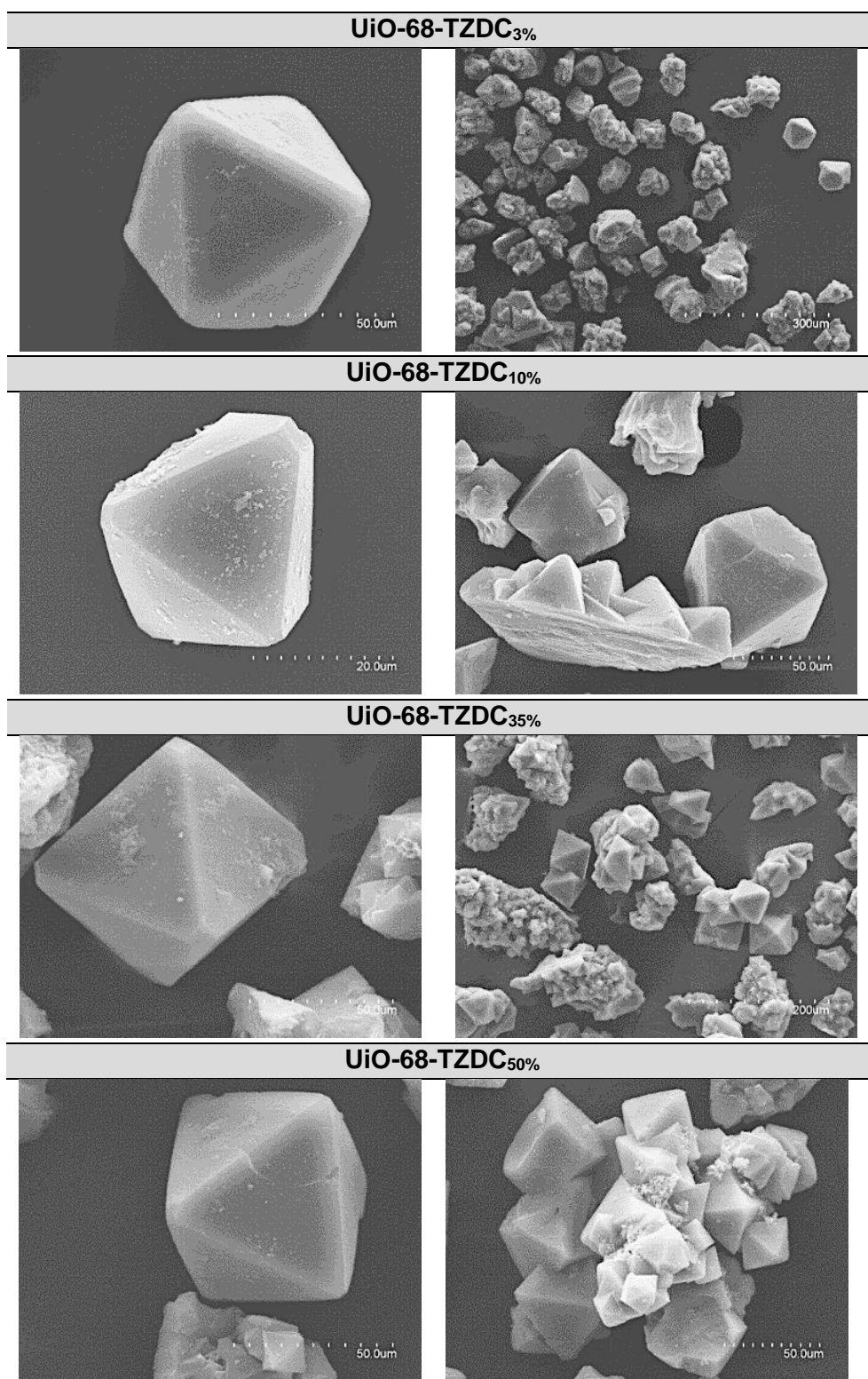


Figure S28. Scanning Electron Microscopy (SEM) images of octahedral crystals of UiO-68-TZDC%.

Analysis of N₂ adsorption/desorption isotherms at 77 K

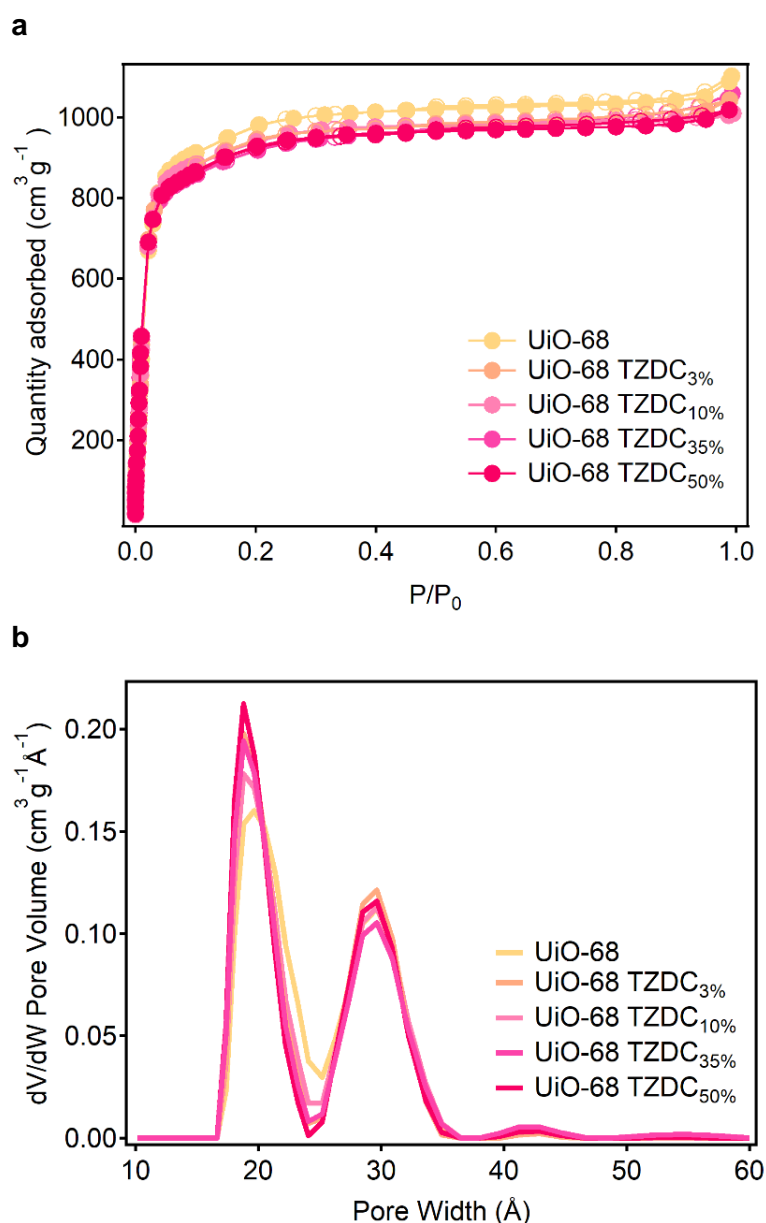


Figure S29. a) Analysis of the N₂ adsorption/desorption isotherm of UiO-68-TZDC% samples compared with UiO-68 direct synthesis at 77 K. b) Pore size distribution of UiO-68-TZDC% samples compared with UiO-68 direct synthesis.

Table S8. Summary of the adsorption analysis.

	UiO-68	UiO-68 TZDC _{3%}	UiO-68 TZDC _{10%}	UiO-68 TZDC _{35%}	UiO-68 TZDC _{50%}
BET surface area (m²·g⁻¹) at P/P₀ = 0.01-0.08	4028	3900	3795	3827	3701
Total pore volume (cm³·g⁻¹) at P/P₀ = 0.96	1.63	1.59	1.54	1.60	1.56
Pore width (Å)	20, 30	19, 30	20, 29	19, 29	19, 29

Chemical stability

The hydrolytical stability of the UiO-68-TZDC_% solids were evaluated by incubation in H₂O:MeOH (4:1) for 24 hours. The PXRDs after this treatment suggest that whereas UiO-68 TZDC sample showed a partial amorphization, the UiO-68 TZDC_% samples remain their crystallinity.

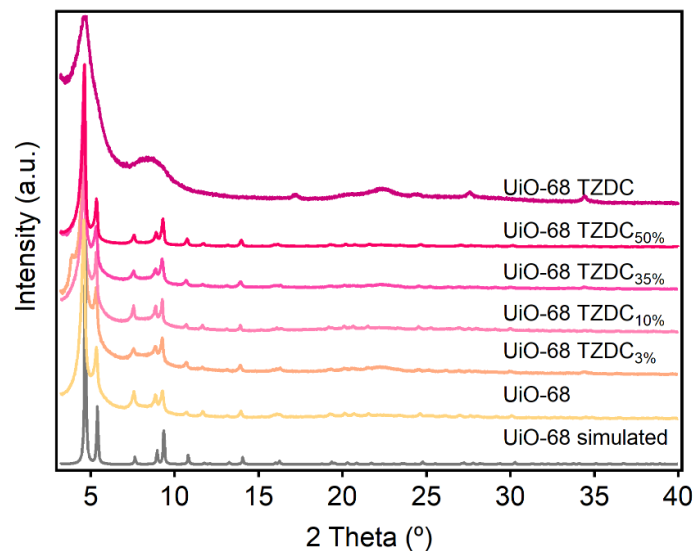


Figure S30. PXRD patterns of the PSE samples after immersion of the solid for 24 hours in H₂O:MeOH (4:1) solution.

S5.3. Checking the maximum exchanged ratio by ^1H NMR and FT-IR.

Following the protocol, 140 mg of as-made UiO-68 was immersed in a DMF solution with 40 equivalents of H_2TZDC and 40 μL of trimethylamine (Et_3N) at 80 $^\circ\text{C}$ during 3 hours under stirring. After time reaction, the solid was thoroughly washed with fresh DMF (40 mL \times 5) and analysed.

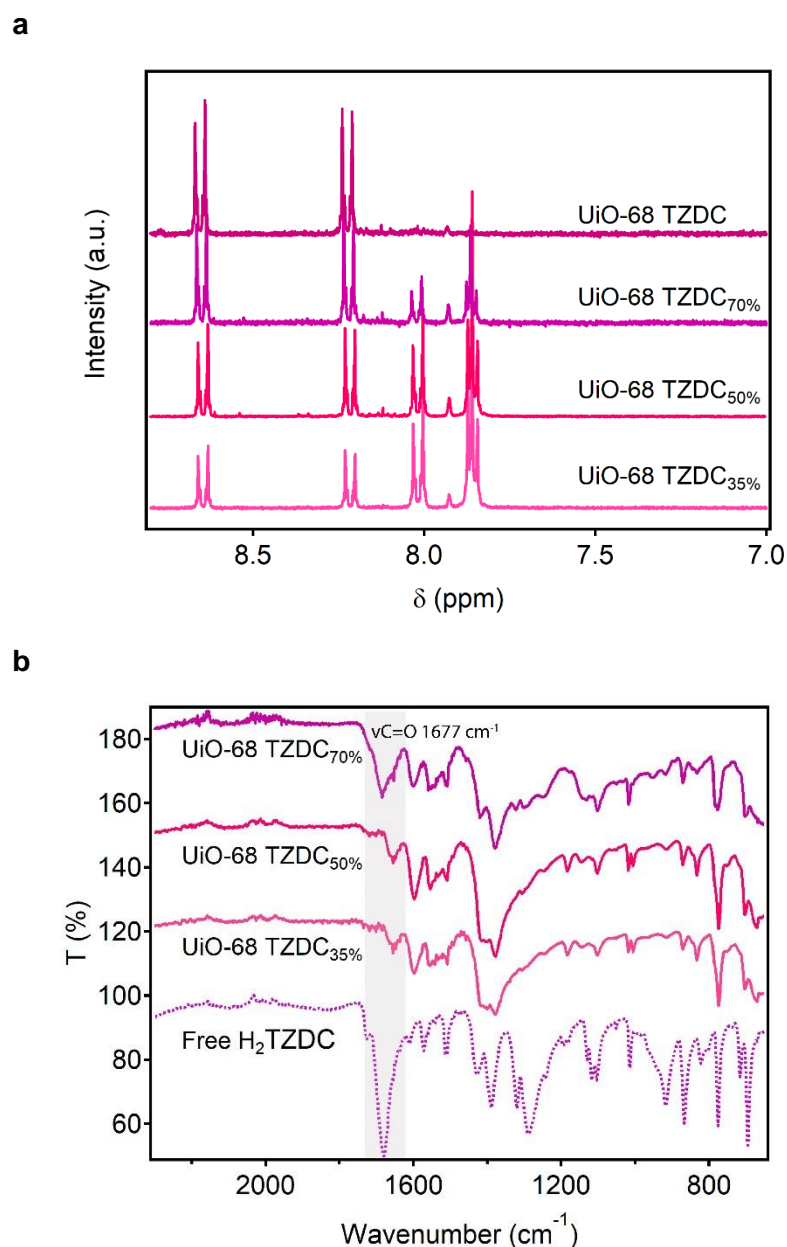


Figure S31. a) TZDC incorporation was calculated by ^1H NMR spectroscopy. b) IR analysis confirms the presence of free TZDC in UiO-68 TZDC_{70%}. The sample shows intense peak of carbonyl stretching at $\nu\text{C}=\text{O} = 1677 \text{ cm}^{-1}$ according to free linker vibration (semi-transparent box).

S5.4. Study of the kinetic's origin of UiO-68-TZDC10%

To confirm whether or not, the formation of core-shell architectures was kinetically controlled we synthesized and characterized another set of UiO-68-TZDC_{10%} crystals by prolonging the exchange time to 6, 12 and 24 hours whilst fixing the stoichiometric equivalents of H₂TZDC in solution.

Synthesis of UiO-68-TZDC_{10%} (6, 12 and 24 h)

130 mg of as-made UiO-68 were immersed in 70 mL of a solution of H₂TZDC (15 mg, 0.75 equiv) in DMF, followed by addition of 40 μ L of trimethylamine (Et₃N) at 80 °C under stirring during 6, 12 or 24 h respectively. The exchanged solid was thoroughly washed with fresh DMF (40 mL \times 5) and kept in hexane. *This protocol is equivalent to the original synthesis reported except for the reaction time.* The differences between UiO-68-TZDC_{10%} prepared after 3 and 24 hours of reaction were already visible by naked eye. The decrease in intensity of the pink color for the second anticipates a higher dilution of TZDC across the crystal compared to the brighter pink in UiO-68-TZDC_{10%}(3h), that suggests a higher concentration of the linker in the crystal surface.

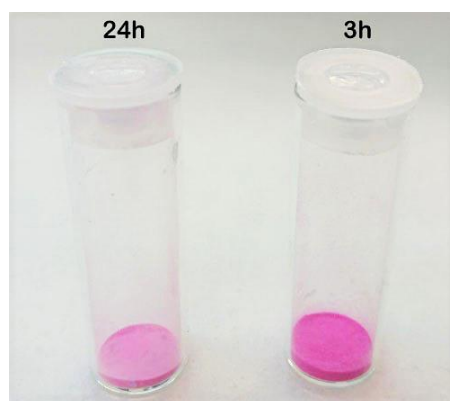


Figure S32. Changes in the colour of the crystals by naked eye.

Kinetic change of TZDC content in bulk and on surface as exchange time

Table S9. Changes in the chemical composition of UiO-68-TZDC_{10%} at different reaction times. The bulk content of TZDC was quantified with 1H-NMR analysis of digested crystals. The relative ratio of TZDC in the surface of the crystals was calculated from the total areas of N_{1s} and Zr_{3d} in the XPS spectra.

Framework	TZDC _{10%} (3 h)	TZDC _{10%} (6 h)	TZDC _{10%} (12 h)	TZDC _{10%} (24 h)
Bulk content (NMR)	11.1	10.8	12.2	11.4
N_{1s}/Zr_{3d} Surface ratio (XPS)	0.657	0.601	0.452	0.331

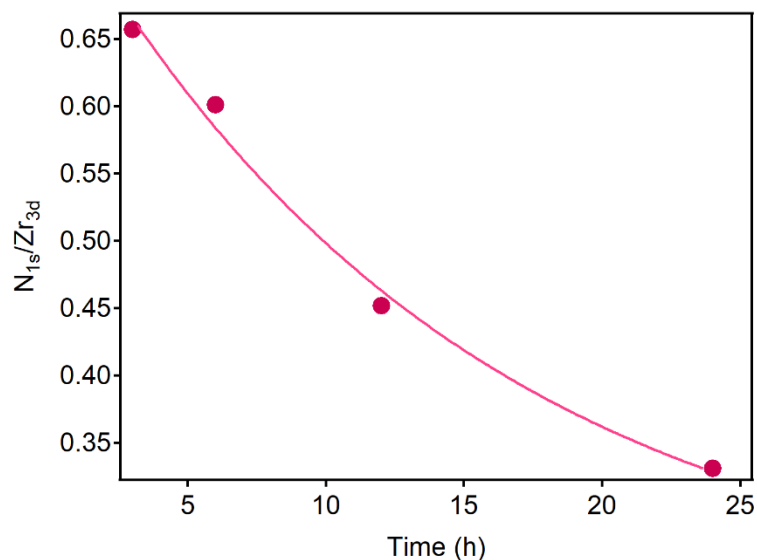


Figure S33. Exponential decrease of TZDC surface content in crystals of UiO-68-TZDC_{10%} as a function of the exchange time after 3, 6, 12 and 24 h. The relative ratio of TZDC in the surface of the crystals was calculated from the total areas of N_{1s} and Zr_{3d} in the XPS spectra.

Fourier Transformed Infrared Spectroscopy (FT-IR).

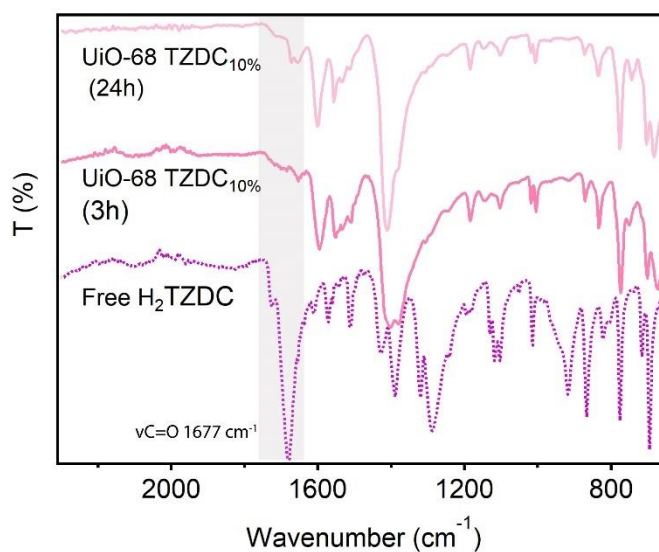


Figure S34. FT-IR spectra of UiO-68-TZDC_{10%} prepared after 3 and 24 hours of reaction and the linker H₂TZDC discard the presence of free linker in the 24 h sample.

Powder X-Ray Diffraction (PXRD)

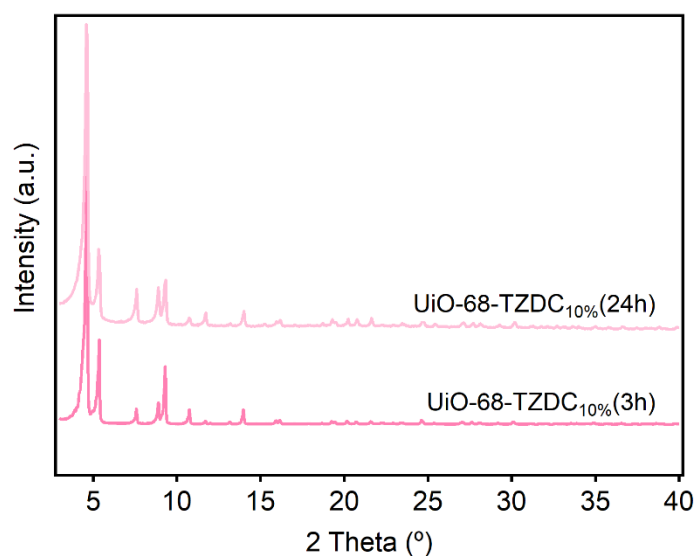


Figure S35. PXRD patterns of UiO-68 TZDC_{10%} (3h) and (24h).

Scanning Electron Microscopy (SEM-EDX)

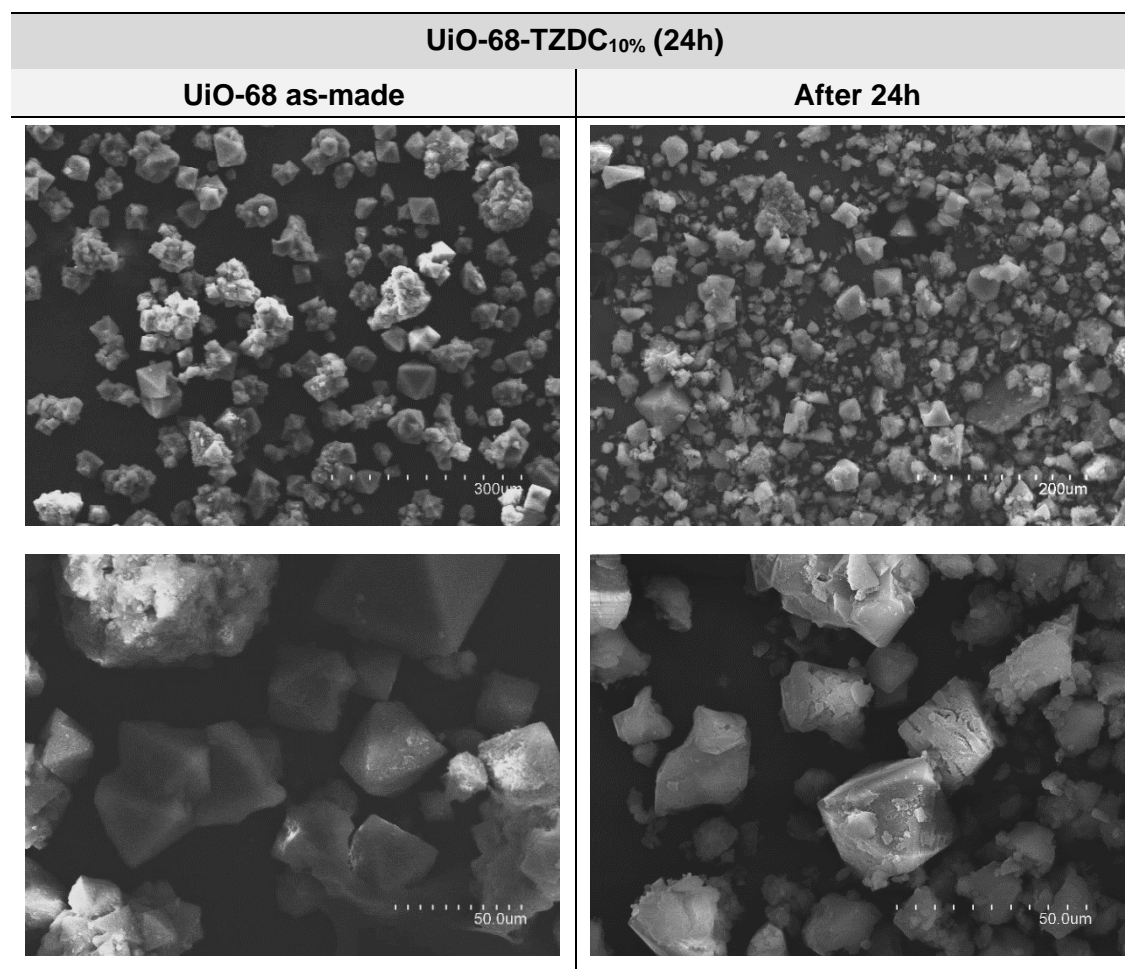


Figure S36. Scanning Electron Microscopy (SEM) images reveals weak damaged crystals after 24 h of reaction.

Analysis of N₂ adsorption/desorption isotherms at 77 K

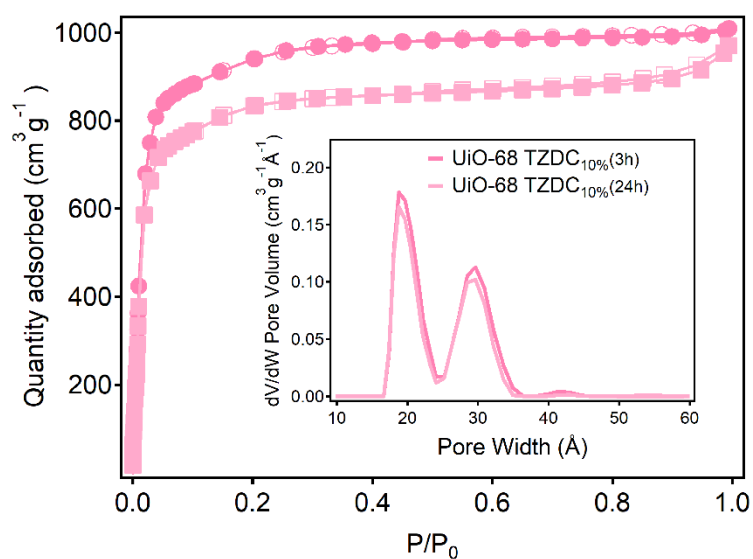


Figure S37. N₂ gas isotherms and pore size distribution of UiO-68-TZDC_{10%} (3h) and (24h). UiO-68-TZDC_{10%}(24h) displays a small reduction of near 11% in the experimental BET value due to a light change in the structural stability.

Table S10. Comparison of the adsorption parameters of UiO-68-TZDC_{10%} (3h and 24h).

	UiO-68-TZDC _{10%} (3h)	UiO-68-TZDC _{10%} (24h)
BET surface area (m²·g⁻¹) at P/P₀ = 0.01-0.08	3795	3420
Total pore volume (cm³·g⁻¹) at P/P₀ = 0.96	1.54	1.42
Pore width (Å)	20, 29	19, 29

S6. Interplay between linker-controlled sensitization and photocatalytic properties

S6.1. DFT calculations

All structural calculation was performed using dispersion-corrected density functional theory (DFT-D3) with the Vienna ab initio simulation package (VASP),^{5,6} and employing the Perdew–Burke–Ernzerhof (PBE) functional.⁷ The recommended GW PAW pseudopotentials⁸ were used for all geometry and electronic calculations. A plane wave basis set was employed with a kinetic energy cut-off of 500 eV, and a Γ -point grid was used to sample the Brillouin zone. Electronic calculations was moreover performed with a $2\times 2\times 2$ Γ -centered grid and PBE functional, although this functional is a qualitative approach, hybrid functional calculations on Zr-MOF have shown PBE to display the correct trends.^{9,10} To investigate the effect of tetrazine doping has on the electronic structure, molecular substitutions were manually installed to the TPDC linker on experimentally determined unit cell of UiO-68, $[(Zr_6O_4(OH)_4)_4(TPDC)_{24}]$, and both lattice parameters and atomic positions were further relaxed.

Table S11. Summary of calculated band-gap values of family of UiO-68-TZDC%.

Sample	No. TZDC	Theoretical Band Gap (eV)
UiO-68	0	2.52
UiO-68-TZDC _{4%}	1	1.37
UiO-68-TZDC _{8%}	2	1.36
UiO-68-TZDC _{13%}	3	1.36
UiO-68-TZDC _{17%}	4	1.36
UiO-68-TZDC _{33%}	8	1.36
UiO-68-TZDC _{42%}	10	1.35
UiO-68-TZDC _{50%}	12	1.35
UiO-68-TZDC	24	1.35

S6.2. UV-Vis experiments

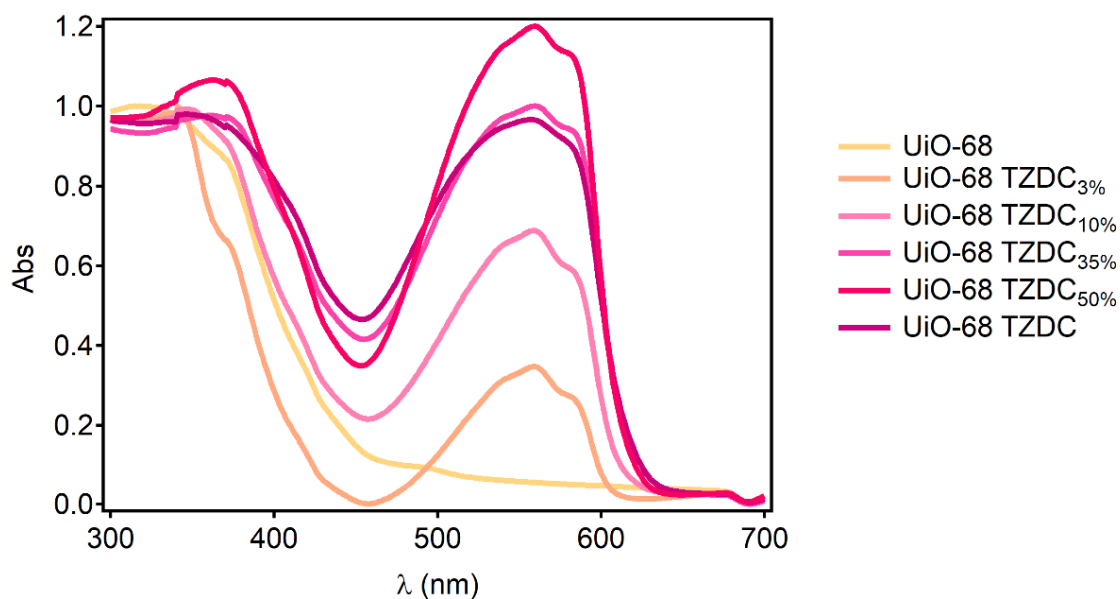


Figure S38. UV-Vis spectrum of UiO-68-TZDC% show a maximum at 560 nm as UiO-68 TZDC direct synthesis.

Experimental Optical Band-Gap Calculation

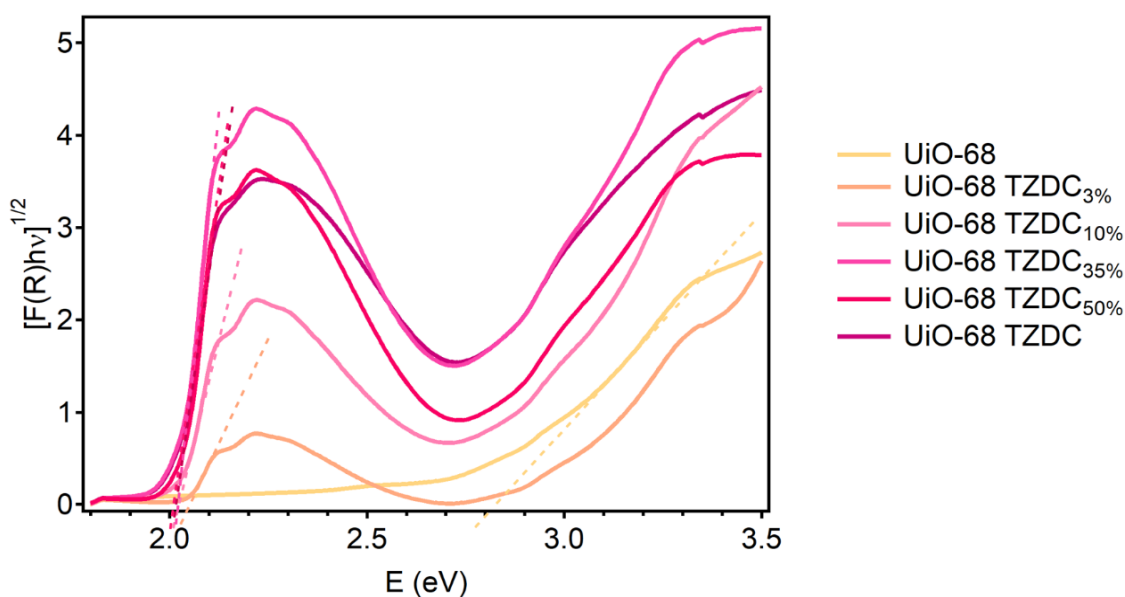


Figure S39. a) Kubelka-Munk function of UiO-68 samples. The dotted line corresponds to the regression fitting of the linear part of the plot. The optical band-gap of UiO-68 TPDC was 2.80 eV, whereas for UiO-68-TZDC% samples it was around 2.0 eV, close to UiO-68 TZDC experimental optical band gap.

Table S12. Summary of experimental optical band-gap values calculated by Kubelka-Munk function.

Sample	Optical Band Gap (eV)
UiO-68	2.80
UiO-68-TZDC_{3%}	2.05
UiO-68-TZDC_{10%}	2.05
UiO-68-TZDC_{35%}	2.03
UiO-68-TZDC_{50%}	2.03
UiO-68-TZDC	2.02

S7. Spatial arrangement of linkers in the crystal

S7.1. Fluorescence microscopy studies

For these experiments, the emission spectra of TPDC and TZDC were collected at two separate excitation wavelengths, 405 and 559 nm, to maximize light absorption in each case. As shown in the spectra below (**Figure S40**), the emission of TPDC is centered at 500 nm (blue) whereas the emission of TZDC is centered at 740 nm (red). These differences in energy of the emission lines are important for a clear mapping of the linker distribution in our case by discriminating their emissions.

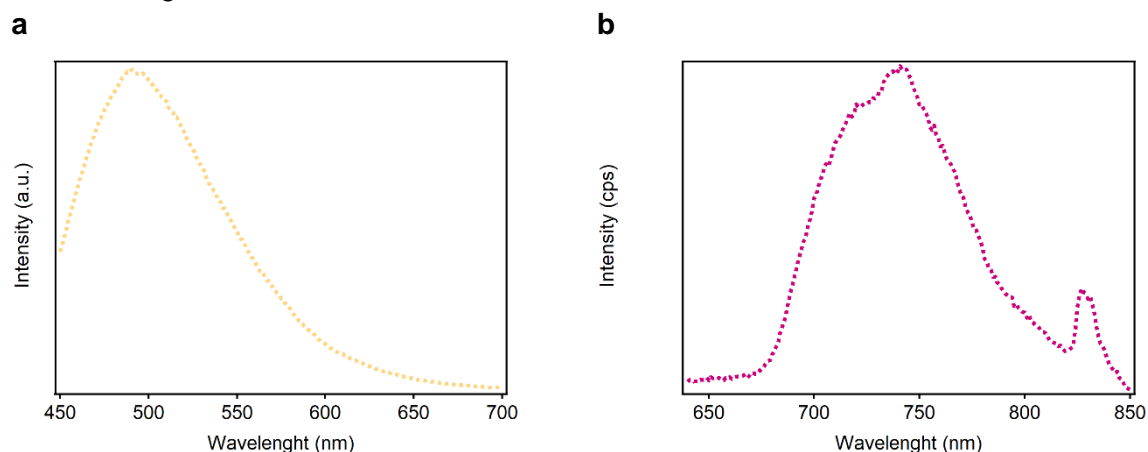


Figure S40. Emission spectra of a) TPDC and b) TZDC in solution.

S7.2. Confocal microscopy studies

Two types of confocal microscopy experiments were carried out. The external crystal surface and defective regions were examined by using freshly made samples. In turn, for the analysis of the microstructures arising from PSE it was necessary to use ultramicrotomy. The crystals were then placed in the bottom of a cylindrical mold and covered with uncured epoxy. The mold was then placed in an oven at 60 °C for 24 hours to allow the resin to cure. The first approach was to dissect the crystals using an ultramicrotome at 10 μm increments until the center of the crystal was at the surface of the resin. Due to the hardness of the crystal and the method's limitations for this type of samples, the samples were deteriorated. Accordingly, we opted for polishing the crystals' molds for minimum changes to their morphology.

External crystal surface analysis

The UiO-68 TZDC% samples were excited at $\lambda = 559$ nm and the emission was collected in 575-675 nm of λ range (red channel). Fluorescence intensity images were taken at different heights, with 1.08 μm of separation between the different planes, from the external surface to 36.72 μm inside the crystal, showing the three-dimensional intensity distribution of the crystals. 35 images were taken, but only 18 were select to simplify.

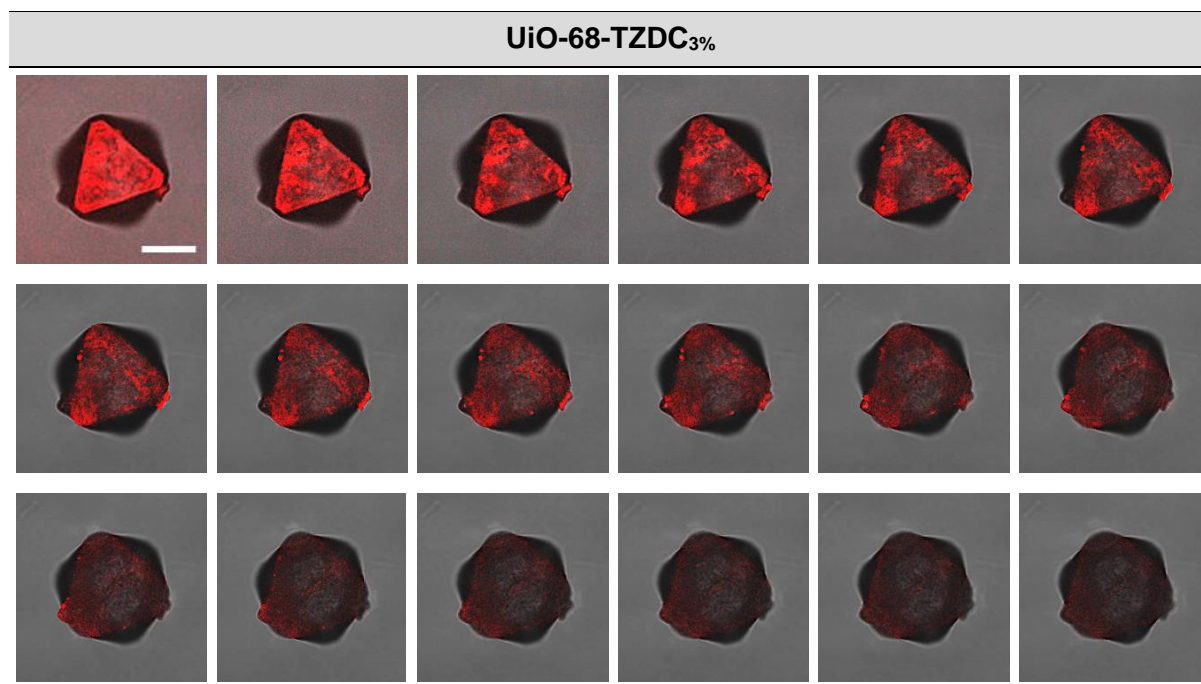


Figure S41. Confocal images of UiO-68 TZDC_{3%}. Z= 0 to Z= -36.72 μm show the edges, vertices, and cracks in the higher fluorescence intensity in the edges, vertices and cracks indicating that these regions likely have a concentrated defect sites. Scale bar correspond to 25 μm .

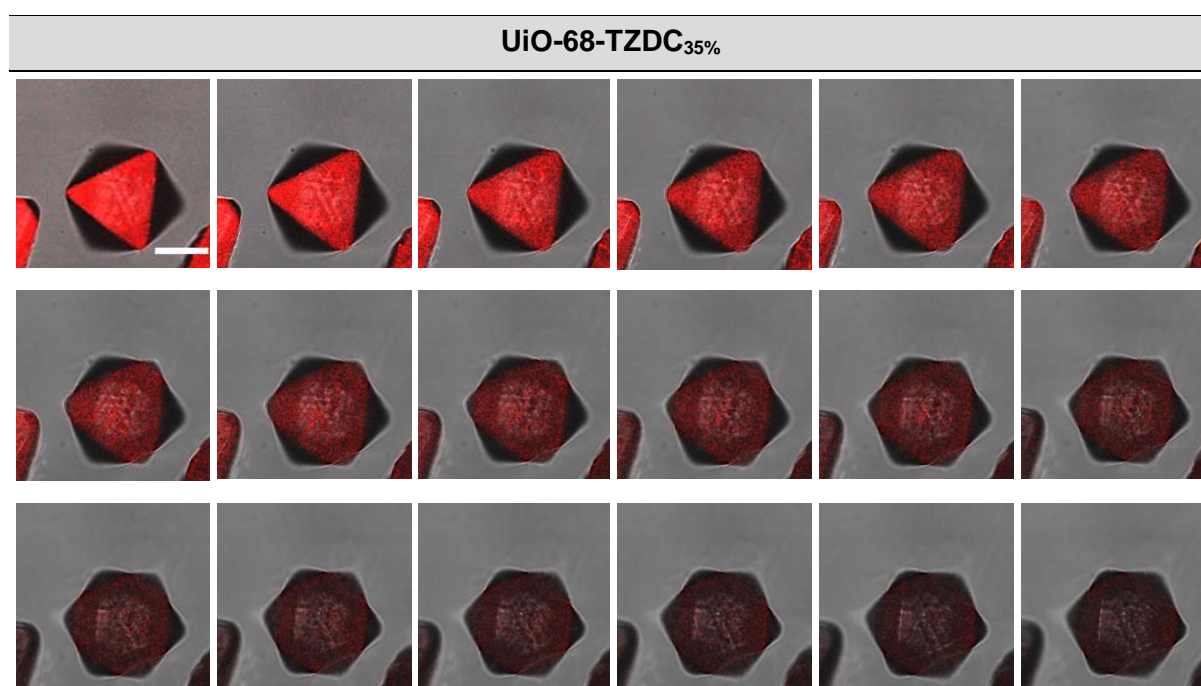


Figure S42. Confocal images of UiO-68 TZDC_{35%}. Z= 0 to Z= -36.72 μm show a uniform distribution of the TZDC linker over the crystal surface. Scale bar correspond to 25 μm .

Comprehensive analysis of the resultant microstructure in polished crystals

The emission of UiO-68 was collected in 425-475 nm range (blue channel). Whereas the emission of UiO-68-TZDC was collected in the 575-675 nm range (red channel).

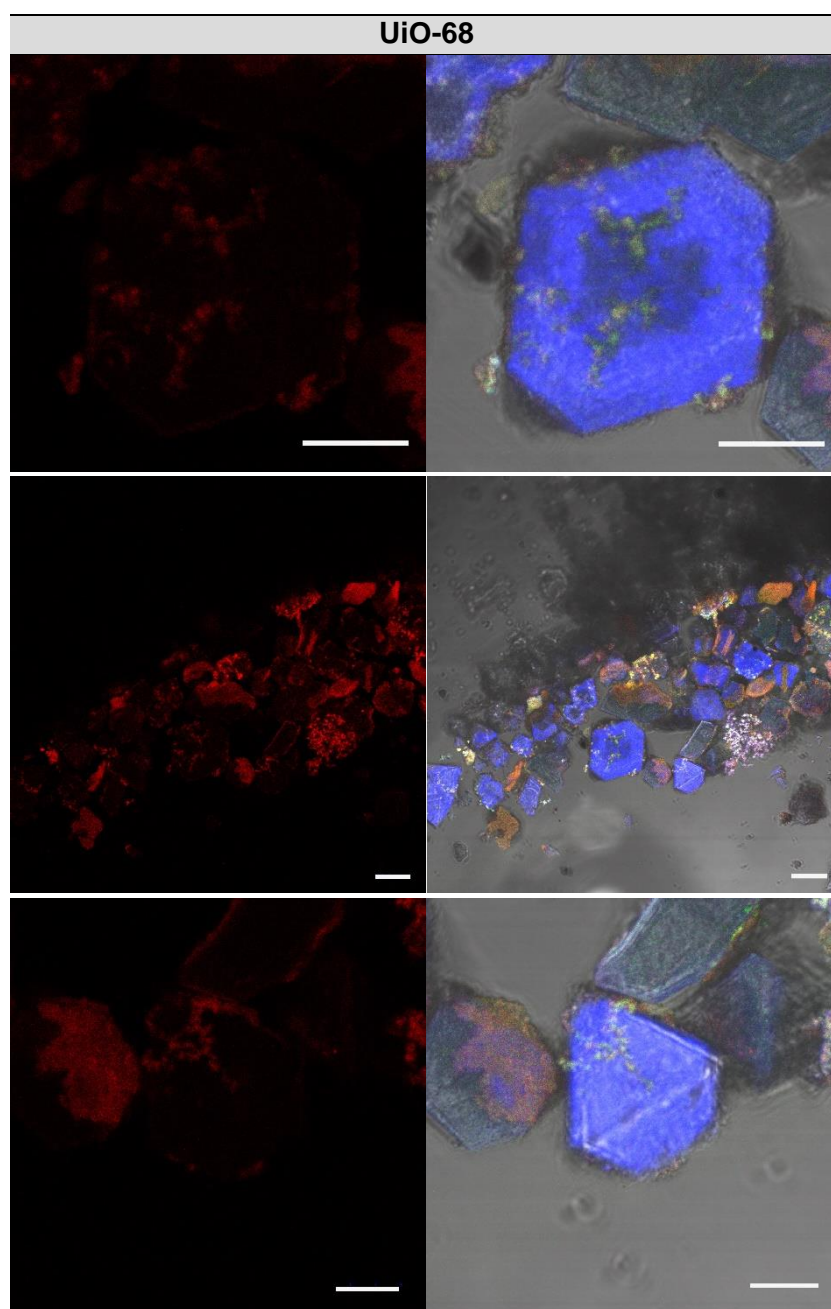


Figure S43. Confocal images of UiO-68 polished crystals' molds. Scale bars correspond to 25 μm . The left column correspond to red channel and the right to the total of channels (red, blue and transmittance light).

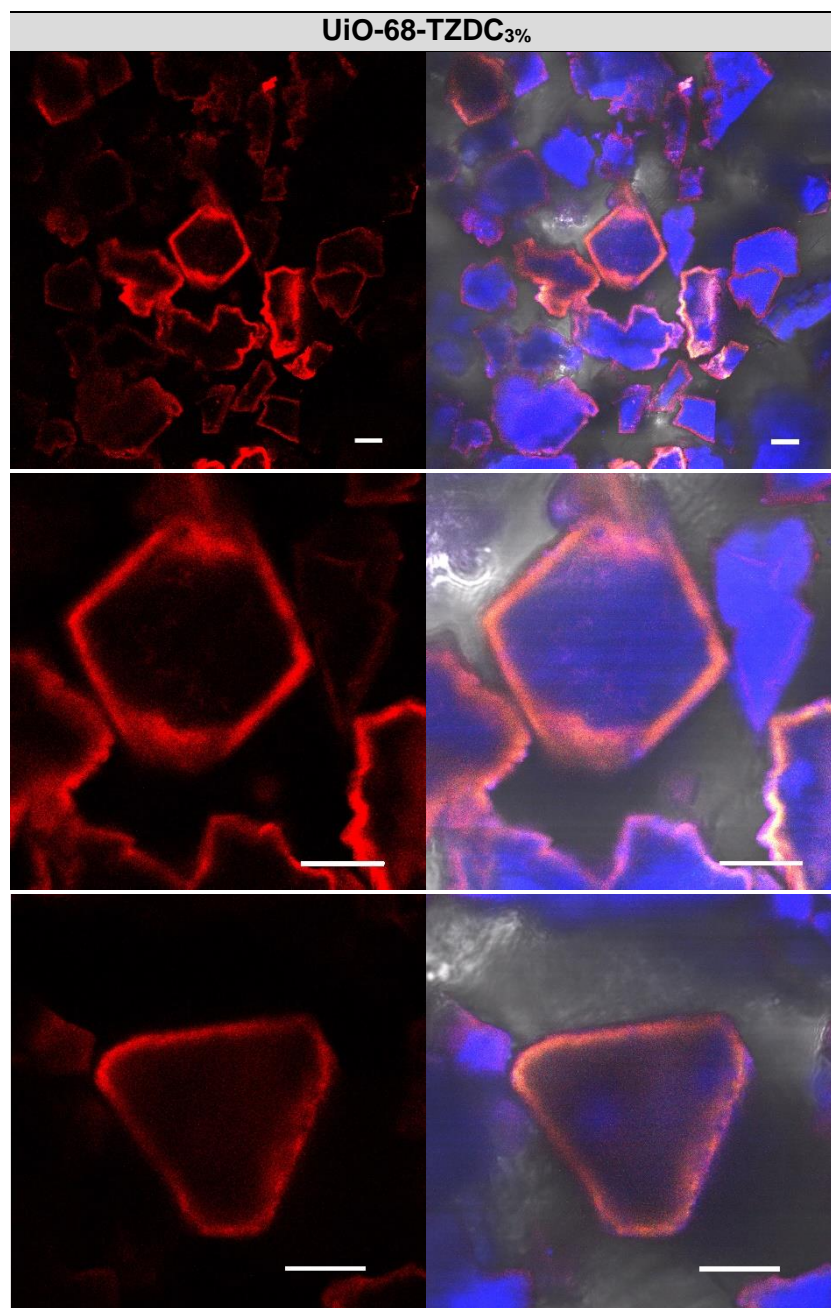


Figure S44. Confocal images of UiO-68-TZDC_{3%} polished crystals' molds. Scale bars correspond to 25 μ m.

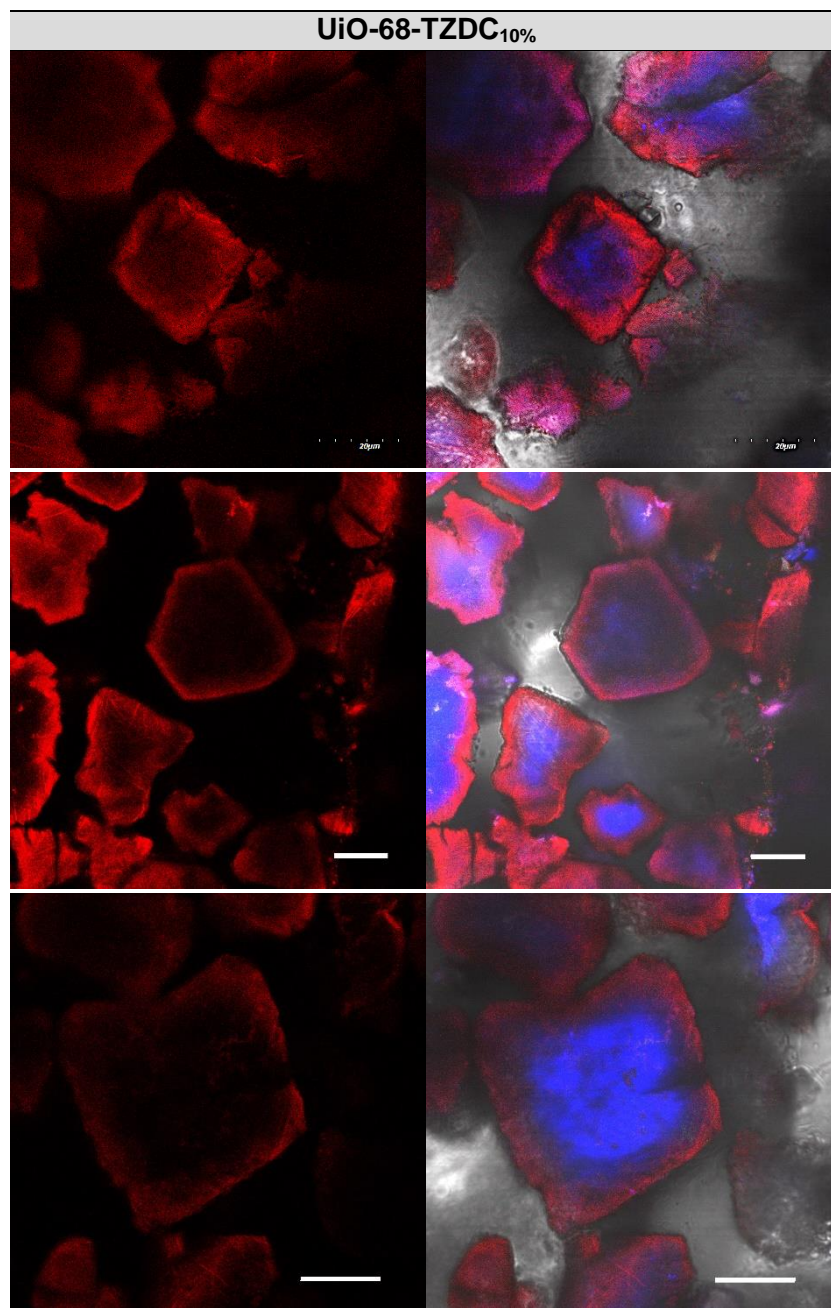


Figure S45. Confocal images of UiO-68-TZDC_{10%} polished crystals' molds. Scale bars correspond to 25 μm.

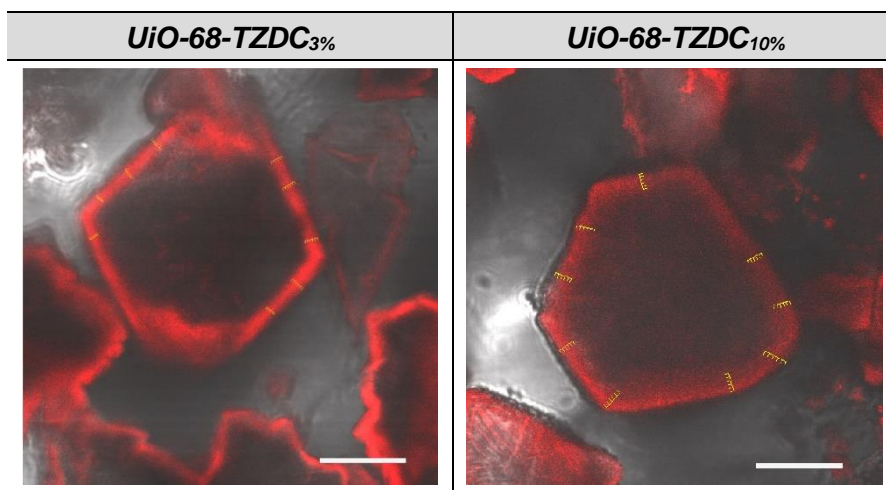


Figure S46. Rough estimation of the thickness of the shell. The shell in the 3% sample ($2.93 \pm 0.50 \mu\text{m}$) is slightly thicker than the 10% case ($4.67 \pm 0.63 \mu\text{m}$), suggesting that the concentration of TZDC might be controlling the shell thickness for short reaction times (3 hours).

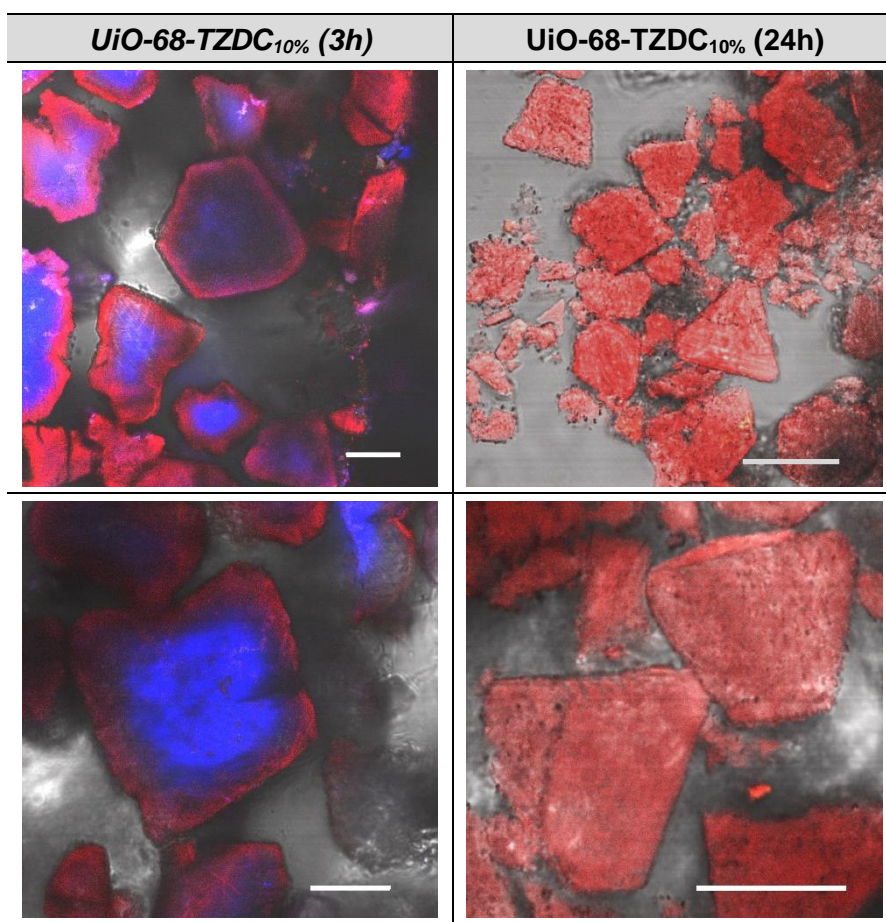


Figure S47. Compared to the asymmetric core-shell distribution present after 3 hours, the longer reaction time seems to favour the diffusion of TZDC across the crystal for a more homogeneous distribution not distinguishable in *UiO-68-TZDC*_{10%}(24h). Scale bar correspond to 25 μm .

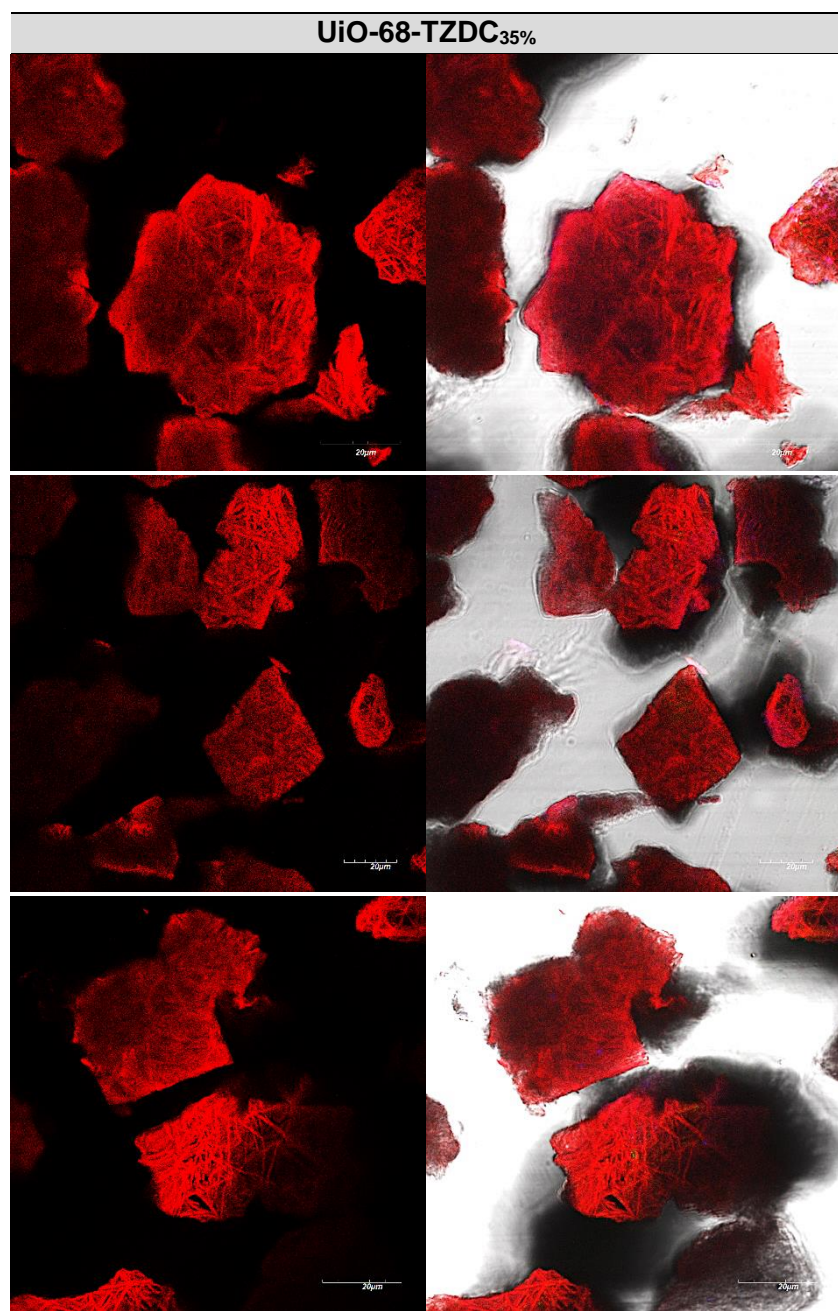


Figure S48. Confocal images of UiO-68-TZDC_{35%} polished crystals' molds. Scale bars correspond to 25 μm .

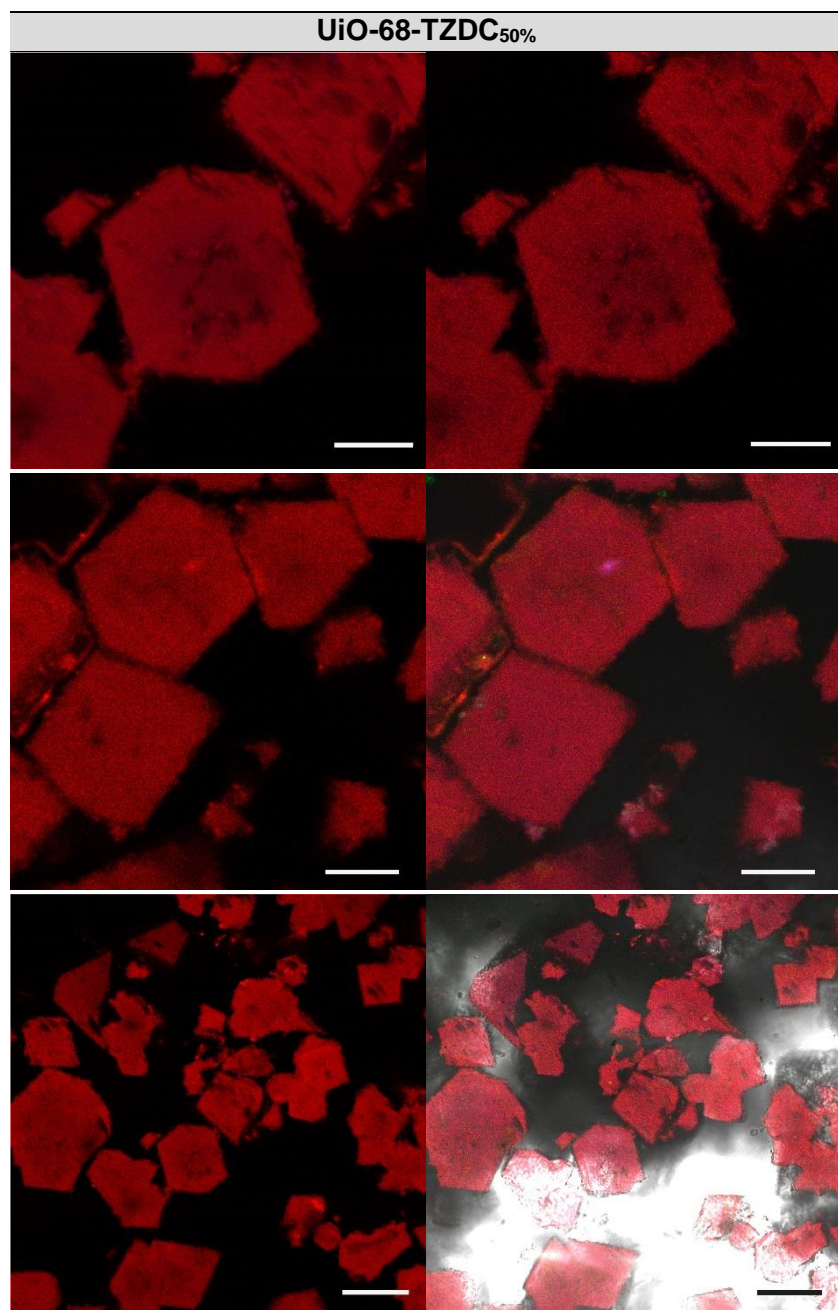


Figure S49. Confocal images of UiO-68-TZDC_{50%} polished crystals' molds. Scale bars correspond to 25 μm .

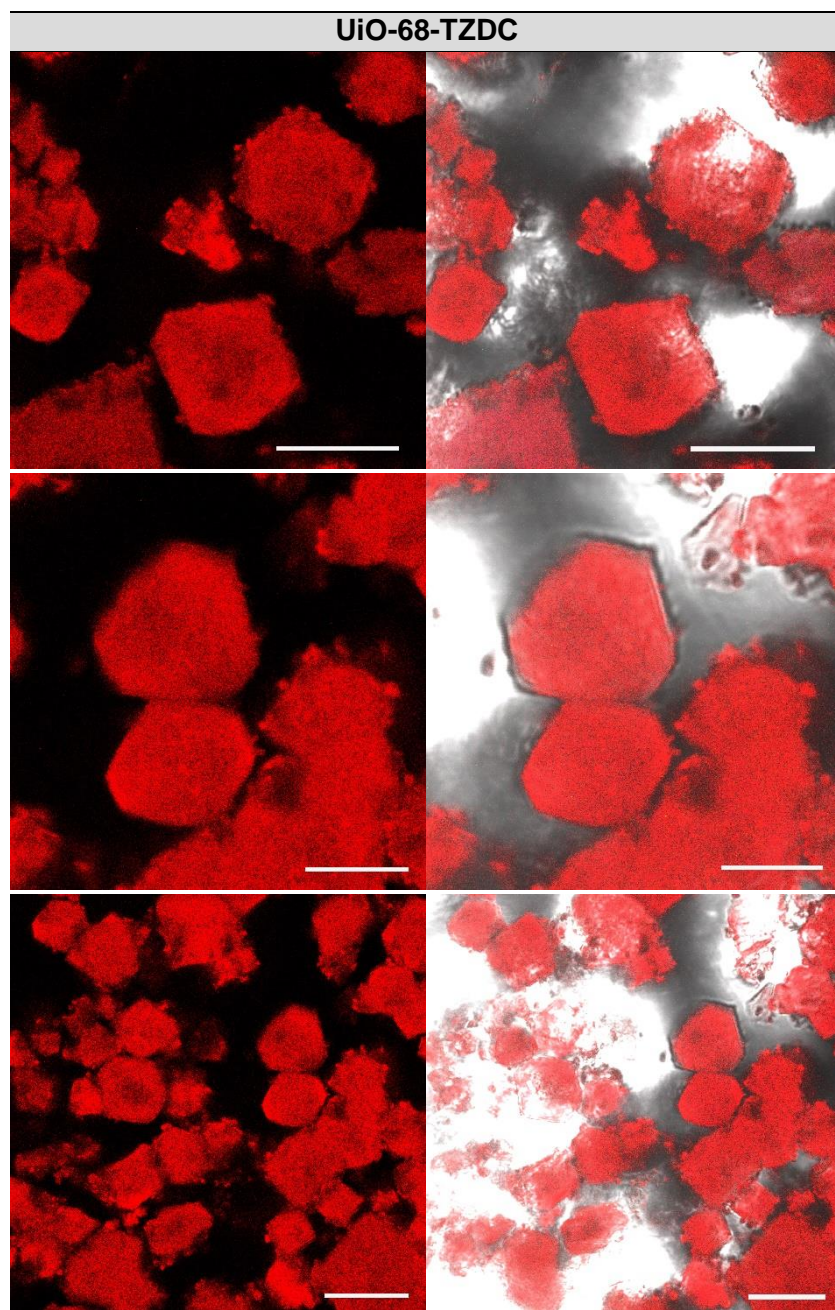


Figure S50. Confocal images of UiO-68-TZDC polished crystals' molds. Scale bars correspond to 10 μm .

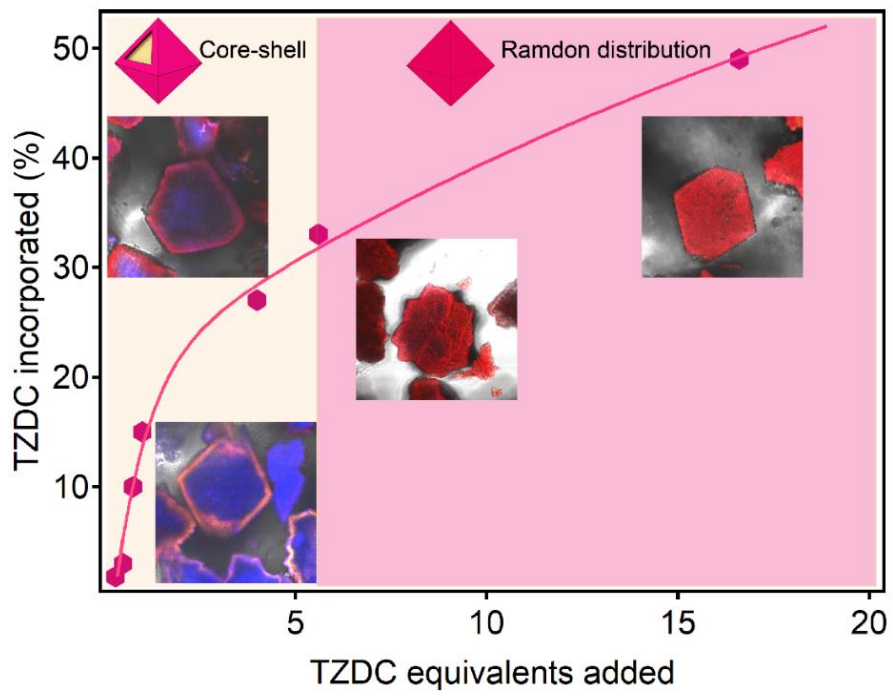


Figure S51. Resultant microstructures at a glance.

S8. Photocatalytic experiments

Methyl viologen reduction

Photoinduced electron transfer experiments were carried out using MOF dispersions (0.2 mg/mL) in water/methanol mixtures (4:1, v/v%) containing MV²⁺ (0.15 mM). The MOF dispersions containing MV²⁺ were sonicated, placed in a quartz cuvette capped with rubber septum and Ar purged for 15 minutes prior irradiation with a 300 W Xe lamp. The UV-Vis absorbance of the cuvettes was measured at different irradiation times. The photoinduced electron transfer measurements were followed by the decrease of the MV²⁺ absorption band centered at 260 nm as well as the increase of the MV^{•+} radical cation absorption bands at 395 and 605 nm.

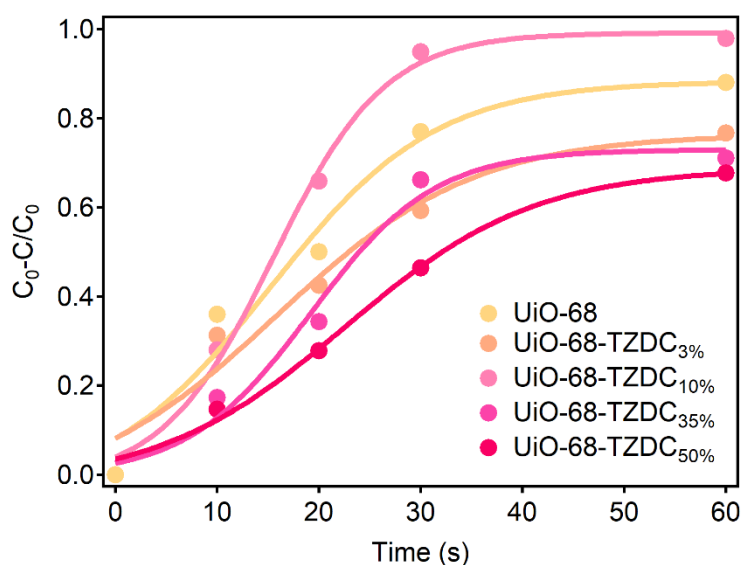


Figure S52. Photocatalytic methyl viologen reduction yields in 1 minute of reaction of UiO-68 and multivariate UiO-68-TZDC_x solids (x = 3, 10, 35 and 50%).

H₂ production

A quartz photoreactor equipped with a manometer was loaded with sonicated dispersions of the corresponding MOFs at 1 mg/mL concentration in H₂O:MeOH (4:1, v/v%) mixture. Prior irradiation the dispersions were purged with Ar for 15 minutes and pressurized at a final pressure of 1.3 bar. The photoreactor was located under the spot UV-Vis light of an optic fiber from a 300 W Xe lamp at 110 mW/cm² for 6.5 h. The H₂ evolution was followed by injecting 250 μL of the reactor gases in an Agilent 490 MicroGC with a TC detector and Ar as carrier gas (MolSieve 5A column). Quantification of the percentage of each gas was based on prior calibration of the system injecting mixtures of H₂ and Ar with known percentage of gases. Quantum efficiency measurements were carried out measuring the lamp photon flux using a calibrated Si diode and taking into account the produced H₂.

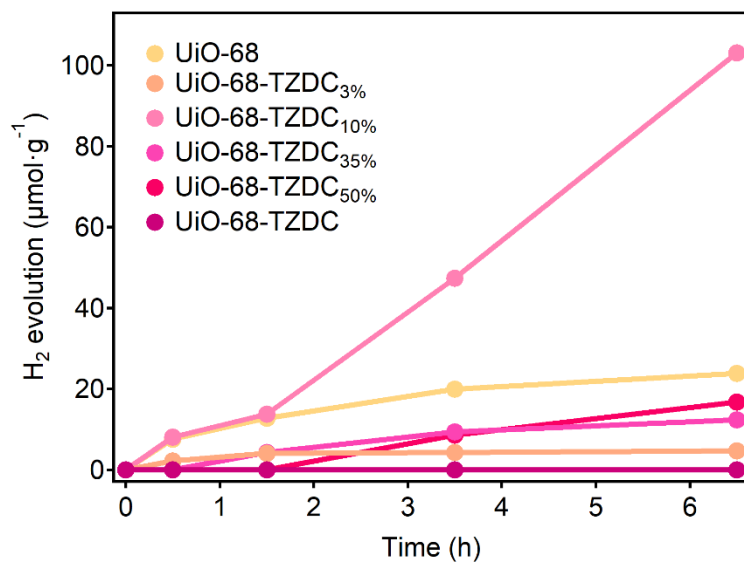


Figure S53. Photocatalytic H₂ production after 6.5 hours of irradiation for UiO-68 and multivariate UiO-68-TZDC_x solids (x = 3, 10, 35 and 50%).

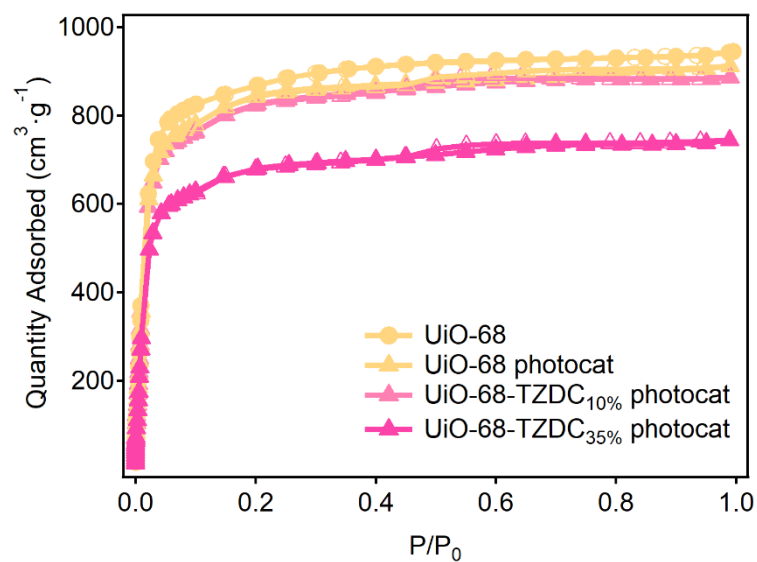


Figure S54. N₂ adsorption/desorption isotherm analysis of UiO-68, UiO-68-TZDC_{10%} and UiO-68-TZDC_{35%} after the photocatalytic experiments.

ICP-MS experiments

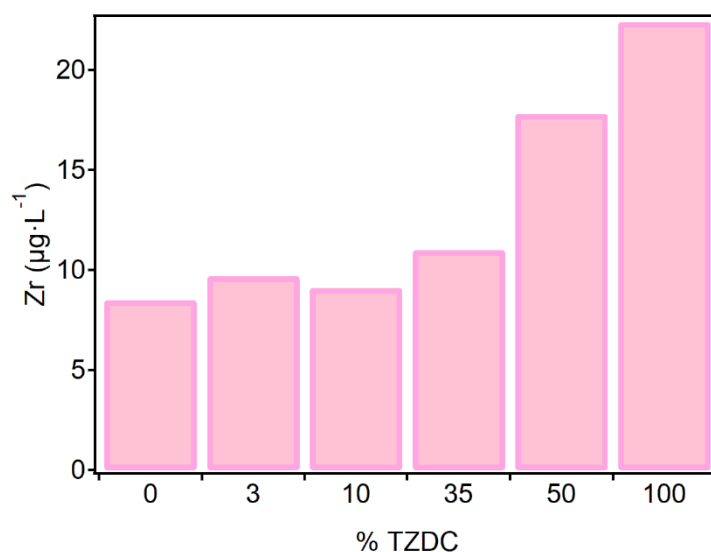


Figure S55. Metal leaching of UiO-68, UiO-68-TZDC and multivariate UiO-68-TZDC_x solids ($x = 3, 10, 35$ and 50%) determined by ICP-MS of the supernatant after soaking in H₂O:MeOH (4:1, v/v%) solutions for 24h.

Table S13. ICP-MS values of metal leaching of UiO-68, UiO-68-TZDC and multivariate UiO-68-TZDC_x solids ($x = 3, 10, 35$ and 50%)

Framework	TPDC	TZDC _{3%}	TZDC _{10%}	TZDC _{35%}	TZDC _{50%}	TZDC
Zr (µg·mL ⁻¹)	8.5	9.7	9.1	11.0	17.8	22.4

XPS experiments

Table S14. Changes in the chemical composition of UiO-68, UiO-68-TZDC and multivariate UiO-68-TZDC_{x%}. The bulk content of TZDC was quantified with ¹H-NMR analysis of digested crystals. The relative ratio of TZDC in the surface of the crystals was calculated from the total areas of N_{1s} and Zr_{3d} in the XPS spectra.

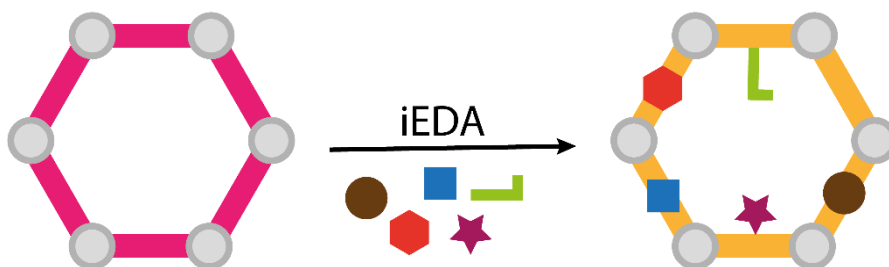
Framework	TPDC	TZDC _{3%}	TZDC _{10%}	TZDC _{35%}	TZDC _{50%}	TZDC
Bulk content (NMR)	0	2.73	11.1	34.5	47.8	100
N _{1s} /Zr _{3d}	0	0.323	0.657	1.133	1.124	0.978
Surface ratio (XPS)	0	0.323	0.657	1.133	1.124	0.978

References

- (1) Liu, J.; Lukose, B.; Shekhah, O.; Arslan, H. K.; Weidler, P.; Gliemann, H.; Bräse, S.; Grosjean, S.; Godt, A.; Feng, X.; Müllen, K.; Magdau, I.-B.; Heine, T.; Wöll, C. A Novel Series of Isoreticular Metal Organic Frameworks: Realizing Metastable Structures by Liquid Phase Epitaxy. *Sci. Rep.* **2012**, *2*, 921.
- (2) Calahorro, A. J.; Fernández, B.; García-Gallarín, C.; Melguizo, M.; Fairen-Jimenez, D.; Zaragoza, G.; Salinas-Castillo, A.; Gómez-Ruiz, S.; Rodríguez-Diéguez, A. Towards a Potential 4,4'-(1,2,4,5-Tetrazine-3,6-Diyl) Dibenzoic Spacer to Construct Metal-Organic Frameworks. *New J. Chem.* **2015**, *39*, 6453–6458.
- (3) Tanko, J. M. Encyclopedia of Electrochemistry, Volume 8: Organic Electrochemistry Edited by Hans J. Schäfer (Universität Münster). Series Edited by Allen J. Bard and Martin Stratmann. *J. Am. Chem. Soc.* **2005**, *127*, 4538–4538.
- (4) Jia, J.; Gutiérrez-Arzaluz, L.; Shekhah, O.; Alsadun, N.; Czaban- Józwiak, J.; Zhou, S.; Bakr, O. M.; Mohammed, O. F.; Eddaoudi, M. Access to Highly Efficient Energy Transfer in Metal-Organic Frameworks via Mixed Linkers Approach. *J. Am. Chem. Soc.* **2020**, *142*, 8580–8584.
- (5) Kresse, G.; Furthmüller, J. Efficiency of Ab-Initio Total Energy Calculations for Metals and Semiconductors Using a Plane-Wave Basis Set. *Comput. Mater. Sci.* **1996**, *6*, 15– 50.
- (6) Kresse, G.; Furthmüller, J. Efficient Iterative Schemes for Ab Initio Total-Energy Calculations Using a Plane-Wave Basis Set. *Phys. Rev. B: Condens. Matter Mater. Phys.* **1996**, *54*, 11169– 11186.
- (7) Perdew, J. P.; Burke, K.; Ernzerhof, M. Generalized Gradient Approximation Made Simple. *Phys. Rev. Lett.* **1996**, *77*, 3865– 3868.
- (8) Lejaeghere, K.; Bihlmayer, G.; Björkman, T.; Blaha, P.; Blügel, S. Reproducibility in density functional theory calculations of solids. *Science* **2016**, *351*, 1415 .
- (9) De Vos, A.; Hendrickx, K.; Van Der Voort, P.; Speybroeck, V. Van; Lejaeghere, K. Missing Linkers: An Alternative Pathway to UiO-66 Electronic Structure Engineering. *Chem. Mater.* **2017**, *29*, 3006–3019.
- (10) Hendrickx, K.; Vanpoucke, D. E. P.; Leus, K.; Lejaeghere, K.; Van, A.; Deyne, Y.-D.; Speybroeck, V. Van; Van Der Voort, P.; Hemelsoet, K. Understanding Intrinsic Light Absorption Properties of UiO-66 Frameworks: A Combined Theoretical and Experimental Study. *Inorg. Chem.* **2015**, *54*, 10701–10710.

Chapter 4:

Exploiting tetrazine tag to enrich pore complexity: from pyridazine networks to fulleretic materials



1. Motivation

Besides the intrinsic properties of *s*-tetrazines presented in the previous chapter, their chemical reactivity also offers interesting perspectives in the context of MOF functionalization. These molecules can act as dienes in inverse Electron-Demand Diels-Alder (iEDDA). Diels-Alder reactions are [4+2]-cycloaddition in which a diene (in our case *s*-tetrazines) and a dienophile (alkene or alkyne) react to form a six-membered ring by suprafacial interaction of 4π -electrons of the diene with the 2π -electrons of the dienophile. Considering the electronic properties of the reactants which may contain electron-donating group (EDG) or electron withdrawing group (EWG) and, consequently, the reactants' frontier molecular orbitals, two types of Diels-Alder reactions are possible: *i*) normal Electron Demand Diels-Alder reaction (nEDDA), and *ii*) inverse Electron-Demand Diels-Alder (iEDDA) (Figure 4.1 a). Compared to the nEDDA reaction, in which an electron-rich diene reacts with an electron-poor dienophile; the iEDDA reaction relies on the reaction of an electron-rich dienophile with an electron-poor diene. The ability of tetrazines to react with unsaturated compounds was first revealed in 1959 by Lindsey et al.¹ This Diels-Alder mechanism may be described as a 1,4-addition of the $-\text{C}=\text{N}=\text{N}=\text{C}-$ diene system of the tetrazine to an appropriate alkene, yielding a highly strained bicyclic intermediate. The adduct undergoes a retro-Diels-Alder reaction to afford the corresponding 4,5-dihydropyridazine, which either isomerises to the corresponding 1,4-dihydro-isomers or is oxidized to give a pyridazine product in addition to the formation of molecular nitrogen (Figure 4.1 b). However, when the reaction takes place with an alkyne dienophile, it directly yields to the respective pyridazine.

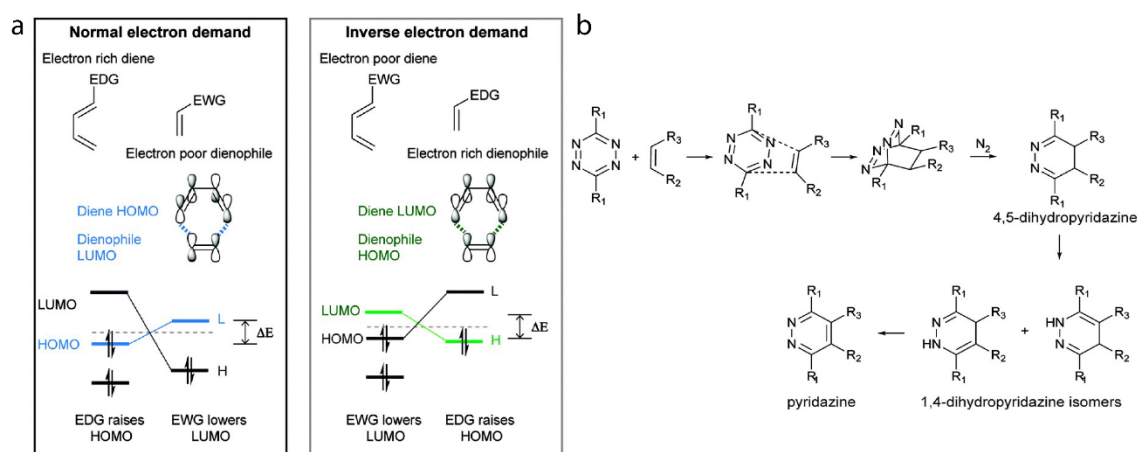


Figure 4.1. Mechanism of IEDDA reaction. a) Frontier molecular orbital of normal and inverse electron demand Diels-Alder reaction. EDG = electron-donating group, EWG = electron-withdrawing group. b) Schematic representation of the reaction between a dienophile and a tetrazine. Extracted from ref 2.

The features of this reaction can be tailored by the chemical properties of the reagents. The presence of EDG or EWG modifies the orbital energies to variable

HOMOdienophile–LUMOdienene energy differences and, as a result, the iEDDA reactivity. The strain and steric effects can also have an impact. The strained dienophiles are more reactive due to their pre-distorted conformation towards the transition structures. Therefore, less distortion energies are needed for the dienophile to react. In turn, substrates with increasing steric hindrance difficult the reactivity, and alkenes and alkynes dienophiles are thus more reactive than the corresponding internal ones.

The reactivity of tetrazines as dienes in iEDDA reactions has been thoroughly studied in solution, with particular focus on the targeted synthesis of natural products,² and bioconjugation reactions,³ probably due to the intrinsic features of the reaction. This type of reactions require no catalyst, offer fast kinetics, orthogonality, quantitative transformations under mild conditions, and inoffensive side products (N₂), so they may be considered as “click chemistry” reactions. As a result, tetrazines are a promising molecule for being used as a chemical tag in post-synthetic covalent modifications (PSM) of reticular solids. Tetrazine moiety complement the traditional employed groups such as amino,⁴ aldehyde⁵, azide⁶ or alkyne.⁷ PSM is an universal route used to incorporate a broad variety of functional groups to pre-assembled reticular solids.^{8,9} This strategy offers significant advantages compared to the direct synthesis methodologies. It is more respectful with the structural integrity of the framework and offers more precise control over the type and density of the functional groups that can be incorporated to the organic and/or inorganic components of the net. Moreover, it enables the production of frameworks that are sometimes not accessible by direct synthesis. Hence, this strategy is an excellent tool for engineering the pore chemistry and physical properties of MOFs.¹⁰

The use of tetrazine reactivity in MOFs chemistry is based almost exclusively on the incorporation of dienophiles as olefins^{11,12} for specific reasons such as increasing their hydrophobicity for membrane fabrication,¹³ as well as, increasing CO₂ adsorption for higher CO₂/N₂ selectivity,¹⁴ or controlling framework interpenetration.¹⁵ However, generic post-functionalization routes based on tetrazine tags are still missing. In this regard, we decided to use the tetrazine framework UiO-68-TZDC (presented in **Chapter 3**) as a platform to explore the versatility of this reactivity to tailor the chemistry of mesopores with diverse chemical functionalities. The reticulation of the tetrazine in the organic backbone also opens the possibility to study the effect of the reticulation in the iEDDA reactivity.

2. Summary of the key results:

The results of this chapter are in the process of being published in “Lerma-Berlanga, B.†; R. Ganivet, C.†; Almora-Barrios, N.; Vismara, R.; A. R. Navarro, J.; Tatay, S.; M. Padial, N. and Martí-Gastaldo, C. Tetrazine linkers as plug-and-play tags for general framework functionalization and C₆₀ conjugation”. In this work, we reported

the versatility of UiO-68-TZDC as a platform to host different pore functionalities incorporated by post synthetic iEDDA covalent modifications. Besides, the tetrazine coordination offers the possibility of studying the influence over the iEDDA reactivity of the nanostructured diene, which is not accessible in conventional organic-chemistry experiments.

Initially, the iEDDA reactivity of UiO-68-TZDC was tested using 2,5-norbornadiene (NBD) as model substrate. We reacted the MOF crystals under different synthetic conditions (solvent, temperature, time and even dienophile equivalents per tetrazine linker). The optimal parameters were determined based on PXRD patterns. The best compromise between clean functionalization and negligible impact to the crystallinity of the framework was reached at 40 °C, with poor impact of the rest of parameters. We assumed that reactivity in the framework was controlled by the same mechanism that operates in solution (*Figure 4.2. a*). That resulted in the formation of a pyridazine core (PZDC), which was associated with the loss of the dark pink colour related to TZDC. The resultant yellow solid was digested, and the solution was analysed by ¹H-NMR. The disappearance of the TZDC signals, and the appearance of new ones associated with PZDC product confirmed the total conversion (*Figure 4.2. b*). The characterization techniques such as SEM, PXRD and N₂ adsorption showed the negligible changes in morphology, cell parameters, and structural robustness, respectively, after the reaction took place. Regarding stability, UiO-68-PZDC displayed higher chemical robustness than UiO-68-TZDC, comparable to that of pristine UiO-68. Probably, it was attributed to the reduction of the central ring polarity which was responsible of the interactions of the framework with water. As for the thermal decomposition profiles they do not display significant changes.

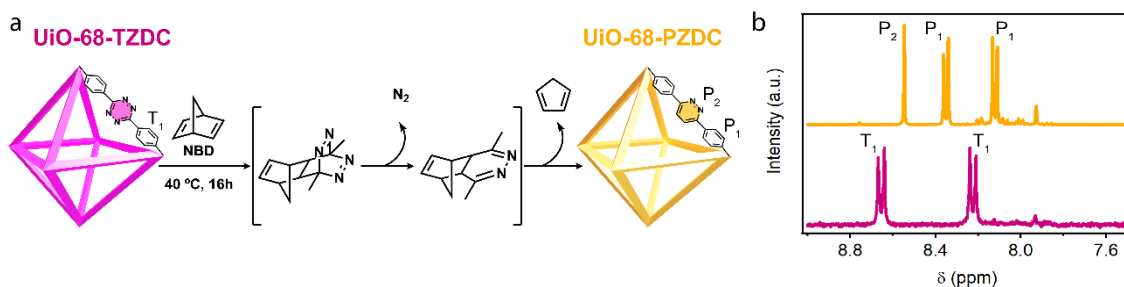


Figure 4.2. a) Mechanism of the iEDDA reaction between UiO-68-TZDC and NBD for post-synthetic modification of the framework. b) ¹H-NMR spectra before/after reaction.

For a better understanding the effect of TZDC reticulation over iEDDA reactivity with NBD, the reaction was monitored in controlled time intervals of up to 24 hours. The gradual discoloration of the MOF (*Figure 4.3. a*), which might be considered representative of the progress of the iEDDA reaction, was followed by UV-Vis solid-state diffuse reflectance spectroscopy measurements (*Figure 4.3. b*). Later, we designed alternative experiments to obtain a direct comparison of the conversion degree in the MOF and in the free ligand. For that, the amount of MOF and linker

were fixed to ensure the same effective concentration of the tetrazine units in both experiments. The reaction conditions were given by the solubility limitations of the linker. Thus, we opted for reactions in DMF at 70 °C. As described above, the reactions were monitored in controlled time intervals of up to 24 hours. The products for each reaction time were digested and analysed by $^1\text{H-NMR}$. The integration of pyridazine peak area by using fumaric acid as an internal standard enabled the quantification of the rate of conversion (%). In both cases, the kinetic rate profiles of PZDC formation with reaction time showed an exponential profile indicative of a pseudo-first order reaction with a plateau near 95 % of PZDC formed. The analysis of the kinetic curves showed that the reaction proceeded much faster in the case of the MOF, even with the expected limitations for the diffusion of the dienophile into the framework. In order to rule out the catalytic effect of Zr(IV) ions, we carried out an additional test with the free linker in presence of ZrCl_4 . The results showed the negligible effect on the reaction rate for the free linker (*Figure 4.3. c*).

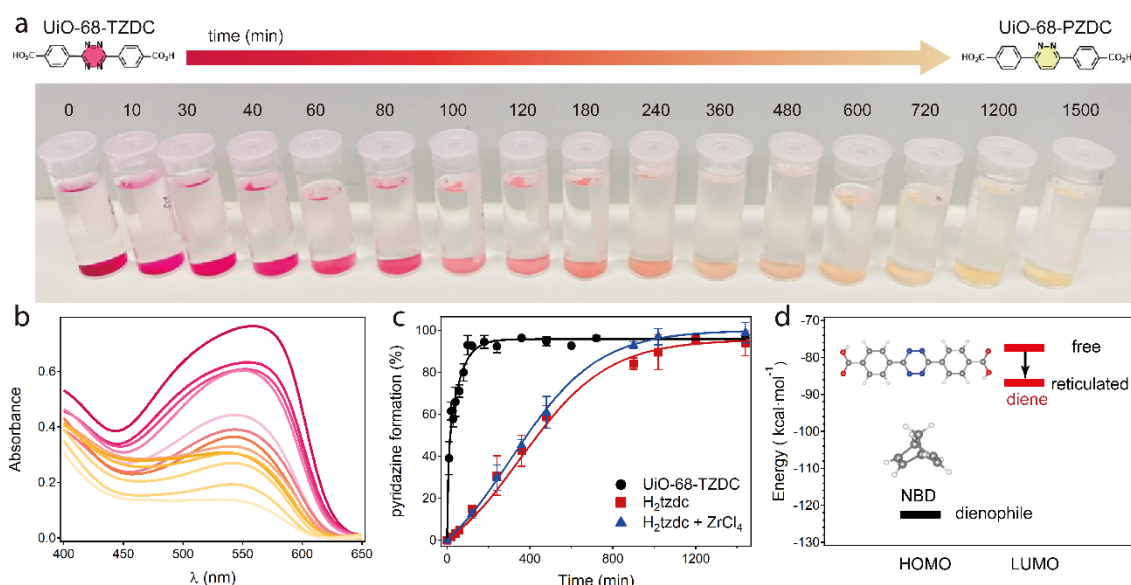


Figure 4.3. a) Progressive change in colour with time of UiO-68-TZDC crystals by iEDDA reaction with NBD in ether at 40 °C. b) Evolution of the UV-Vis diffuse reflectance spectra of the solid. c) Kinetic profile for the formation of pyridazine for UiO-68-TZDC compared to the H_2tzdc linker in equivalent conditions in DMF at 70 °C. Percentages of conversion were quantified by $^1\text{H-NMR}$ analysis. e) DFT calculation showing the effect of reticulation in shifting the energy of the diene LUMO for an increase in the reaction rate. Inset: structure calculated for H_2tzdc and for NBD.

In view of those results, we argued the accelerated reactivity in UiO-68-TZDC can be attributed to a sum of different reasons: *i*) increase of diene accessibility, and *ii*) electronic factors. Reticulation of TZDC in the framework was certainly effective in preventing π - π stacking of the diene molecules in solution, that may favour its accessibility, as well as the reactivity. Regarding electronic factors, the metal coordination may modulate the energies of frontier molecular orbitals. DFT-VASP calculations were employed to analyse the electronic effect of Zr(IV) coordination in

shifting the LUCO of UiO-68-TZDC, that was centred at the tetrazine linker. The results showed a decrease in energy of 3.8 kcal·mol⁻¹ compared to the free linker. That narrowed the gap between frontier orbitals, LUMO from the diene and HOMO from the dienophile, and consequently, it increased the reaction rate (*Figure 4.3. d*). Those computational studies were done by Neyvis Almora-Barrios. Although we could not exclude the effect of free carboxylic groups in disfavoured the reactivity of free H₂tzdc, the electronic effect seemed to be the most likely reason for the enhanced UiO-68-TZDC reactivity.

Following those experiments, we analysed the versatility of the iEDDA reaction for the PSM of UiO-68-TZDC. For that, we tested an ample range of functionalized alkene/alkyne dienophiles. Those scope led to multiple pore environments in UiO-68-PZDC derivates which incorporated functionalities such as fused rings, hydroxy groups, phenyl rings, succinimide, carboxylic terminated groups, aliphatic chains, and even chiral moieties. The formation of the iEDDA reaction products were examined by ¹H-NMR. The analysis of the signals confirmed the disappearance of the TZDC signals, and the appearance of new ones associated with the desired products. Those results suggested a conversion rate close to 95 %, except for the alkene unstrained dienophiles which presented poorer reactivity and required more drastic conditions to achieve higher yields. The formation of the products was additionally confirmed by mass spectrometry, as well as a clear conversion was proved by elemental and TGA analysis of activated solids. The PXRD (*Figure 4.4. a*), SEM-images and N₂ isotherms of the crystals after PSM reaction confirmed the retainment of the crystallinity, morphology, and the structural robustness, respectively, showing a minimum impact to the original structure.

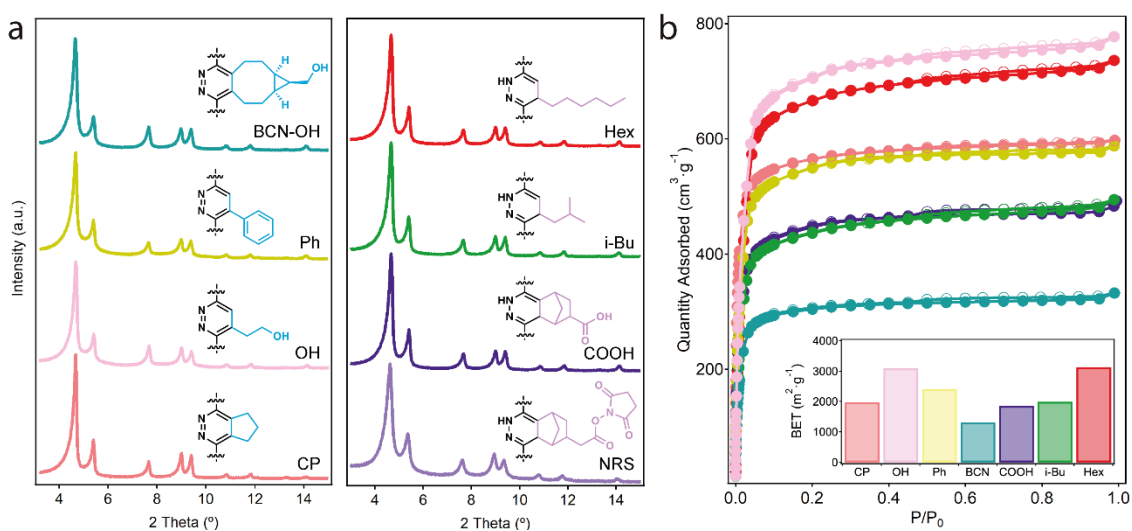


Figure 4.4. a) PXRD patterns of UiO-68-PZDC derivatives confirm minimum impact to crystallinity after iEDDA reaction in all cases. Decorating groups in mesoporous cavities (*inset*). b) N₂ isotherms at 77 K and experimental BET surface areas (*inset*).

Regarding surface areas, the values oscillate from 3100 to 1300 m²·g⁻¹ (*Figure 4.4. b*). Those changes were associated to the incorporation of bulky substituents to the framework cavities and were in good agreement with the effect of steric crowding in the pore volume calculated from framework models. Those were generated computationally by Neyvis Almora-Barrios with Materials Studio R2 and analysed by Sergio Tatay with *zeo++*.¹⁶

We used the versatility of the UiO-68-TZDC platform to go one step further and introduce nanocarbon units in a controlled manner. The spherical shape, high degree of symmetry and number of double bonds of C₆₀ make it an ideal dienophile for the construction of supramolecular architectures by iEDDA. In contrast to the previous methods in which fullerene was encapsulated in the pores by infiltration or mechanical grinding, our approach enabled the creation of supramolecular architectures in which fullerene positions were fixed by the reactivity of the organic component of the framework. The interesting properties of fullerenes are well-known. C₆₀ is an electron acceptor which also possesses good thermal stability, consequently these properties have resulted in its application in organic solar cells,¹⁷ superconductors,¹⁸ and ferromagnetic materials.¹⁹ In addition, fullerene compounds may be a good candidate to perform gas sorption and separation when diluted in porous matrices due to the excellent gas binding interactions of C₆₀.²⁰

The synthetic conditions described above were adapted taking into account the low solubility of fullerenes. As a result, we produced UiO-68-PZDC(C₆₀) framework by covalent anchoring of C₆₀ molecules. The reaction induced a change in the colour of the crystals from pink to brownish which was an indicative of the covalent conjugation (*Figure 4.5. a*). Different tests were performed to confirm the successful functionalization. Firstly, UiO-68-PZDC(C₆₀) crystals were conscientiously washed with toluene to remove the unreacted fullerene encapsulated or physisorbed. Even after that process, the crystals remained brown. The UV-Vis solid spectrum of UiO-68-PZDC(C₆₀) revealed features at different wavenumbers when compared to pristine C₆₀ suggesting electronic changes. The SS-MAS-¹³CNMR spectra of crystals showed the presence of new broad signals around 142 ppm that can be attributed to sp²-carbons of bonded fullerene (*Figure 4.5. b*). The covalent functionalization was further confirmed by mass spectrometry of digested crystals. The positive MALDI-TOF spectrum presented a peak centred at m/z = 1033 associated to hydrated monoadducts of pyridazine which fragmentation generated a peak m/z = 720 of neat fullerene molecules (*Figure 4.5. c*). For better understanding of the structure of that fulleretic material, we used a structural model generated with Materials Studio as an initial input for the Rietveld refinement of a high-resolution powder diffraction data set. That refinement was carried out by Rebecca Vismara. UiO-68-PZDC(C₆₀) was isostructural to UiO-68-TZDC but displayed slightly elongated cell axis and the covalent conjugation of C₆₀ units to the tetrazine ring for the formation of H₂pzdc-C₆₀ units (*Figure 4.5. d, e*). The occupancy factors of fullerene molecules were refined freely to account for the total functionalization.

The model converged for the formation of nearly up to 50 % of pyridazine units (PZDC-C₆₀) getting a crystallographic unit cell formula of [Zr₆O₄(OH)₄(PZDC-C₆₀)₃(TZDC)₃]. That degree of functionalization was in excellent agreement with the elemental and thermogravimetric analysis of the crystals.

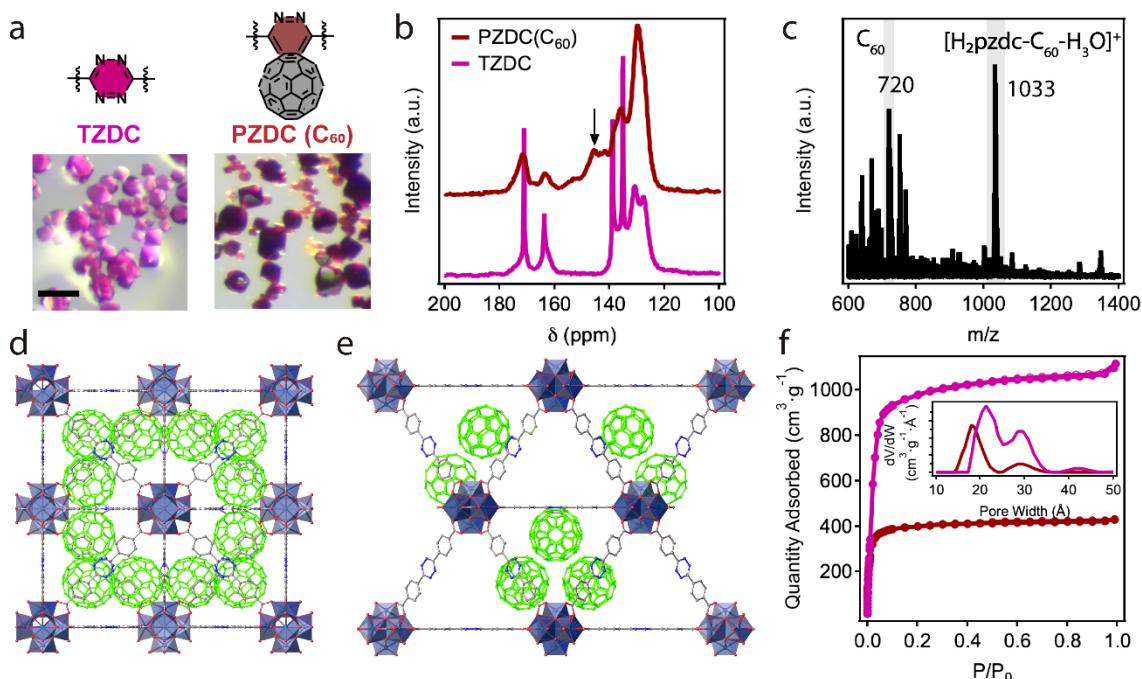


Figure 4.5. a) Crystals of UiO-68-TZDC before and after reaction with fullerene. Scale bars correspond to 50 μm . b) Solid-state ^{13}C -NMR spectra of UiO-68-TZDC and UiO-68-PZDC(C₆₀) revealing the appearance of an additional band in the sp^2 carbon region. d) Mass spectra of UiO-68-PZDC(C₆₀) crystals digested in acid. Structure of UiO-68-PZDC(C₆₀) along d) 100 and e) 110 showing the distribution of fullerenes in half the tetrahedral cavities characteristic of UiO-type frameworks. The symmetry was reduced from $Fm-3m$ to $P23$ for the sake of clarity. The solvent molecules and hydrogen atoms have been omitted for clarity. f) Experimental N_2 isotherms of UiO-68-TZDC and PZDC(C₆₀) at 77 K and the corresponding NLDFT-PSD graphs (inset).

In addition, the accessible porosity of the crystals was consistent to the conjugation of three C₆₀ molecules to the edges of 50% of the tetrahedral cavities. The material showed a type-I isotherm with retention of micro (1.8 nm) and mesoporosity (2.9 nm) with an experimental surface area of near 1700 $\text{m}^2\cdot\text{g}^{-1}$ and a pore volume reduction near to 50% compared to pristine UiO-68-TZDC (0.65 and 1.51 $\text{cm}^3\cdot\text{g}^{-1}$, respectively) (Figure 4.5. f inset). Additional experiments were performed to understand the persistent percentage of functionalization. For that, we extended the reaction time to five days which resulted in a very similar functionalization, suggesting that the upper limit was not controlled by diffusion limitations, but it was imposed by the steric crowding of the pore and the repulsive intermolecular interactions. That result was corroborated with an alternative experiment using UiO-68-TZDC_{44%} (see Chapter 3), a multivariate MOF which contained approximately half of the reactive linkers. For that case, the results showed a complete functionalization when tetrazine moieties were diluted in the framework.

3. References

- (1) Lindsey, R. A. C. and R. V. Reactions of Tetrazines with Unsaturated Compounds. A New Synthesis of Pyridazines. *J. Am. Chem. Soc.* **1959**, *81* (16), 4342–4346.
- (2) Oliveira, B. L.; Guo, Z.; Bernardes, G. J. L. Inverse Electron Demand Diels-Alder Reactions in Chemical Biology. *Chem. Soc. Rev.* **2017**, *46* (16), 4895–4950.
- (3) Zhang, J.; Shukla, V.; Boger, D. L. Inverse Electron Demand Diels-Alder Reactions of Heterocyclic Azadienes, 1-Aza-1,3-Butadienes, Cyclopropenone Ketals, and Related Systems. A Retrospective. *J. Org. Chem.* **2019**, *84* (15), 9397–9445.
- (4) Wang, Z.; Cohen, S. M. Postsynthetic Covalent Modification of a Neutral Metal-Organic Framework. *J. Am. Chem. Soc.* **2007**, *129* (41), 12368–12369.
- (5) Huang, A.; Caro, J. Covalent Post-Functionalization of Zeolitic Imidazolate Framework ZIF-90 Membrane for Enhanced Hydrogen Selectivity. *Angew. Chem. Int. Ed.* **2011**, *50* (21), 4979–4982.
- (6) Goto, Y.; Sato, H.; Shinkai, S.; Sada, K. “ Clickable ” Metal - Organic Framework. *J. Am. Chem. Soc.* **2008**, *130*, (44), 14354–14355.
- (7) Li, B.; Gui, B.; Hu, G.; Yuan, D.; Wang, C. Postsynthetic Modification of an Alkyne-Tagged Zirconium Metal-Organic Framework via a Click Reaction. *Inorg. Chem.* **2015**, *54* (11), 5139–5141.
- (8) Tanabe, K. K.; Cohen, S. M. Postsynthetic Modification of Metal–Organic Frameworks—a Progress Report. *Chem. Soc. Rev.* **2011**, *40* (2), 498–519.
- (9) Kalaj, M.; Cohen, S. M. Postsynthetic Modification: An Enabling Technology for the Advancement of Metal-Organic Frameworks. *ACS Cent. Sci.* **2020**, *6* (7), 1046–1057.
- (10) Mandal, S.; Natarajan, S.; Mani, P.; Pankajakshan, A. Post-Synthetic Modification of Metal–Organic Frameworks Toward Applications. *Adv. Funct. Mater.* **2021**, *31* (4), 1–22.
- (11) Vinu, M.; Sivasankar, K.; Prabu, S.; Han, J. L.; Lin, C. H.; Yang, C. C.; Demel, J. Tetrazine-Based Metal-Organic Frameworks as Scaffolds for Post-Synthetic Modification by the Click Reaction. *Eur. J. Inorg. Chem.* **2019**, *5*, 461–466.
- (12) Chen, C.; Allen, C. A.; Cohen, S. M. Tandem Postsynthetic Modification of Metal-Organic Frameworks Using an Inverse-Electron-Demand Diels-Alder Reaction. *Inorg. Chem.* **2011**, *50* (21), 10534–10536.
- (13) Feng, L.; Lo, S. H.; Tan, K.; Li, B. H.; Yuan, S.; Lin, Y. F.; Lin, C. H.; Wang, S. L.; Lu, K. L.; Zhou, H. C. An Encapsulation-Rearrangement Strategy to Integrate Superhydrophobicity into Mesoporous Metal-Organic Frameworks. *Matter* **2020**, *2* (4), 988–999.
- (14) Zhang, Y. J.; Nie, H. X.; Yu, M. H.; Chang, Z. Post-Synthetic Modification of Tetrazine Functionalized Porous MOF for CO₂ Sorption Performances Modulation. *J. Solid State Chem.* **2021**, *300*, 122257.
- (15) Jędrzejowski, D.; Pander, M.; Nitek, W.; Bury, W.; Matoga, D. Turning Flexibility into Rigidity: Stepwise Locking of Interpenetrating Networks in a MOF Crystal through Click Reaction. *Chem. Mater.* **2021**, *33* (18), 7509–7517.
- (16) Willems, T. F.; Rycroft, C. H.; Kazi, M.; Meza, J. C.; Haranczyk, M. Algorithms and Tools for High-Throughput Geometry-Based Analysis of Crystalline Porous Materials. *Microporous Mesoporous Mater.* **2012**, *149* (1), 134–141.
- (17) Khlyabich, P. P.; Burkhart, B.; Thompson, B. C. Efficient Ternary Blend Bulk Heterojunction Solar Cells with Tunable Open-Circuit Voltage. *J. Am. Chem. Soc.* **2011**, *133* (37), 14534–14537.
- (18) Buntar, V.; Sauerzopf, F. M.; Weber, H. W.; Halushka, M.; Kuzmany, H. Mixed State Parameters

- of Single Crystalline Rb₃ C₆₀ Fullerene Superconductors. *Phys. Rev. B - Condens. Matter Mater. Phys.* **2005**, 72 (2), 1–6.
- (19) Nakano, S.; Kitagawa, Y.; Kawakami, T.; Okumura, M.; Nagao, H.; Yamaguchi, K. Theoretical Studies on Electronic States of Rh-C₆₀. Possibility of a Room-Temperature Organic Ferromagnet. *Molecules* **2004**, 9 (9), 792–807.
- (20) Yuan, Y.; Cui, P.; Tian, Y.; Zou, X.; Zhou, Y.; Sun, F.; Zhu, G. Coupling Fullerene into Porous Aromatic Frameworks for Gas Selective Sorption. *Chem. Sci.* **2016**, 7 (6), 3751–3756.

Publication 3:

***Tetrazine linkers as plug-and-play tags for
general framework functionalization and C₆₀
conjugation***

Under revision

Tetrazine linkers as plug-and-play tags for general framework functionalization and C₆₀ conjugation

Belén Lerma-Berlanga,^{†,‡} Carolina R. Ganivet,^{†,‡} Neyvis Almora-Barrios,[†] Rebecca Vismara,[§] Jorge A. R. Navarro,[§] Sergio Tatay,[†] Natalia M. Padial,[†] Carlos Martí-Gastaldo.^{†,*}

[†] Functional Inorganic Materials Team, Instituto de Ciencia Molecular (ICMol). Universitat de València. Catedrático José Beltrán-2, 46980, Paterna (Spain)

[§] Departamento de Química Inorgánica. Universidad de Granada. Av. Fuentenueva S/N, 18071, Granada (Spain).

KEYWORDS Metal-Organic Frameworks • tetrazine tags • Click chemistry • Diels-Alder • Fullerene

ABSTRACT: The value of covalent post-synthetic modification in expanding the chemistry and pore versatility of reticular solids is well documented. Here we use mesoporous crystals of UiO-68-TZDC to demonstrate the value of tetrazine connectors for all-purpose inverse electron-demand Diels-Alder ligation chemistry. Our results suggest a positive effect of tetrazine reticulation over its reactivity for quantitative one-step functionalization with a broad scope of alkene or alkyne dienophiles into pyridazine and dihydropyridazine frameworks. This permit generating multiple pore environments with diverse chemical functionalities and the expected accessible porosities, that is also extended to the synthesis of crystalline fulleretic materials by covalent conjugation of fullerene molecules.

Introduction

Post-synthetic modification (PSM) is a universal tool for functionalizing and expanding the pore chemistry of reticular solids as Metal-Organic Frameworks (MOFs) and Covalent Organic Frameworks (COFs).^{1,2} The organic components in these networks offer appealing opportunities for the implementation of new chemical functionalities that are respectful with the original structure and in most cases not accessible by direct synthesis. This is for instance the case of nanocarbons as fullerene or nanographenes, whose functionalization and purification to obtain soluble linkers is quite laborious and time-consuming. Covalent PSM generally requires adequate chemical tags in the organic strut for covalent functionalization in presence of soluble reagents.³ These tags have been traditionally restricted to amino or aldehyde groups for imine condensation,⁴ acylation⁵ alkylation⁶ or conversion to hydrazones⁷ to cite a few. The incorporation of azide or alkyne tags has been also central to the introduction of click chemistry to PSM. This route enables quantitative conjugation of a broad range of molecules by azide-alkyne 1,3-dipolar cycloaddition reactions under mild conditions in presence of Cu(I) as catalyst.^{8,9} In this regard, the inverse Electron-Demand Diels-Alder (iEDDA) reaction between electron-poor dienes, as 1,2,4,5-tetrazines, and electron-rich dienophiles is an excellent alternative for metal-free click reactions. This reaction does not require a catalyst, offers fast kinetics, orthogonality with other click reactions, quantitative transformations under mild conditions, and inoffensive side products for minimum impact to the clicked frameworks.¹⁰ iEDDA has been thoroughly studied in solution with particular focus on targeted synthesis of natural products¹¹ and bioconjugation reactions,¹² however, generic post-functionalization routes for MOFs are

still missing. Precedents are based almost exclusively in the incorporation of dienophiles as olefins to amino-tagged MOFs for subsequent reaction with tetrazine.^{13,14} This tandem approach requires two steps and is quite limiting in the scope of dienes accessible, thus limiting versatile engineering of pore chemistry. The alternative integration of dienes to the MOF structure would be arguably more adequate for all-purpose ligation chemistry but the number of candidates remains still very limited.¹⁵⁻¹⁷ We recently reported the synthesis of UiO-68-TZDC crystals by reticulation of 4,4'-(1,2,4,5-tetrazine-3,6-diyl)dibenzoic acid (H₂tzdc) diene linkers into a mesoporous framework.¹⁸ Here we present this tetrazine MOF as an ideal platform towards the generalization of iEDDA PSM chemistry for one-step functionalization with a broad scope of alkene/alkyne dienophiles to generate multiple pore environments with diverse chemical functionalities (**Figure 1a**). Our route can be also extended to the covalent conjugation of C₆₀ molecules, that is directed by reaction with the tetrazine tags in the linker for the synthesis of porous, fulleretic crystals by precise positioning of the nanocarbons (**Figure 1b**).

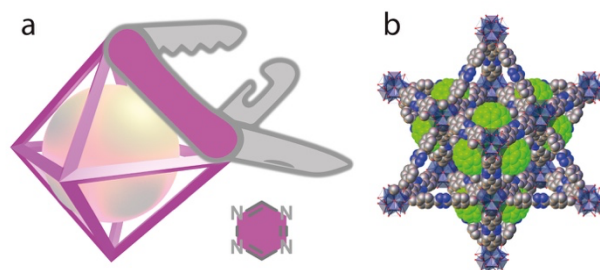


Figure 1. a) Use of tetrazine linkers as plug-and-play tags for general framework functionalization. b) Structure of UiO-68-TZDC(C₆₀) after one-step conjugation of fullerene molecules in green.

Results and Discussion

iEDDA reactivity of UiO-68-TZDC.

We initially used 2,5-norbornadiene (NBD) as model substrate to optimize the iEDDA reaction with UiO-68-TZDC (**Figure 2a**). We reacted the MOF crystals in different solvents (*N,N*-dimethylformamide, ether or acetonitrile) and variable temperatures (40, 60, 70 or 80 °C), reaction times (8 or 16h), or dienophile equivalents per tetrazine linker (1:3 or 1:50), followed by thorough washing with ether and storage in hexane. According to the X-ray diffraction (PXRD) patterns of all samples, the best compromise between clean functionalization with negligible impact to the crystallinity of the framework was reached at 40 °C, with poor impact of the rest of parameters. Based on these tests, we selected reactions at 40 °C in ether stirring during 16 h in a shaker, with a 1:3 ratio as the optimum conditions. As shown in **Figure 2a**, the first step of the reaction involves a Diels-Alder [4+2] cycloaddition with inverse electron-demand resulting in a highly strained bicyclic adduct. Nevertheless, the distortion is mostly perpendicular to the long-axis of the ligand, thus preventing strain-induced disassembly of the MOF. This is also the case for tetrazine-edged supramolecular cages, as beautifully demonstrated by Nitschke and co-workers.¹⁹ The initially formed adduct is then rapidly converted in a retro-Diels-Alder step (upon release of N₂) to the corresponding dihydropyridazine intermediate that spontaneously rearomatizes via a second retro-Diels-Alder reaction to eliminate a molecule of cyclopentadiene. In this case, NBD acts as an ethyne equivalent for the formation of pyridazine (PZDC). Quantitative formation of the PZDC MOF was confirmed by ¹H-NMR of the crystals after digestion in D₂SO₄/DMSO-*d*₆ solutions. **Figure 2b** shows the appearance of the signal intrinsic to the pyridazine nucleus accompanied by the deshielding of the hydrogens in the aromatic rings adjacent to the PZDC core as result of the lower electron density. Despite the desymmetrization of the tetrazine linker, the spectrum shows the same pattern and multiplicity. Optical microscopy and SEM imaging (**Figure S2**) confirmed that the size and morphology of UiO-68-PZDC crystals are retained after the reaction. This is consistent with the negligible changes to unit cell parameters calculated by LeBail refinement of the PXRD patterns before and after the reaction (**Figure 2c**). iEDDA reaction yields a significant color change from pink to light yellow concomitant to the clean conversion of the tetrazine ring into pyridazine. Disappearance of the characteristic signal of tetrazine core was also confirmed by solid-state diffuse reflectance spectroscopy (**Figure 3b**). UiO-68-PZDC was solvent-exchanged with hexane and evacuated at 10⁻⁶ Torr overnight. It displays a non-hysteretic type-I N₂ isotherm with a multipoint BET surface area of near 4200 m²·g⁻¹, almost coincident with the 4300 m²·g⁻¹ displayed by pristine UiO-68-TZDC (**Figure S3**). Regarding stability in humid environments, UiO-68-PZDC shows higher chemical robustness than UiO-68-TZDC comparable to that of pristine UiO-68 (**Figures S4 and S5**) and we attribute these differences to the changes in polarity of the central ring for minimizing the interaction of the framework with polar solvents as water. As for the thermal decomposition

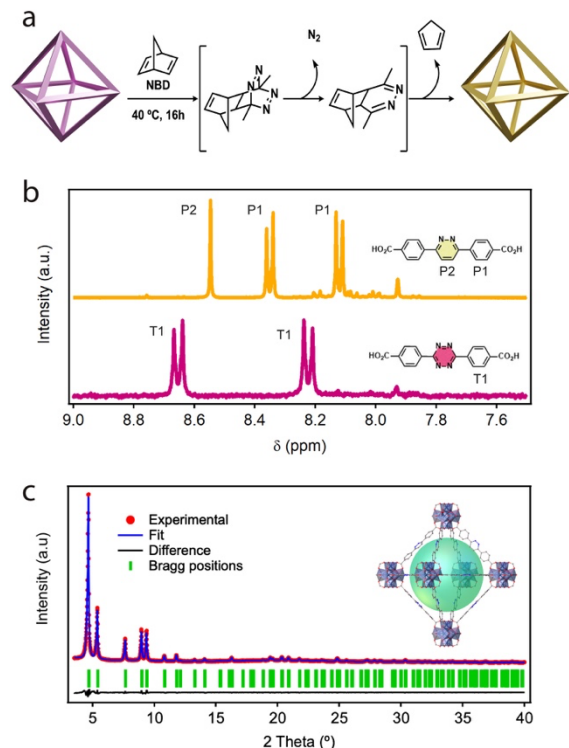


Figure 2. a) Mechanism of the iEDDA reaction between UiO-68-TZDC and NBD for post-synthetic modification of the framework. b) ¹H-NMR spectra before/after reaction. c) PXRD LeBail refinement of UiO-68-PZDC. Fm-3m, a = b = c = 32.66080 Å, α = β = γ = 90°, Rp = 3.04 %, Rwp = 4.03 %, Rexp = 2.47 %, Chi2 = 2.66, GoF = 1.63.

profiles do not display significant changes in thermal stability (**Figure S1**).

Kinetic study and effect of reticulation over reactivity.

For a better understanding of the effect of reticulating TZDC over iEDDA reactivity with NBD we monitored the reaction in controlled time intervals of up to 24 hours. **Figure 3a** shows the gradual change in color with time of the dispersions of UiO-68-TZDC crystals associated to the disappearance of the characteristic n → π* absorption band of the tetrazine ring at 558 nm. This change is consistent with the UV-Vis solid reflectance measurements of the MOF at variable times of reaction (**Figures 3b and 3c**). The decrease in intensity of the absorption maximum with time seems to follow a fast regime at short reaction times up to 180 min, where there is a decrease in the slope for slower TZDC degradation. Though the discoloration of the MOF might be considered representative of the progress of the iEDDA reaction, we chose to run another kinetic experiment that accounted for the actual formation of PZDC and provided a meaningful comparison with the reactivity of the free linker in the same conditions. We opted for reactions in DMF at 70 °C to avert the limited solubility of H₂tzdc dicarboxylic acid in ether. The amount of MOF was fixed to ensure an effective concentration of the linker in the heterogeneous solid/liquid phase equivalent to the homogeneous experiments in solution (9 mM).

We quantified the product of the reaction with time by integration of the ¹H-NMR peak area of pyridazine by using

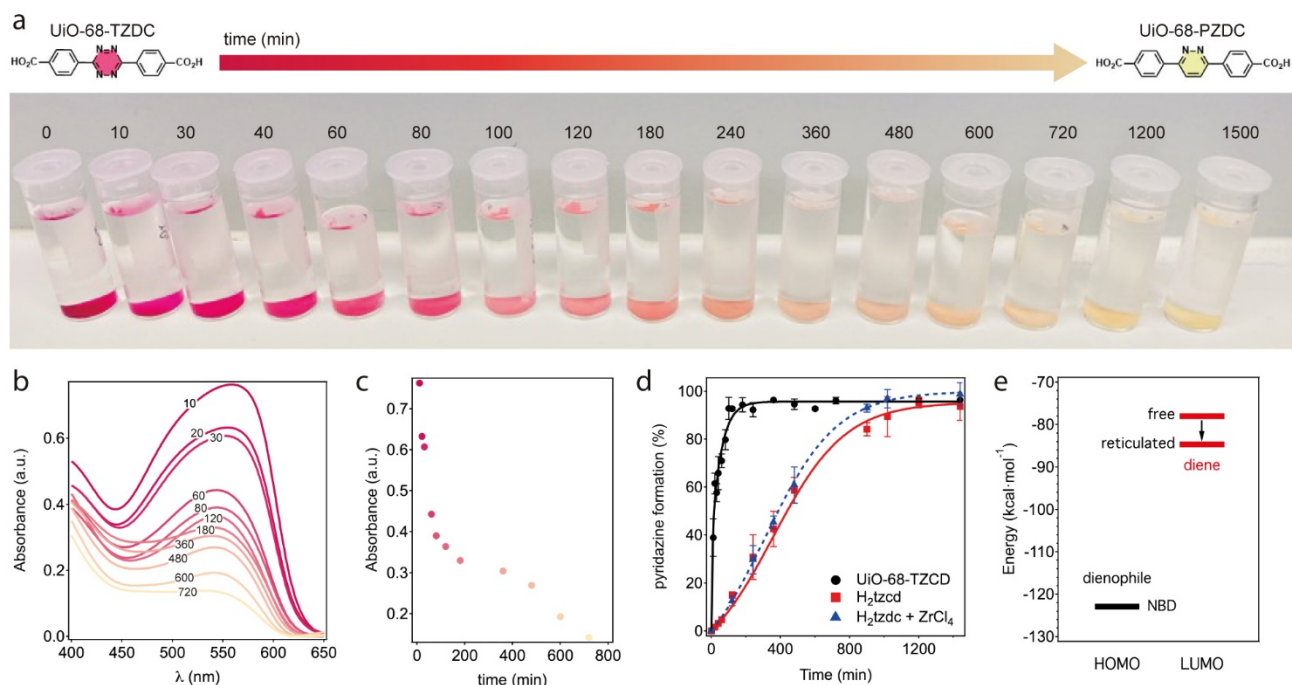


Figure 3. a) Progressive change in colour with time of UiO-68-TZDC crystals by iEDDA reaction with NBD in ether at 40 °C. b) Evolution of the UV-Vis diffuse reflectance spectra of the solid and c) decrease of intensity of the tetrazine absorption band. d) Kinetic profile for the formation of pyridazine for UiO-68-TZDC compared to the H₂tzdc linker in equivalent conditions in DMF at 70 °C. Percentages of conversion were quantified by ¹H-NMR analysis. e) DFT calculation showing the effect of reticulation in shifting the energy of the LUMO of the diene for an increase in the reaction rate.

fumaric acid as an internal standard (**Section S3.1**). **Figure 3d** shows the rate of PZDC formation with time by reaction of NBD with UiO-68-TZDC or H₂tzdc. Both experiments show an exponential profile indicative of a pseudo-first order reaction with a plateau near 95 % of PZDC formation. Even though the PSM reaction must be limited by the diffusion of the dienophile the reaction proceeds much faster in the case of the mesoporous MOF. We performed an additional test in presence of ZrCl₄ to rule out the catalytic effect of Zr(IV) ions as demonstrated by its negligible effect on the reaction rate for the free linker. We argue the accelerated reactivity in UiO-68-TZDC can be attributed to a sum of different reasons. Reticulation of TZDC in the framework might be certainly effective in preventing π-π stacking of the diene molecules in solution, that might disfavor reactivity. However, the key factor in controlling iEDDA reactivity between electron-deficient 1,2,4,5-tetrazines and alkenes is the energy difference between the LUMO of the first and the HOMO of the dienophile.^[19] For a given alkene, electron-withdrawing substituents in the tetrazine can lower the LUMO energy for stronger interactions and higher reactivity. We used density functional theory (DFT) as implemented in VASP for analyzing the electronic effect of metal coordination in shifting the LUMO of UiO-68-TZDC, that is centered at the tetrazine linker (See **Supplementary Section S3.2**. for computational details). We observe a decrease in energy of 3.8 kcal·mol⁻¹ compared to the free linker for a narrowing of the gap between frontier orbitals and subsequent increase in the reaction rate (**Figure 3e**). Compared to the shift of 2.3 kcal·mol⁻¹ reported for di-pyridine substituted tetrazines,^[20] the reticulation of the linker in the MOF seems to be more effective in lowering the LUMO energy. Although we cannot exclude the effect of free

carboxylic groups in disfavoring the reactivity of free H₂tzdc, this electronic effect seems to be the most likely reason for the enhanced UiO-68-TZDC and NBD reactivity.

iEDDA generalization and substrate scope.

Encouraged by our results, we decided to illustrate the versatility of the iEDDA reaction for PSM modification of UiO-68-TZDC with an ample range of substrates. We selected alkene and alkyne dienophiles that encompassed changes in substituents, ring strain and steric effect, all relevant to fine-tuning the LUMO_{diene}-HOMO_{dienophile} energy gap and Diels-Alder reactivity. Our scope included a first group of alkenes as 4-(cyclopent-1-en-1-yl)morpholine, 2,3-dihydrofuran and trimethyl((1-phenylvinyl)oxy)silane and the strained cycloalkyne (1 α ,8 α ,9 β)-Bicyclo[6.1.0]non-4-yne-9-methanol, all amenable to rearomatization for the generation of pyridazine (PZDC) units. This was complemented with substituted norbornenes as 5-norbornene-2-acetic acid succinimidyl ester and 5-norbornene-2-carboxylic acid and unstrained alkenes as 4-methyl-1-pentene or 1-octene, more prone to generate dihydropyridazines (HPZDC). The transformation of tetrazine linkers in functionalized PZDC or HPZDC rings was analyzed by ¹H-NMR (**Supplementary Section 4.2**).

Integration of the signals confirms the disappearance of the TZDC signals, and the appearance of new ones associated with the products. Suggesting a conversion rate close to 95 %, except for the unstrained dienophiles 4-methyl-1-pentene and 1-octene. This is not surprising and agrees well with the poorer reactivity documented for these non-cyclic,

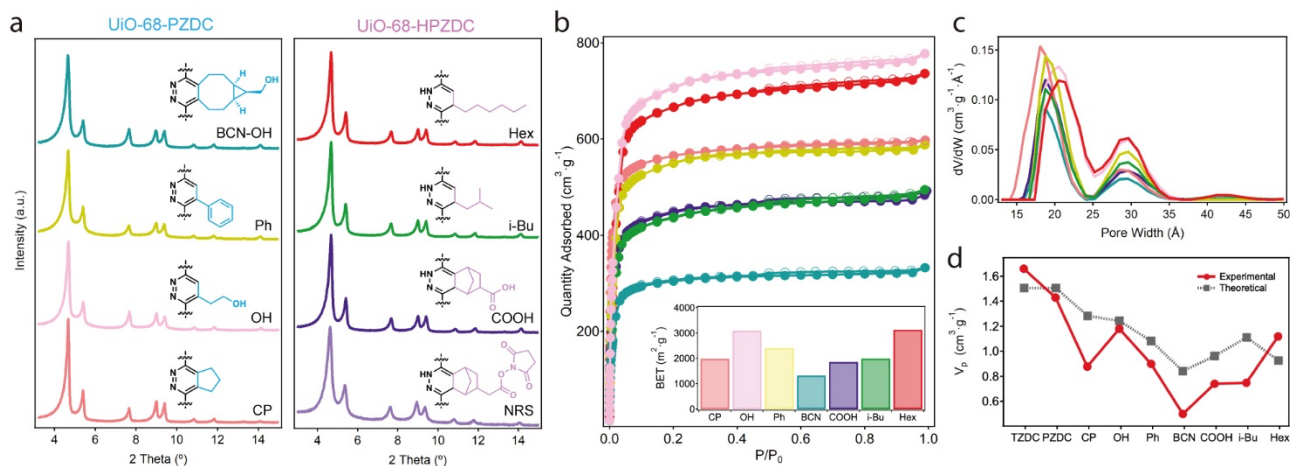


Figure 4. a) PXRD patterns of UiO-68-PZDC and HPZDC MOFs confirming minimum impact to crystallinity after iEDDA reaction in all cases. b) N_2 isotherms at 77 K and experimental BET surface areas (*inset*). c) PSD analysed by NLDFT. d) Experimental variation of pore volume with functionalization and comparison with the theoretical changes calculated from simulated crystallographic files.

electron-poor molecules,¹⁰ that would require more drastic condition or a higher number of equivalents to achieve higher yields. The formation of the iEDDA reaction products was additionally confirmed by mass spectrometry (**Table S5**). The CHN analysis of the crystals after evacuation of the solvent are also consistent with a clean functionalization (**Table S6**), that imposes small changes to the thermal stability of the functionalized frameworks according to their TGA profiles in air (**Table S7**). The PXRD of the crystals after PSM reaction (**Figure 4a**) confirmed that the crystallinity was retained in all cases with minimum impact to the original structure for a rich collection of groups decorating the mesoporous cavities of UiO-68-PZDC and HPZDC that include fused rings (CP), alkyl hydroxy (OH) and phenyl rings (Ph), succinimide (NRS) or carboxylic terminated groups (COOH), and isobutyl (*i*-Bu) or hexyl (Hex) chains, respectively. A special mention goes to UiO-68-PZDC(BCN-OH), which apart from ring-fused pyridazines and useful points of guest recognition through its -OH groups, presents stereocenters within the cavities for the generation of chiral frameworks. We selected 7 candidates to confirm the retention of porosity after PSM reaction and evacuation. All samples measured display type-I isotherms with surface areas ranging from 3100 to 1300 $m^2 \cdot g^{-1}$ (**Figure 4b**). We also observe a shift in the pore size of the microporous cavities that oscillate between 2.1 and 1.8 nm (**Figure 4c**). These changes are associated to the incorporation of bulky substituents to the framework cavities and agree well with the effect of steric crowding in the pore volume calculated from the PZDC and HPZDC framework models, that were generated computationally and analysed with zeo++ (**Figure 4d**).²⁰

Tetrazine-controlled covalent conjugation of C_{60} for crystalline fulleretic materials.

Built upon these results, we speculated on the possibility of extending our approach to fullerene molecules for covalent conjugation to the framework. Crystalline fulleretic frameworks are interesting materials in molecular electronics, photosensitization, biomedicine or organic photovoltaics based on the combination of the excellent electron-acceptor ability, high charge mobility or broad light absorption

of fullerene with the periodic order, high surface areas, chemical tunability and rich pore chemistry of reticular solids.²¹ To date, the synthetic strategies to incorporate C_{60} to MOFs can be summarized into coordinative or non-coordinative immobilization. The first relies on the derivatization of fullerene with coordinating functional groups as pyridyl or carboxylate and their use as organic connectors to direct framework assembly.²²⁻²⁴ This approach suffers from the intrinsic restrictions to C_{60} functionalization and the limited solubility of these molecules in the synthetic conditions conventionally used in MOF chemistry. Also, the use of soft metal ions often leads to poor framework stability toward solvent evacuation for non-permanent porosities. Non-coordinative encapsulation of fullerene guests by infiltration²⁵⁻³¹ or mechanochemical grinding³² is arguable more adequate to exploit the rich variety of MOF topologies and porosity metric available. However, it suffers from diffusion limitations, which often impose poor loadings per unit cell, and the absence of specific binding sites that result in disordered guest positioning inside the pore not amenable to X-ray analysis.

We argued tetrazine linkers might be ideal plug-and-play tags for the covalent conjugation of pristine C_{60} molecules, that circumvented these limitations and enabled efficient one-step incorporation of fullerene combined with covalent anchoring for spatial control. We adapted the synthetic conditions described above to the singular solubility of fullerene (**Section S5.1**).

UiO-68-TZDC crystals were reacted with six equivalents of commercial grade C_{60} in toluene. The mixture was incubated in a shaking oven for 3 days at 40 °C, followed by Soxhlet washing with toluene overnight, filtration and storage in hexane. The reaction induced a change in the color of the crystals from pink to brownish that was indicative of successful functionalization (**Figure 5a**). Covalent conjugation to the framework was confirmed with solid-state magic angle spinning ^{13}C -NMR spectroscopy (**Figure 5c**). Comparison of the spectra of UiO-68-PZDC(C_{60}) crystals with the parent MOF confirms the appearance of an additional band in the sp^2 carbon region. Even though it is impossible to confirm a specific symmetry for the monoadduct after the cycloaddition, the reaction of [6,6] rather

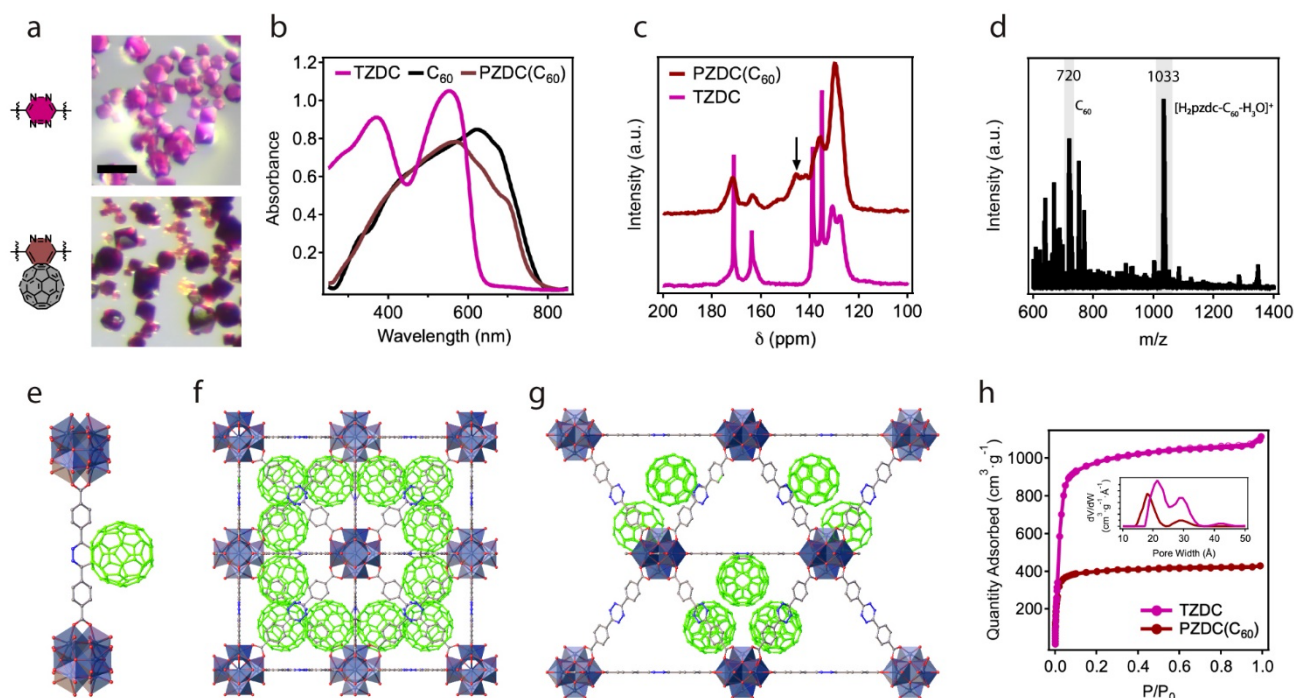


Figure 5. a) Crystals of UiO-68-TZDC before (*top*) and after (*bottom*) reaction with fullerene. Scale bars correspond to 50 μm . b) Solid-state UV-Vis diffuse reflectance spectra of UiO-68-PZDC(C₆₀) suggesting the incorporation of fullerene. c) Solid-state ¹³C-NMR spectra of UiO-68-TZDC and UiO-68-PZDC(C₆₀) crystals digested in acid. d) Mass spectra of UiO-68-PZDC(C₆₀) crystals digested in acid. e) View of the H₂pzdc-C₆₀ units that result from the covalent grafting of fullerene (in green) to tetrazine connectors. Structure of UiO-68-PZDC(C₆₀) along f) 100 and g) 110 showing the distribution of fullerenes in half the tetrahedral cavities characteristic of UiO-type frameworks. The symmetry was reduced from *Fm-3m* to *P23* for the sake of clarity. The solvent molecules and hydrogen atoms have been omitted for clarity. h) Experimental N₂ isotherms of UiO-68-TZDC and PZDC(C₆₀) at 77 K and the corresponding NLDFT-PSD graphs (inset).

than [5,6] π -bonds are expected to be more favorable from thermodynamic and kinetic standpoints.³³ Functionalization was further confirmed by mass spectrometry of the crystals after digestion in a DMSO/H₂SO₄ mixture (**Figure 5d**). The positive MALDI-TOF spectrum confirms covalent ligation of C₆₀ to the tetrazine linker for hydrated monoadducts of pyridazine [H₂pzdc-C₆₀-H₃O]⁺ linkers at $m/z = 1033$, and pristine fullerene at 720 possibly due to the molecule fragmentation upon ionization (see **Supplementary Section 5.2** for further discussion). We used tandem mass spectrometry to confirm that neat fullerene molecules were generated from the fragmentation of the monoadduct and not associated to ineffective functionalization or its occlusion in the mesopores of the MOF.

Although the reaction does not impose changes to the size or morphology of the crystals, our experiments with synchrotron radiation (ALBA, BL13-XALOC) revealed very weak x-Ray diffraction at resolutions higher than 1.47 \AA . For better understanding of the structure of the fulleretic material, we used a structural model generated with Materials Studio as initial input for the Rietveld refinement of a high-resolution powder diffraction data set. As shown in **Supplementary Section 5.3**, the refinement converged with excellent statistics for a cubic *Fm-3m* space group with cell parameters $a = 32.5556(2)$ \AA ($R_{\text{Bragg}} = 0.010$, $R_p = 0.033$ and $R_{\text{wp}} = 0.046$). UiO-68-PZDC(C₆₀) is isostructural to UiO-68-TZDC but displays slightly elongated cell axis and the covalent conjugation of C₆₀ units to the tetrazine ring for the formation of H₂pzdc-C₆₀ units (**Figure 5e**).

The occupancy factors of fullerene molecules were refined freely to account for the total functionalization. The

model converged for the formation of near to 50 % of pyridazine PZDC-C₆₀ units for a crystallographic unit cell formula of [Zr₆O₄(OH)₄(PZDC-C₆₀)₃(TZDC)₃]. This degree of functionalization is in excellent agreement with the elemental and thermogravimetric analysis of the crystals (**Section S5.2**). Fullerene molecules are crystallographically disordered and, their electron density is distributed symmetrically across the solid as result of the cubic symmetry. To simplify the analysis, we reduced the symmetry to a *P23* space group whilst retaining the net occupancy factors a clearer overview of the distribution of fullerene units. As shown in **Figures 5f and 5g**, UiO-68-PZDC(C₆₀) shows a regular conjugation of three C₆₀ molecules to the edges of 50 % of the tetrahedral cavities that are characteristic of UiO-type frameworks. This is in excellent agreement with the accessible porosity of the crystals. The material shows a type-I isotherm with retention of micro (1.8 nm) and mesoporosity (2.9 nm) for an experimental surface area of near 1700 $\text{m}^2\cdot\text{g}^{-1}$ (**Figure 4h**). Even though the experimental pore volume is reduced to near 50 % compared to pristine UiO-68-TZDC (0.65 and 1.51 $\text{cm}^3\cdot\text{g}^{-1}$, respectively), the porosity available would be in principle compatible with the loading of additional molecules, as demonstrated by the presence of solvent molecules in the as-synthesized structure.

We speculated that the loading of three molecules of C₆₀ per unit cell could be fixed by the diffusion limitations imposed by the steric crowding of the pore, and the repulsive intermolecular interactions that might prevent further functionalization. To confirm this point, we synthesised alternative sets of UiO-68-PZDC(C₆₀) by extending the reaction time to 5 days. CHN and TGA data confirm very similar

functionalization degrees, between 50 and 55 %, suggesting that this upper limit is controlled by steric impediments. This was corroborated with a control experiment by using multivariate UiO-68 crystals that combined reactive (TZDC) and non-reactive (TPDC) linkers. UiO-68-TZDC_{44%} was prepared according to our reported protocol,¹⁸ and reacted with fullerene by following the conditions described above. Our results confirm complete derivatization of the tetrazine rings when diluted with terphenyl linkers, suggesting the possibility of fine tuning C₆₀ incorporation in multivariate fulleretic materials (**Section S5.4**).

Conclusions

We have demonstrated the general value of tetrazine linkers as plug-and-play tags for general framework functionalization in one-step. The compatibility of these electron deficient linkers with the inverse Diels-Alder reaction can be considered as a rapid, highly efficient post-synthetic route for the generation of a rich diversity of pore environments. Our results also suggest that the reticulation of 1,2,4,5-tetrazine linkers in mesoporous frameworks might have an electronic effect over iEDDA reactivity with a broad range of dienophiles, which results in quantitative transformations into pyridazine and dihydropyridazine derivatives in all cases. Also important, we demonstrate how this general framework ligation scheme can be a useful tool to produce crystalline fulleretic materials. Compared to other routes, the incorporation of C₆₀ is exclusively controlled by the density and distribution of tetrazine linkers in the solid, which might be an interesting alternative to control their spatial distribution and intermolecular separation for targeted function in molecular electronics or photovoltaics. Provided the compatibility of this reaction with biological applications, we are currently exploring its potential for covalent bioconjugation of enzymes to reticular solids via orthogonal iEDDA ligation chemistry.

ASSOCIATED CONTENT

Supporting Information.

The Supporting Information is available free of charge on the ACS Publications website.

Synthetic and experimental details; physical characterization and supporting tables and figures (PDF)

X-ray crystallographic data for UiO-68-PZDC(C₆₀) (CIF)

AUTHOR INFORMATION

Corresponding Authors

*carlos.marti@uv.es

Author Contributions

These authors contributed equally.

Notes

The authors declare no competing financial interest. CCDC 2167506 contains the supplementary crystallographic data for this paper.

ACKNOWLEDGMENT

This work was supported by the EU (ERC Stg Chem-fs-MOF 714122), the Generalitat Valenciana (PROMETEU/2021/054 & SEJIGENT/2021/059) and the Spanish government (CEX2019-000919-M, PID2020-118117RB-I00 & EUR2021-121999). B.L.-B. thanks the Spanish government for a FPU (FPU16/04162). N.M.P. thanks La Caixa Foundation for a Postdoctoral Junior Leader-Retaining Fellowship (ID 100010434 and fellowship code LCF/BQ/PR20/11770014). R.V. acknowledges the Programa Juan de la Cierva Formación for a postdoctoral fellowship (FJC2020-045043-I). We also thank the University of Valencia for research facilities (NANBIOSIS) and ALBA for the provision of synchrotron radiation facilities (XALOC, proposal 2021095461).

REFERENCES

- (1) Freund, R.; Canossa, S.; Cohen, S. M.; Yan, W.; Deng, H.; Guillerm, V.; Eddaoudi, M.; Madden, D. G.; Fairen-Jimenez, D.; Lyu, H.; Macreadie, L. K.; Ji, Z.; Zhang, Y.; Wang, B.; Haase, F.; Wöll, C.; Zaremba, O.; Andreato, J.; Wuttke, S.; Diercks, C. S. 25 Years of Reticular Chemistry. *Angew. Chem. Int. Ed.* **2021**, *60*, 23946–23974.
- (2) Kalaj, M.; Cohen, S. M. Postsynthetic Modification: An Enabling Technology for the Advancement of Metal–Organic Frameworks. *ACS Cent. Sci.* **2020**, *6*, 1046–1057.
- (3) Cohen, S. M. Postsynthetic Methods for the Functionalization of Metal–Organic Frameworks. *Chem. Rev.* **2011**, *112*, 970–1000.
- (4) Kawamichi, T.; Haneda, T.; Kawano, M.; Fujita, M. X-Ray Observation of a Transient Hemiaminal Trapped in a Porous Network. *Nature* **2009**, *461*, 633–635.
- (5) Wang, Z.; Cohen, S. M. Modulating Metal–Organic Frameworks To Breathe: A Postsynthetic Covalent Modification Approach. *J. Am. Chem. Soc.* **2009**, *131*, 16675–16677.
- (6) McKinlay, A. C.; Morris, R. E.; Horcajada, P.; Férey, G.; Gref, R.; Couvreur, P.; Serre, C. BioMOFs: Metal–Organic Frameworks for Biological and Medical Applications. *Angew. Chem. Int. Ed.* **2010**, *49*, 6260–6266.
- (7) Burrows, A. D.; Frost, C. G.; Mahon, M. F.; Richardson, C. Post-Synthetic Modification of Tagged Metal–Organic Frameworks. *Angew. Chem. Int. Ed.* **2008**, *47*, 8482–8486.
- (8) Goto, Y.; Goto, Y.; Sato, H.; Sato, H.; Shinkai, S.; Sada, K.; Sada, K. “Clickable” Metal–Organic Framework. *J. Am. Chem. Soc.* **2008**, *130*, 14354–14355.
- (9) Savonnet, M.; Bazer-Bachi, D.; Bats, N.; Perez-Pellitero, J.; Jeanneau, E.; Lecocq, V.; Pinel, C.; Farrusseng, D. Generic Postfunctionalization Route from Amino-Derived Metal–Organic Frameworks. *J. Am. Chem. Soc.* **2010**, *132*, 4518–4519.
- (10) Knall, A.-C.; Slugovc, C. Inverse Electron Demand Diels–Alder (IEDDA)-Initiated Conjugation: A (High) Potential Click Chemistry Scheme. *Chem. Soc. Rev.* **2013**, *42*, 5131–5142.
- (11) Zhang, J.; Shukla, V.; Boger, D. L. Inverse Electron Demand Diels–Alder Reactions of Heterocyclic Azadienes, 1-Aza-1,3-Butadienes, Cyclopropenone Ketals, and Related Systems. A Retrospective. *J. Org. Chem.* **2019**, *84*, 9397–9445.
- (12) Oliveira, B. L.; Guo, Z.; Bernardes, G. J. L. Inverse Electron Demand Diels–Alder Reactions in Chemical Biology. *Chem. Soc. Rev.* **2017**, *46*, 4895–4950.
- (13) Chen, C.; Allen, C. A.; Cohen, S. M. Tandem Postsynthetic Modification of Metal–Organic Frameworks Using an Inverse-

Electron-Demand Diels–Alder Reaction. *Inorg. Chem.* **2011**, *50*, 10534–10536.

(14) Roy, P.; Schaate, A.; Behrens, P. Post-Synthetic Modification of Zr-Metal–Organic Frameworks through Cycloaddition Reactions. *Chem. Eur. J.* **2012**, *18*, 6979–6985.

(15) Feng, L.; Lo, S.-H.; Tan, K.; Li, B.-H.; Yuan, S.; Lin, Y.-F.; Lin, C.-H.; Wang, S.-L.; Lu, K.-L.; Zhou, H.-C. An Encapsulation–Rearrangement Strategy to Integrate Superhydrophobicity into Mesoporous Metal–Organic Frameworks. *Matter* **2020**, *2*, 988–999.

(16) Vinu, M.; Sivasankar, K.; Prabu, S.; Han, J.; Lin, C.; Yang, C.; Demel, J. Tetrazine-Based Metal–Organic Frameworks as Scaffolds for Post-Synthetic Modification by the Click Reaction. *Eur. J. Inorg. Chem.* **2020**, *5*, 461–466.

(17) Jędrzejowski, D.; Pander, M.; Nitek, W.; Bury, W.; Matoga, D. Turning Flexibility into Rigidity: Stepwise Locking of Interpenetrating Networks in a MOF Crystal through Click Reaction. *Chem. Mater.* **2021**, *33*, 7509–7517

(18) Lerma-Berlanga, B.; Ganivet, C. R.; Almora-Barrios, N.; Tatay, S.; Peng, Y.; Alberio, J.; Fabelo, O.; González-Platas, J.; García, H.; Padial, N. M.; Martí-Gastaldo, C. Effect of Linker Distribution in the Photocatalytic Activity of Multivariate Mesoporous Crystals. *J. Am. Chem. Soc.* **2021**, *143*, 1798–1806.

(19) Roberts, D. A.; Pilgrim, B. S.; Cooper, J. D.; Ronson, T. K.; Zarra, S.; Nitschke, J. R. Post-Assembly Modification of Tetrazine-Edged FeII 4L6 Tetrahedra. *J. Am. Chem. Soc.* **2015**, *137*, 10068–10071.

(20) Willems, T. F.; Rycroft, C. H.; Kazi, M.; Meza, J. C.; Haranczyk, M. Algorithms and Tools for High-Throughput Geometry-Based Analysis of Crystalline Porous Materials. *Microporous and Mesoporous Mater.* **2012**, *149*, 134–141.

(21) Rice, A. M.; Dolgoplova, E. A.; Shustova, N. B. Fulleretic Materials: Buckyball- and Buckybowl-Based Crystalline Frameworks. *Chem. Mater.* **2017**, *29*, 7054–7061.

(22) Peng, P.; Li, F. F.; Neti, V. S. P. K.; Magana, A. J. M.; Echegoyen, L. Design, Synthesis, and X-Ray Crystal Structure of a Fullerene-Linked Metal–Organic Framework. *Angew. Chem. Int. Ed* **2014**, *53*, 160–163.

(23) Williams, D. E.; Dolgoplova, E. A.; Godfrey, D. C.; Ermolaeva, E. D.; Pellechia, P. J.; Greytak, A. B.; Smith, M. D.; Avdoshenko, S. M.; Popov, A. A.; Shustova, N. B. Fulleretic Well-Defined Scaffolds: Donor–Fullerene Alignment Through Metal Coordination and Its Effect on Photophysics. *Angew. Chem. Int. Ed.* **2016**, *55*, 9070–9074.

(24) Kraft, A.; Roth, P.; Schmidt, D.; Stangl, J.; Müller-Buschbaum, K.; Beuerle, F. Three-Dimensional Metal–Fullerene Frameworks. *Chem. Eur. J.* **2016**, *22*, 5982–5987.

(25) Sun, D.; Tham, F. S.; Reed, C. A.; Boyd, P. D. W. Extending Supramolecular Fullerene–Porphyrin Chemistry to Pillared Metal–Organic Frameworks. *National Acad. Sci.* **2002**, *99*, 5088–5092.

(26) Chae, H.; Siberio-Perez, D.; Kim, J.; Go, Y.; Eddaoudi, M.; Matzger, A.; O’Keeffe, M.; Yaghi, O. M. A Route to High Surface Area, Porosity and Inclusion of Large Molecules in Crystals. *Nature* **2004**, *427*, 523–527.

(27) Constable, E. C.; Zhang, G.; Housecroft, C. E.; Zampese, J. A. Bucky-Blocks: Templating a Coordination Network with C60. *CrystEngComm* **2011**, *14*, 1770–1774.

(28) Li, H.; Hill, M. R.; Huang, R.; Doblin, C.; Lim, S.; Hill, A. J.; Babarao, R.; Falcaro, P. Facile Stabilization of Cyclodextrin Metal–Organic Frameworks under Aqueous Conditions via the Incorporation of C 60in Their Matrices. *Chem. Comm.* **2016**, *52*, 5973–5976.

(29) Goswami, S.; Ray, D.; Otake, K.; Kung, C.-W.; Garibay, S. J.; Islamoglu, T.; Atilgan, A.; Cui, Y.; Cramer, C. J.; Farha, O. K.; Hupp, J. T. A Porous, Electrically Conductive Hexa-Zirconium(IV) Metal–Organic Framework. *Chem. Sci.* **2018**, *341*, 1230444.

(30) Souto, M.; Calbo, J.; Mañas-Valero, S.; Walsh, A.; Espallargas, G. M. Charge-Transfer Interactions between Fullerenes and a Mesoporous Tetrathiafulvalene-Based Metal–Organic Framework. *Beilstein J. Nanotechnol.* **2019**, *10*, 1883–1893.

(31) Lo, S.; Kitao, T.; Nada, Y.; Murata, K.; Ishii, K.; Uemura, T. Chiral Induction in Buckminsterfullerene Using a Metal–Organic Framework. *Angew. Chem. Int. Ed.* **2021**, *60*, 17947–17951.

(32) Martínez, V.; Karadeniz, B.; Biliškov, N.; Lončarić, I.; Muratović, S.; Žilić, D.; Avdoshenko, S. M.; Roslova, M.; Popov, A. A.; Užarević, K. Tunable Fulleretic Sodalite MOFs: Highly Efficient and Controllable Entrapment of C60 Fullerene via Mechanochemistry. *Chem. Mater.* **2020**, *32*, 10628–10640.

(33) Miller, G. P.; Tetreau, M. C. Facile, Completely Regioselective 1,4-Hydrogenations of C60-Diaryltetrazine Monoadducts. *Org. Lett.* **2000**, *2*, 3091–3094.

Supplementary Information

Tetrazine linkers as plug-and-play tags for general framework functionalization and C₆₀ conjugation

Belén Lerma-Berlanga^[a], Carolina R. Ganivet^[a], Neyvis Almora-Barrios^[a], Rebecca Vismara^[b], Jorge A. R. Navarro^[b], Sergio Tatay^[a], Natalia M. Padial^[a], Carlos Martí-Gastaldo^{[a]*}

[a] B. Lerma-Berlanga, Dr. C. R. Ganivet, Dr. N. Almora-Barrios, Dr. S. Tatay, Dr. N. M. Padial, Dr. C. Martí-Gastado

Functional Inorganic Materials Team, Instituto de Ciencia Molecular (ICMol)

Universitat de València

Catedrático José Beltrán-2, 46980, Paterna (Spain)

E-mail: carlos.marti@uv.es

[b] Dr. Rebecca Vismara, Prof. J. A. R. Navarro

Departamento de Química Inorgánica

Universidad de Granada, 18071, Granada (Spain)

Table of contents

Supplementary Information	1
S1. General considerations: starting materials and characterization	4
Materials and reagents	4
Physical and chemical characterization	4
S2. iEDDA reactivity of UiO-68-TZDC	6
S2.1. Synthesis of UiO-68-PZDC	6
S2.2. Chemical characterization	6
Proton Nuclear Magnetic Resonance (¹H-NMR)	6
Elemental Analysis (EA)	6
Thermogravimetric Analysis (TGA)	6
Scanning Electron Microscopy (SEM-EDX)	7
Analysis of N₂ adsorption/desorption isotherms at 77 K	7
Chemical stability	8
Powder X-Ray Diffraction (PXRD)	8
Scanning Electron Microscopy (SEM-EDX)	9
S3. Kinetic study and effect of reticulation over reactivity	9
S3.1. Kinetic experiments	9
S3.2. Computational calculations	14
Model of UiO-68-TZDC	14
Model of H₂tzdc linker and 2,5-norbornadiene (NBD) substrate	15
S4. iEDDA generalization and substrate scope	16
S4.1. Synthesis of UiO-68-PZDC (X) & UiO-68-HPZDC (X)	16
S4.2. Chemical characterization	17
¹H-NMR analysis	17
HR-Mass Spectrometry	21
Elemental Analysis (EA)	23
Thermogravimetric Analysis (TGA)	24
Powder X-Ray Diffraction (PXRD)	25
Scanning Electron Microscopy (SEM-EDX)	25
Analysis of N₂ adsorption/desorption isotherms at 77 K	28
S4.3. Theoretical models	29
Theoretical Pore Size Distribution	29
Structural models of UiO-68-PZDC and HPZDC frameworks	30

S5. Tetrazine controlled C₆₀ conjugation for crystalline fulleretic materials	33
S5.1. Synthesis of UiO-68-PZDC(C ₆₀)	33
S5.2. Chemical characterization	33
SS-MAS-¹³C-NMR	33
MALDI-MS	34
Elemental Analysis (EA)	35
Thermogravimetric Analysis (TGA)	36
Scanning Electron Microscopy (SEM-EDX)	36
Single Crystal X-Ray diffraction experiments	37
S5.3. Rietveld refinement	38
S5.4. Complementary experiments with MTV-UiO-68-TZDC _{44%}	40
Synthesis of UiO-68-TZDC_{44%}	40
Elemental and Thermogravimetric Analysis	40
References	41

S1. General considerations: starting materials and characterization

Materials and reagents

2,5-Norbornadiene, 4-(cyclopent-1-en-1-yl)morpholine, 2,3-dihydrofuran and trimethyl((1-phenylvinyl)oxy)silane, were purchased from TCI Chemicals. (1 α ,8 α ,9 β)-Bicyclo[6.1.0]non-4-yne-9-methanol, 4-Methyl-1-pentene, 1-octene and fullerene (C₆₀) were purchased from Sigma-Aldrich. Hexane and diethylether ($\geq 99.9\%$) were purchased from Scharlab. All reagents and solvents were used without any previous purification unless specified.

Physical and chemical characterization

- Elemental Analysis (EA): Carbon, nitrogen and hydrogen contents were determined by microanalytical procedures using a LECO CHNS.

- Thermogravimetric Analysis (TGA) were carried out with a Mettler Toledo TGA/SDTA 851 apparatus between 25 and 700 °C under ambient conditions (10 °C·min⁻¹ scan rate and an air flow of 30 mL·min⁻¹).

- ¹H-Nuclear Magnetic Resonance (NMR) spectra were recorded on a Bruker Avance III 300 WB spectrometer and were calibrated to the residual solvent peak (DMSO-*d*₆ at 2.50 ppm ¹H-NMR). The following abbreviations were used to explain multiplicities: s = singlet, d = doublet, t = triplet, q = quartet, m = multiplet, br = broad.

- ¹³C-Solid State Nuclear Magnetic Resonance (¹³C-SS-NMR) spectra were recorded on a Bruker Avance III 400 spectrometer WB.

- X-Ray Diffraction (XRD) patterns were collected in a PANalytical X'Pert PRO diffractometer using copper radiation (Cu K α = 1.5418 Å) with an X'Celerator detector, operating at 40 mA and 45 kV. Profiles were collected in the 2° < 2 θ < 40° range with a step size of 0.017°. XRD pattern for refinement was collected for polycrystalline sample using a 0.5 mm glass capillary mounted and aligned in a PANalytical Empyrean diffractometer (Bragg-Brentano geometry) using copper radiation (Cu K α = 1.5418 Å) with an PIXcel detector, operating at 40 mA and 45 kV. Profiles were collected by using a Soller Slit of 0.02° and a divergence slit of 1/4 at room temperature in the angular range 3° < 2 θ < 40° with a step size of 0.017°. LeBail refinements were carried out with the FULLPROF software package.

- Scanning Electron Microscopy (SEM): particle morphologies and dimensions were studied with a Hitachi S4800 scanning electron microscope at an accelerating voltage of 20 kV, over metalized samples with a mixture of gold and palladium for 90 seconds.

- UV-Vis diffuse reflectance spectroscopy (DRS) experiments were performed on a Jasco V-670 spectrophotometer using an integrated Labsphere in the range 200-800 nm.

- High resolution quadrupole time-of-flight mass spectrometer, QTOF (LC-MS/MS). The experiments were carried out with TripleTOF™ 5600 LC/MS/MS System, (AB SCIEX) apparatus. Ionization source: ESI/APCI. Temperature: 450 °C, ion spray voltage (ISVF): 5500.
- Mass spectrometer with MALDI ionization source and time-of-flight analyzer (MS MALDI TOF). Samples were analyzed in a 5800 MALDI TOFTOF (ABSciex) in reflector positive and negative mode, in a range 500 – 2000 m/z, at 2800 – 3500 of laser intensity.
- Gas adsorption measurements were recorded on a Micromeritics 3Flex apparatus at relative pressures up to 1 atm. The sample was degassed overnight at 60 °C and 10^{-6} Torr prior to analysis. Surface area, pore size and volume values were calculated from N₂ adsorption-desorption isotherms (77 K) Specific surface area was calculated by multi-point Brunauer-Emmett-Teller (BET) method. Total pore volume values were taken at $P/P_0=0.96$. Pore size distributions were analysed by using the solid density functional theory (NLDFT) for the adsorption branch by assuming a cylindrical pore model.

S2. iEDDA reactivity of UiO-68-TZDC

S2.1. Synthesis of UiO-68-PZDC

20 mg of UiO-68-TZDC (0.0077 mmol, 1 equiv) were immersed in 5 mL of ether, then 18 equivalents 2,5-norbornadiene (NBD) (0.1384 mmol) were added. The resultant mixture was stirring in a shaker at 40 °C during 16 hours in a 10 mL pyrex glass tube with PTFE lined phenolic caps. After this time, the slight yellow crystals were washed thoroughly with fresh acetone (4 x 10 mL) and then kept 6 days in hexane.

S2.2. Chemical characterization

Proton Nuclear Magnetic Resonance ($^1\text{H-NMR}$)

Before $^1\text{H-NMR}$ analysis, the sample was activated under vacuum at 120 °C for 16 h. After that, 5 mg of activated UiO-68-PZDC were suspended in 0.5 mL of $\text{DMSO-}d_6$. The sample was digested by addition of two drops of $\text{D}_2\text{SO}_4-d_2$ (96-98 wt. %). Finally, the mixture was stirred during 5 minutes at 80 °C. The resulting clear solution was transferred to an NMR tube and $^1\text{H-NMR}$ was recorded.

Elemental Analysis (EA)

UiO-68-PZDC was activated in the vacuum oven at 120°C overnight before the analysis. Elemental analysis for $[\text{Zr}_6\text{O}_4(\text{OH})_4(\text{C}_{18}\text{H}_{12}\text{N}_2\text{O}_4)_6]$: Calc. C (81.2), H (4.9), N (10.9); found: C (84.5), H (5.0) and N (10.5).

Thermogravimetric Analysis (TGA)

The sample was activated in the vacuum oven at 120°C overnight before the analysis.

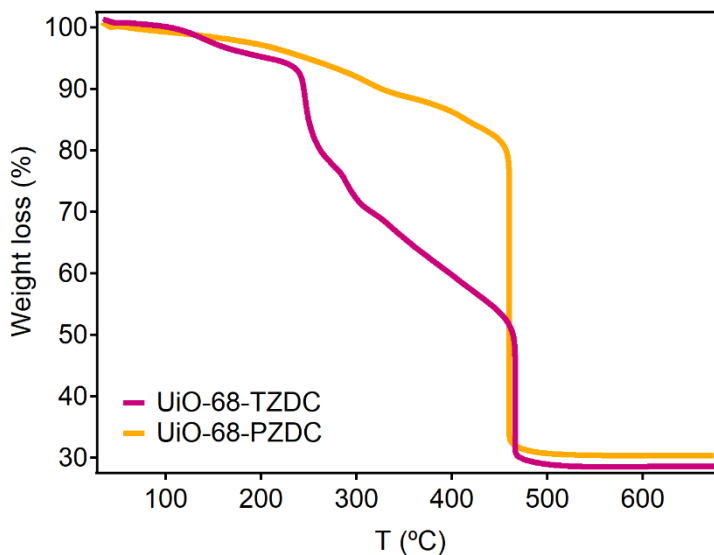


Figure S1. Thermal decomposition profile of UiO-68-TZDC and UiO-68-PZDC. ZrO_2 calc.: 28.42%, exp.: 30.31%.

Scanning Electron Microscopy (SEM-EDX)

SEM images of UiO-68-PZDC confirming that the size and morphology of UiO-68 crystals are retained after the post-synthetic reaction.

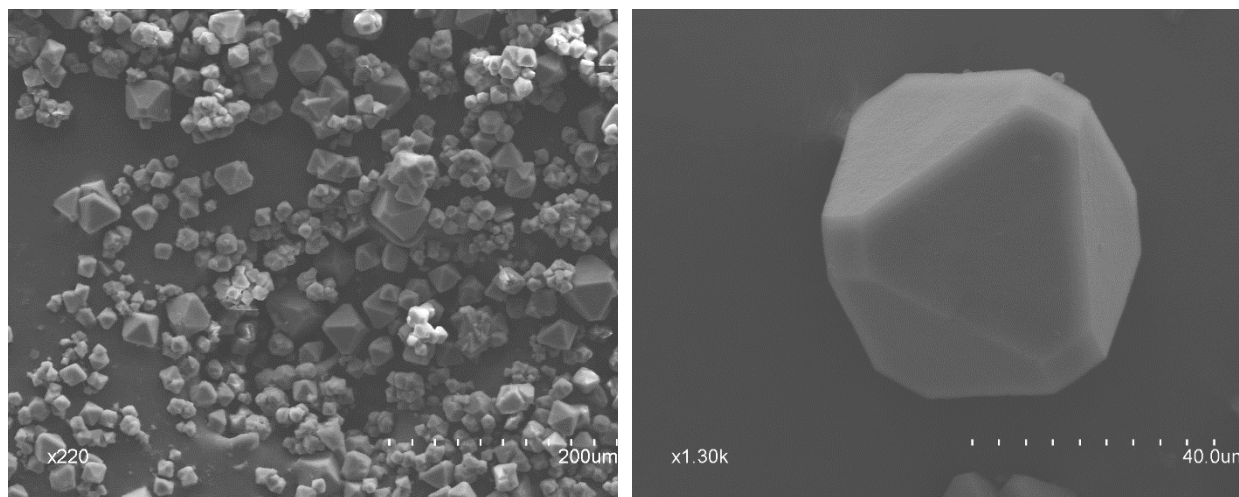


Figure S2. Scanning Electron Microscopy (SEM) images of octahedral crystals of UiO-68-PZDC.

Analysis of N₂ adsorption/desorption isotherms at 77 K

UiO-68-PZDC was degassed overnight at 60 °C and 10⁻⁶ Torr overnight after exchange with hexane. The data in yellow corresponds to the reported isotherm of UiO-68-PZDC.¹

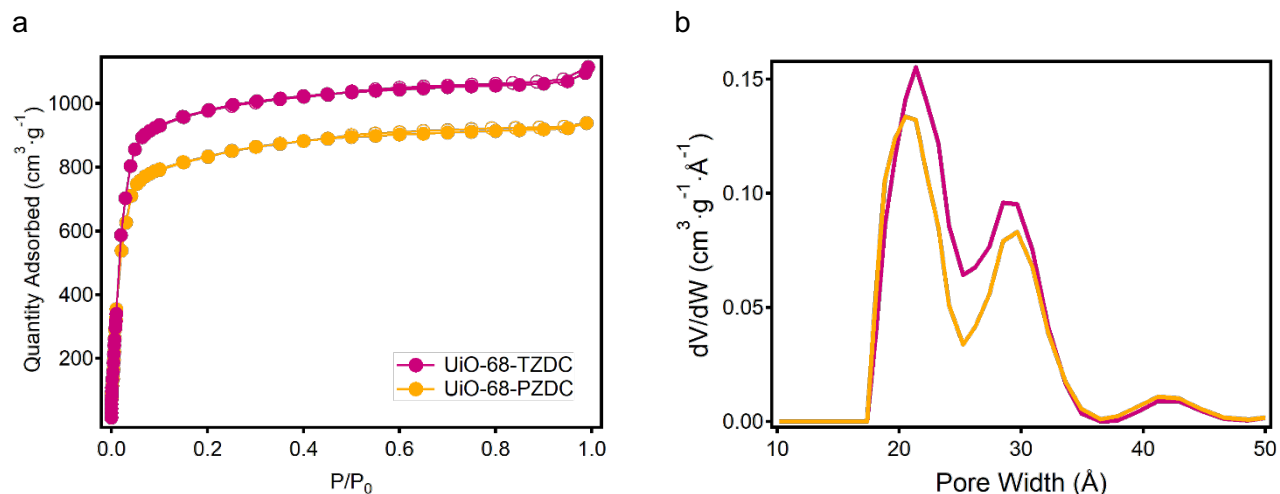


Figure S3. a) N₂ adsorption/desorption isotherms at 77 K and b) pore size distribution calculated assuming a cylindrical pore model of hexane exchanged samples.

Table S1. Summary of the N₂ adsorption analysis.

	UiO-68-TZDC	UiO-68-PZDC
BET surface area (m²·g⁻¹) at P/P₀ = 0.01-0.08	4289	4134
Total pore volume (cm³·g⁻¹) at P/P₀ = 0.96	1.66	1.43
Pore width (nm)	2.1, 2.9	2.1, 3.0

Chemical stability

The hydrolytical stability of the UiO-68-PZDC was evaluated by soaking the material in water (pH = 7) for 24 hours. The PXRD after this treatment suggest that the sample retains the original crystallinity. Compared to the pristine material, UiO-68-TZDC, the framework shows higher chemical robustness after the Diels-Alder reaction, comparable to UiO-68.

Powder X-Ray Diffraction (PXRD)

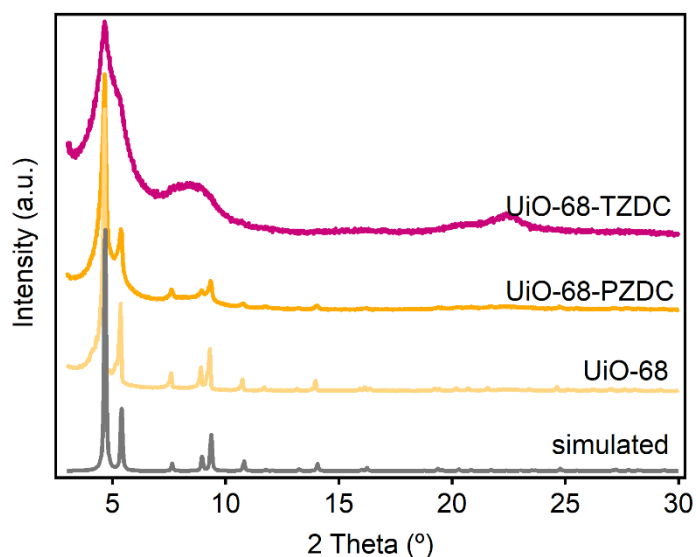


Figure S4. Comparison of the PXRD patterns of the solids after soaking in water for 24 hours.

Scanning Electron Microscopy (SEM-EDX)

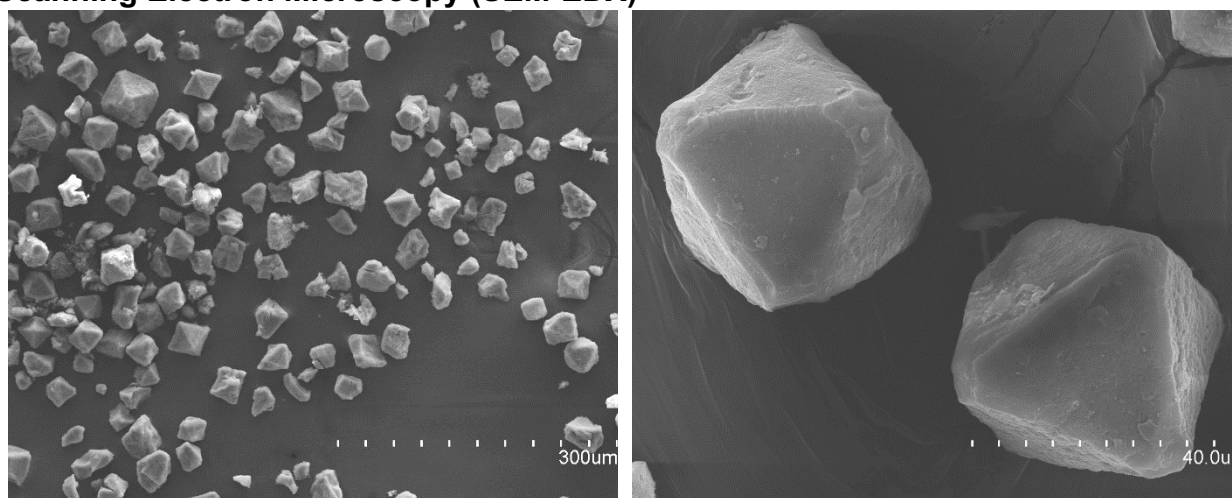


Figure S5. Scanning Electron Microscopy (SEM) images of octahedral crystals of UiO-68-PZDC after being soaked in water for 24 hours, confirm minimum impact to the size of morphology after water treatment.

S3. Kinetic study and effect of reticulation over reactivity

S3.1. Kinetic experiments

NBD was selected as substrate for kinetic experiments. The quantity of MOF and H₂TZDC linker were fixed to ensure identical effective concentration of the tetrazine units in both experiments to get directly comparable results. Initially, both experiments were carried out in diethyl ether. Only the reactions with the MOF showed colour changes. Unfortunately, for H₂TZDC linker experiments any change was observed after 48 hours probably due to the unwavering π - π interactions of organic linker. Therefore, to improve the linker solubility, DMF at 70 °C was select as reaction medium.

MOF kinetic experiments: 10 mg of UiO-68-TZDC (0.0039 mmol, 1 equiv) were immersed in 2.5 mL of ether or DMF, then 3 equivalents per TZDC of 2,5-norbornadiene (NBD) (7.1 μ L, 0.069 mmol) were added. The resultant mixture was stirred at 70 °C in an orbital shaker during different times (0, 0.3, 0.66, 2, 4, 6, 8, 10, 15, 17, 20 and 24 hours) in a 5 mL pyrex glass tube with PTFE lined phenolic caps. Finally, all solids were thoroughly washed with fresh acetone (10 mL \times 4) after the reaction (Figure S6):

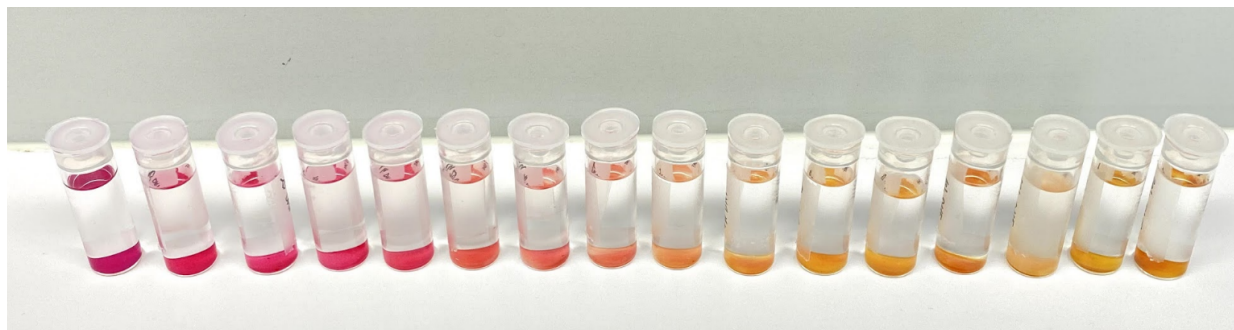


Figure S6. Progressive change in colour with time of UiO-68-TZDC crystals by iEDDA reaction with NBD in DMF at 70 °C.

Linker kinetic experiments: 10.5 mg of H₂TZDC (0.032 mmol, 1 equiv) were immersed in 3.5 mL of DMF, then 3 equivalents 2,5-norbornadiene (NBD) (9.8 μL, 0.096 mmol) were added. The resultant mixture was stirred at 70 °C in an orbital shaker during different times (0, 0.3, 0.66, 2, 4, 6, 8, 10, 15, 17, 20 and 24 hours) in a 5 mL pyrex glass tube with PTFE lined phenolic caps. After the reaction time, the solid was thoroughly washed with fresh acetone (4 × 10 mL) (Figure S7).

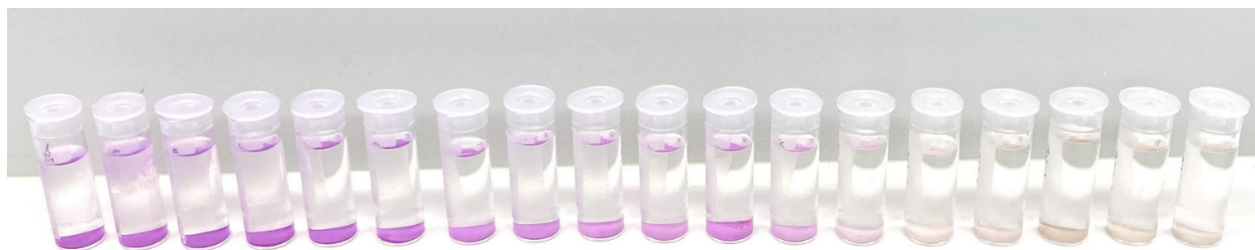


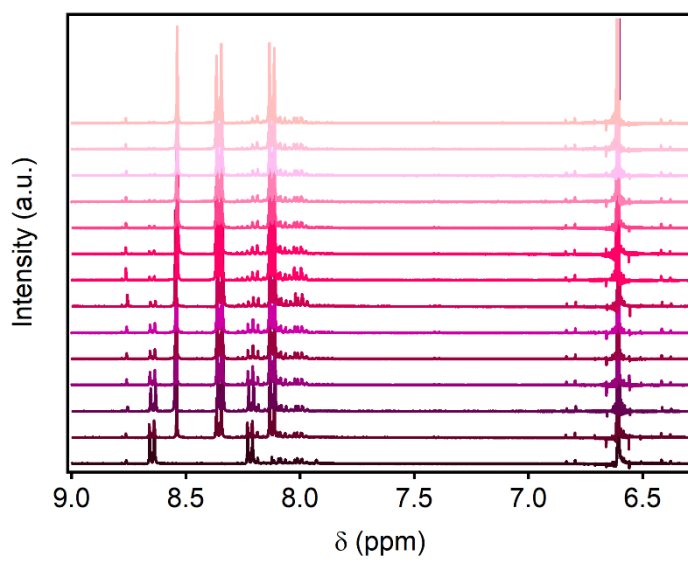
Figure S7. Progressive change in colour with time of H₂TZDC by iEDDA reaction with NBD in DMF at 70 °C.

Additional experiments in presence of ZrCl₄ were done to test the catalytic effect of Zr(IV) ions. 10.5 mg of H₂TZDC (0.032 mmol, 1 equiv) were immersed in 3.5 mL of DMF, then 3 equivalents 2,5-norbornadiene (NBD) (9.8 μL, 0.096 mmol) and 7.5 mg of ZrCl₄ (0.032 mmol, 1 equiv) were added. The resultant mixture was stirred at 70 °C during different times (2, 4, 6, 8, 15, 17 and 24 hours) in a 5 mL pyrex glass tube with PTFE lined phenolic caps. After the reaction time, the solid was thoroughly washed with fresh acetone (4 × 10 mL).

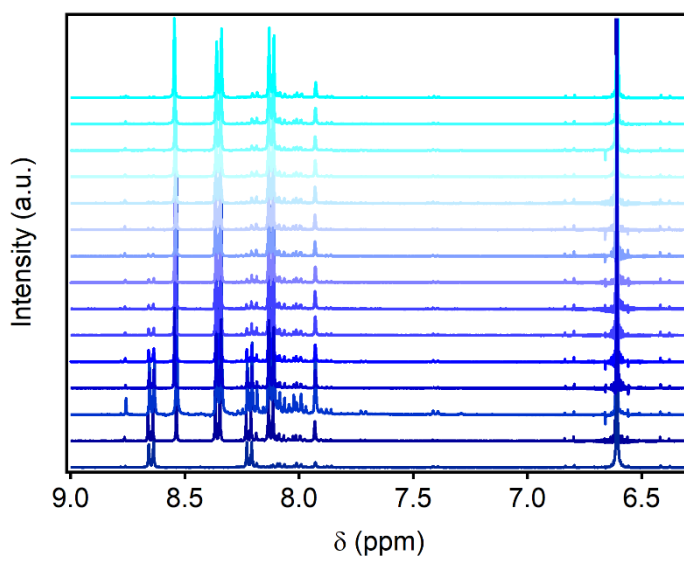
We quantified the product of the reaction (4,4'-(pyridazine-3,6-diyl)dibenzoic acid) with time by integration of the ¹H-NMR peak area of pyridazine compound by using fumaric acid as an internal standard. Pyridazine signals were selected for the quantification because the lower solubility and chemical stability in the reaction medium of TZDC made its quantification difficult.

For that, the resultant solids (MOF and linker) were activated in the vacuum oven at 120 °C for 2 hours. Then, 2 mg of dry solids were weighed in an analytical precision balance and suspended in 0.6 mL of a fumaric solution (0.02M in DMSO-*d*₆). After that, the samples were digested by addition of two drops of D₂SO₄-*d*₂ (96-98 wt. %). The mixture was stirred for 5 minutes at 80 °C. Then, the resulting clear solutions were transferred to an NMR tube and ¹H-NMR was recorded.

a



b



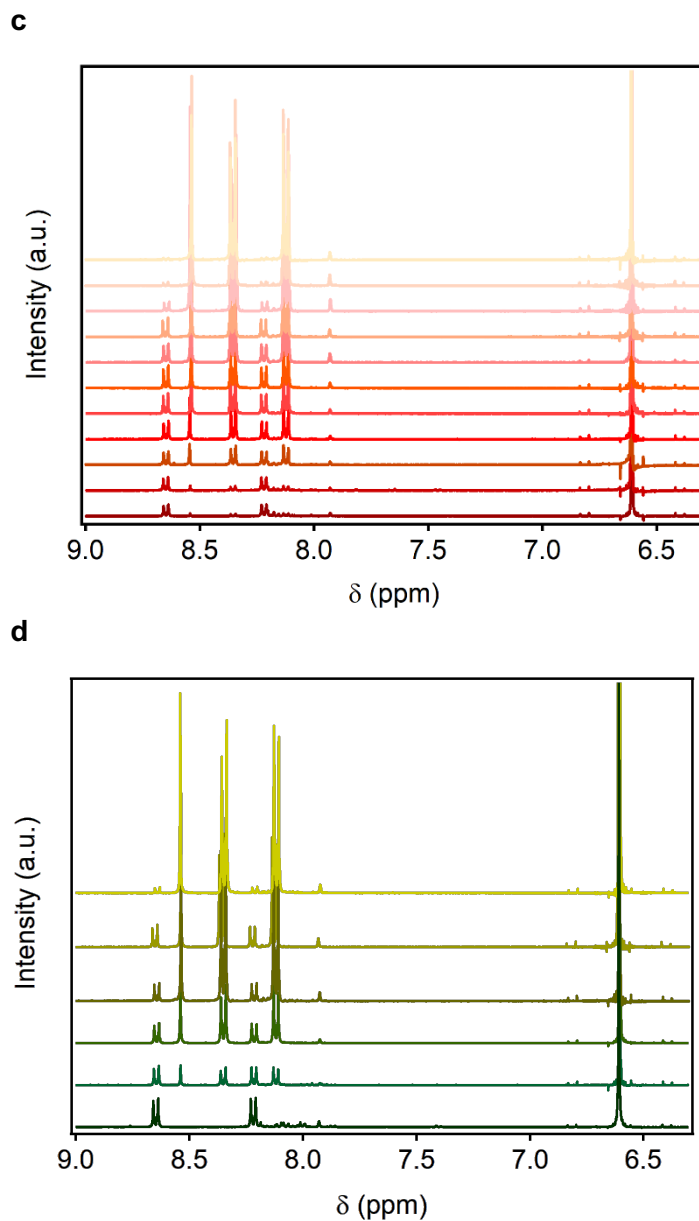


Figure S8. ^1H NMR spectra of resultant digested solids, spectrum from bottom to up corresponds to an increase of reaction time. a) Resultant solids of UiO-68-TZDC in ether at 40 °C. b) Resultant solids of UiO-68-TZDC in DMF at 70 °C. c) Resultant solids of H_2tzdc in DMF at 70 °C and d) Resultant solids of $\text{H}_2\text{tzdc}/\text{ZrCl}_4$ in DMF at 70 °C.

The % of pyridazine formation was calculated from the integration values of pyridazine (doublet centred at 8.34 ppm) and fumaric acid (singlet at 6.6 ppm) signals at different reaction times by following the equation below:

$$\% \text{ pzdc conversion}_{t=x} = \frac{\frac{\text{Integral of the pzdc}_{t=x}}{\text{Integral of the fumaric}_{t=x}}}{\frac{\text{Integral of the pzdc}_{t=24}}{\text{Integral of the fumaric}_{t=24}}} \times 100$$

An example of the calculation of the formation of pyridazine is shown below.

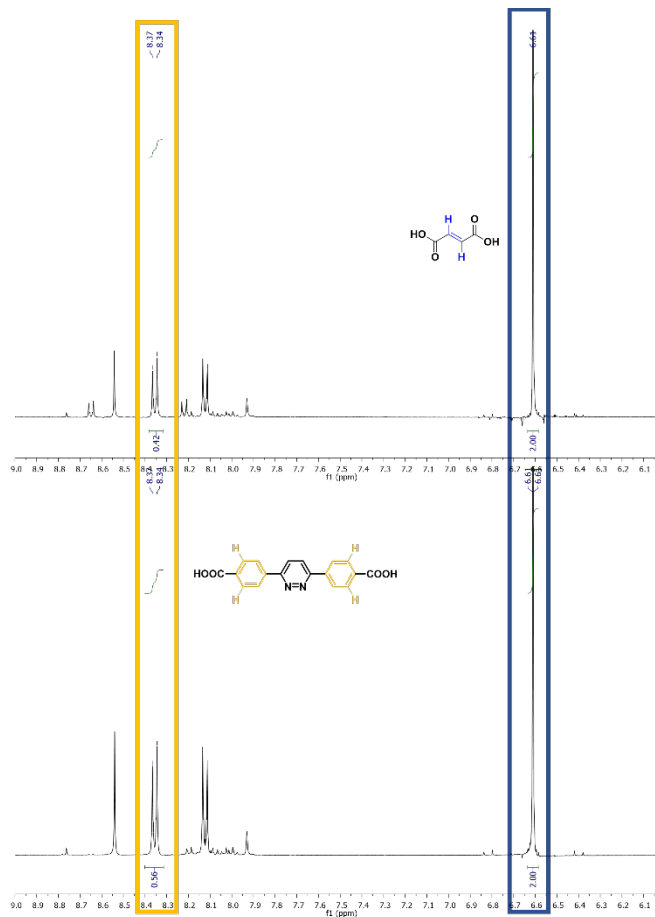


Figure S9. $^1\text{H-NMR}$ of resultant solids of UiO-68-TZDC reaction in DMF at 70 °C after digestion, top for $t = 20$ min and bottom for $t = 24$. The selected signal of pyridazine is framed in yellow and for fumaric acid in blue.

$$\% \text{ pzdc conversion}_{t=20 \text{ min}} = \frac{\frac{0.42}{2}}{\frac{0.56}{2}} \times 100 = 73 \%$$

S3.2. Computational calculations

Model of UiO-68-TZDC

We used the crystallographic structure reported¹ (CCDC 2023345) to build an orthorhombic unit cell containing two Zr_6 clusters as displayed below.

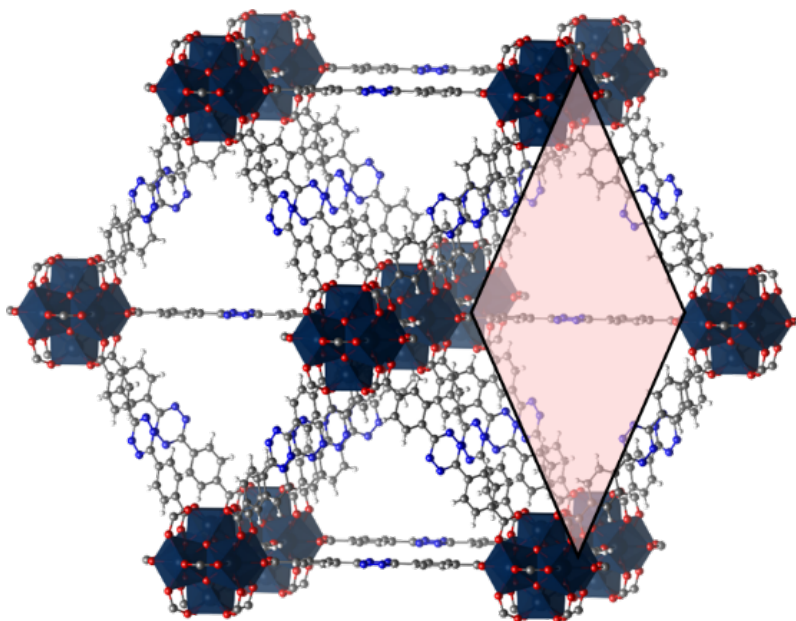


Figure S10. Perspective along [101] showing the conventional unit cell of a UiO-68-TZDC crystal with four Zr_6 -clusters. A reduced unit cell used in this work, with only two Zr_6 -clusters, is shown by a pink background. Cell parameters: $a = 32.4741 \text{ \AA}$; $b = c = 22.963 \text{ \AA}$.

The calculation was performed using dispersion-correlated density functional theory (DFT-D3) with VASP code²⁻⁵ and employing the Perdew–Burke–Ernzerhof (PBE) functional.⁶ The recommended GW PAW pseudopotentials⁷ were used. The kinetic energy cutoff for the plane-wave basis set expansion was chosen as 500 eV, and Γ points were used for integrations in the reciprocal space, due to the large size of the unit cell of the direct lattice. Single-point HSE06 screened hybrid functional^{8,9} DFT calculations were carried out on the optimised geometries of UiO-68-TZDC structure for calculating accurate electronic structure.

In contrast to molecular quantum-chemical calculation, within periodic boundary conditions, the electron energy levels calculated with VASP are given with respect to an internal energy reference. To align the HOCO and LUCO with the vacuum scale, it is necessary to evaluate the electrostatic potential in the vacuum region represented by an empty space within the simulation cell. This was performed following the method of Butler *et al.*^{10,11}

Table S2. Calculated HOCO and LUCO gives for VASP and with respect to the vacuum level (kcal/mol).

UiO-68-TZDC	from VASP	After band alignment ($\Phi_{av}(r) = 43.00$)
HOCO	-106.19	-149.19
LUCO	-38.45	-81.45

Model of H₂tzdc linker and 2,5-norbornadiene (NBD) substrate.

The electronic structure of the H₂tzdc linker and 2,5-norbornadiene (NBD) substrate in molecular form (see Figure S11 and S12) were obtained from calculation with HSE06 hybrid functional using VASP.

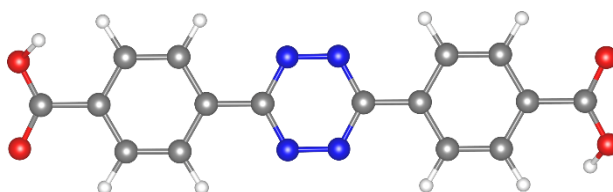


Figure S11. Structure calculated of H₂tzdc linker.

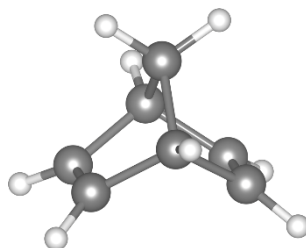


Figure S12. Structure calculated of NBD substrate.

Table S3. Calculated HOMO and LUMO from VASP (kcal/mol).

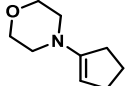

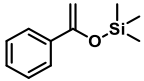
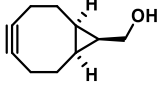
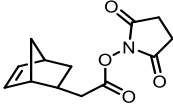
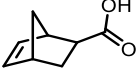
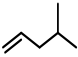
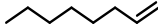
	H ₂ tzdc	NBD
HOMO	-153.21	-123.06
LUMO	-77.70	-2.10

S4. iEDDA generalization and substrate scope

S4.1. Synthesis of UiO-68-PZDC(X) & UiO-68-HPZDC(X)

20 mg of UiO-68-TZDC (0.0077 mmol, 1 equiv) were immersed in 5 mL of solvent, then 18 equivalents (0.1384 mmol) of dienophiles were added. Less reactive, non-cyclic alkenes required at least 90 equiv to detect signals indicative of the formation of the product. The resultant mixtures were stirred in the shaker during 16 hours in 10 mL pyrex glass tubes with PTFE lined phenolic caps. After time reaction, the solids were thoroughly washed with fresh acetone (10 mL × 4) and then kept in hexane.

Table S4. Summary of dienophiles and reaction conditions tested.

Compound	Dienophiles	Scheme	Solvent	Quantity	Temp (° C)	% Transf
UiO-68-PZDC(CP)	4-(cyclopent-1-en-1-yl)morpholine		Ether	20.0 μL	40	97
UiO-68-PZDC(OH)	2,3-dihydrofuran		Ether	10.5 μL	40	94
UiO-68-PZDC(Ph)	trimethyl((1-phenylvinyl)oxy)silane		Ether	28.4 μL	40	93
UiO-68-PZDC(BCN-OH)	(1α,8α,9β)-Bicyclo[6.1.0]non-4-yne-9-methanol, BCN-OH		Ether	20.8 mg	40	95
UiO-68-HPZDC(NRS)	5-Norbornene-2-acetic acid succinimidyl ester		DMF	17.3 mg	40	94
UiO-68-HPZDC(COOH)	5-Norbornene-2-carboxylic acid		DMF	19.1 mg	40	97
UiO-68-HPZDC(<i>i</i> -Bu)	4-Methyl-1-pentene		Ether	87.5 μL	40	70
UiO-68-HPZDC(Hex)	1-octene		Ether	110 μL	40	38

S4.2. Chemical characterization

¹H-NMR analysis

For ¹H-NMR analysis the same procedure was followed as for UiO-68-PZDC. 5 mg of activated sample were suspended in 0.5 mL of DMSO-*d*₆. After that, the sample was digested by addition of two drops of D₂SO₄-*d*₂ (96-98 wt. %). The mixture was stirred for 5 minutes at 80 °C. Then, the resulting clear solution was transferred to an NMR tube and ¹H-NMR was recorded.

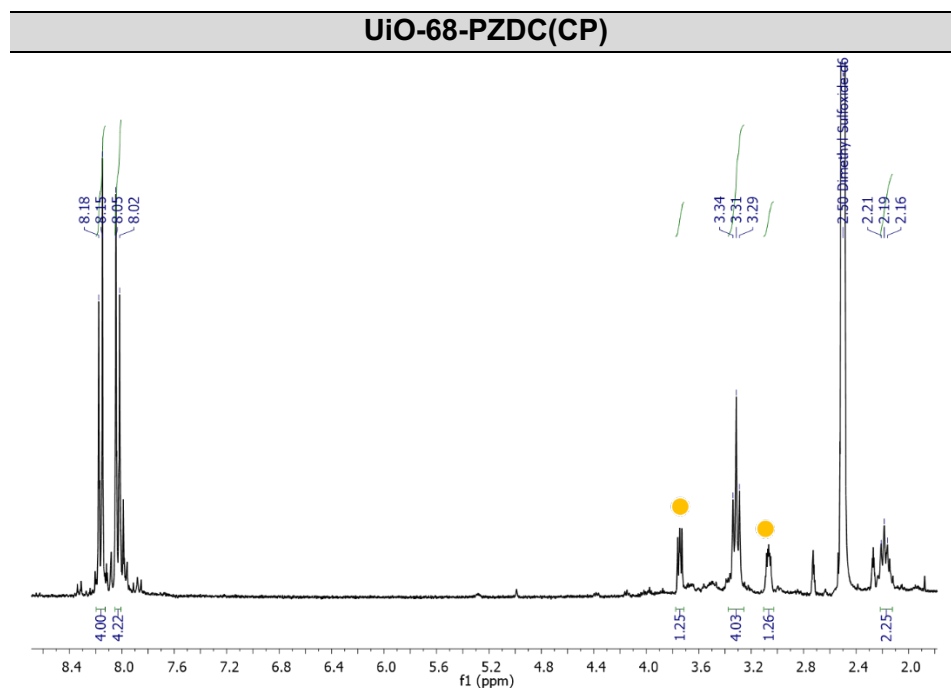


Figure S13. ¹H-NMR spectrum of UiO-68-PZDC(CP). ¹H-NMR (300 MHz, DMSO-*d*₆) δ 8.16 (d, *J* = 8.6 Hz, 4H), 8.03 (d, *J* = 8.6 Hz, 4 H), 3.31 (t, *J* = 7.5 Hz, 4H), 2.18 (q, *J* = 6.2 Hz, 2H). The signals 3.75 (m) and 3.07 (m) (showed as yellow circle) denote that morpholine remains inside the pores after washed and activation treatment.

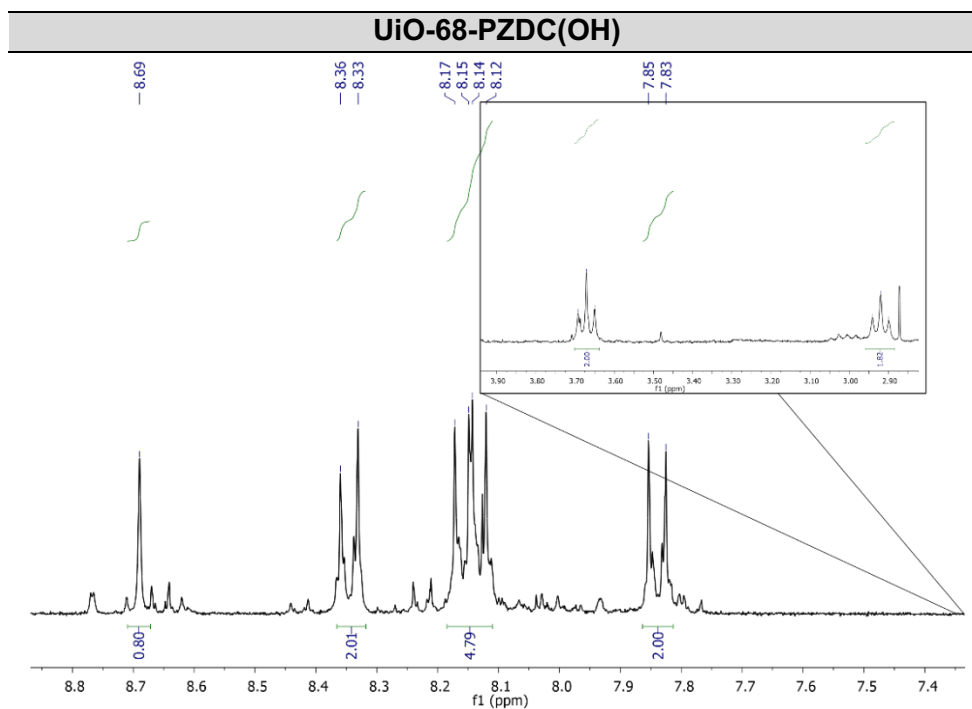


Figure S14. $^1\text{H-NMR}$ spectrum of UiO-68-PZDC(OH). $^1\text{H-NMR}$ (300 MHz, $\text{DMSO-}d_6$) δ 8.69 (s, 1H), 8.35 (d, $J = 8.7$ Hz, 2H), 8.15 (dd, $J = 8.6, 6.8$ Hz, 4H), 7.84 (d, $J = 8.6$ Hz, 2H), 3.67 (t, $J = 6.4$ Hz, 2H), 2.92 (t, $J = 6.2$ Hz, 2H).

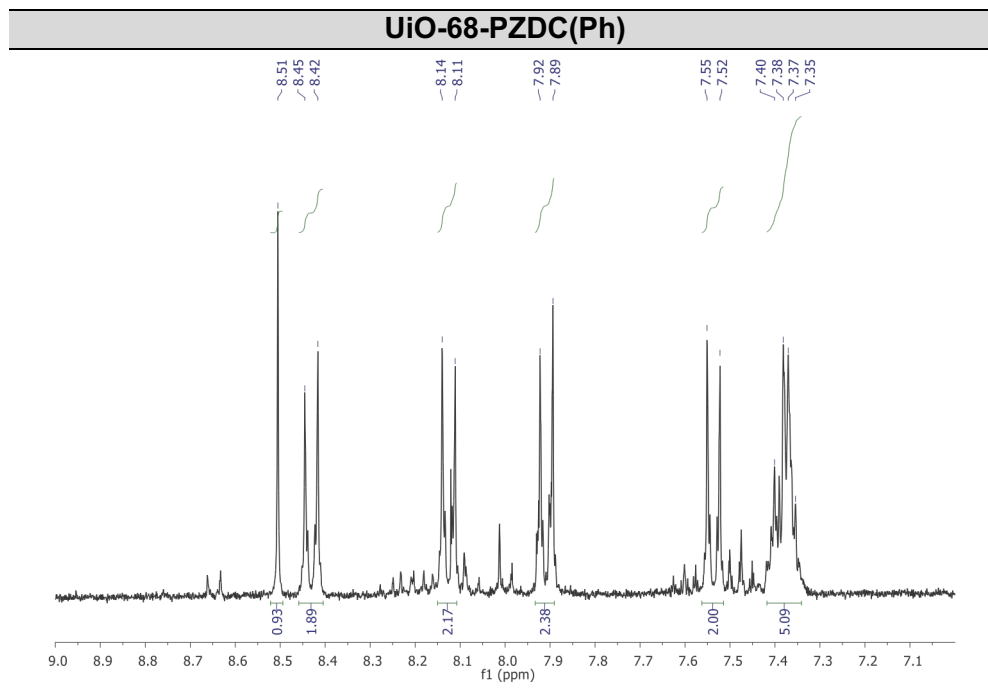


Figure S15. $^1\text{H-NMR}$ spectrum of UiO-68-PZDC(Ph). $^1\text{H NMR}$ (300 MHz, $\text{DMSO-}d_6$) δ 8.51 (s, 1H), 8.43 (d, $J = 8.7$ Hz, 2H), 8.13 (d, $J = 8.7$ Hz, 2H), 7.91 (d, $J = 8.6$ Hz, 2H), 7.54 (d, $J = 8.6$ Hz, 2H), 7.38 (dd, $J = 8.7, 5.3$ Hz, 5H).

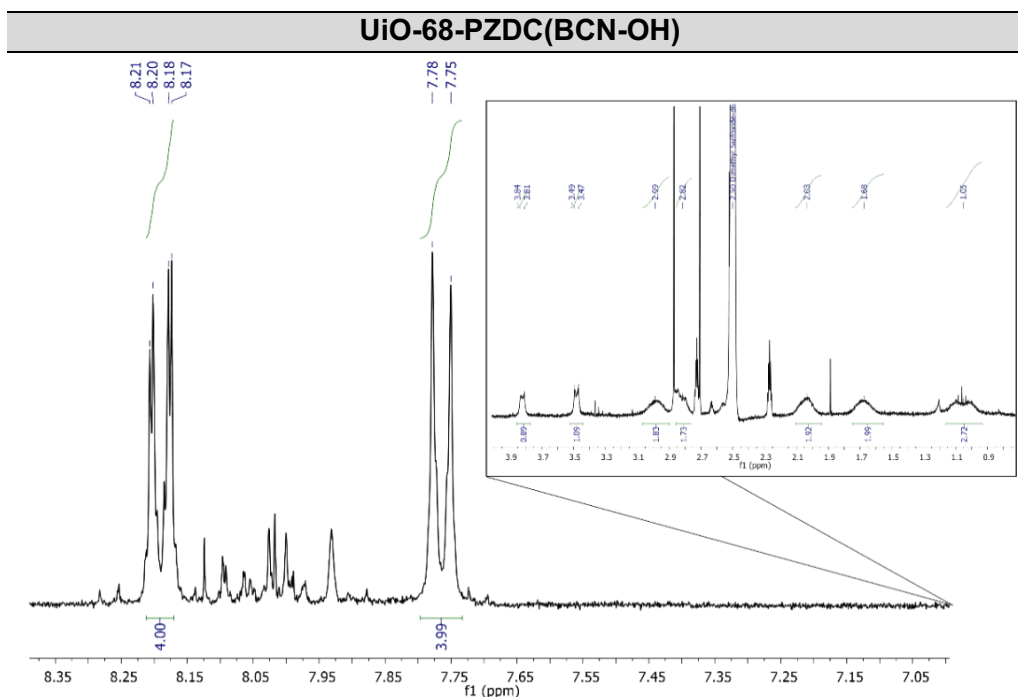


Figure S16. $^1\text{H-NMR}$ spectrum of UiO-68-PZDC(BCN-OH). $^1\text{H-NMR}$ (300 MHz, $\text{DMSO-}d_6$) δ 8.19 (dd, $J = 8.5, 1.5$ Hz, 4H), 7.76 (d, $J = 8.4$ Hz, 4H), 3.82 (d, $J = 8.4$ Hz, 1H), 3.48 (brd, $J = 7.2$ Hz, 1H), 2.99 (brd, 2H), 2.82 (b, 2H), 2.03 (b, 2H), 1.68 (b, 2H), 1.05 (b, 2H).

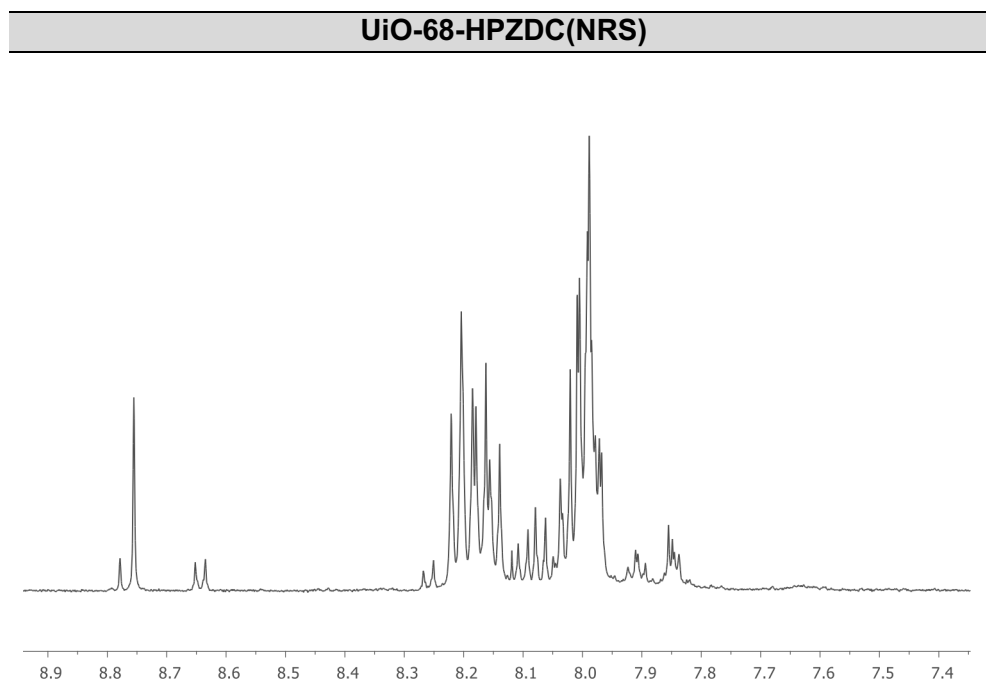


Figure S17. $^1\text{H-NMR}$ spectrum of UiO-68-HPZDC(NRS) shows the disappearance of the signal intrinsic to the tetrazine linker.

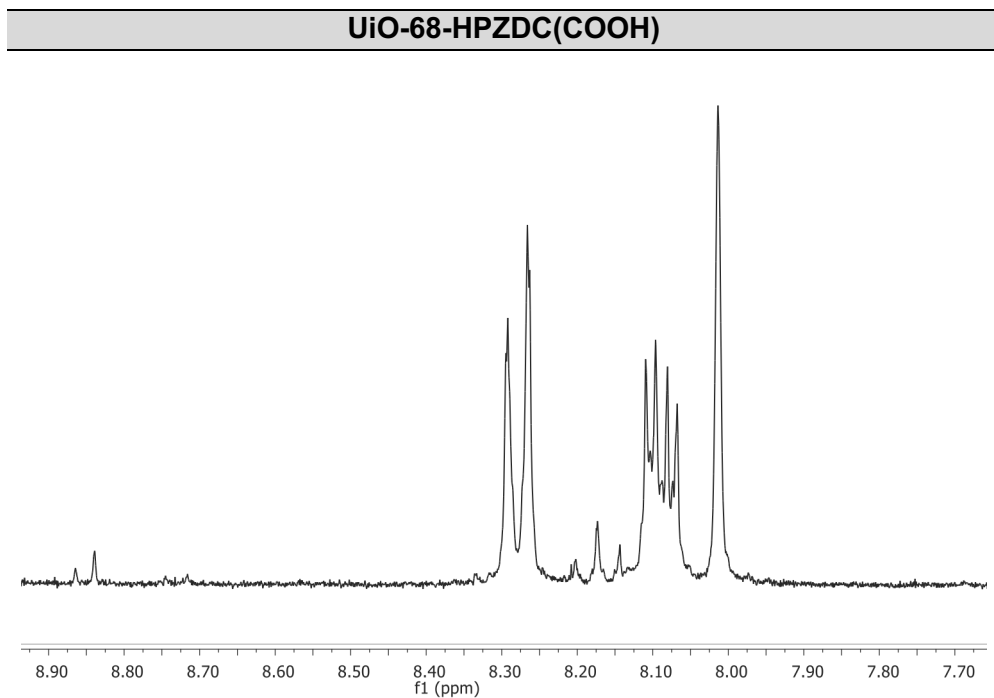


Figure S18. $^1\text{H-NMR}$ spectrum of UiO-68-HPZDC(COOH) shows the disappearance of the signal intrinsic to the tetrazine linker.

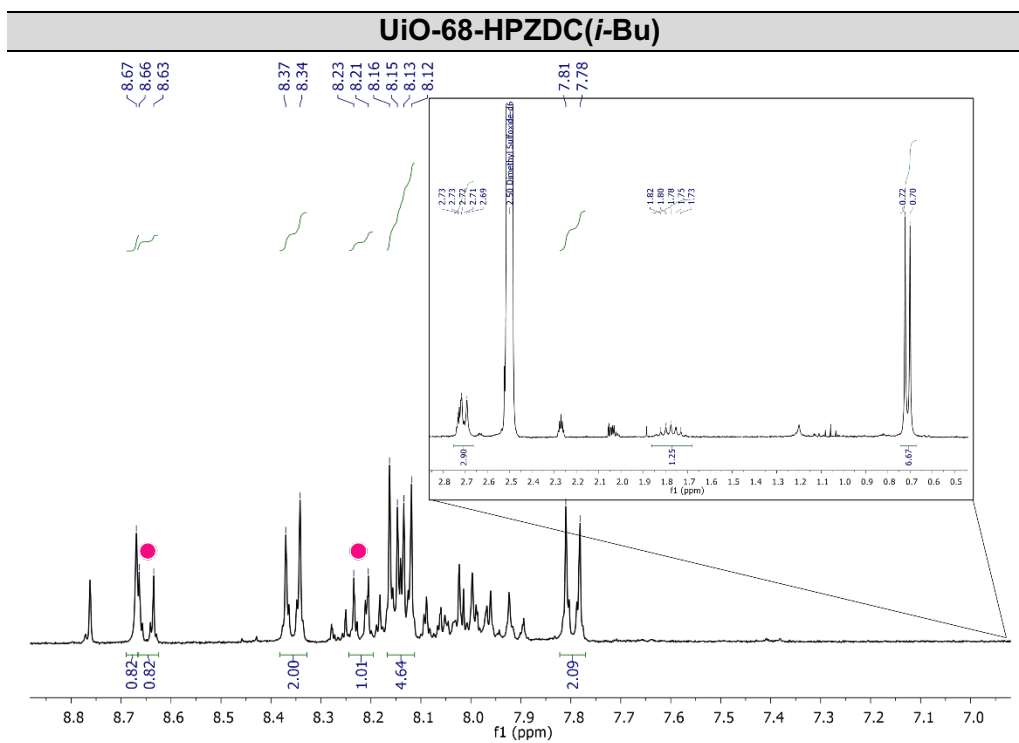


Figure S19. $^1\text{H-NMR}$ spectrum of UiO-68-HPZDC(*i*-Bu). $^1\text{H-NMR}$ (300 MHz, $\text{DMSO-}d_6$) δ 8.67 (s, 1H), 8.36 (d, $J = 8.7$ Hz, 2H), 8.14 (dd, $J = 8.6, 4.6$ Hz, 4H), 7.80 (d, $J = 8.5$ Hz, 2H), 2.73 (m, 2H), 1.78 (dt, $J = 13.5, 6.8$ Hz, 1H), 0.71 (d, $J = 6.6$ Hz, 6H). The signals 8.65 (d, $J = 8.8$ Hz, 1H) and 8.22 (d, $J = 8.8$ Hz, 1H) correspond to unreacted UiO-68-TZDC (shown as pink circles). The % of transformation (70 %) was calculated from the integration value of the aromatic signal for each molecule.

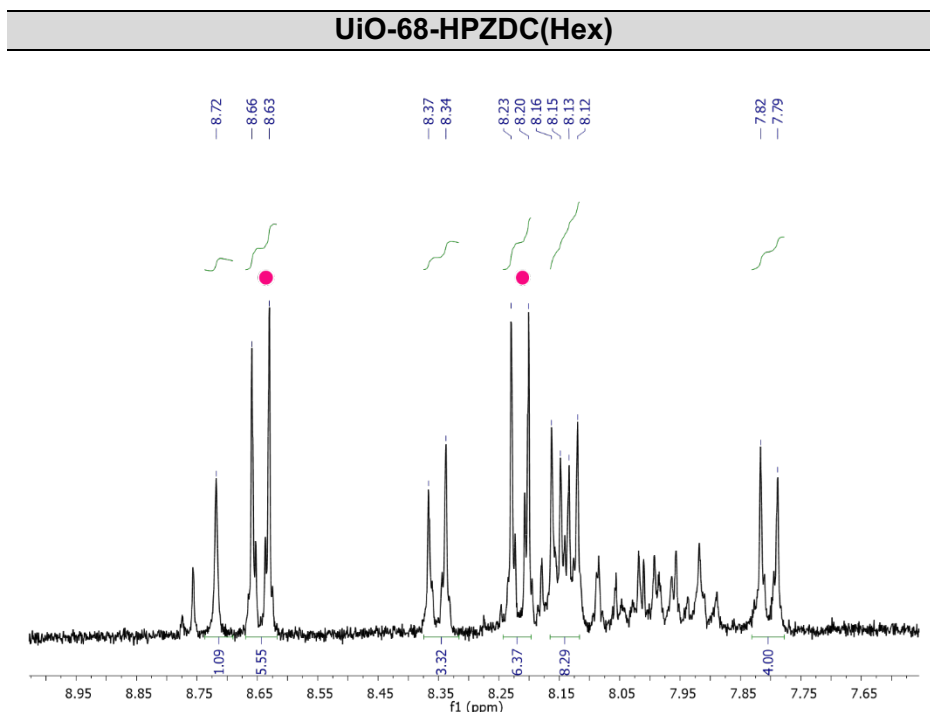


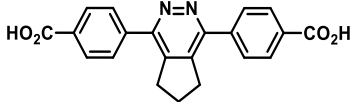
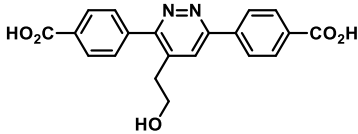
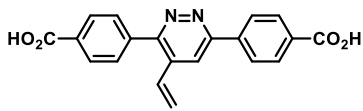
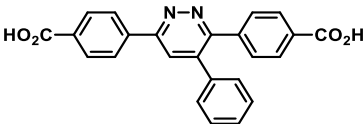
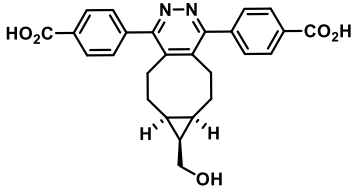
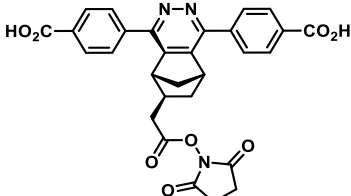
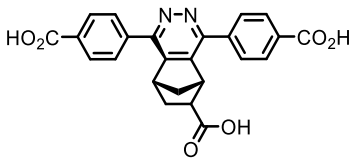
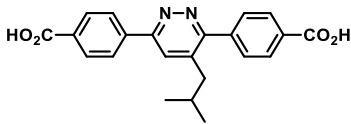
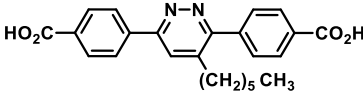
Figure S20. $^1\text{H-NMR}$ spectrum of UiO-68-HPZDC(Hex). $^1\text{H-NMR}$ (300 MHz, $\text{DMSO-}d_6$) δ 8.72 (s, 1H), 8.22 (d, $J = 8.7$ Hz, 6H), 8.14 (dd, $J = 8.6, 4.3$ Hz, 8H), 7.80 (d, $J = 8.5$ Hz, 4H). The signals 8.64 (d, $J = 8.7$ Hz, 6H), 8.35 (d, $J = 8.7$ Hz, 4H), below to unreacted UiO-68-TZDC (shown as pink circles). The % of transformation (38 %) was calculated from the integration value of the aromatic signal for each molecule.

HR-Mass Spectrometry

The samples were digested using the same protocol as used for $^1\text{H-NMR}$ measurements. Once the samples were dissolved in DMSO, an aliquot was taken and dispersed in methanol. The positive mode was studied.

The HR-MS results confirm the formation of desired products. In case of UiO-68-HPZDC(X) samples, the analysis reveals that after digestion process the dihydropyridazines core is oxidated to pyridazine. For its part, UiO-68-PZDC(OH), the alkene derivate resultant of alcohol elimination is obtained.

Table S5. Expected product of Diels-Alder reaction. The values of m/z are consistent with the chemical formula proposed.

Compound	Molecule	Chemical Formula and Exact mass	m/z positive
(CP)		C ₂₁ H ₁₆ N ₂ O ₄ 360.11	361.12
(OH)		C ₂₀ H ₁₆ N ₂ O ₅ 364.11	347.10
		C ₂₀ H ₁₄ N ₂ O ₄ 346.10	
(Ph)		C ₂₄ H ₁₆ N ₂ O ₄ 396.11	397.12
(BCN-OH)		C ₂₆ H ₂₄ N ₂ O ₅ 444.17	445.18
(NRS)		C ₂₉ H ₂₃ N ₃ O ₈ 541.15	542.16
(COOH)		C ₂₄ H ₁₈ H ₂ O ₆ 430.12	431.12
(<i>i</i> -Bu)		C ₂₂ H ₂₀ N ₂ O ₄ 376.14	377.15
(Hex)		C ₂₄ H ₂₄ N ₂ O ₄ 404.17	405.18

Elemental Analysis (EA)

For clarity, only the samples in which the transformation was complete were analyzed by AE and TGA techniques. Prior to analysis, samples were activated in the vacuum oven at 120°C overnight. The results confirm the clean functionalization of the tetrazine core to pyridazine and dihydropyridazine derivatives. The table below confirms the consistency between calculated and experimental values.

Table S6. Calculated and experimental percentages of C, H and N for each compound. The calculated percentages are based on the proposed formula.

Compound	Formula	%C _{cal}	%C _{exp}	%H _{cal}	%H _{exp}	%N _{cal}	%N _{exp}
(CP)	[Zr ₆ O ₄ (OH) ₄ (C ₂₁ H ₁₆ N ₂ O ₄) ₆]	84.9	82.4	5.6	6.7	9.4	10.9
(OH)	[Zr ₆ O ₄ (OH) ₄ (C ₂₀ H ₁₄ N ₂ O ₅) ₆]	84.9	84.1	5.2	6.7	8.5	9.3
(Ph)	[Zr ₆ O ₄ (OH) ₄ (C ₂₄ H ₁₄ N ₂ O ₄) ₆]	87.1	85.6	4.4	5.6	8.5	8.7
(BCN-OH)	[Zr ₆ O ₄ (OH) ₄ (C ₂₆ H ₂₂ N ₂ O ₅) ₆]	86.0	85.3	6.3	6.8	7.7	7.9
(NRS)	[Zr ₆ O ₄ (OH) ₄ (C ₂₉ H ₂₂ N ₃ O ₈) ₆]	84.3	83.9	5.5	6.3	10.2	9.8
(COOH)	[Zr ₆ O ₄ (OH) ₄ (C ₂₄ H ₁₇ N ₂ O ₆) ₆]	86.3	84.7	5.3	6.4	8.4	8.9

Thermogravimetric Analysis (TGA)

The samples were activated in the vacuum oven at 120°C overnight before the analysis.

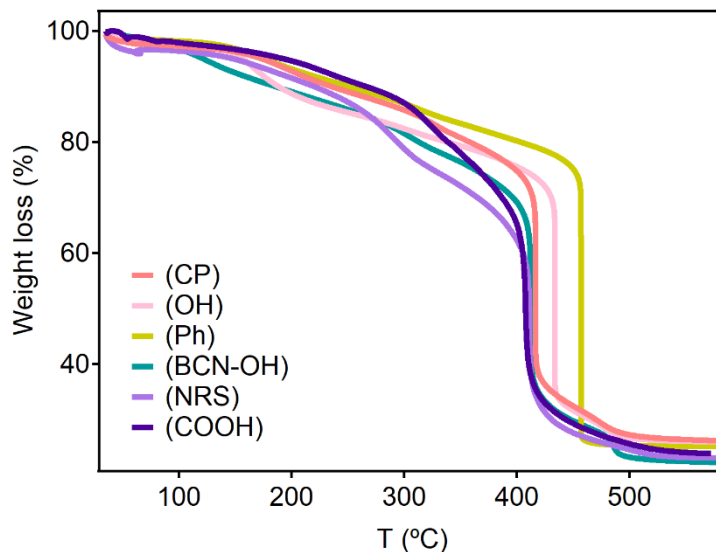


Figure S21. Thermal decomposition profile of UiO-68-PZDC and HPZDC frameworks.

Table S7. Calculated and experimental percentages of ZrO_2 . The calculated percentages are based on the formula proposed.

Compound	% ZrO_2 calculated	% ZrO_2 experimental
(CP)	26.02	26.25
(OH)	22.09	22.06
(Ph)	25.91	25.79
(BCN-OH)	23.53	25.12
(NRS)	18.76	22.98
(COOH)	22.67	23.87

Powder X-Ray Diffraction (PXRD)

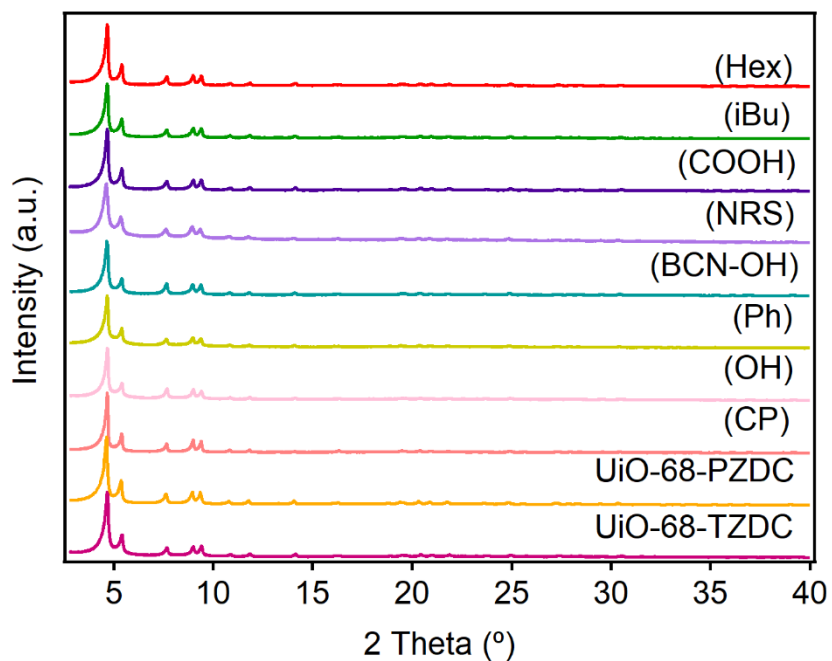
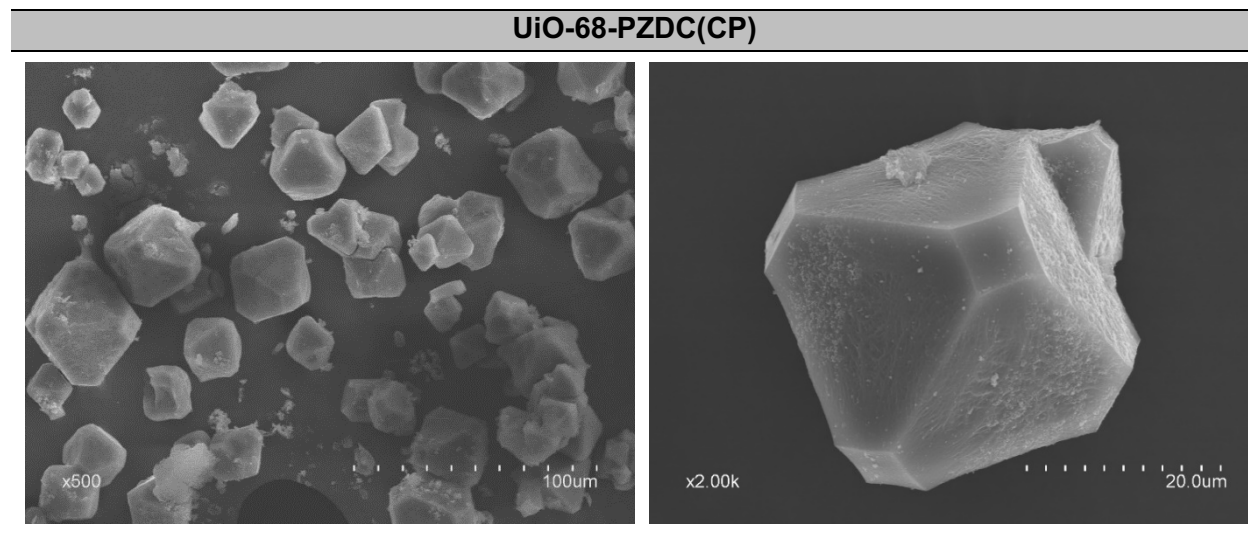
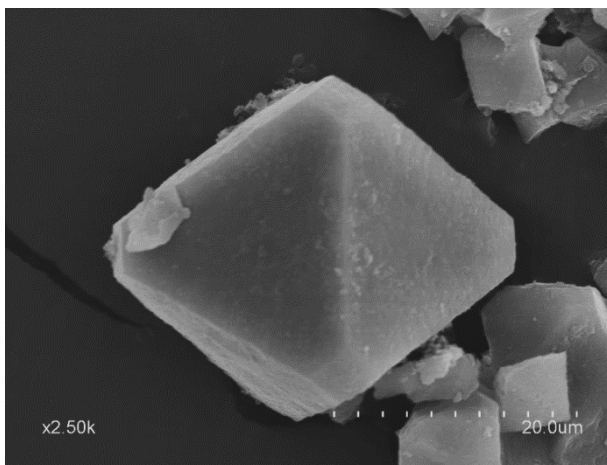
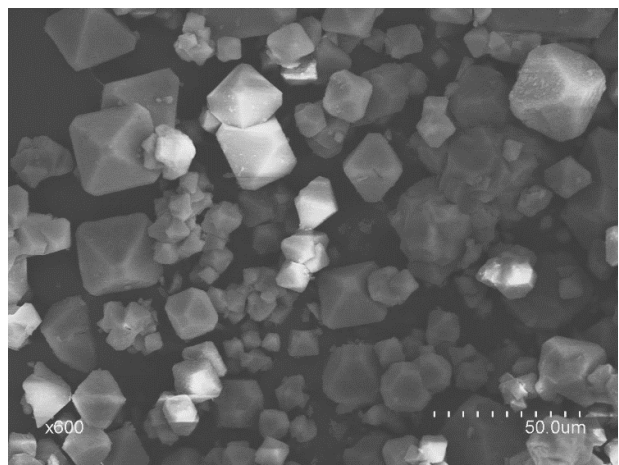


Figure S22. PXRD patterns of UiO-68-PZDC and HPDC MOFs confirming minimum impact to crystallinity upon iEDDA reaction in all cases.

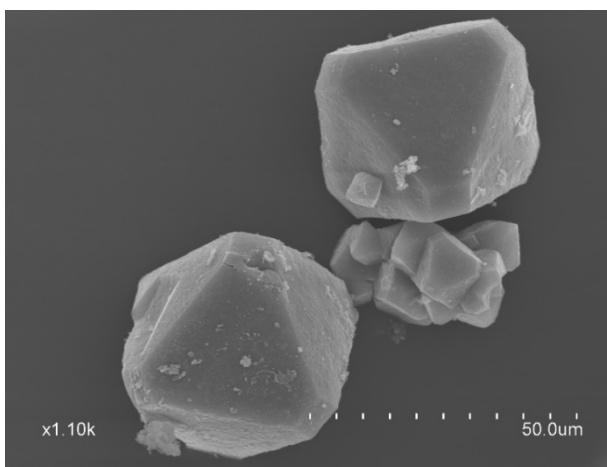
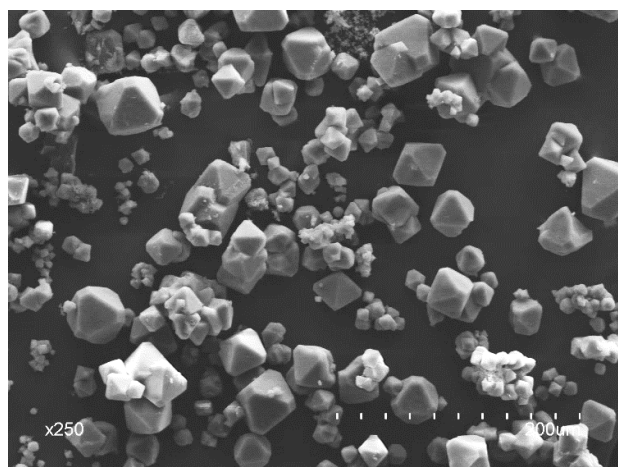
Scanning Electron Microscopy (SEM-EDX)



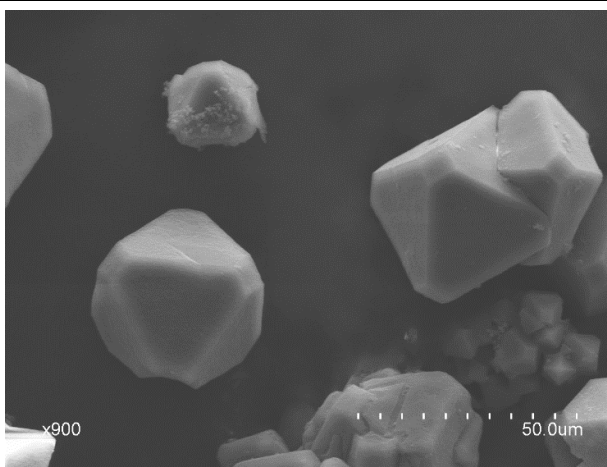
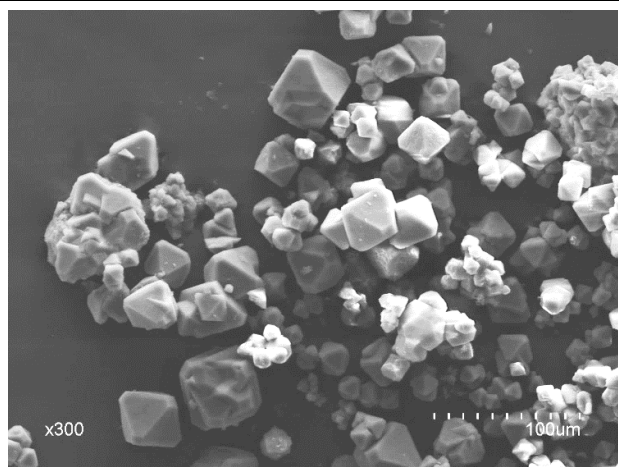
UiO-68-PZDC(OH)



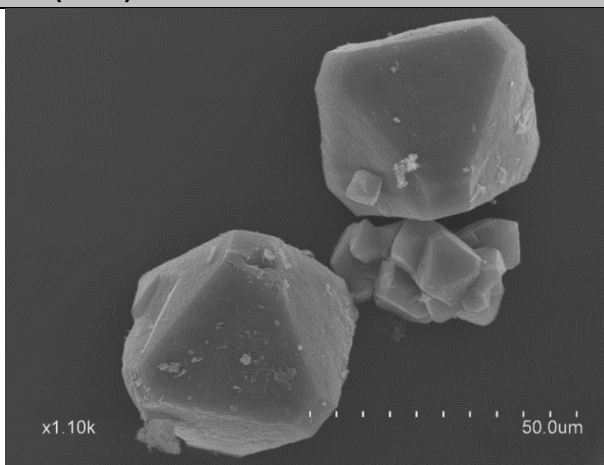
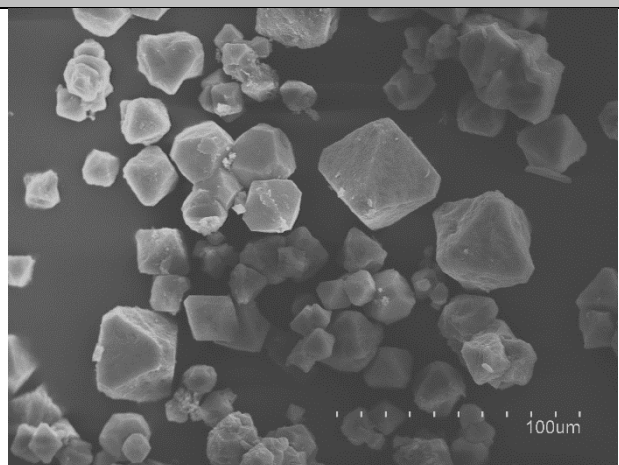
UiO-68-PZDC(Ph)



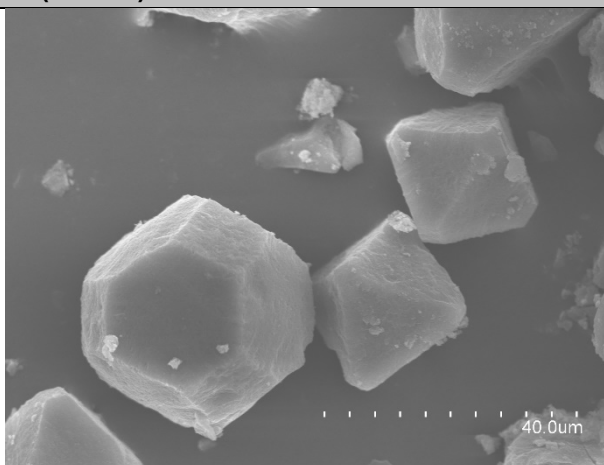
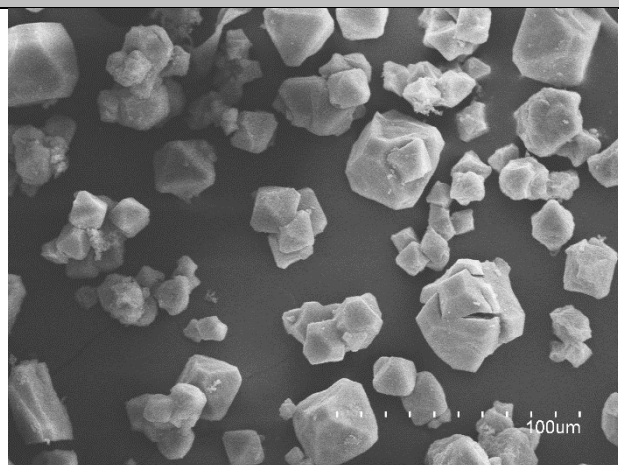
UiO-68-PZDC(BCN-OH)



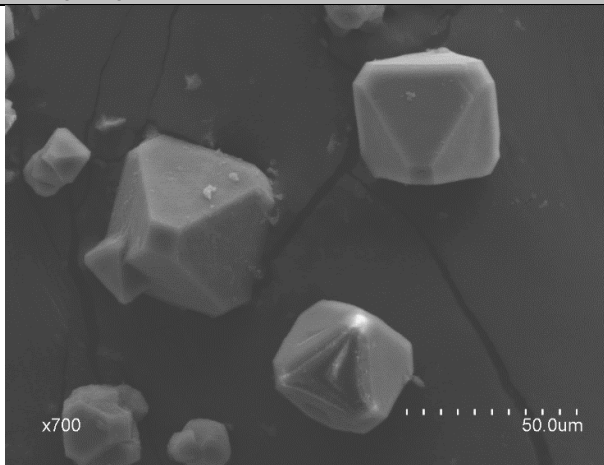
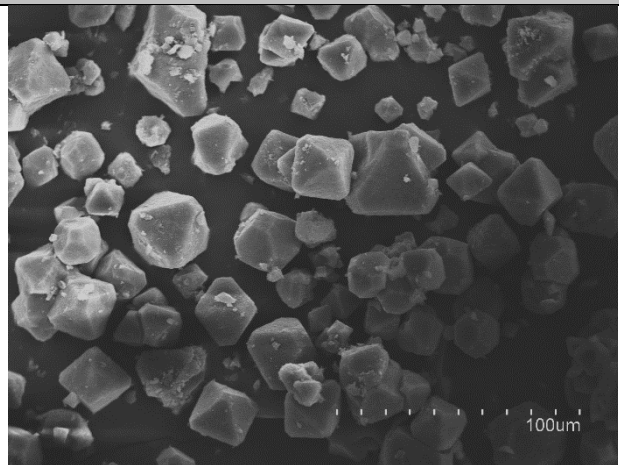
UiO-68-HPZDC(NRS)



UiO-68-HPZDC(COOH)



UiO-68-HPZDC(*i*Bu)



UiO-68-HPZDC(Hex)

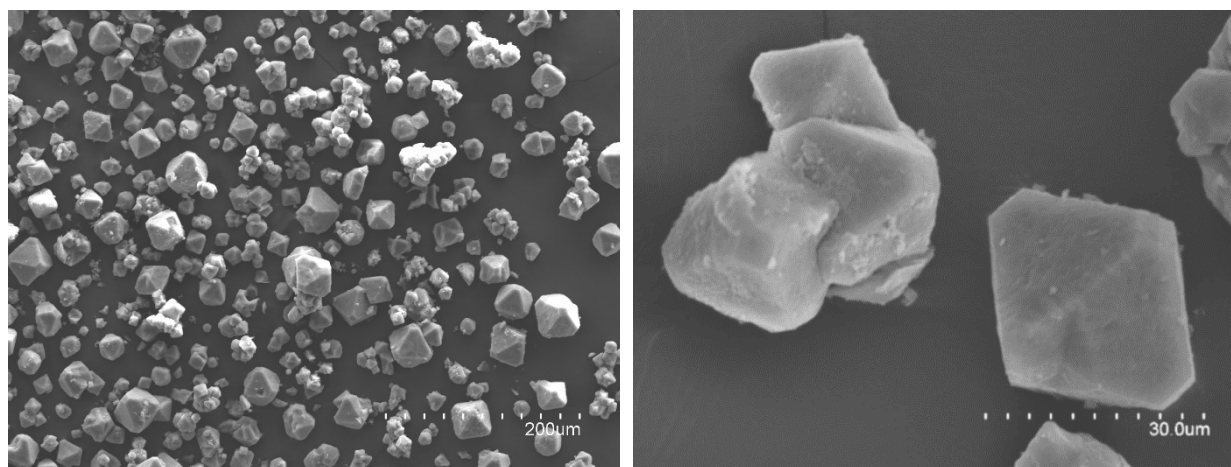


Figure S23. Scanning Electron Microscopy (SEM) images of crystal of UiO-68-PZDC and HPZDC. Lower magnification confirms minimum impact to morphology upon iEDDA reaction in all cases. Higher magnification shows the particle size oscillates between 20-50 μm across the series.

Analysis of N_2 adsorption/desorption isotherms at 77 K

Table S8. Summary of the experimental adsorption parameters of resultant solids.

Compound	BET surface area ($\text{m}^2\cdot\text{g}^{-1}$)	Vp total at $P/P_0 = 0.96$ ($\text{cm}^3\cdot\text{g}^{-1}$)	Pore width (nm)
(CP)	2313	0.92	1.8, 2.9
(OH)	3099	1.18	2.0, 2.9
(Ph)	2422	0.90	1.9, 2.9
(BCN-OH)	1327	0.50	1.9, 2.9
(COOH)	1862	0.74	1.9, 2.9
(i-Bu)	1999	0.75	1.9, 2.9
Hex	3132	1.12	2.1, 2.9

The abnormally low values obtained for UiO-68-PZDC(CP) are associated to the occlusion of morpholine molecules inside the pore, as confirmed with $^1\text{H-NMR}$ (Figure S13). The high BET value obtained for UiO-68-HPZDC(Hex) might be linked to a comparatively lower degree of functionalization as discussed in the main text.

S4.3. Theoretical models

Theoretical Pore Size Distribution

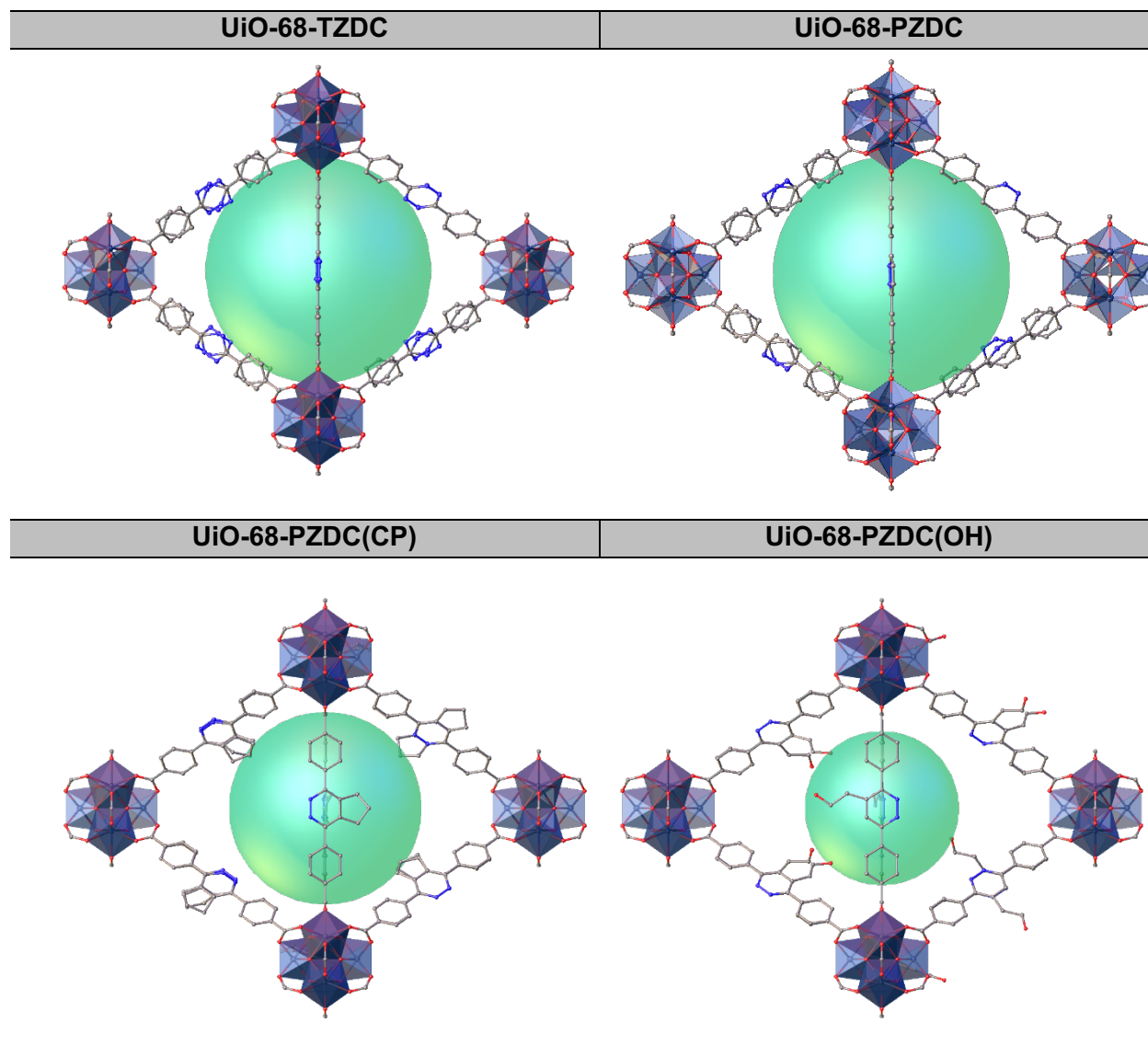
Surface area (chan_radious=probe_radious=1.69 and num_samples=2000) and probe-occupiable volume (chan_radious=probe_radious=1.69 and num_samples=5000) were obtained by analysing computationally generated models of UiO-68-PZDC and UiO-68-HPZDC (Supplementary Section S6.2) by using Zeo++.¹²

Table S9. Summary of the adsorption parameters calculated from the crystallographic models of UiO-68-PZDC and HPZDC frameworks.

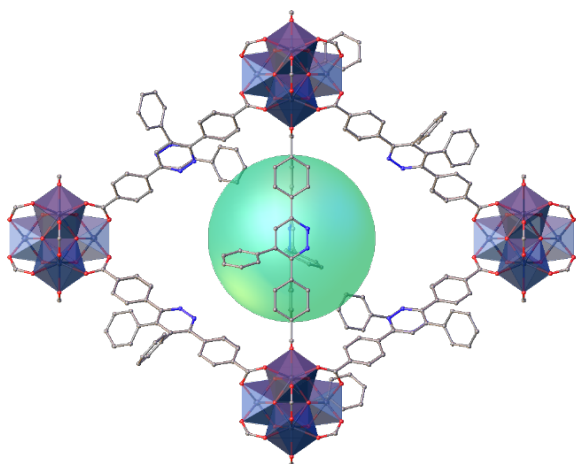
Compound	BET surface area (m ² ·g ⁻¹)	Vp total (cm ³ ·g ⁻¹)
UiO-68-TZDC	4360	1.51
UiO-68-PZDC	4076	1.51
(CP)	4225	1.28
(OH)	4315	1.24
(Ph)	4013	1.08
(BCN-OH)	3705	0.84
(NRS)	2889	0.62
(COOH)	3538	0.96
(i-Bu)	4084	1.11
(Hex)	3852	0.93

Structural models of UiO-68-PZDC and HPZDC frameworks

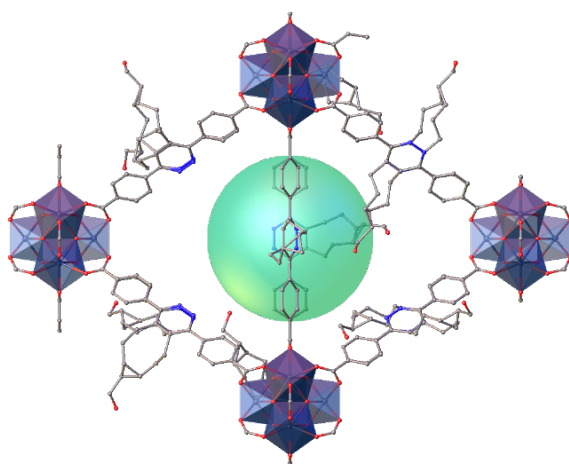
The structural models were created with Materials Studio 2017 R2¹³ by using the reported structure of UiO-68-TZDC (CCDC 2023345)¹ as starting model.



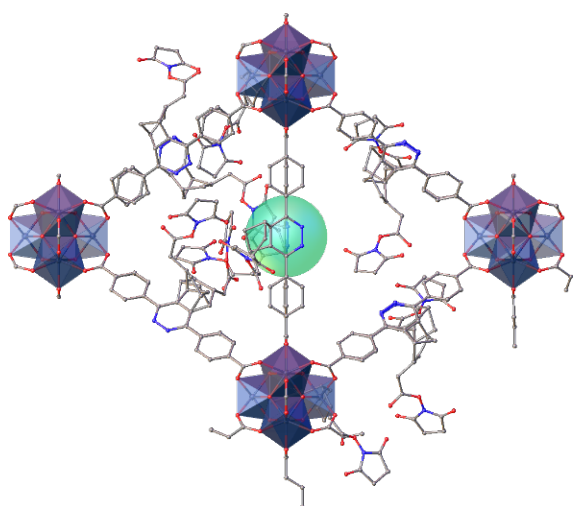
UiO-68-PZDC(Ph)



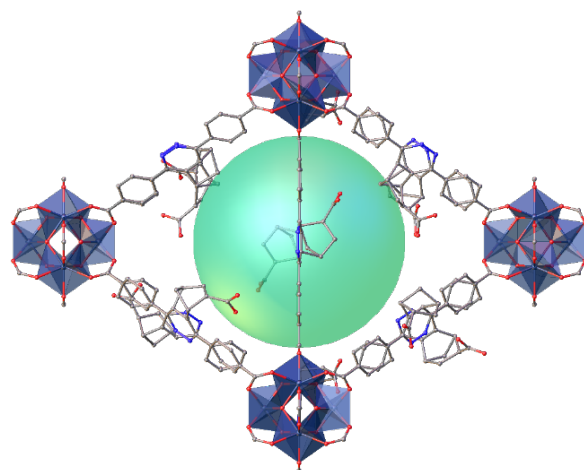
UiO-68-PZDC(BCN-OH)



UiO-68-HPZDC(NRS)



UiO-68-HPZDC(COOH)



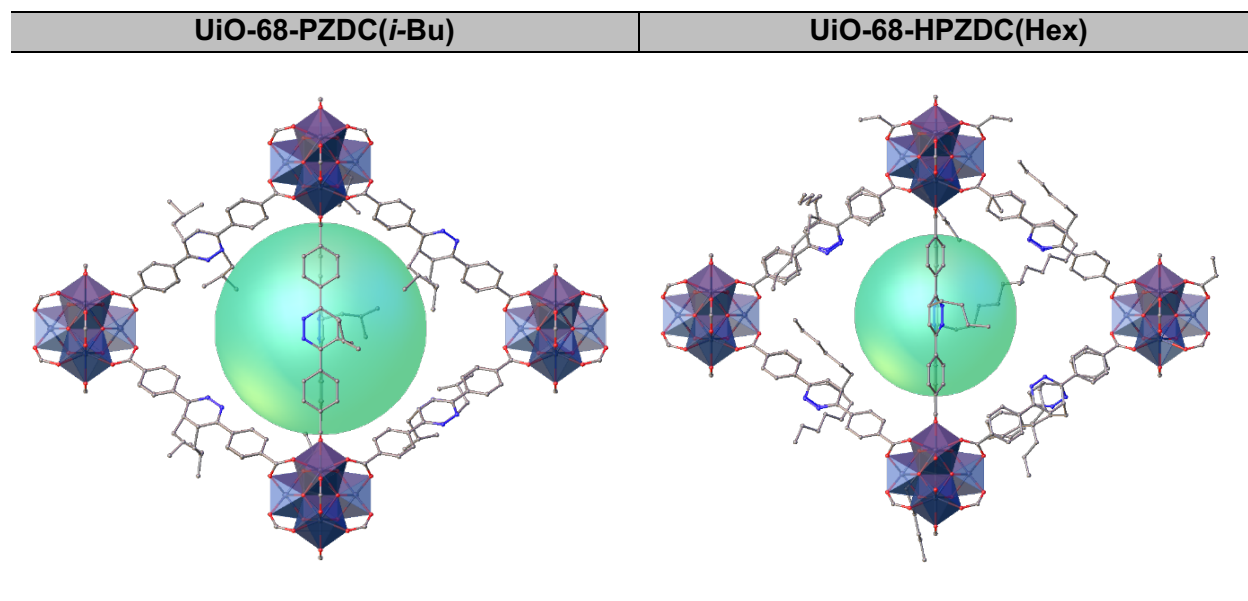


Figure S24. Crystallographic models representative of the changes in pore chemistry and accessible porosity across the UiO-68-PZDC and HPZDC frameworks generated by iEDDA reaction.

S5. Tetrazine controlled C₆₀ conjugation for crystalline fulleretic materials

S5.1. Synthesis of UiO-68-PZDC(C₆₀)

20 mg of UiO-68-TZDC (0.0077 mmol, 1 equiv) were immersed in a solution of 6 equivalents of C₆₀ (0.0462 mmol) in 15 mL of toluene. The resultant mixture was stirring in a shaker at 40 °C during 72 hours in a 25 mL pyrex bottle. After this time, the brown crystals were washed by soxhlet extraction with toluene overnight. Then, UiO-68-PZDC(C₆₀) crystals were kept in hexane for further analysis.

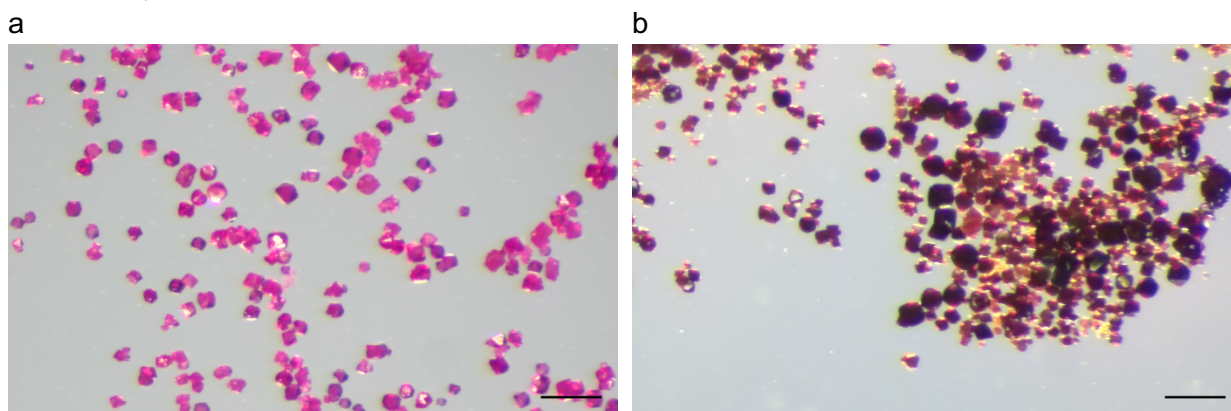


Figure S25. Picture of as-made crystals of a) UiO-68-TZDC and b) UiO-68-PZDC(C₆₀) acquired with an optical microscope. Crystals display a hexagonal morphology and micrometric size (close to 20 μm). Scale bars correspond to 100 μm .

A complementary experiment using the above experimental conditions was performed. In this case, UiO-68 was stirring in a shaker at 40 °C during 72 hours in C₆₀ solution, the resultant brown crystals were washed by soxhlet with toluene overnight. The result was completely different from those obtained for UiO-68-TZDC. Whereas in the case of tetrazine-based MOF, the resultant crystals remained brownish after toluene extraction; UiO-68 crystals recovered its original yellow colour. This finding may be considered as an indirect probe that fullerene was covalent binding to the network and rule out the occlusion inside the pores.

S5.2. Chemical characterization

SS-MAS-¹³C-NMR

For this measurement, both samples, pristine UiO-68-TZDC and functionalized UiO-68-PZDC(C₆₀) were diluted in KBr. Thus, it was required less amount of sample to fill the available large SS-NMR's holder. This dilution involved the broadening of signals, this effect was accentuated for UiO-68-PZDC(C₆₀), which preparation was trickier.

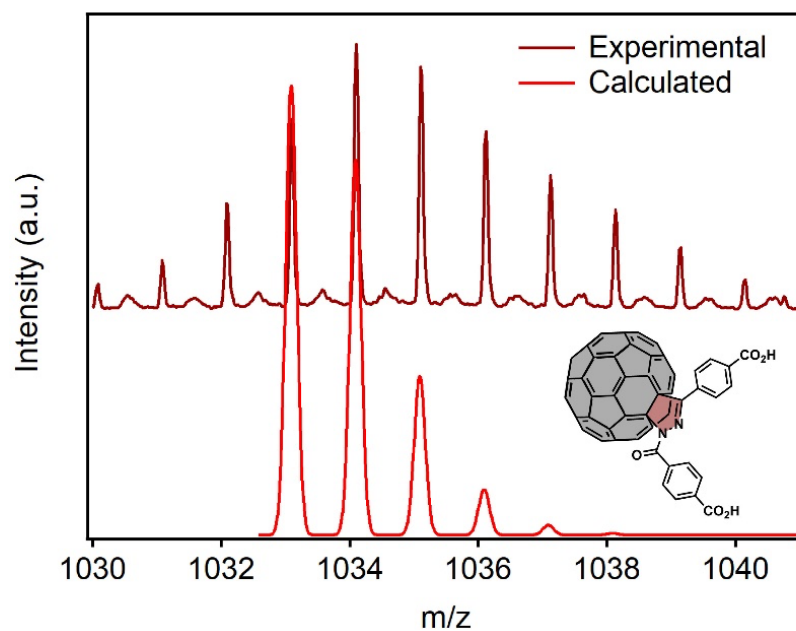
The presence of new broad signals around 142 ppm are attributed to sp² -carbons of bonded fullerene^{14,15}.

MALDI-MS

For MALDI-MS analysis, the sample was digested using the same protocol detailed above. UiO-68-PZDC(C_{60}) was digested in DMSO/ H_2SO_4 solution, 1 μ L of this sample was diluted 1:10 with acetonitrile (ACN). 1 μ L of the diluted sample was spotted onto the MALDI plate and allowed to air-dry at room temperature and after 1 μ L of matrix (trans-2-[3-(4-tert-Butylphenyl)-2-methyl-2-propenylidene]malononitrile, DCTB (Bruker), in 70% ACN, 0.1% Trifluoroacetic acid, TFA) was spotted onto the same MALDI plate position and allowed to air-dry at room temperature.

Positive mode spectrum showed the peak associated with the formation of the fullerene monoadduct with the tetrazine ligand at 1033 m/z. This m/z value corresponds to the mass of the monoadduct and a molecule of water in acid media [$H_2pzdc-C_{60}-H_3O$] $^+$. However, we suspect that the harsh acid conditions of the digestions promote a hydration and a rearrangement of the fullerene linker.¹⁶ The extra water molecule results in the formation of an amide group through one oxygen atom addition to a 2-pyrazoline ring fused by its 4,5-positions to C_{60} , and the placement of two hydrogen atoms at the fullerene cage. Indeed, in view of the mixture of species with similar m/z values present at the isotopic pattern, we also suggest multiple hydrogen additions to the C_{60} moiety.

a



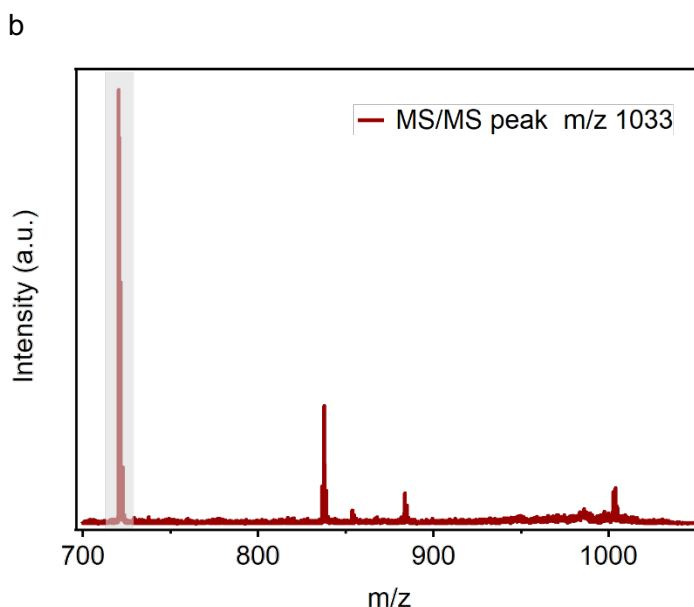


Figure S26. a) Positive MALDI-MS spectrum of digested UiO-68-PZDC(C₆₀) (top), calculated spectrum of hydrated monoadduct proposed, [H₂pzdc-C₆₀-H₃O]⁺ (down). b) Positive MS/MS spectrum of 1033 m/z peak confirmed that neat fullerene molecules were generated from the fragmentation of the monoadduct.

Elemental Analysis (EA)

For elemental analysis, samples were activated in the vacuum oven at 120°C overnight before the analysis. Based on EA results, we proposed a molecular formula which involved 50 - 55 % of functionalization. Elemental analysis for [Zr₆O₄(OH)₄(C₇₆H₈N₂O₄)₃(C₁₆H₈N₄O₄)₃] ≡ [Zr₆O₄(OH)₄(PZDC-C₆₀)₃(TZDC)₃], calc. C (91.6), H (1.5), N (6.9); found: C (90.8), H (2.9) and N (6.3).

The percentage of functionalization was reproducible under selected synthetic conditions. Moreover, similar C₆₀ incorporation value was reached in complementary experiments in which the reaction time was extended to 5 days. The UiO-68-PZDC(C₆₀) crystals were synthesized by extending the reaction time to 5 days.

Table S10. Experimental percentages of C, H and N for UiO-68-PZDC(C₆₀) prepared under different conditions.

Sample	Functionalization protocol	%C _{exp}	%H _{exp}	%O _{exp}
UiO-68-PZDC(C ₆₀)	Shaker 40 °C, 3 days (original)	90.8	2.9	6.3
UiO-68-PZDC(C ₆₀)-5 days	Shaker 40 °C, 5 days	90.6	3.2	6.2

Thermogravimetric Analysis (TGA)

For thermogravimetric analysis, samples were activated in the vacuum oven at 120°C overnight before the analysis. Calculated value of ZrO₂ was based on accepted molecular formula [Zr₆O₄(OH)₄(C₇H₈N₂O₄)₃(C₁₆H₈N₄O₄)₃]: ZrO₂ calculated = 15.8 %; ZrO₂ experimental = 16.7 %. The EA and TGA results were consistent with a functionalization between 50 - 55 %. It is worth mentioning the remarkable change in thermal stability observed for the functionalized material, which is a clear proof of the chemical modification undergone by the pillars of the network.

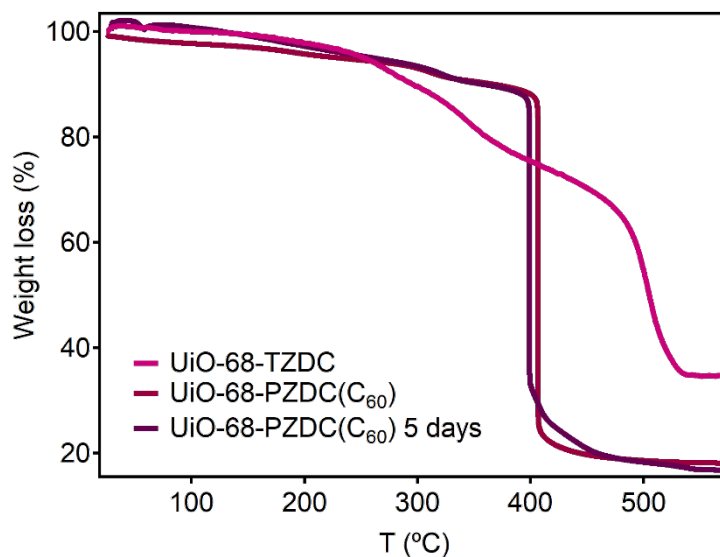


Figure S27. Thermal decomposition profile of original UiO-68-TZDC and UiO-68-PZDC(C₆₀) (solid line) and UiO-68-PZDC(C₆₀) (dotted line).

Scanning Electron Microscopy (SEM-EDX)

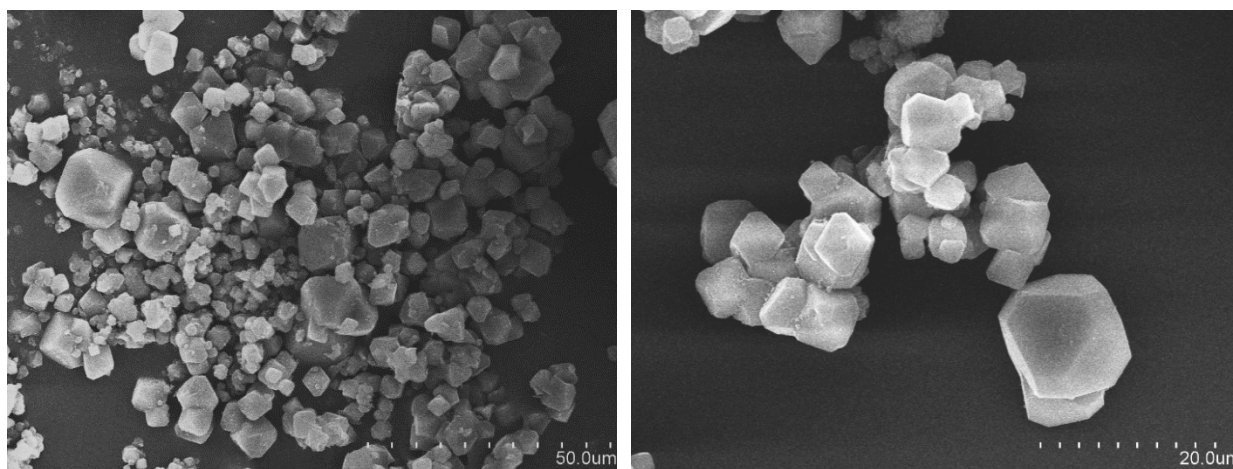


Figure S28. Scanning Electron Microscopy (SEM) images of crystal of UiO-68-PZDC(C₆₀).

Single Crystal X-Ray diffraction experiments

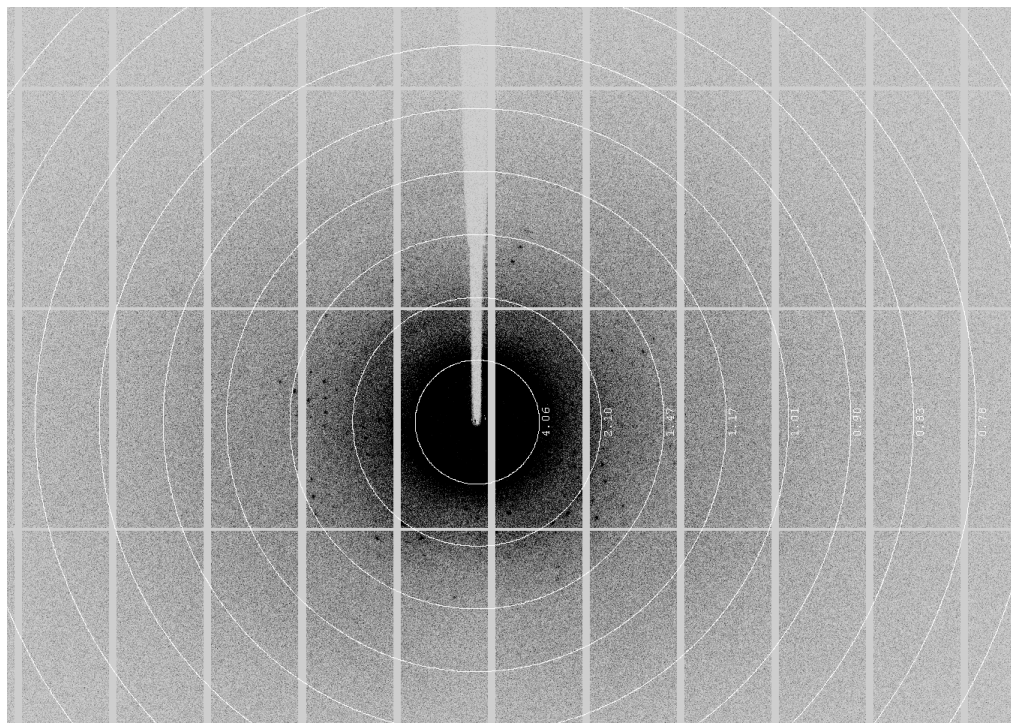


Figure S29. Images of diffraction experiments with synchrotron radiation (ALBA, BL13-XALOC) showed very weak x-Ray diffraction at resolutions higher than 1.47 Å.

S5.3. Rietveld refinement

The comparison between the as-synthesised PXRD pattern of UiO-68-PZDC(C₆₀) and the pristine UiO-68-TZDC suggested that the two MOFs are isostructural. A whole powder pattern refinement with the Le Bail method¹⁷ using the program TOPAS-R v.3¹⁸ confirmed the hypothesized space group and was used to retrieve the unit cell parameters of UiO-68-PZDC(C₆₀). According to the computed crystal structure in *Fm-3m* symmetry the asymmetric unit and the preliminary structure were built. As first approximation, the position and orientation of Zr cluster and of the linker were fixed according to the computational model. The crystallographically independent portion of TZDC(C₆₀) was described as rigid body in *z-matrix* formalism as implemented in TOPAS-R. Then, a combined Monte Carlo/Simulated Annealing approach¹⁹ was used to locate the solvent molecules in the preliminary framework. To simulate the solvent, the two hexane molecules were described as rigid bodies and their positions of the centre of mass and orientations were let to vary. The structure refinement was then carried out with the Rietveld method, as implemented in TOPAS-R v.3. Average values were initially assigned to bond distances and angles for both the linker and solvent [Bond distances for the rigid body describing the linkers: C–C 1.36 Å; exocyclic C–C 1.45 Å; C–H 1.05 Å; C–O 1.23 Å]. During the final Rietveld refinement stages, bond distances (except for the C–H distances) were refined in a restrained range of values [Bond distances for the rigid body describing the linkers: C–C 1.34–1.43 Å; exocyclic C–C min 1.40–1.60 Å; C–O 1.23–1.26 Å]. A Chebyshev polynomial function was successfully used for the background description. A refined, isotropic thermal parameter was assigned to the metal atoms; lighter atoms were given an isotropic thermal parameter 2.0 Å² higher. The Fundamental Parameters Approach²⁰ was used to model the peak profile. The occupancy of the ligand was let free to refine except for the atoms of the carboxylate group, whose site occupation factors were fixed to the ones of the cluster atoms assuming that the missing linkers are replaced by formates. To retrieve the relative the content of pyridazine PZDC-C₆₀ units in respect to TZDC, the occupancy factors of fullerene molecule was let to vary. The final Rietveld refinement plot is shown in Figure S31, and the crystallographic details are summarized in Table S11.

TableS11. Crystallographic data and Rietveld refinement of UiO-68-PZDC(C₆₀).

UiO-68-PZDC(C ₆₀)	
CCDC Number	2167506
Empirical formula	Zr ₆ O ₄₀ C _{368.5} N _{11.9} H _{258.6}
Formula weight (g mol ⁻¹)	15842.24
Crystallographic system	Cubic
Space group	<i>Fm-3m</i>
a, b, c (Å)	32.5556(2)
V (Å ³)	34504(7)
Z, Z'	64, 8
ρ (g cm ⁻³)	0.290
Temperature (K)	298
Wavelength (Å)	1.540596
2θ range (°)	3.5-105
Number of reflections	1052
Number of structural/total variables	47
F(000)	3072
R _{Bragg}	0.010
R _p	0.033
R _{wp}	0.046
GoF	4.080

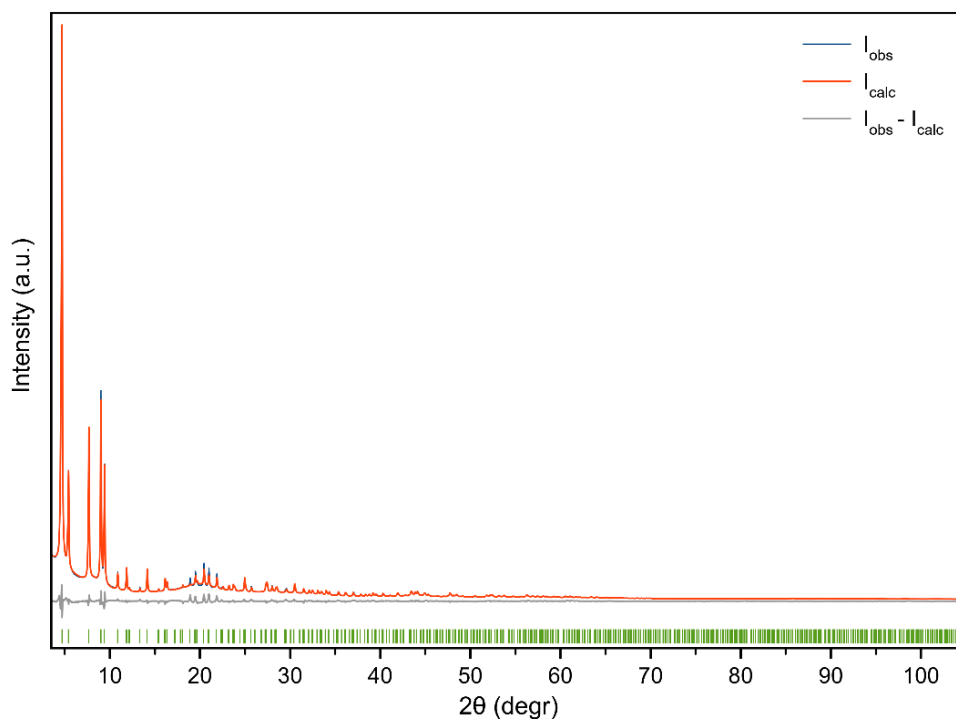


Figure S30. Experimental (blue line), calculated (red line), difference plot [(I_{obs}-I_{calc})] (black line, bottom panel) and Bragg positions (green ticks) for the Rietveld refinement of experimental diffraction data of UiO-68-PZDC(C₆₀) hexane exchanged collected at room temperature.

S5.4. Complementary experiments with MTV-UiO-68-TZDC_{44%}

Synthesis of UiO-68-TZDC_{44%}

20 mg of UiO-68-TZDC_{44%} (prepared according to our reported protocol¹) (0.0077 mmol, 1 equiv) were immersed in a solution of 6 equivalents of C₆₀ (0.0462 mmol) in 15 mL of toluene. The resultant mixture was stirring in a shaker at 40 °C during 72 hours in a 25 mL pyrex bottle. After this time, the brown crystals were washed by soxhlet extraction with toluene overnight. Then, UiO-68-TZDC_{44%}(C₆₀) crystals were kept in hexane for further analysis.

Elemental and Thermogravimetric Analysis

As in the previous case, the same was activated in the vacuum oven at 120°C overnight before the analysis. Based on EA and TGA results, we proposed a molecular formula which involved a complete functionalization. $[\text{Zr}_6\text{O}_4(\text{OH})_4(\text{C}_{76}\text{H}_8\text{N}_2\text{O}_4)_{2.64}(\text{C}_{20}\text{H}_{12}\text{O}_4)_{3.36}]$ calc. C (95.8), H (2.0), N (2.20); found: C (94.5), H (2.7) and N (2.8). This affirmation was supported by TGA results: ZrO₂ calculated = 19.0 %; ZrO₂ experimental = 19.3 %.

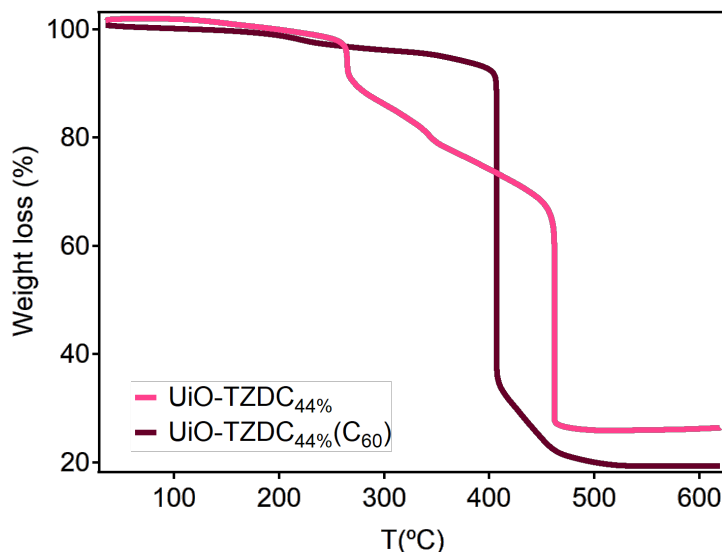
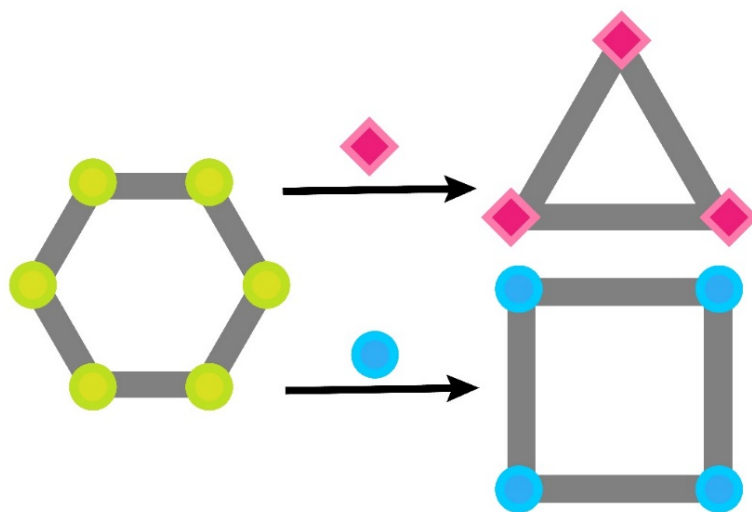


Figure S31. Thermal decomposition profile of MTV-UiO-68-TZDC_{44%} and UiO-68-TZDC_{44%}(C₆₀) frameworks.

References

1. Lerma-Berlanga, B.; Ganivet, C. R.; Almora-Barrios, N.; Tatay S.; Peng, Y.; Albero, J.; Fabelo, O.; González-Platas, J.; García, H.; Padial, N. M.; Martí-Gastaldo C.; *J Am Chem Soc.* **2021**, 143, 1798-1806.
2. Kresse, G.; Furthmüller, J. *Comput. Mater. Sci.* **1996**, 6, 15-50.
3. Kresse, G.; Furthmüller, J. *Phys. Rev. B: Condens. Matter Mater. Phys.* **1996**, 54, 11169-11186.
4. Grimme, S.; Antony, J.; Ehrlich, S.; Krieg, H. *J. Chem. Phys.* **2010**, 132 (15), 154104.
5. Bucko, T.; Hafner, J.; Lebegue, S.; Angyan, J. G. *J. Phys. Chem. A* **2010**, 114 (43), 11814-11824.
6. Perdew, J. P.; Burke, K.; Ernzerhof, M. *Phys. Rev. Lett.* **1996**, 77, 3865-3868.
7. Lejaeghere, K.; Bihlmayer, G.; Björkman, T.; Blaha, P.; Blügel, S.; *Science* **2016**, 351, 1415.
8. Heyd, J.; Scuseria, G. E.; Ernzerhof, M.; *J. Chem. Phys.* **2003**, 118, 8207-8215.
- 9.. Krukau, A. V.; Vydrov, O. A.; Izmaylov A. F.; Scuseria, G. E.; *J. Chem. Phys.* **2006**, 125, 224106.
10. Butler, K. T.; Hendon, C. H.; Walsh, A.; *J. Am. Chem. Soc.* **2014**, 136, 2703-2706.
11. Butler, K. T.; Walsh, A.; Frost, J. M.; *MacroDensity*, **2017**.
12. Martin, R. L.; Smit B.; Haranczyk, M.; *J Chem Inf Model* **2011**, 52, 308-318
13. Meunier, M.; *Mol. Simulat.* **2008**, 34, 887-888.
14. Tycko, R.; Haddon, R. C.; Dabbagh, G.; Glarum, S. H.; Douglass, D. C.; Mujsce, A. M.; *J. Phys. Chem.* **1991**, 95, 2, 518-520.
15. Huang, T.; Jin, B.; Fang Peng, R.; Di Chen, C.; Zong Zheng, R.; He, Y.; Jin Chu, S.; *Polymers* **2015**, 7(5), 896-908.
16. Yasujiro, M; Mitsuharu, S.; Yves, R.; Koichi, K.; *Bull. Chem. Soc. Jpn.* **2003**, 76, 1669–1672.
17. Le Bail, A.; Duroy, H.; Fourquet, J.L.; *Materials Research Bulletin* 23, **1988**, 447-452.
18. TOPAS-R v.3, Karlsruhe, Germany, **2005**.
19. Coelho, A.; *J. Appl. Crystallogr.* **2000**, 33, 899–908.
20. Cheary, W.; Coelho, A. A.; *J. Appl. Crystallogr.* **1998**, 31, 851.

Chapter 5:
***Metal-Induced Dynamic
Topological Transformations in
Heterometallic
Ti-MOFs***



1. Motivation

The rapid increase in the number of reported MOF structures has broadened their applicability in different fields such as gas storage,^{1,2} separation,³⁻⁵ or catalysis.^{6,7} It is precisely this feasibility that has accentuated their limitations, requiring enhanced thermal, mechanical or hydrolytic stabilities⁸ and increasing levels of complexity. The chemistry of the secondary building units (SBUs) can be used to improve the thermodynamic stability and tune the chemical reactivity of MOFs. For instance, inorganic clusters based on tetravalent metals such as Ti(IV), Zr(IV), and Hf(IV) are less prone to hydrolysis due to strong M-O bonds. Among these metals, the intrinsic properties of titanium make Ti-MOFs even more appealing because high stability might be combined with a tailorable electronic structure, photoactivity, or chemical reactivity. The synthesis of predesigned Ti-MOFs from targeted SBUs remains very challenging due to the high reactivity of Ti salts, which generally lead to ill-defined amorphous phases under solvothermal conditions. Therefore, the number of reported titanium frameworks is considerably low when is compared to Zr-MOFs. Given that scenario, it is not surprising that there are no well-established routes to introduce heterogeneity into mixed-metal titanium frameworks. The success of one-step synthesis is based on the use of metal ions with similar charges and ionic radii. Whereas incorporation of other metals into Ti-MOFs by post-synthetic exchange is hindered by high stable Ti-O coordination bonds which results in grafting to the SBU, incomplete metal replacement⁹ or undesired formation of titanium oxide coatings.¹⁰

In this regard, transmetalation reactions have been exclusively focused in homometallic MOFs for either labile nodes (e. g. $[\text{Zn}_4\text{O}(\text{CO}_2)_6]$ in MOF-5¹¹) or robust SBUs (e. g. $[\text{Zr}_6\text{O}_4(\text{OH})_4(\text{CO}_2)_{12}]$ in UiO-MOFs⁹) that compromise the stability of the resulting material or limit the metal exchange rate, respectively. Thus, we propose the use of MUV-10(Ca),¹² a heterometallic Ti-MOF, as reagent in post synthetic transmetalation reactions. That MOF presents tetranuclear clusters $[\text{Ti}_2\text{Ca}_2(\text{O})_2(\text{H}_2\text{O})_4(\text{CO}_2)_8]$ where combine soft (Ca^{2+}) and hard (Ti^{4+}) metal sites, so MUV-10 permits the controlled metal exchange in soft positions. Moreover, post-synthetic methods are perfectly compatible with MUV-10 due to its chemical and thermal robustness, which allow us to carry out reactions on it without altering its structural integrity and crystallinity.

2. Summary of the key results

The findings of this chapter were published in “M. Padial, N;[†] Lerma-Berlanga B.;[†] Almora-Barrios N.; Castells-Gil J.; da Silva I.; de la Mata M.; I. Molina S.; Hernández-Saz J.; Platero-Prats A. E.; Tatay S.; and Martí-Gastaldo C.; “*Heterometallic titanium-organic frameworks by metal-induced dynamic topological transformations*”. *J. Am. Chem. Soc.* **2020**, *142* (14), 6638-6648”. In that publication we introduced a pioneering methodology for the synthesis of heterometallic titanium frameworks by metal-exchange reaction of MOF crystals at mild

temperatures without altering the chemical stability of the resultant framework. Post synthetic transmetallation in MUV-10 modifies the points of extension of the SBU and thus the resulting framework topology. The different transformation stages were carefully studied at different times for one month to understand the origin of the dynamic topological transformation phenomena. That experimental analysis was complemented by the computational studies which also evaluated the effect of the metal in directing the transformation.

Initially, Mn(II) ions were selected as initial test to evaluate the ability of Ti_2Ca_2 cluster to undergo transmetalation due to Mn(II) was the only divalent first-row transition metal cation for which MUV-10(Mn)¹² could be prepared by direct synthesis. For that, MUV-10(Ca) crystals were immersed in a methanolic solution of $Mn(NO_3)_2$ for 10 and 30 days prior to analysis. The SEM-EDX analysis revealed a homogeneous Ca replacement with a ratio far from complete substitution. Further analysis by SEM, XRPD and N_2 adsorption confirmed the retention of the original structure and hydrolytic stability. In order to study the compatibility of MUV-10 cluster with the incorporation of other transition-metals ions, same experiments were carried out using Co(II) methanolic solutions. In that case, a pink solid was collected after 10 days. In contrast to the previous case, SEM-EDX measurements showed practically a complete Ca exchange for Ti:Co ratios close to 1:2. In addition, microscopic images suggested a change in morphology associated with the transformation. The reaction with cobalt induced the formation of micrometer-sized crystals with an octahedral morphology that grew at expense of the outer surface of MUV-10(Ca) crystals (*Figure 5.1. a*), suggesting a crystal-to-crystal transformation without redissolution. PXRD Rietveld refinement of the newly phase confirmed a topological change for the formation of a heterometallic Ti-MOF isostructural with MIL-100 which presented $[TiCo_2(\mu_3-O)(CO_2)_6(H_2O)_3]$ trimers. We referred to that new material as MUV-101(Co). The metal exchange generated a new 6-c SBU. That led to the formation of a new topology compatible with the structural information encoded in the newly formed metal cluster and the 3-c organic linker common on both frameworks. To study that phenomenon in detail, crystals were isolated for different soaking times (from 1 to 30 days) and the transformation at different stages was analysed confirming kinetic control over the topological transformation process. At early stages, both phases coexisted and progressively MUV-101(Co) grew directed by MUV-10 crystals which acted as scaffold template. The progressive changes, as a function of exchange time, were evidenced by PXRD, TGA and N_2 adsorption. The 30-day samples showed properties comparable to those of MIL-100 (*Figure 5.1. b-e*). X-ray absorption spectroscopy (XAS) discarded phase segregation as confirmed by the presence of heterobimetallic $TiCo_2$ clusters and confirmed the expected coordination geometry for trimeric clusters in the structure of MIL-100. (*Figure 5.1. f, g*). XAS data were collected in ALBA and SOLEIL synchrotrons and were analysed by Ana E. Platero Prats and Sergio Tatay.

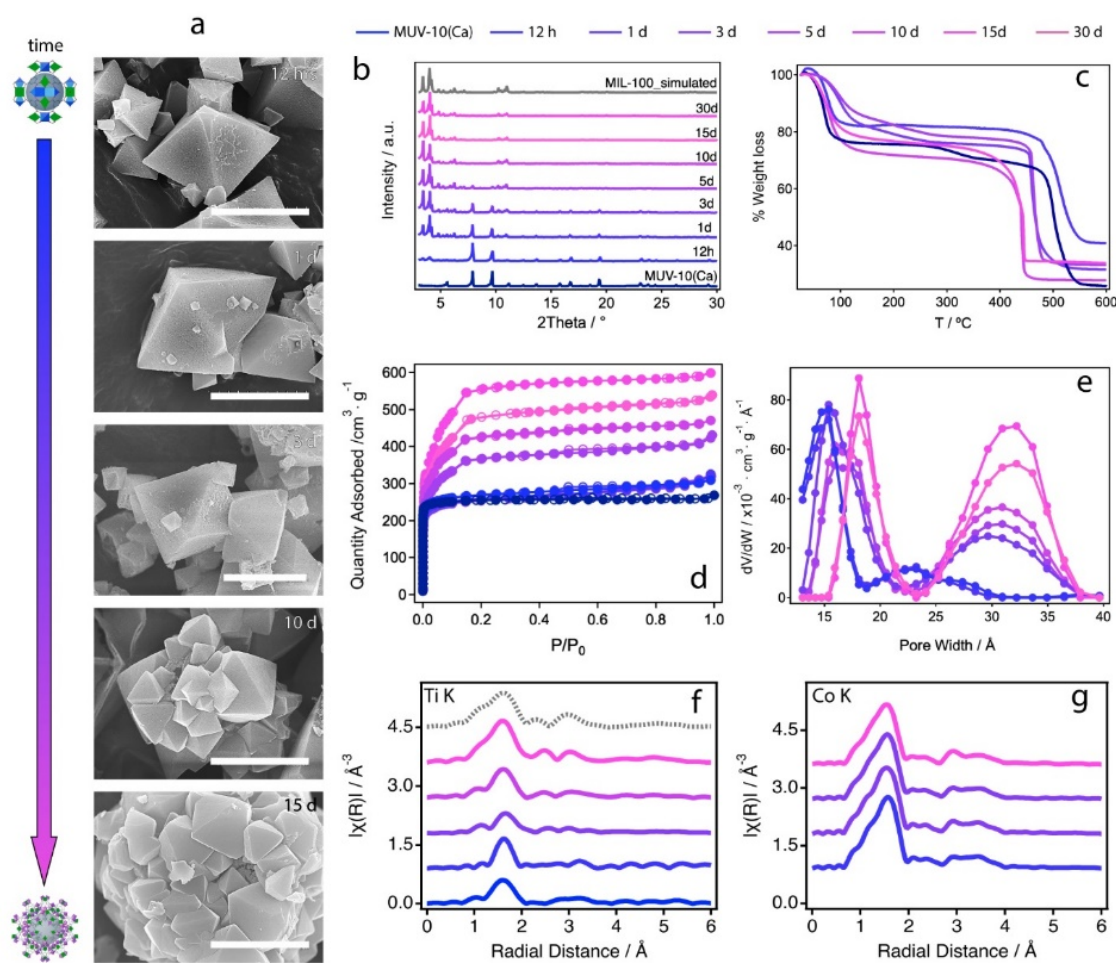


Figure 5.1. Dynamic topological transformation of MUV-10(Ca) to MUV-101(Co) with time: a) SEM images showing the progressive transformation of the crystals (scale bars 3 μm). Analysis of the transformation at different reaction times: b) PXRDs showing the transformation of MUV-10(Ca) into MUV-101(Co); c) change in the thermal stability of materials as result of the dilution of Ti-O bonds in TiCo_2 in comparison to Ti_2Ca_2 SBUs; d) N_2 isotherms at 77 K showing the progressive increase in surface area; e) pore size distribution (PSD) showing the evolution in pore size until the formation of a mesoporous framework; f, g) EXAFS Ti and Co K-edge spectra of MUV-101(Co) at different stages of the transformation. The spectrum of MIL-100(Ti) was used for comparison and is shown as a dashed grey line.

Computational studies were essential to rationalize the origin of that transformation. The surface terminations in MUV-10 crystals and thermodynamics of the SBU transformation were analysed by Neyvis Almora-Barrios combining molecular mechanics simulations based on interatomic potentials and quantum-mechanical methods based on DFT. Computational results suggested that metal exchange reactions in MUV-10 were dominated by the terminations of the dominant (111) surfaces where exposed metal (ligand free) and ligand-capped terminations required for topological transformation coexist (Figure 5.2. a, b, c). For thermodynamic calculations we proposed two reactions, one being the formation of heterometallic tetramer (Ti_2M_2) present in MUV-10, and other being the formation of heterometallic trimers (TiM_2) reminiscent of MIL-100. We calculated the enthalpy

energies for the process of cation exchange in methanol solution for different common divalent first-row transition metal ions ($M^{2+} = \text{Mn, Fe, Co, Ni, Cu, and Zn}$). The formation of an isostructural cluster was only thermodynamically favourable for Mn, probably due to higher preference of Ca and Mn for heptacoordinated capped-trigonal-prismatic (CTP) geometry (Figure 5.2. d). Calculations for the rest of the metals showed a thermodynamically favourable TiM_2 SBU formation (Figure 5.2. e). While Fe, Co, and Ni metals displayed similar enthalpies for trimer formation; the small stabilization for the formation of TiZn_2 suggested that that material might be produced under kinetic control. Finally, Cu was the only metal for which the formation of the heterometallic trimer was not energetically favourable. The instability of Ti_2Cu_2 SBU proposed the formation of an alternative SBU compatible with the 3-c connected btc linker.

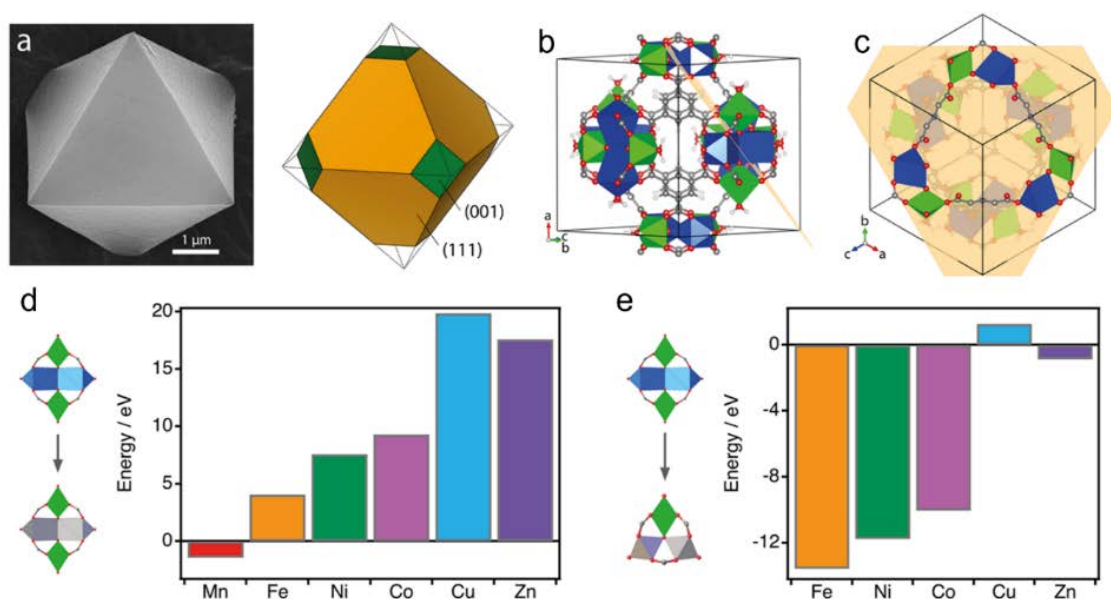


Figure 5.2. a) Experimental and theoretical morphology of a crystal of MUV-10(Ca). b) Perspective showing the cleavage of the cubic cell and the resulting c) $\{111\}$ surface termination combining metal and ligand free reactive sites. d) Energy balance for the exchange of Ca^{2+} sites in Ti_2Ca_2 SBUs with $M^{2+} = \text{Mn, Fe, Co, Ni, Cu, and Zn}$. e) Enthalpy changes for the formation of TiM_2 from Ti_2Ca_2 SBUs.

The value of those theoretical predictions was proven by additional experiments. For that, MUV-10(Ca) crystals were soaked in concentrated solutions of Fe(II), Ni(II), Zn(II), and Cu(II) nitrate salts using the same conditions described above. The analysis of resultant solids after 10 and 30 days showed that Fe, Ni, and Zn exhibited a similar behaviour to Co. SEM-EDX and PXRD measurements confirmed the gradual exchange of Ca^{2+} , which becomes complete for MUV-101(Zn) after 10 days and after 30 days for MUV-101(Ni). MUV-101(Fe)-30d showed incomplete transformation possibly since the difficulties in stabilising Fe^{2+} in solution for the long reaction times. According to enthalpy values, MUV-101(Zn) seemed to be a kinetic product which could only be prepared by diffusion-controlled metal exchange. For its part,

the Cu transformation was tracked in more detail. To that end, solids at different reaction times between 1 hour and 5 days were analysed. As was observed for Co transmetallation, the process involved morphological changes in the crystal seeds. SEM-EDX measurements confirmed the formation of intertwined cubes at the faces of MUV-10(Ca) crystals (*Figure 5.3. a*) and a Ti:Cu ratio of close to 1:4 for 5 d sample. PXRD analysis supported the formation of new phase isostructural with HKUST, which referred to as MUV-102(Cu). The progressive changes as a function of exchange time were followed by PXRD, TGA and N₂ adsorption (*Figure 5.3. b, e*) demonstrating that the transformation in MUV-102(Cu) was much faster compared to MUV-101(Co); just one day was enough to achieve the full transformation. The final metal composition of MUV-102(Cu) implied the formation of one heterometallic TiCu cluster counterbalanced by the coordination of O²⁻ capping linkers, [TiCu(CO₂)₂(O)(H₂O)], per 2.5 homometallic Cu₂ units, [Cu₂(CO₂)₂(H₂O)₂]. The presence of heterometallic SBUs was corroborated by XAS (*Figure 5.3. c, d*) and EPR measurements. MUV-102(Cu) together with MUV-101(Zn) confirmed the ability of MUV-10 of metal-induced topological transformation to enable the formation of MOFs not accessible by direct synthesis.

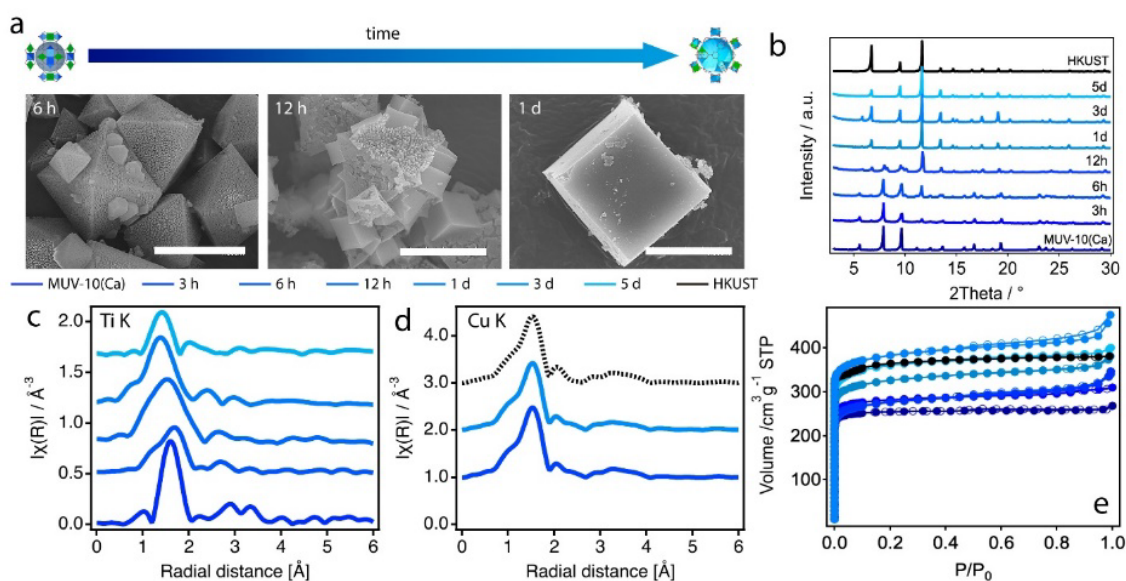


Figure 5.3. Dynamic topological transformation of MUV-10(Ca) to MUV-102(Cu). a) SEM images showing the progress of the transformation with time for the formation of cube-like crystals of MUV-102(Cu). Scale bars: 3 μm . Analysis of the MOF transformation at different reaction times: b) PXRDs showing the transformation of MUV-10(Ca) into MUV-102(Cu) with time and comparison with commercial HKUST (black); c, d) EXAFS Ti and Cu-K edges spectra of MUV-102(Cu) at different stages of transformation. The spectrum of homometallic HKUST was used for comparison and is showed as a dashed black line; e) N₂ isotherms at 77 K showing the progressive increase in surface area and pore volume with time until matching that of HKUST (black line).

3. References

- (1) Mason, J. A.; Oktawiec, J.; Taylor, M. K.; Hudson, M. R.; Rodriguez, J.; Bachman, J. E.; Gonzalez, M. I.; Cervellino, A.; Guagliardi, A.; Brown, C. M.; Llewellyn, P. L.; Masciocchi, N.; Long, J. R. Methane Storage in Flexible Metal-Organic Frameworks with Intrinsic Thermal Management. *Nature* **2015**, *527* (7578), 357–361.
- (2) Tian, T.; Zeng, Z.; Vulpe, D.; Casco, M. E.; Divitini, G.; Midgley, P. A.; Silvestre-Albero, J.; Tan, J. C.; Moghadam, P. Z.; Fairen-Jimenez, D. A Sol-Gel Monolithic Metal-Organic Framework with Enhanced Methane Uptake. *Nat. Mater.* **2018**, *17* (2), 174–179.
- (3) Li, L.; Lin, R. B.; Krishna, R.; Li, H.; Xiang, S.; Wu, H.; Li, J.; Zhou, W.; Chen, B. Ethane/Ethylene Separation in a Metal-Organic Framework with Iron-Peroxo Sites. *Science* **2018**, *362* (6413), 443–446.
- (4) Gu, C.; Hosono, N.; Zheng, J. J.; Sato, Y.; Kusaka, S.; Sakaki, S.; Kitagawa, S. Nanoporous Materials: Design and Control of Gas Diffusion Process in a Nanoporous Soft Crystal. *Science* **2019**, *363* (6425), 387–391.
- (5) Cadiau, A.; Belmabkhout, Y.; Adil, K.; Bhatt, P. M.; Pillai, R. S.; Shkurenko, A.; Martineau-Corcus, C.; Maurin, G.; Eddaoudi, M. Molecular Sorption: Hydrolytically Stable Fluorinated Metal-Organic Frameworks for Energy-Efficient Dehydration. *Science* **2017**, *356* (6339), 731–735.
- (6) Diercks, C. S.; Liu, Y.; Cordova, K. E.; Yaghi, O. M. The Role of Reticular Chemistry in the Design of CO₂ Reduction Catalysts. *Nat. Mater.* **2018**, *17* (4), 301–307.
- (7) Zhao, M.; Yuan, K.; Wang, Y.; Li, G.; Guo, J.; Gu, L.; Hu, W.; Zhao, H.; Tang, Z. Metal-Organic Frameworks as Selectivity Regulators for Hydrogenation Reactions. *Nature* **2016**, *539* (7627), 76–80.
- (8) Howarth, A. J.; Liu, Y.; Li, P.; Li, Z.; Wang, T. C.; Hupp, J. T.; Farha, O. K. Chemical, Thermal and Mechanical Stabilities of Metal-Organic Frameworks. *Nat. Rev. Mater.* **2016**, *1* (15018), 1–16.
- (9) Santaclara, J. G.; Olivos-suarez, A. I.; Gonzalez-nelson, A.; Osadchii, D.; Nasalevich, M. A.; Veen, M. A. Van Der; Kapteijn, F.; Sheveleva, A. M.; Veber, S. L.; Fedin, M. V.; Murray, A. T.; Hendon, C. H.; Walsh, A.; Gascon, J. Revisiting the Incorporation of Ti(IV) in UiO-Type Metal – Organic Frameworks: Metal Exchange versus Grafting and Their Implications on Photocatalysis. *Chem. Mater.* **2017**, *29*, (21), 8963–8967.
- (10) Denny, M. S.; Parent, L. R.; Patterson, J. P.; Meena, S. K.; Pham, H.; Abellan, P.; Ramasse, Q. M.; Paesani, F.; Gianneschi, N. C.; Cohen, S. M. Transmission Electron Microscopy Reveals Deposition of Metal Oxide Coatings onto Metal-Organic Frameworks. *J. Am. Chem. Soc.* **2018**, *140* (4), 1348–1357.
- (11) Brozek, C. K.; Dincă, M. Thermodynamic Parameters of Cation Exchange in MOF-5 and MFU-4l. *Chem. Commun.* **2015**, *51* (59), 11780–11782.
- (12) Castells-Gil, J.; Padiál, N. M.; Almora-Barrios, N.; Albero, J.; Ruiz-Salvador, A. R.; González-Platas, J.; García, H.; Martí-Gastaldo, C. Chemical Engineering of Photoactivity in Heterometallic Titanium-Organic Frameworks by Metal Doping. *Angew. Chem.* **2018**, *130* (28), 8589–8593.

Publication 4:

***Heterometallic Titanium-Organic
Frameworks by Metal-Induced
Dynamic Topological
Transformations***

J. Am. Chem. Soc., **2020**, *142* (14), 6638-
6648

Heterometallic Titanium–Organic Frameworks by Metal-Induced Dynamic Topological Transformations

Natalia M. Padial,^{*,} Belén Lerma-Berlanga,[•] Neyvis Almora-Barrios, Javier Castells-Gil, Iván da Silva, María de la Mata, Sergio I. Molina, Jesús Hernández-Saz, Ana E. Platero-Prats, Sergio Tatay, and Carlos Martí-Gastaldo^{*}



Cite This: *J. Am. Chem. Soc.* 2020, 142, 6638–6648



Read Online

ACCESS |



Metrics & More

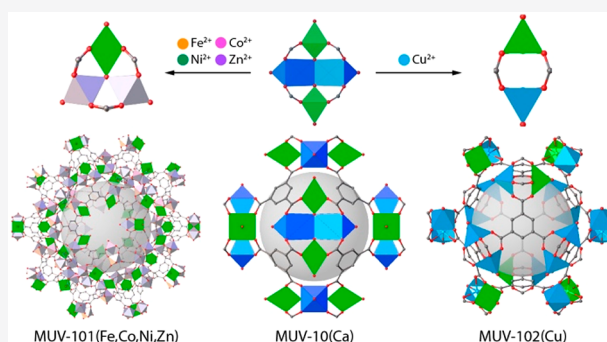


Article Recommendations



Supporting Information

ABSTRACT: Reticular chemistry has boosted the design of thousands of metal and covalent organic frameworks for unlimited chemical compositions, structures, and sizable porosities. The ability to generate porous materials at will on the basis of geometrical design concepts is responsible for the rapid growth of the field and the increasing number of applications derived. Despite their promising features, the synthesis of targeted homo- and heterometallic titanium–organic frameworks amenable to these principles is relentlessly limited by the high reactivity of this metal in solution that impedes the controlled assembly of titanium molecular clusters. We describe an unprecedented methodology for the synthesis of heterometallic titanium frameworks by metal-exchange reactions of MOF crystals at temperatures below those conventionally used in solvothermal synthesis. The combination of hard (titanium) and soft (calcium) metals in the heterometallic nodes of MUV-10(Ca) enables controlled metal exchange in soft positions for the generation of heterometallic secondary building units (SBUs) with variable nuclearity, controlled by the metal incorporated. The structural information encoded in the newly formed SBUs drives an MOF-to-MOF conversion into bipartite nets compatible with the connectivity of the organic linker originally present in the crystal. Our simulations show that this transformation has a thermodynamic origin and is controlled by the terminations of the (111) surfaces of the crystal. The reaction of MUV-10(Ca) with first-row transition metals permits the production of crystals of MUV-101(Fe,Co,Ni,Zn) and MUV-102(Cu), heterometallic titanium MOFs isostructural with archetypal solids such as MIL-100 and HKUST. In comparison to de novo synthesis, this metal-induced topological transformation provides control over the formation of hierarchical micro-/mesopore structures at different reaction times and enables the formation of heterometallic titanium MOFs not accessible under solvothermal conditions at high temperature, thus opening the door for the isolation of additional titanium heterometallic phases not linked exclusively to trimesate linkers.



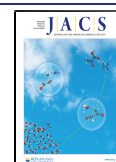
INTRODUCTION

Metal–organic frameworks (MOFs) are crystalline extended structures assembled by the linkage of inorganic polynuclear clusters, termed secondary building units (SBUs), and organic linkers. For the last 15 years, the principles of reticular chemistry have guided the design of thousands of MOFs by rationalizing the combination of SBUs and organic linkers with variable extension points into predetermined topologies.¹ Reticular chemistry provides control over the design of materials at a molecular level for a rich landscape of chemical compositions, structures, and sizable porosities for direct application in gas storage,^{2,3} separation,^{4–6} or catalysis.^{7,8} The rapid growth of the MOF field has built upon two main design strategies. The first, the isorecticular approach, is based on the reticulation of sizable organic linkers of the same geometry and connectivity. It makes it possible to control the metrics and functionality of a specific framework topology that is fixed by

the structural information encoded in the inorganic SBU.⁹ The second, the SBU approach, is more general in conception, as it permits targeting multiple MOF topologies also amenable to isorecticular functionalization, by controlling the geometry and connection points of the two building units in the framework.^{10,11} The successful translation of these geometric design principles to the synthesis of binary MOFs relies on finding the experimental conditions that reproduce the structural information encoded in the two chemical building units targeted. This is not a problem for the organic linker, which

Received: January 6, 2020

Published: March 14, 2020



will retain its geometry and connectivity in solution, but predicting the formation of persistent metal–oxo clusters under crystal growth formation conditions is not straightforward. The chemistry of SBUs intrinsic to archetypical families of MOFs such as $[\text{Cu}_2(\text{H}_2\text{O})_2(\text{RCO}_2)_2]$ (HKUST),¹² $[\text{Cr}_3\text{O}(\text{H}_2\text{O})_3(\text{RCO}_2)_6]$ (MIL-100, MIL-101),^{13,14} $[\text{Zn}_4\text{O}(\text{RCO}_2)_6]$ (MOF-5),⁹ and $[\text{Zr}_6\text{O}_4(\text{OH})_4(\text{RCO}_2)_{12}]$ (UiO)¹⁵ is well understood and central to the thousands of works related to these materials published in the last years.

With the advance of the field, the application of MOFs has stressed their limitations, calling for enhanced thermal, mechanical, or hydrolytical stabilities and increasing levels of complexity.^{16,17} The chemistry of the SBU can be used to improve the thermodynamic stability and tune the chemical reactivity of MOFs. For instance, inorganic clusters based on trivalent metals such as Ti(IV), Zr(IV), and Hf(IV) are less prone to hydrolysis due to strong M–O bonds. Among these metals, titanium is less toxic, more abundant, and redox active. Still, the synthesis of predesigned titanium frameworks from targeted SBUs remains very challenging due to the high reactivity of Ti salts, which generally lead to ill-defined amorphous phases under solvothermal conditions. On the other hand, complexity at the SBU can be achieved by the combination of two or more metals in heterometallic clusters for mixed-metal MOFs that can outperform their monometallic counterparts in different applications such as gas storage, separation, and heterogeneous catalysis.^{18,19} The intrinsic properties of Ti-MOFs make this possibility even more appealing, as high stability might be combined with a tailorable electronic structure, photoactivity, or chemical reactivity. However, the limitations of the chemistry of titanium are even more restrictive in this case and there is no straightforward route for their synthesis. The success of one-step synthesis relies on the use of metal ions with similar charges and ionic radii. The high polarizing power of Ti^{4+} prevents a direct reaction with other metals that would likely result in poor control over their distribution in the final material for the formation of segregated phases. In turn, incorporation of other metals into Ti-MOFs by postsynthetic exchange would be inadequate due to the high stability of Ti–O coordination bonds, whereas the incorporation of Ti^{4+} in preformed materials would not allow for complete metal replacement and lacks control over the positioning of titanium atoms in the structure,²⁰ which can result in a spurious deposition of metal oxide coatings.²¹

We report an unprecedented methodology for the synthesis of heterometallic titanium frameworks amenable to the principles of reticular chemistry. Instead of relying on the serendipitous discovery of mixed-metal clusters by trial and error, we use MOF crystals to direct the formation of SBUs with variable connection points by transmetalation reactions at 65 °C. The combination of hard and soft metals in the heterometallic nodes of MUV-10 (MUV, Materials of Universidad de Valencia) enables controlled metal exchange in soft positions while the structural integrity is retained. The offset in the coordination geometry upon metal replacement generates a thermodynamically metastable state that evolves into the formation of SBUs of decreased nuclearity and dependent on the metal incorporated. The structural information encoded in the newly formed SBUs drives the formation of bipartite nets compatible with the connectivity of the organic linker originally present in the crystal. This metal-induced topological transformation is a dynamic phenomenon

and can be controlled with time until complete transformation of the material.

RESULTS AND DISCUSSION

Metal-Exchange Reactions in Heterometallic SBUs Combining Labile and Robust Coordination Sites. As commented above, the *de novo* synthesis of heterometallic MOFs is restricted to metals with similar reactivity in solution that allow for a concomitant reaction and avoid the formation of homometallic frameworks. Postsynthetic metal exchange is a more versatile route that enables the incorporation of a broader range of metals for heterometallic compositions not accessible by direct synthesis. Metal exchange reactions typically involve soaking of the MOF in concentrated solutions of the metal to be incorporated. The degree of exchange (often incomplete) is kinetically and thermodynamically controlled by the stability constants of the substituting cations and the strength of the M–O bond in the cluster. This is why precedents of MOF transmetalation are mostly focused on labile SBUs more prone to hydrolysis and metal replacement.^{22,23} In contrast, robust MOFs with SBUs featuring strong $\text{M}^{\text{IV}}\text{–O}$ bonds, such as $[\text{Zr}_6\text{O}_4(\text{OH})_4(\text{RCO}_2)_{12}]$, are less likely to undergo metal exchange at the cluster and can suffer from uncontrolled grafting at defective positions²⁰ or induce the undesired formation of an oxide coating.²¹ Thus far, transmetalation reactions have been exclusively focused in homometallic MOFs for either labile or robust SBUs that compromise the stability of the resulting material or limit the metal exchange rate, respectively.

We hypothesized that these limitations might be circumvented by using heterometallic SBUs. The combination of soft (M^{2+}) and hard (M^{4+}) metals at different coordination sites in the cluster might translate into quantitative metal replacement without altering the structure or jeopardizing the chemical stability of the framework.

We decided to explore this concept for the heterometallic titanium framework MUV-10(Ca).²⁴ This microporous solid can be synthesized in high yields from the direct reaction of a calcium salt with different titanium sources. It displays a three-dimensional *the* topology built from the linking of eight-connected $[\text{Ti}_2\text{Ca}_2(\text{O})_2(\text{H}_2\text{O})_4(\text{RCO}_2)_8]$ heterometallic SBUs with *btc* linkers (*btc* = benzene-1,3,5-tricarboxylate anion). In comparison to the labile and robust coordination sites in Zn_4 and Zr_6 clusters, Ti_2Ca_2 combines hard Ti^{4+} ions in octahedral sites and capped-trigonal-prismatic soft Ca^{2+} centers more prone to metal exchange (Figure 1). Our recent work

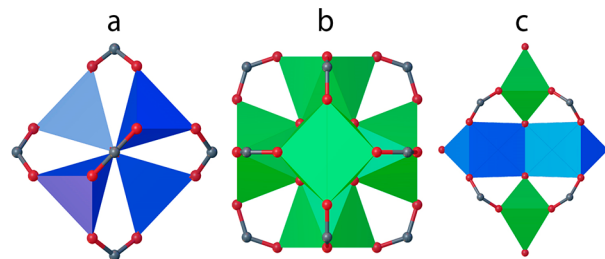


Figure 1. Secondary building units used in transmetalation reactions. Structures of the metal–oxo clusters: (a) $[\text{Zn}_4\text{O}(\text{RCO}_2)_6]$, Zn_4 ; (b) $[\text{Zr}_6\text{O}_4(\text{OH})_4(\text{RCO}_2)_{12}]$, Zr_6 ; (c) $[\text{Ti}_2\text{Ca}_2(\text{O})_2(\text{H}_2\text{O})_4(\text{RCO}_2)_8]$, Ti_2Ca_2 (this work). Blue and green metal sites denote labile (Zn^{2+} , Ca^{2+}) and robust (Zr^{4+} , Ti^{4+}) metal exchange positions, respectively, red denotes O, and gray denotes C.

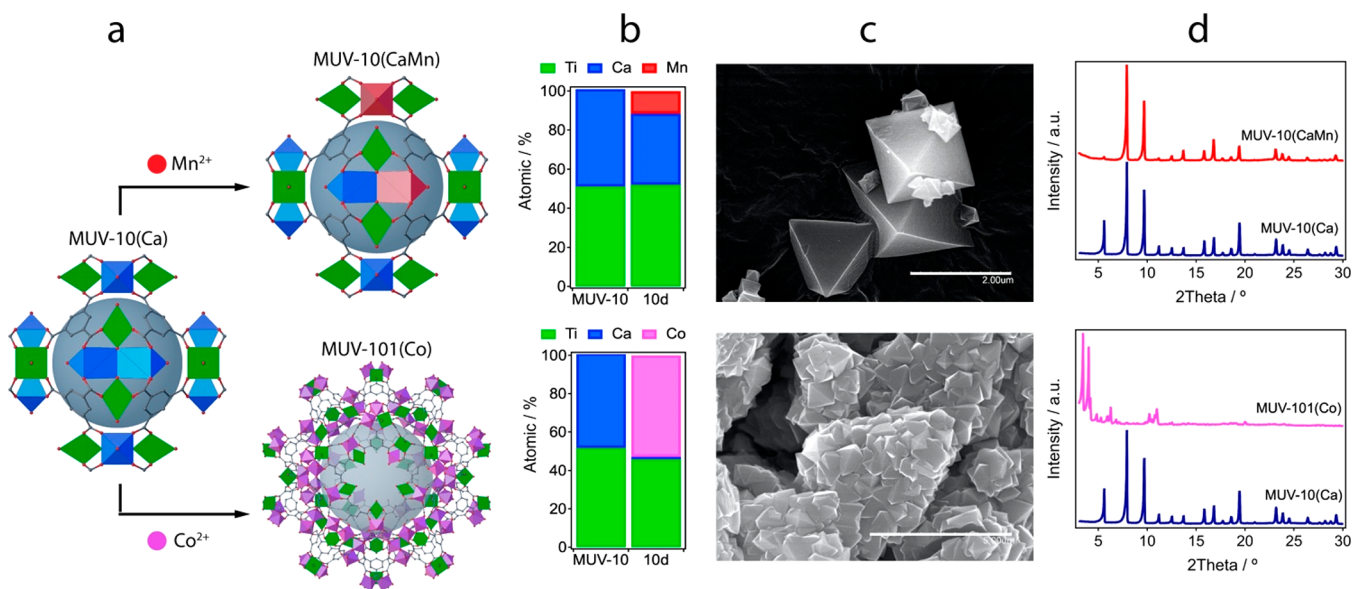


Figure 2. Metal exchange reactions with MUV-10(Ca) crystals: (a) reaction of MUV-10(Ca) in methanolic solutions of Mn^{2+} yields partial metal exchange with retention of the original structure, whereas the same reaction with Co^{2+} drives a topological transformation into MUV-101(Co); (b) experimental metal replacement after 10 days; (c) SEM images of the crystals; (d) PXRD after the experiment.

demonstrated the difficulties in producing other heterometallic solids by direct synthesis with divalent first-row transition-metal cations. In contrast to Fe(II), Co(II), Ni(II), Cu(II), and Zn(II), only MUV-10(Mn) could be prepared due to the preference of Mn ions toward a heptacoordinated capped-trigonal-prismatic (CTP) geometry.^{24,25} We decided to investigate if same solid could be prepared by transmetalation of the calcium phase. Crystals of MUV-10(Ca) were immersed in concentrated solutions of $\text{Mn}(\text{NO}_3)_2$ in MeOH (0.2 M) at 65 °C. The resulting MUV-10(CaMn) crystals were filtered and cleaned after 10 days and 30 days for further analyses. We evaluated the degree of metal exchange with X-ray energy dispersive spectroscopy (EDX; section S3.1 in the Supporting Information). The incorporation of Mn is concomitant with a decrease in Ca. Metal exchange is slightly more favorable at longer soaking times; Ca replacement increases from 11.6% (10 days) up to 13.0% after 30 days (Figure 2b, top). In comparison to the postsynthetic modification of Zn_4 clusters in MOF-5,²⁶ total exchange is far from complete, suggesting thermodynamic control over the transmetalation reaction. The metal distribution was also analyzed with EDX. Mapping throughout the crystals reveals a homogeneous distribution of both metals, ruling out metal clustering at the surface or the formation of segregated phases (section S3.2 in the Supporting Information). Scanning electron microscopy (SEM) confirms that the crystals retained the morphology and micrometer size of the starting material after metal exchange, suggesting a crystal-to-crystal reaction rather than recrystallization in the presence of the new metal (Figure 2c, top). Retention of the original structure was confirmed by powder X-ray diffraction (PXRD) Le Bail refinement of the samples at variable soaking times (Figure 2d (top) and section S3.3 in the Supporting Information). The absence of additional peaks discards the formation of an additional phase upon metal exchange. The changes in the relative intensities of the [100] reflection possibly originates from a preferential orientation of the crystals, as we avoided grinding to prevent amorphization. Crystals were activated by using the protocol reported for

MUV-10(Ca) to analyze the effect of metal exchange over the porosity of the solid (section S3.4 in the Supporting Information). The N_2 isotherm collected confirmed that MUV-10(CaMn) retained the original porosity with an insignificant effect on the BET surface area and the experimental pore diameter. Also important, PXRD data of the crystals after soaking in concentrated HCl and NaOH(aq) solutions confirm that transmetalation does not compromise the hydrolytic stability of the parent solid that originates from the presence of robust Ti–O nodes (section S3.5 in the Supporting Information).

In order to demonstrate if the cluster in MUV-10 might be compatible with the incorporation of other transition-metal ions to access chemical compositions not accessible by direct synthesis, we next attempted the same experiments in the presence of Co^{2+} . Soaking of MUV-10(Ca) in methanolic solutions of $\text{Co}(\text{NO}_3)_2 \cdot 6\text{H}_2\text{O}$ (0.2 M) at 65 °C resulted in the formation of a pink solid already after 10 days. In comparison to partial replacement for the Mn case, the EDX analysis revealed that after this time metal exchange became quantitative for the case of Co with only slight traces of unexchanged calcium, close to 0.1% (Figure 2b, bottom). Quantitative metathesis has been reported for labile $[\text{Cd}_4\text{O}]^{6+}$ units²² in MOF single crystals, but this drastic increase in substitution on moving from Mn^{2+} to Co^{2+} was unanticipated. To investigate its origin, we inspected the crystals with SEM after the reaction. In comparison to transmetalation with Mn, which does not influence the original morphology, reaction with cobalt induces the formation of a cluster of micrometer-sized crystals with an octahedral morphology that completely occupy the original space of the seeding MUV-10(Ca) crystal (Figure 2c, bottom). EDX mapping of the crystals is again consistent with the formation of a single phase with a homogeneous distribution of Ti and Co throughout the newly formed crystals and complete depletion of Ca. However, PXRD reveals the complete transformation of the original material into a new phase that displays high crystallinity (Figure 2d, bottom). Rather than metal exchange, in the

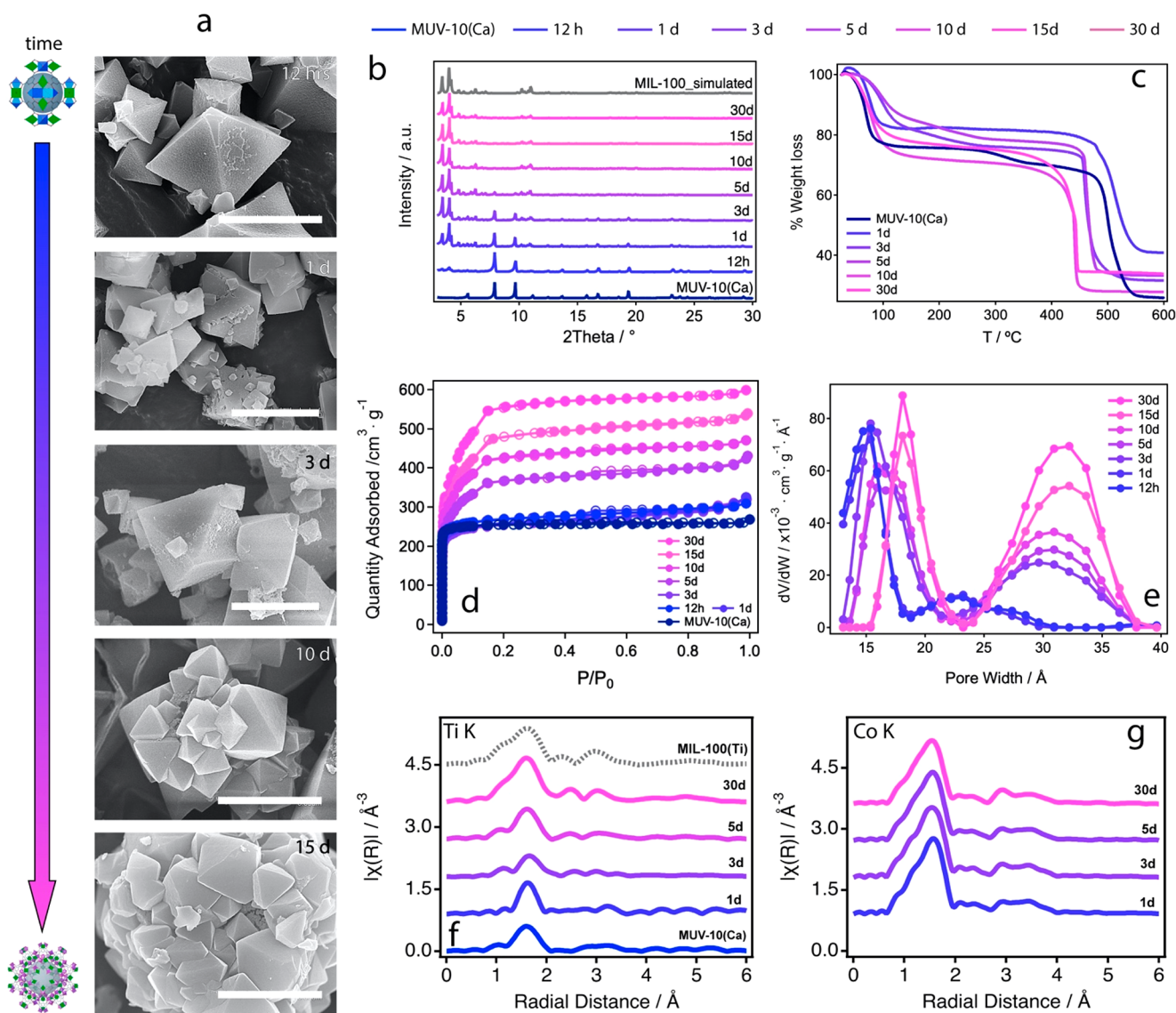


Figure 3. Dynamic topological transformation of MUV-10(Ca) to MUV-101(Co): (a) SEM images showing the progressive transformation of the crystals with time (scale bars 3 μm). Analysis of the transformation at different reaction times: (b) PXRDs showing the transformation of MUV-10(Ca) into MUV-101(Co) with time; (c) change in the chemical stability of the final material as result of the dilution of Ti–O bonds in TiCo_2 in comparison to Ti_2Ca_2 SBUs; (d) N_2 adsorption/desorption isotherms at 77 K showing the progressive increase in surface area with time; (e) pore size distribution (PSD) showing the evolution in pore size until the formation of a mesoporous framework; (f, g) EXAFS Ti and Co K-edge spectra of MUV-101(Co) at different stages of the transformation. The spectrum of MIL-100(Ti) was used for comparison and is shown as a dashed gray line. For a clearer analysis of the different stages of transformation see section S4 in the Supporting Information.

presence of Co^{2+} , MUV-10(Ca) seems to act as a templating scaffold that directs the growth of a new phase that we will refer to as MUV-101(Co). In fact, PXRD Rietveld refinement of this newly formed phase confirmed that transmetalation induces a topological change for the formation of a heterometallic titanium–organic framework isostructural with MIL-100 (zeotypic *mtn* topology; section S4.4 in the Supporting Information).¹³

Dynamic Topological Transformation of MUV-10 to MUV-101. We next investigated this phenomenon by isolating the crystals for different soaking times and analyzing the transformation at the different stages (section S4 in the Supporting Information). SEM images reveal the formation of a corrugated surface on the facets of MUV-10(Ca) crystals after 12 h of exposure to methanolic solutions of Co(II) (Figure 3a). We observe the formation of small crystallization

nuclei on the surface and edges of the crystal after 1 day, which evolve with time into micrometer-sized crystals with octahedral morphologies that can already be visualized after 3 days. Newly formed crystals seem to keep growing continuously at expense of the original MOF to produce a cluster of intertwined crystals after 15 days that keeps the original size and shape of the MUV-10(Ca) templating scaffold (Figure S55 in the Supporting Information). Overall, microscopic images suggest that both phases coexist and the formation of the MUV-101 phase proceeds by transformation of one crystal into the other rather than crystallization from redissolution of MUV-10 in the reaction medium. We cannot visualize the dissolution of the original crystals before the formation of the new crystals. Additional experiments with larger crystals show the particularities of the transformation more clearly (Figure S56 in the Supporting Information). This analysis was comple-

mented with EDX measurements as a function of the soaking time to account for the changes in chemical composition concomitant with the transformation of MUV-10 (section S4.2 in the Supporting Information). The data show a rapid incorporation of Co, which reaches a plateau at around 60 atom % after 15 days, parallel with the complete removal of calcium from the crystals. The relative titanium content decreases from 50 to 40 atom % until it stabilizes for a relative Ti:Co ratio close to 1:2. Single-point spectra of the chemical composition throughout the crystals are indicative of a homogeneous distribution of both metals in the expected ratio.

The study of the MUV-101 phase by single-crystal diffraction was not possible due to the intertwined nature of the crystals formed. Nevertheless, the structure was determined instead by refinement of high-resolution PXRD data collected by using synchrotron radiation (ALBA, BL04-MSPD) and using the structure reported for MIL-100(Ti) as a starting model (CCDC 1871195).²⁷ Rietveld refinement converged with excellent residual values ($R_{wp} = 3.95\%$, $R_{exp} = 1.77\%$) to a cubic $Fd\bar{3}m$ space group with the cell parameter $a = 73.5784(8)$ Å (section S4.4 in the Supporting Information). MUV-101(Co) is isostructural with the prototypical MIL-100 family. Accordingly, heterometallic 6-c $TiCo_2$ SBUs are connected to six 3-c btc linkers to produce a zeolitic framework with an *mnt* topology, which combines two types of mesoporous cages of 2.4 and 2.9 nm interconnected in three dimensions. However, in MIL-100 phases, the introduction of M^{3+} (Cr, Fe, Al)^{13,28,29} or M^{4+} (Ti)²⁷ metals into the homometallic SBU $[M_3(\mu_3-O)(X)(H_2O)_2(RCO_2)_6]$ is counterbalanced by the coordination of different capping linkers ($X = F^-, Cl^-, OH^-, O^{2-}$) to the axial position of the metal positions for a neutral structure. In MUV-101(Co), the combination of Co^{2+} and Ti^{4+} drives the formation of $[TiCo_2(\mu_3-O)(H_2O)_3(RCO_2)_6]$ clusters with possibly only water molecules acting as terminal ligands. The metallic ratio fixed by this formula agrees well with the experimental value determined by EDX. A phase transformation was also evaluated by PXRD of the crystals at increasing soaking times. Figure 3b shows that the [220] and [311] low- θ diffraction lines characteristic of the MUV-101 phase, isostructural with MIL-100, are already seen after only 12 h and become clearly visible after 1 day. From that point, MUV-10 and MUV-101 phases coexist up to 5 days of reaction, whereas the reflections [110] and [111] characteristic of MUV-10 are no longer visible. Rietveld refinements were used to calculate the relative phase percentages in these intermediate states. As shown in section S4.6 in the Supporting Information, the formation of MUV-101(Co) increases at the expense of MUV-10(Ca) for relative percentages of 3, 11, 65 and 98 atom % after 1, 3, 10, and 30 days, respectively.

The gradual conversion of the Ti_2Ca_2 cluster in MUV-10 into $TiCo_2$ in MUV-101(Co) is also correlated with changes in the thermal stability of the solid isolated at different reaction times. Thermogravimetric analyses (TGA; Figure 3c and section S4.7 in the Supporting Information) show a progressive decrease in the decomposition temperature upon incorporation of cobalt from 500 °C for MUV-10 down to a minimum of 440 °C in fully transformed MUV-101(Co) after 30 days. We argue that this is possibly due to the dilution of the relative percentage of robust Ti–O bonds in the metal-oxo clusters, which decreases from 45% in MUV-10(Ca) to 33% in MUV-101. Nonetheless, the thermal stability of MUV-101(Co) is significantly higher than that of other homometallic

phases such as Fe^{3+} and Cr^{3+} , which decompose between 300 and 350 °C.^{13,28} We next collected standard N_2 isotherms for all of the solids to investigate the effect of a phase transformation on their porosity (Figure 3d and section S4.8 in the Supporting Information). All solids display a type I isotherm with increasing gas uptakes for higher degrees of transformation. The reaction time gradually increases the multipoint BET surface area and pore volume values from 1054 $m^2 \cdot g^{-1}$ and 0.47 $cm^3 \cdot g^{-1}$ for MUV-101(Co)-12h, respectively, almost identical with those of the MUV-10(Ca) phase, to almost double these values for MUV-101(Co)-30d with 2043 $m^2 \cdot g^{-1}$ and 0.92 $cm^3 \cdot g^{-1}$. This value is consistent with the values reported for MIL-100 phases and confirms complete MOF-to-MOF conversion. The effect of this dynamic transformation on the porosity can be more easily visualized by looking into the pore size distribution (PSD). As shown in Figure 3e, at short reaction times between 12 h and 1 day the PSD is dominated by a broad distribution of micropores centered at 1.5 nm and incipient mesoporosity between 2 and 3 nm. This intermediate stage is reminiscent of MUV-10(Ca) with an incipient formation of MUV-101(Co) and agrees well with the coexistence of both phases anticipated by Rietveld analyses. The onset of mesoporosity is also consistent with the opening of a small hysteresis loop in the N_2 isotherm of these samples for the range $P/P_0 = 0.4-1.0$ (Figure S45 in the Supporting Information). From 3 days and onward the PSD reveals the formation of a mesoporous material with two pore sizes. The smaller pores increase up to 1.5–1.8 nm, whereas the largest pores lie close to 3.2 nm, consistent with the prevalence of the MUV-101 phase at these stages. Overall, the sorption data suggest that this topological transformation might be useful to gain dynamic control over the formation of hierarchical micro-/mesopore structures at intermediate stages of the transformation. We also confirmed that the stability of the final material toward water degradation was not compromised by running stability tests by soaking MUV-101(Co)-30d crystals in acid, neutral, and basic aqueous solutions (section S4.9 in the Supporting Information).

One of the main limitations in the synthesis of mixed-metal frameworks, by either direct or postsynthetic methods, is the likeliness of producing segregated single-component phases rather than a homogeneous distribution of the metals at an atomic level in the structure of the heterometallic MOF.¹⁸ This problem is generally not discoverable by the characterization techniques used and requires more advanced tools such as X-ray absorption and high-resolution spectroscopies.²¹ We used EXAFS (Ti and Co K-edges) to correlate the degree of transformation with the changes to the local composition and structure of the SBUs with time (Figure 3fg and section S4.10 in the Supporting Information). Ti and Co K-edge EXAFS data collected on the MUV-101 phase at 77 K demonstrate the presence of heterobimetallic $TiCo_2$ clusters, with Ti–Co distances of ca. 2.94 Å (Table S8 in the Supporting Information). This intermetallic distance in the heterometallic cluster of MUV-101 is significantly shorter than the Ti–Ti distances seen in homometallic MIL-100(Ti) (i.e., 3.47 Å)²⁷ and agrees well with our DFT models and the crystallographic data reported for other heterometallic $TiCo_2$ clusters,³⁰ ruling out the formation of segregated phases. The detailed analyses of the Ti K-edge XANES region indicate the presence of a three-component pre-edge feature at 4971.5 eV after long transmetalation times, characteristic of centrosymmetric six-coordinated Ti^{4+} centers.^{31,32} The intermediate stages of

transformation show more distorted octahedral geometries. With regard to the local structure of the cobalt centers in MUV-101(Co), Co K-edge XANES data show the presence of a pre-edge feature at 7709.2 eV after equivalent reaction times indicative of Co^{2+} with slightly distorted octahedral geometries, consistent with the formation of TiCo_2 clusters.³³ For a better understanding of the transformation process at the nanoscale, we next used scanning transmission electron microscopy (STEM) with EDX to collect high-resolution elemental maps throughout a slice of the crystals (Figure 4). MUV-101(Co)-

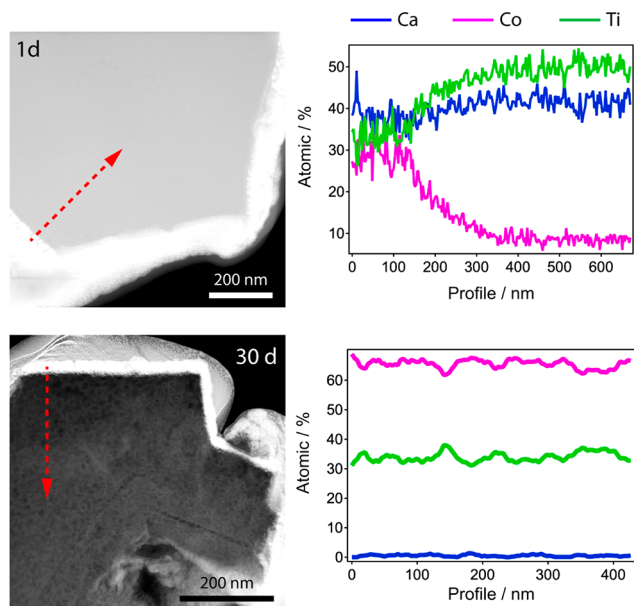


Figure 4. STEM-EDX of FIB-sectioned lamellae of MUV-101(Co)-1d and -30d showing the relative distribution of Ca (blue), Co (pink), and Ti (green) from the external surface to the inside of the crystal.

1d and -30d crystals were isolated, washed thoroughly, and sectioned with a focused ion beam (FIB). STEM-EDX of the lamellae at an early stage of the transformation confirms that the material grown on the external surface of the crystal is richer in cobalt and poorer in calcium in comparison to the interior. This spatial control over chemical composition agrees well with a diffusion-controlled process in which metal exchange induces the formation of MUV-101(Co) at the expense of MUV-10(Ca) crystals. We do not observe any signatures that account for the deposition of amorphous oxide coatings or segregation of phases, confirming the homogeneity of the process also at the nanoscale. Moreover, STEM-EDX spectral maps at different regions inside several crystals confirm the formation of a new material upon metal exchange with relative Ti, Co, and Ca contents consistent with the EDX analyses of bulk crystals (section S4.11 in the Supporting Information).

Origin of the Topological Transformation. To put our results in context, we looked at the literature for other examples of MOF transformations by metal exchange reactions. Zhang and co-workers recently reported the transformation of HKUST into MIL-100. In this case, the poor stability of HKUST in the reaction medium induces the decomposition and redissolution of the crystals by hydrolysis in the presence of Fe^{3+} , which is concomitant with the growth of nanoparticles of MIL-100(Fe).³⁴ In our case, the MOF transformation proceeds by crystal-to-crystal transformation

from a chemically stable precursor.²⁴ The epitaxial growth of MOFs first reported by Kitagawa and co-workers³⁵ involves exposure to metal solutions of MOF crystals with surfaces that are end-capped by linkers capable of coordinating the incoming metal. As a result, the outer surface of the crystal seeds the growth of an isostructural shell that is hybridized with the original core into a single mixed-metal crystal, provided there is an excellent match between both lattices. In our case, the crystals of MUV-10(Ca) (*the*; cubic, $Pm\bar{3}$, $a = 15.8362(8)$ Å) act as a templating scaffold and direct a topological transformation into MUV-101 (*mtn*; cubic, $Fd\bar{3}m$, $a = 73.5784(8)$ Å). In comparison to epitaxial growth, this process is driven by the generation of a new 6-c SBU, resulting in the formation of a new topology compatible with the structural information encoded in newly formed metal cluster and the 3-c organic linker common to both frameworks.

Intrigued by the differences with other MOF-to-MOF transformations available, we decided to rationalize the origin of this phenomenon by analyzing the surface terminations in MUV-10 crystals and studying the thermodynamics of the transformation of the SBU. We calculated the energies of (111), (001), and (110) surfaces representative of a cubic system with atomistic simulation techniques and used them to predict the equilibrium shape of the crystal through the Wulff construction method (see section S5 in the Supporting Information for computational methods).³⁶ As shown in Figure S5b, our results predict the formation of truncated octahedral crystals with preferential formation of (111) facets and small contributions from (001), with the latter being responsible for truncation of the octahedral symmetry. The expression of (001) facets is not visible from SEM pictures, which show MUV-10 crystals with regular octahedral morphologies (Figure 5a). This deviation from our model is possibly due to the effect of the solvent or the modulator (acetic acid) over the crystallization of the MOF, which was not considered in our calculations and might disfavor the stabilization of (001) surfaces. Accordingly, metal exchange reactions in MUV-10 shall be dominated by the terminations of the dominant (111) surfaces. Cleavage of the crystal along this direction by using the GDIS package³⁷ reveals the coexistence of exposed metal (ligand free) and ligand-capped terminations compatible with the ligand or metal-exchange reactions required for a structural transformation (Figure 5c,d). Similar terminations have been reported for other cubic MOFs such as UiO and HKUST.^{38,39} To confirm this point, we performed additional metal exchange experiments with single crystals that reveal more clearly the nucleation of small seeds of MUV-101(Co) in the (111) facets of the octahedra (section S4.12 in the Supporting Information).

Our experimental results confirm the formation of heterometallic MUV-10(Mn) or MUV-101(Co) phases depending on the metal incorporated into the SBU. We hypothesized that an MOF-to-MOF transformation might be ascribed to the instability of the heterometallic Ti_2M_2 cluster that is generated when Ca^{2+} is replaced with Co^{2+} rather than Mn^{2+} . Accordingly, we calculated the energy balance for the replacement of Ca^{2+} nodes in $[\text{Ti}_2\text{Ca}_2(\mu_3\text{-O})_2(\text{H}_2\text{O})_4(\text{RCO}_2)_8]$ by these two metals. As shown in Figure 5e, the formation of an isostructural cluster is only thermodynamically favorable for Mn^{2+} , whereas it is disfavored for Co^{2+} . These differences likely originate from the higher preference of Ca and Mn for a 7-fold CTP coordination environment in comparison to other first-row transition-metal ions such as

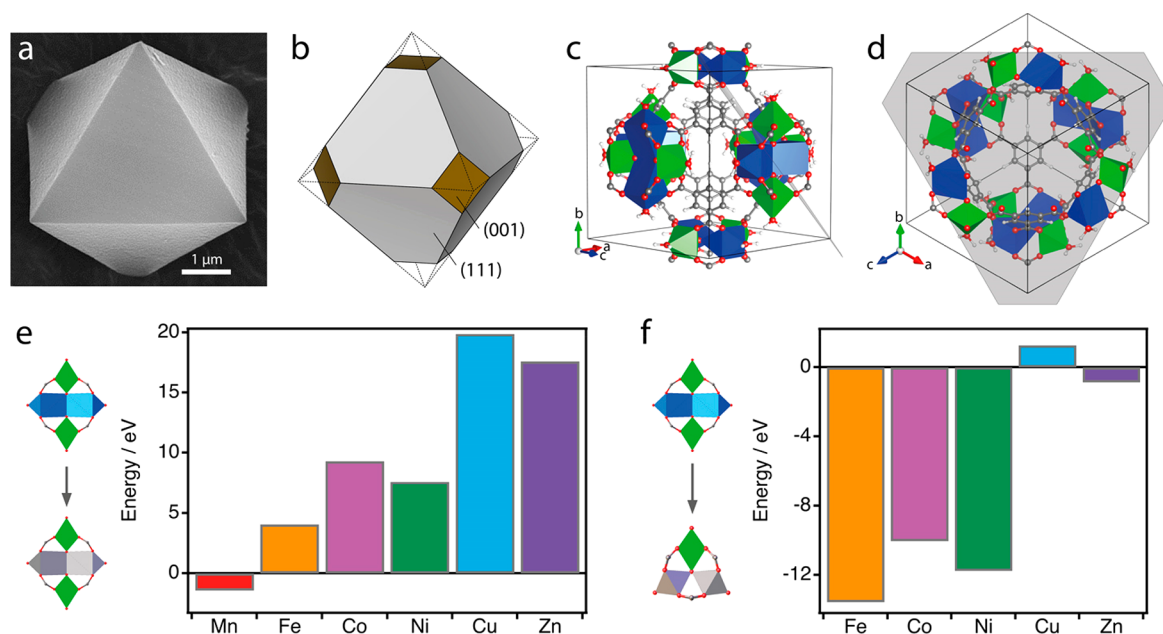


Figure 5. Origin of the topological transformation. (a) Experimental and (b) theoretical morphology of a crystal of MUV-10(Ca) calculated with the Wulff method. Differences are likely ascribed to the effect of the modulator used in the synthesis. (c) Perspective showing the cleavage of the cubic cell and the resulting (d) {111} surface termination combining metal and ligand free reactive sites. (e) Energy balance for the exchange of Ca^{2+} sites in $[\text{Ti}_2\text{Ca}_2(\mu_3\text{-O})_2(\text{H}_2\text{O})_4(\text{RCO}_2)_8]$ (Ti_2Ca_2) SBUs with Mn^{2+} (red), Fe^{2+} (orange), Co^{2+} (magenta), Ni^{2+} (green), Cu^{2+} (blue), and Zn^{2+} (purple). Except for Mn^{2+} , metal exchange would generate unstable coordination environments in isostructural clusters. (f) Enthalpy changes for the formation of $[\text{TiM}_2(\mu_3\text{-O})(\text{H}_2\text{O})_3(\text{RCO}_2)_6]$ (TiM_2) from Ti_2Ca_2 SBUs. Formation of TiM_2 metal–oxo clusters is disfavored for Cu^{2+} and thermodynamically possible for Fe^{2+} , Co^{2+} , Ni^{2+} , and Zn^{2+} with a significant preference for the first three.

cobalt. We ascribe these differences to changes in the ionic radii, which decrease from 1.06 and 0.90 Å for Ca^{2+} and Mn^{2+} to 0.65 Å for Co^{2+} .⁴⁰ In comparison to Co^{2+} , the electronic preference of Mn for this coordination geometry agrees well with the structural trends extracted from the Cambridge Structural Database for heptacoordination across the transition-metal series.²⁵ We argue that this thermodynamic instability triggers the transformation of Ti_2Co_2 into more stable TiCo_2 SBUs. This was further confirmed by calculating the enthalpy for the formation of $[\text{TiCo}_2(\mu_3\text{-O})(\text{H}_2\text{O})_3(\text{RCO}_2)_6]$ from $[\text{Ti}_2\text{Ca}_2(\mu_3\text{-O})_2(\text{H}_2\text{O})_4(\text{RCO}_2)_8]$ clusters (Figure 5f), which indicates that the formation of the heterometallic TiCo_2 SBU is thermodynamically more favorable. Overall, this suggests that the transformation probably proceeds by metal exchange at the (111) surface of the crystal. Metal replacement would generate an offset in the coordination geometry of the Ti_2Co_2 heterometallic clusters that would evolve into the formation of more stable TiCo_2 SBUs. This would be the thermodynamic driving force guiding the formation of MUV-101(Co). In comparison to the microporosity of MUV-10(Ca), the mesoporosity of MUV-101(Co) shall enable more favorable diffusion of mass for quantitative transformation from the outside to the inside of MUV-10(Ca) crystals.

To gain a more general understanding of the effect of the metal over the transformation phenomenon, we extended the calculations to other common divalent first-row transition-metal ions ($\text{M}^{2+} = \text{Fe}, \text{Ni}, \text{Cu}, \text{Zn}$). Calcium exchange for the formation of heterometallic MUV-10(Ca) Ti_2M_2 clusters is also disfavored for these metals, following the order $\text{Cu} > \text{Zn} \gg \text{Co} > \text{Ni} > \text{Fe}$ with positive enthalpies of formation ranging from 19.9 to 4.1 eV for Cu and Fe, respectively (Figure 5e). These enthalpy changes are consistent with our previous

periodic calculations for metal exchange in MUV-10(Ca).^{24,25} In turn, the calculated formation enthalpies of TiM_2 from Ti_2M_2 display different trends depending on the metal identity (Figure 5f). The formation of TiM_2 SBUs is thermodynamically more favorable for Fe, Ni, and Co, with energies ranging -13.6 to -10.0 eV, suggesting that these heterometallic phases of MUV-101 should also be synthetically accessible. However, the small stabilization for the formation of TiZn_2 (-0.9 eV) suggests that this material might be difficult to produce under thermodynamic control. Finally, Cu is the only metal for which the formation of the heterometallic trimer is not energetically favorable. This is in line with the low crystal field stabilization energies expected for Cu^{2+} and Zn^{2+} .⁴¹ Given the instability of Ti_2Cu_2 SBUs, our simulations suggest that the exchange of MUV-10(Ca) crystals with copper might induce the formation of an alternative SBU for a different bipartite net compatible with the 3-c connectivity of btc linkers.

Effect of the Metal in Directing the Transformation.

We performed additional metal exchange reactions to test the value of our theoretical predictions. MUV-10(Ca) crystals were soaked in concentrated solutions of Fe(II), Ni(II), and Zn(II) nitrate salts using the same conditions described above (section S6 in the Supporting Information). As anticipated by our calculations, all metals display a similar behavior and trigger the formation of colored crystals that are visible after 10 days, except for Zn. SEM-EDX and PXRD confirm the gradual exchange of Ca^{2+} , which becomes complete after 10 days for MUV-101(Zn) and 30 days for quantitative formation of crystals of MUV-101(Ni). MUV-101(Fe)-30d shows close to 13 atom % of calcium, indicative of an incomplete transformation, in good agreement with the presence of a residual fraction of the MUV-10 phase in the PXRD (Figure S61 in the Supporting Information). This is possibly due to the difficulties

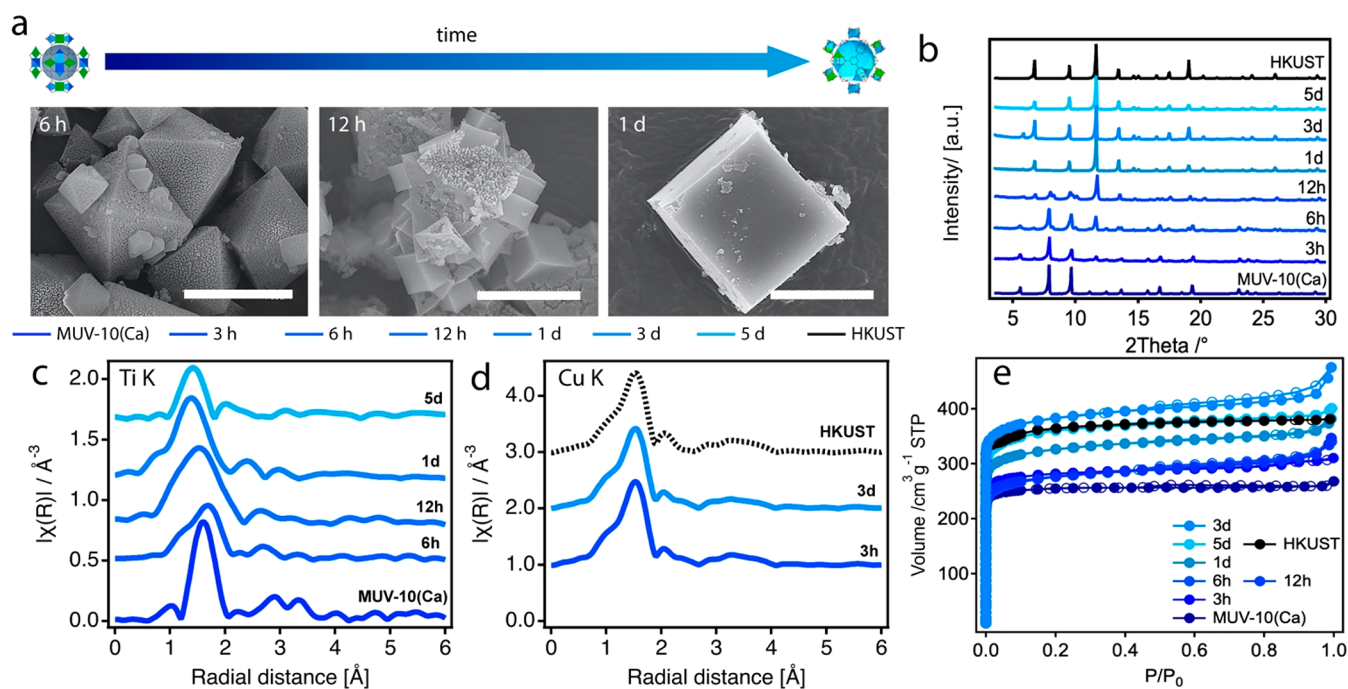


Figure 6. Dynamic topological transformation of MUV-10(Ca) to MUV-102(Cu). (a) SEM images showing the progress of the transformation with time for the formation of cubelike crystals of MUV-102(Cu) (scale bars 3 μm). Analysis of the MOF transformation at different reaction times: (b) PXRDs showing the transformation of MUV-10(Ca) into MUV-102(Cu) with time and comparison with commercial HKUST (black); (c, d) EXAFS Ti and Cu K-edge spectra of MUV-102(Cu) at different stages of transformation. The spectrum of homometallic HKUST was used for comparison and is shown as a dashed black line. (e) N_2 adsorption/desorption isotherms at 77 K showing the progressive increase in surface area and pore volume with time until they match those of HKUST (black line). For a clearer analysis of the different stages of transformation see section S7 in the Supporting Information.

in stabilizing Fe^{2+} in solution for the long reaction times used in the experiment. N_2 isotherms of MUV-101(Ni)-30d and MUV-101(Zn)-10d are indicative of mesoporous solids with BET values and pore sizes consistent with the formation of highly crystalline heterometallic MIL-100 phases. MUV-101(Fe)-30d shows a significantly smaller surface area as a result of the incomplete transformation. Overall, these results confirm the general value of MUV-10(Ca) as a precursor for inducing the formation of mesoporous, heterometallic titanium–organic frameworks by metal exchange at low temperature. To check if these phases were kinetic in nature, we also attempted to produce MUV-101(Fe,Co,Ni,Zn) MOFs by direct synthesis at high temperature. Whereas MUV-101(Fe,Co,Ni) can be prepared by solvothermal reactions of titanium isopropoxide with the metal salts and btc in DMF,⁴² MUV-101(Zn) can only be isolated by a metal exchange reaction with MUV-10(Ca) at 65 $^\circ\text{C}$. These results agree well with our theoretical predictions that reveal a clear thermodynamic preference for the formation of $[\text{TiM}_2(\mu_3\text{-O})(\text{H}_2\text{O})_3(\text{RCO}_2)_6]$ SBUs for Fe, Co, and Ni, whereas Zn is significantly less favorable.²⁵ As a result, this heterometallic phase can only be isolated by diffusion-controlled metal exchange rather than under thermodynamic control at high temperatures.

We next investigated the effect of Cu^{2+} on the transformation. Our calculations above suggest that the formation of TiCu_2 clusters is not favorable; therefore, we expected significant differences in the product of the metal exchange reaction. For a clearer overview of the process, we analyzed the progress of the reaction by isolating the product at different reaction times between 1 h and 5 days (section S7 in the Supporting Information). SEM measurements confirm the

formation of intertwined cubes at the facets of MUV-10(Ca) that become larger with time up to around 5 μm (Figure 6a). In comparison to MUV-101(Co), the reaction with Cu^{2+} is roughly 3 times faster. The copper content reaches a plateau close to 80% between 1 and 5 days, concomitant with the complete depletion of calcium from the crystals, for a final Ti:Cu ratio of close to 1:4 (section S7.2 in the Supporting Information). These differences in the morphology of the crystals and relative metal ratio in comparison to MUV-101(Fe,Co,Ni,Zn) indicated the formation of a different phase in the case of copper. This was first analyzed with PXRD (Figure 6b), suggesting complete transformation after 1 day into a highly crystalline material that we will refer to as MUV-102(Cu). Figure S81 in the Supporting Information shows the Le Bail refinement of the sample after 5 days, confirming that the resulting material is isostructural with HKUST (*tbo*; cubic, $Fm\bar{3}m$, $a = 26.343(5)$ \AA). This MOF is built from the linking of 4-c paddlewheel $[\text{Cu}_2(\text{CO}_2)_2(\text{H}_2\text{O})_2]$ SBUs and 3-c btc organic molecules. The total metal content corresponds to the incorporation of 20 atom % of titanium in MUV-102(Cu), suggesting the formation of one heterometallic TiCu cluster per 2.5 homometallic Cu_2 units. Just as with MUV-101(Fe,Co,Ni,Zn) or MIL-100(Ti), we argue that the excess of positive charge that results from the replacement of Cu^{2+} with Ti^{4+} might be counterbalanced by the coordination of O^{2-} capping linkers to titanium for a heterometallic $[\text{TiCu}(\text{RCO}_2)_2(\text{O})(\text{H}_2\text{O})]$ SBU. The formation of a heterometallic cluster agrees well with the evolution of the Ti K-edge EXAFS data with the reaction time (Figure 6c,d), which indicate the presence of Ti–Cu distances at ca. 2.84 \AA for long reaction times, in agreement with our DFT models for MUV-102(Cu) (Table S16 and section S7.6 in the Supporting Information).

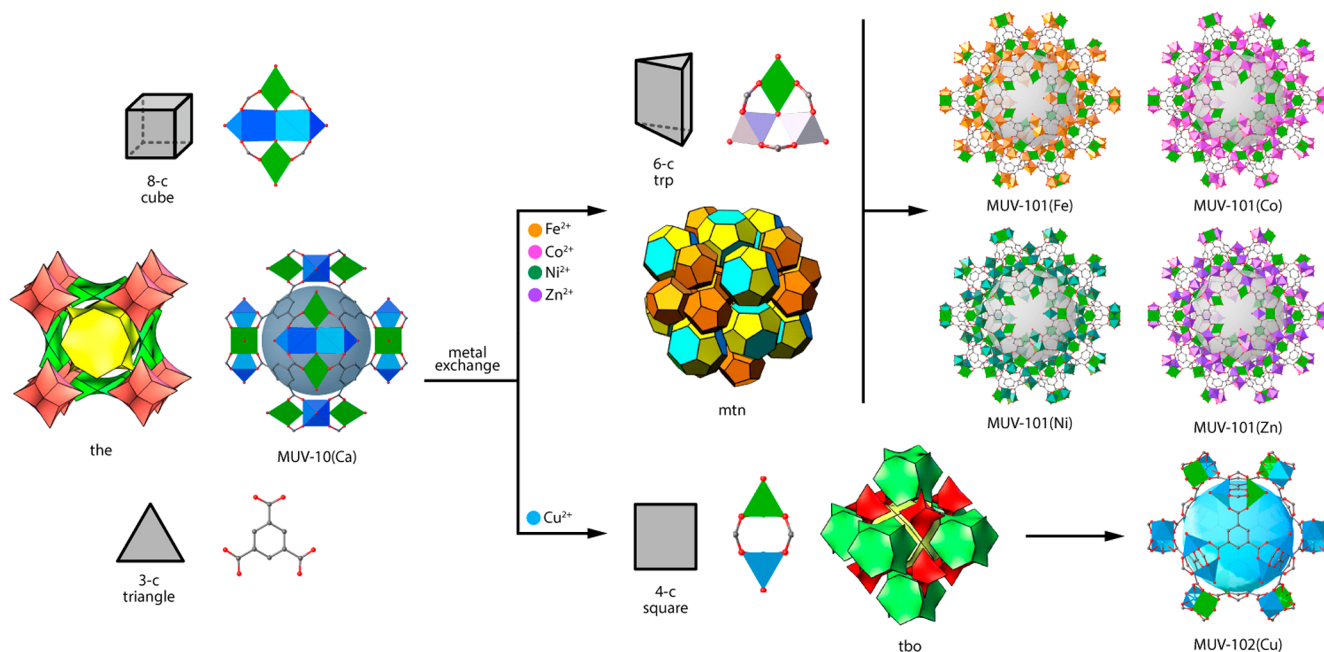


Figure 7. Topological transformation chart. Graphical overview of the binary heterometallic titanium–organic frameworks described in this work and their corresponding topologies and building units. By the principles of reticular chemistry, the transformation of the 8-c Ti_2Ca_2 metal–oxo cluster in MUV-10(Ca) into 6-c TiM_2 and 4-c TiCu units by metal exchange reactions drives the formation of the binary frameworks dictated by the local symmetries of 3-c btc units and the newly formed SBUs. All topologies shown have been taken from the Reticular Chemistry Structure Resource (RCSR; <http://rcsr.anu.edu.au/>).

Additionally, Ti and Cu K-edge XANES data demonstrated the simultaneous presence of highly distorted Ti(IV) six-^{31,32} and five-coordinated Cu(II) centers^{43,44} in MUV-102(Cu). The formation of heterometallic paddlewheel units is also consistent with the presence of uncoupled cupric $S = 1/2$ signals already present in the electron spin resonance spectra of MUV-102(Cu) after 6 h (section S7.7 in the Supporting Information). We discarded the formation of nanometer-thick oxide coatings upon transformation with STEM-EDX analyses. High-resolution spectral maps collected from FIB-sectioned crystals also confirm the formation of an outer shell of Cu that deepens into the crystal for increasing reaction times (section S7.8 in the Supporting Information). The formation of this binary *tbo* framework is consistent with N_2 gas sorption measurements. MUV-102(Cu) samples formed after transformations from 1 h to 5 days display type isotherms intrinsic to microporous materials with BET surface area values and pore sizes increasing from $1000 \text{ m}^2\cdot\text{g}^{-1}$ and a micropore centered at 0.8 nm for MUV-102(Cu)-1h, characteristic of MUV-10, to $1509 \text{ m}^2\cdot\text{g}^{-1}$ and bimodal microporosity centered at 0.9 and 1.1 nm after complete transformation in MUV-102(Cu)-5d. We measured the porosity of a commercial sample of HKUST (Basolite C300) soaked in MeOH for 5 days at room temperature to confirm the excellent match in porosity between both samples (Figure 6e and section S7.9 in the Supporting Information). The low titanium doping does not notably affect the thermal and chemical stability of MUV-102(Cu), which displays a decomposition temperature of 302 °C and the same limitations toward water hydrolysis as homometallic HKUST (sections S7.10 and S7.11 in the Supporting Information). As with MUV-101(Zn), we could not prepare this heterometallic analogue of HKUST by direct synthesis, confirming again the ability of metal-induced topological transformation to enable the formation of MOFs not accessible by *de novo* synthesis.

CONCLUSION

The synthesis of titanium frameworks still remains limited by the difficulties in controlling the high reactivity of Ti^{4+} ions in solution, which precludes the formation of persistent SBUs with the symmetry and connectivity required to target predefined topologies. We have shown the general value of MUV-10(Ca) as a precursor for directing the formation of mesoporous or microporous heterometallic titanium–organic frameworks at low temperature by exchange reactions with first-row transition metals. Metal exchange at the soft positions of the cluster induces a MOF-to-MOF transformation that is controlled by the formation of thermodynamically favored heterometallic clusters. As summarized in Figure 7, the nuclearity and nodes of connection of the resulting metal clusters are controlled by the metal incorporated and direct the assembly of binary frameworks according to the principles of reticular chemistry. In comparison to direct synthesis, this metal-induced topological transformation is a dynamic phenomenon and can be used to gain control over the formation of hierarchical micro-/mesopore structures by controlling the extent of transformation with time for the synthesis of mixed phases. Our results also suggest that this method enables the formation of heterometallic titanium MOFs that are not accessible under solvothermal conditions at high temperature, thus opening the door to the synthesis of additional titanium heterometallic phases not limited to trimesate linkers. On the basis of the advantageous properties of titanium and the intrinsic advantages of mixed-metal MOFs over their homometallic counterparts in applications such as gas storage/separation and heterogeneous catalysis,^{18,19} we are confident that this approach might represent a turning point for the synthesis and general applications of titanium frameworks in a broad context.

■ ASSOCIATED CONTENT

Supporting Information

The Supporting Information is available free of charge at <https://pubs.acs.org/doi/10.1021/jacs.0c00117>.

Synthetic and experimental details, physical characterization, and supporting tables and figures as described in the text (PDF)

X-ray crystallographic data for MUV-101(Co) (CIF)

■ AUTHOR INFORMATION

Corresponding Authors

Natalia M. Padial – *Functional Inorganic Materials Team, Instituto de Ciencia Molecular (ICMol), Universitat de València, Paterna 46980, València, Spain*; orcid.org/0000-0001-6067-3360; Email: nmpadial@scripps.edu

Carlos Martí-Gastaldo – *Functional Inorganic Materials Team, Instituto de Ciencia Molecular (ICMol), Universitat de València, Paterna 46980, València, Spain*; orcid.org/0000-0003-3203-0047; Email: carlos.marti@uv.es

Authors

Belén Lerma-Berlanga – *Functional Inorganic Materials Team, Instituto de Ciencia Molecular (ICMol), Universitat de València, Paterna 46980, València, Spain*

Neyvis Almora-Barríos – *Functional Inorganic Materials Team, Instituto de Ciencia Molecular (ICMol), Universitat de València, Paterna 46980, València, Spain*; orcid.org/0000-0001-5269-2705

Javier Castells-Gil – *Functional Inorganic Materials Team, Instituto de Ciencia Molecular (ICMol), Universitat de València, Paterna 46980, València, Spain*; orcid.org/0000-0001-7931-3867

Iván da Silva – *ISIS Facility, Rutherford Appleton Laboratory, Didcot, Oxfordshire OX11 0QX, United Kingdom*

María de la Mata – *Departamento de Ciencia de los Materiales e I.M. y Q.I., Facultad de Ciencias, IMEYMAT, Universidad de Cádiz, 11510 Cádiz, Spain*; orcid.org/0000-0002-1581-4838

Sergio I. Molina – *Departamento de Ciencia de los Materiales e I.M. y Q.I., Facultad de Ciencias, IMEYMAT, Universidad de Cádiz, 11510 Cádiz, Spain*

Jesús Hernández-Saz – *Departamento de Ingeniería y Ciencia de los Materiales y del Transporte, Escuela Politécnica Superior, Universidad de Sevilla, 41011 Sevilla, Spain*; orcid.org/0000-0002-6630-7203

Ana E. Platero-Prats – *Departamento de Química Inorgánica and Condensed Matter Physics Center (IFIMAC), Universidad Autónoma de Madrid, 28049 Madrid, Spain*; orcid.org/0000-0002-2248-2739

Sergio Tatay – *Functional Inorganic Materials Team, Instituto de Ciencia Molecular (ICMol), Universitat de València, Paterna 46980, València, Spain*

Complete contact information is available at: <https://pubs.acs.org/doi/10.1021/jacs.0c00117>

Author Contributions

• N.M.P. and B.L.-B. contributed equally.

Notes

The authors declare no competing financial interest.

■ ACKNOWLEDGMENTS

This work was supported by the EU (ERC Stg Chem-fs-MOF 714122) and Spanish government (MDM-2015-0538, CTQ2017-83486-P & RTI2018-098568-A-I00). S.T., B.L.-B., and J.C.-G. thank the Spanish government for a Ramón y Cajal Fellowship (RYC-2016-19817) and FPU (FPU16/04162) and FPI Scholarships (CTQ2014-59209-P). N.M.P. thanks the European Union for a Marie Skłodowska-Curie Global Fellowship (H2020-MSCA-IF-2016-GF-749359-EnanSET). A.E.P.-P. acknowledges a TALENTO grant (2017-T1/IND5148) from Comunidad de Madrid. We acknowledge SOLEIL and ALBA for provision of synchrotron radiation facilities and we thank Dr. Valérie Briois for assistance in using beamlines ROCK (proposal 20180480), Dr. Laura Simonell at BL22-CLAESS (proposal 2018022634), and Dr. Catalin Popescu at BL04-MSPD. Work at SOLEIL was supported by a public grant overseen by the French National Research Agency (ANR) as part of the “Investissements d’Avenir” program (ANR10-EQPX45). We also thank the BSC-RES for computational resources. We are grateful to Dr. Victor Rubio-Giménez and Maria Romero-Ángel (Instituto de Ciencia Molecular) for their help with the EXAFS experiments. M.M. and S.I.M. thank the support from Junta de Andalucía (Research group INNANOMAT, TEP-946). M.M. also acknowledges Ministry of Science and Innovation for her Juan de la Cierva postdoctoral fellowship.

■ REFERENCES

- (1) Yaghi, O. M.; O’Keeffe, M.; Ockwig, N.; Chae, H.; Eddaoudi, M.; Kim, J. Reticular Synthesis and the Design of New Materials. *Nature* **2003**, *423*, 705–714.
- (2) Mason, J. A.; Oktawiec, J.; Taylor, M. K.; Hudson, M. R.; Rodriguez, J.; Bachman, J. E.; Gonzalez, M. I.; Cervellino, A.; Guagliardi, A.; Brown, C. M.; Llewellyn, P. L.; Masciocchi, N.; Long, J. R. Methane Storage in Flexible Metal-Organic Frameworks with Intrinsic Thermal Management. *Nature* **2015**, *527*, 357–361.
- (3) Tian, T.; Zeng, Z.; Vulpe, D.; Casco, M. E.; Divitini, G.; Mirdley, P. A.; Silvestre-Albero, J.; Tan, J.-C.; Moghadam, P. Z.; Fairen-Jimenez, D. A Sol-Gel Monolithic Metal-Organic Framework with Enhanced Methane Uptake. *Nat. Mater.* **2018**, *17*, 174–179.
- (4) Gu, C.; Hosono, N.; Zheng, J.-J.; Sato, Y.; Kusaka, S.; Sakaki, S.; Kitagawa, S. Design and Control of Gas Diffusion Process in a Nanoporous Soft Crystal. *Science* **2019**, *363*, 387–391.
- (5) Li, L.; Lin, R.-B.; Krishna, R.; Li, H.; Xiang, S.; Wu, H.; Li, J.; Zhou, W.; Chen, B. Ethane/Ethylene Separation in a Metal-Organic Framework with Iron-Peroxy Sites. *Science* **2018**, *362*, 443–446.
- (6) Cadiau, A.; Belmabkhout, Y.; Adil, K.; Bhatt, P. M.; Pillai, R. S.; Shkurenko, A.; Martineau-Corcoss, C.; Maurin, G.; Eddaoudi, M. Hydrolytically Stable Fluorinated Metal-Organic Frameworks for Energy-Efficient Dehydration. *Science* **2017**, *356*, 731–735.
- (7) Diercks, C. S.; Liu, Y.; Cordova, K. E.; Yaghi, O. M. The Role of Reticular Chemistry in the Design of CO₂ Reduction Catalysts. *Nat. Mater.* **2018**, *17*, 301–307.
- (8) Zhao, M.; Yuan, K.; Wang, Y.; Li, G.; Guo, J.; Gu, L.; Hu, W.; Zhao, H.; Tang, Z. Metal-Organic Frameworks as Selectivity Regulators for Hydrogenation Reactions. *Nature* **2016**, *539*, 76–80.
- (9) Eddaoudi, M.; Kim, J.; Rosi, N.; Vodak, D.; Wachter, J.; O’Keeffe, M.; Yaghi, O. M. Systematic Design of Pore Size and Functionality in Isoreticular MOFs and Their Application in Methane Storage. *Science* **2002**, *295*, 469–472.
- (10) O’Keeffe, M.; Yaghi, O. M. Deconstructing the Crystal Structures of Metal-Organic Frameworks and Related Materials into Their Underlying Nets. *Chem. Rev.* **2012**, *112*, 675–702.
- (11) Kalmutzki, M. J.; Hanikel, N.; Yaghi, O. M. Secondary Building Units as the Turning Point in the Development of the Reticular Chemistry of MOFs. *Sci. Adv.* **2018**, *4*, No. eaat9180.

- (12) Chui, S.; Lo, F.; Charmant, J.; Orpen, A. A Chemically Functionalizable Nanoporous Material $[\text{Cu}_3(\text{TMA})_2(\text{H}_2\text{O})_3]_n$. *Science* **1999**, *283*, 1148–1150.
- (13) Férey, G.; Serre, C.; Mellot-Draznieks, C.; Millange, F.; Surblé, S.; Dutour, J.; Margiolaki, I. A Hybrid Solid with Giant Pores Prepared by a Combination of Targeted Chemistry, Simulation, and Powder Diffraction. *Angew. Chem., Int. Ed.* **2004**, *43*, 6296–6301.
- (14) Férey, G.; Mellot-Draznieks, C.; Serre, C.; Millange, F.; Dutour, J.; Surblé, S.; Margiolaki, I. A Chromium Terephthalate-Based Solid with Unusually Large Pore Volumes and Surface Area. *Science* **2005**, *309*, 2040–2042.
- (15) Cavka, J.; Jakobsen, S.; Olsbye, U.; Guillou, N.; Lamberti, C.; Bordiga, S.; Lillerud, K. A New Zirconium Inorganic Building Brick Forming Metal Organic Frameworks with Exceptional Stability. *J. Am. Chem. Soc.* **2008**, *130*, 13850–13851.
- (16) Howarth, A. J.; Liu, Y.; Li, P.; Li, Z.; Wang, T. C.; Hupp, J. T.; Farha, O. K. Chemical, Thermal and Mechanical Stabilities of Metal-Organic Frameworks. *Nature Rev. Mater.* **2016**, *1*, 15018.
- (17) Furukawa, H.; Cordova, K. E.; O’Keeffe, M.; Yaghi, O. M. The Chemistry and Applications of Metal-Organic Frameworks. *Science* **2013**, *341*, 1230444.
- (18) Abednatanzi, S.; Derakhshandeh, P.; Depauw, H.; Coudert, F.-X.; Vrieland, H.; Voort, P.; Leus, K. Mixed-Metal Metal-Organic Frameworks. *Chem. Soc. Rev.* **2019**, *48*, 2535–2565.
- (19) Masoomi, M.; Morsali, A.; Dhakshinamoorthy, A.; García, H. Mixed-Metal MOFs: Unique Opportunities in Metal-organic Framework Functionality and Design. *Angew. Chem., Int. Ed.* **2019**, *58*, 15188–15205.
- (20) Santaclara, J. G.; Olivos-Suarez, A. I.; Nelson, A.; Osadchii, D.; Nasalevich, M. A.; van der Veen, M. A.; Kapteijn, F.; eveleva, A.; Veber, S. L.; Fedin, M. V.; Murray, A. T.; Hendon, C. H.; Walsh, A.; Gascon, J. Revisiting the Incorporation of Ti(IV) in UiO-Type Metal-Organic Frameworks: Metal Exchange versus Grafting and Their Implications on Photocatalysis. *Chem. Mater.* **2017**, *29*, 8963–8967.
- (21) Denny, M. S.; Parent, L. R.; Patterson, J. P.; Meena, S.; Pham, H.; Abellan, P.; Ramasse, Q. M.; Paesani, F.; Gianneschi, N. C.; Cohen, S. M. Transmission Electron Microscopy Reveals Deposition of Metal Oxide Coatings onto Metal-Organic Frameworks. *J. Am. Chem. Soc.* **2018**, *140*, 1348–1357.
- (22) Das, S.; Kim, H.; Kim, K. Metathesis in Single Crystal: Complete and Reversible Exchange of Metal Ions Constituting the Frameworks of Metal-Organic Frameworks. *J. Am. Chem. Soc.* **2009**, *131*, 3814–3815.
- (23) Brozek, C. K.; Dincă, M. Ti^{3+} , $\text{V}^{2+/3+}$, $\text{Cr}^{2+/3+}$, Mn^{2+} , and Fe^{2+} Substituted MOF-5 and Redox Reactivity in Cr- and Fe-MOF-5. *J. Am. Chem. Soc.* **2013**, *135*, 12886–12891.
- (24) Castells-Gil, J.; Padiál, N. M.; Almora-Barrios, N.; Albero, J.; Ruiz-Salvador, R. A.; González-Platas, J.; García, H.; Martí-Gastaldo, C. Chemical Engineering of Photoactivity in Heterometallic Titanium-Organic Frameworks by Metal Doping. *Angew. Chem., Int. Ed.* **2018**, *57*, 8453–8457.
- (25) Cremades, E.; Echeverría, J. & Alvarez, S. The trigonal prism in coordination chemistry. *Chem. - Eur. J.* **2010**, *16*, 10380–10396.
- (26) Brozek, C. K.; Dincă, M. Thermodynamic Parameters of Cation Exchange in MOF-5 and MFU-4 L. *Chem. Commun.* **2015**, *51*, 11780–11782.
- (27) Castells-Gil, J.; Padiál, N. M.; Almora-Barrios, N.; da Silva, I.; Mateo, D.; Albero, J.; García, H.; Martí-Gastaldo, C. De Novo Synthesis of Mesoporous Photoactive Titanium(IV)-Organic Frameworks with MIL-100 Topology. *Chem. Sci.* **2019**, *10*, 4313–4321.
- (28) Horcajada, P.; Surblé, S.; Serre, C.; Hong, D.-Y.; Seo, Y.-K.; Chang, J.-S.; Grenèche, J.-M.; Margiolaki, I.; Férey, G. Synthesis and Catalytic Properties of MIL-100(Fe), an Iron(III) Carboxylate with Large Pores. *Chem. Commun.* **2007**, 2820–2822.
- (29) Volkringer, C.; Popov, D.; Loiseau, T.; Férey, G.; Burghammer, M.; Riekkel, C.; Haouas, M.; Taulelle, F. Synthesis, Single-Crystal X-Ray Microdiffraction, and NMR Characterizations of the Giant Pore Metal-Organic Framework Aluminum Trimesate MIL-100. *Chem. Mater.* **2009**, *21*, 5695–5697.
- (30) Hong, K.; Bak, W.; Moon, D.; Chun, H. Bistable and Porous Metal-Organic Frameworks with Charge-Neutral AcsNet Based on Heterometallic $\text{M}_3\text{O}(\text{CO}_2)_6$ Building Blocks. *Cryst. Growth Des.* **2013**, *13*, 4066–4070.
- (31) Farges, F.; Brown, G. E. Coordination Chemistry of Titanium (IV) in Silicate Glasses and Melts: IV. XANES Studies of Synthetic and Natural Volcanic Glasses and Tektites at Ambient Temperature and Pressure. *Geochim. Cosmochim. Acta* **1997**, *61*, 1863–1870.
- (32) Henderson, G. S.; de Groot, F.; Moulton, B. X-Ray Absorption Near-Edge Structure (XANES) Spectroscopy. *Rev. Mineral. Geochem.* **2014**, *78*, 75–138.
- (33) Hunault, M.; Vercamer, V.; Haverkort, M.; Arrio, M.-A.; Brouder, C.; Calas, G.; Juhin, A. Tracking the Signature of Low Symmetry Environments in the XAS K Pre-Edge. *J. Phys.: Conf. Ser.* **2016**, *712*, 012005.
- (34) Li, W.; Zhang, Y.; Zhang, C.; Meng, Q.; Xu, Z.; Su, P.; Li, Q.; Shen, C.; Fan, Z.; Qin, L.; Zhang, G. Transformation of Metal-Organic Frameworks for Molecular Sieving Membranes. *Nat. Commun.* **2016**, *7*, 11315.
- (35) Furukawa, S.; Hirai, K.; Nakagawa, K.; Takashima, Y.; Matsuda, R.; Tsuruoka, T.; Kondo, M.; Haruki, R.; Tanaka, D.; Sakamoto, H.; Shimomura, S.; Sakata, O.; Kitagawa, S. Heterogeneously Hybridized Porous Coordination Polymer Crystals: Fabrication of Heterometallic Core-Shell Single Crystals with an In-Plane Rotational Epitaxial Relationship. *Angew. Chem., Int. Ed.* **2009**, *48*, 1766–1770.
- (36) Herring, C. Some Theorems on the Free Energies of Crystal Surfaces. *Phys. Rev.* **1951**, *82*, 87–93.
- (37) Fleming, S.; Rohl, A. GDIS: A Visualization Program for Molecular and Periodic Systems. *Z. Kristallogr. - Cryst. Mater.* **2005**, *220*, 580–584.
- (38) Zhang, D.; Zhu, Y.; Liu, L.; Ying, X.; Hsiung, C.-E.; Sougrat, R.; Li, K.; Han, Y. Atomic-Resolution Transmission Electron Microscopy of Electron Beam-Sensitive Crystalline Materials. *Science* **2018**, *359*, 675–679.
- (39) Amirjalayer, S.; Tafipolsky, M.; Schmid, R. Surface Termination of the Metal-Organic Framework HKUST-1: A Theoretical Investigation. *J. Phys. Chem. Lett.* **2014**, *5*, 3206–3210.
- (40) Shannon, R. Revised Effective Ionic Radii and Systematic Studies of Interatomic Distances in Halides and Chalcogenides. *Acta Crystallogr., Sect. A: Cryst. Phys., Diffr., Theor. Gen. Crystallogr.* **1976**, *32*, 751–767.
- (41) Cotton, A. F. I - Ligand Field Theory. *J. Chem. Educ.* **1964**, *41* (9), 466.
- (42) Castells-Gil, J. M.; Padiál, N.; Almora-Barrios, N.; Gil-San-Millán, R.; Torres, V.; Romero-Ángel, M.; da Silva, I.; Waerenborgh, J. C.; Jagiello, J.; Tatay, S. R.; Navarro, J. A.; Martí-Gastaldo, C. Heterometallic Titanium-Organic Frameworks as Dual Metal Catalysts for Synergistic Non-Buffered Hydrolysis of Nerve Agent Simulants. Submitted for publication (2020).
- (43) Todaro, M.; Sciortino, L.; Gelardi, F.; Buscarino, G. Determination of Geometry Arrangement of Copper Ions in HKUST-1 by XAFS During a Prolonged Exposure to Air. *J. Phys. Chem. C* **2017**, *121*, 24853–24860.
- (44) Borfecchia, E.; Maurelli, S.; Gianolio, D.; Groppo, E.; Chiesa, M.; Bonino, F.; Lamberti, C. Insights into Adsorption of NH_3 on HKUST-1 Metal-Organic Framework: A Multitechnique Approach. *J. Phys. Chem. C* **2012**, *116*, 19839–19850.

Supporting Information

Heterometallic titanium-organic frameworks by metal-induced dynamic topological transformations

Natalia M. Padial,^{†,‡,§,*} Belén Lerma-Berlanga,^{†, #} Neyvis Almora-Barrios,[†] Javier Castells-Gil,[†]
Iván da Silva,[§] María de la Mata,[◇] Sergio I. Molina,[◇] Jesús Hernández-Saz,[‡] Ana E. Platero-Prats,^{∇,▫} Sergio Tatay,[†] Carlos Martí-Gastaldo^{†,*}

[†] Functional Inorganic Materials Team, Instituto de Ciencia Molecular (ICMol), Universitat de València, Paterna 46980, València, Spain.

[§] ISIS Facility, Rutherford Appleton Laboratory, Chilton, Didcot, Oxfordshire, OX11 0QX, United Kingdom.

[◇] Departamento de Ciencia de los Materiales e I.M. y Q.I., Facultad de Ciencias, IMEYMAT, Universidad de Cádiz, Campus Río San Pedro, s/n, 11510, Cádiz, Spain.

[‡] Departamento de Ingeniería y Ciencia de los Materiales y del Transporte, Escuela Politécnica Superior, Universidad de Sevilla, 41011, Sevilla, Spain.

[∇] Departamento de Química Inorgánica, Universidad Autónoma de Madrid, 28049, Madrid, Spain.

[▫] Condensed Matter Physics Center (IFIMAC), Universidad Autónoma de Madrid, 28049, Madrid, Spain.

[‡] (present address) Department of Chemistry, Scripps Research, 10550 North Torrey Pines Road, La Jolla, CA 92037, United States.

These authors contributed equally

*carlos.marti@uv.es

TABLE OF CONTENTS

S1. GENERAL CONSIDERATIONS: STARTING MATERIALS AND CHARACTERIZATION.....	S4
S1.1. Materials and reagents	S4
S1.2. Physical and chemical characterization	S4
S2. GENERAL PROCEDURE TO THE TRANSMETALLATION OF MUV-10(Ca) WITH Mⁿ⁺	S6
S3. TRANSMETALATION OF MUV-10(Ca) WITH Mn²⁺	S7
S3.1. Experimental metal content	S7
S3.2. Scanning Electron Microscopy (SEM) and single point mapping.....	S8
S3.3. Powder X-Ray Difracttion (PXRD).....	S9
S3.4. Analysis of N ₂ adsorption/desorption isotherms at 77 K	S11
S3.5. Chemical stabillity.....	S13
S4. TRANSFORMATION OF MUV-10(Ca) IN MUV-101(Co) BY METAL EXCHANGE WITH Co²⁺	S14
S4.1. MUV-101(Co) at a Glance.....	S14
S4.2. Evolution of metal content with time	S15
S4.3. Scanning Electron Microscopy (SEM) and single point mapping.....	S17
S4.4. Rietveld refinement and crystallographic data of MUV-101(Co)	S24
S4.5. Powder X-Ray Difracttion (PXRD).....	S26
S4.6.Rietveld quantification of the relative percentage of MUV-10/MUV-101 phases at intermediate stages of transformation.	S30
S4.7.Thermogravimetric Analysis (TGA) and changes to the termal stability of the solid with the degree of transformation.	S34
S4.8. Analysis of N ₂ adsorption/desorption isotherms at 77 K and porosity changes with the degree of transformation.....	S37
S4.9. Chemical stability.....	S44
S4.10. EXAFS data analysis and fitting.	S45
S4.11. STEM-EDX and high-resolution elemental maps.....	S47
S4.12. Tranformation in single crystals.....	S49
S5. COMPUTATIONAL METHODS.....	S51
S6. TRANSFORMATION OF MUV-10(Ca) IN MUV-101(Fe, Ni, Zn) BY METAL EXCHANGE WITH Fe²⁺, Ni²⁺AND Zn²⁺.	S53
S6.1. MUV-101(Fe)	S54
S6.2. MUV-101(Ni)	S57
S6.3. MUV-101(Zn).....	S60
S7. TRANSFORMATION OF MUV-10(Ca) IN MUV-102(Cu) BY METAL EXCHANGE WITH Cu²⁺	S65
S7.1. MUV-102(Cu) at a glance	S65

S7.2. Evolution of metal content with time	S66
S7.3. Scanning Electron Microscopy (SEM) and EDAX	S68
S7.4. Le Bail refinement of MUV-102(Cu)	S75
S7.5. Powder X-Ray Difracttion (PXRD).....	S76
S7.6. EXAFS data analysis and fitting	S80
S7.7. Electron Spin Resonance	S82
S7.8. STEM-EDX data and analysis.....	S82
S7.9. Analysis of N ₂ adsorption/desorption isotherms at 77 K and porosity changes with the degree of transformation.....	S84
S7.10. Thermogravimetric Analysis (TGA) and changes to the termal stability of the solid with the degree of transformation	S89
S7.11. Chemical stability.....	S92
S8. REFERENCES	S93

S1. GENERAL CONSIDERATIONS: STARTING MATERIALS AND CHARACTERIZATION

S1.1. Materials and reagents

Benzene-1,3,5-tricarboxylic acid (98%) was purchased from TCI Europe. CaCl_2 anhydrous, granular ($\geq 93\%$), $\text{MnCl}_2 \cdot 4\text{H}_2\text{O}$ ($\geq 99\%$), $\text{Co}(\text{NO}_3)_2 \cdot 6\text{H}_2\text{O}$ ($\geq 98\%$), $\text{Cu}(\text{NO}_3)_2 \cdot 3\text{H}_2\text{O}$ (99%), FeCl_2 (98%), $\text{Ni}(\text{NO}_3)_2 \cdot 6\text{H}_2\text{O}$ ($\geq 98.5\%$), $\text{Zn}(\text{NO}_3)_2 \cdot 6\text{H}_2\text{O}$ ($\geq 99\%$), acetic acid 99% and titanium (IV) isopropoxide were purchased from Sigma-Aldrich. *N,N*-Dimethylformamide ($\geq 99.8\%$), and methanol ($\geq 99.9\%$) were purchased from Scharlab. Ultrapure water from Milli-Q equipment was used when required. All reagents and solvents were used without any previous purification unless specified.

S1.2. Physical and chemical characterization

- Inductively coupled plasma optical emission spectrometry (ICP-OES) was performed ex situ at the CAI de Técnicas Geológicas of the Universidad Complutense de Madrid. Solids were digested by immersion in HNO_3 , followed by heating at $100\text{ }^\circ\text{C}$ for 24 h in a closed Teflon digestion vessel. Analysis was performed on a SPECTRO Arcos ICP-OES analyzer.

- Scanning Electron Microscopy (SEM) and single point energy-dispersive X-Ray analysis (EDX): particle morphologies, dimensions and mapping were studied with a Hitachi S-4800 scanning electron microscope at an accelerating voltage of 20 kV, over metalized samples with a mixture of gold and palladium during 90 seconds.

- Powder X-Ray diffraction (PXRD) patterns were collected in a PANalytical X'Pert PRO diffractometer using copper radiation ($\text{Cu K}\alpha = 1.5418\text{ \AA}$) with an X'Celerator detector, operating at 40 mA and 45 kV. Profiles were collected in the $3^\circ < 2\theta < 40^\circ$ range with a step size of 0.017° . LeBail refinements were carried out with the FULLPROF software package. Rietveld refinements were carried out with Topas Academic 6 program (<http://www.topas-academic.net/>). The diffraction data used for the Rietveld refinement of the structure of MUV-101(Co) were collected in ALBA synchrotron (beamline BL04 – MSPD, $\lambda = 0.44265540\text{ \AA}$) with a step size of 0.003° using a 0.7 mm glass capillary and a MAD26 High Resolution Detector. Rietveld quantification of the relative fraction of MUV-10(Ca)/MUV-101(Co) phases at intermediate transformation stages was obtained from diffraction data collected in the same line ($\lambda = 0.41289619\text{ \AA}$) with a step size of 0.006° using a 0.7 mm glass capillary.

- Thermogravimetric analysis (TGA) were carried out with a Mettler Toledo TGA/SDTA 851 apparatus between 25 and $800\text{ }^\circ\text{C}$ under ambient conditions ($10\text{ }^\circ\text{C}\cdot\text{min}^{-1}$ scan rate and an air flow of $30\text{ mL}\cdot\text{min}^{-1}$).

- N_2 adsorption measurements were collected at 77 K with a Micromeritics 3Flex apparatus. Samples were exchanged with MeOH and degassed overnight at $150\text{ }^\circ\text{C}$ and 10^{-6} Torr in a Multisorb station prior to analysis.

- X-Ray Absorption Spectroscopy (XAS). Transmission geometry XAS measurements for combined X-ray Absorption Near Edge Structure (XANES) and Extended X-Ray Absorption Fine Structure (EXAFS) analyses were performed at ROCK beamline at the SOLEIL synchrotron and at the CLAESS beamline at the ALBA synchrotron. Data were collected at 77 K to minimize the signal to noise ratio. Ti *K*-edge XAFS spectra were acquired from 4850 to 5770 eV, resulting in a *k*-range up to 12 \AA^{-1} . Cu and Co *K*-edge XAFS spectra were acquired from 8800 to 9785 eV and 7555 and 8555 eV, respectively, resulting in a *k*-range up to 15 \AA^{-1} .

¹. The data analysis and background removal were performed within ATHENA and ARTEMIS.¹ The Fourier transform of the *k*-space EXAFS data were fitted to structural models using the FEFF9 code.²

-X-band (~ 9.3 GHz) Electron Spin Resonance spectra were collected in polycrystalline samples at 77 K with a Bruker ELEXYS E580 spectrometer.

- High-resolution scanning transmission electron microscopy. The chemical composition and elemental distribution of the samples have been analyzed under scanning transmission electron microscopy (STEM) conditions at 200 kV by means of X-Ray spectroscopy (EDX). The samples were coated with a Pt/Pd protective layer in a Leica EM SCD500 instrument and, then, TEM specimens were obtained by focus ion beam (FIB) in a Zeiss Auriga Cross-Beam Station operated at 30 kV, following the in situ lift-out method.³ Preliminary studies were carried out using a Jeol2100, while higher quality compositional maps were obtained either in a Themis Titan FEI microscope (MUV-101(Co)-30d in Figure 4b) or in a FEI TALOS F200S (MUV-101(Co)-1d in Figure 4a), equipped with Super-X energy dispersive X-ray spectrometry systems including silicon drift detectors (FEI ChemiSTEM), provided with their specific software for acquisition and data processing (Oxford INCA® and Thermo Fisher Velox® software, respectively). The Titan microscope employed is equipped with four EDX detector segments, achieving a higher collection solid angle than that of the Talos instrument equipped with only two EDX detector segments (and, thus, poorer efficiency). The measurements were performed by spectrum imaging (i.e., scanning the electron probe on the area of interest and collecting one EDX spectrum every pixel) optimizing the pixel size and exposure time for every case, rendering 2D maps of the different constituents after data processing.

S2. GENERAL PROCEDURE TO THE TRANSMETALLATION OF MUV-10(Ca) WITH M^{n+}

Crystals of MUV-10(Ca) were synthesized by following the synthesis reported,¹⁹ washed by soxhlet extraction with MeOH overnight and dried under vacuum at room temperature prior to metal exchange reactions. After this treatment, 100 mg of polycrystalline powder was suspended in 10 mL of 0.2 M methanolic solutions of the corresponding metal ($M(\text{NO}_3)_2 \cdot x\text{H}_2\text{O}$ ($M = \text{Co}, \text{Cu}, \text{Ni}$ and Zn), MCl_2 ($M = \text{Mn}$ and Fe)) and kept static in the oven at 65 °C. The mixture was kept in these conditions at variable time. Samples were isolated by centrifugation, washed 3 times by resuspending in fresh solvent and dried at room temperature under vacuum.

S3. TRANSMETALATION OF MUV-10(Ca) WITH Mn²⁺

S3.1. Experimental metal content

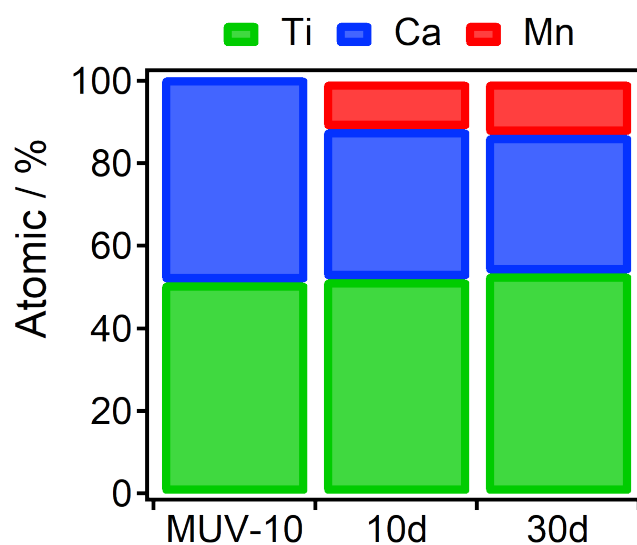


Figure S1. Experimental metal content in MUV-10(CaMn) after 0, 10 and 30 days of reaction. Experimental metal content in MUV-10(CaMn) determined by EDX analysis.

Table S1. Experimental metal content determined by EDX analysis.

Sample	^[a] Normalized	
	Mn [at. %]	Ca [at. %]
MUV-10(CaMn)-10d	11.6 ± 0.1	36.3 ± 0.1
MUV-10(CaMn)-30d	13.0 ± 0.1	31.6 ± 0.2

^[a] Calculated by normalizing to total M²⁺ content.

S3.2. Scanning Electron Microscopy (SEM) and single point mapping

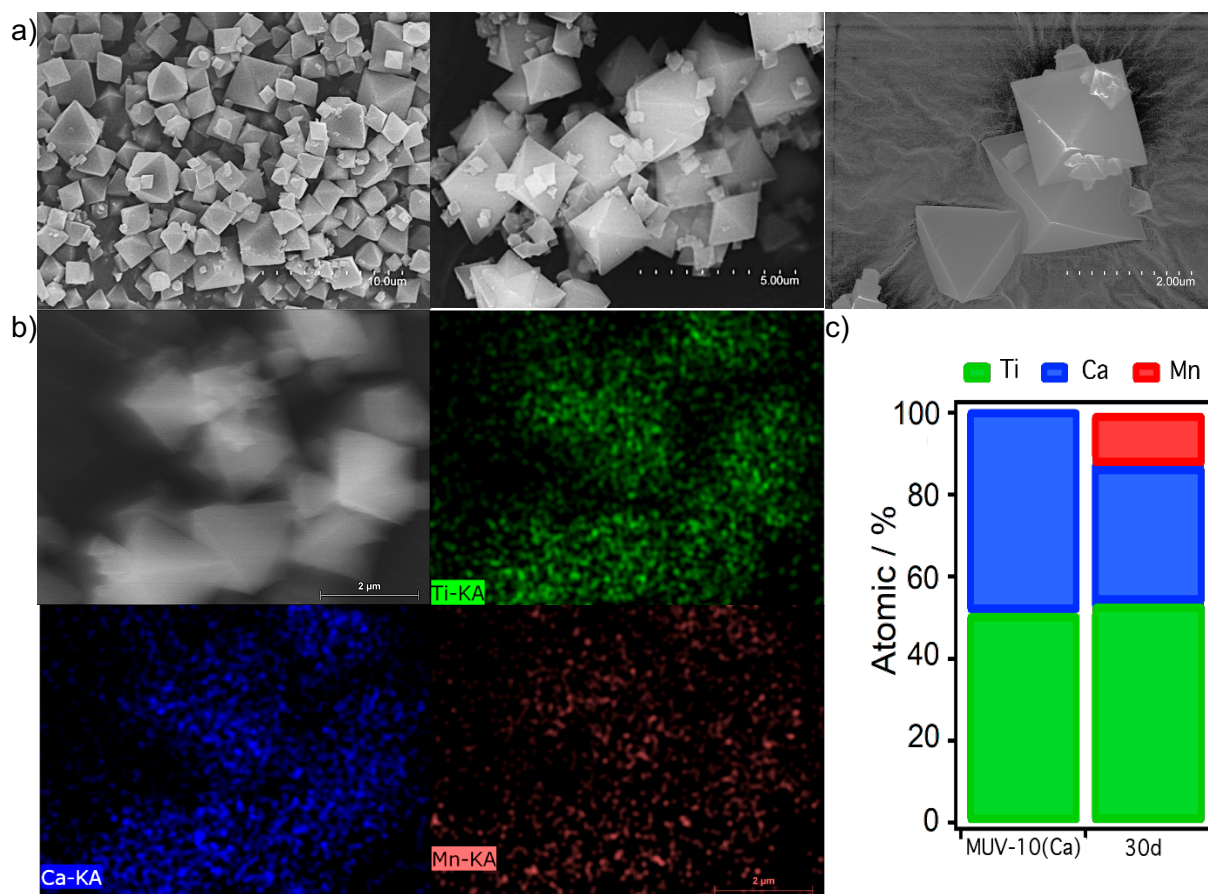
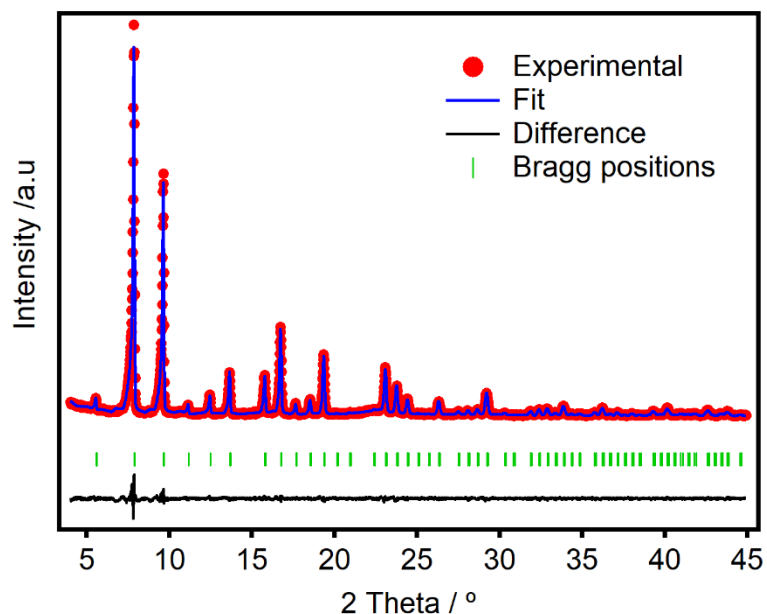
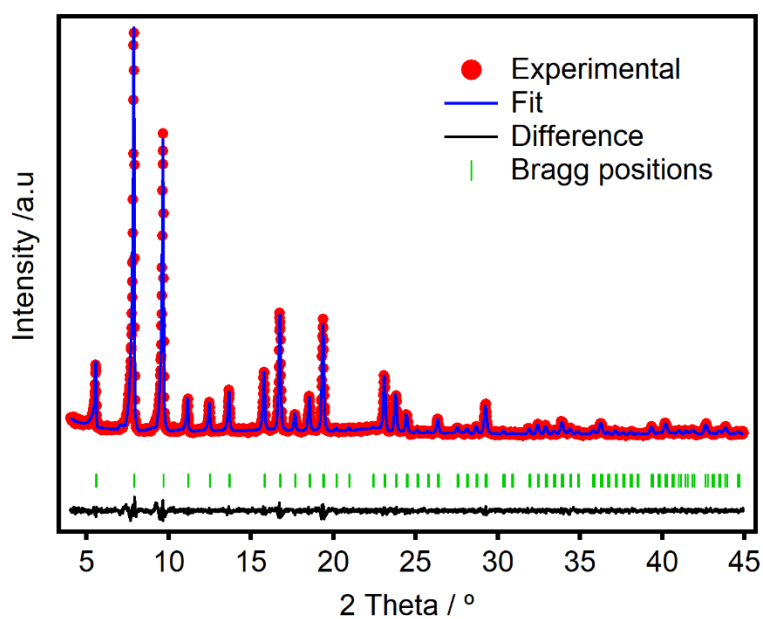


Figure S2. (a) SEM microscopy, (b) mapping and (c) energy-dispersive X-Ray analysis (EDX) of MUV-10(MnCa) after 30 days. Mapping of Mn (red), and Ca (blue) confirms that metal distribution is homogeneous throughout the crystals.

S3.3. Powder X-Ray Diffraction (PXRD)



Cubic, Pm-3; $a = b = c$ 15.8691 Å; $\alpha = \beta = \gamma = 90^\circ$; $V = 3996.3076$ Å³; $R_e = 5.47$ %, $R_p = 7.28$ %, $R_{wp} = 4.85$ %, $GoF = 1.5$.



Cubic, Pm-3; $a = b = c$ 15.8572 Å; $\alpha = \beta = \gamma = 90^\circ$; $V = 3987.3174$ Å³; $R_e = 7.15$ %, $R_p = 9.74$ %, $R_{wp} = 7.49$ %, $GoF = 1.3$.

Figure S3. Experimental (red dots), calculated (blue line), difference plot $[(obs - calc)]$ (black line, bottom panel) and Bragg positions (green ticks, bottom panel) for the LeBail refinement of experimental diffraction data of MUV-10(CaMn) after: (top) 10 days and (bottom) 30 days.

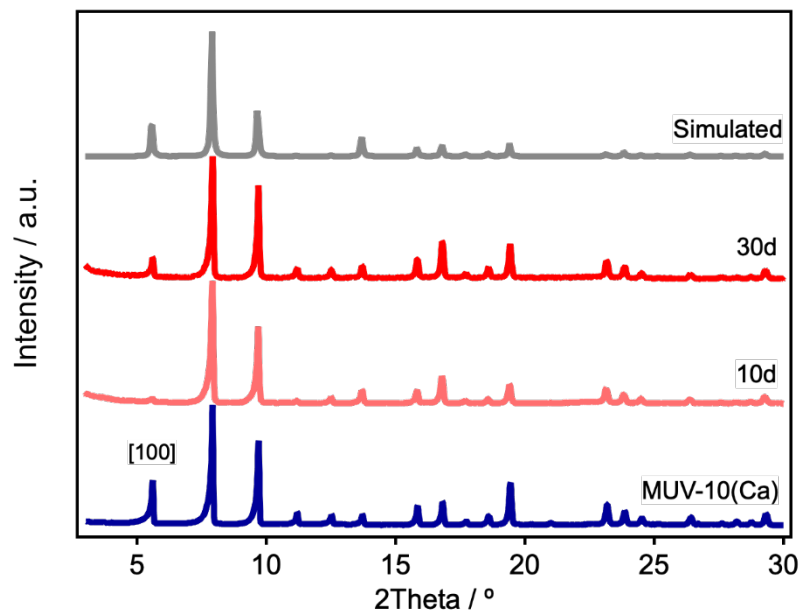


Figure S4. PXRD of MUV-10(Ca) simulated from CCDC1819267⁴ (grey), MUV-10(CaMn) after 10 days and after 30 days confirming the structural integrity of the material after metal exchange.

S3.4. Analysis of N₂ adsorption/desorption isotherms at 77 K

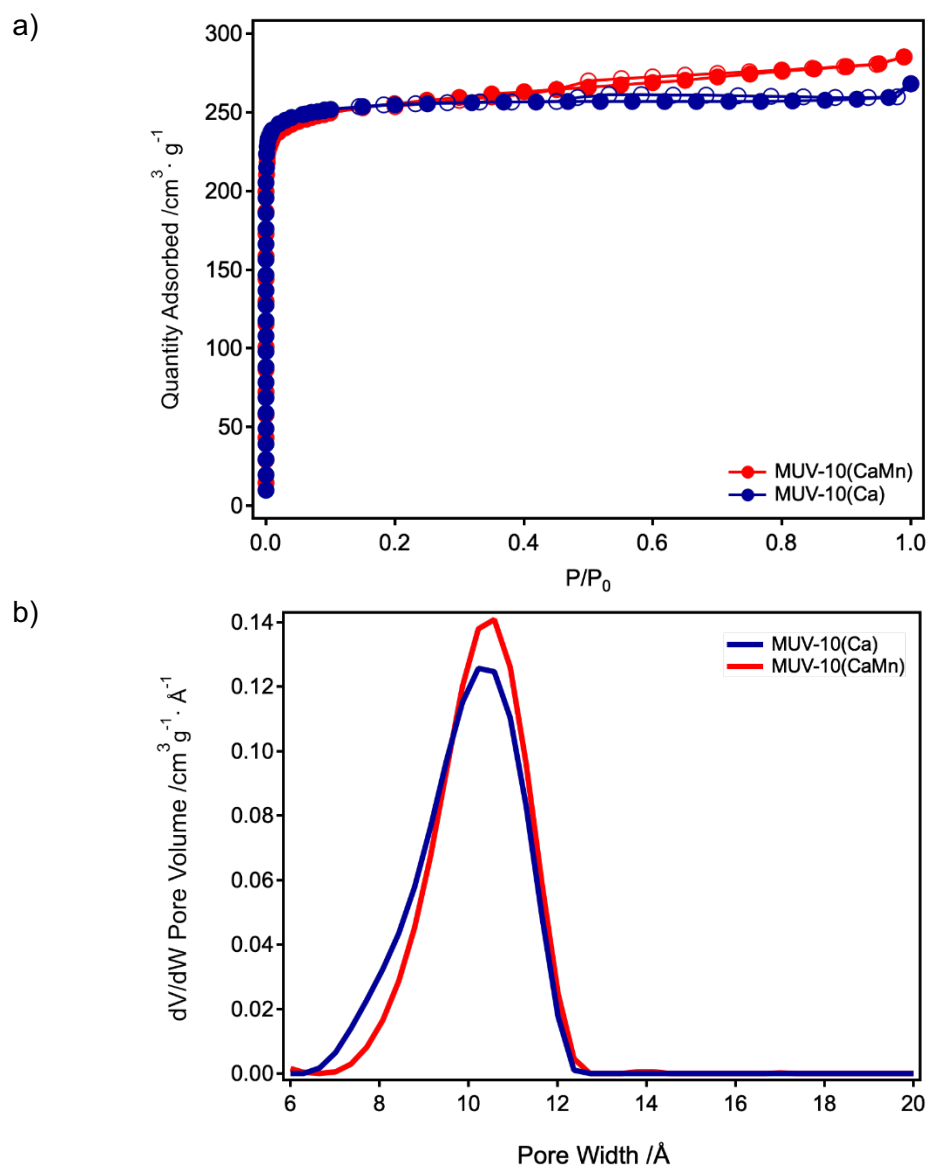


Figure S5. Analysis of the N₂ adsorption/desorption isotherm of MUV-10(Ca) and MUV-10(CaMn)-30d at 77 K. Total pore volume (V_t) was estimated at $P/P_0=0.96$. a) N₂ adsorption isotherm, b) Pore size distribution (PSD) was analysed by using the solid density functional theory (NLDFT) for the adsorption branch by assuming a cylindrical pore model.

Table S2. Main parameters calculated from the multi-point BET analysis and PSD analysis.

Sample	SA_{BET} [m ² ·g ⁻¹]	V_t [cm ³ ·g ⁻¹]	PSD _{NLDFT} [nm]	
			micro	meso
MUV-10(Ca)	1041	0.40	1.1	---
MUV-10(CaMn)-30d	1018	0.43	1.1	---

S3.5. CHEMICAL STABILITY

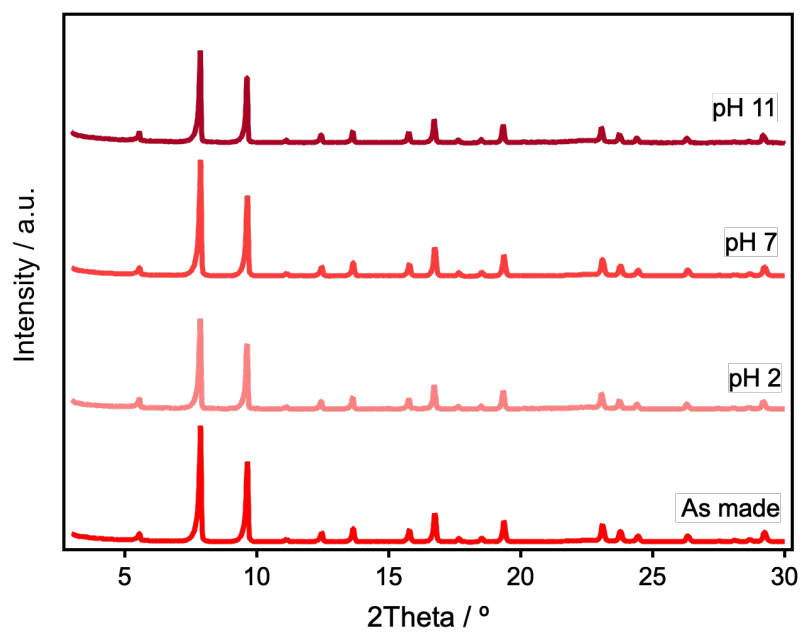
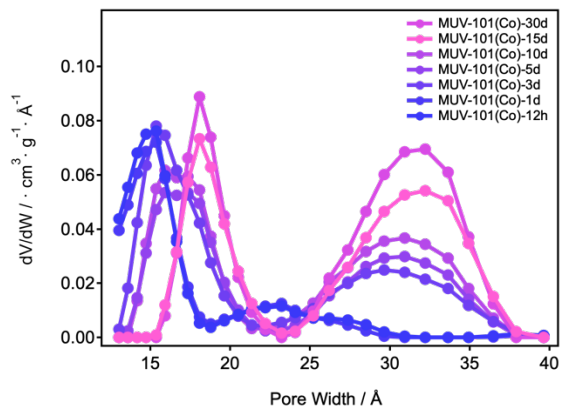
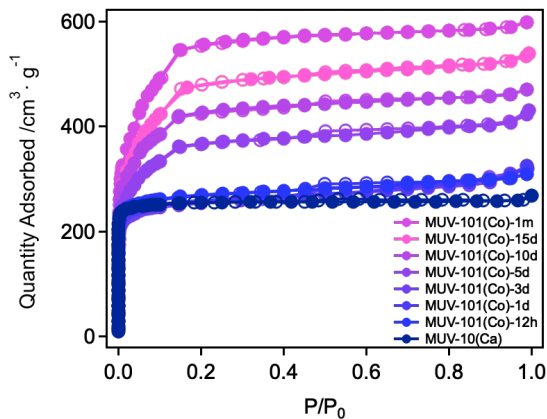
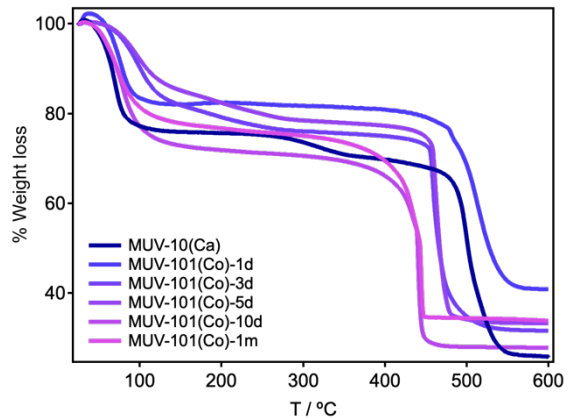
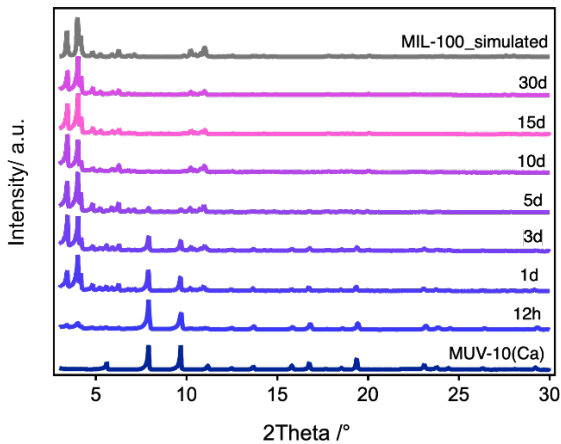
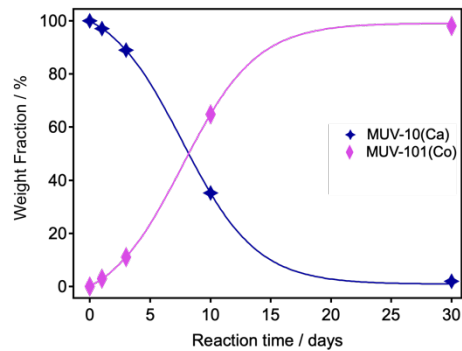
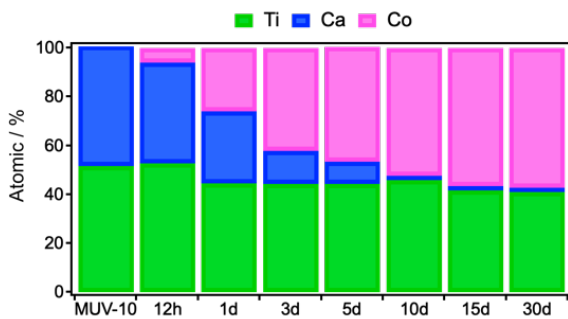
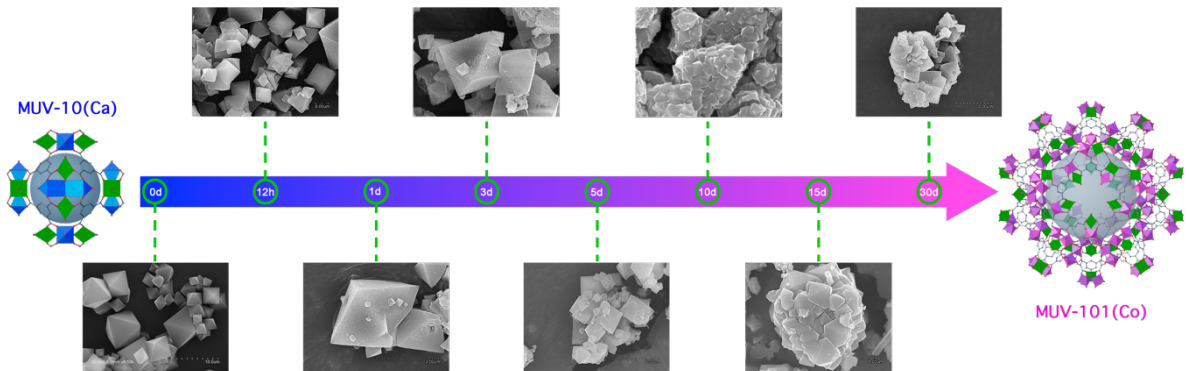


Figure S6. PXRD of MUV-10(CaMn)-30d after soaking in aqueous solution at pH 2, 7 and 11 during 24 hours ruling out structural degradation of the solid after metal exchange.

S4. TRANSFORMATION OF MUV-10(Ca) IN MUV-101(Co) BY METAL EXCHANGE WITH Co^{2+}

S4.1. MUV-101(Co) at a Glance



S4.2. Evolution of metal content with time

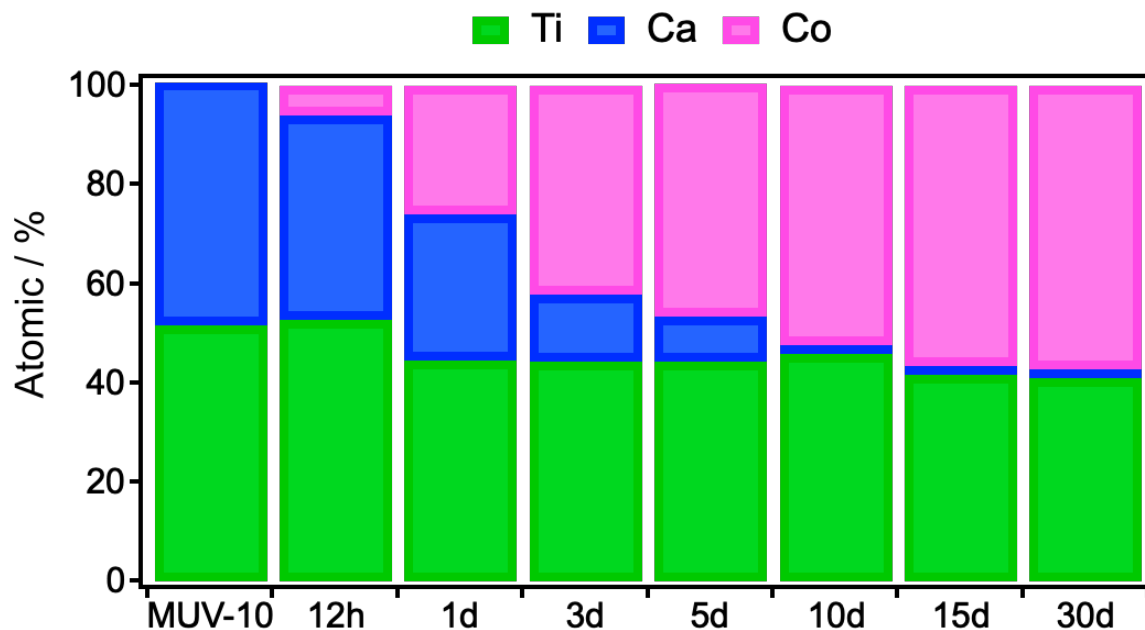


Figure S7. Evolution of the metal content (calcium, titanium and cobalt) in the crystals isolated for the different stages of transformation of MUV-10(Ca) into MUV-101(Co). Experimental values were determined by EDX analysis with a Hitachi S-4800 scanning electron microscope at an accelerating voltage of 20 keV.

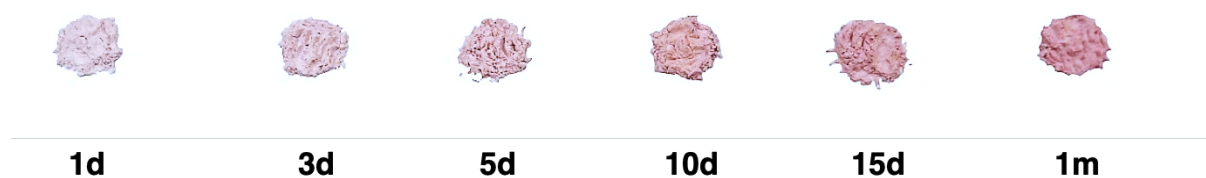


Figure S8. The incorporation of cobalt concomitant to the formation of in MUV-101(Co) is associated to a gradual color change from white to pink.

Table S3. Experimental metal content determined by EDX analysis.

Sample	^[a] Normalized		
	Ca [%]	Ti [%]	Co [%]
MUV-101(Co)-12h	41.1 ± 0.3	52.9 ± 0.4	6.0 ± 0.1
MUV-101(Co)-1d	29.4 ± 0.1	44.6 ± 0.2	26.1 ± 0.1
MUV-101(Co)-3d	13.5 ± 0.1	44.4 ± 0.3	42.1 ± 0.4
MUV-101(Co)-5d	10.6 ± 0.1	45.9 ± 0.4	43.5 ± 0.4
MUV-101(Co)-10d	3.3 ± 0.1	42.1 ± 0.3	54.7 ± 0.5
MUV-101(Co)-15d	0.9 ± 0.0	45.7 ± 0.4	53.5 ± 0.5
MUV-101(Co)-30d	0.1 ± 0.0	41.2 ± 0.2	58.8 ± 0.3

^[a] Calculated by normalizing to total M²⁺ content.

ICP-OES confirmed the evolution of the metal content observed by EDX analysis. Both techniques provide consistent values with small deviations within the experimental error. The 1d, 3d and 5d samples were selected because their drastic changes in the metal content .

Table S4. Comparison of metal content determined by EDX analysis and ICP-OES.

Time	^[a] EDX			ICP-OES		
	Ca [%]	Ti [%]	Co [%]	Ca [%]	Ti [%]	Co [%]
1 d	29.4	44.6	26.1	28.3	42.5	29.2
3 d	13.5	44.4	42.1	15.1	48.3	36.6
5 d	10.6	45.9	43.5	12.4	44.7	42.9

^[a] Calculated by normalizing to total M²⁺ content.

S4.3. Scanning Electron Microscopy (SEM) and single point mapping

Scanning Electron microscopy and single point energy-dispersive X-Ray analysis (EDX) of the transformation of MUV-10(Ca) into MUV-101(Co) from 12 hours to 30 days. Analysis was performed with a Hitachi S-4800 scanning electron microscope at an accelerating voltage of 20 keV. Mapping of Ti (green), Ca (blue) and Co (pink) confirm that metal distribution is homogeneous throughout the crystals.

MUV-101(Co)-12h

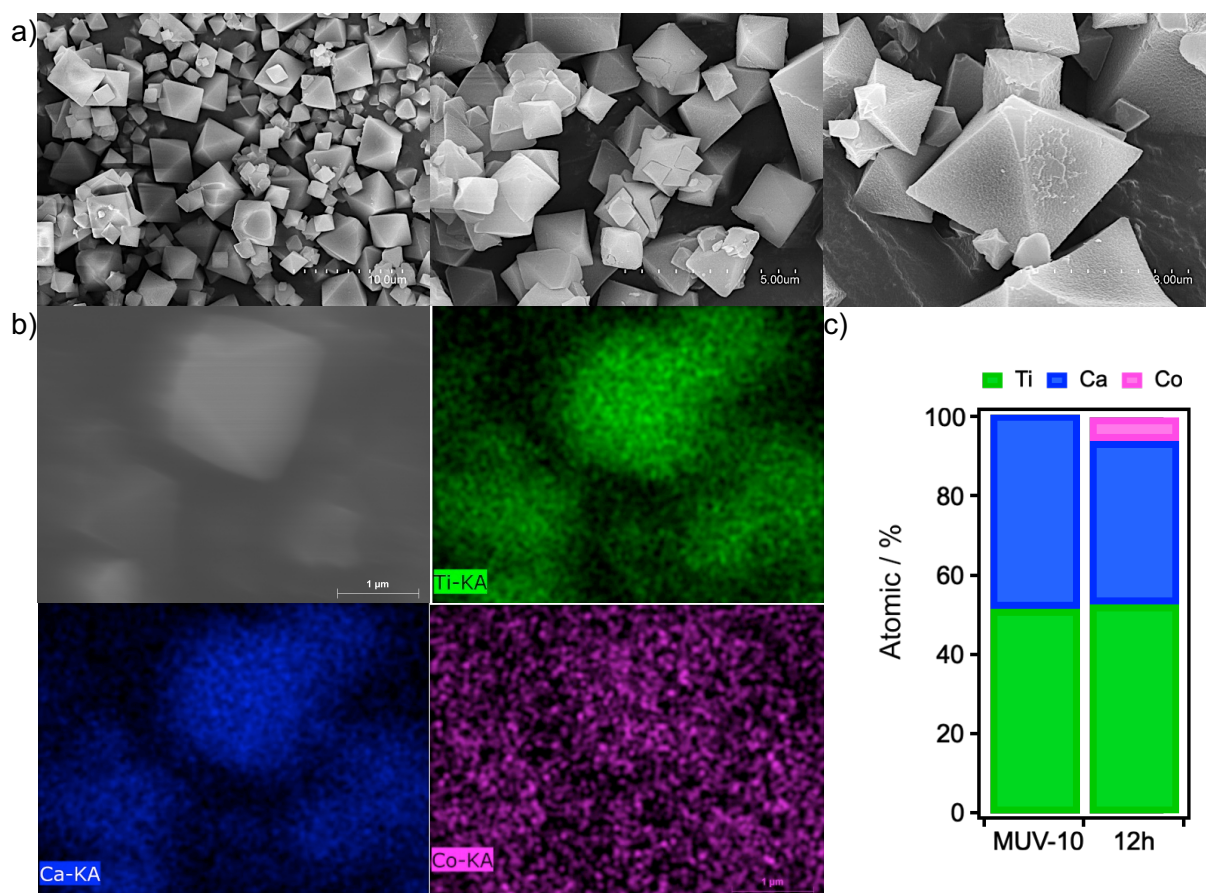


Figure S9. MUV-101(Co)-12h: a) SEM images; b) Mapping of Ti (green), Ca (blue) and Co (pink); c) experimental atomic percentage from point and shoot EDX analysis for diferent crystals.

MUV-101(Co)-1d

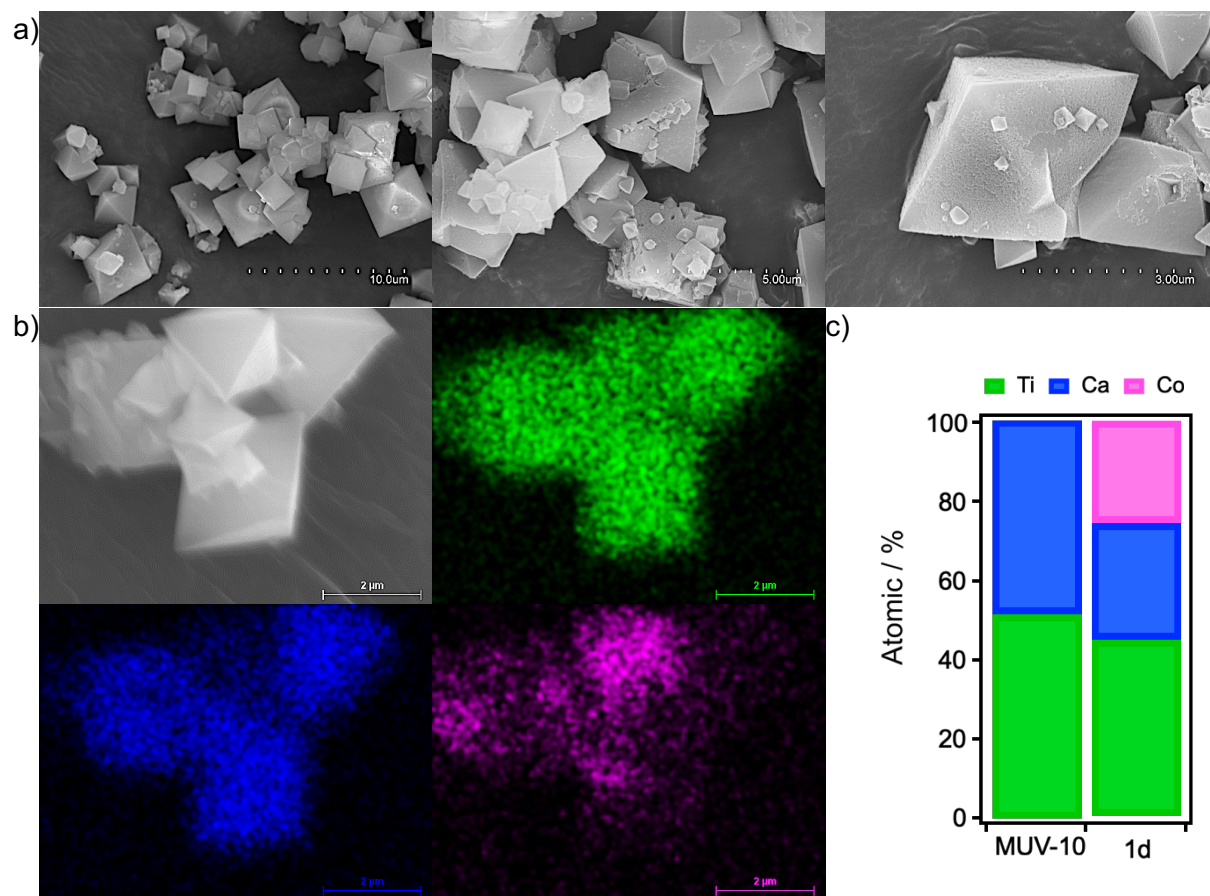


Figure S10. MUV-101(Co)-1d: a) SEM images; b) Mapping of Ti (green), Ca (blue) and Co (pink); c) experimental atomic percentage from point and shoot EDX analysis for different crystals.

MUV-101(Co)-3d

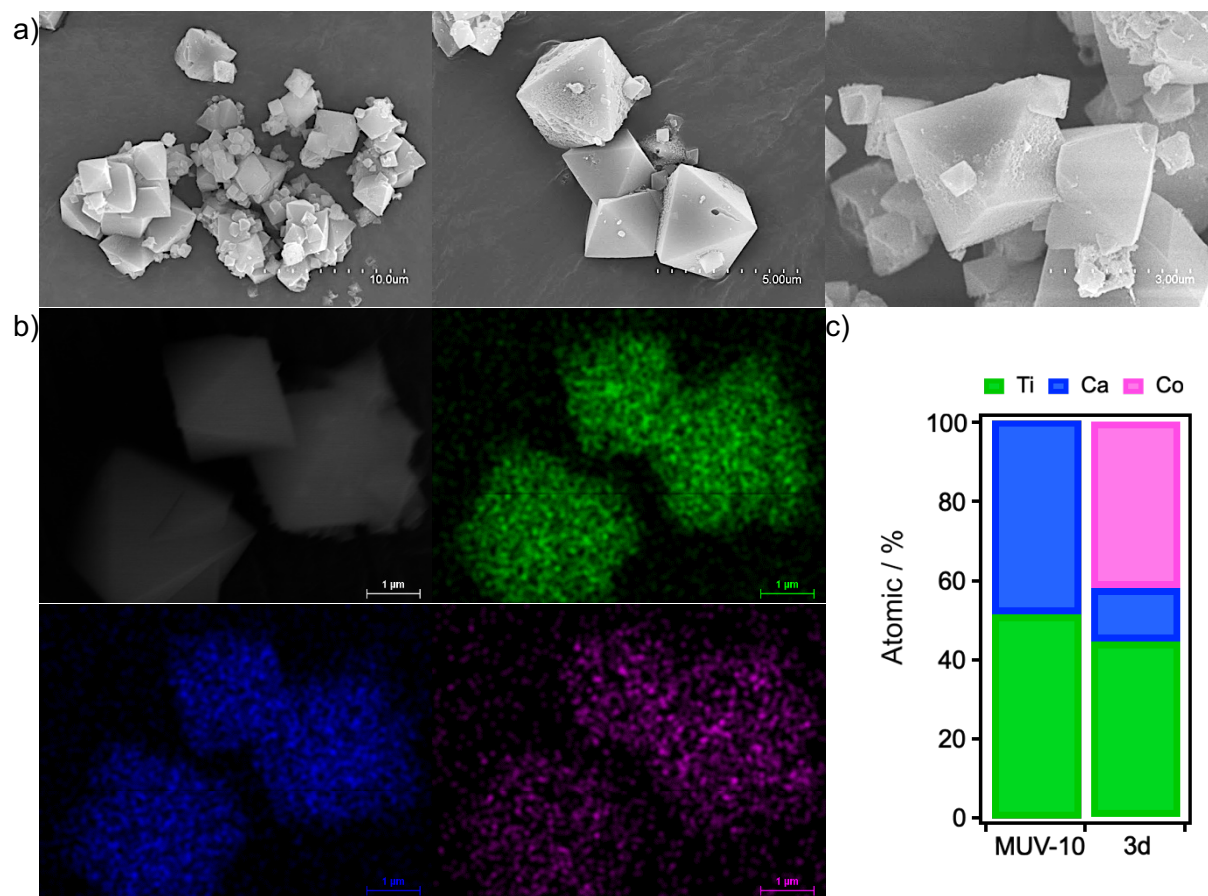


Figure S11. MUV-101(Co)-3d: a) SEM images; b) Mapping of Ti (green), Ca (blue) and Co (pink); c) experimental atomic percentage from point and shoot EDX analysis for different crystals.

MUV-101(Co)-5d

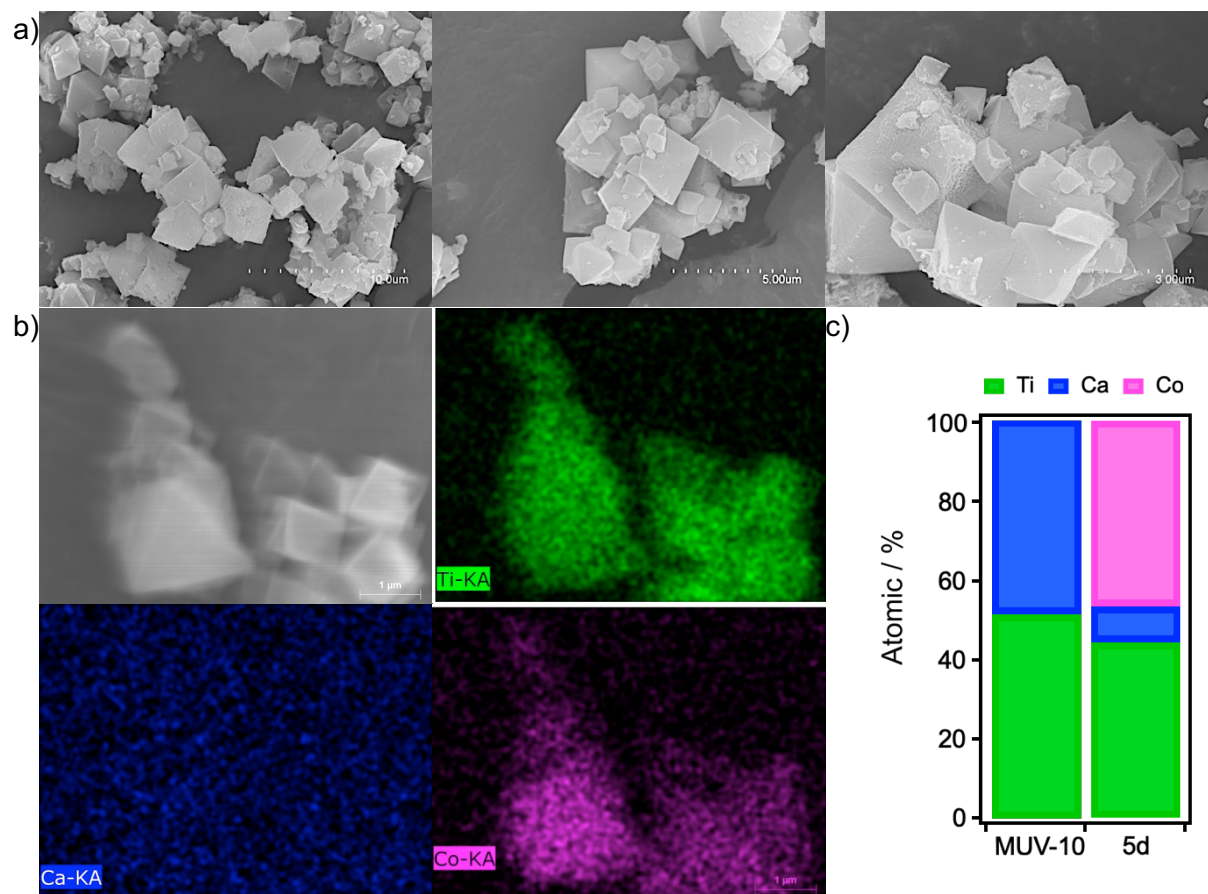


Figure S12. MUV-101(Co)-5d: a) SEM images; b) Mapping of Ti (green), Ca (blue) and Co (pink); c) experimental atomic percentage from point and shoot EDX analysis for different crystals.

MUV-101(Co)-10d

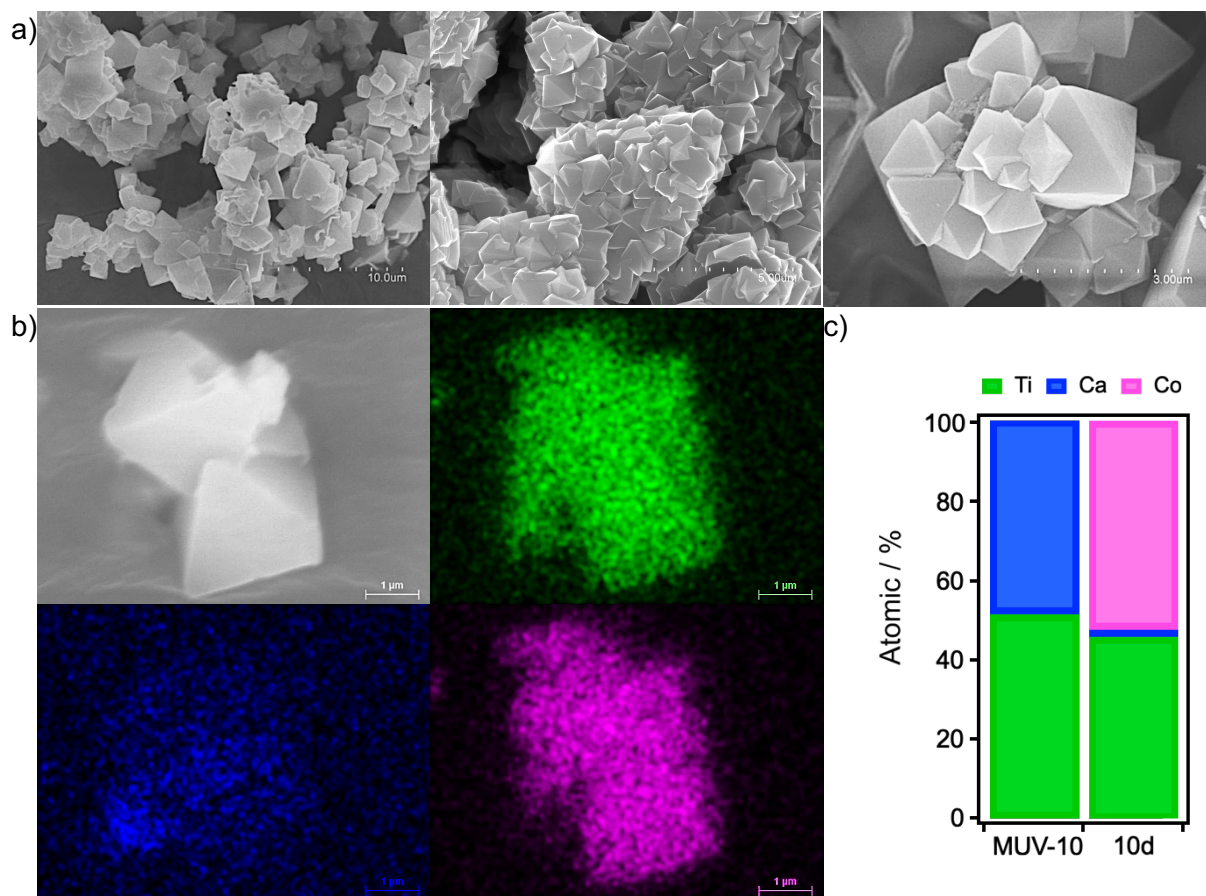


Figure S13. MUV-101(Co)-10d: a) SEM images; b) Mapping of Ti (green), Ca (blue) and Co (pink); c) experimental atomic percentage from point and shoot EDX analysis for different crystals.

MUV-101(Co)-15d

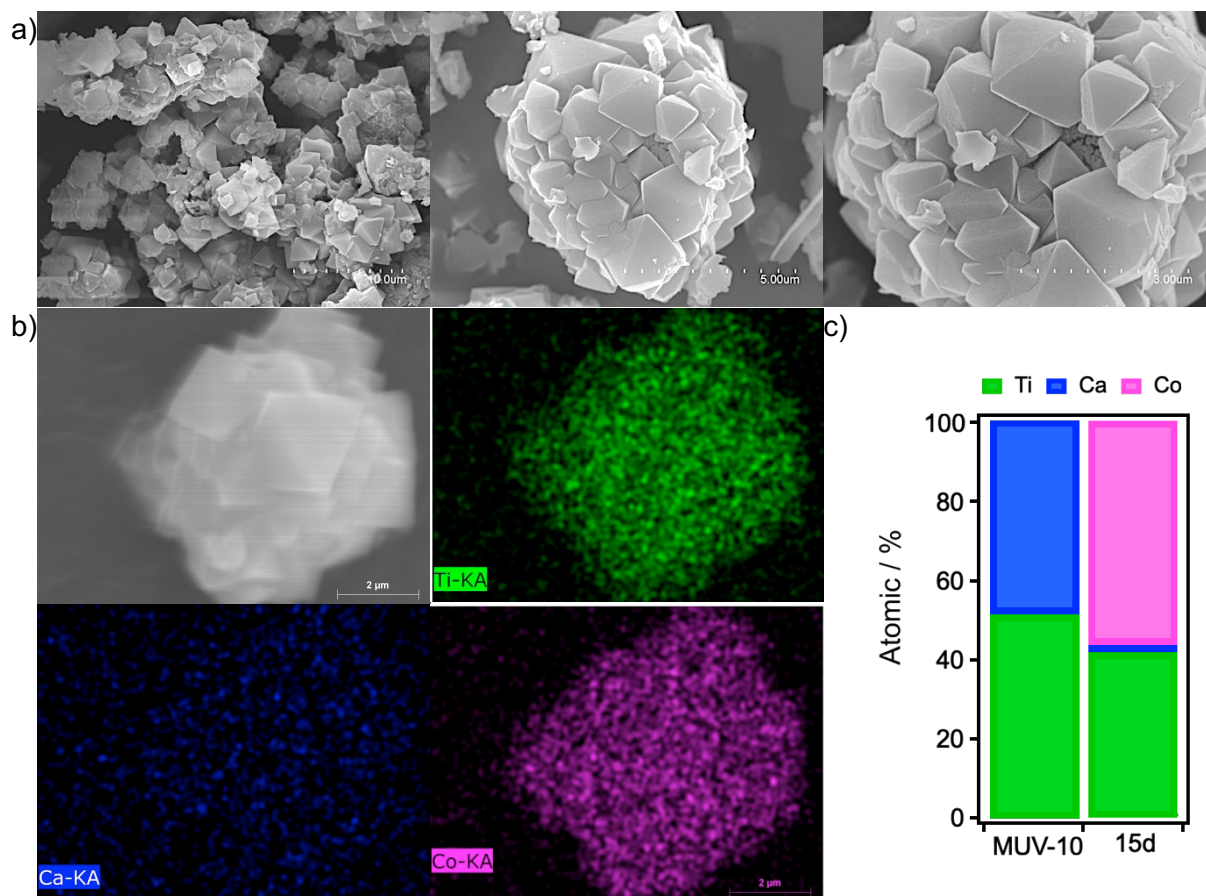


Figure S14. MUV-101(Co)-15d: a) SEM images; b) Mapping of Ti (green), Ca (blue) and Co (pink); c) experimental atomic percentage from point and shoot EDX analysis for different crystals.

MUV-101(Co)-30d

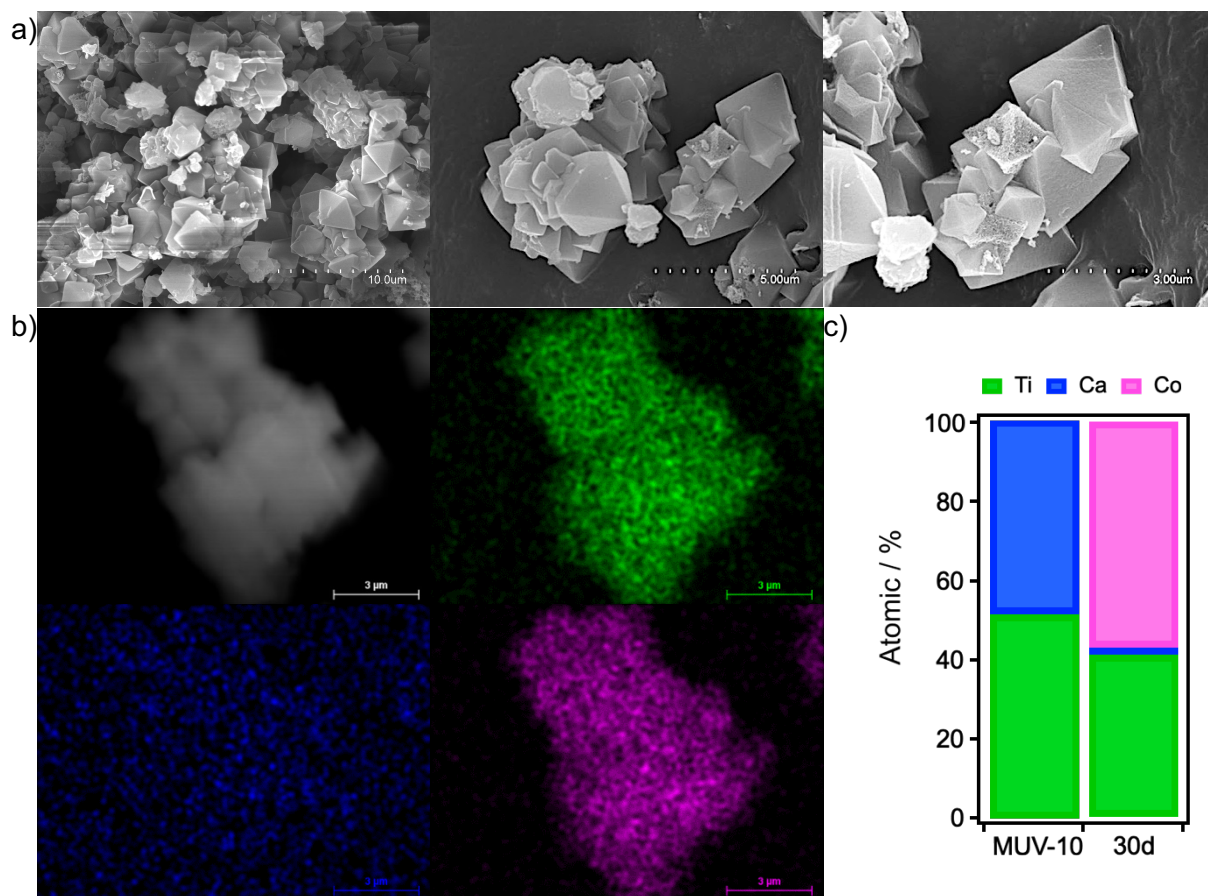


Figure S15. MUV-101(Co)-30d: a) SEM images; b) Mapping of Ti (green), Ca (blue) and Co (pink); c) experimental atomic percentage from point and shoot EDX analysis for different crystals.

S4.4. Rietveld refinement and crystallographic data of MUV-101(Co)

PXRDs were collected in ALBA synchrotron (beamline BL04 – MSPD, $\lambda = 0.44265540 \text{ \AA}$) with a step size of 0.003° using a 0.7 mm glass capillary and a MAD26 High Resolution Detector. The structure reported for MIL-100(Ti) (CCDC 1871195)⁵ was used as the starting model to guide Rietveld refinement, which was carried out with Topas Academic 6 program (<http://www.topas-academic.net/>). The six crystallographically independent organic linkers were modelled using semi-rigid bodies, where selected bond distances, bond angles and torsion angles could be refined. Fixed occupancies of 1/3 and 2/3 were assigned to Ti and Co atoms, respectively, which are sharing crystallographic sites in the crystal structure. Some distance restraints were needed to be included in the refinement, in order to keep the Ti/Co-O bond distances within reasonable values. After the framework structure was well described in the refinement, the approximate water molecules' positions in the pores were found by means of difference Fourier maps. These water molecules were described as single O atoms, which could freely translate inside the pores. Background was fitted with a 24-coefficients Chebyshev polynomial and peak shapes were modelled with a Thompson-Cox-Hasting pseudo-Voigt profile function. Crystallographic parameters from the final Rietveld refinement are summarized below.

Table S5. Crystallographic data and Rietveld refinement of MUV-101(Co).

CCDC id code	1965235
Empirical formula	$C_{306}H_{102}O_{272}Ti_{17}Co_{34}, O_{118.8}$
Formula weight	12848.29
Cryst. Syst.	Cubic
Space group	Fd-3m
a, Å	73.5784(8)
α, °	90
V, Å³	398338(13)
Z	16
Temperature, K	298
Wavelength, Å	0.44265540
2θ range, °	0.15 - 15
Number of reflections	2259
Number of structural/total variables	151 / 182
R_p, %	5.13
R_{wp}, %	7.00
R_{exp}, %	3.95
GoF	1.77

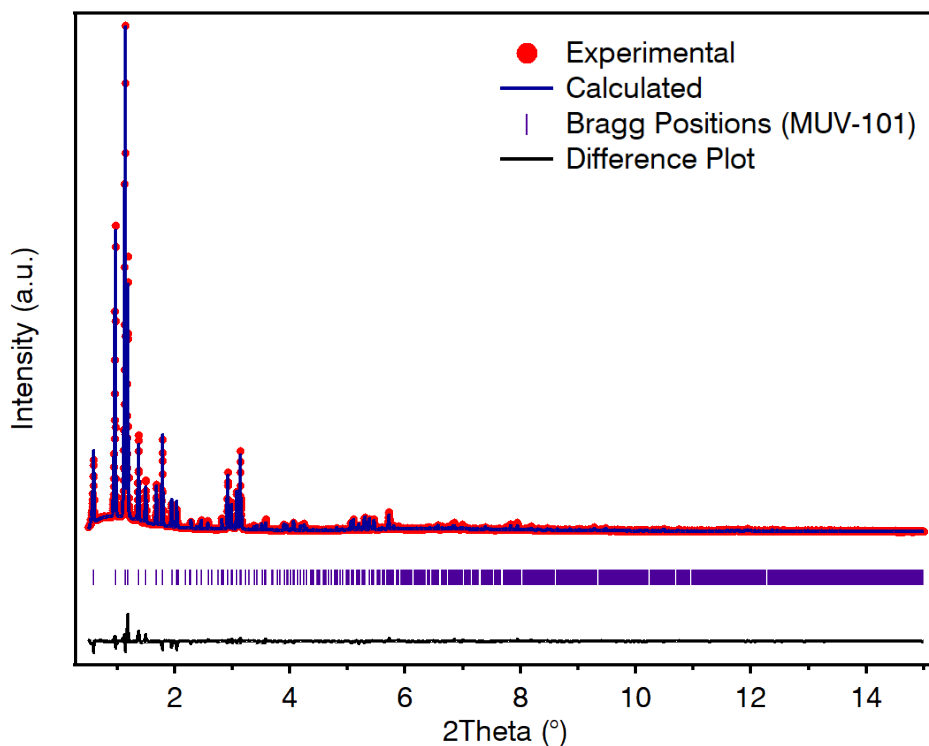


Figure S16. Experimental (red dots), calculated (blue line), difference plot $[(I_{obs}-I_{calc})]$ (black line, bottom panel) and Bragg positions (blue ticks, bottom panel) for the Rietveld refinement of the experimental diffraction data of activated MUV-101(Co)-40d.

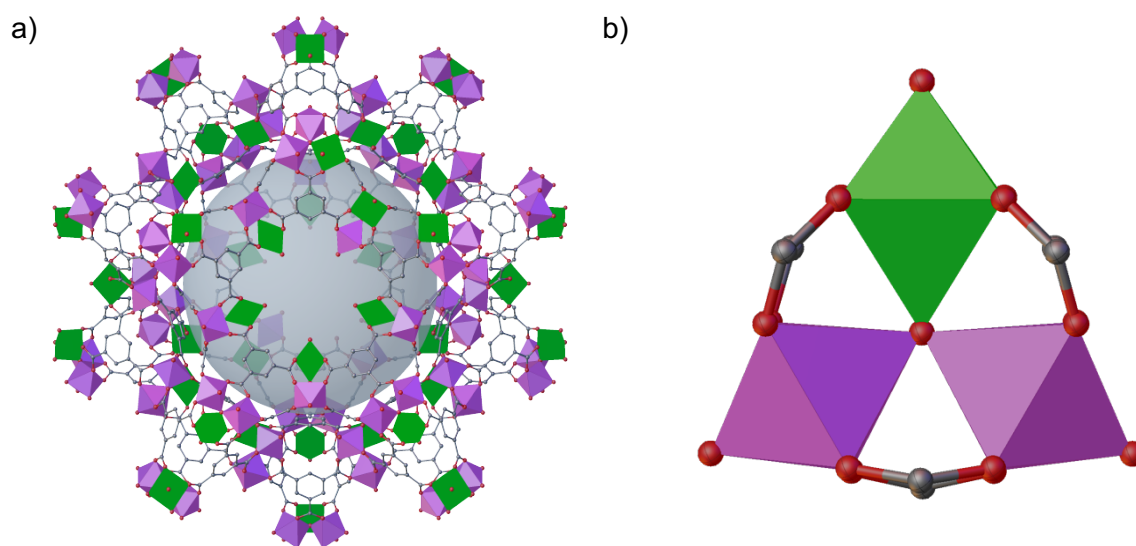


Figure S17. a) Structure of MUV-101(Co) built from from the interlinking of b) heterometallic 6-c $[\text{TiCo}_2(\mu_3\text{-O})(\text{RCO}_2)_6(\text{H}_2\text{O})_3]$ SBUs with 3-c trimesate linkers.

S4.5. Powder X-Ray Diffraction (PXRD)

MUV-101(Co)-12h

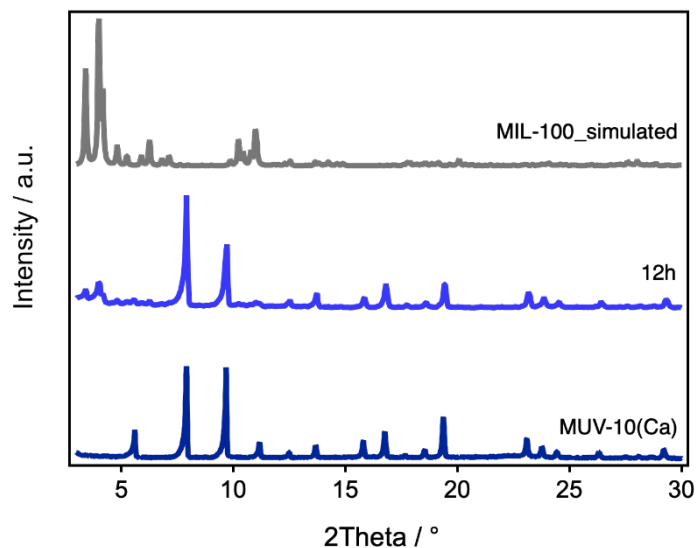


Figure S18. PXRD comparison of MUV-10(Ca) (bottom), MUV-101(Co)-12h (middle) and simulated MIL-100 (top).

MUV-101(Co)-1d

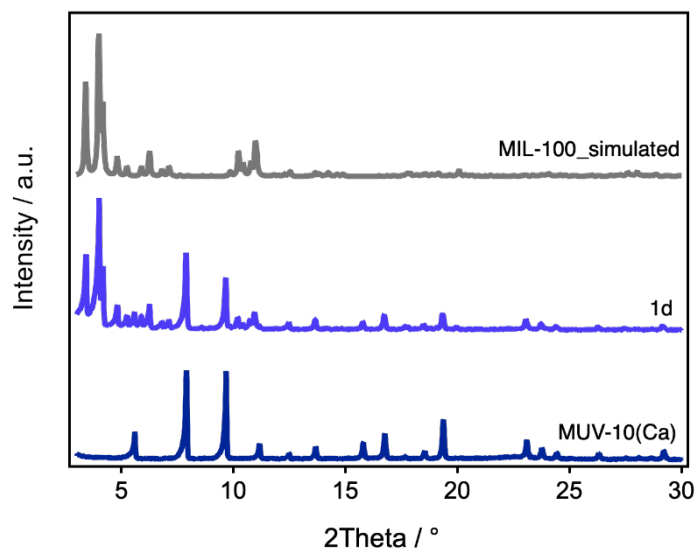


Figure S19. PXRD comparison of MUV-10(Ca) (bottom), MUV-101(Co)-1d (middle) and simulated MIL-100 (top).

MUV-101(Co)-3d

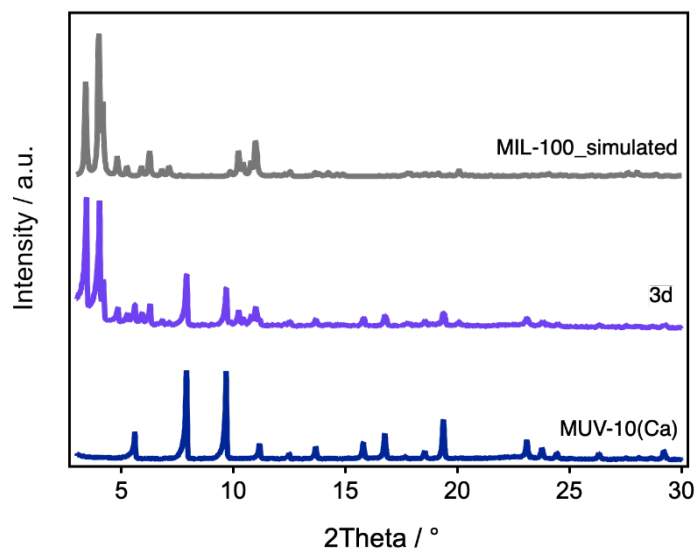


Figure S20. PXRD comparison of MUV-10(Ca) (bottom), MUV-101(Co)-3d (middle) and simulated MIL-100 (top).

MUV-101(Co)-5d

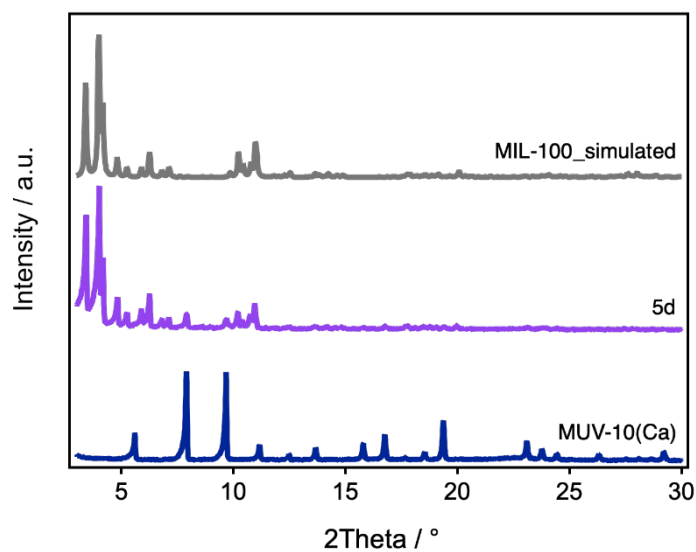


Figure S21. PXRD comparison of MUV-10(Ca) (bottom), MUV-101(Co)-5d (middle) and simulated MIL-100 (top).

MUV-101(Co)-10d

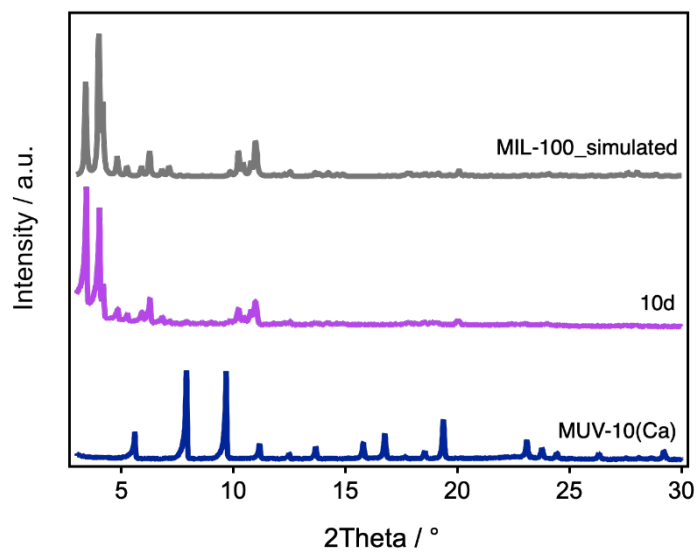


Figure S22. PXRD comparison of MUV-10(Ca) (bottom), MUV-101(Co)-10d (middle) and simulated MIL-100 (top).

MUV-101(Co)-15d

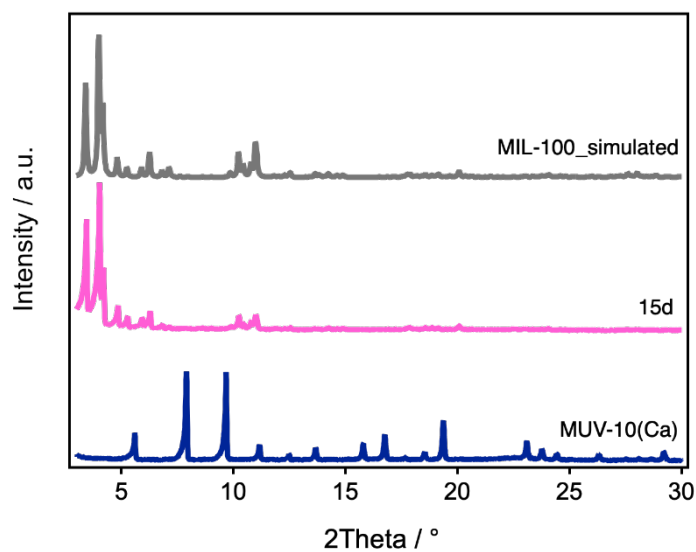


Figure S23. PXRD comparison of MUV-10(Ca) (bottom), MUV-101(Co)-15d (middle) and simulated MIL-100 (top).

MUV-101(Co)-30d

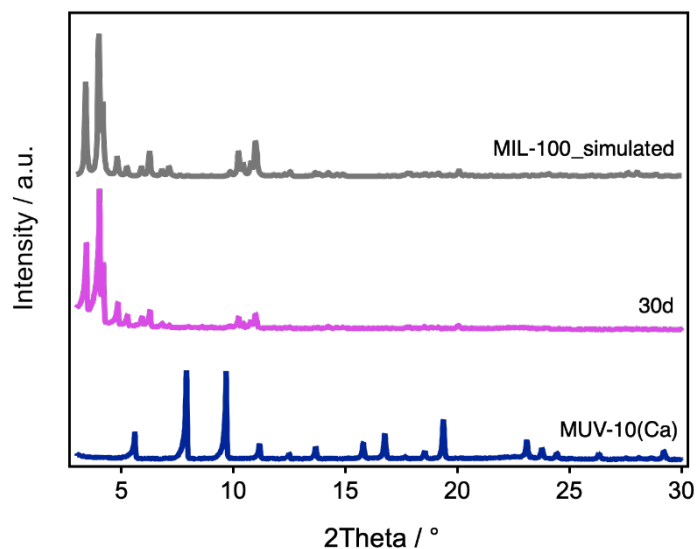


Figure S24. PXRD comparison of MUV-10(Ca) (bottom), MUV-101(Co)-30d (middle) and simulated MIL-100 (top).

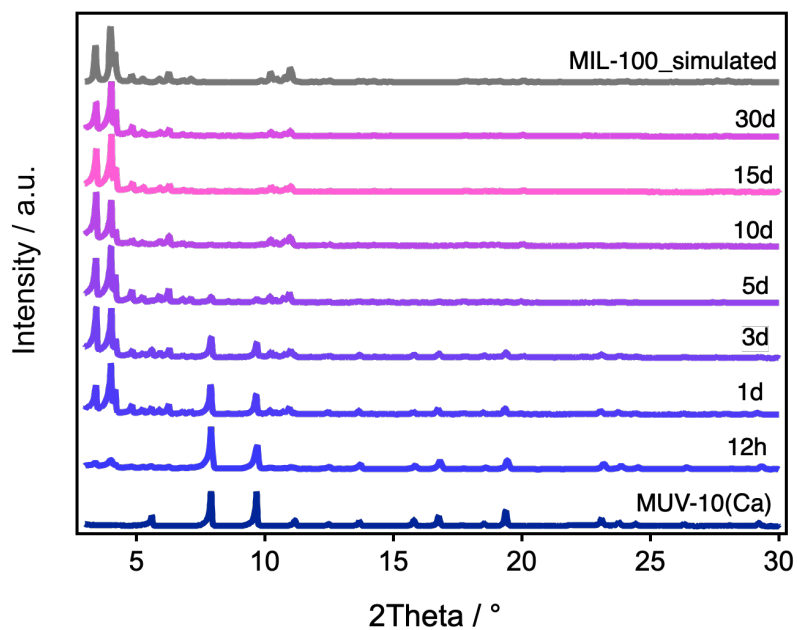
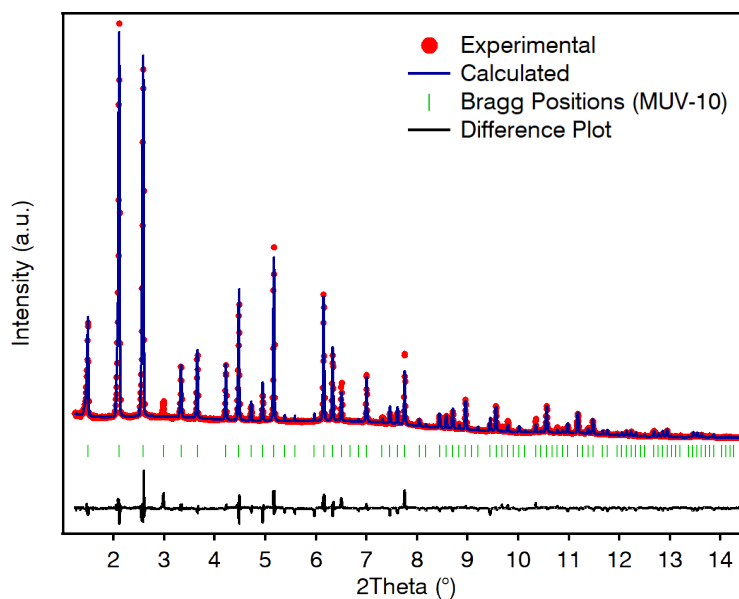


Figure S25. PXRD comparison of the transformation of MUV-10(Ca) into MUV-101(Co) from 12 hours to 30 days.

S4.6. Rietveld quantification of the relative percentage of MUV-10/MUV-101 phases at intermediate stages of transformation

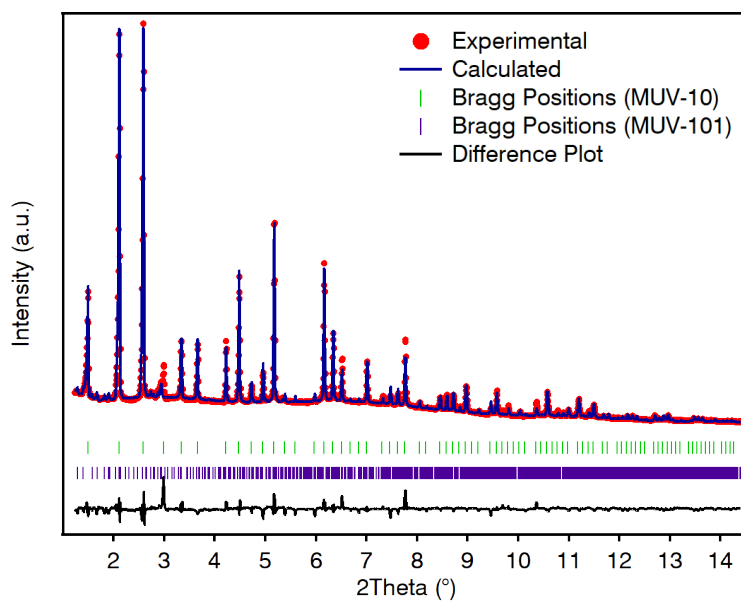
PXRDs were collected in ALBA synchrotron (beamline BL04 – MSPD, $\lambda = 0.41289619 \text{ \AA}$) with a step size of 0.006° using a 0.7 mm glass capillary and a MAD26 High Resolution Detector. The percentage of phases were calculated by Rietveld refinement. carried out with Topas Academic 6 program (<http://www.topas-academic.net/>). Background was fitted with a 24-coefficients Chebyshev polynomial and peak shapes were modelled with a Thompson-Cox-Hasting pseudo-Voigt profile function. Experimental (red dots), calculated (blue line), difference plot $[(\text{obs}-\text{calc})]$ (black line, bottom panel) and Bragg positions (green ticks, bottom panel) for the Le Bail refinement of experimental diffraction data used to calculate the relative phase percentages of the transformation of MUV-10(Ca) into MUV-101(Co) after 1, 3, 10 and 30 days.



0 Days: Rietveld Refinement of MUV-10(Ca), 100 %, MUV-101(Co), 0 %. Cubic, $Pm\bar{3}$; $a = b = c = 15.8642 \text{ \AA}$; $\alpha = \beta = \gamma = 90^\circ$; $V = 3992.608 \text{ \AA}^3$; $R_{\text{exp}} = 2.98 \%$, $R_p = 3.09 \%$, $R_{\text{wp}} = 4.89 \%$, $\text{GoF} = 1.64$.

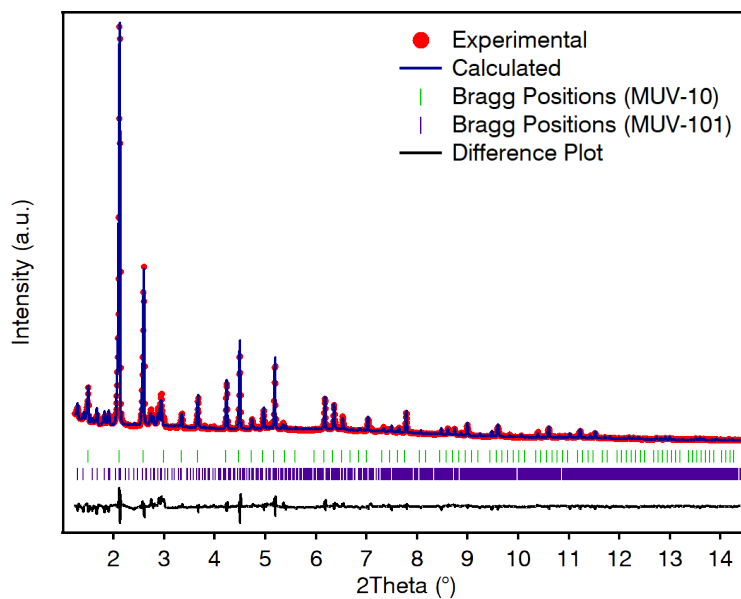
Figure S26. Rietveld refinement of MUV-10(Ca).

a)



1 Day: Rietveld Refinement of MUV-101(Co)-1d, MUV-10(Ca): 97.03 %, MUV-101(Co): 2.97 %. $R_{\text{exp}} = 2.74$ %, $R_p = 3.03$ %, $R_{\text{wp}} = 4.90$ %, $\text{GoF} = 1.79$.

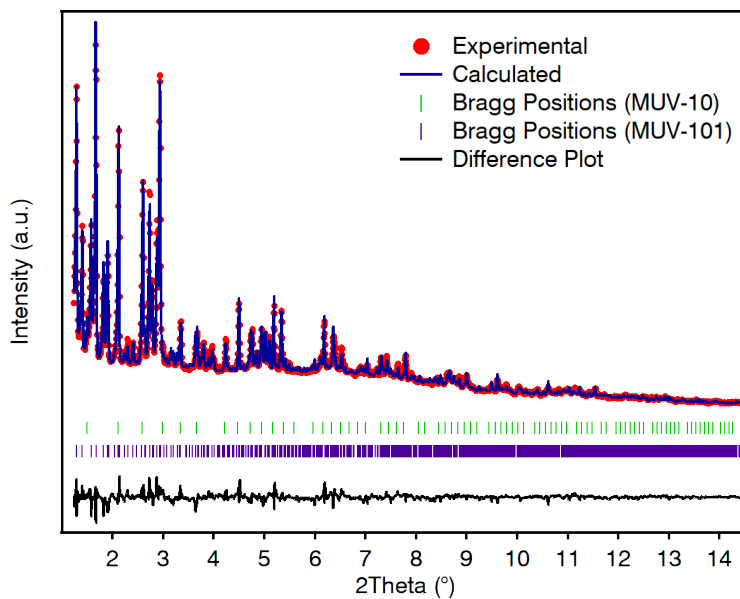
b)



3 Days: Rietveld Refinement of MUV-101(Co)-3d, MUV-10(Ca): 88.90 %, MUV-101(Co): 11.10 %. $R_{\text{exp}} = 2.65$ %, $R_p = 4.30$ %, $R_{\text{wp}} = 5.94$ %, $\text{GoF} = 2.24$.

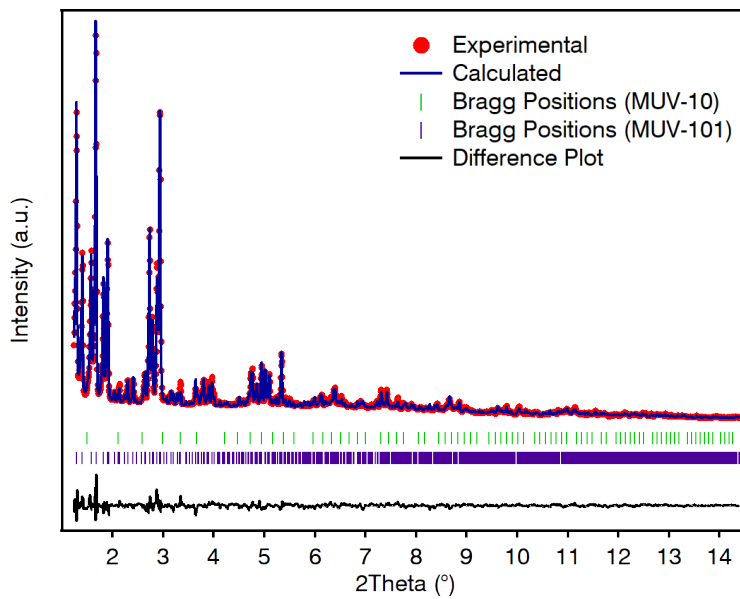
Figure S27. Rietveld refinement of a) MUV-101(Co)-1d and b) MUV-101(Co)-3d.

a)



10 Days: Rietveld Refinement of MUV-101(Co)-10d, MUV-10(Ca): 35.21 %, MUV-101 (Co): 64.79 %. $R_{\text{exp}} = 2.81$ %, $R_p = 3.10$ %, $R_{\text{wp}} = 4.22$ %, $\text{GoF} = 1.50$.

b)



30 Days: Rietveld Refinement of MUV-101(Co)-30d, MUV-10: 1.94 %, MUV-101: 98.06 %. $R_{\text{exp}} = 2.59$ %, $R_p = 3.93$ %, $R_{\text{wp}} = 5.12$ %, $\text{GoF} = 1.98$.

Figure S28. Rietveld refinement of a) MUV-101(Co)-10d and b) MUV-101(Co)-30d.

Table S6. Summary of the data calculated from the Rietveld refinements.

Sample	MUV-10(Ca) [%]	MUV-101(Co) [%]	R_{exp} [%]	R_p [%]	R_{wp} [%]	GoF
MUV-10(Ca)	100	0	2.98	3.09	4.89	1.64
MUV-101(Co)-1d	97.03	2.97	2.74	3.03	4.90	1.79
MUV-101(Co)-3d	88.90	11.10	2.65	4.30	5.94	2.24
MUV-101(Co)-10d	35.21	64.79	2.81	3.10	4.22	1.50
MUV-101(Co)-30d	1.94	98.06	2.59	3.93	5.12	1.98

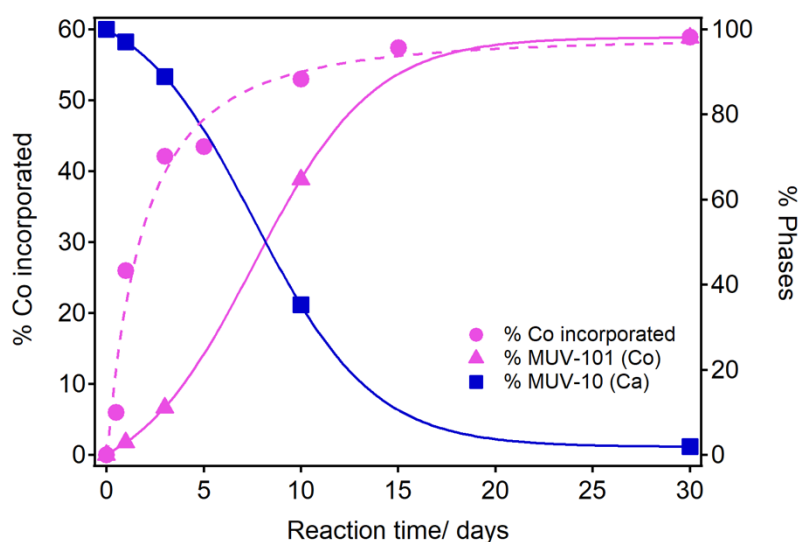


Figure S29. Comparison of the kinetic profiles of the metal exchange (dashed line) and the variation in the relative fractions of MUV-10(Ca) and MUV-101(Co) phases (solid lines) at the different stages of transformation studied. Whereas the first follows the expected behavior with a linear increase to reach saturation after 5 days, the profile of the crystallographic analysis is closer to a S-type curve because the incorporation of Co(II) is not linearly correlated with the formation of MUV-101(Co) at the early stages of transformation.

S4.7. Thermogravimetric Analysis (TGA) and changes to the thermal stability of the solid with the degree of transformation

TGA curves were recorded on activated solids at a ramp rate of 5 °C/min on a Mettler Toledo TGA/SDTA 851e/SF/1100 apparatus between 25 and 600 °C under synthetic air.

MUV-101(Co)-1d

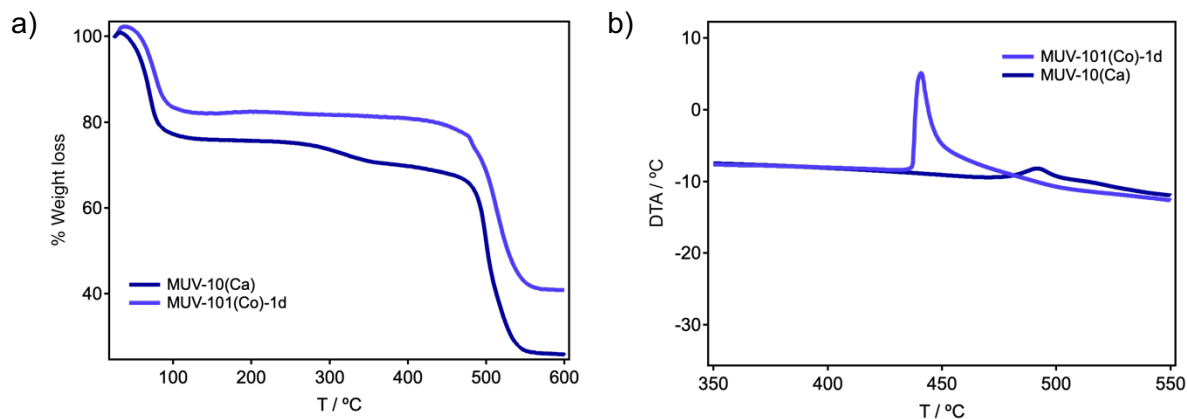


Figure S30. a) Thermogravimetric analysis and b) DTA of MUV-101(Co)-1d compared with MUV-10(Ca).

MUV-101(Co)-3d

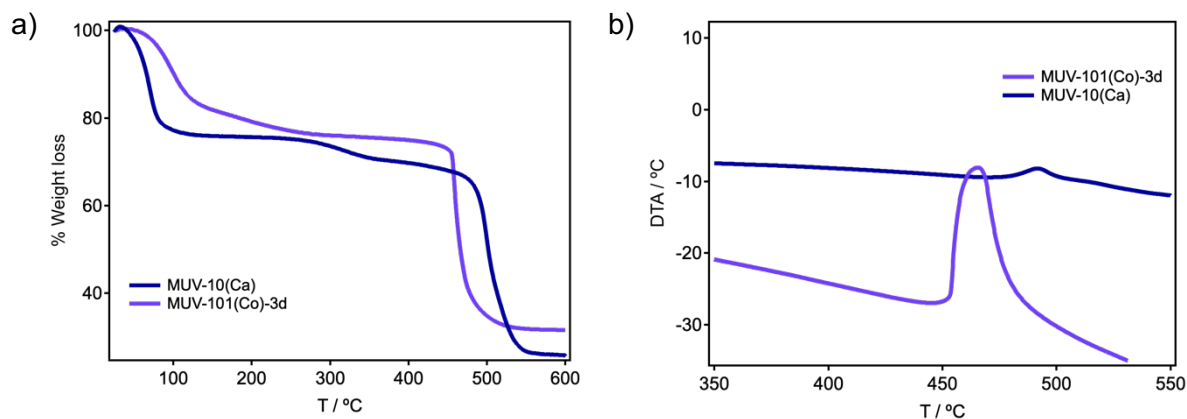


Figure S31. a) Thermogravimetric analysis and b) DTA of MUV-101(Co)-3d compared with MUV-10(Ca).

MUV-101(Co)-5d

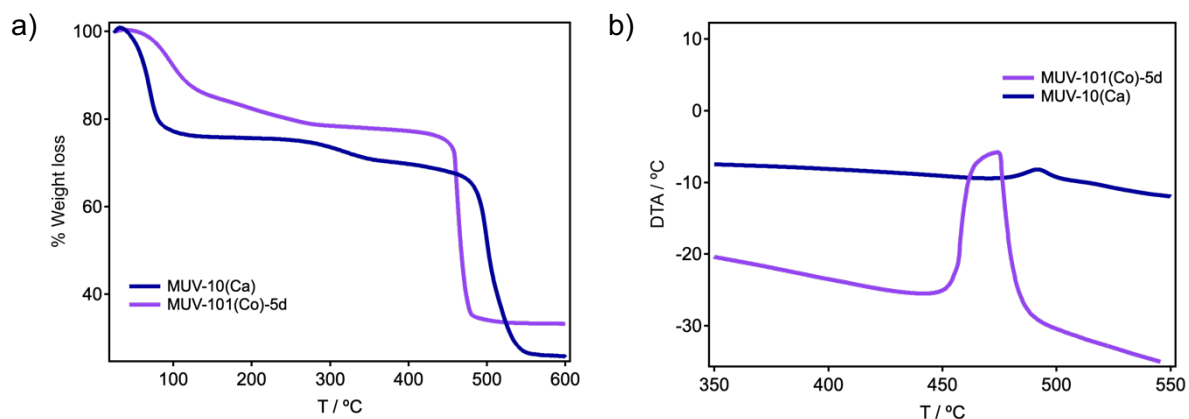


Figure S32. a) Thermogravimetric analysis and b) DTA of of MUV-101(Co)-5d compared with MUV-10(Ca).

MUV-101(Co)-10d

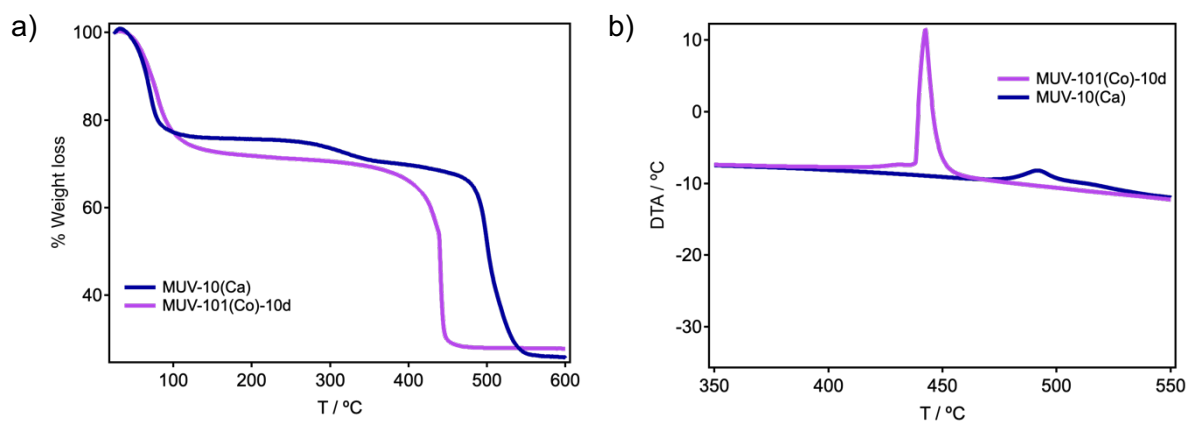


Figure S33. a) Thermogravimetric analysis and b) DTA of MUV-101(Co)-10d compared with MUV-10(Ca).

MUV-101(Co)-30d

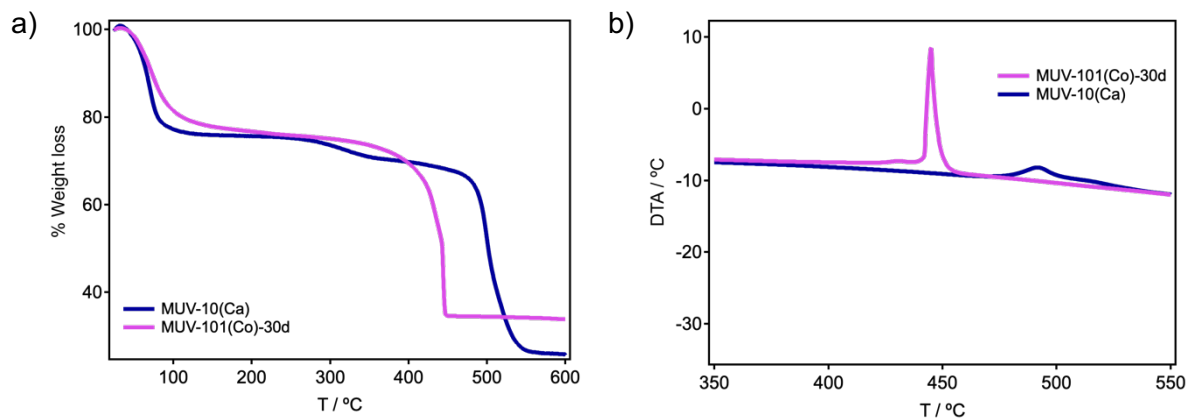


Figure S34. a) Thermogravimetric analysis and b) DTA of MUV-101(Co)-30d compared with MUV-10(Ca)

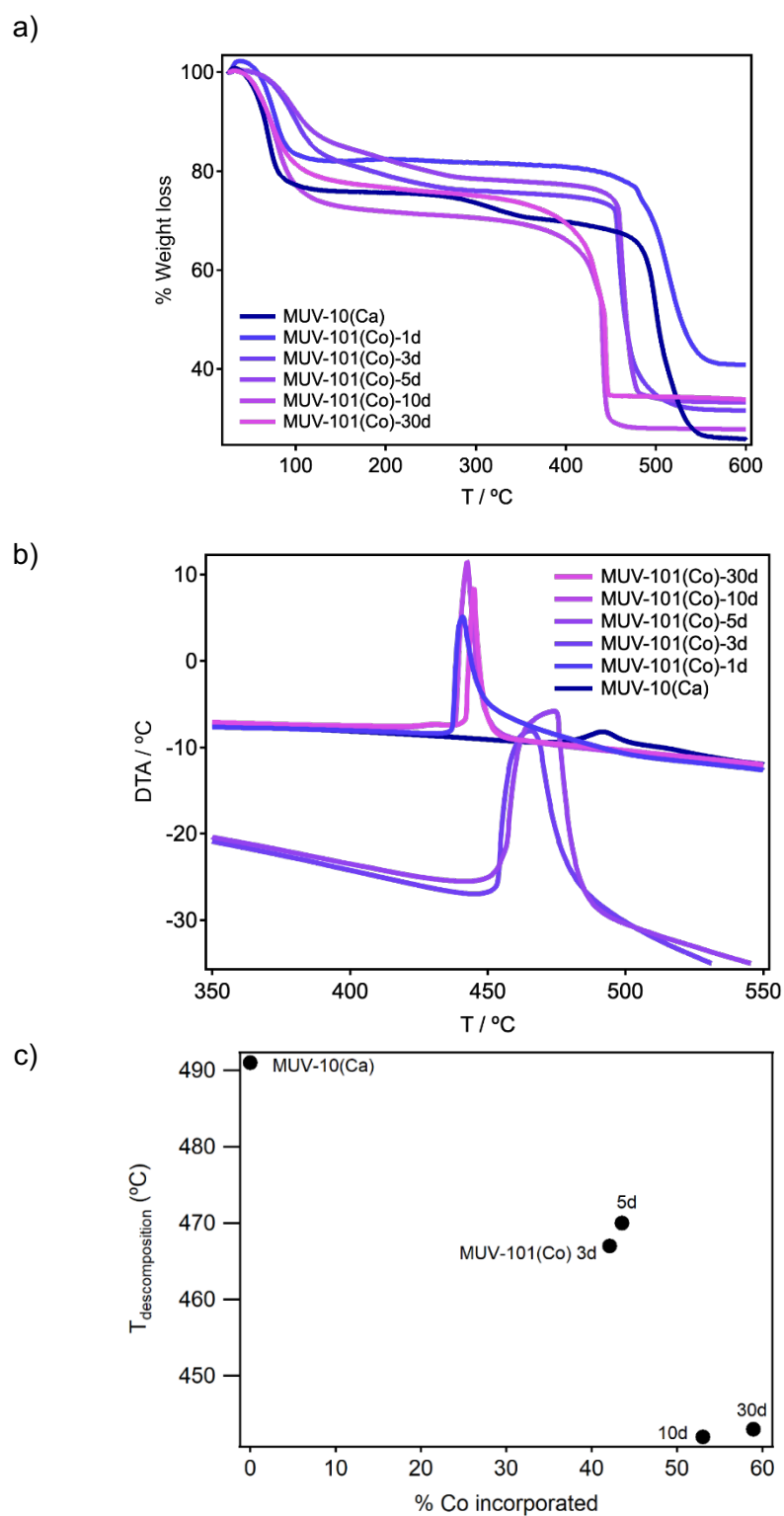


Figure S35. a) Overlay of TGA profiles and b) shift in temperature of the endothermic peak in the differential thermal analysis of MUV-10(Ca) and MUV-101(Co) after metal exchange for 1 to 30 days. c) Decrease in the temperature of decomposition of the MOF with Co % as estimated from EDX analysis.

S4.8. Analysis of N₂ adsorption/desorption isotherms at 77 K and porosity changes with the degree of transformation

MUV-101(Co)-12h

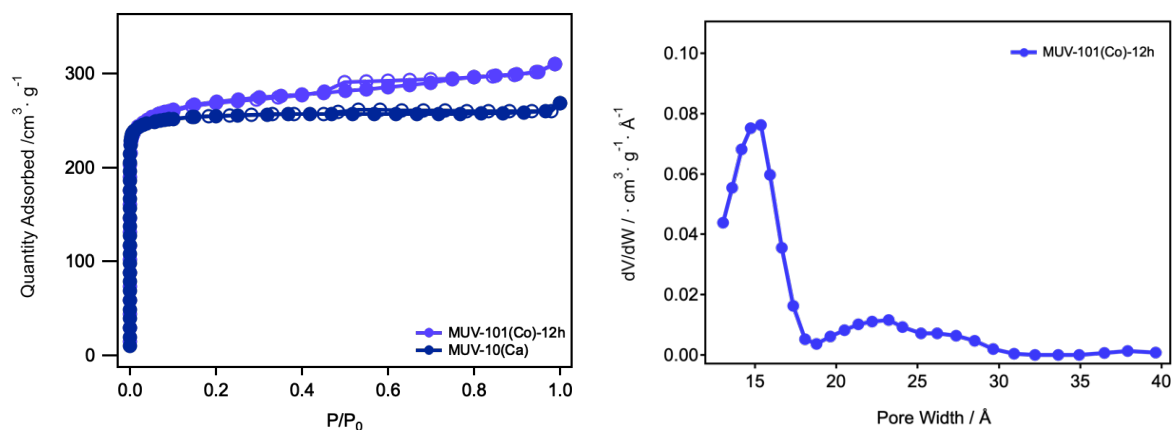


Figure S36. a) N₂ adsorption isotherm of MUV-101(Co)-12h compared with MUV-10(Ca); b) Pore size distribution (PSD).

MUV-101(Co)-1d

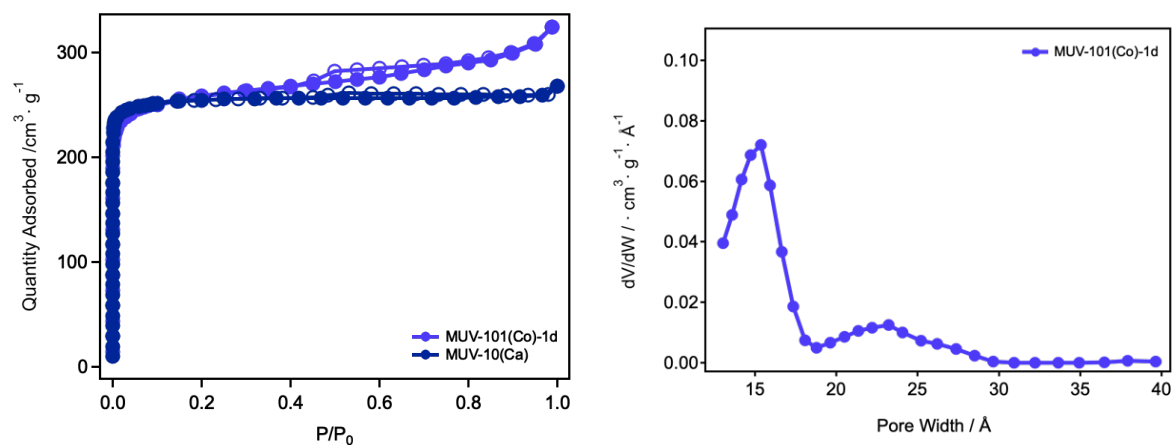


Figure S37. a) N₂ adsorption isotherm of MUV-101(Co)-1d compared with MUV-10(Ca); b) Pore size distribution (PSD).

MUV-101(Co)-3d

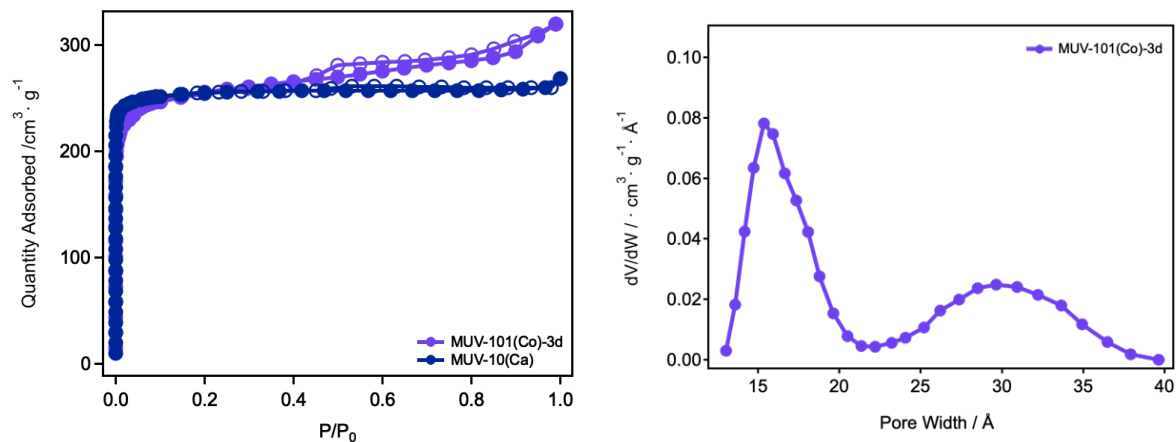


Figure S38. a) N₂ adsorption isotherm of MUV-101(Co)-3d compared with MUV-10(Ca); b) Pore size distribution (PSD).

MUV-101(Co)-5d

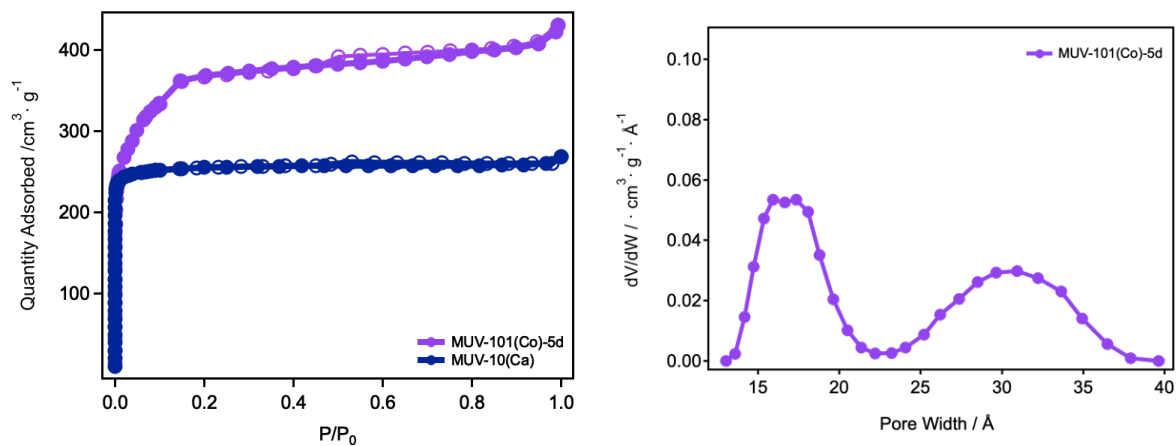


Figure S39. a) N₂ adsorption isotherm of MUV-101(Co)-5d compared with MUV-10(Ca); b) Pore size distribution (PSD).

MUV-101(Co)-10d

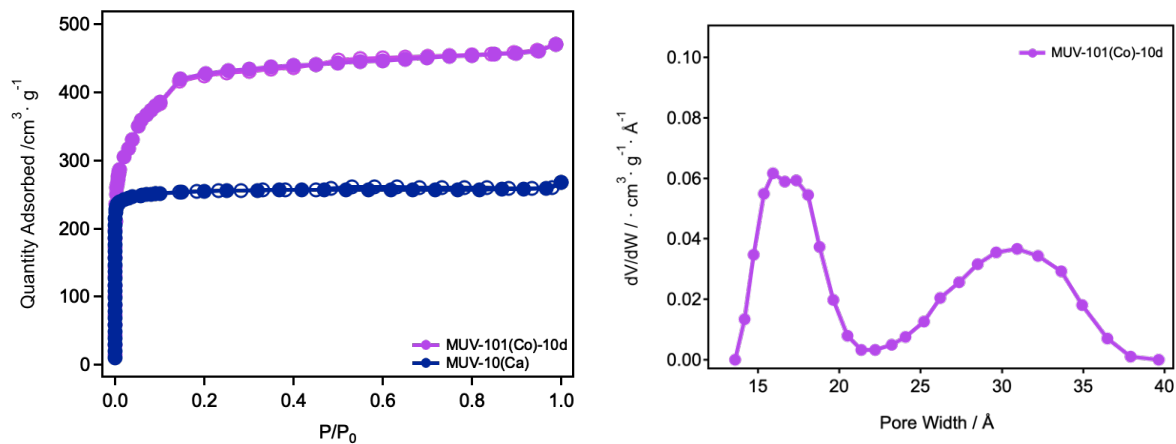


Figure S40. a) N₂ adsorption isotherm of MUV-101(Co)-10d compared with MUV-10(Ca); b) Pore size distribution (PSD).

MUV-101(Co)-15d

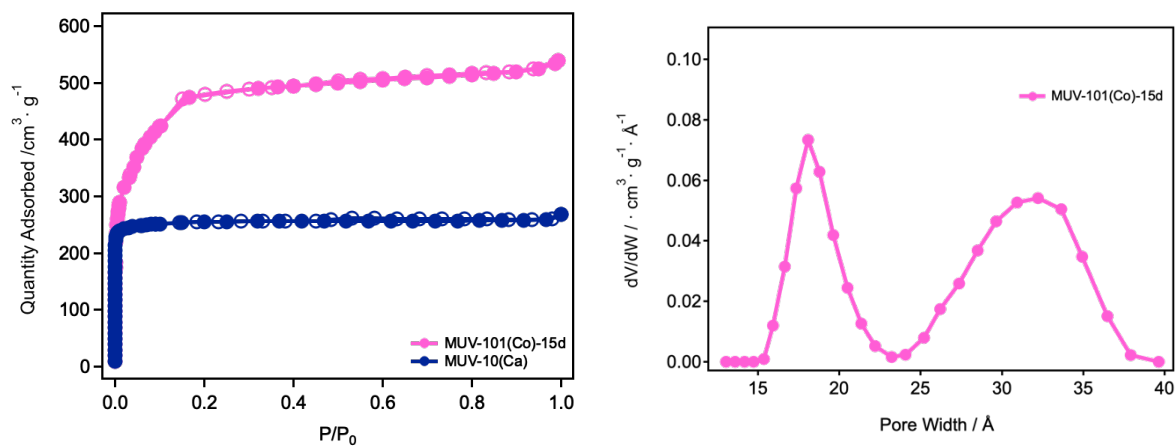


Figure S41. a) N₂ adsorption isotherm of MUV-101(Co)-15d compared with MUV-10(Ca); b) Pore size distribution (PSD).

MUV-101(Co)-30d

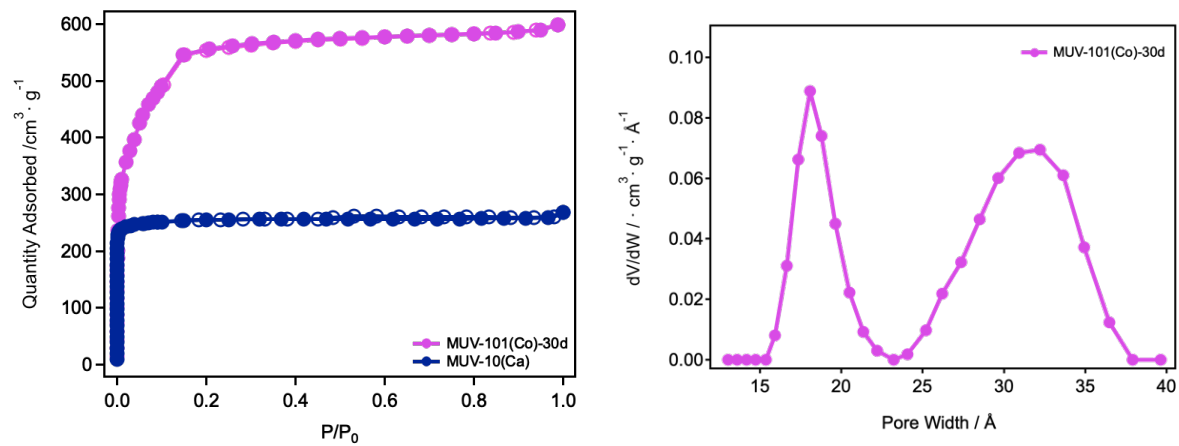


Figure S42. a) N₂ adsorption isotherm of MUV-101(Co)-30d compared with MUV-10(Ca); b) Pore size distribution (PSD).

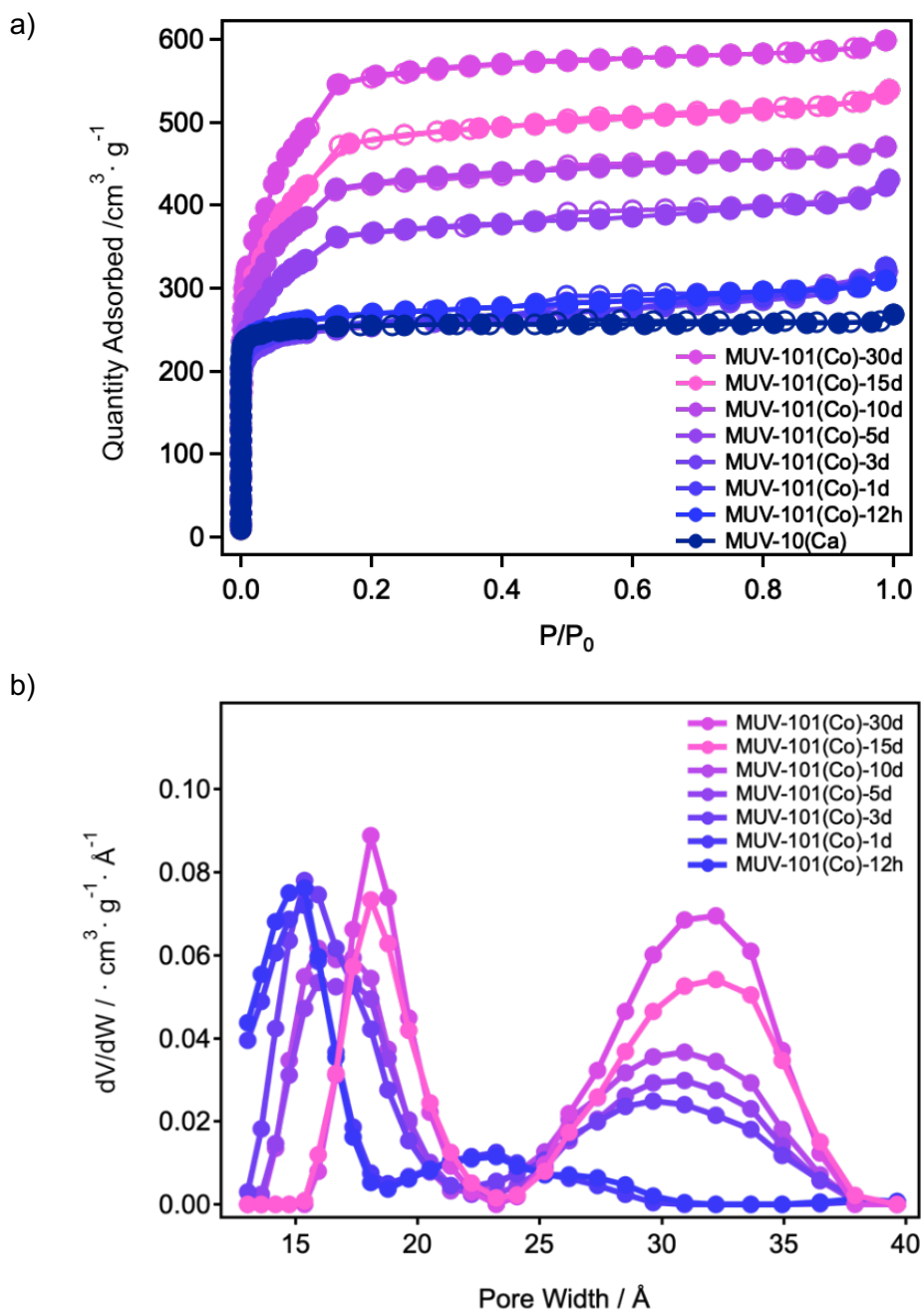


Figure S43. General comparison of a) N_2 adsorption isotherms and b) Pore size distributions for the transformation of MUV-10(Ca) into MUV-101(Co) for all the transformation stages analysed.

Table S7. Summary of the analysis of the N₂ adsorption/desorption isotherms at 77 K of MUV-10(Ca) and MUV-101(Co) materials produced at different reaction times. Specific surface area (SA) was calculated with the multi-point Brunauer-Emmett-Teller (BET) method. Total pore volume (V_t) was estimated at P/P₀=0.96. The pore size distribution (PSD) was analysed by using the solid density functional theory (NLDFT) for the adsorption branch by assuming a cylindrical pore model.

Sample	SA _{BET} [m ² ·g ⁻¹]	V _t [cm ³ ·g ⁻¹]	PSD _{NLDFT} [nm]	
			micro	meso
MUV-10(Ca)	1041	0.40	1.1	---
MUV-101(Co)-12h	1054	0.47	1.5	2.4
MUV-101(Co)-1d	1019	0.48	1.5	2.5
MUV-101(Co)-3d	988	0.48	1.5	2.5
MUV-101(Co)-5d	1237	0.63	1.7	3.0
MUV-101(Co)-10d	1554	0.72	1.7	3.1
MUV-101(Co)-15d	1766	0.81	1.8	3.2
MUV-101(Co)-30d	2043	0.92	1.8	3.2

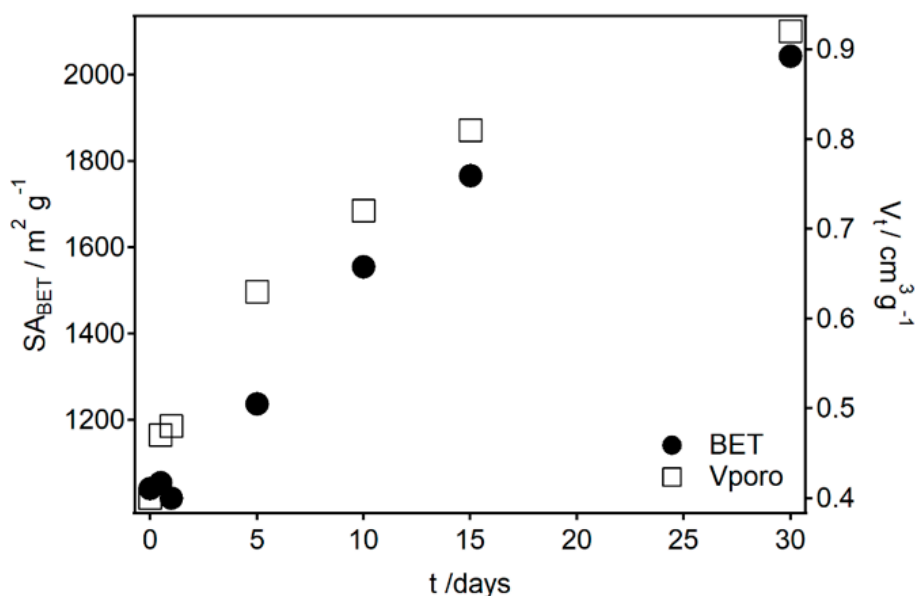


Figure S44. Graphical representation of the changes of the surface area and pore volume with the reaction time for the transformation of MUV-10(Ca) into MUV-101(Co).

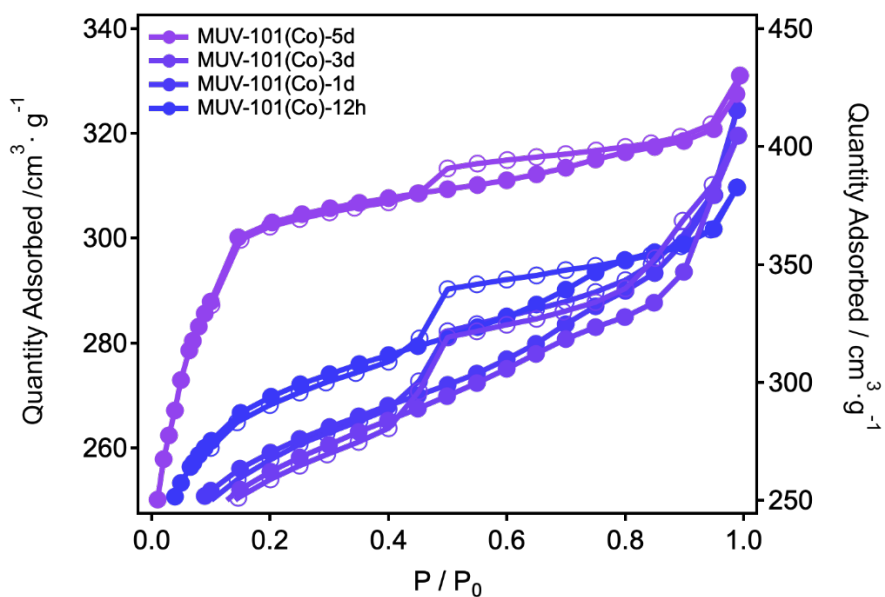


Figure S45. Opening of a hysteresis loop in MUV-101(Co)-12 h, 1d, 3d and 5d indicative of the generation of mesoporosity at these transformation stages. For clarity we have represented the samples in separate axis: 12 h, 1 d and 3 d in Y-1 (left) and 5 d in Y-2 (right).

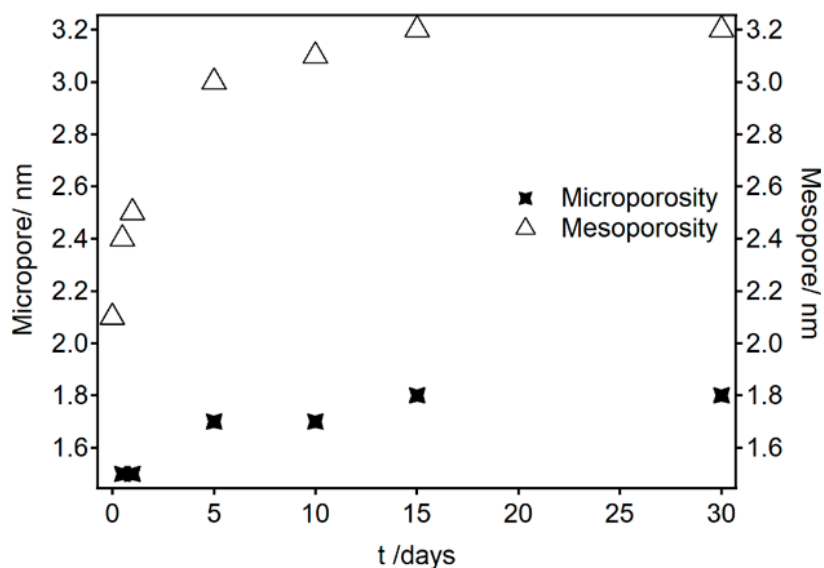


Figure S46. Graphical representation of the changes with reaction time in the micro- and mesoporosity in MUV-101(Co) extracted from PSD data.

S4.9. Chemical Stability

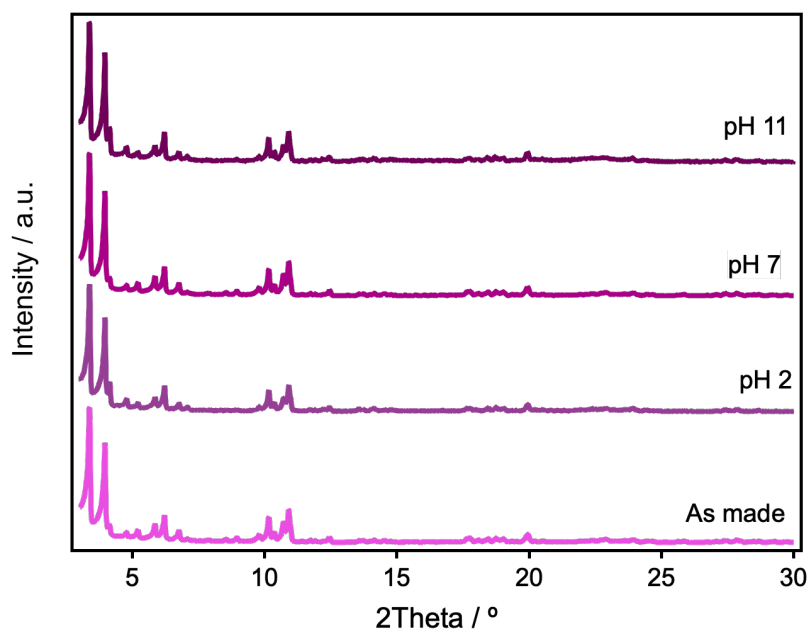


Figure S47. Comparison of PXRD of as-made MUV-101(Co)-30d and after soaking in an aqueous solution at pH 2, 7 and 11 during 24 hours ruling out structural degradation in the pH range studied.

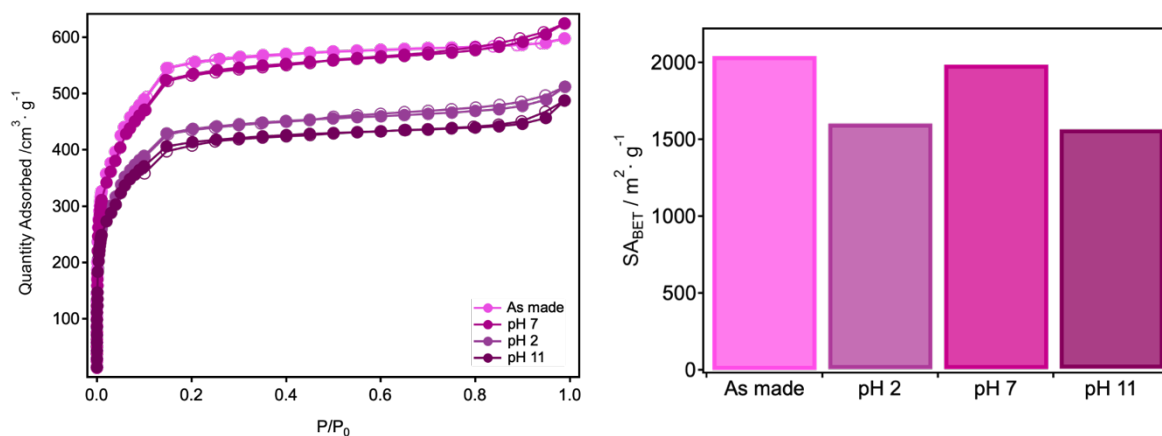


Figure S48. N₂ adsorption/desorption isotherms (left) and calculated BET surface area values (right) of MUV-101(Co)-30d after water treatment at neutral, acid and basic pH.

S4.10. EXAFS data analysis and fitting

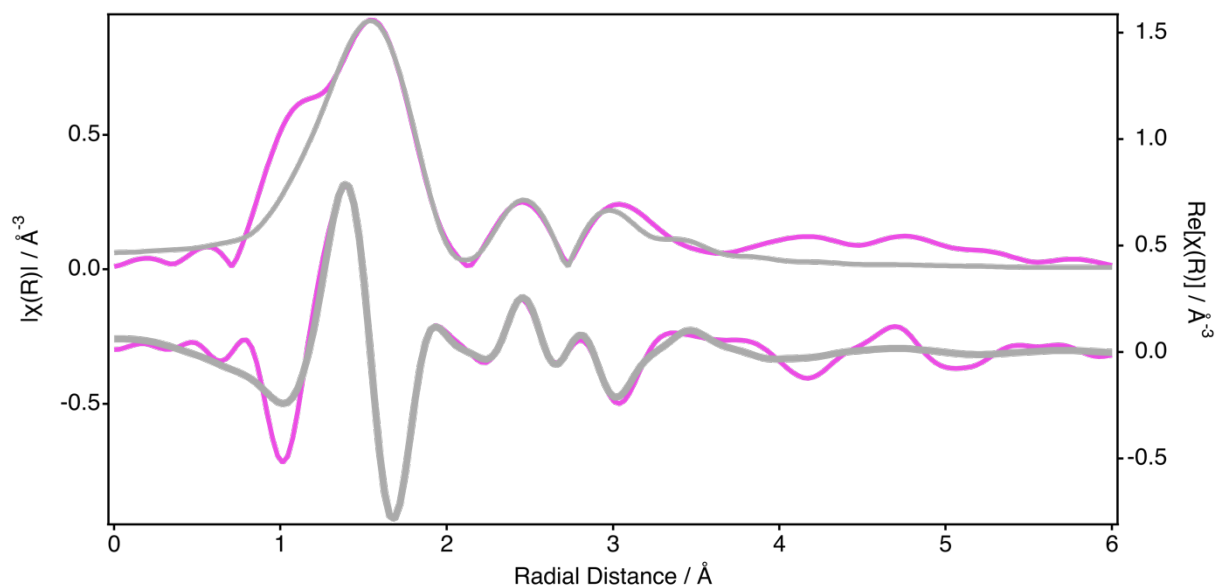


Figure S49. Ti K-edge magnitude and real part of R space for MUV-101(Co)-30d. Gray line experimental fit to the data.

Table S8. Parameters of the coordination shells around Ti atoms in MUV101-(Co)-30d: average number of neighbour atoms (N), distance (R), and Debye-Waller factor (σ^2).

Path	N	R / Å	σ^2 / Å ²
Ti-(μ_3 -O)	1	1.67	0.040
Ti-O	4	1.96	0.015
Ti-Oax	1	2.38	0.015
Ti-C	4	2.74	0.002
Ti-Co	2	2.94	0.040

Table S9. DFT computed interatomic distances for optimized MIL-100(Ti) and MUV-101(Co) clusters. Distances in the table are reported in Angstroms.

Cluster	d(Ti-Ti) /d(Co-Co)	d(Ti-Co)	d(Ti- μ^3 -O) /d(Co- μ^3 -O)	d(Ti-Oax) /d(Co-Oax)	d(Ti-O) /d(Co-O)
MIL-100(Ti)	3.842	-	2.221	1.824	2.022
MUV-101(Co)	3.280	3.266	1.724/1.976	2.342/2.255	2.000/2.023

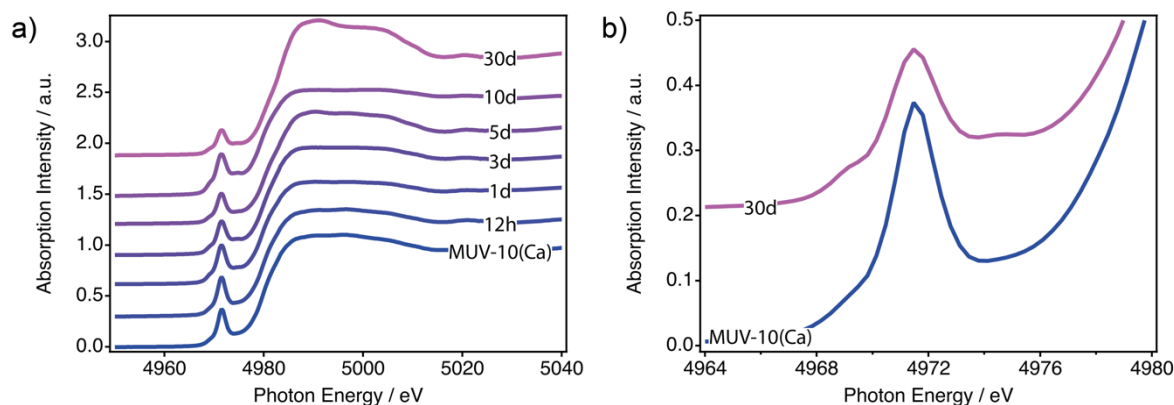


Figure S50. a, b) XANES Ti-K edge spectra of MUV-101(Co) at different stages of transformation.

Table S10. Ti K-edge XANES analyses for MUV-101(Co) samples. CN stands for coordination number.

Sample	Pre-edge (eV)	Edge (eV)	Pre-edge/edge height ^a	Pre-edge components	CN
MUV-10(Ca)	4971.0	4979.5	0.34	3	6
MUV-101(Co)-12h	4971.6	4979.8	0.38	3	6 ^a
MUV-101(Co)-1d	4971.0	4979.2	0.38	3	6 ^a
MUV-101(Co)-3d	4971.5	4979.8	0.29	3	6 ^a
MUV-101(Co)-5d	4971.5	4979.9	0.29	3	6 ^a
MUV-101(Co)-10d	4971.5	4980.2	0.37	3	6 ^a
MUV-101(Co)-30d	4971.5	4980.6	0.20	3	6

^a Distorted octahedral geometries.^{6,7}

Table S11. Co K-edge XANES analyses for MUV-101(Co) systems.

Sample	Pre-edge 1s→3d (eV)	Edge (eV)	Pre-edge/edge height ^a	CN
MUV-101(Co)-1d	7709.5	7721.1	0.025	6 ^a
MUV-101(Co)-3d	7708.9	7720.6	0.026	6 ^a
MUV-101(Co)-5d	7709.4	7721.1	0.026	6 ^a
MUV-101(Co)-15d	7709.2	7720.8	0.029	6 ^a

^a Distorted octahedral geometries.^{6,7}

S4.11. STEM-EDX and high-resolution elemental maps

MUV-101(Co)-1d

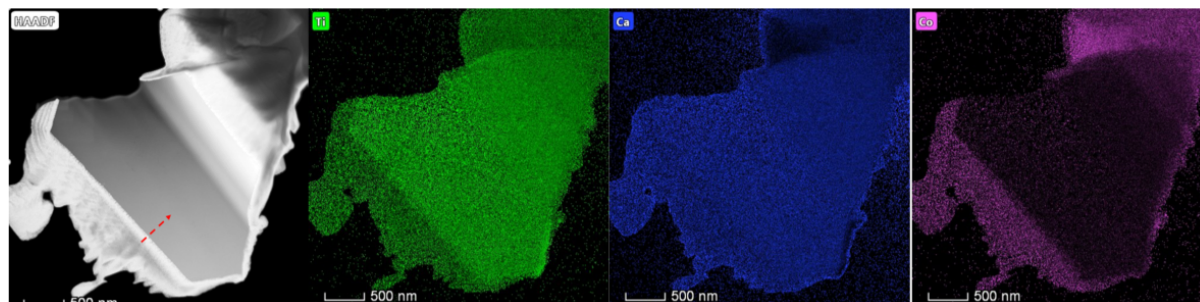


Figure S51. STEM image of a sectioned lamellae of MUV-101(Co)-1d and high resolution element mapping. EDX line analysis: 49 % (Ti, green); 44 % (Ca, blue) and 7 % (Co, purple).

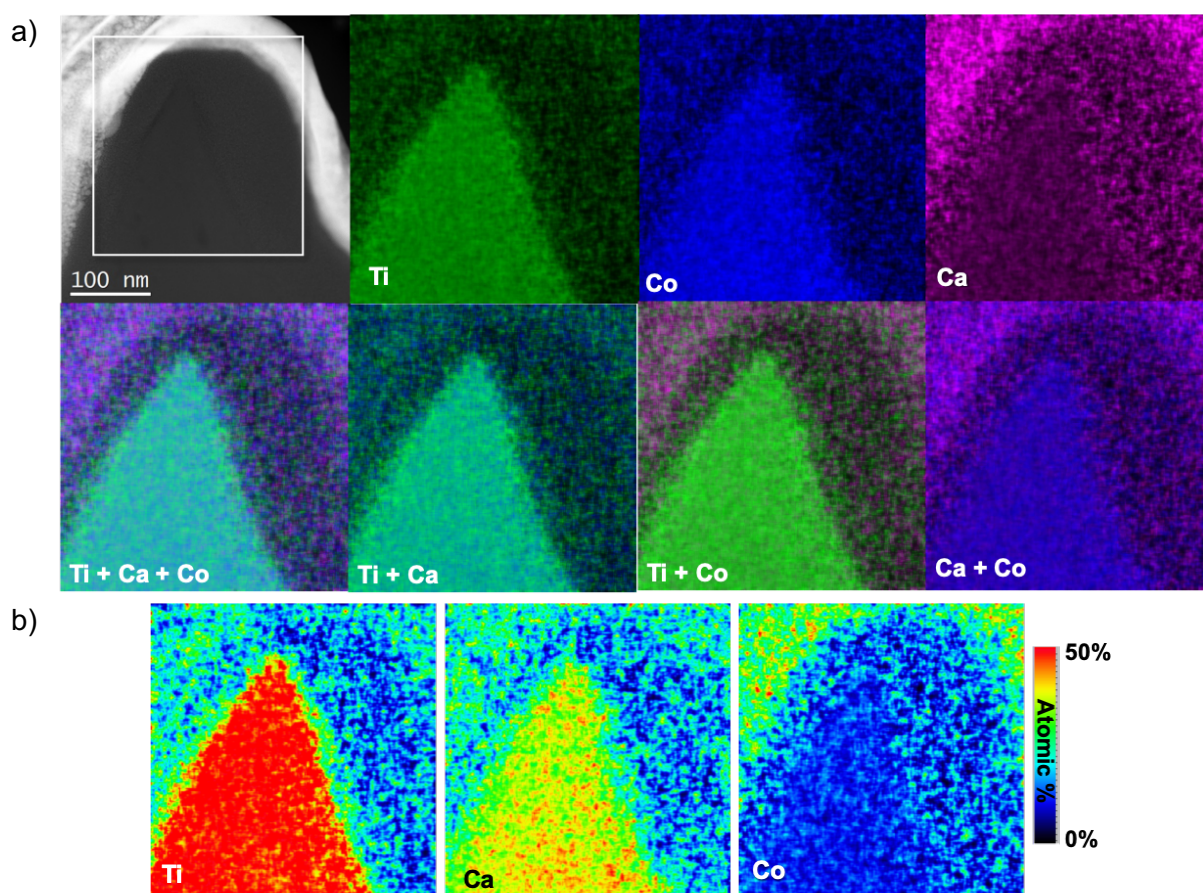


Figure S52. a) STEM image of a sectioned lamellae of MUV-101(Co)-1d and high resolution element mapping. EDX area analysis: 50 % (Ti, green); 39 % (Ca, blue) and 11 % (Co, purple). b) Temperature compositional map.

MUV-101(Co)-30d

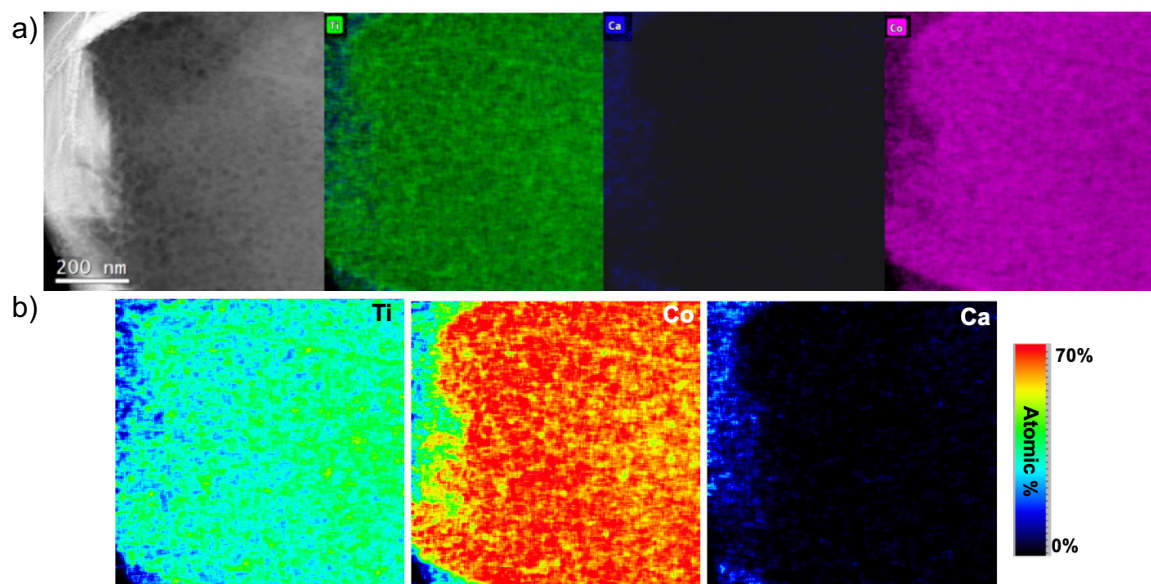


Figure S53. a) STEM image of a sectioned lamellae of MUV-101(Co)-30d and high resolution element mapping. EDX line analysis: 33 % (Ti, green); 0 % (Ca, blue) and 67 % (Co, purple). b) Temperature compositional map.

S4.12. Transformation in single crystals

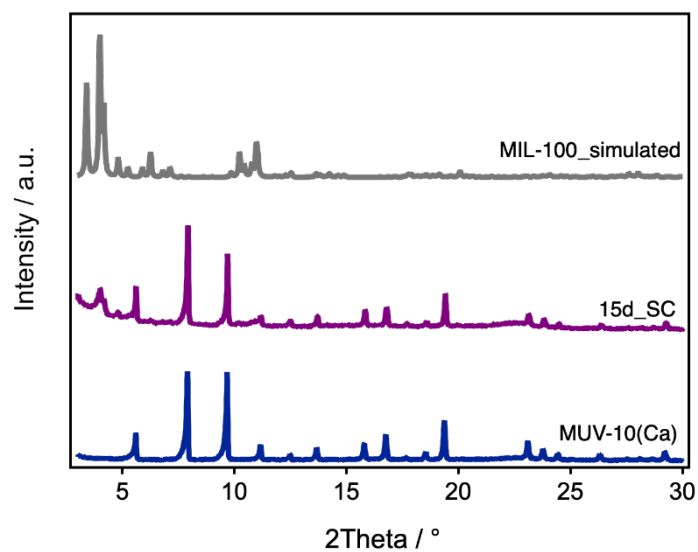


Figure S54: PXRD of MUV-10(Ca) (bottom), MUV-101(Co)-15d obtained from the transformation of single crystals (middle) and simulated MIL-100 (top).

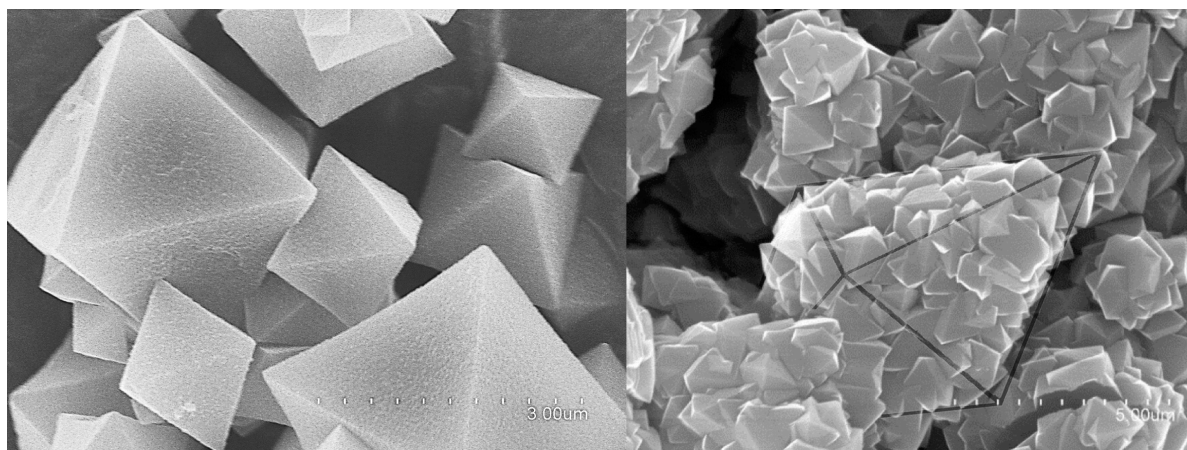


Figure S55. Comparison of the size of the crystals of: a) MUV-10(Ca) at the beginning of the reaction and b) MUV-101(Co) after the transformation is complete.

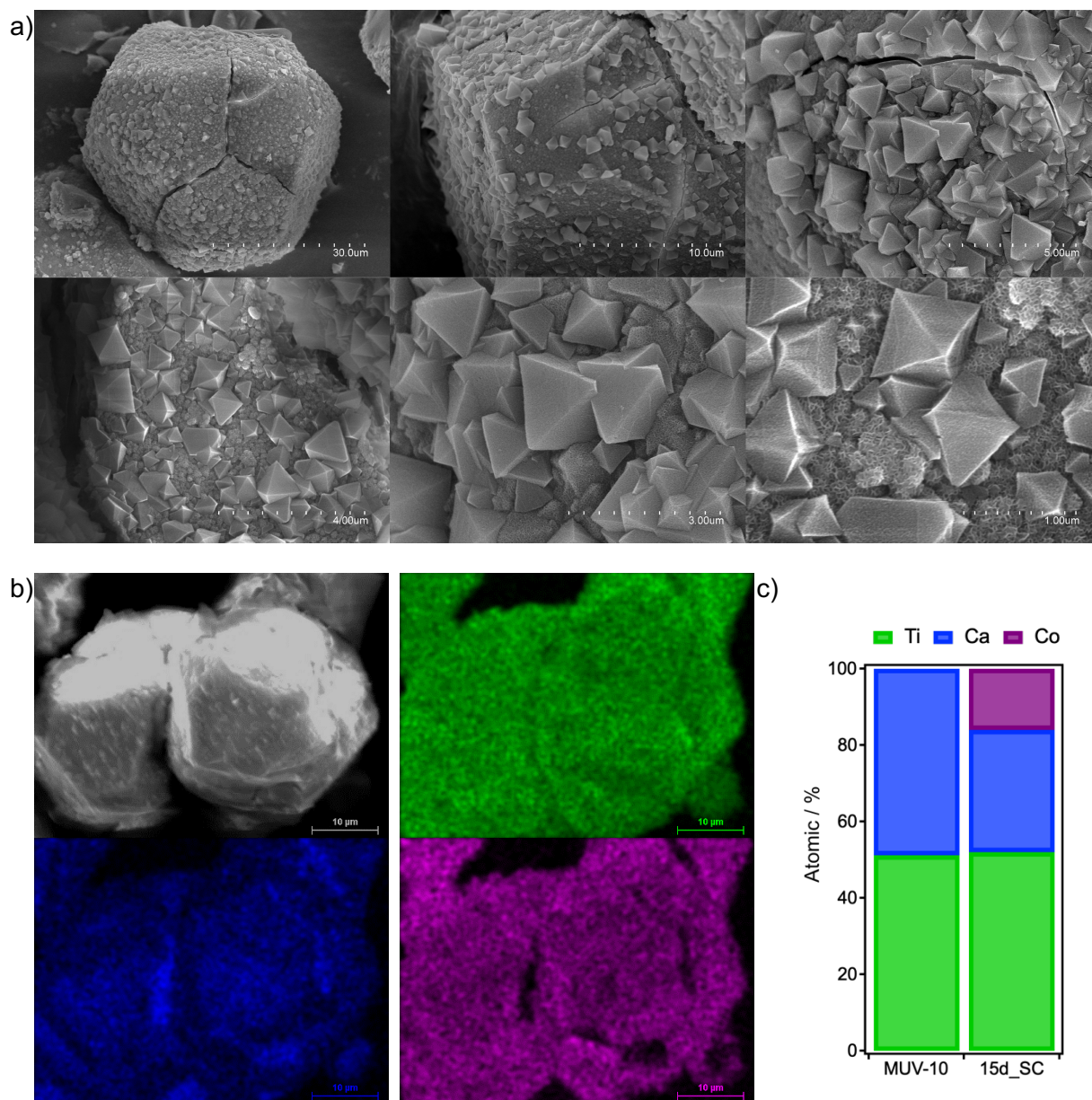


Figure S56. MUV-101(Co)-15d obtained by metal exchange of single crystals of MUV-10(Ca): a) SEM images; b) Area mapping of Ti (green), Ca (blue) and Co (pink); c) experimental atomic percentage from point and shoot EDX analysis for diferent crystals.

S5. COMPUTATIONAL METHODS

The surface properties of MUV-10 and the thermodynamic stability of this materials upon metal exchange reaction with different metal cations, M^{2+} , was analysed by using a combination of computational techniques, molecular mechanics simulations based on interatomic potentials and quantum-mechanical methods based on the density functional theory (DFT).

Surface Models

From crystal structure of the bulk of MUV-10, a single surface was created by employing GDIS software.⁸ In practice, the solid is divided into region 1, which contains the surface and all layers of atoms below it that exhibit a significant atomic relaxation, and region 2, which contains the rest of the bulk material where it is assumed that no displacements from the three-dimensional crystal structure are induced (Supplementary Figure S56). This method is the most efficient and precise for atomistic techniques. Several model surfaces were built by cutting the bulk MOF with different spatial orientations; (001), (110) and (111) and the surface energies calculated by using the Universal Force Field, as implemented in GULP code.⁹

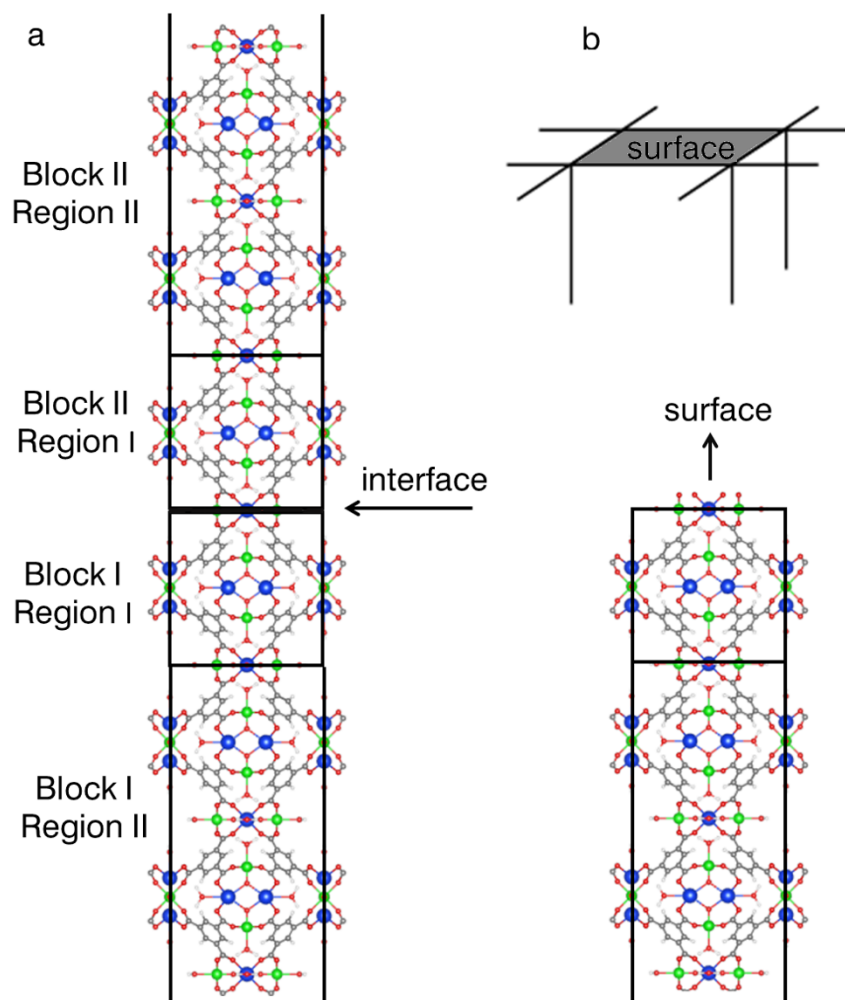


Figure S57. Schematic representation of MUV-10: a) complete crystal and b) half crystal, exposing a surface periodic in two dimensions.

Surface Stabilities

The calculated surface energies for the (001), (110) and (111) surfaces are listed in Supplementary Table 11. The surface (111) is most stable and will be mainly the most exposed in the morphology.

Table S12. Surface energies in J/m² for a list of low-index surfaces.

Surface	γ
(001)	3.95
(110)	5.38
(111)	3.01

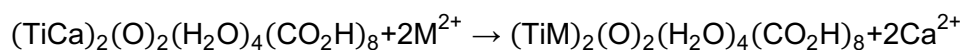
Crystal Morphology

The calculated surface energies were used to obtain the equilibrium crystal morphology of MUV-10 through the Wulff construction method¹⁰ and the crystal morphology model was created with the VESTA (Visualization for Electronic and Structural Analysis) version 3.1.4 package.¹¹

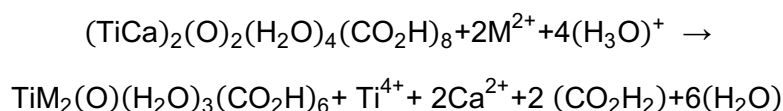
Thermodynamics of metal exchange

The calculations were performed on the cluster models, using density functional theory (DFT) as implemented in the Vienna ab initio simulation package (VASP).^{12,13} We employed the generalized gradient approximation (GGA) with the Perdew-Burke-Erzerhof functional (PBE) functional¹⁴ complemented by the dispersion PBE-D3 term as presented by Grimme.^{15,16} The projector augmented wave (PAW) method¹⁷ was used to describe the frozen core electrons and their interaction with the valence electrons. The kinetic energy cutoff for the plane-wave basis set expansion was chosen as 500 eV. For Mn²⁺, Fe²⁺, Co²⁺, Ni²⁺ and Cu²⁺, we considered all possible spin states, whereas Zn²⁺ is not spin-polarised. The solvation energy of each cation metals and anions in methanol solution were calculated using Gaussian09.¹⁸

To investigate the thermodynamic of the metal exchange reaction with retention of the SBU in MUV-10, we calculated the enthalpies energies for the process of cation exchange in methanol solution, according to the following reaction:



Enthalpy changes for the formation of [TiM₂(μ_3 -O)(H₂O)₃(CO₂)₆] heterometallic clusters consistent with the topological transformation of MUV-10 to MUV-101 were calculated according to the following reactions:



S6. TRANSFORMATION OF MUV-10(Ca) IN MUV-101(Fe, Ni, Zn) BY METAL EXCHANGE WITH Fe²⁺, Ni²⁺ AND Zn²⁺

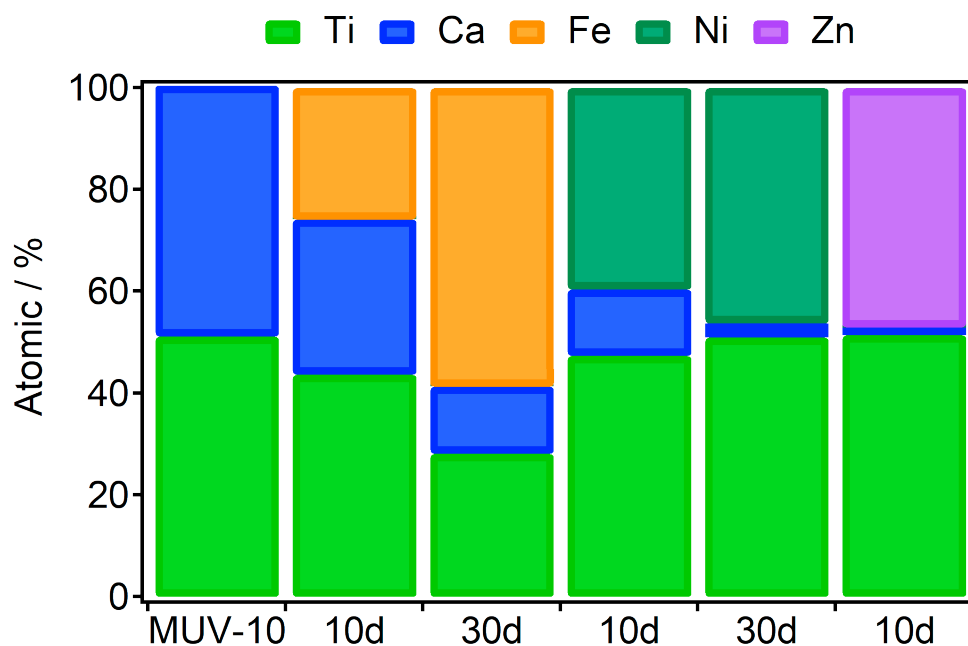


Figure S58. Evolution of the metal content in the crystals isolated after 10 and 30 days of transformation of MUV-10(Ca) into MUV-101(Fe) and MUV-101(Ni) and 10 days for MUV-101(Zn). Experimental values were determined by EDX analysis with a Hitachi S-4800 scanning electron microscope at an accelerating voltage of 20 keV.

Table S13. Experimental metal content determined by EDX analysis. M=Fe, Ni or Zn.

Sample	Time	[a]Normalized		
		Ca [%]	Ti [%]	M [%]
MUV-101(Fe)	10d	30.5 ± 0.4	43.7 ± 0.3	25.8 ± 0.4
	30d	13.2 ± 0.2	28.1 ± 0.4	58.7 ± 0.9
MUV-101(Ni)	10d	13.1 ± 0.1	47.3 ± 0.1	39.6 ± 0.2
	30d	2.8 ± 0.1	51.0 ± 0.6	46.2 ± 0.3
MUV-101(Zn)	10d	0.2 ± 0.1	57.4 ± 0.2	42.4 ± 0.1

[a] Calculated by normalizing to total M²⁺ content.

S6.1. MUV-101(Fe)

Scanning Electron Microscopy (SEM) and single point mapping

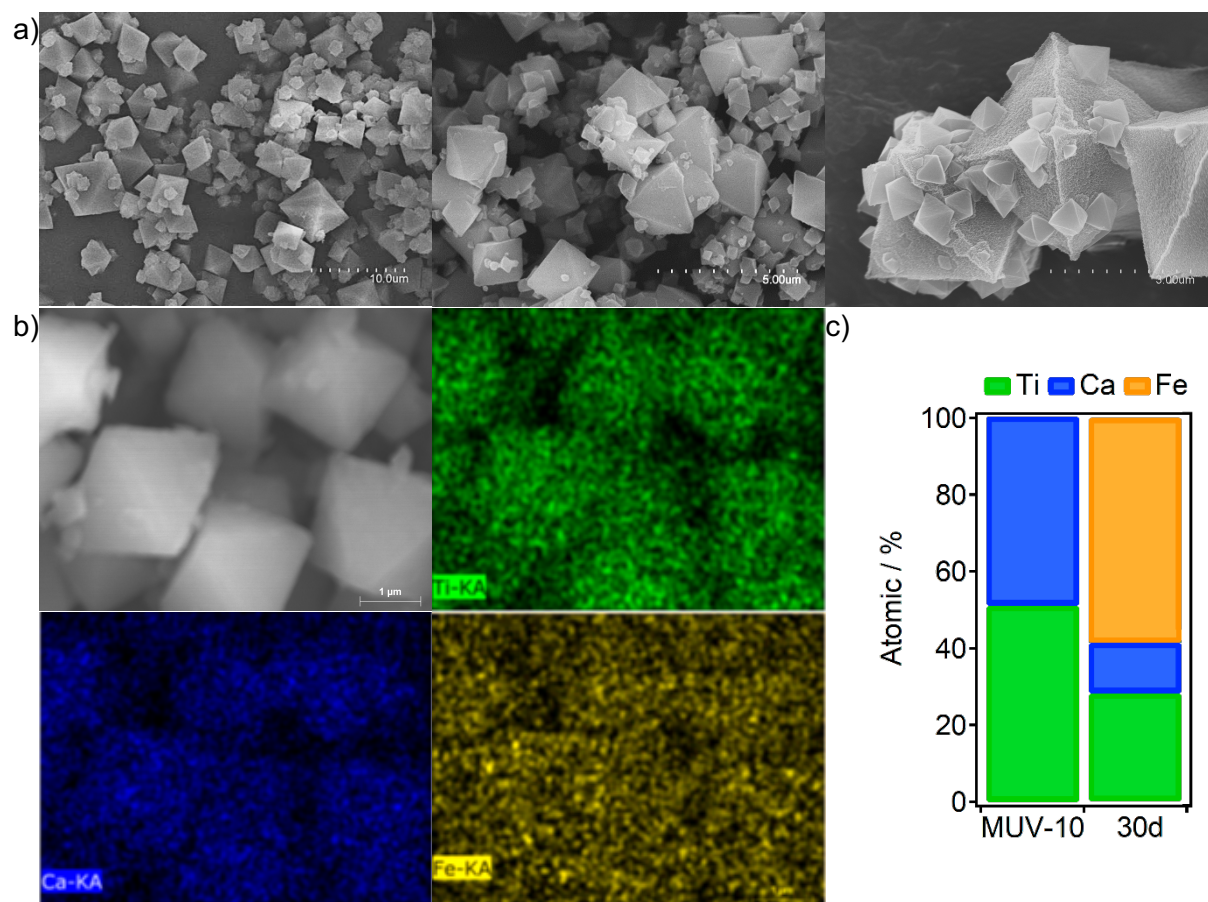
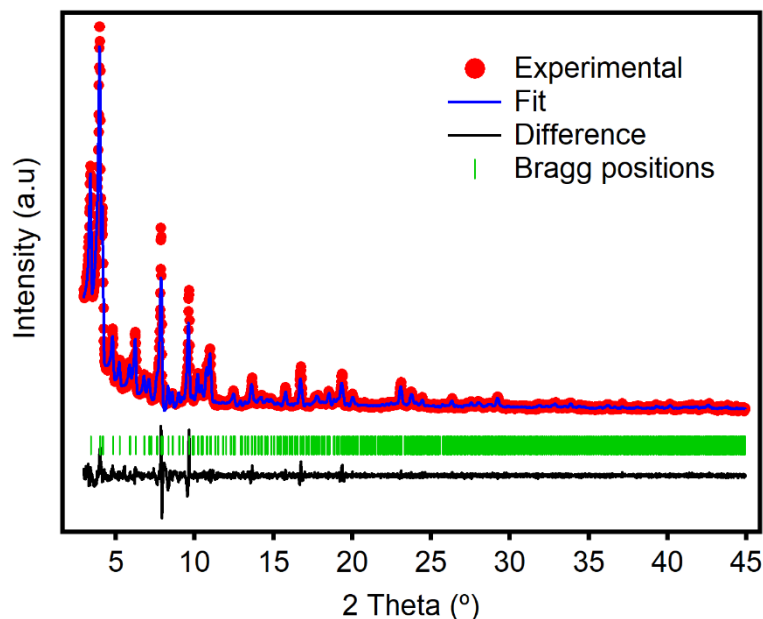


Figure S59. MUV-101(Fe)-30d: a) SEM images; b) Area mapping of Ti (green), Ca (blue) and Fe (orange); c) experimental atomic percentage from point and shoot EDX analysis for different crystals.

LeBail Refinement and Powder X-Ray Diffraction (PXRD)



Cubic, F d -3 m; $a = b = c$ 73.4759 Å; $\alpha = \beta = \gamma = 90^\circ$; $V = 39976.7812 \text{ \AA}^3$; $R_e = 6.22 \%$, $R_p = 7.00 \%$, $R_{wp} = 10.9 \%$, $GoF = 1.76$. Statistics are abnormally high due to the presence of a contaminant fraction of MUV-10(Ca) in the sample.

Figure S60. Experimental (red dots), calculated (blue line), difference plot $[(I_{obs} - I_{calc})]$ (black line, bottom panel) and Bragg positions (green ticks, bottom panel) for the Le Bail refinement of experimental diffraction data of MUV-101(Fe) after 30 days.

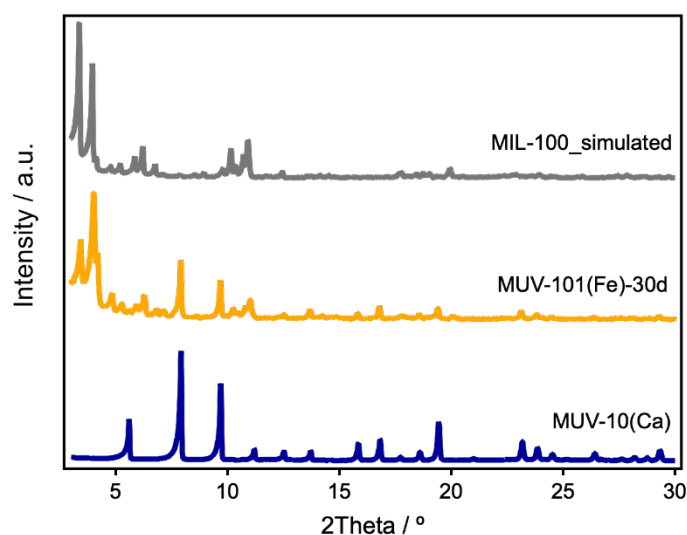


Figure S61. PXRD comparison of MUV-10(Ca) (bottom), MUV-101(Fe) (middle) and simulated MIL-100 (top).

Analysis of N₂ adsorption/desorption isotherms at 77 K

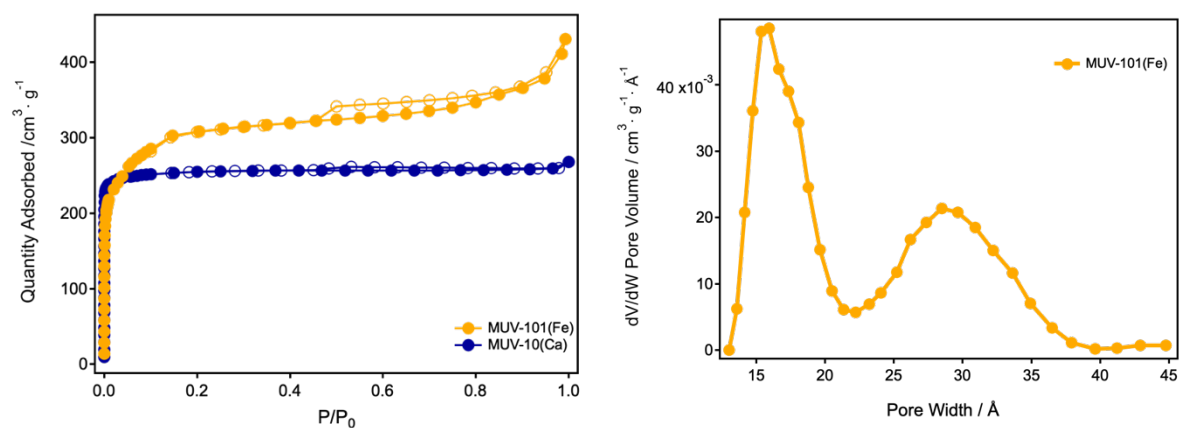


Figure S62. a) N₂ adsorption isotherm of MUV-101(Fe) compared with MUV-10(Ca); b) Pore size distribution (PSD).

S6.2. MUV-101(Ni)

Scanning Electron Microscopy (SEM) and single point mapping

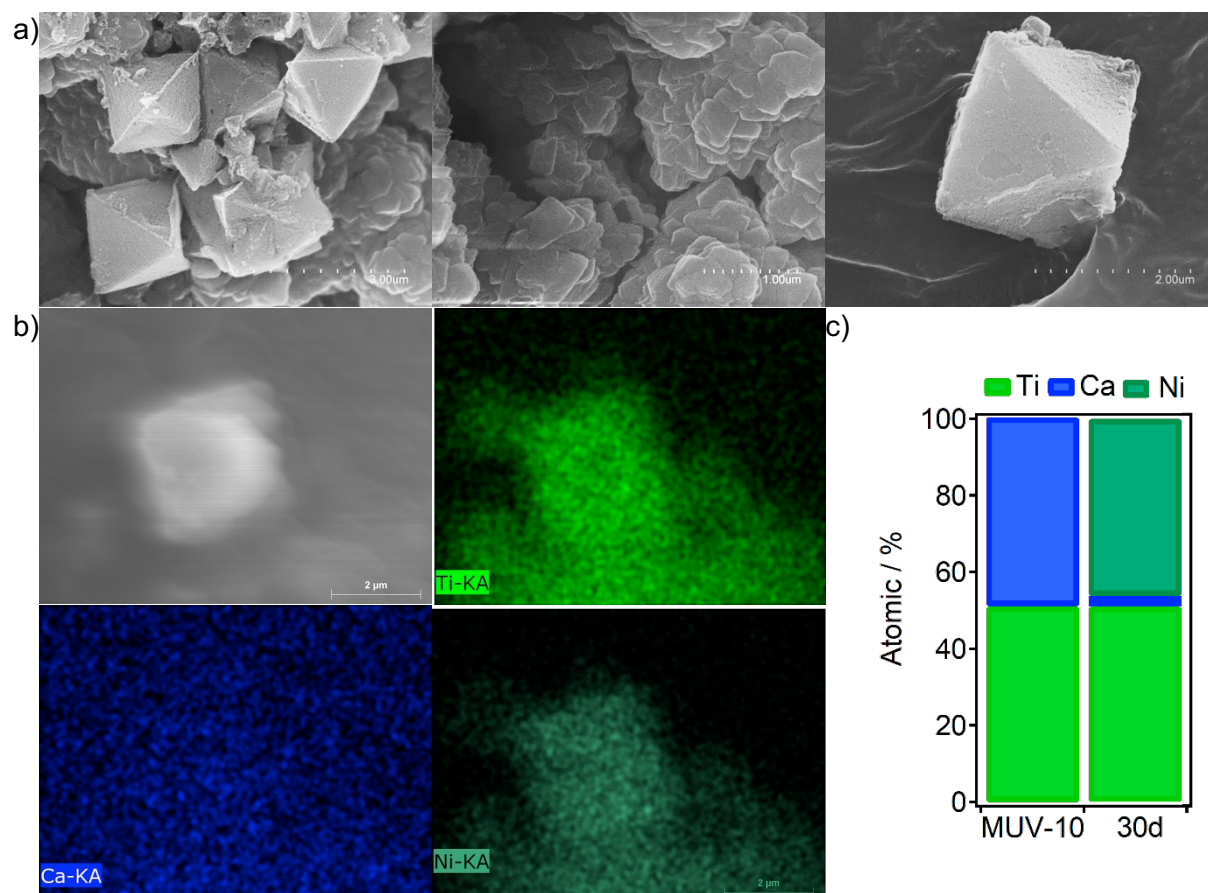
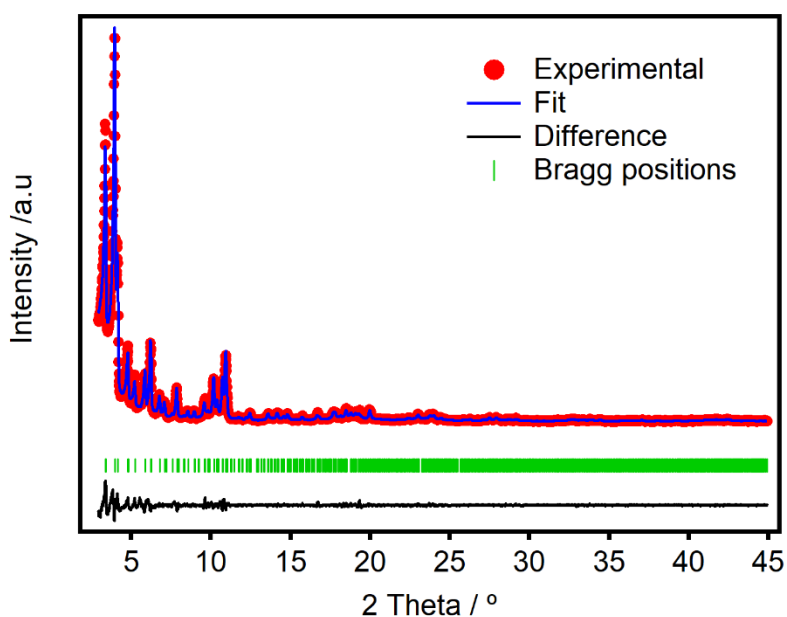


Figure S63. MUV-101(Ni)-30d: a) SEM images; b) Area mapping of Ti (green), Ca (blue) and Ni (dark green) confirm that metal distribution is homogeneous throughout the crystals; c) experimental atomic percentage from point and shoot EDX analysis for diferent crystals.

LeBail Refinement and Powder X-Ray Diffraction (PXRD)



Cubic, F d -3 m; $a = b = c$ 73.6659 Å; $\alpha = \beta = \gamma = 90^\circ$; $V = 39976.7812 \text{ \AA}^3$; $R_e = 5.98\%$, $R_p = 7.93\%$, $R_{wp} = 4.88\%$, $GoF = 1.6$.

Figure S64. Experimental (red dots), calculated (blue line), difference plot $[(I_{obs}-I_{calc})]$ (black line, bottom panel) and Bragg positions (green ticks, bottom panel) for the Le Bail refinement of experimental diffraction data of MUV-101(Ni) after 30 days.

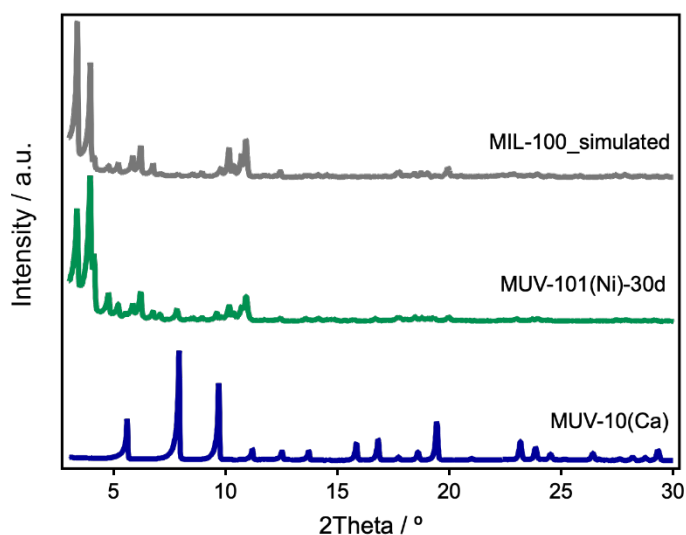


Figure S65. PXRD comparison of MUV-10(Ca) (bottom), MUV-101(Ni) (middle) and simulated MIL-100 (top).

Analysis of N₂ adsorption/desorption isotherms at 77 K

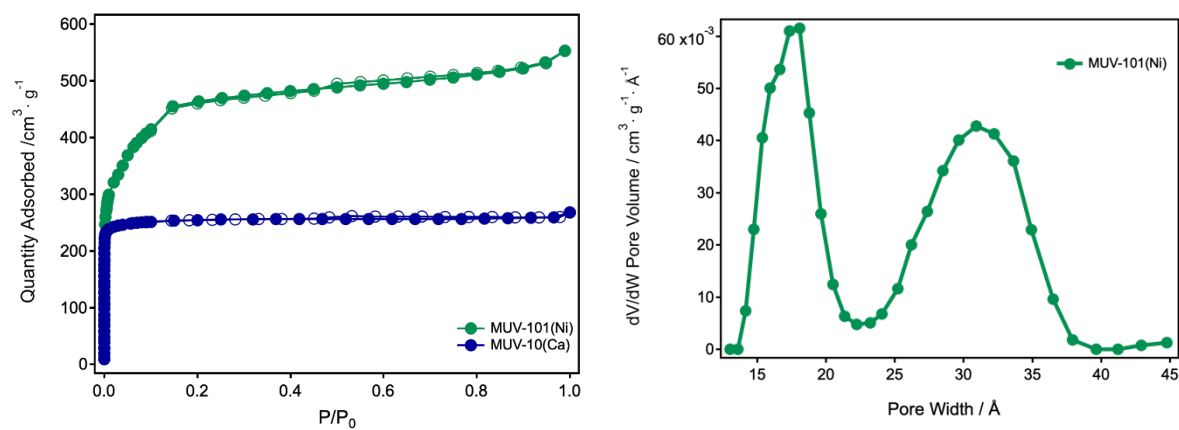


Figure S66. a) N₂ adsorption isotherm of MUV-101(Ni) compared with MUV-10(Ca); b) Pore size distribution (PSD).

S6.3. MUV-101(Zn)

Scanning Electron Microscopy (SEM) and single point mapping

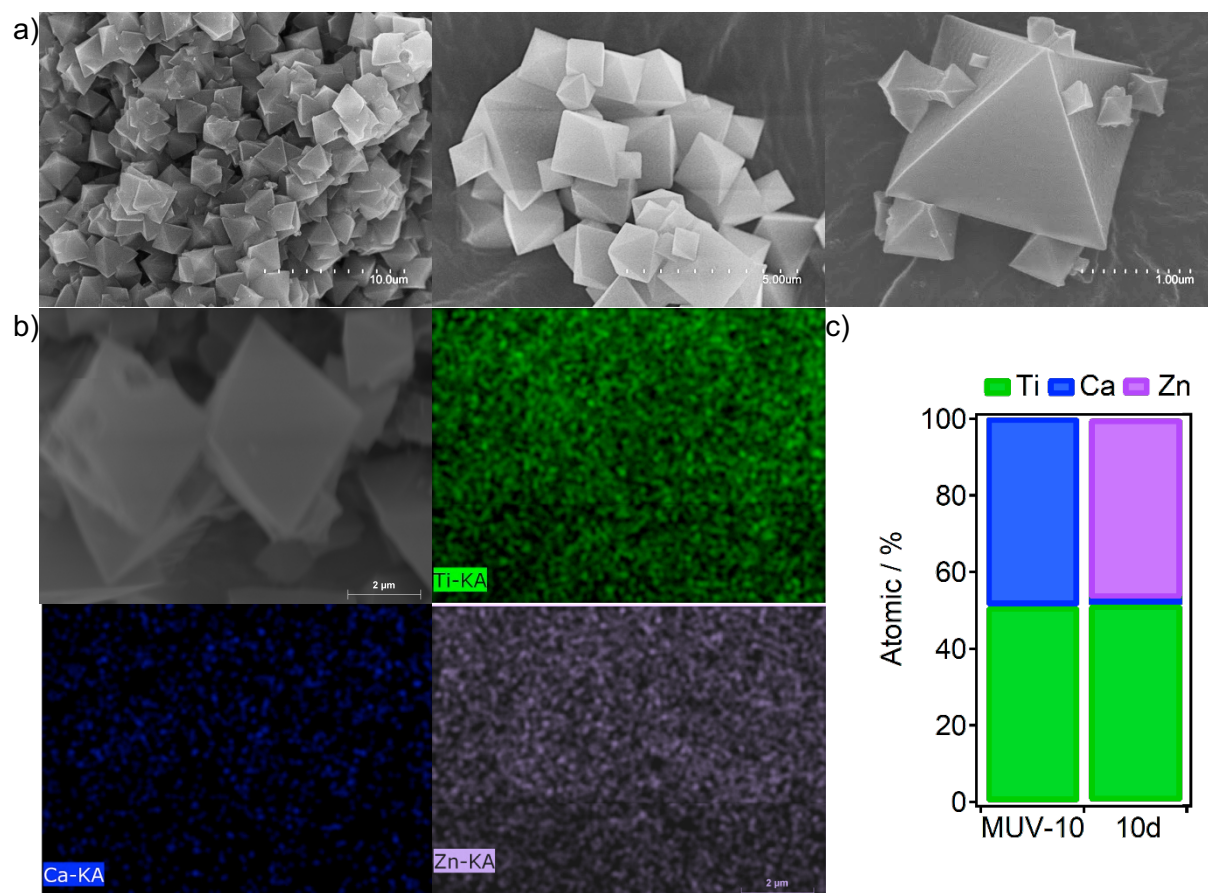
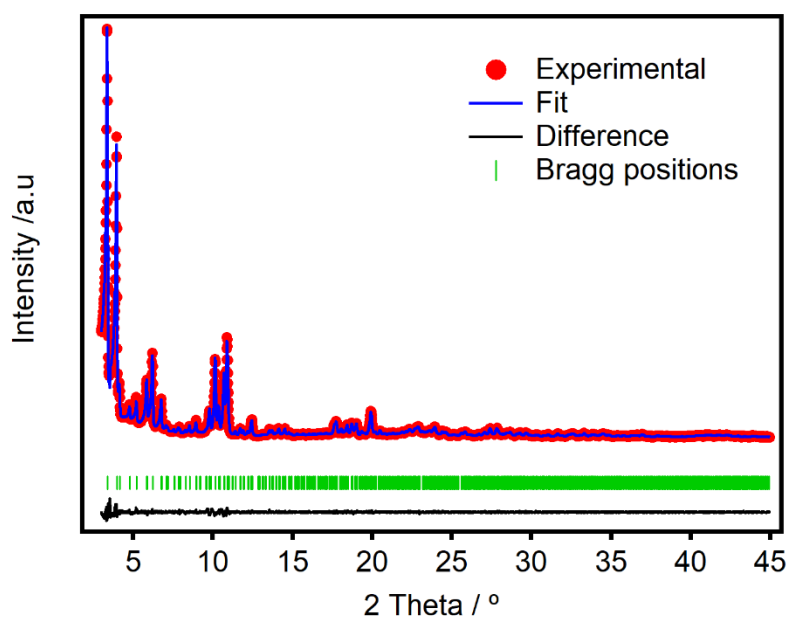


Figure S67. MUV-101(Zn)-10d: a) SEM images; b) Area mapping of Ti (green), Ca (blue) and Zn (violet); c) experimental atomic percentage from point and shoot EDX analysis for different crystals.

LeBail Refinement and Powder X-Ray Diffraction (PXRD)



Cubic, F d -3 m; $a = b = c$ 73.9281 Å; $\alpha = \beta = \gamma = 90^\circ$; $V = 40324.6906 \text{ \AA}^3$; $R_e = 2.91\%$, $R_p = 3.93\%$, $R_{wp} = 2.67\%$, $GoF = 1.5$.

Figure S68. Experimental (red dots), calculated (blue line), difference plot $[(I_{obs} - I_{calc})]$ (black line, bottom panel) and Bragg positions (green ticks, bottom panel) for the Le Bail refinement of experimental diffraction data of MUV-101(Zn) after 10 days.

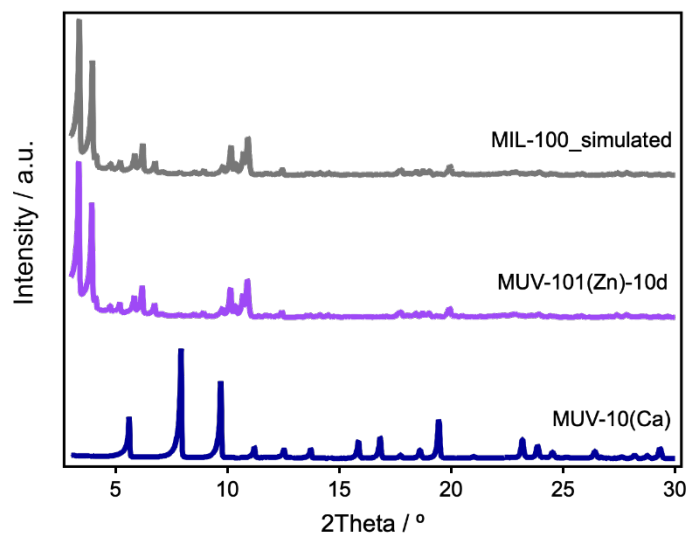


Figure S69. PXRD comparison of MUV-10(Ca) (bottom), MUV-101(Zn) (middle) and simulated MIL-100 (top).

Analysis of N₂ adsorption/desorption isotherms at 77 K

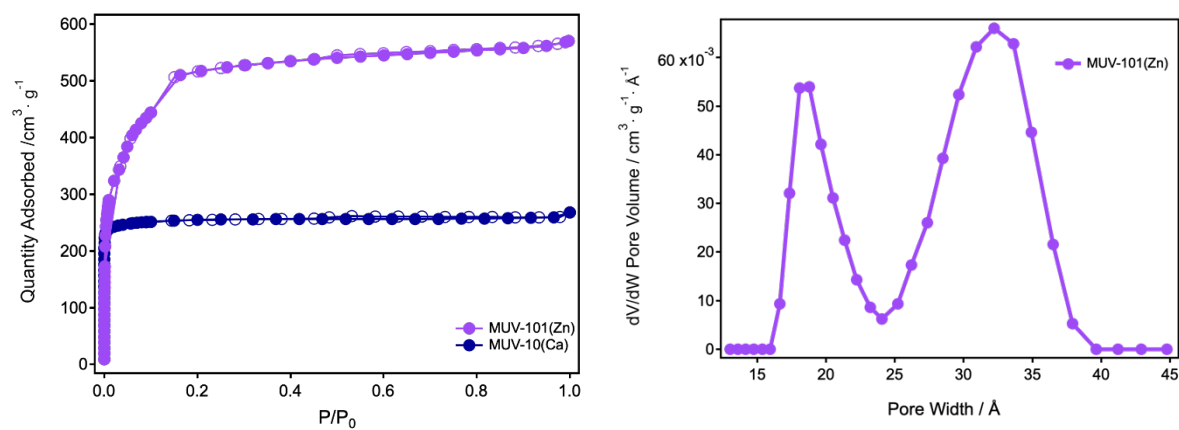


Figure S70: a) N₂ adsorption isotherm of MUV-101(Zn) compared with MUV-10(Ca); b) Pore size distribution (PSD).

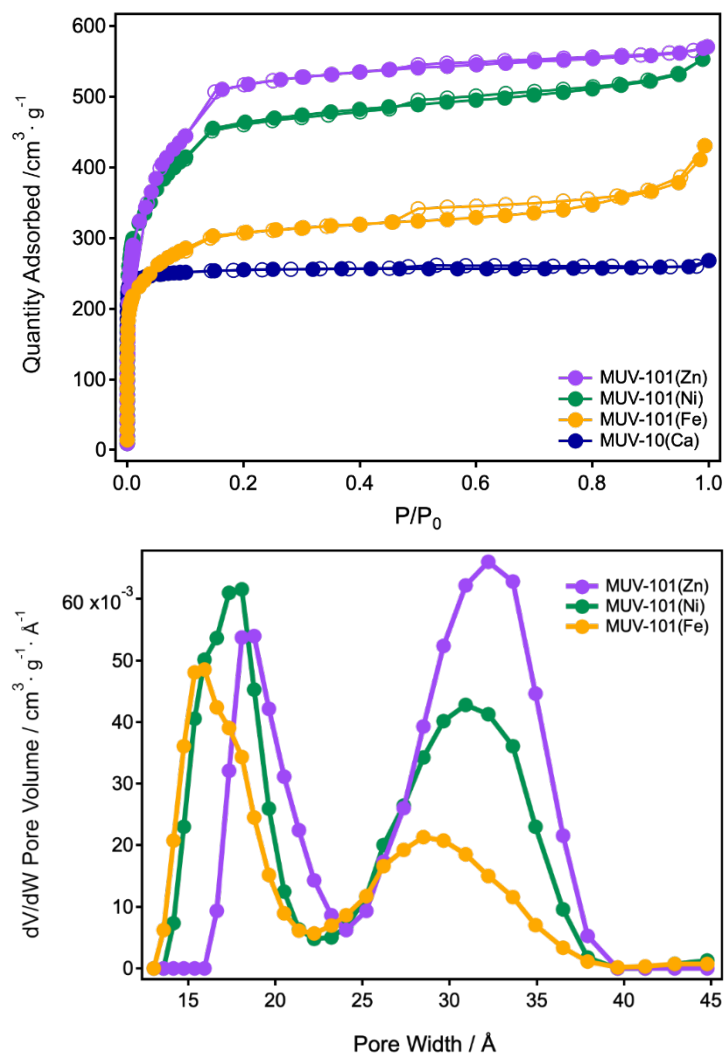


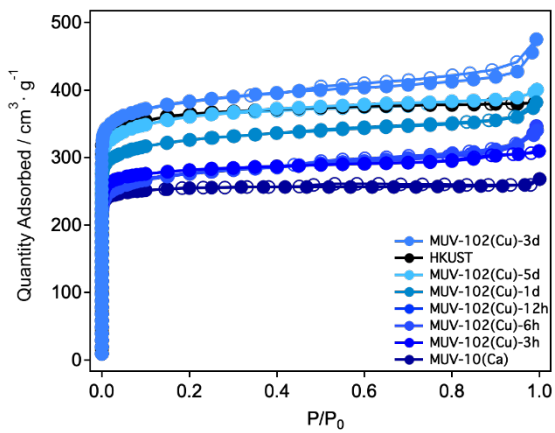
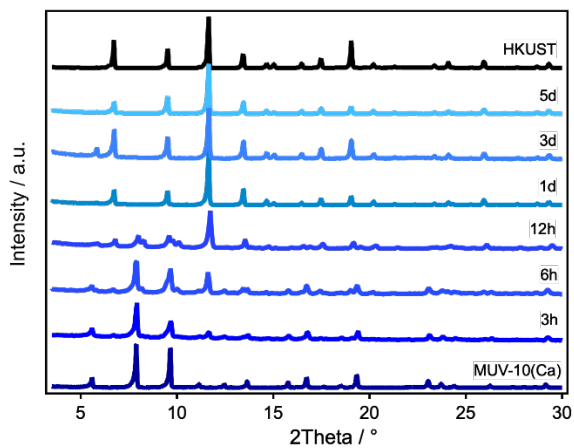
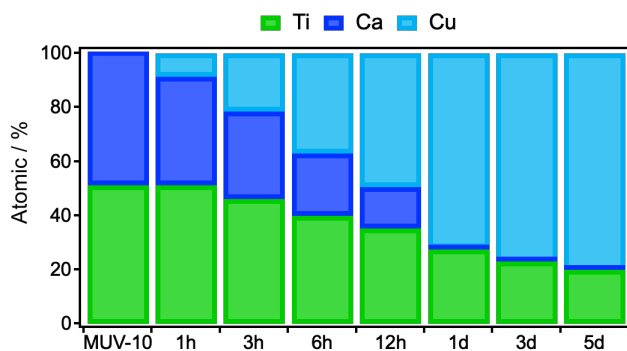
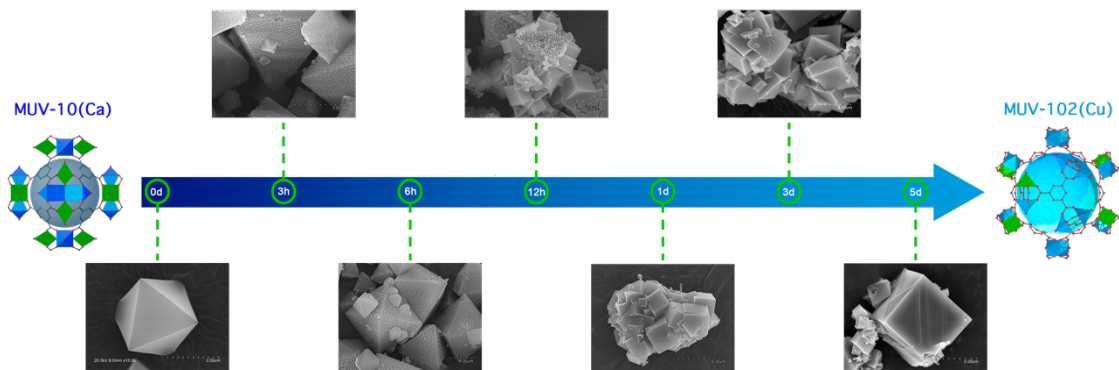
Figure S71. General comparison of N_2 adsorption isotherms (top) and pore size distributions (bottom) of MUV-101(Fe), MUV-101(Ni) and MUV-101(Zn).

Table S14. Summary of the analysis of the N₂ adsorption/desorption isotherm of MUV-101(Zn) after 10 days and MUV-101(Fe, Ni) after 30 days at 77 K. Specific surface area (SA) was calculated with the multi-point Brunauer-Emmett-Teller (BET) method. Total pore volume (V_t) was estimated at P/P₀=0.96. Pore size distribution (PSD) was analysed by using the solid density functional theory (NLDFT) for the adsorption branch by assuming a cylindrical pore model.

Sample	SA _{BET} [m ² ·g ⁻¹]	V _t [cm ³ ·g ⁻¹]	PSD _{NLDFT} [nm]	
			micro	meso
MUV-101(Fe)	1137	0.59	1.6	2.9
MUV-101(Ni)	1716	0.82	1.8	3.1
MUV-101(Zn)	1865	0.87	1.8	3.2

S7. TRANSFORMATION OF MUV-10(Ca) IN MUV-102(Cu) BY METAL EXCHANGE WITH Cu^{2+}

S7.1. MUV-102(Cu) at a glance



S7.2. Evolution of metal content with time

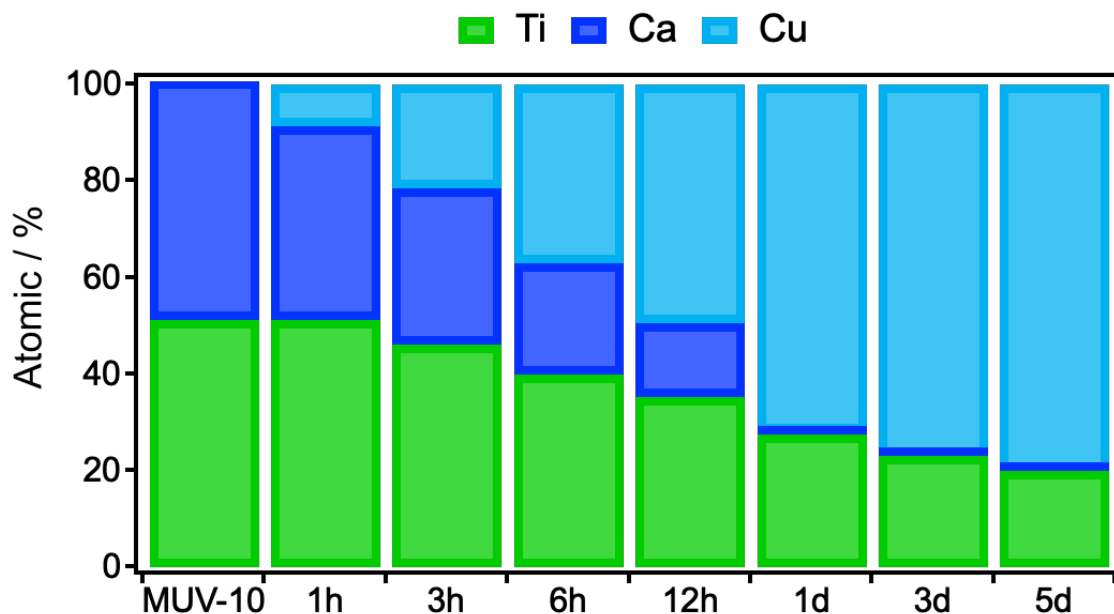


Figure S72. Evolution of the metal content (calcium, titanium and copper) in the crystals isolated for the different stages of transformation of MUV-10(Ca) into MUV-102(Cu). Experimental values were determined by EDX analysis with a Hitachi S-4800 scanning electron microscope at an accelerating voltage of 20 keV.

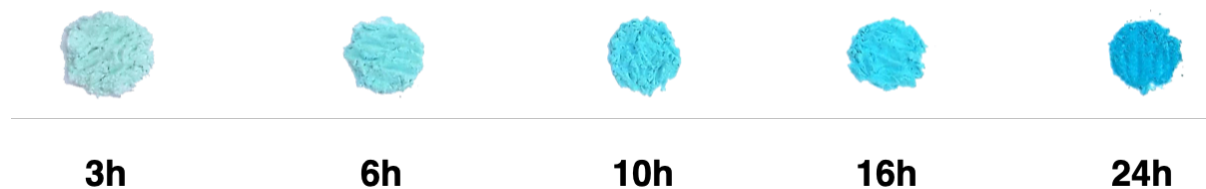


Figure S73. The incorporation of copper concomitant to the formation of MUV-102(Cu) is associated to a gradual color change from white to blue.

Table S15. Experimental metal content determined by EDX analysis.

Sample	^[a] Normalized		
	Ca [%]	Ti [%]	Cu [%]
MUV-102(Cu)-1h	40.3 ± 0.2	51.2 ± 0.1	8.5 ± 0.1
MUV-102(Cu)-3h	32.4 ± 0.1	46.1 ± 0.3	21.5 ± 0.3
MUV-102(Cu)-6h	23.0 ± 0.1	40.0 ± 0.0	37.0 ± 0.3
MUV-102(Cu)-12h	15.2 ± 0.3	35.5 ± 0.1	49.5 ± 0.1
MUV-102(Cu)-1d	0.5 ± 0.1	27.5 ± 0.1	72.0 ± 0.1
MUV-102(Cu)-3d	0.5 ± 0.1	27.5 ± 0.1	73.0 ± 0.1
MUV-102(Cu)-5d	0.0 ± 0.3	20.0 ± 0.2	80 ± 0.2

^[a] Calculated by normalizing to total M²⁺ content.

S7.3. Scanning Electron Microscopy (SEM) and EDAX

Scanning Electron microscopy and single point energy-dispersive X-Ray analysis (EDX) of the transformation of MUV-10(Ca) into MUV-102(Cu) from 1 hour to 5 days. Analysis was performed with a Hitachi S-4800 scanning electron microscope at an accelerating voltage of 20 keV. Mapping of Ti (green), Ca (blue) and Cu (yellow) confirm that metal distribution is homogeneous throughout the crystals.

MUV-102(Cu)-1h

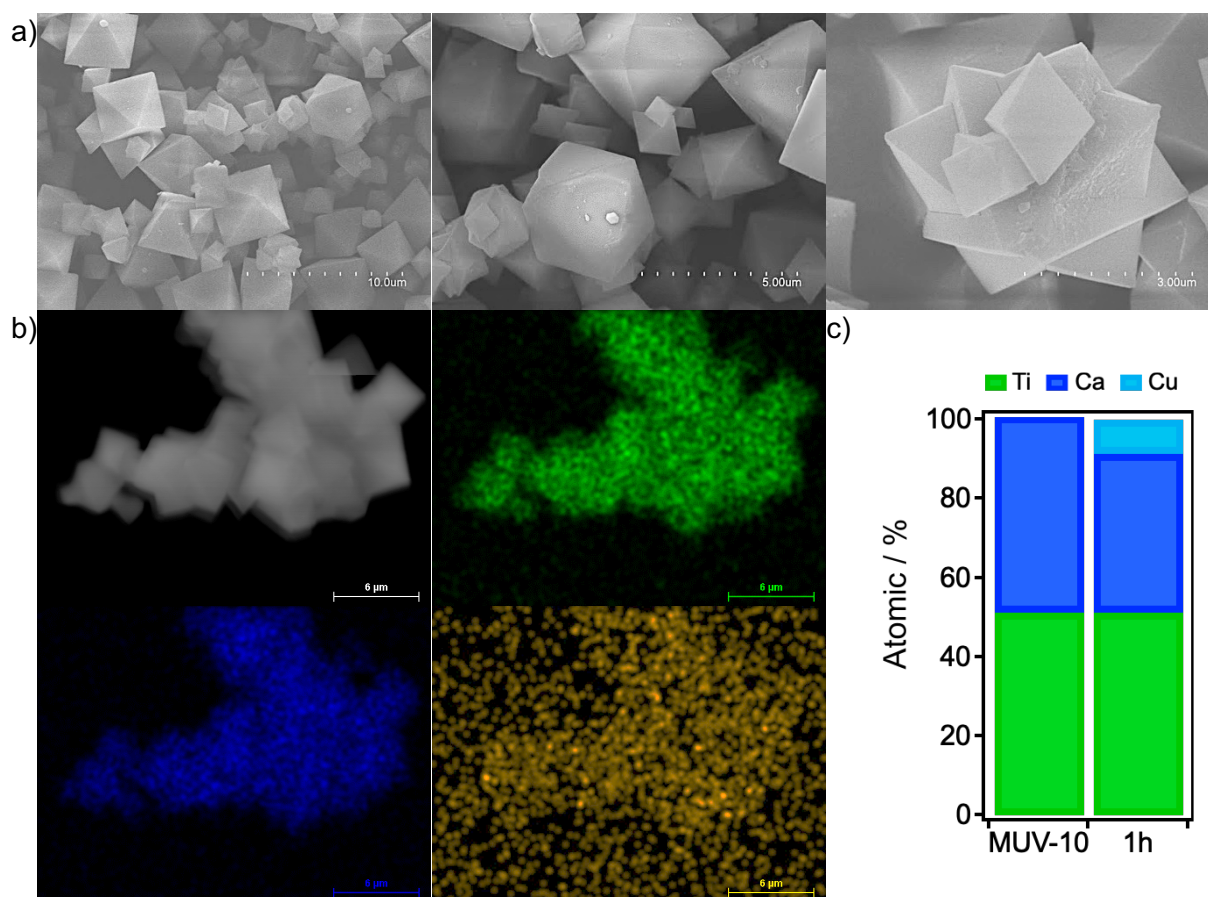


Figure S74. MUV-102(Cu)-1h: a) SEM images; b) Area Mapping of Ti (green), Ca (blue) and Cu (yellow); c) experimental atomic percentage from point and shoot EDX analysis for diferent crystals.

MUV-102(Cu)-3h

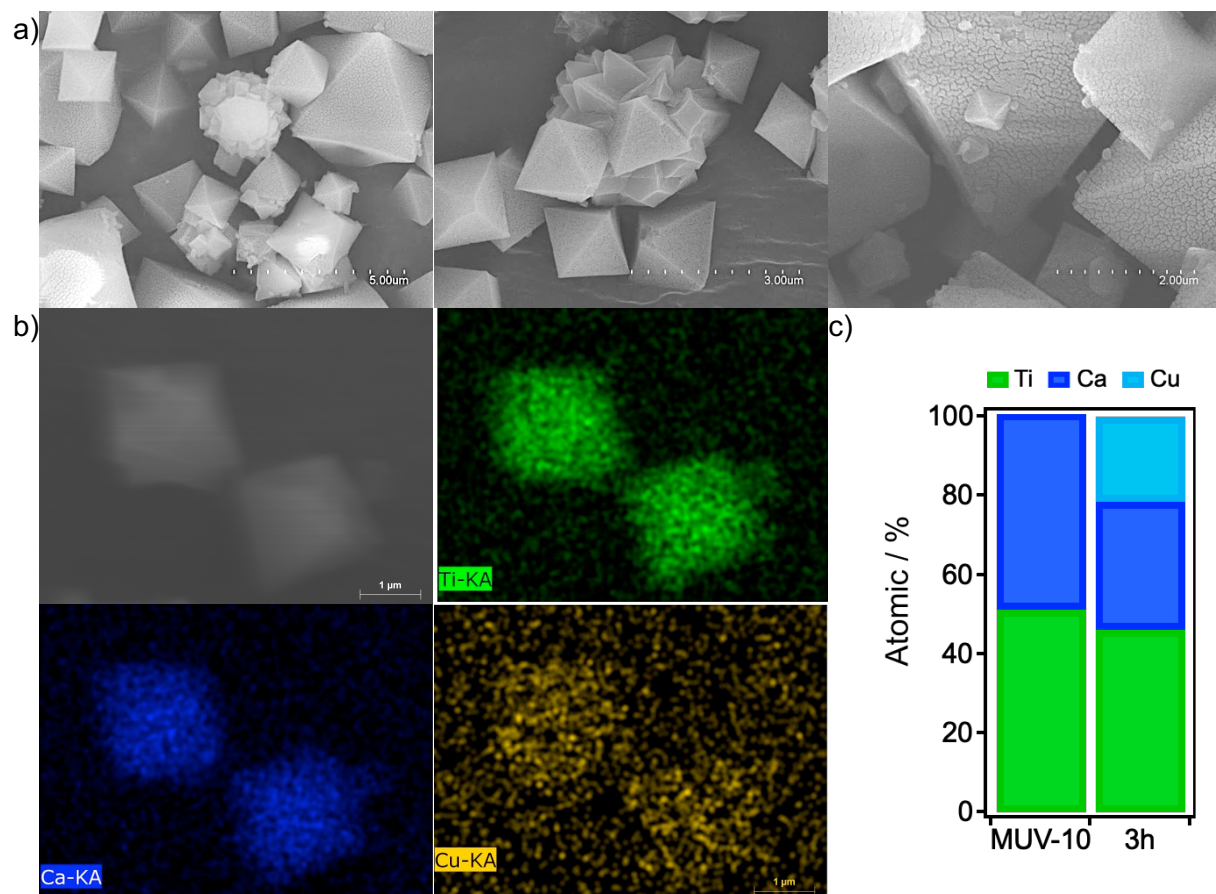


Figure S75. MUV-102(Cu)-3h: a) SEM images; b) Area mapping of Ti (green), Ca (blue) and Cu (yellow); c) experimental atomic percentage from point and shoot EDX analysis for different crystals.

MUV-102(Cu)-6h

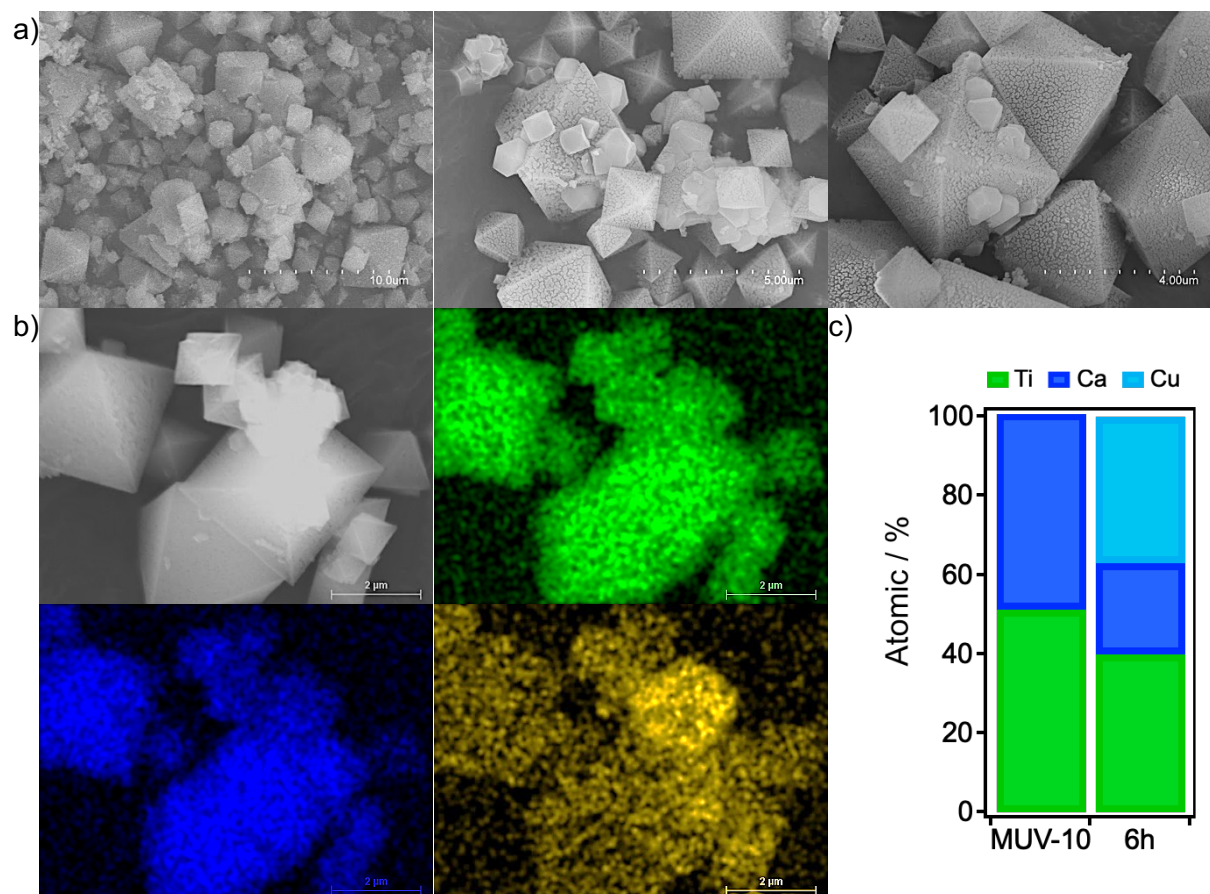


Figure S76. MUV-102(Cu)-6h: a) SEM images; b) Area mapping of Ti (green), Ca (blue) and Cu (yellow); c) experimental atomic percentage from point and shoot EDX analysis for different crystals.

MUV-102(Cu)-12h

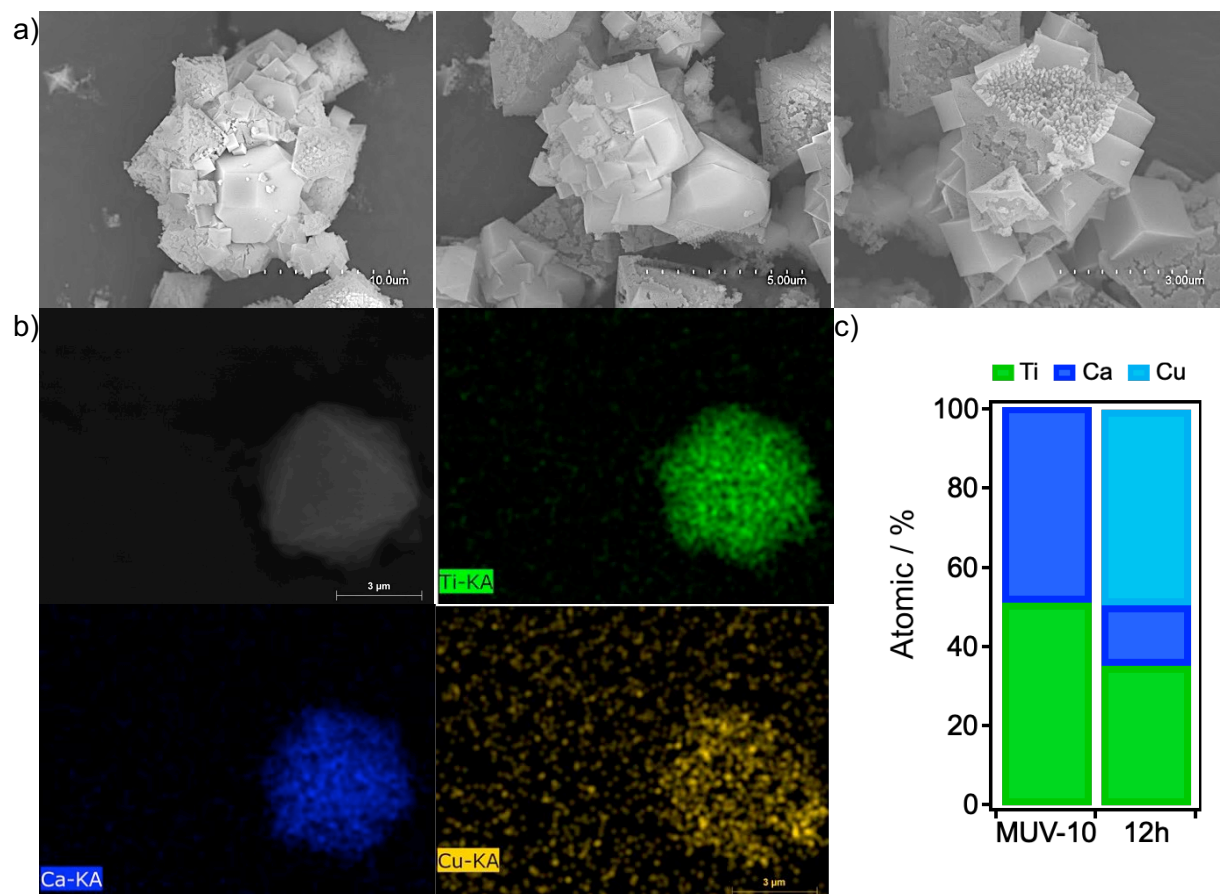


Figure S77. MUV-102(Cu)-12h: a) SEM images; b) Area mapping of Ti (green), Ca (blue) and Cu (yellow); c) experimental atomic percentage from point and shoot EDX analysis for different crystals.

MUV-102(Cu)-1d

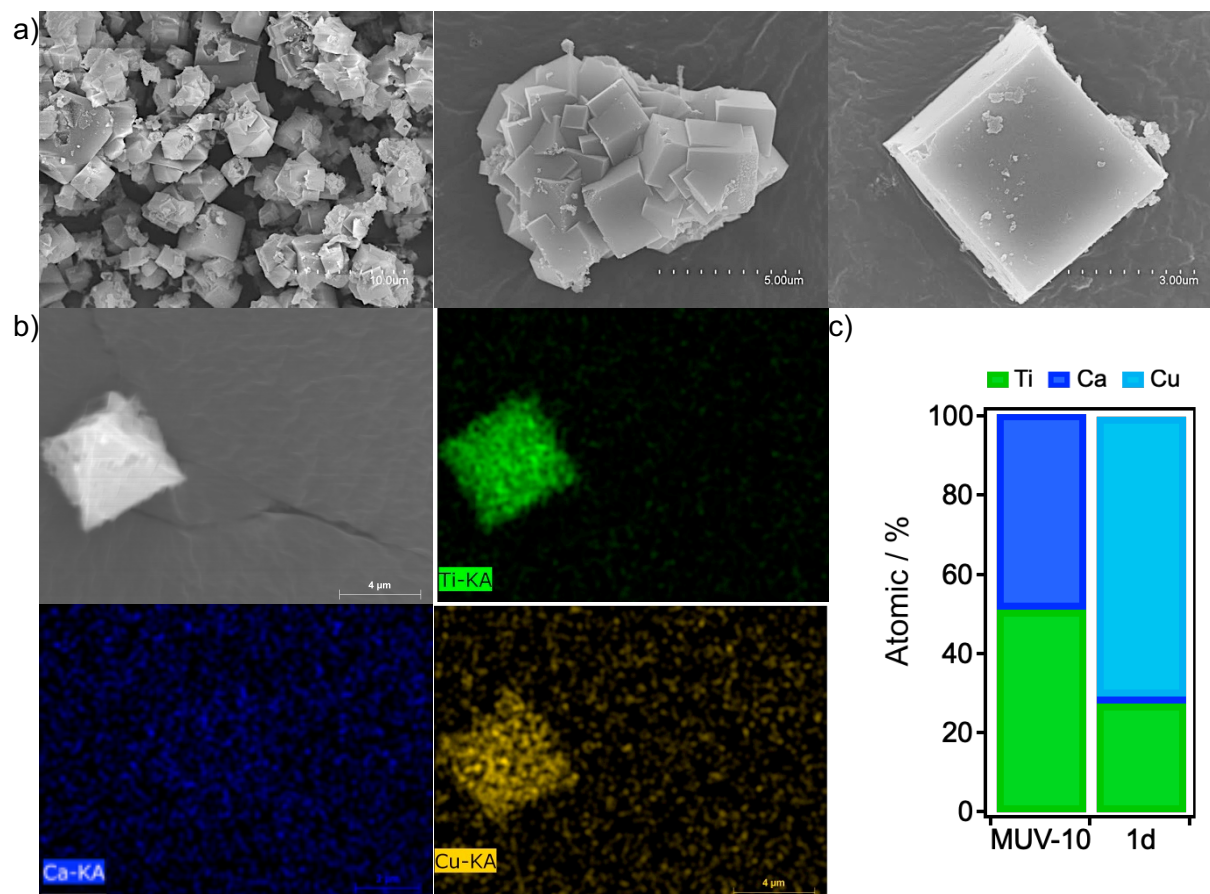


Figure S78. MUV-102(Cu)-1d: a) SEM images; b) Area mapping of Ti (green), Ca (blue) and Cu (yellow); c) experimental atomic percentage from point and shoot EDX analysis for different crystals.

MUV-102(Cu)-3d

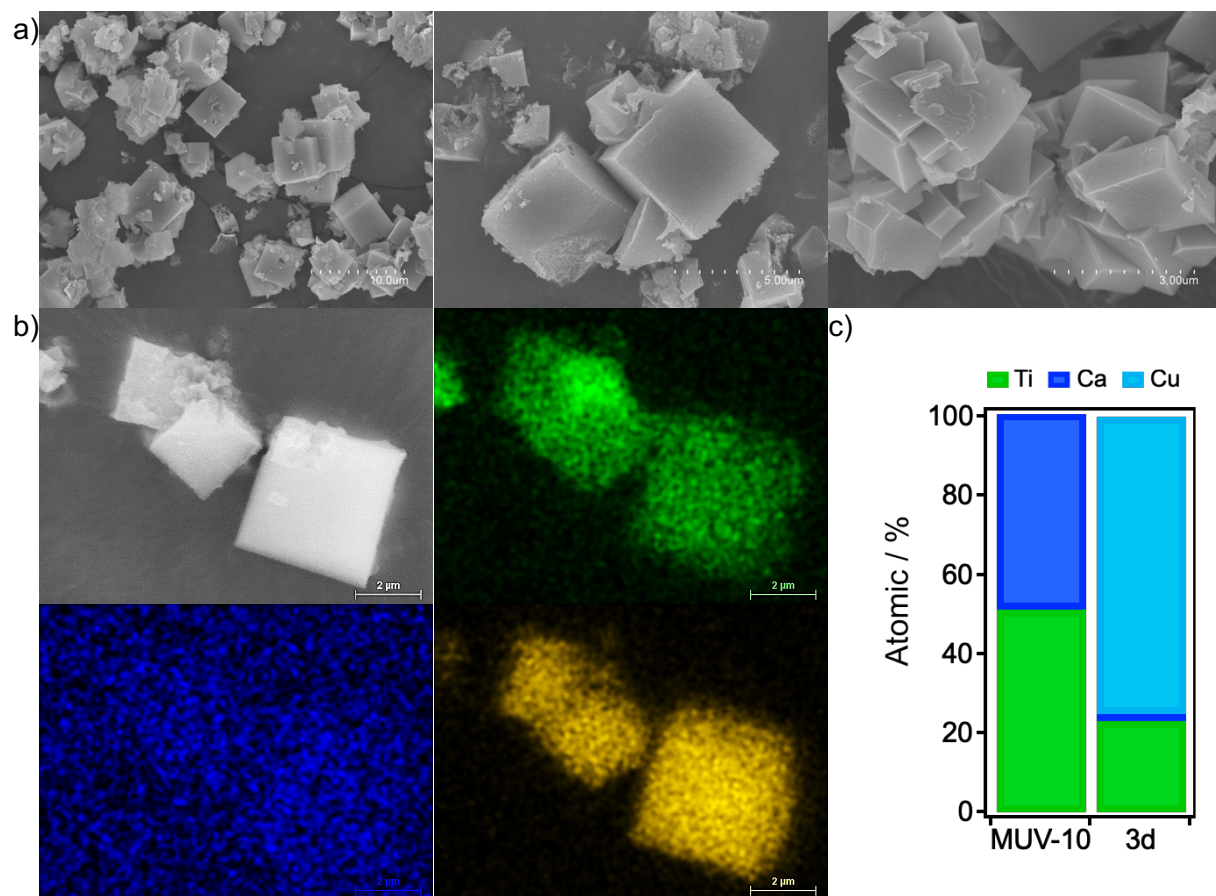


Figure S79. MUV-102(Cu)-3d: a) SEM images; b) Area mapping of Ti (green), Ca (blue) and Cu (yellow); c) experimental atomic percentage from point and shoot EDX analysis for different crystals.

MUV-102(Cu)-5d

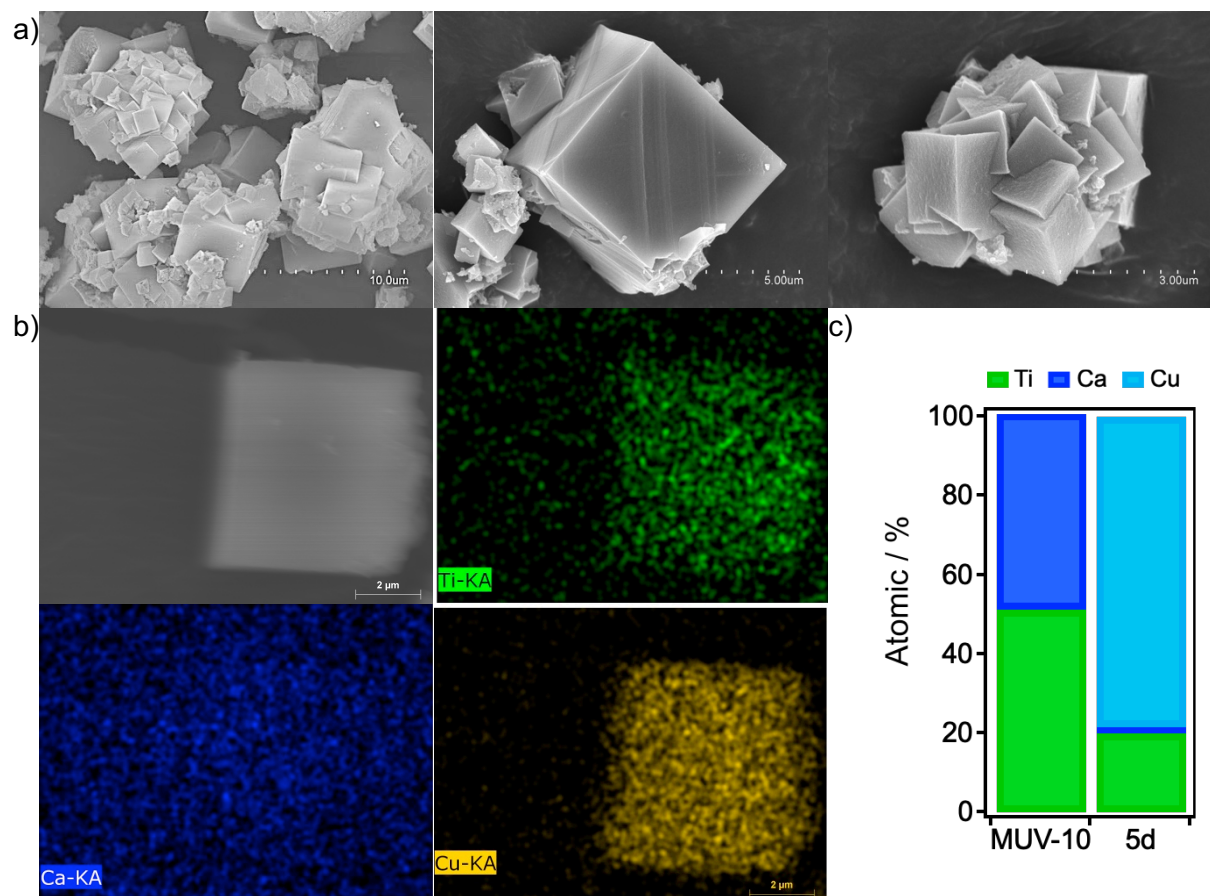
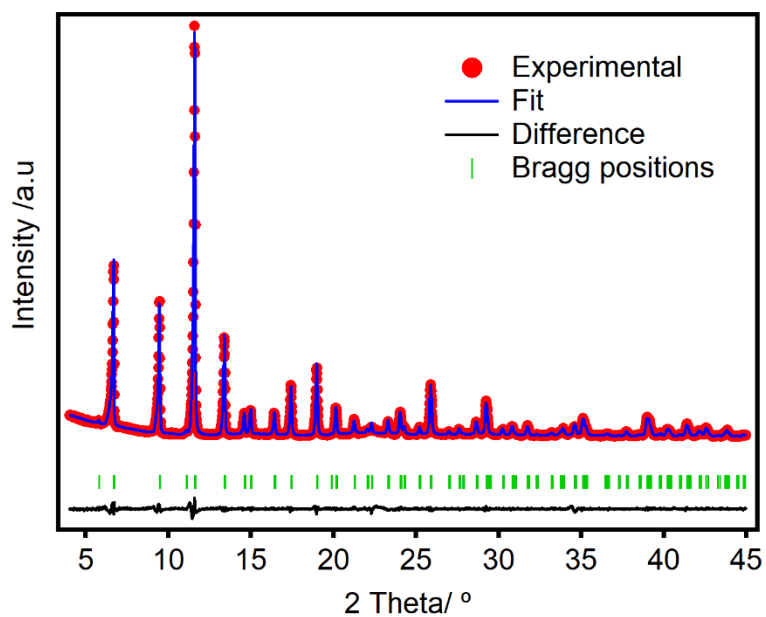


Figure S80: MUV-102(Cu)-5d: a) SEM images; b) Area mapping of Ti (green), Ca (blue) and Cu (yellow); c) experimental atomic percentage from point and shoot EDX analysis for different crystals.

S7.4. Le Bail refinement of MUV-102(Cu)



Cubic, $Fm\bar{3}m$; $a = b = c = 26.4195 \text{ \AA}$; $\alpha = \beta = \gamma = 90^\circ$; $V = 18440.4863 \text{ \AA}^3$; $R_e = 4.44\%$, $R_p = 6.40\%$, $R_{wp} = 3.29\%$, $GoF = 1.9$.

Figure S81. Experimental (red dots), calculated (blue line), difference plot $[(I_{obs} - I_{calc})]$ (black line, bottom panel) and Bragg positions (green ticks, bottom panel) for the Le Bail refinement of experimental diffraction data of MUV-102(Cu) after 5 days.

S7.5. Powder X-Ray Diffraction (PXRD)

MUV-102(Cu)-3h

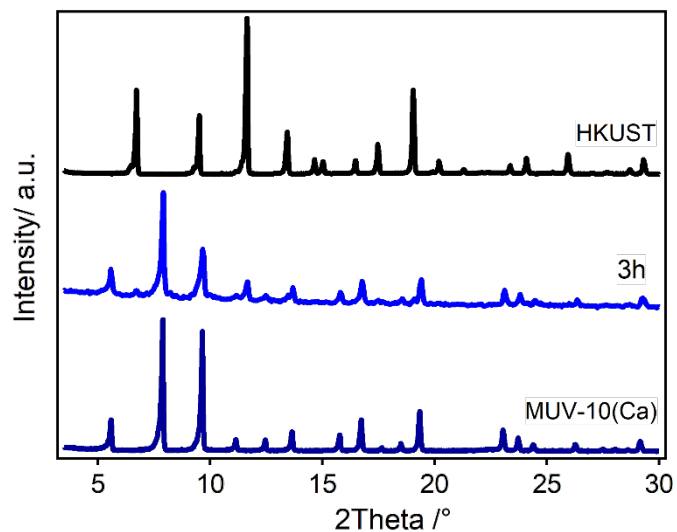


Figure S82. PXRD comparison of MUV-10(Ca) (bottom), MUV-102(Cu)-3h (middle) and commercial HKUST (top).

MUV-102(Cu)-6h

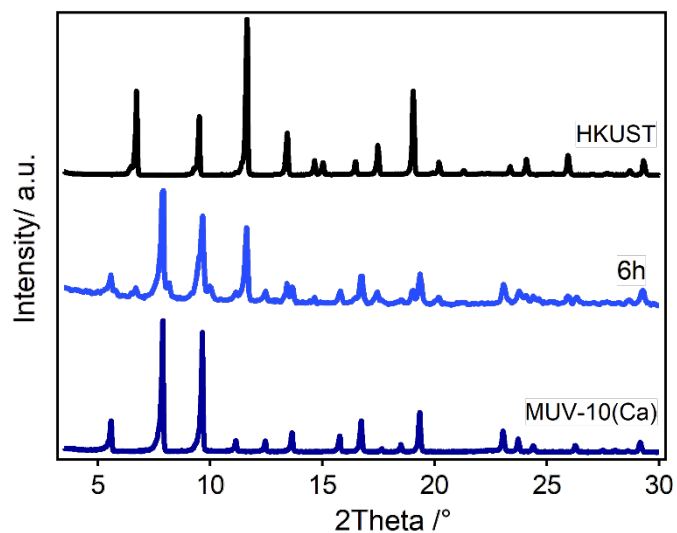


Figure S83. PXRD comparison of MUV-10(Ca) (bottom), MUV-102(Cu)-6h (middle) and commercial HKUST (top).

MUV-102(Cu)-12h

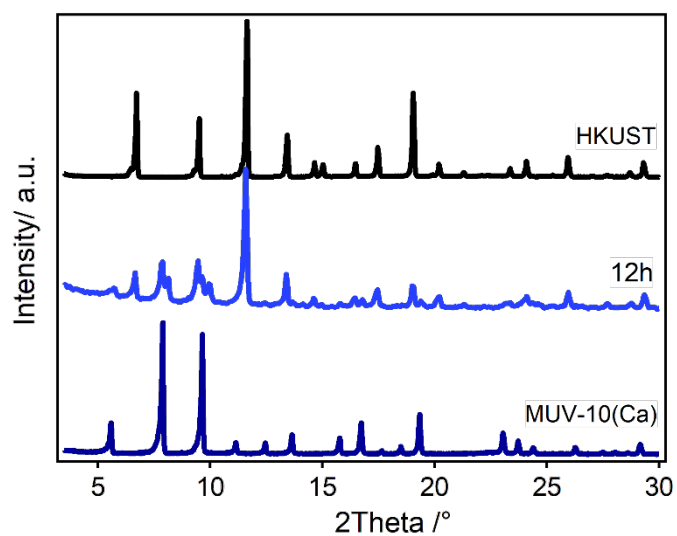


Figure S84. PXRD comparison of MUV-10(Ca) (bottom), MUV-102(Cu)-12h (middle) and commercial HKUST (top).

MUV-102(Cu)-1d

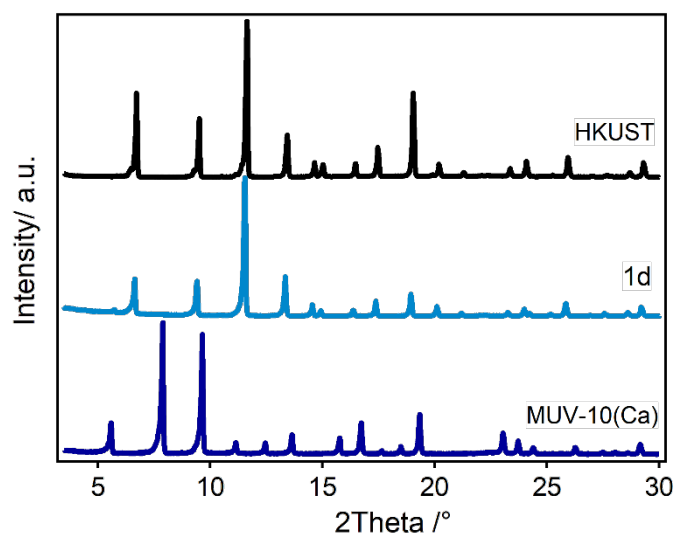


Figure S85. PXRD comparison of MUV-10(Ca) (bottom), MUV-102(Cu)-1d (middle) and commercial HKUST (top).

MUV-102(Cu)-3d

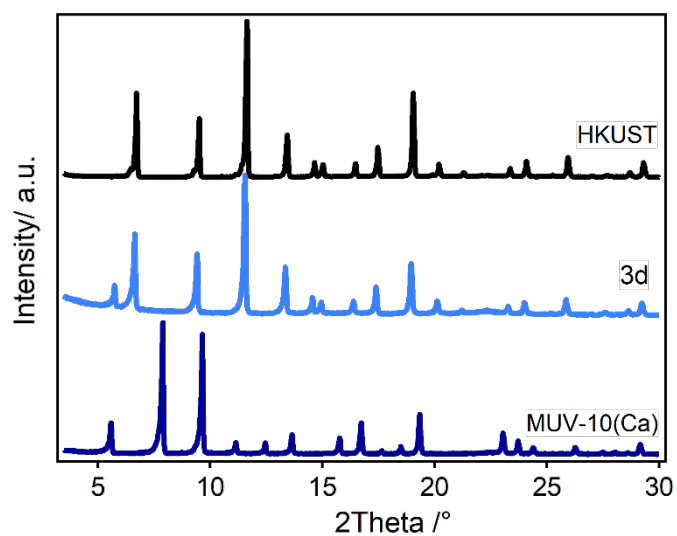


Figure S86. PXRD comparison of MUV-10(Ca) (bottom), MUV-102(Cu)-3d (middle) and commercial HKUST (top).

MUV-102(Cu)-5d

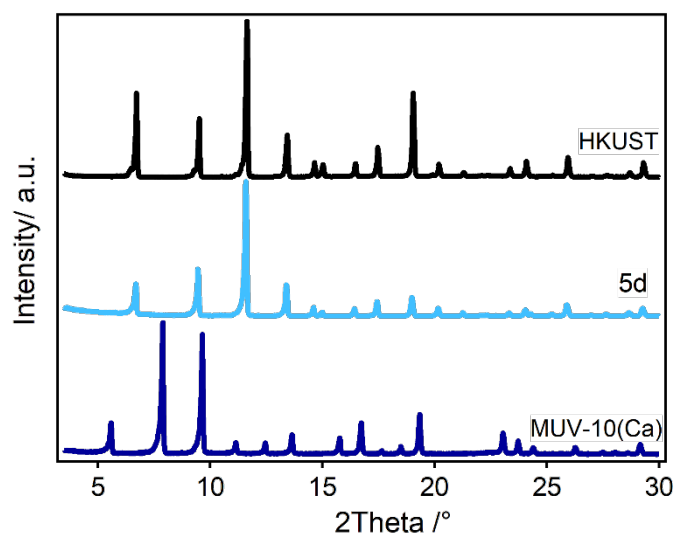


Figure S87. PXRD comparison of MUV-10(Ca) (bottom), MUV-102(Cu)-5d (middle) and commercial HKUST (top).

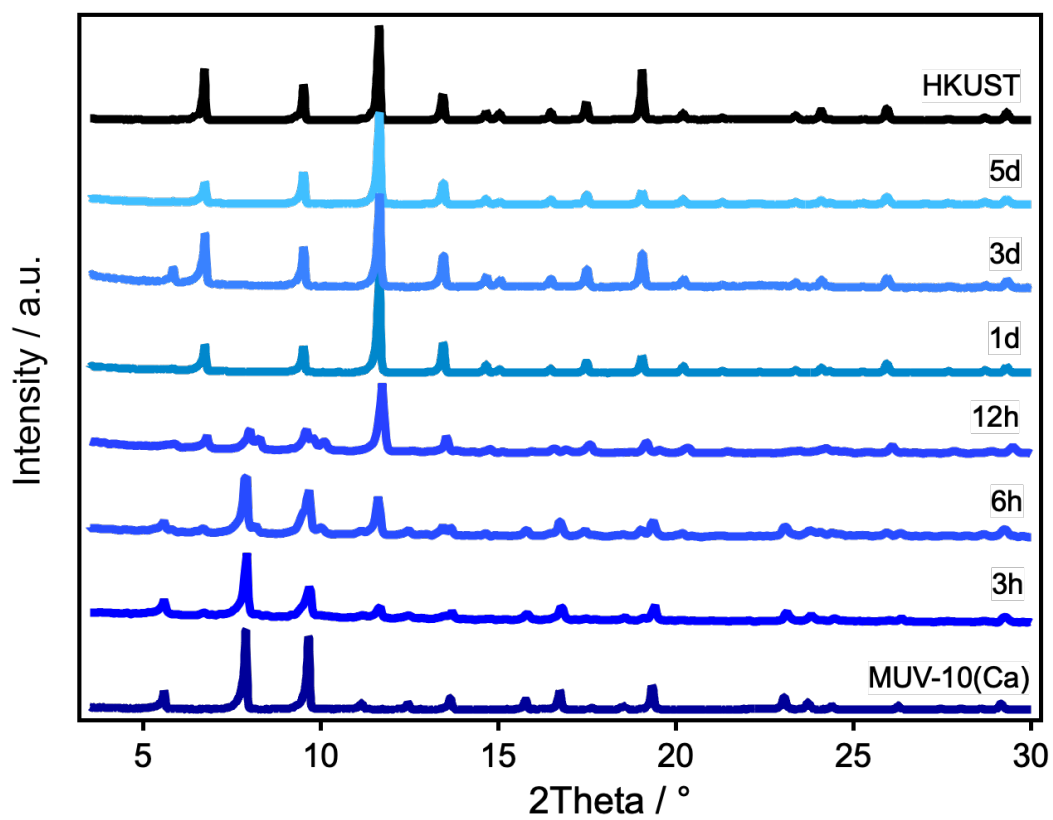


Figure S88. PXRD comparison of the transformation of MUV-10(Ca) into MUV-102(Cu) from 3 hours to 5 days.

S7.6. EXAFS data analysis and fitting

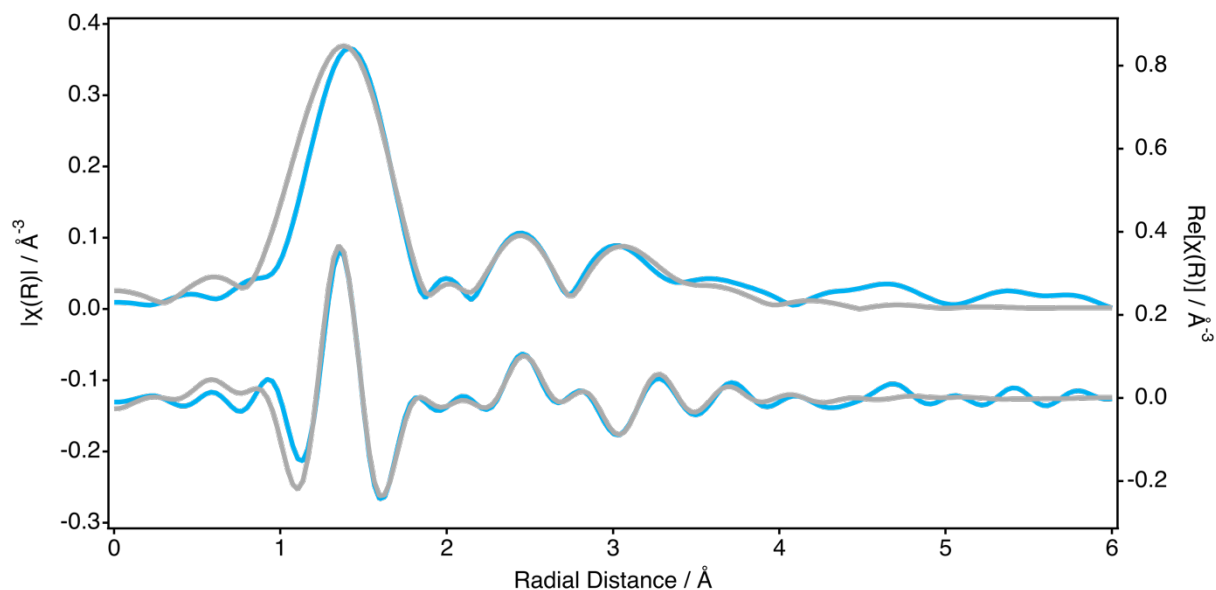


Figure S89. Ti K-edge magnitude and real part of R space for MUV-102(Cu)-5d. Gray line experimental fit to the data.

Table S16. Parameters of the coordination shells around Fe atoms in MUV-102(Cu)-5d: average number of neighbour atoms (N), distance (R), and Debye-Waller factor (σ^2).

Path	N	R / Å	σ^2 / Å ²
Ti-O	4	2.84	0.015
Ti-Cu	1	2.84	0.015
Ti-Oax	1	1.79	0.001
Ti-C	4	3.41	0.03

Table S17. DFT computed interatomic distances for optimized HKUST and MUV-102(Cu) in primitive cell. Distances are in the table are reported in Angstroms.

Cluster	d(Cu-Cu) / d(Ti-Cu)	d(Ti-Oax)	d(Cu-O) / d(Ti-O)
HKUST	2.495	-	1.966
MUV-102(Cu)	2.479/2.907	1.623	1.954/2.038

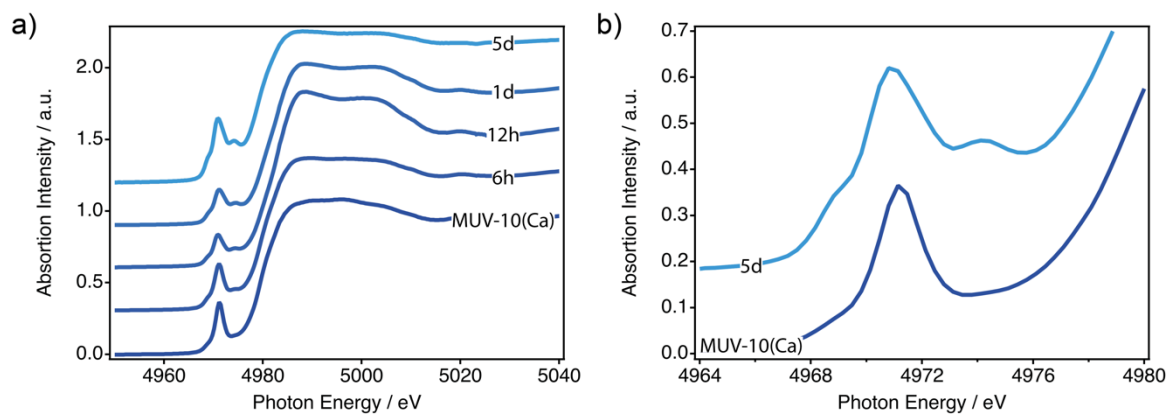


Figure S90. a, b) XANES Ti-K edges spectra of MUV-102(Cu) at different stages of transformation.

Table S18. Ti K-edge XANES analyses for MUV-102(Cu) systems. CN stands for coordination number.

Sample	Pre-edge (eV)	Edge (eV)	Pre-edge/edge height ^a	Pre-edge components	CN
MUV-10	4971.0	4979.5	0.34	3	6
MUV-102(Cu)-6h	4971.4	4979.7	0.32	3	6
MUV-102(Cu)-12h	4971.2	4980.9	0.18	3	6
MUV-102(Cu)-1d	4971.5	4980.3	0.22	3	6
MUV-102(Cu)-5d	4971.3	4979.4	0.40	3	6 ^a

^a Distorted octahedral geometry.^{7,19}

Table S19. Cu K-edge XANES analyses for MUV-102(Cu) systems. CN stands for coordination number.

Sample	Pre-edge 1s→3d (eV)	Pre-edge 1s→4p (eV)	Edge (eV)	CN
HKUST	4977.6	8986.1	8992.1	5
MUV-102(Cu)-3h	4977.6	8987.2	8992.3	5
MUV-102(Cu)-3d	4977.8	8987.3	8992.5	5

S7.7. Electron Spin Resonance

The incorporation of diamagnetic Ti^{4+} ions to generate heterometallic $\text{Ti}^{4+}\text{-Cu}^{2+}$ paddle wheel units is expected to leave uncompensated $S = \frac{1}{2}$ spins in MUV-102(Cu) that can be detected with ESR. In turn, the antiferromagnetically coupled $\text{Cu}^{2+}\text{-Cu}^{2+}$ pairs in the paddle wheel units of homometallic HKUST-1 shall result in a ESR silent $S = 0$ ground state at low temperatures. As shown below, the spectra of MUV-102(Cu)-6h and 3d confirms the presence of paramagnetic Cu^{2+} units indicative of the formation of the heterometallic TiCu cluster compared to the minimum contribution of this signal in the spectrum of HKUST-1. This signal has been previously attributed to the presence of extraframework $[\text{Cu}(\text{OH}_2)_6]^{2+}$ complexes.²⁰

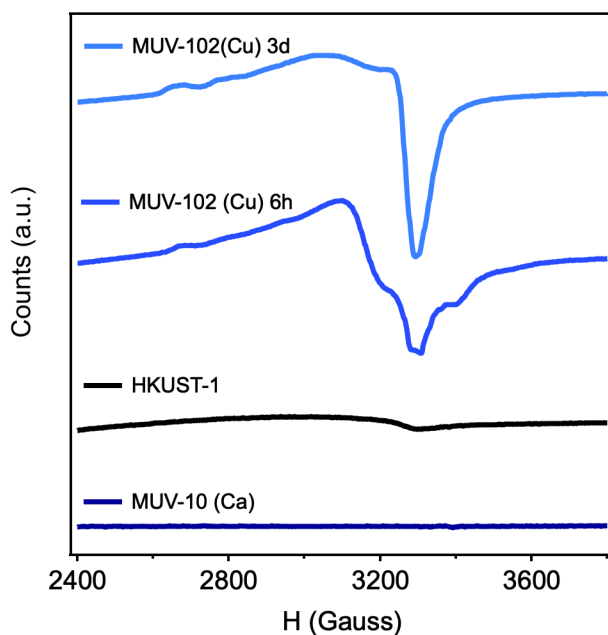


Figure S91. EPR spectra of MUV-10(Ca), HKUST-1 and MUV-102(Cu) 6h and 3d confirming the presence of cupric $S = \frac{1}{2}$ signals in the last two indicative of the formation of heterometallic TiCu clusters in MUV-102(Cu).

S7.8. STEM-EDX data and analysis

MUV-102(Cu)-6h

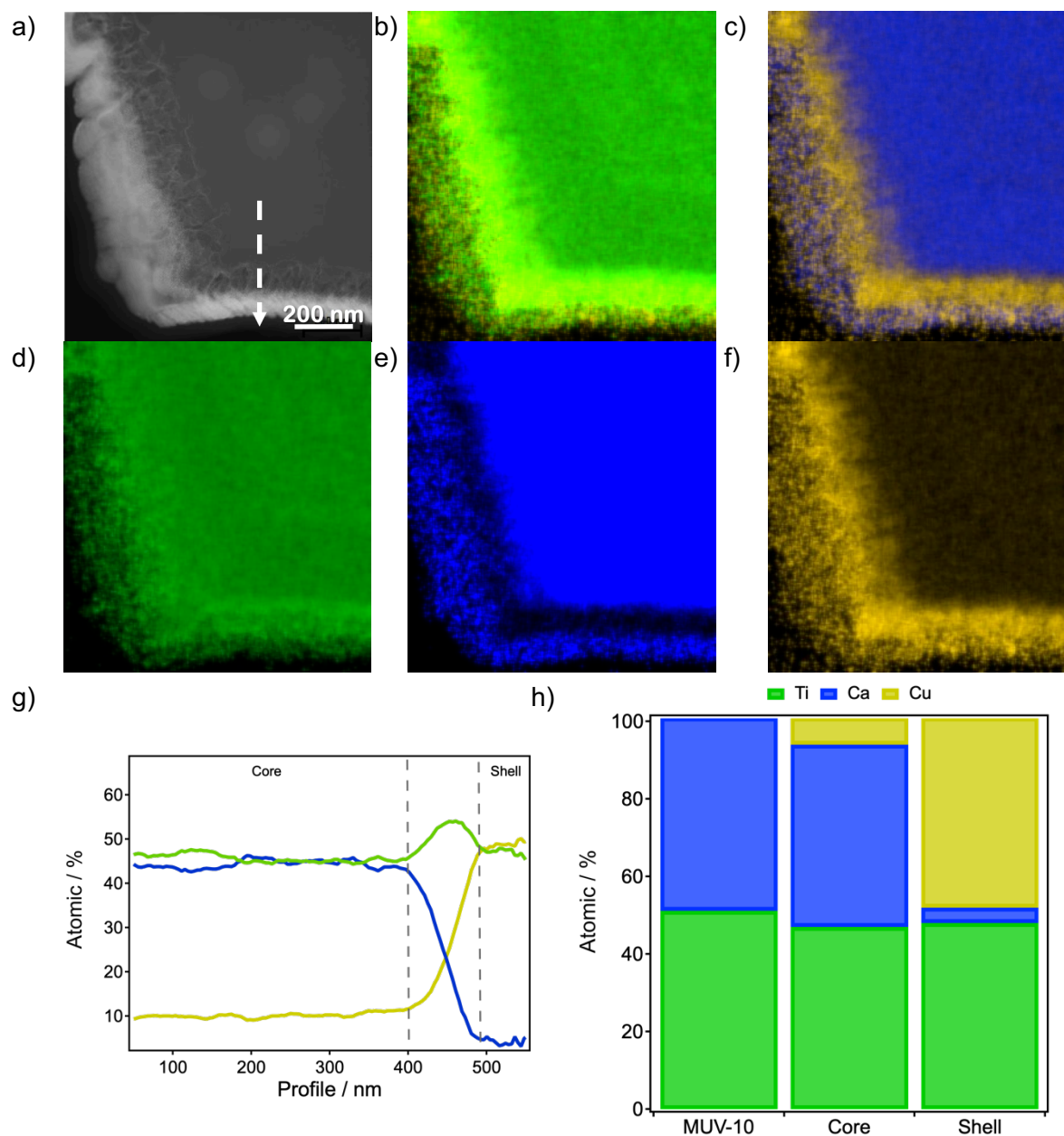


Figure S92. a) STEM image of a sectioned lamellae of MUV-102(Cu)-6h and high resolution element mapping: b) Ti + Cu; c) Ca +Cu; d) Ti (green); e) Ca (blue); f) Cu (yellow); g) relative distribution of metal contents across the crystal from the core (0-400 nm) to the shell (490-550 nm) and h) Visual representation of the metal content in both areas compared to MUV-10(Ca).

S7.9. Analysis of N₂ adsorption/desorption isotherms at 77 K and porosity changes with the degree of transformation

MUV-102(Cu)-3h

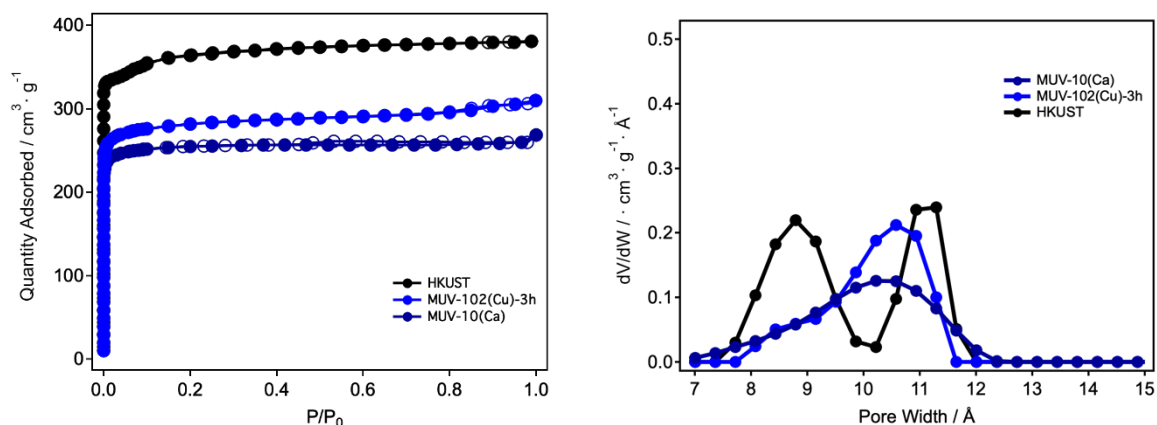


Figure S93. a) N₂ adsorption isotherm of MUV-102(Cu)-3h compared with MUV-10(Ca) and commercial HKUST soaked during 5 days in MeOH at room temperature; b) Pore size distribution (PSD).

MUV-102(Cu)-6h

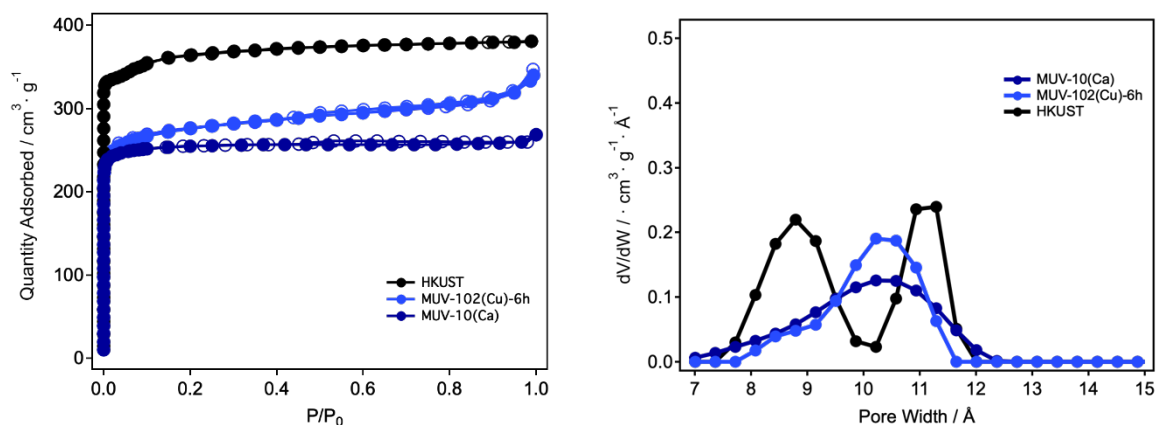


Figure S94. a) N₂ adsorption isotherm of MUV-102(Cu)-6h compared with MUV-10(Ca) and commercial HKUST soaked during 5 days in MeOH at room temperature; b) Pore size distribution (PSD).

MUV-102(Cu)-12h

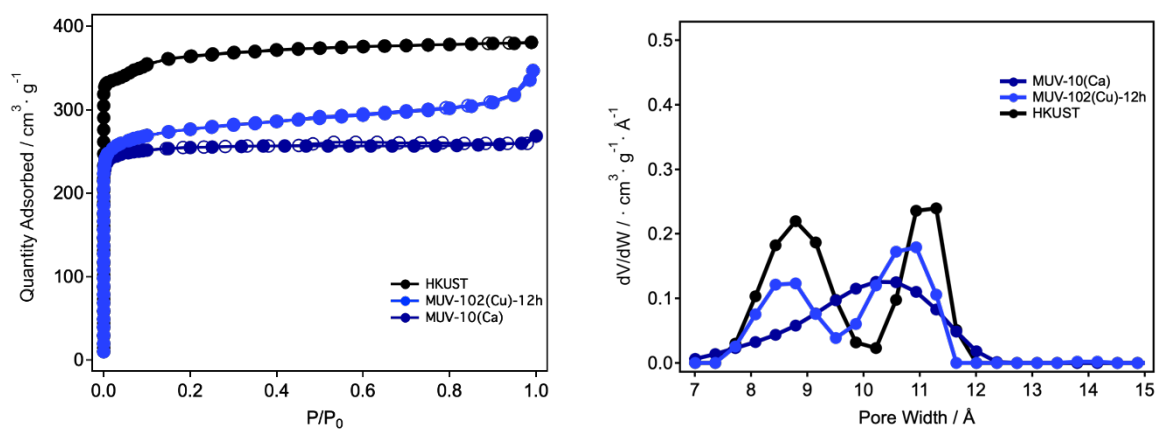


Figure S95. a) N₂ adsorption isotherm of MUV-102(Cu)-12h compared with MUV-10(Ca) and commercial HKUST soaked during 5 days in MeOH at room temperature; b) Pore size distribution (PSD).

MUV-102(Cu)-1d

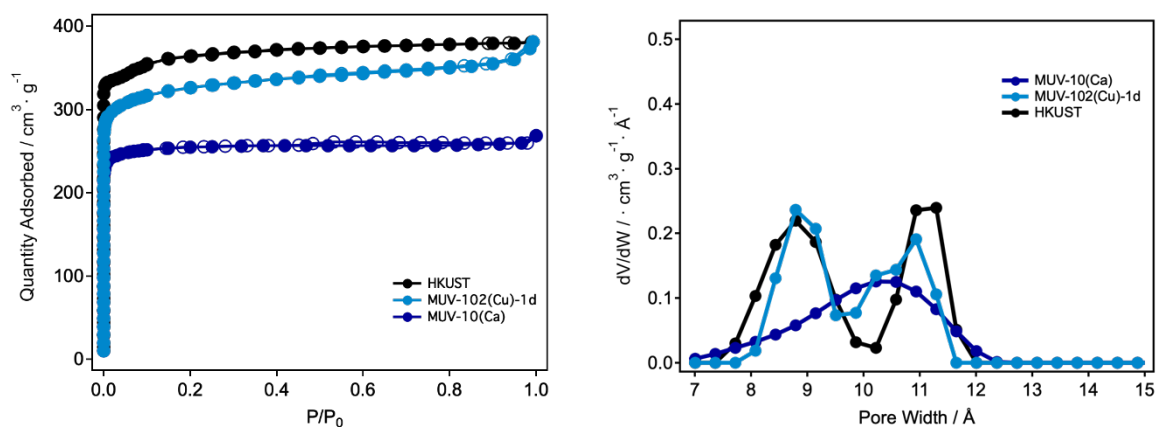


Figure S96. a) N₂ adsorption isotherm of MUV-102(Cu)-1d compared with MUV-10(Ca) and commercial HKUST soaked during 5 days in MeOH at room temperature; b) Pore size distribution (PSD).

MUV-102(Cu)-3d

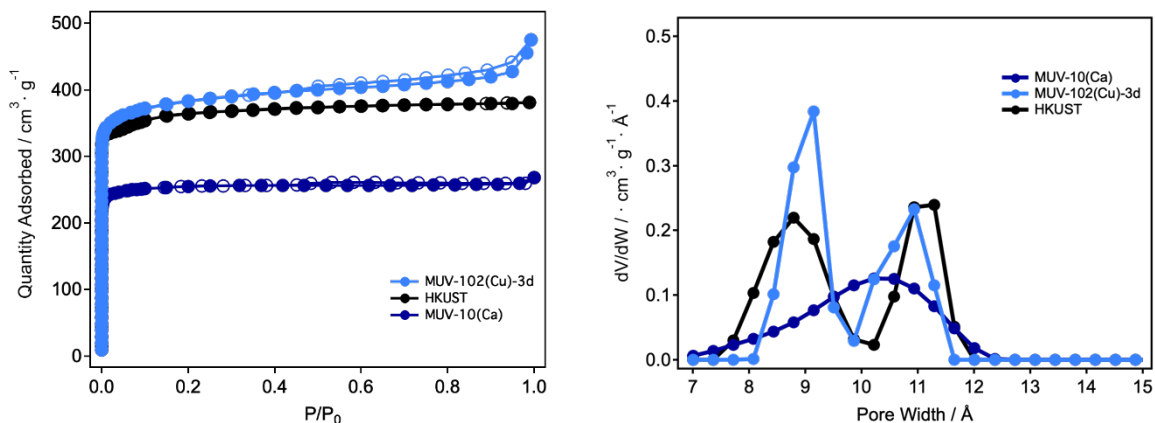


Figure S97. a) N₂ adsorption isotherm of MUV-102(Cu)-3d compared with MUV-10(Ca) and commercial HKUST soaked during 5 days in MeOH at room temperature; b) Pore size distribution (PSD).

MUV-102(Cu)-5d

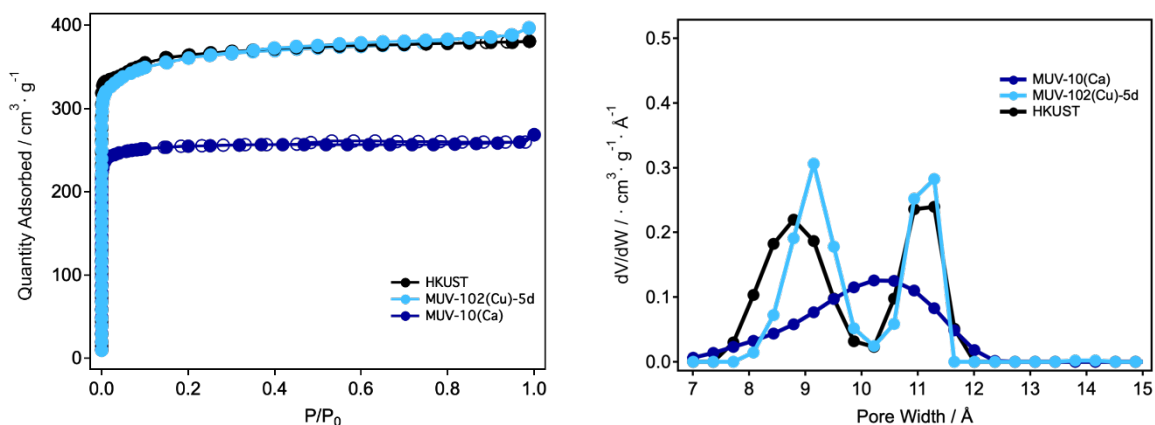


Figure S98. a) N₂ adsorption isotherm of MUV-102(Cu)-5d compared with MUV-10(Ca) and commercial HKUST soaked during 5 days in MeOH at room temperature; b) Pore size distribution (PSD).

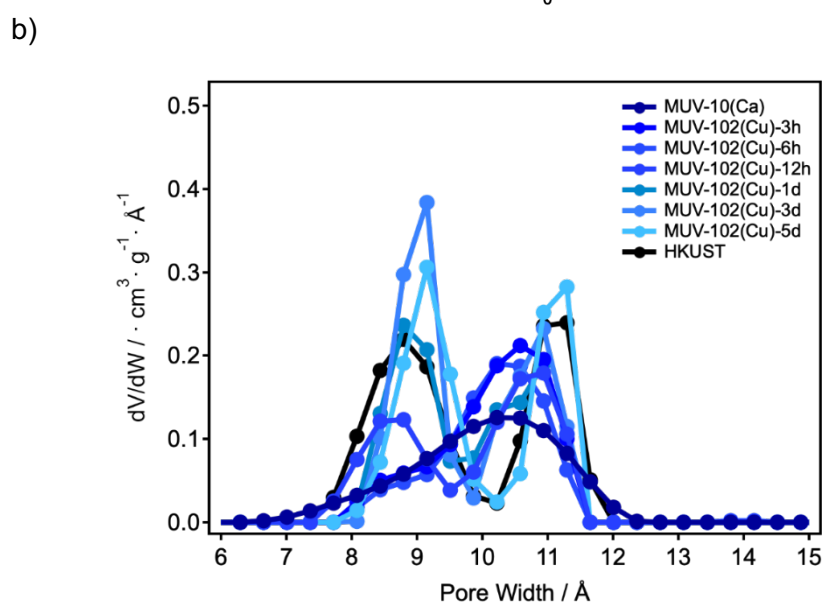
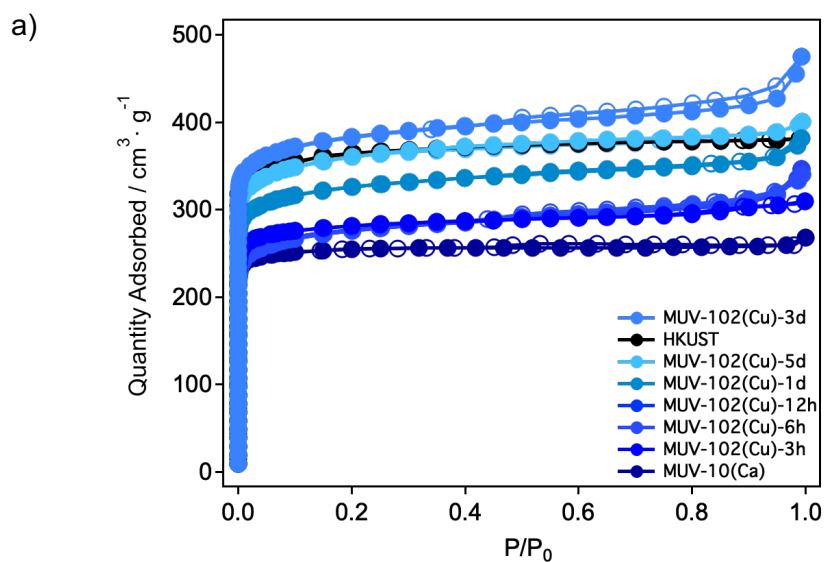


Figure S99. General comparison of a) N_2 adsorption isotherms and b) Pore size distribution for the transformation of MUV-10(Ca) into MUV-102(Cu) from 3 hours to 5 days of metal exchange reaction.

Table S20. Summary of the analysis of the N₂ adsorption/desorption isotherms at 77 K of MUV-102(Cu) materials produced at different reaction times. Specific surface area (SA) was calculated with the multi-point Brunauer-Emmett-Teller (BET) method. Total pore volume (V_t) was estimated at P/P₀=0.96. Pore size distribution (PSD) was analysed by using the solid density functional theory (NLDFT) for the adsorption branch by assuming a cylindrical pore model.

Sample	SA _{BET} [m ² ·g ⁻¹]	V _t [cm ³ ·g ⁻¹]	PSD _{NLDFT} [nm]	
			micro	micro'
HKUST 5d MeOH	1438	0.59	0.89	1.1
MUV-102(Cu)-1h	997	0.40	---	1.1
MUV-102(Cu)-3h	1137	0.47	---	1.1
MUV-102(Cu)-6h	1078	0.50	---	1.0
MUV-102(Cu)-12h	1091	0.50	0.85	1.1
MUV-102(Cu)-1d	1280	0.56	0.89	1.1
MUV-102(Cu)-3d	1509	0.66	0.91	1.1
MUV-102(Cu)-5d	1403	0.60	0.91	1.1

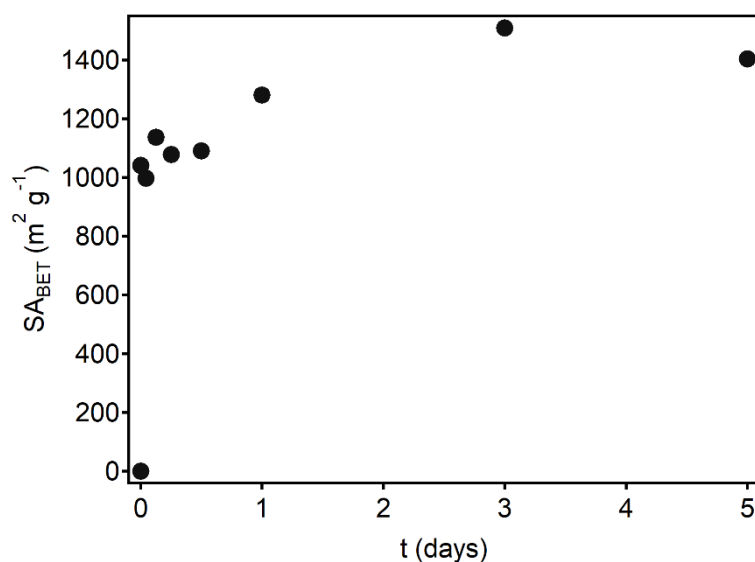


Figure S100. Graphical representation of the changes in the surface area with reaction time for the transformation of MUV-10(Ca) into MUV-102(Cu).

S7.10. Thermogravimetric Analysis (TGA) and changes to the thermal stability of the solid with the degree of transformation

TGA curves were recorded on activated solids at a ramp rate of 5 °C/min on a Mettler Toledo TGA/SDTA 851e/SF/1100 apparatus between 25 and 600 °C under synthetic air.

MUV-102(Cu)-3h

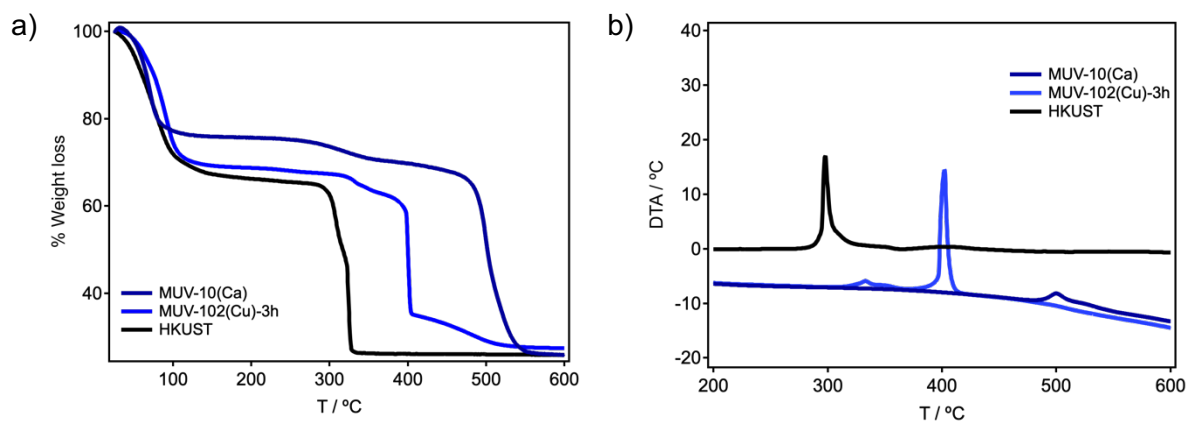


Figure S101. a) Thermogravimetric analysis and b) DTA of MUV-102(Cu)-3h compared with MUV-10(Ca) and commercial HKUST.

MUV-102(Cu)-6h

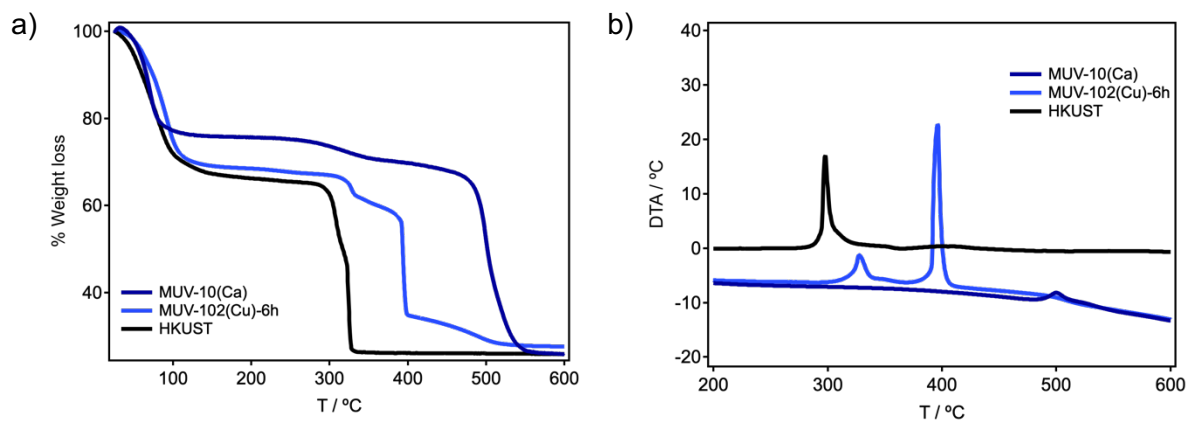


Figure S102. a) Thermogravimetric analysis and b) DTA of MUV-102(Cu)-6h compared with MUV-10(Ca) and commercial HKUST.

MUV-102(Cu)-12h

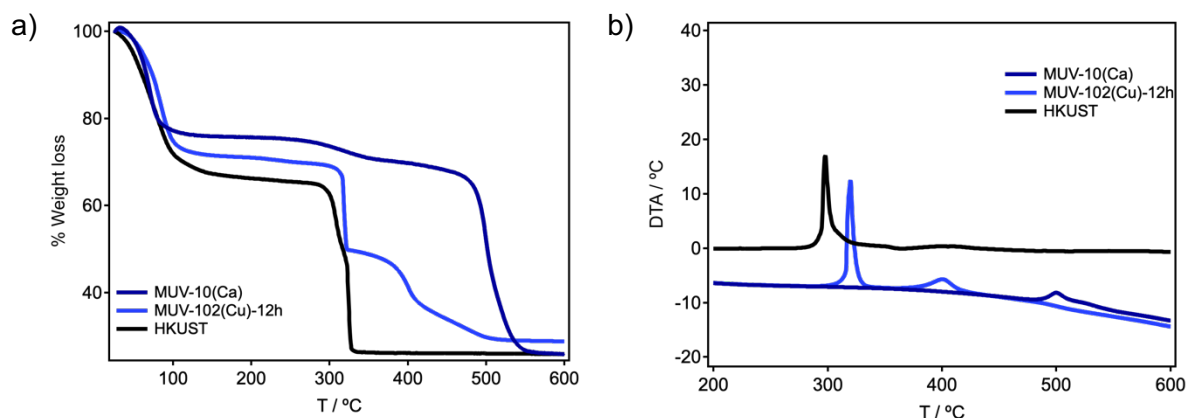


Figure S103. a) Thermogravimetric analysis and b) DTA of MUV-102(Cu)-12h compared with MUV-10(Ca) and commercial HKUST.

MUV-102(Cu)-1d

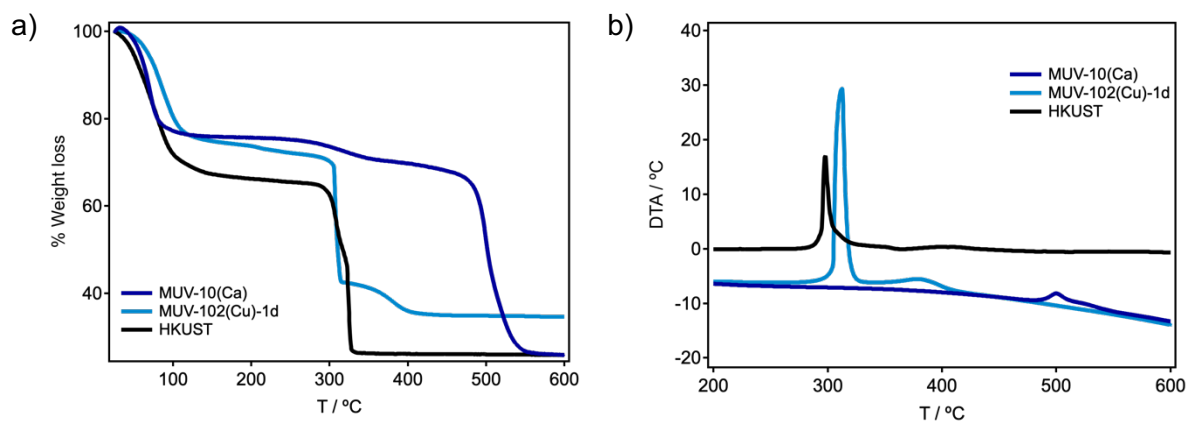


Figure S104. a) Thermogravimetric analysis and b) DTA of MUV-102(Cu)-1d compared with MUV-10(Ca) and commercial HKUST.

MUV-102(Cu)-5d

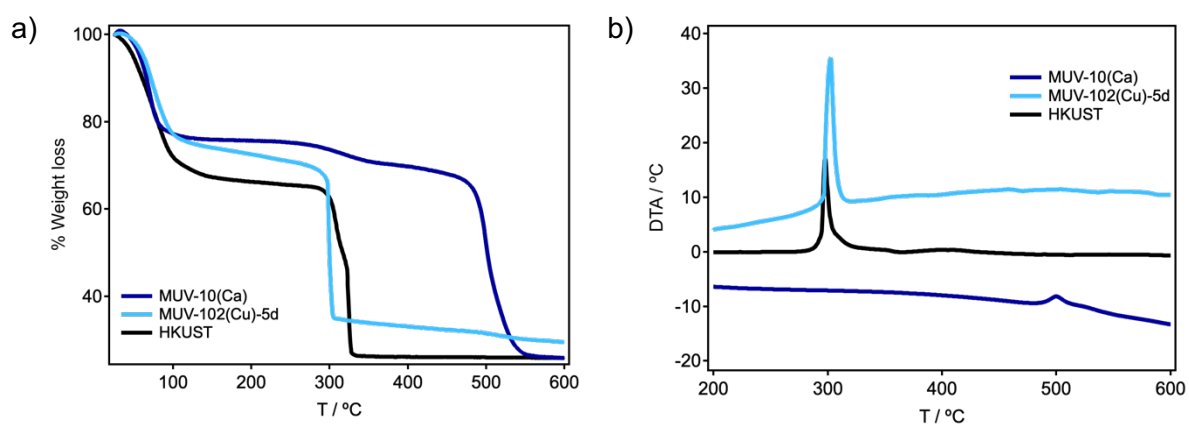


Figure S105. a) Thermogravimetric analysis and b) DTA of MUV-102(Cu)-5d compared with MUV-10(Ca) and commercial HKUST.

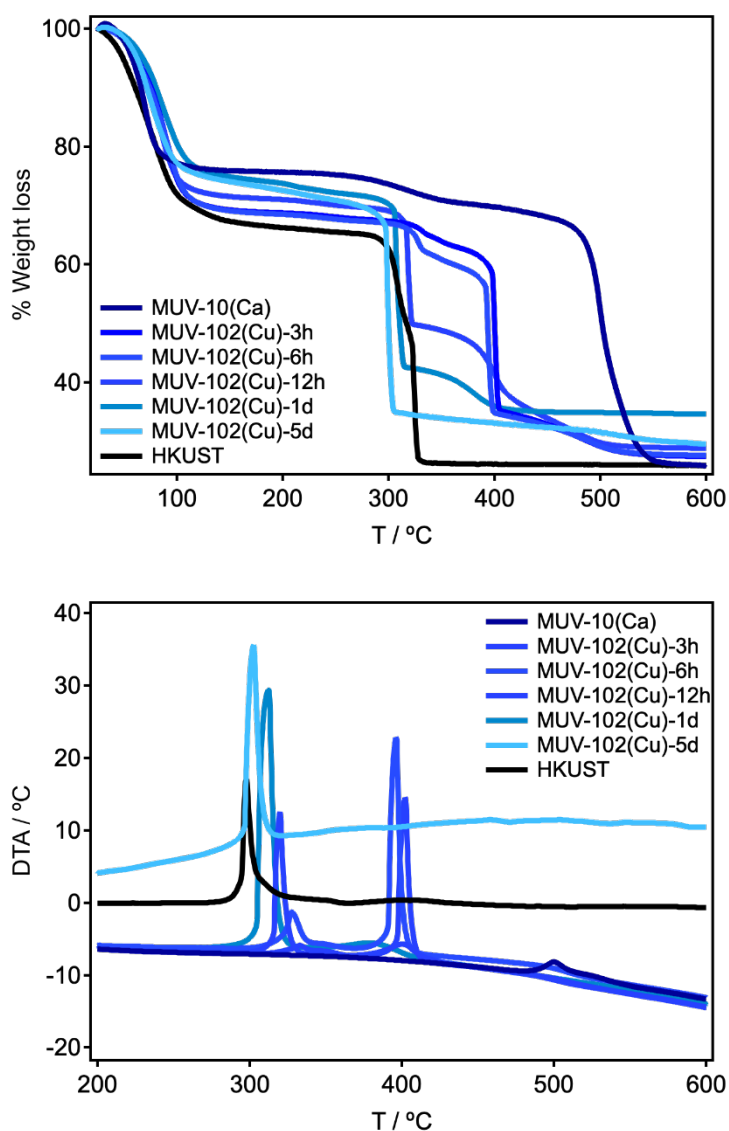


Figure S106. a) Comparison of the thermal decomposition profiles of MUV-10(Ca) and MUV-102(Cu) at different transformation stages and b) shift in temperature of the endothermic peak in the differential thermal analysis of MUV-10(Ca) and MUV-102(Cu) after metal exchange for 3 hours to 5 days. Compared to MUV-10(Ca), the thermal stability of MUV-102(Cu) is progressively reduced with the Cu% incorporated down to a minimum very close to the decomposition temperature of homometallic HKUST.

S7.11. Chemical stability

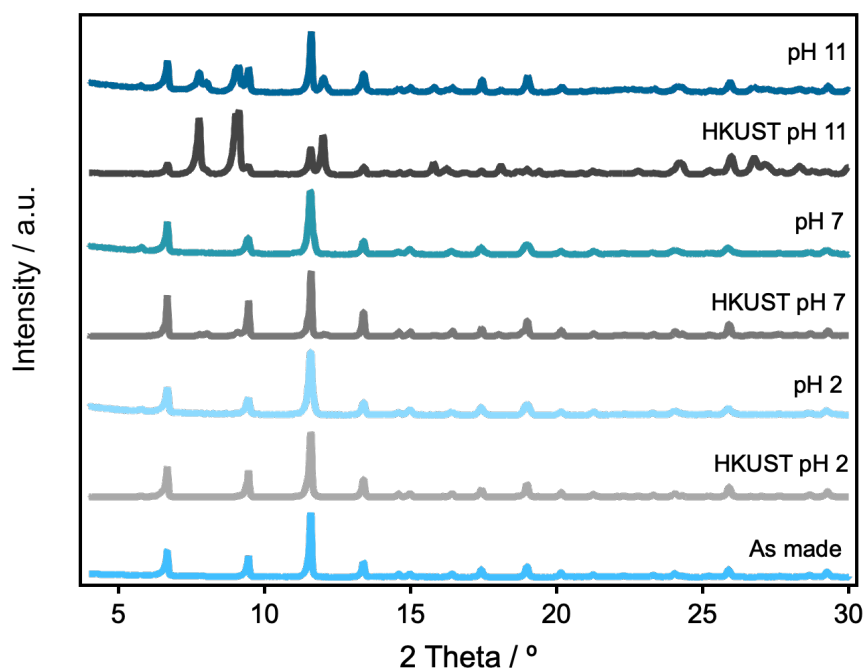


Figure S107. Comparison of the PXRDs of HKUST and MUV-102(Cu)-5d after soaking in an aqueous solution at pH 2, 7 and 11 during 24 hours. The heterometallic phase shows the same limitations towards water hydrolysis than homometallic HKUST.

S8. REFERENCES

1. Ravel, B. & Newville, M. ATHENA, ARTEMIS, HEPHAESTUS: data analysis for X-ray absorption spectroscopy using IFEFFIT. *J. Sync. Rad.* **2005**, *12*, 537–541.
2. Rehr, J. J., Kas, J. J., Vila, F. D., Prange, M. P. & Jorissen, K. Parameter-free calculations of X-ray spectra with FEFF9. *Phys. Chem. Chem. Phys.* **2010**, *12*, 5503–5513.
3. Langford, R. . & Clinton, C. In situ lift-out using a FIB-SEM system. *Micron* **2004**, *35*, 607–611.
4. Castells-Gil, J.; Padial, N. M.; Almora-Barrios, N.; Albero, J.; Ruiz-Salvador, R. A.; González-Platas, J.; García, H.; Martí-Gastaldo, C. Chemical Engineering of Photoactivity in Heterometallic Titanium–Organic Frameworks by Metal Doping. *Angew. Chem. Int. Ed.* **2018**, *57*, 8453–8457.
5. Castells-Gil, J.; Padial, N. M.; Almora-Barrios, N.; da Silva, I.; Mateo, D.; Albero, J.; García, H.; Martí-Gastaldo, C. De Novo Synthesis of Mesoporous Photoactive Titanium(IV)–Organic Frameworks with MIL-100 Topology. *Chem. Sci.* **2019**, *10*, 4313–4321.
6. Farges, F. & Brown, G. E. Coordination chemistry of titanium (IV) in silicate glasses and melts: IV. XANES studies of synthetic and natural volcanic glasses and tektites at ambient temperature and pressure. *Geochim. Cosmochim. Ac.* **1997**, *61*, 1863–1870.
7. Henderson, G. S., de Groot, F. & Moulton, B. X-ray Absorption Near-Edge Structure (XANES) Spectroscopy. *Rev. Mineralogy Geochem.* **2014**, *78*, 75–138.
8. Fleming, S. & Rohl, A. GDIS: a visualization program for molecular and periodic systems. *Zeitschrift Für Kristallographie – Cryst. Mater.* **2005**, *220*, 580–584.
9. Gale, J. D. GULP: A computer program for the symmetry-adapted simulation of solids. *J. Chem. Soc. Faraday Trans.* **1997**, *93*, 629–637.
10. Wulff, G. XXV. Zur Frage der Geschwindigkeit des Wachstums und der Auflösung der Krystallflächen. *Zeitschrift Für Kristallographie – Cryst. Mater.* **1901**, *34*, 449–530.
11. Momma, K. & Izumi, F. VESTA 3 for three-dimensional visualization of crystal, volumetric and morphology data. *J. Appl. Crystallogr.* **2011**, *44*, 1272–1276.

12. Kresse, G. & Furthmüller, J. Efficiency of ab-initio total energy calculations for metals and semiconductors using a plane-wave basis set. *Comput. Mater. Sci.* **1996**, *6*, 15-50.
13. Kresse, G. & Furthmüller, J. Efficient iterative schemes for ab initio total-energy calculations using a plane-wave basis set. *Phys. Rev. B* **1996**, *54*, 11169-11186.
14. Perdew, J. P., Burke, K. & Ernzerhof, M. Generalized gradient approximation made simple. *Phys. Rev. Lett.* **1996**, *77*, 3865-3868.
15. Grimme, S., Antony, J., Ehrlich, S. & Krieg, H. A consistent and accurate ab initio parametrization of density functional dispersion correction (DFT-D) for the 94 elements H-Pu. *J. Chem. Phys.* **2010**, *132*, 154104.
16. Bučko, T., Hafner, J., Lebègue, S. & Ángyán, J. G. Improved description of the structure of molecular and layered crystals: Ab initio DFT calculations with van der Waals corrections. *J. Phys. Chem. A* **2010**, *114*, 11814-11824.
17. Blöchl, P. Projector augmented-wave method. *Phys. Rev. B* **1994**, *50*, 17953-17979.
18. Frisch, M.J.; Trucks, G. W.; Schlegel, H. B.; Scuseria, G. E.; Robb, M. A. ; Cheeseman, J. R.; Scalmani, G. ; Barone, V.; Petersson, G. A. ; Nakatsuji, H.; Li, X.; Caricato, M.; Marenich, A.; Bloino, J.; Janesko, B. G. ; Gomperts, R.; Mennucci, B.; Hratchian, H. P.; Ortiz, J. V.; Izmaylov, A. F.; Sonnenberg, J. L.; Williams-Young, D.; Ding, F.; Lipparini, F.; Egidi, F.; Goings, J.; Peng, B.; Petrone, A.; Henderson, T.; Ranasinghe, D.; Zakrzewski, V. G.; Gao, J.; Rega, N.; Zheng, G.; Liang, W.; Hada, M.; Ehara, M.; Toyota, K.; Fukuda, R.; Hasegawa, J.; Ishida, M.; Nakajima, T.; Honda, Y.; Kitao, O.; Nakai, H.; Vreven, T.; Throssell, K.; Montgomery, J. A.; Peralta, Jr., J. E.; Ogliaro, F.; Bearpark, M.; Heyd, J. J.; Brothers, E.; Kudin, K. N.; Staroverov, V. N.; Keith, T.; Kobayashi, R.; Normand, J.; Raghavachari, K.; Rendell, A.; Burant, J. C.; Iyengar, S. S.; Tomasi, J.; Cossi, M.; Millam, J. M.; Klene, M.; Adamo, C.; Cammi, R.; Ochterski, J. W.; Martin, R. L; Morokuma, K.; Farkas, O.; Foresman, J. B.; Fox, D. J. Gaussian 09, Revision A.02. Gaussian, Inc., Wallingford CT, **2016**.

19. Hunault, M., Vercamer V., Haverkort M.W., Arrio M-A., Brouder C., Calas G., Juhin A. Tracking the signature of low symmetry environments in the XAS K pre-edge. *J. Phys. Conf. Ser.* **2016**, 712, 012005.
20. Pöpl, A., Kunz, S., Himsl, D., Hartmann, M. CW and Pulsed ESR Spectroscopy of Cupric Ions in the Metal–Organic Framework Compound $\text{Cu}_3(\text{BTC})_2$ *J. Phys. Chem. C* 2008, 112, 2678-2684.

Chapter 6:

Conclusions

The work developed in this thesis was design for expanding the chemical complexity of reticular materials based on Group IV metals, in particular on Ti(IV) and Zr(IV). The high charge density and bond polarization of those metals result in strong metal-ligand bonds, and consequently in chemical and thermal robust reticular solids. These features make them suitable platforms to translate chemical complexity into targeted function without compromising the structure, crystallinity, or porosity of the original materials.

The **first chapter** provided an overview of the rise of chemical complexity in reticular solids, especially in Metal-Organic Frameworks (MOFs). The description starts with the study of *binary* networks, continues presenting networks of intermediate complexity, such as *multivariate* and *multicomponent* frameworks, and advances in complexity up to *hybrid multicomponent* frameworks. The discussion includes the presentation of the characterization techniques used for deciphering the organic and inorganic variance. Moreover, it highlights the importance of the structural richness and intrinsic properties of complex MOFs to extend their applications in relevant research fields.

In the **second chapter**, we described the first example of a permanently porous titanium-organic polyhedra. The synthesis of this cMUV-11 demonstrated the effect of variations in the synthesis conditions on modulating the dimensionality of the resulting solid. Starting from the same organic and metal precursors as MUV-11, the use of shorter reaction times, milder temperature, and an alternative modulator resulted in the reduction of dimensionality from 2D extended framework to discrete cubes of cMUV-11. The presence of vertex-to-vertex H-bonds between complementary hydroxamic groups was the responsible of intramolecular packing of cMUV-11. The evacuation protocol found was respectful of that intercage-packing and ensured a surface area value and PSD in agreement with the crystallographic analysis. The value of $1020 \text{ m}^2 \cdot \text{g}^{-1}$ of BET was close from the highest reported so far. Stability tests of cMUV-11 confirmed the ability of hydroxamate chelates to form stable Ti(IV) nodes to provide excellent resistance toward the hydrolysis. Moreover, our results pointed out that the reduction in dimensionality did not compromise the thermal stability of the Ti-cage. So, cMUV-11 was postulated as robust platform to prepare multivariate-MOPs by the combination of functionalized organic ligands in different ratios. The functionalization of the original hydroxamic linker with hydrogen-bond donor (-NH₂) and acceptor (-OCH₃) groups allowed to tailor pore chemistry. By direct synthesis of the mixture of two ligands, we produced mixed-linker cages with an incorporation rate controlled by the concentration of the ligands in solution. Although the introduction of the functional groups gave rise to isostructural phases to cMUV-11, the functionalization of those cages results in variable responses towards solvent evacuation. The -OCH₃ functionalization led to more stable crystalline arrangements. Regarding chemical and thermal stability of multivariate cages, negligible variations were detected according to computational calculations. The meaningful study of activation protocol illustrated the detrimental

effect of the presence of -NH₂ group on BET surface area values; in turn, -OCH₃ functionalization below 50 % yielded surface areas of nearly 1200 m²·g⁻¹.

Even though those MOPs showed low solubility in conventional solvents, the incorporation of functionalities, as -NH₂ groups, makes them more susceptible to undergo post synthetic modifications that may increase the solubility. That opens promising perspectives for the use of cMUV-11 derivatives as ideal platform to engineer photocatalytic performance in porous solids by using only molecular concepts exclusive of homogeneous catalysis.

In **chapter three**, we demonstrated the value of the use of High-Throughput (HT) methodologies to accelerate the exploration of the chemical space intrinsic to MOF synthesis and ensure high reproducibility by systematic design of experiments. That approach allowed us to test more than 100 conditions for the optimizing the formation of single-crystals of two mesoporous frameworks: UiO-68 and its tetrazine derivate UiO-68-TZDC [TZDC = 4,4'-(1,2,4,5-tetrazine-3,6-diyl)dibenzoic acid]. The analysis of properties of the single-linker phases revealed the necessity of combining both units in the same material to produce a photoactive material without compromising its chemical stability or porosity, both important to photocatalytic applications. The value of post synthetic linker exchanged methods was proven with the preparation of multivariate UiO-68-TZDC% from UiO-68 crystals. The fine tuning of the synthetic exchange conditions permitted to control the relative ratio and spatial distribution of parent (TPDC) and exchanged (TZDC) linkers. The isolation of single crystal of UiO-68 and UiO-68-TZDC were particularly important in understanding the dynamic exchange reactions and the origin of the asymmetric linker distribution. The fluorescence experiments showed that the formation of *core-shell* microstructures was dominated by kinetic control; being favoured by low linker-exchange concentrations and short reaction times. Above a threshold concentration of TZDC, even short times produced homogeneous distributions. MTV-UiO-68-TZDC% (% = 3-50%) materials constituted an ideal set of samples for studying the effect linker distribution in the photocatalytic activity due to their comparable electronic structure and their different photoactive linker distribution over the crystal. UiO-68 derivatives were tested on methyl viologen reduction and H₂ production. UiO-68-TZDC_{10%} *core-shell* displayed the best photocatalytic performance, over UiO-68-TZDC_{10%} *homogeneous* and even over the pure UiO-68-TZDC. Those result suggested a complex scenario in which the performance was controlled not only by photoactive linker (TZDC) but also by its distribution inside the crystal. So, our work demonstrated the impact of linker distribution on encoding MOF properties.

In **chapter four**, we used the UiO-68-TZDC as a platform to demonstrate the general value of tetrazine tags for framework covalent functionalization in one-step. The inverse Electron-Demand Diels-Alder (iEDDA) reactivity of tetrazine enabled quantitative and inoffensive side-products modifications under mild conditions, which ensure the crystallinity and porosity of the resulting materials. The high

versatility of the process allowed the introduction of a wide range of chemical functionalities as hydroxyl, phenyl, succinimide, terminal carboxylic groups, aliphatic chains, and even chiral centres. As a result, multiple pore environments were created in resultant pyridazine and dihydropyridazine derivatives. The kinetic study of the conversion in the MOF and in the free linker revealed the positive effect of tetrazine reticulation over its reactivity. Moreover, our methodology assisted the preparation of crystalline fullerene porous materials by the incorporation of C₆₀ molecules with high loadings by covalent grafting. Compared to the coordinative or non-coordinative synthetic strategies used for immobilizing C₆₀ in MOFs, the reported method overcame the limitations presented by the synthesis of fullerene-derived materials: *i*) laborious synthesis of fullerene containing linkers; *ii*) limited solubility of those molecules which can result in problems in purification and in the MOF synthesis; *iii*) poor loadings per unit cell due to diffusion limitations or *iv*) disordered guest positioning inside the pore not amenable to X-ray analysis. Furthermore, the incorporation of C₆₀ was exclusively controlled by the density and distribution of tetrazine linkers in the solid, which allowed to control their spatial distribution and intermolecular separation for targeted function in multivariate frameworks.

In the **chapter five**, we introduced a new methodology for the synthesis of heterometallic titanium frameworks by post-synthetic metal-exchange reactions. Our results illustrated the value of MUV-10(Ca) in acting as a directing platform for the formation of mesoporous or microporous heterometallic titanium organic frameworks. The presence of Ti₂Ca₂ heterometallic cluster with hard (titanium) and soft (calcium) metals permitted restricting metal exchange reactions to the soft positions in the metal-oxo cluster for the generation of heterometallic SBUs with variable nuclearity, controlled by the metal incorporated. So, our approach represented a new strategy to introduce metal variance in the inorganic component of the framework whilst respecting the geometric principles of reticular chemistry. In contrast to direct synthesis, this methodology allowed the formation of heterometallic titanium MOFs that were not accessible under conventional solvothermal conditions at high temperature, as it was reflected by the isolation of MUV-101 (Zn) and MUV-102 (Cu), isostructural to MIL-100 and HKUST, respectively. So, those results anticipated the possibility of designing and synthesising new heterometallic titanium frameworks, not only limited to three connected trimesic linkers, following the principles of reticular chemistry. In addition, the careful control over topological transformation might be useful to gain dynamic control over the formation of hierarchical micro-/mesopore structures at intermediate stages of the transformation which may be relevant in some specific applications as gas store/separation or heterogeneous catalysis.

Resumen de la tesis doctoral

La presente tesis doctoral titulada “*Estudio de la complejidad químicas en sólidos reticulares del grupo IV*” (en inglés *Exploring Chemical Complexity in Group IV Reticular Solids*) se ha realizado mediante compendio de publicaciones. Está estructurada en cinco capítulos, además de un capítulo final de conclusiones y resúmenes en castellano y valenciano.

El primer capítulo consiste en una introducción que muestra una visión general sobre el concepto de *Complejidad Química* en redes sintéticas. Para adentrarnos en esta área es necesario definir previamente el concepto de Química Reticular (*Reticular Chemistry*), topología (*Topology*) y expansión isoreticular (*Isoreticular expansion*), así como las herramientas necesarias para diseñar y preparar estructuras que sean periódicas, cristalinas y porosas entre las que destacan, en el contexto de la presente tesis, las redes metal-orgánicas (*Metal-Organic Frameworks (MOFs)*), las redes covalente-orgánicas (*Covalent Organic Frameworks (COFs)*) y los poliedros metal-orgánicos (*Metal-Organic Polyhedra (MOPs)*). A continuación, se realiza una clasificación en orden creciente de los distintos tipos de redes porosas en función de la variabilidad que existe en la composición de éstas. Así pues, el capítulo comienza con la descripción de las redes más sencillas, las *redes binarias*, pasando por las redes de complejidad intermedia, *redes multivarianza* y *redes multicomponente*, hasta llegar a las más complejas, *redes multicomponente con incorporación de multivarianza*. De este modo se pretende dar una visión incremental en el concepto de complejidad química que refleje las dificultades que existen tanto desde un punto de vista del diseño experimental de las redes como en la caracterización de éstas y de los avances que se han llevado a cabo en el área en los últimos años.

Los resultados experimentales también se presentan en orden creciente de complejidad química. En el Capítulo 2 se describe la síntesis de una serie de MOPs que presentan *multivarianza* gracias a la combinación de ligandos orgánicos con diferentes funcionalizaciones en proporciones controladas. Los capítulos 3 y 4 recogen los trabajos centrados en la modificaciones del material conocido como UiO-68-TZDC (TZDC: 4,4'-(1,2,4,5-tetrazine-3,6-diyl)dibenzoate), un MOF de zirconio derivado del UiO-68 que incorpora en su ligando el grupo tetrazina (TZDC). En ambas publicaciones se aborda la complejidad química a partir de modificaciones enfocadas en el ligando orgánico. Mientras que en el Capítulo 3 se demuestra cómo la variación de las condiciones de intercambio post-sintético de ligando permite controlar la distribución espacial de los ligandos activos e inactivos con luz visible en la estructura resultante; en el Capítulo 4, se explora la reactividad del anillo de tetrazina que forma parte del ligando TZDC para generar nuevos entornos de poros y así cambiar las propiedades y con ello, las aplicaciones del material resultante. Por último, en el Capítulo 5 se presenta una metodología para introducir variabilidad en los nodos metálicos. Este enfoque, basado en el MOF heterometalico MUV-10, modifica la conectividad, nuclearidad y los puntos de extensión de la unidad de construcción secundaria (*SBU, del inglés Secondary Building Units*) y, por tanto, la topología de la red resultante.

A continuación, se detallan los aspectos más importantes desarrollados en cada uno de los capítulos.

Durante el capítulo introductorio, **Capítulo 1**, nos centraremos en el tipo de redes sintetizadas a lo largo de la presente tesis, es decir, en las *redes metal-orgánicas* y en los *poliedros metal-orgánicos*. Estos sólidos reticulares poseen en común que están constituidas por un *componente orgánico o ligando* y un componente inorgánico que puede ser un *metal o un clúster metálico*. Así pues, las *redes binarias*, constituidas por dos componentes, son consideradas como punto de partida para introducir la complejidad química debido a la gran variabilidad que pueden presentar tanto en el componente orgánico como en el inorgánico. El siguiente grado de complejidad se consigue con la introducción de diversidad en uno de estos componentes, es decir, incorporando diferentes funcionalizaciones en el ligando, dando lugar a una aproximación orgánica, o diferentes metales/clústeres metálicos, produciéndose así una aproximación inorgánica. El empleo de una de estas aproximaciones origina lo que se conoce como *redes multivarianza*, o combinación de diferentes componentes químicos en número y proporciones variables que respetan la estructura original de la red. Alternativamente, cuando se combinan componentes de diferente topología, conectividad y/o tamaño da lugar a *redes multicomponentes* ya sea mediante la diversidad de ligandos o metales. El grado de complejidad superior se alcanza cuando estas últimas incorporan el concepto de *multivarianza* dando lugar a las *redes híbridas multicomponente*. Conforme vamos adentrándonos en el capítulo introductorio, la discusión se centra en la necesidad de realizar un análisis detallado de estas redes para determinar el grado de complejidad química que poseen. Para ello se introducen técnicas de caracterización específicas tanto para el estudio de los componentes orgánicos como de los inorgánicos. Estas técnicas se clasifican en función de la información que proporcionan sobre la red relacionado con *i)* la presencia de componentes de múltiple naturaleza en la misma estructura, *ii)* la proporción en la que se encuentran, *iii)* su cuantificación o *iv)* la distribución que poseen la diversidad de componentes a lo largo de la red. Además, para el caso específico de los metales también se realiza un estudio del entorno metálico y del estado de oxidación del mismo. La última parte de este capítulo demuestra cómo el control en la complejidad química de las redes sintetizadas permite modificar sus propiedades e implementación en aplicaciones concretas. El dominio del entorno químico del poro, que se genera cuando se crea la red compleja permite introducir diferentes funcionalizaciones que pueden actuar en paralelo o de forma cooperativa, puede dar lugar a fenómenos sinérgicos. De esta manera, la complejidad en las redes metal-orgánicas permite que estos materiales se acerquen cada vez más a los sistemas biológicos reales, ampliando así su rango de aplicación para dar soluciones concretas a problemas cotidianos de relevancia social. Así pues, durante este apartado se refleja el valor de la incorporación de complejidad y heterogeneidad en las propiedades de los MOFs en algunas de las áreas de aplicación concretas como son la separación y almacenamiento de gases, la catálisis heterogénea, la remediación ambiental o la preparación de dispositivos luminiscentes.

En el **segundo capítulo** se describe el primer ejemplo descrito hasta la fecha de un poliedro metal-orgánico (MOP) poroso basado en titanio (IV), cMUV-11, de las siglas del nombre en inglés de *cage-type Material of Universidad de València*. Este nuevo MOP es un ejemplo ideal para introducir el concepto de complejidad en el componente orgánico mediante la combinación de ligandos que poseen distintos grupos funcionales. En este contexto, los materiales porosos tipo MOP han despertado un gran interés debido a que poseen una de las propiedades más relevantes de los MOFs, la porosidad, combinada con la naturaleza molecular de los sistemas discretos, lo que les confiere potenciales propiedades en reconocimiento anfitrión-huésped, separación y almacenamiento de gases, catálisis o su implementación en membranas. A pesar de las potenciales aplicaciones que poseen los materiales tipo MOPs todavía están relativamente inexploradas en comparación con el resto de los sólidos porosos extendidos como los MOFs y los COFs. Una de las principales causas de esto está relacionado con las propiedades químicas y estructurales de las cajas metal-orgánicas. Lograr la evacuación de las moléculas de disolvente de su interior evitando su agregación o reorganización, o incluso su colapso estructural en estado sólido no suele ser un proceso trivial. Por tanto, debido a esta complejidad los MOPs suelen carecer de altos valores de áreas superficiales. Además, en términos de estabilidad, la obtención de sistemas químicamente estables se reduce a estrategias concretas, restringiendo así su diversidad química. Por todo ello, hasta lo que alcanza nuestro conocimiento, únicamente se han descrito 14 tipos de poliedros regulares para describir el ensamblado de MOPs, mientras que por el contrario se conocen más de 100.000 estructuras cristalinas de MOFs con una amplia gama de topologías. Ante esta situación decidimos ampliar la diversidad química de los poliedros porosos robustos introduciendo el grupo funcional hidroxámico como conector metálico. La combinación del grupo hidroxámico con metales altamente cargados como el Ti(IV) ofrece la posibilidad de ensamblar redes robustas, como ya quedó ejemplificado por el MUV-11 (*MUV* de las siglas en inglés *Material of Universidad de València*), reportado recientemente por nuestro grupo.

Los resultados de este capítulo fueron publicados bajo el título “*Permanent porosity in hydroxamate titanium-organic polyhedral*” y referencia: Lerma-Berlanga, B.; Castell-Gil, J. R. Ganivet, C.; Almora-Barrios, N.; González-Platas, J.; Fabelo, O.; M. Padial, N. y Martí-Gastaldo, C.; *J. Am. Chem. Soc.* **2021**, *143* (50), 21195-21199. En este trabajo se preparó el cMUV-11 mediante la reacción directa de isopropóxido de titanio (IV) con el ligando ácido benceno-1,4-dihidroxámico (*p*-H₄bdha) en *N,N*-dimetilformamida (DMF) anhidro utilizando ácido benzoico como modulador en condiciones solvotermales. Tras 18 h de reacción a 100 °C se obtuvieron cristales octaédricos de color rojo intenso de 100 μm de tamaño medio. La calidad de los cristales permitió determinar de su estructura mediante difracción de rayos X de monocristal. cMUV-11 consistió en cajas neutras discretas con fórmula [Ti₈(*p*-H₂bdha)₈(*p*-bdha)₄]. Las cajas se pueden describir como cubos distorsionados. Los ocho vértices están compuestos por nodos simples de titanio en un entorno octaédrico distorsionado (TiL₃), impuesto por el anillo de quelato formado por el grupo hidroxamato con el titanio, y unidos por 12 ligandos *p*-H₄bdha parcialmente

desprotonados. En el cristal, las cajas moleculares se organizan formando una red tridimensional dirigida a través de enlaces de hidrógeno que implicaban grupos hidroxámicos complementarios de las aristas adyacentes. Este empaquetamiento dió origen a una red de topología *pcb* con cavidades microporosas intrínsecas a los cubos.

Las técnicas de caracterización empleadas, análisis termogravimétrico (ATG) y espectroscopía de plasma de acoplamiento inductivo (en inglés *Inductively coupled plasma mass spectrometry, ICP*) mostraron la alta estabilidad térmica y química de cMUV-11 comparable con los valores de otros MOFs de titanio descritos. La estabilidad estructural se evaluó mediante medidas de difracción de rayos X de polvo y adsorción de N₂ de las muestras previamente intercambiadas con disolventes volátiles (acetona, hexano y éter dietílico). A pesar de que los patrones de difracción de las muestras evacuadas mostraron un ensanchamiento de las líneas de difracción, tras sumergir la muestra de nuevo en DMF se recuperó la difracción original, confirmando así la flexibilidad de los enlaces H que controlan el empaquetamiento de cMUV-11. La elección del disolvente de intercambio y las condiciones de activación fueron claves para obtener la porosidad esperada. El intercambio de la muestra con acetona condujo a una isoterma reversible de tipo I con un área superficial BET de 1020 m²·g⁻¹ cercana al valor más alto reportado en MOPs hasta el momento. El análisis de los datos por el método NLDFT mostró una distribución de tamaño de poro centrada en 1.5 nm, en concordancia con las dimensiones de la cavidad microporosa estimada a partir del análisis cristalográfico.

El impacto del disolvente empleado durante el intercambio previo a la activación del material posee un efecto notable sobre su porosidad, esto evidenció la necesidad de controlar las interacciones entre los poliedros. Para demostrar esto, se prepararon una serie de MOPs combinando ligandos con diversas funcionalidades: el grupo amino (-NH₂) se seleccionó por sus propiedades donador de H y el metoxi (-OCH₃) como aceptor. Así pues, mediante el uso combinado de ligandos con diferentes grupos funcionales se consigue modular el entorno químico de las cajas al incorporar grupos funcionales con distinta capacidad para formar enlaces de hidrógeno en proporciones controladas. Los sistemas cMUV-11-NH₂-X% y cMUV-11-OCH₃-X% (X= 10, 20, 50, 60) se prepararon por síntesis directa utilizando combinaciones binarias del ligando correspondiente, *p*-H₄bdha-NH₂ o *p*-H₄bdha-OCH₃, con el ligando original (*p*-H₄bdha). El análisis mediante resonancia magnética nuclear de protón (¹H-RMN) de las muestras previamente digeridas permitió evaluar el porcentaje de incorporación real del ligando funcionalizado *p*-bdha-X. El estudio de la tendencia de incorporación de cada ligando sugirió un impacto visible del sustituyente en el proceso de empaquetamiento. A pesar de esto, las cajas multivariadas se aislaron como monocristales de tamaño, color y morfologías similares al material original. El análisis de las muestras confirmó su pureza y homogeneidad. Además, el análisis cristalográfico de cMUV-11-NH₂-50% y -OCH₃-50% confirmó la obtención de redes isoestructurales a cMUV-11 y descartó alteraciones significativas a nivel de la red de enlaces de hidrógeno. Este mismo efecto se observa en las variaciones insignificantes obtenidas en el cálculo de la estructura electrónica mediante DFT; apoyadas por las mínimas variaciones

observadas experimentalmente en la estabilidad química y térmica de los tres derivados.

En cuanto a la estabilidad estructural, cMUV-11-X también presentaron una reorganización estructural en estado sólido reflejada en cambios en el patrón de difracción de rayos X. El impacto de la funcionalización del ligando orgánico en el empaquetamiento se demuestra en la respuesta ante la evacuación del disolvente, y, consecuentemente, en los valores de porosidad. Para la serie cMUV-11-NH₂-X% sólo las muestras intercambiadas con hexano y con porcentajes ≤ 20 % de grupos aminos mostraron una porosidad permanente con valores BET máximos de 620 m²·g⁻¹. Por el contrario, las muestras cMUV-11-OCH₃ con una carga inferior al 50 % presentaron áreas superficiales más elevadas que el cMUV-11, cercanas a los 1200 m²·g⁻¹. De este modo, se demostró el impacto de las interacciones entre cajas en la modulación de la porosidad para esta familia de MOPs.

Durante el **tercer capítulo** se estudia el efecto que produce la incorporación de un anillo de 1,2,4,5-tetrazina en el ligando orgánico sobre las propiedades químicas y fotocatalíticas de una red metal-orgánica de tipo UiO-68. Además, han sintetizado redes multivarianza que permiten analizar el impacto que tiene la distribución del anillo de 1,2,4,5-tetrazina a lo largo del cristal en las propiedades de las mismas. A pesar de que las aril-s-tetrazinas fueron descubiertas a finales del siglo XIX, ha sido en las últimas décadas cuando la comunidad científica ha mostrado interés en su implementación como bloques de construcción para el diseño de nuevos materiales moleculares funcionales. Las aril-s-tetrazinas pueden actuar como una antena de luz visible con un comportamiento redox pudiéndose reducir reversiblemente debido a su carácter deficiente en electrones. Tanto sus valores del potencial de reducción como la cinética del proceso, así como la posición máxima de la banda de absorción pueden ser modulados mediante el uso de sustituyentes por lo que pueden llegar a ser excelentes candidatos para incorporarse en aplicaciones relacionadas con procesos de generación de luz, sensores, células solares, y polímeros electro/fotoactivos. Así pues, en este capítulo se combina un ligando orgánico derivado de tetrazina con un metal del grupo (IV), el circonio, para desarrollar nuevos fotocatalizadores heterogéneos porosos y estables. La síntesis de MOF basados en tetrazina se puede llevar a cabo por síntesis directa o por métodos post sintéticos. Estos últimos ofrecen la posibilidad de controlar las distribuciones de ligando en el cristal de los sólidos multivarianza resultantes; lo cual permitiría modular las propiedades fotocatalíticas del material.

Los resultados de este capítulo se publicaron bajo el título "Effect of Linker Distribution in the Photocatalytic Activity of Multivariate Mesoporous Crystals" y referencia: Lerma-Berlanga, B.; R. Ganivet C.; Almora-Barrios N.; Tatay S.; Peng Y.; Albero J.; Fabelo O.; González-Platas J.; García H.; M. Padial N. y Martí-Gastaldo, C. *J. Am. Chem. Soc.* **2021**, *143* (4), 1798–1806. En este trabajo presentamos la optimización de las condiciones sintéticas para la preparación de cristales de UiO-68 (UiO: University of Oslo), usando H₂TPDC (1,1':4',1''-terphenyl)-4,4''-dicarboxylic acid en inglés) y UiO-68-TZDC, un análogo fotoactivo del material anterior basado en un derivado dicarboxílico de la tetrazina, H₂TZDC (1,2,4,5-

tetrazine-3,6-diyl)-4,4'-dibenzoic en inglés). El estudio de las propiedades químicas de estos materiales demostró la necesidad de combinar ambos ligandos en una misma estructura para poder preparar un material con la suficiente estabilidad estructural y química como para emplearse como fotocatalizador. Las muestras UiO-68-TZDC_% multivarianza mostraron propiedades mejoradas en comparación con sus homólogos puros.

Así pues, los materiales UiO-68 y UiO-68-TZDC se prepararon en condiciones solvotermales. La implementación de metodologías de análisis de alto volumen de muestra (*High-Throughput Screening* en inglés) permitió acelerar el cribado sistemático de los parámetros sintéticos y alcanzar una alta reproducibilidad en la síntesis de los materiales. Los cristales de UiO-68 se aislaron como octaedros de color amarillo pálido de tamaño comprendido entre 20 y 50 μm utilizando 40 equivalentes de modulador y calentando a 100 $^{\circ}\text{C}$ durante 72 h. Dichas condiciones sólo requirieron una ligera reducción de los equivalentes de modulador, de 40 a 10, para producir UiO-68-TZDC como cristales octaédricos de color rosa de menor tamaño (10-20 μm). El análisis cristalográfico mediante difracción de rayos X determinó parámetros cristalográficos muy similares para ambos materiales con topología *fcu* característica de esta familia de materiales tipo UiO.

El análisis del efecto del ligando sobre el comportamiento químico de los MOFs binarios mostró que la presencia del núcleo de tetrazina en el conector orgánico disminuía la estabilidad térmica y química de la estructura. Mientras que el UiO-68 se descomponía en el aire por encima de los 500 $^{\circ}\text{C}$, UiO-68-TZDC mostraba una descomposición gradual a partir de los 250 $^{\circ}\text{C}$. Por otra parte, la estabilidad hidrolítica de los sólidos se evaluó mediante la incubación de las muestras en agua durante 24 h. Los difractogramas de rayos X de polvo tras este tratamiento mostraron una amorfización parcial para el UiO-68-TZDC. El efecto negativo del ligando TZDC también fue confirmado mediante ICP, mostrando una lixiviación de Zr^{+4} superior tras la incubación en medio acuoso. A pesar de las diferencias observadas para las dos redes, tras la optimización del proceso de activación se obtuvieron valores esperados de áreas superficiales BET, alrededor de los 4000 $\text{m}^2\cdot\text{g}^{-1}$. Además, el análisis de adsorción de CO_2 reveló mayor afinidad en el caso de UiO-68-TZDC. El análisis de las fases binarias mostró la necesidad del empleo de ambos ligandos para producir redes multivarianza que combinaran las propiedades de ambas redes: absorción de luz en el rango del visible, estabilidad química y elevada porosidad, todo ello relevante para su uso en fotocatalisis.

La familia de muestras MTV-UiO-68-TZDC_% se preparó a partir de experimentos post-sintéticos de intercambio de ligando (en inglés *Solvent-Assisted Ligand Exchange, SALE*) utilizando cristales de UiO-68 como precursores y diferentes cantidades de ligando H_2TZDC . Las condiciones suaves de intercambio fueron respetuosas con la estructura y porosidad original. Además, la coexistencia de ambos ligandos mejoró la estabilidad química de los materiales. El impacto del dopaje de tetrazina en la estructura electrónica de los materiales resultantes se estudió mediante cálculos DFT. Los cálculos mostraron que niveles bajos de intercambio de TZDC son suficientes para modificar la estructura electrónica y las

propiedades ópticas de los híbridos. Esta tendencia teórica estaba de acuerdo con los valores experimentales del *band gap* óptico medidos mediante espectroscopia de reflectancia difusa y calculados empleando la función Kubelka-Munk.

Para estudiar la complejidad química de las estructuras multivarianza resultantes a nivel de un único cristal se realizaron medidas de microscopía confocal de fluorescencia y espectroscopia de fotoelectrones emitidos por rayos X (en inglés *X-ray Photoelectron Spectroscopy, XPS*). Las imágenes registradas en el microscopio confocal mostraron disposiciones espaciales concretas para el ligando original (TPDC) y el intercambiado (TZDC) en función de los niveles de dopaje. Las muestras con porcentajes de tetrazina más bajos mostraron una distribución asimétrica de los ligandos que originaban microestructuras de tipo *core-shell*/TPDC-TZDC, con recubrimiento ligeramente más gruesos para niveles de dopaje más altos. Para las muestras con niveles de TZDC superiores al 35 % se observaron distribuciones de ligando homogéneas. Paralelamente, se realizaron experimentos para estudiar el origen de la formación de distribuciones asimétricas. Para ello, se preparó un nuevo conjunto de cristales MTV-UiO-68-TZDC% manteniendo fijo los equivalentes de TZDC en disolución y modificando los tiempos de intercambio. Se observó que los tiempos de reacción prolongados favorecían la difusión de TZDC a través del cristal formando una distribución más homogénea. De esta manera, los resultados indicaron que la distribución del ligando no sólo estaba controlada por la concentración de TZDC en la disolución, sino también por el tiempo de intercambio.

Las muestras MTV-UiO-68-TZDC% constituyeron una plataforma idónea para estudiar el efecto de la distribución del ligando sobre la actividad catalítica de las redes ya que todos los sólidos poseen estructura electrónica y un valor de *bandgap* óptico común. Así pues, se realizaron dos ensayos catalíticos diseñados para la reducción del metil viológeno y producción de H₂ mostraron que la mayor actividad catalítica se alcanzaba para la muestra UiO-68-TZDC_{10%} con una distribución asimétrica *core-shell*. Los análisis de las muestras tras los ensayos catalíticos sugirieron que el rendimiento catalítico se podía explicar mediante un equilibrio entre la concentración superficial del ligando fotoactivo (shell de TZDC) y la estabilidad del material (core de UiO-68).

En el **cuarto capítulo** se demuestra la importancia de las tetrazinas como grupo funcional en la modificación postsintética de redes metal-orgánicas. Entre las muchas cualidades de las s-tetrazinas, algunas de ellas comentadas en el capítulo anterior, cabe destacar su reactividad como dieno en las reacciones de tipo Diels-Alder de demanda electrónica inversa (*iEDDA*, siglas de su nombre en inglés *inverse Electron-Demand Diels-Alder*). Este tipo de reacción pericíclica de cicloadición entre un dieno y un dienófilo posee algunas ventajas que la hacen viable para llevarla a cabo sobre materiales porosos respetando la integridad de la red: no necesitan un catalizador, ofrecen una cinética rápida, ortogonalidad, transformaciones cuantitativas en condiciones suaves y productos secundarios inofensivos (N₂). Por lo tanto, la tetrazina se presenta como un grupo funcional complementario a los utilizados convencionalmente para llevar a cabo modificaciones covalentes post sintéticas las cuales se han restringido a unos pocos grupos como son el grupo

amino, aldehído, azida o alquino. Hasta la fecha, el uso de la reactividad post-sintética de la tetrazina en los MOFs se basaba casi exclusivamente en la incorporación de olefinas con fines concretos, como es la integración de la hidrofobicidad requerida para la fabricación de membranas, la modulación de la capacidad de adsorción de CO₂ para conseguir una mayor selectividad en la separación de CO₂/N₂ o para el control de la interpenetración de las redes. A pesar de ello, todavía no se habían descrito rutas genéricas de post funcionalización en MOFs basadas en el grupo tetrazina. En este sentido, proponemos emplear el UiO-68-TZDC, sintetizado en el capítulo anterior, como plataforma para explorar esta reactividad y modificar el entorno de los poros con diversas funcionalidades químicas. Además, el UiO-68-TZDC permite estudiar el efecto de reticulación de la tetrazina sobre la reactividad iEDDA.

Los resultados de este capítulo están en proceso de ser publicados bajo el título "Tetrazine linkers as plug-and-play tags for general framework functionalization and C₆₀ conjugation." y su lista de autores es la siguiente: Lerma-Berlanga, B.;[†] R. Ganivet, C.;[†] Almora-Barrios, N.; Vismara, R.; A. R. Navarro, J.; Tatay, S.; M. Padial, N. y Martí-Gastaldo, C. En este trabajo, se muestra la versatilidad del material UiO-68-TZDC como plataforma para albergar diferentes funcionalidades químicas en el poro incorporadas por modificaciones covalentes post-sintéticas de tipo iEDDA. Inicialmente, la reactividad iEDDA de UiO-68-TZDC fue probada con un exceso de equivalentes de 2,5-norbornadieno (NBD), considerado dienófilo modelo en este tipo de reacciones. Durante la reacción se produce un cambio de color, de rosa, característico del MOF original, a amarillo característico de la transformación de la tetrazina a piridazina (PZDC). La transformación total a piridazina fue confirmada tras la digestión de los cristales mediante espectrometría de masas de alta resolución y resonancia magnética nuclear de protón (¹H-RMN). Las condiciones sintéticas óptimas se determinaron por un compromiso entre una funcionalización completa y un bajo impacto en la cristalinidad del material resultante. Las condiciones de reacción seleccionadas fueron tiempos de reacción de 16 horas con agitación a 40 °C utilizando un exceso de 3 equivalentes de dienófilo. El resultante UiO-68-PZDC fue caracterizado por imágenes de microscopio de barrido electrónico (en inglés *Scanning Electron Microscopy, SEM*), difracción de rayos X de polvo, adsorción de N₂ y análisis termogravimétrico, ATG. Los resultados de la caracterización del nuevo material no mostraron cambios significativos respecto al UiO-68-TZDC original, lo que confirmó una modificación respetuosa con la estructura del material.

Para comprender el efecto de la reticulación del ligando de TZDC sobre la reactividad en las reacciones iEDDA, se llevó a cabo un estudio de la reacción entre el MOF y el sustrato NBD en intervalos de tiempo controlados durante 24 horas, observándose un cambio de color gradual de rosa a amarillo pálido indicando el progreso de la reacción hacia la formación de piridazina. Además, se realizaron ensayos control sometiendo a las mismas condiciones, tiempo y temperatura el ligando libre y así tener una comparación directa del grado de conversión en el MOF y en el ligando libre y, por tanto, determinar el efecto de la reticulación. El análisis mediante ¹H-RMN de los sólidos digeridos a los diferentes tiempos de reacción (t=

0, 10, 20, 30, 40, 60, 80, 100, 120, 180, 240, 360, 480, 600, 720, 1200 y 1500 minutos) empleando como patrón interno el ácido fumárico, permitió llevar a cabo la cuantificación del producto formado, y con ello el grado de conversión de tetrazina a piridazina, y así elaborar los perfiles cinéticos de formación de piridazina. A pesar de que en ambos casos los perfiles se ajustaban a una reacción de pseudo-primer orden con una meseta cerca del 95 % de conversión; la cinética fue más rápida en el caso del MOF, incluso con la limitación de la difusión del dienófilo a través de los poros. Para corroborar los efectos positivos de la reticulación en la reactividad del anillo de tetrazina, se realizó un control adicional con el ligando libre en presencia de $ZrCl_4$, que sirvió para descartar el efecto catalítico de los iones $Zr(IV)$ en el proceso. Así pues, el aumento de la velocidad observado se puede explicar en base a la suma de varios factores: *i)* mayor accesibilidad del dieno, gracias a que la reticulación disminuye las interacciones π - π entre tetrazinas, *ii)* efectos electrónicos atribuidos a la a la coordinación del ligando al centro metálico. Además, respecto a este efecto, los cálculos DFT-VASP realizados mostraron una disminución de la energía del orbital LUMO en el UiO-68-TZDC que se tradujo en una reducción de la diferencia de energía entre el LUMO del dieno y el HOMO del dienófilo favoreciendo así la termodinámica de la reacción.

A continuación, se estudió la versatilidad de la reacción iEDDA para la modificación de la red UiO-68-TZDC empleando una amplia gama de dienófilos. Los experimentos generaron una variedad de derivados del UiO-68-PZDC con entornos de poros diversos, entre los cuales se incluían funcionalidades como anillos fusionados, grupos hidroxilo, fenilos, succinimida, carboxílicos terminales, cadenas alifáticas e incluso centros quirales. El análisis por 1H -RMN de los sólidos resultantes mostró la desaparición de las señales propias de la TZDC y la aparición de las nuevas asociadas a los productos formados, esto, se confirmó mediante espectrometría de masas de alta resolución (HRMS), análisis elemental y análisis termogravimétrico. El posterior análisis de los derivados por difracción de rayos X de polvo, imágenes de SEM y adsorción de N_2 confirmaron una cristalinidad, morfología y robustez estructural comparable a la estructura original. Además, la versatilidad de la plataforma UiO-68-TZDC para introducir modificaciones permitió ir más allá de estos sustratos moleculares e introducir unidades nanocarbonadas de forma controlada. Las condiciones sintéticas empleadas anteriormente fueron adaptadas a la singular solubilidad de los fullerenos y nos permitió sintetizar el derivado UiO-68-PZDC(C_{60}), con moléculas de C_{60} covalentemente unidas al anillo de piridazina. Las medidas de espectroscopia UV-Vis junto a las de resonancia magnética de carbono y espectrometría de masas confirmaron la formación del monoadducto entre el fullereno y el anillo de piridazina del ligando. Para comprender mejor la estructura del derivado fullerético, se realizó un refinamiento Rietveld a partir de una medida de difracción de polvo de alta resolución. Los resultados mostraron que UiO-68-PZDC(C_{60}) era isoestructural a UiO-68-TZDC pero con valores de celda ligeramente alargados y la presencia de unidades de $H_2pzdc-C_{60}$ debido a conjugación covalente de las unidades de C_{60} al anillo de tetrazina. Los factores de ocupación de las moléculas de fullereno se refinaron libremente para tener en cuenta la funcionalización total. El modelo convergió para la formación de cerca del

50% de unidades de piridazina, obteniéndose una fórmula unidad de $[\text{Zr}_6\text{O}_4(\text{OH})_4(\text{PZDC}-\text{C}_{60})_3(\text{TZDC})_3]$. Este grado de funcionalización estaba de acuerdo con los valores experimentales del análisis elemental y termogravimétrico de los cristales. Además, los valores porosidad accesible, tamaño y volumen de poro eran consistentes con la conjugación de tres moléculas de C_{60} en los bordes del 50 % de las cavidades tetraédricas. Se realizaron experimentos adicionales para comprender el origen de este porcentaje de funcionalización persistente. La ampliación del tiempo de reacción a cinco días dio lugar a un porcentaje muy similar, lo que sugirió que este límite superior de funcionalización no estaba controlado por las limitaciones de difusión, sino que venía impuesto por el impedimento estérico del poro y las interacciones intermoleculares repulsivas. Este resultado se corroboró con un experimento alternativo utilizando UiO-68-TZDC_{44%} (descrito en el capítulo 3), el cual mostró una funcionalización completa cuando los ligandos TZDC estaban diluidos en la estructura.

Finalmente, el **capítulo cinco** muestra la versatilidad de los nodos heterometálicos del MUV-10 para experimentar transformaciones post sintéticas que permiten incorporar nuevos metales y obtener diferentes topologías de manera dirigida venciendo así las limitaciones que impone la síntesis directa a la formación de ciertas redes. La síntesis de MOFs de titanio prediseñados a partir de SBUs específicas sigue siendo un gran desafío debido a la alta reactividad de los precursores de titanio, que en condiciones de síntesis solvotermales conducen, generalmente, a fases amorfas y/o a la formación de óxido de titanio. Además, las rutas para introducir heterogeneidad en los nodos de titanio homometálicos son todavía escasas. En la mayoría de los casos, las reacciones de síntesis directa se basan principalmente en combinaciones de titanio con iones metálicos con cargas y radios iónicos similares. En cuanto a las reacciones post sintéticas, la incorporación de otros metales se ve dificultada por la alta estabilidad de los enlaces de coordinación Ti-O, lo que da lugar a una sustitución incontrolable y/o a la formación de una capa de óxido no deseada. Esto podría explicar la baja diversidad química de los MOFs basados en dicho metal. Como posible alternativa, nosotros proponemos el uso de MUV-10(Ca), un MOF heterometálico de Ti, como reactivo en reacciones de transmetalación post sintéticas. Este MOF presenta clústeres tetranucleares $[\text{Ti}_2\text{Ca}_2(\text{O})_2(\text{H}_2\text{O})_4(\text{CO}_2)_8]$, donde se combinan sitios metálicos blandos (Ca^{2+}) y duros (Ti^{4+}). De este modo, MUV-10 puede ser considerado un excelente candidato para dirigir la formación de nodos metálicos con puntos de conexión variables gracias a la mayor facilidad que ofrece el Ca^{2+} frente al Ti^{4+} para el intercambio. Así, nuestra aproximación contribuiría a mejorar la diversidad química de los MOFs basados en titanio, considerados excelentes candidatos para ampliar el rango de aplicación de los materiales porosos debido a su alta estabilidad química y térmica.

Los resultados descritos en el quinto capítulo se publicaron bajo el título "Heterometallic titanium-organic frameworks by metal-induced dynamic topological transformations" y referencia: M. Padiál, N.;[†] Lerma-Berlanga, B.;[†] Almora-Barrios, N.; Castells-Gil, J.; da Silva, I.; de la Mata, M.; I. Molina, S.; Hernández-Saz, J.; Platero-Prats, A. E.; Tatay, S.; y Martí-Gastaldo, C. *J. Am. Chem. Soc.* **2020**, *142* (14), 6638-6648. En este trabajo se presentó una nueva metodología para la síntesis

de redes heterometálicas de titanio (IV) mediante la reacción post sintética de intercambio de metales. Se estudiaron cuidadosamente las diferentes etapas de transformación (desde 1 día a 1 mes) para comprender el origen del fenómeno de la transformación topológica observada. Este análisis experimental se complementó con estudios computacionales que evaluaron el papel de la naturaleza del metal para dirigir dicha transformación.

La capacidad de transmetalación del clúster Ti_2Ca_2 se comenzó a probar con Mn(II), el único catión divalente de la primera serie de metales de transición para el que se pudo preparar el MUV-10(Mn) por síntesis directa. Para ello, se sumergieron cristales de MUV-10(Ca) en una disolución de $Mn(NO_3)_2$ en metanol a distintos tiempos comprendidos entre 1 y 30 días. El grado de transmetalación de las muestras se analizó por SEM-EDX. Los resultados mostraron una sustitución homogénea del Ca con una proporción alejada de la sustitución completa. Posteriormente, se extendió el estudio a otros metales de transición. Los mismos experimentos realizados con Mn(II) se llevaron a cabo con Co (II). Tras 10 días de intercambio se aisló un sólido rosa. La caracterización a nivel de composición y morfología se realizó mediante SEM-EDX donde se observó que se había producido un intercambio de Ca prácticamente completo con un ratio Ti:Co cercana a 1:2. Además, se observaron cambios en la morfología de los cristales. Los cristales octaédricos de MUV-10 quedaron recubiertos de cristales octaédricos de menor tamaño. El refinamiento de los datos de difracción de polvo de la nueva fase por el método Rietveld confirmó la formación de un MOF de titanio heterometálico isoestructural a MIL-100 compuesto por clusters de trímeros $[TiCo_2(\mu_3-O)(CO_2)_6(H_2O)_3]$, denominado MUV-101(Co). Para estudiar este cambio topológico en detalle, se aislaron los cristales a diferentes tiempos de intercambio. En las primeras etapas, ambas fases coexistieron y progresivamente el crecimiento de MUV-101(Co) fue dirigido por los cristales de MUV-10, que actuaron como semilla de crecimiento (en inglés conocido como *seeding template*). Los cambios progresivos se siguieron mediante medidas de difracción de rayos X de polvo, ATG y adsorción de N_2 . La muestra de 30 días mostró propiedades comparables a la fase homometálica descrita para MIL-100 (Co). La espectroscopia de absorción de rayos X descartó la segregación de fases, confirmando la presencia de clústeres bimetálicos de $TiCo_2$ y se confirmó la geometría de coordinación esperada para el trímero metálico del MIL-100.

Los estudios computacionales fueron esenciales para racionalizar el origen del cambio de topología en la red asociado a la reacción de transmetalación. Los cálculos teóricos indicaron que las reacciones de intercambio de metales en MUV-10 estaban dominadas por las terminaciones de las superficies del cristal (111), donde coexisten el metal expuesto (libre de ligando) y las terminaciones de ligando necesarias para la transformación topológica. Complementariamente, se estudió el efecto de la naturaleza del metal en la preferencia de transformación del clúster de Ti_2Ca_2 hacia Ti_2M_2 (presente en MUV-10) o TiM_2 (presente en MIL-100). Para ello se examinaron diferentes iones divalentes de la primera serie de transición ($M^{2+} = Mn, Fe, Co, Ni, Cu$ y Zn). La formación de un clúster isoestructural a MUV-10 sólo fue termodinámicamente favorable para el Mn, probablemente debido a la mayor

preferencia del Ca y el Mn por la geometría heptacordinada trigonal-prismática (CTP). En cambio, los cálculos para el Fe, el Co, el Ni y el Zn mostraron su preferencia por la formación del trímero TiM_2 . El Cu fue el único metal para el que la formación del trímero heterometálico no fue energéticamente favorable, lo que sugirió la formación de un nodo alternativo compatible con el ligando trimésico (con tres puntos de conexión).

Para comprobar el valor de estos resultados teórico, se llevaron a cabo experimentos adicionales en los que el MUV-10 se sumergió en disoluciones de sales de Fe(II), Ni(II), Zn(II) y Cu(II) en las mismas condiciones que para los iones anteriores. El análisis de los sólidos tras 10 y 30 días de intercambio evidenció unos resultados experimentales acorde a las tendencias calculadas teóricamente. El Fe, el Ni y el Zn mostraron un comportamiento similar al encontrado para el Co, dando lugar a estructuras de tipo MIL-100. Debido al comportamiento excepcional esperado para el Cu, se realizó un seguimiento más detallado de su transformación. Para ello, se analizaron los sólidos a diferentes tiempos de reacción (desde 1 h hasta 5 d). Las medidas de SEM-EDX confirmaron la formación de cubos entrelazados en las caras de los cristales octaédricos de MUV-10(Ca) y una relación Ti:Cu cercana a 1:4 para la muestra tras 5 d de intercambio. El análisis estructural por rayos X de polvo confirmó la formación de una nueva fase isoestructural a HKUST que se denominó MUV-102(Cu). Los cambios en función del tiempo de intercambio fueron seguidos por difracción de rayos X de polvo, ATG y adsorción de N_2 . Estos resultaron evidenciar una mayor velocidad de transformación en MUV-102(Cu) que en MUV-101(Co); sólo un día fue suficiente para lograr la transformación completa. La composición metálica final de MUV-102(Cu) implicó la formación de nodos mixtos formado por un clúster heterometálico de TiCu compensado por las cargas del ligando O^{2-} , $[TiCu(CO_2)_2(O)(H_2O)]$, y por 2,5 unidades homometálicas de Cu_2 , $[Cu_2(CO_2)_2(H_2O)_2]$. La presencia de nodos heterometálicas fue corroborada por la absorción de rayos X y las mediciones de resonancia paramagnética electrónica. Este último compuesto, el MUV-102(Cu), junto con el MUV-101(Zn) confirmaron la capacidad del MUV-10 para producir MOFs no accesibles por síntesis directa a través de transformaciones topológicas inducidas por el nodo bimetálico.

Resum de la tesi doctoral

La present tesi doctoral titulada “Estudi de la complexitat químiques en sòlids reticulars del grup IV” (en anglés *Exploring Chemical Complexity in Group IV Reticular Solids*) s'ha realitzat mitjançant compendi de publicacions. Està estructurada en cinc capítols, a més d'un capítol final de conclusions i resums en castellà i valencià.

El primer capítol consisteix en una introducció que mostra una visió general sobre el concepte de *Complexitat Química* en xarxes sintètiques. Per a endinsar-nos en aquesta àrea és necessari definir prèviament el concepte de Química Reticular (*Reticular Chemistry*), topologia (*Topology*) i expansió isoreticular (*Isoreticular Expansion*), així com les eines necessàries per a dissenyar i preparar estructures que siguin periòdiques, cristal·lines i poroses entre les quals destaquen, en el context de la present tesi, les *xarxes metall-orgàniques* (*Metall-Organic Frameworks (MOFs)*), les *xarxes covalent-orgàniques* (*Covalent Organic Frameworks (COFs)*) i els *poliedres metall-orgànics* (*Metall-Organic Polyhedra (MOPs)*). A continuació, es realitza una classificació en ordre creixent dels diferents tipus de xarxes poroses en funció de la variabilitat que existeix en la composició d'aquestes. Així doncs, el capítol comença amb la descripció de les xarxes més senzilles, les *xarxes binàries*, passant per les xarxes de complexitat intermèdia, *xarxes multivariància* i *xarxes multicomponent*, fins a arribar a les més complexes, *xarxes multicomponent amb incorporació de multivariància*. D'aquesta manera es pretén donar una visió incremental en el concepte de complexitat química que reflectisca les dificultats que existeixen tant des d'un punt de vista del disseny experimental de les xarxes com en la caracterització d'aquestes i dels avanços que s'han dut a terme en l'àrea en els últims anys.

Els resultats experimentals també es presenten en ordre creixent de complexitat química. En el Capítol 2 es descriu la síntesi d'una sèrie de MOPs que presenten *multivariància* gràcies a la combinació de lligants orgànics amb diferents funcionalitats en proporcions controlades. Els capítols 3 i 4 recullen els treballs centrats en la modificacions del material conegut com UiO-68-TZDC (TZDC: 4,4'-(1,2,4,5-tetrazine-3,6-diyl)dibenzoate), un MOF de zirconi derivat del UiO-68 que incorpora en el seu lligant el grup tetrazina (TZDC). En estes dues publicacions s'aborda la complexitat química a partir de modificacions enfocades en el lligant orgànic. Mentre que en el Capítol 3 es demostra com la variació de les condicions d'intercanvi post-sintètic de lligant permet controlar la distribució espacial dels lligants actius i inactius amb llum visible en l'estructura resultant; en el Capítol 4, s'explora la reactivitat de l'anell de tetrazina que forma part del lligant TZDC per a generar nous entorns de porus i així canviar les propietats i amb això, les aplicacions del material resultant. Finalment, en el Capítol 5 es presenta una metodologia per a introduir variabilitat en els nodes metàl·lics. Aquesta aproximació, basat en el MOF heterometàlic MUV-10, modifica la connectivitat, nuclearidad i els punts d'extensió de la unitat de construcció secundària (SBU, de l'anglès *Secondary Building Units*) i, per tant, la topologia de la xarxa resultant.

A continuació, es detallen els aspectes més importants desenvolupats en cadascun dels capítols.

Durant el capítol introductori, **Capítol 1**, ens centrarem en el tipus de xarxes sintetitzades al llarg de la present tesi, és a dir, en les *xarxes metall-orgàniques* i en els *poliedres metall-orgànics*. Aquests sòlids reticulars posseeixen en comú que estan constituïts per un component orgànic o lligant i un component inorgànic que pot ser un metall o un clúster metàl·lic. Així doncs, les *xarxes binàries*, constituïdes per dos components, són considerades com a punt de partida per a introduir la complexitat química a causa de la gran variabilitat que poden presentar tant en el component orgànic com en l'inorgànic. El següent grau de complexitat s'aconsegueix amb la introducció de diversitat en un d'aquests components, és a dir, incorporant diferents funcionalitats en el lligant, donant lloc a una aproximació orgànica, o diferents metalls/clústers metàl·lics, produint-se així una aproximació inorgànica. L'ús d'una d'aquestes aproximacions origina el que es coneix com a *xarxes multivariància*, o combinació de diferents components químics en número i proporcions variables que respecten l'estructura original de la xarxa. Alternativament, quan es combinen components de diferent topologia, connectivitat i/o grandària dona lloc a *xarxes multicomponents* ja siga mitjançant la diversitat de lligants o metalls. El grau de complexitat superior s'aconsegueix quan aquestes últimes incorporen el concepte de multivariància donant lloc a les *xarxes híbrides multicomponent*. Conforme anem endinsant-nos en el capítol introductori, la discussió es centra en la necessitat de realitzar una anàlisi detallada d'aquestes xarxes per a determinar el grau de complexitat química que posseeixen. Per a això s'introdueixen tècniques caracterització específiques tant per a l'estudi dels components orgànics com dels inorgànics. Aquestes tècniques es classifiquen en funció de la informació que proporcionen sobre la xarxa relacionat amb *i)* la presència de components de múltiple naturalesa en la mateixa estructura, *ii)* la proporció en la qual es troben, *iii)* la seua quantificació o *iv)* la distribució que posseeixen la diversitat de components al llarg de la xarxa. A més, per al cas específic dels metalls també es realitza un estudi de l'entorn metàl·lic i de l'estat d'oxidació d'aquest. L'última part d'aquest capítol demostra com el control en la complexitat química de les xarxes sintetitzades permet modificar les seues propietats i implementació en aplicacions concretes. El domini de l'entorn químic del porus, que es genera quan es crea la xarxa permet introduir diferents funcionalitats que poden actuar en paral·lel o de manera cooperativa, pot donar lloc a fenòmens sinèrgics. D'aquesta manera, la complexitat en les xarxes metall-orgàniques permet que aquests materials s'acosten cada vegada més als sistemes biològics reals, ampliant així el seu rang d'aplicació per a donar solucions concretes a problemes quotidians de rellevància social. Així doncs, durant aquest apartat es mostra el valor de la incorporació de complexitat i heterogeneïtat en les propietats dels MOFs en algunes de les àrees d'aplicació concretes com són la separació i emmagatzematge de gasos, la catàlisi heterogènia, la remediació ambiental o la preparació de dispositius luminescents.

En el **segon capítol** es descriu el primer exemple descrit fins a la data d'un poliedre metall-orgànic (MOP) porós basat en titani (IV), cMUV-11, de les sigles del nom en anglés de *cage-type Material of Universitat de València*. Aquest nou MOP és un exemple ideal per a introduir el concepte de complexitat en el component orgànic mitjançant la combinació de lligants que posseeixen diferents grups funcionals. En aquest context, els materials porosos tipus MOP han despertat un gran interès pel fet que posseeixen una de les propietats més rellevants dels MOFs, la porositat, combinada amb la naturalesa molecular dels sistemes discrets, la qual cosa els confereix potencials propietats en reconeixement amfitrió-hoste, separació i emmagatzematge de gasos, catàlisi o la seua implementació en membranes. Malgrat les potencials aplicacions que posseeixen els materials tipus MOPs encara estan relativament inexplorades en comparació amb la resta dels sòlids porosos estesos com els MOFs i els COFs. Una de les principals causes d'això està relacionat amb les propietats químiques i estructurals de les caixes metall-orgàniques. Aconseguir l'evacuació de les molècules de dissolvent del seu interior evitant la seua agregació o reorganització, o fins i tot el seu col·lapse estructural en estat sòlid no sol ser un procés trivial. Per tant, a causa d'aquesta complexitat els MOPs solen mancar d'alts valors d'àrees superficials. A més, en termes d'estabilitat, l'obtenció de sistemes químicament estables es redueix a estratègies concretes, restringint així la seua diversitat química. Per tot això, fins al que aconseguim el nostre coneixement, únicament s'han descrit 14 tipus de poliedres regulars per a descriure l'assemblat de MOPs, mentre que per contra es coneixen més de 100.000 estructures cristal·lines de MOFs amb una àmplia gamma de topologies. Davant aquesta situació decidim ampliar la diversitat química dels poliedres porosos robustos introduint el grup funcional hidroxàmic com a connector metàl·lic. La combinació del grup hidroxàmic amb metalls altament carregats com el Ti(IV) ofereix la possibilitat d'assemblar xarxes robustes, com ja va quedar exemplificat pel MUV-11 (MUV de les sigles en anglés *Material of Universitat de València*), reportat recentment pel nostre grup.

Els resultats d'aquest capítol van ser publicats sota el títol "*Permanent porosity in hydroxamate titanium-organic polyhedral*" i referència: Lerma-Berlanga, B.; Castell-Gil, J. R. Ganivet, C.; Almora-Barris, N.; González-Plates, J.; Fabelo, O.; M. Padià, N. i Martí-Gastaldó, C.; *J. Am. Chem. Soc.* 2021, 143 (50), 21195-21199. En aquest treball es va preparar el cMUV-11 mitjançant la reacció directa del isopropòxid de titani (IV) amb el lligant àcid benzé-1,4-dihidroxàmic (*p*-H₄bdha) en *N,N*-dimetilformamida (DMF) anhidre utilitzant àcid benzoic com a modulador en condicions solvotermals. Després de 18 h de reacció a 100 °C es van obtenir cristalls octaèdrics de color roig intens de 100 µm de grandària. La qualitat dels cristalls va permetre determinar de la seua estructura mitjançant difracció de raigs X de monocristall. cMUV-11 va consistir en caixes neutres discretes amb fórmula [Ti₈(*p*-H₂bdha)₈(*p*-bdha)₄]. Estes caixes metall-orgàniques es poden descriure com a cubs distorsionats on els huit vèrtexs estan compostos per nodes simples de titani en un entorn octaèdric distorsionat (TiL₃), imposat per l'anell de quelat format pel grup hidroxàmic amb el titani, i units per 12 lligants *p*-H₄bdha parcialment desprotonats. En el cristall, les caixes moleculars s'organitzen formant una xarxa

tridimensional dirigida a través d'enllaços d'hidrogen que impliquen grups hidroxàmics complementaris de les arestes adjacents. Aquest empaquetament va originar una xarxa de topologia *pcb* amb cavitats microporoses intrínseques als cubs.

Les tècniques de caracterització emprades, anàlisi termogravimètric i espectroscòpia de plasma d'acoblament inductiu van mostrar l'alta estabilitat tèrmica i química de cMUV-11 comparable amb els valors d'uns altres MOFs de titani descrits. L'estabilitat estructural es va avaluar mitjançant mesures de difracció de raigs X de pols i adsorció de N₂ de les mostres prèviament intercanviades amb dissolvents volàtils (acetona, hexan i èter dietílic). A pesar que els patrons de difracció de les mostres evacuades van mostrar un eixamplament de les línies de difracció, després de submergir la mostra de nou en DMF es va recuperar la difracció original, confirmant així la flexibilitat dels enllaços H que controlen l'empaquetament de cMUV-11. L'elecció del dissolvent d'intercanvi i les condicions d'activació van ser claus per a obtenir la porositat esperada. L'intercanvi de la mostra amb acetona va conduir a una isoterma reversible de tipus I amb una àrea superficial BET de 1020 m²·g⁻¹ pròxima al valor més alt reportat en MOPs fins al moment. L'anàlisi de les dades pel mètode NLDFIT va mostrar una distribució de grandària de porus centrada en 1.5 nm, en concordança amb les dimensions de la cavitat microporosa estimada a partir de l'anàlisi cristal·logràfic.

L'impacte del dissolvent empleat durant l'intercanvi previ a l'activació del material posseeix un efecte notable sobre la seua porositat final, la qual cosa va evidenciar la necessitat de controlar les interaccions entre els poliedres. Per a demostrar això, es van preparar una sèrie de MOPs combinant lligants amb diverses funcionalitats: el grup amino (-NH₂) es va seleccionar per les seues propietats donador d'H i el metoxi (-OCH₃) com a acceptor. Així doncs, mitjançant l'ús combinat de lligants amb diferents grups funcionals s'aconsegueix modular l'entorn químic de les caixes en incorporar grups funcionals amb diferent capacitat per a formar enllaços d'hidrogen en proporcions controlades. Els sistemes cMUV-11-NH₂-X% i cMUV-11-OCH₃-X% (X= 10, 20, 50, 60) es van preparar per síntesi directa utilitzant combinacions binàries del lligant corresponent, *p*-H₄bdha-NH₂ o *p*-H₄bdha-OCH₃, amb el lligant original (*p*-H₄bdha). L'anàlisi mitjançant ressonància magnètica nuclear de protó (¹H-RMN) de les mostres prèviament digerides va permetre avaluar el percentatge d'incorporació real del lligant modificat *p*-bdha-X. L'estudi de la tendència d'incorporació de cada lligant va suggerir un impacte visible del substituent en el procés d'empaquetament. Malgrat això, les caixes multivariància es van aïllar com a monocristalls de grandària, color i morfologies similars al material original. L'anàlisi de les mostres va confirmar la seua puresa i homogeneïtat. A més, l'anàlisi cristal·logràfic de cMUV-11-NH₂-50% i -OCH₃-50% va confirmar l'obtenció de xarxes isoestructurals a cMUV-11 i va descartar alteracions significatives a nivell de la xarxa d'enllaços d'hidrogen. Aquest mateix efecte s'observa en les variacions insignificants obtingudes en el càlcul de l'estructura electrònica mitjançant DFT; secundades per les mínimes variacions observades experimentalment en l'estabilitat química i tèrmica dels tres derivats.

Quant a l'estabilitat estructural, cMUV-11-X també van presentar una reorganització estructural en estat sòlid reflectida en canvis en el patró de difracció de raigs X. L'impacte de la modificació del lligant orgànic en l'empaquetament es demostra en la resposta davant l'evacuació del dissolvent, i, conseqüentment, en els valors de porositat. Per a la sèrie cMUV-11-NH₂-X% només les mostres intercanviades amb hexan i amb percentatges ≤ 20% de grups amins van mostrar una porositat permanent amb valors BET màxims de 620 m²·g⁻¹. Per contra, les mostres cMUV-11-OCH₃ amb una càrrega inferior al 50 % van presentar àrees superficials més elevades que el cMUV-11, pròximes als 1200 m²·g⁻¹. D'aquesta manera, es va demostrar l'impacte de les interaccions entre caixes en la modulació de la porositat per a aquesta família de MOPs.

Durant el **tercer capítol** s'estudia l'efecte que produeix la incorporació d'un anell de 1,2,4,5-tetrazina en el lligant orgànic sobre les propietats químiques i fotocatalítiques d'una xarxa metall-orgànica de tipus UiO-68. A més, han sintetitzat xarxes multivariància que permeten analitzar l'impacte que té la distribució de l'anell de 1,2,4,5-tetrazina al llarg del cristall en les propietats d'aquestes. A pesar que les aril-s-tetrazines van ser descobertes a la fi del segle XIX, ha sigut en les últimes dècades quan la comunitat científica ha mostrat interès en la seua implementació com a blocs de construcció per al disseny de nous materials moleculars funcionals. Les aril-s-tetrazines poden actuar com una antena de llum visible amb un comportament redox podent-se reduir reversiblement a causa del seu caràcter deficient en electrons. Tant els seus valors del potencial de reducció com la cinètica del procés, així com la posició màxima de la banda d'absorció poden ser modulats mitjançant l'ús de substituents pel que poden arribar a ser excel·lents candidats per a incorporar-se en aplicacions relacionades amb processos de generació de llum, sensors, cèl·lules solars, i polímers electro/fotoactivos. Així doncs, en aquest capítol es combina un lligant orgànic derivat de tetrazina amb un metall del grup (IV), el zirconi, per a desenvolupar nous fotocatalitzadors heterogenis porosos i estables. La síntesi de MOF basats en tetrazina es pot dur a terme per síntesi directa o per mètodes post sintètics. Aquests últims ofereixen la possibilitat de controlar les distribucions de lligant en el cristall dels sòlids multivariància resultants; la qual cosa permetria modular les propietats fotocatalítiques del material.

Els resultats d'aquest capítol es van publicar sota el títol "Effect of Linker Distribution in the Photocatalytic Activity of Multivariate Mesoporous Crystals" amb referència: Lerma-Berlanga, B.; R. Ganivet C.; Almora-Barrios N.; Tatay S.; Peng Y.; Albero J.; Fabelo O.; González-Platas J.; García H.; M. Padial N. i Martí-Gastaldo, C. *J. Am. Chem. Soc.* **2021**, *143* (4), 1798–1806". En aquest treball presentem l'optimització de les condicions sintètiques per a la preparació de cristalls de UiO-68 (UiO: University of Oslo), usant H₂TPDC (1,1':4',1''-terphenyl)-4,4''-dicarboxylic acid) i UiO-68-TZDC, un anàleg fotoactiu del primer basat en un ligando derivat dicarboxílic de la tetrazina, H₂TZDC (1,2,4,5-tetrazine-3,6-diyl)-4,4'-dibenzoic). L'estudi de les propietats químiques d'aquests materials va mostrar la necessitat de combinar tot dos lligants en una mateixa estructura per a poder preparar un material amb la suficient estabilitat estructural i química com per a emprar-se com

fotocatalizador. Les mostres UiO-68-TZDC% multivariància van mostrar propietats millorades en comparació amb els seus homòlegs purs.

Així doncs, els materials UiO-68 i UiO-68-TZDC es van preparar en condicions solvotermals. La implementació de metodologies d'anàlisis d'alt volum de mostra (*High-Throughput Screening* en anglés) va permetre accelerar la exploració sistemàtica dels paràmetres sintètics i aconseguir una alta reproductibilitat en la síntesi dels materials. Els cristalls de UiO-68 es van aïllar com a octaedres de color groc pàl·lid de grandària compresa entre 20 i 50 μm utilitzant 40 equivalents de modulador i calfant a 100 $^{\circ}\text{C}$ durant 72 h. Aquestes condicions només van requerir una lleugera reducció dels equivalents de modulador, de 40 a 10, per a produir UiO-68-TZDC com a cristalls octaèdrics de color rosa de menor grandària (10-20 μm). L'anàlisi cristal·logràfic mitjançant difracció de raigs X va determinar paràmetres cristal·logràfics molt similars per a tots dos materials amb topologia *fcu* característica d'aquesta família de materials tipus UiO.

L'anàlisi de l'efecte del lligant sobre el comportament químic dels MOFs binaris va mostrar que la presència del nucli de tetrazina en el connector orgànic disminuïa l'estabilitat tèrmica i química de l'estructura. Mentre que el UiO-68 es descomponia en l'aire per damunt dels 500 $^{\circ}\text{C}$, UiO-68-TZDC mostrava una descomposició gradual a partir dels 250 $^{\circ}\text{C}$. D'altra banda, l'estabilitat hidrolítica dels sòlids es va avaluar mitjançant la incubació de les mostres en aigua durant 24 h. Els difractogrames de raigs X de pols després d'aquest tractament van mostrar una amortització parcial del UiO-68-TZDC. L'efecte negatiu del lligant TZDC també va ser confirmat mitjançant ICP, mostrant una lixiviació de Zr^{+4} superior després de la incubació al mig aquós. Malgrat les diferències observades per a les dues xarxes, després de l'optimització del procés d'activació es van obtenir valors esperats d'àrees superficials BET, al voltant dels 4000 $\text{m}^2\cdot\text{g}^{-1}$. A més, l'anàlisi d'adsorció de CO_2 va revelar major afinitat en el cas de UiO-68-TZDC. L'anàlisi de les fases binàries va mostrar la necessitat de l'ús de tots dos lligants per a produir xarxes multivariància que combinaren les propietats de totes dues xarxes: absorció de llum en el rang del visible, estabilitat química i elevada porositat, tot això rellevant per al seu ús en fotocatalisis.

La família de mostres MTV-UiO-68-TZDC% es va preparar a partir d'experiments post-sintètics d'intercanvi de lligant (en anglés *Solvent-Assisted Ligand Exchange, SALE*) utilitzant cristalls de UiO-68 com a precursors i diferents quantitats de lligant H_2TZDC . Les condicions suaus d'intercanvi van ser respectuoses amb l'estructura i porositat original. A més, la coexistència de tots dos lligants va millorar l'estabilitat química dels materials. L'impacte del dopatge de tetrazina en l'estructura electrònica dels materials resultants es va estudiar mitjançant càlculs DFT. Els càlculs van mostrar que nivells baixos d'intercanvi de TZDC són suficients per a modificar l'estructura electrònica i les propietats òptiques dels híbrids. Aquesta tendència teòrica estava d'acord amb els valors experimentals del banda òptica mesurats mitjançant espectroscòpia de reflectància difusa i calculats emprant la funció Kubelka-Munk.

Per a estudiar la complexitat química de les estructures multivariància resultants a nivell d'un únic cristall es van realitzar mesures de microscòpia confocal de fluorescència i espectroscòpia de fotoelectrons emesos per raigs X (en anglés *X-ray Photoelectron Spectroscopy, XPS*). Les imatges registrades en el microscopi confocal van mostrar disposicions espacials concretes per al lligant original (TPDC) i l'intercanviat (TZDC) en funció dels nivells de dopatge. Les mostres amb percentatges de tetrazina més baixos van mostrar una distribució asimètrica dels lligants que originaven microestructures de tipus *core-shell*/TPDC-TZDC, amb recobriment lleugerament més gruixuts per a nivells de dopatge més alts. Per a les mostres amb nivells de TZDC superiors al 35 % es van observar distribucions de lligant homogènies. Paral·lelament, es van realitzar experiments per a estudiar l'origen de la formació de distribucions asimètriques. Per a això, es va preparar un nou conjunt de cristalls MTV-UiO-68-TZDC% mantenint fix els equivalents de TZDC en dissolució i modificant els temps d'intercanvi. Es va observar que els temps de reacció prolongats afavorien la difusió de TZDC a través del cristall formant una distribució més homogènia. D'aquesta manera, els resultats van indicar que la distribució del lligant no sols estava controlada per la concentració de TZDC en la dissolució, sinó també pel temps d'intercanvi.

Les mostres MTV-UiO-68-TZDC% van ser una plataforma idònia per a estudiar l'efecte de la distribució del lligant sobre l'activitat catalítica de les xarxes ja que tots els sòlids posseeixen estructura electrònica i un valor de banda òptica comú. Així doncs, es van realitzar dos assajos catalítics dissenyats per a la reducció del metil viológen i producció d'H₂ van mostrar que la major activitat catalítica s'aconseguia per a la mostra UiO-68-TZDC_{10%} amb una distribució asimètrica *core-shell*. Les anàlisis de les mostres després dels assajos catalítics van suggerir que el rendiment catalític es podia explicar mitjançant un equilibri entre la concentració superficial del lligant fotoactiu (TZDC) i l'estabilitat del material (centre dels cristalls formats principalment per UiO-68).

En el **quart capítol** es demostra la importància de les tetrazines com a grup funcional en la modificació postsintètica de xarxes metall-orgàniques. Entre les moltes qualitats de les s-tetrazinas, algunes d'elles comentades en el capítol anterior, cal destacar la seua reactivitat com a dieno en les reaccions de tipus Diels-Alder de demanda electrònica inversa (iEDDA, sigles del seu nom en anglés *inverse Electron-Demand Diels-Alder*). Aquest tipus de reacció pericíclica de cicloaddició entre un dieno i un dienófilo posseeix alguns avantatges que la fan viable per a dur-la a terme sobre materials porosos respectant la integritat de la xarxa: no necessiten un catalitzador, ofereixen una cinètica ràpida, ortogonalitat, transformacions quantitatives en condicions suaus i productes secundaris inofensius (N₂). Per tant, la tetrazina es presenta com un grup funcional complementari als utilitzats convencionalment per a dur a terme modificacions covalents post sintètiques les quals s'han restringit a uns pocs grups com són el grup amino, aldehyd, azida o alquino. Fins hui, l'ús de la reactivitat post-sintètica de la tetrazina en els MOFs es basava quasi exclusivament en la incorporació d'olefines amb finalitats concrets, com és la integració de la hidrofobicitat requerida per a la fabricació de membranes, la modulació de la capacitat d'adsorció de CO₂ per a aconseguir una major

selectivitat en la separació de CO₂/N₂ o per al control de la interpenetració de les xarxes. Malgrat això, encara no s'havien descrit rutes genèriques de post modificació en MOFs basades en el grup tetrazina. En aquest sentit, proposem emprar el UiO-68-TZDC, sintetitzat en el capítol anterior, com a plataforma per a explorar aquesta reactivitat i modificar l'entorn dels porus amb diverses funcionalitats químiques. A més, el UiO-68-TZDC permet estudiar l'efecte de reticulació de la tetrazina sobre la reactivitat iEDDA.

Els resultats d'aquest capítol estan en procés de ser publicats sota el títol "Tetrazine linkers as plug-and-play tags for general framework functionalization and C₆₀ conjugation." Els seus autors són els següents: Lerma-Berlanga, B.;[†] R. Ganivet, C.;[†] Almora-Barrios, N.; Vismara, R.; A. R. Navarro, J.; Tatay, S.; M. Padial, N. i Martí-Gastaldo, C. En aquest treball, es mostra la versatilitat del material UiO-68-TZDC com a plataforma per a albergar diferents funcionalitats químiques en el porus incorporades per modificacions covalents post-sintètiques de tipus iEDDA. Inicialment, la reactivitat iEDDA del UiO-68-TZDC va ser provada amb un excés d'equivalents de 2,5-norbornadieno (NBD), considerat dienófilo model en aquest tipus de reaccions. Durant la reacció es produeix un canvi de color, de rosa, característic del MOF original, a groc característic de la transformació de la tetrazina a piridazina (PZDC). La transformació total a piridazina va ser confirmada després de la digestió dels cristalls mitjançant espectrometria de masses d'alta resolució i ressonància magnètica nuclear de protó (¹H-RMN). Les condicions sintètiques òptimes es van determinar per un compromís entre una modificació completa i un baix impacte en la cristal·linitat del material resultant. Les condicions seleccionades van ser un temps de reacció de 16 hores amb agitació a 40 °C utilitzant un excés de 3 equivalents de dienófilo. El resultat UiO-68-PZDC va ser caracteritzat per imatges de microscopi d'escombratge electrònic (en anglès *Scanning Electron Microscopy, SEM*), difracció de raigs X de pols, adsorció de N₂ i anàlisi termogravimètric. Els resultats de la caracterització del nou material no van mostrar canvis significatius respecte al UiO-68-TZDC original, la qual cosa va confirmar una modificació respectuosa amb l'estructura del material.

Per a comprendre l'efecte de la reticulació del lligant de TZDC sobre la reactivitat en les reaccions iEDDA, es va dur a terme un estudi de la reacció entre el MOF i el substrat NBD en intervals de temps controlats durant 24 hores, observant-se un canvi de color gradual de rosa a groc pàl·lid indicant el progrés de la reacció cap a la formació de piridazina. A més, es van realitzar assajos control sotmetent a les mateixes condicions, temps i temperatura el lligant lliure i així tindre una comparació directa del grau de conversió en el MOF i en el lligant lliure i, per tant, determinar l'efecte de la reticulació. L'anàlisi mitjançant ¹H-RMN dels sòlids digerits als diferents temps de reacció (t= 0, 10, 20, 30, 40, 60, 80, 100, 120, 180, 240, 360, 480, 600, 720, 1200 y 1500 minuts) emprant com a patró intern l'àcid fumàric, va permetre dur a terme la quantificació del producte format, i amb això el grau de conversió de tetrazina a piridazina, i així elaborar els perfils cinètics de formació de piridazina. A pesar que en tots dos casos els perfils s'ajustaven a una reacció de pseudo-primer ordre amb un altilplà prop del 95% de conversió; la cinètica va ser més ràpid en el cas del MOF, fins i tot amb la limitació de la difusió del dienófilo a

través dels porus. Per a corroborar els efectes positius de la reticulació en la reactivitat de l'anell de tetrazina, es va realitzar un control addicional amb el lligant lliure en presència de $ZrCl_4$, que va servir per a descartar l'efecte catalític dels ions $Zr(IV)$ en el procés. Així doncs, l'augment de la velocitat observat es pot explicar sobre la base de la suma de diversos factors: i) major accessibilitat del dieno, gràcies a que la reticulació disminueix les interaccions π - π entre tetrazinas, ii) efectes electrònics atribuïts a la a la coordinació del lligant al centre metàl·lic. A més, respecte a aquest efecte, els càlculs DFT-VASP realitzats van mostrar una disminució de l'energia de l'orbital LUMO en el UiO-68-TZDC que es va traduir en una reducció de la diferència d'energia entre el LUMO del dieno i el HOMO del dienófilo afavorint així la termodinàmica de la reacció.

A continuació, es va estudiar la versatilitat de la reacció iEDDA per a la modificació de la xarxa UiO-68-TZDC emprant una àmplia gamma de dienófilos. Els experiments van generar una varietat de derivats del UiO-68-PZDC amb entorns de porus diversos, entre els quals s'inclouen funcionalitats com a anells fusionats, grups hidroxil, fenilos, succinimida, carboxílics terminals, cadenes alifàtiques i fins i tot centres quirals. L'anàlisi per 1H -RMN dels sòlids resultants va mostrar la desaparició dels senyals propis de la TZDC i l'aparició de les noves associades als productes formats, això, es va confirmar mitjançant espectrometria de masses d'alta resolució, anàlisi elemental i anàlisi termogravimètric. El posterior anàlisi dels derivats per difracció de raigs X de pols, imatges de SEM i adsorció de N_2 van confirmar una cristal·linitat, morfologia i robustesa estructural comparable a l'estructura original. A més, la versatilitat de la plataforma UiO-68-TZDC per a introduir modificacions va permetre anar més enllà d'aquests substrats moleculars i introduir unitats nanocarbonades de manera controlada. Les condicions sintètiques emprades anteriorment van ser adaptades a la singular solubilitat dels fullerenos i ens va permetre sintetitzar el seu derivat UiO-68-PZDC(C_{60}), amb molècules de C_{60} covalentment unides a l'anell de piridazina. Les mesures d'espectroscòpia UV-Vis al costat de les de ressonància magnètica de carboni i espectrometria de masses van confirmar la formació del monoadducte entre el fullereno i l'anell de piridazina del lligant. Per a comprendre millor l'estructura del derivat fullerètic, es va realitzar un refinament Rietveld a partir d'una mesura de difracció de pols d'alta resolució. Els van resultar van mostrar que UiO-68-PZDC(C_{60}) era isoestructural a UiO-68-TZDC però amb valors de cel·la lleugerament allargats i la presència d'unitats de $H_2pzdc-C_{60}$ a causa de conjugació covalent de les unitats de C_{60} a l'anell de tetrazina. Els factors d'ocupació de les molècules de fullereno es van refinar lliurement per a tindre en compte la modificació total. El model va convergir per a la formació de prop del 50% d'unitats de piridazina, obtenint-se una fórmula unitat de $[Zr_6O_4(OH)_4(PZDC-C_{60})_3(TZDC)_3]$.

Aquest grau de modificació concordava amb els valors experimentals de l'anàlisi elemental i termogravimètric dels cristalls. A més, els valors porositat accessible, grandària i volum de porus eren consistents amb la conjugació de tres molècules de C_{60} en les vores del 50 % de les cavitats tetraèdriques. Es van realitzar experiments addicionals per a comprendre l'origen d'aquest percentatge de modificació persistent. L'ampliació del temps de reacció a cinc dies va donar lloc a un

percentatge molt similar, la qual cosa va suggerir que aquest límit superior de modificació no estava controlat per les limitacions de difusió, sinó que venia imposat per l'impediment estèric del porus i les interaccions intermoleculares repulsives. Aquest resultat es va corroborar amb un experiment alternatiu utilitzant UiO-68-TZDC_{44%} (descriu en el capítol 3), el qual va mostrar una modificació completa quan els lligants de TZDC estaven diluïts en l'estructura.

Finalment, el **capítol cinc** mostra la versatilitat dels nodes heterometàlics del MUV-10 per a experimentar transformacions post sintètiques que permeten incorporar nous metalls i obtenir diferents topologies de manera dirigida venent així les limitacions que imposa la síntesi directa a la formació d'unes certes xarxes. La síntesi de MOFs de titani predissenyats a partir de SBUs específiques continua sent un gran desafiament degut a l'alta reactivitat dels precursors de titani, que en condicions de síntesis solvotermals condueixen, generalment, a fases amorfes i/o a la formació d'òxid de titani. A més, les rutes per a introduir heterogeneïtat en els nodes de titani homometàlics són encara escasses. En la majoria dels casos, les reaccions de síntesi directa es basen principalment en combinacions de titani amb ions metàl·lics amb càrregues i radis iònics similars. Quant a les reaccions post sintètiques, la incorporació d'altres metalls es veu dificultada per l'alta estabilitat dels enllaços de coordinació Ti-O, la qual cosa dona lloc a una substitució incontrolable i/o a la formació d'una capa d'òxid no desitjada. Això podria explicar la baixa diversitat química dels MOFs basats en aquest metall. Com a possible alternativa, nosaltres proposem l'ús de MUV-10(Ca), un MOF heterometàlic de Ti, com a reactiu en reaccions de transmetal·lació post sintètiques. Aquest MOF presenta clústers tetranuclears $[\text{Ti}_2\text{Ca}_2(\text{O})_2(\text{H}_2\text{O})_4(\text{CO}_2)_8]$, on es combinen llocs metàl·lics blans (Ca^{2+}) i durs (Ti^{4+}). D'aquesta manera, MUV-10 pot ser considerat un excel·lent candidat per a dirigir la formació de nodes metàl·lics amb punts de connexió variables gràcies a la major facilitat que ofereix el Ca^{2+} enfront del Ti^{4+} per a l'intercanvi. D'aquesta manera, la nostra aproximació contribuiria a millorar la diversitat química dels MOFs basats en titani, considerats excel·lents candidats per a ampliar el rang d'aplicació dels materials porosos a causa de la seua alta estabilitat química i tèrmica.

Els resultats descrits en el cinqué capítol es van publicar sota el títol "Heterometallic titanium-organic frameworks by metal-induced dynamic topological transformations" i referència: M. Padial, N.;[†] Lerma-Berlanga, B.;[†] Almora-Barrios, N.; Castells-Gil, J.; da Silva, I.; de la Mata, M.; I. Molina, S.; Hernández-Saz, J.; Platero-Prats, A. E.; Tatay, S.; i Martí-Gastaldo, C. *J. Am. Chem. Soc.* **2020**, *142* (14), 6638-6648. En aquest treball es va presentar una nova metodologia per a la síntesi de xarxes heterometàliques de titani (IV) mitjançant la reacció post sintètica d'intercanvi de metalls. Es van estudiar acuradament les diferents etapes de transformació (des d'1 dia a 1 mes) per a comprendre l'origen del fenomen de la transformació topològica observada. Aquesta anàlisi experimental es va complementar amb estudis computacionals que van avaluar el paper de la naturalesa del metall per a dirigir aquesta transformació.

La capacitat de transmetal·lació del clúster Ti_2Ca_2 es va començar a provar amb Mn(II), l'únic catió divalent de la primera sèrie de metalls de transició per al qual es va poder preparar el MUV-10(Mn) per síntesi directa. Per a això, es van submergir cristalls de MUV-10(Ca) en una dissolució $Mn(NO_3)_2$ en metanol a diferents temps compresos entre 1 i 30 dies. El grau de transmetal·lació de les mostres es va analitzar per SEM-EDX. Els resultats van mostrar una substitució homogènia del Ca amb una proporció allunyada de la substitució completa.

Posteriorment, es va estendre l'estudi a altres metalls de transició. Els mateixos experiments realitzats amb Mn(II) es van dur a terme amb Co (II). Després de 10 dies d'intercanvi es va aïllar un sòlid rosa. La caracterització a nivell de composició i morfologia es va realitzar mitjançant SEM-EDX on es va observar que s'havia produït un intercanvi de Ca pràcticament complet amb un ràtio Ti:Co pròxima a 1:2. A més, es van observar canvis en la morfologia dels cristalls. Els cristalls octaèdrics de MUV-10 van quedar recoberts de cristalls octaèdrics de menor grandària. El refinament de les dades de difracció de pols de la nova fase pel mètode Rietveld va confirmar la formació d'un MOF de titani heterometàlic isoestructural a MIL-100 compost per clústers de trímers $[TiCo_2(\mu_3-O)(CO_2)_6(H_2O)_3]$, denominat MUV-101(Co). Per a estudiar aquest canvi topològic detalladament, es van aïllar els cristalls a diferents temps d'intercanvi. En les primeres etapes, totes dues fases van coexistir i progressivament el creixement de MUV-101(Co) va ser dirigit pels cristalls de MUV-10, que van actuar com a llavor de creixement. Els canvis progressius es van seguir mitjançant mesures de difracció de raigs X de pols, anàlisis termogravimètric i adsorció de N_2 . La mostra de 30 dies va mostrar propietats comparables a la fase homometàlica descrita per a MIL-100 (Co). L'espectroscòpia d'absorció de raigs X va descartar la segregació de fases, confirmant la presència de clústers bimetal·lics de $TiCo_2$ i es va confirmar la geometria de coordinació esperada per al trímer metal·lic del MIL-100.

Els estudis computacionals van ser essencials per a racionalitzar l'origen del canvi de topologia en la xarxa associat a la reacció de transmetal·lació. Els càlculs teòrics van indicar que les reaccions d'intercanvi de metalls en MUV-10 estaven dominades per les terminacions de les superfícies del cristall (111), on coexisteixen el metall exposat (lliure de lligant) i les terminacions de lligant necessàries per a la transformació topològica. Complementàriament, es va estudiar l'efecte de la naturalesa del metall en la preferència de transformació del clúster de Ti_2Ca_2 cap a Ti_2M_2 (present en MUV-10) o TiM_2 (present en MIL-100). Per a això es van examinar diferents ions divalents de la primera sèrie de transició ($M^{2+} = Mn, Fe, Co, Ni, Cu$ y Zn). La formació d'un clúster isoestructural a MUV-10 només va ser termodinàmicament favorable per al Mn, probablement a causa de la major preferència del Ca i el Mn per la geometria heptacordinada trigonal-prismàtica (CTP). En canvi, els càlculs per al Fe, el Co, el Ni i el Zn van mostrar la seua preferència per la formació del trímer TiM_2 . El Cu va ser l'únic metall per al qual la formació del trímer heterometàlic no va ser energèticament favorable, la qual cosa va suggerir la formació d'un node alternatiu compatible amb el lligant trimésic (amb tres punts de connexió). Per a comprovar el valor d'aquests resultats teòrics, es van dur a terme experiments addicionals en els quals el MUV-10 es va submergir en

dissolucions de sals de Fe(II), Ni(II), Zn(II) i Cu(II) en les mateixes condicions que per als ions anteriors. L'anàlisi dels sòlids després de 10 i 30 dies d'intercanvi va evidenciar uns resultats experimentals concorde a les tendències calculades teòricament. El Fe, el Ni i el Zn van mostrar un comportament similar al trobat per al Co, donant lloc a estructures de tipus MIL-100. A causa del comportament excepcional esperat per al Cu, es va realitzar un seguiment més detallat de la seua transformació. Per a això, es van analitzar els sòlids a diferents temps de reacció (des de 1 h fins a 5 d). Les mesures de SEM-EDX van confirmar la formació de cubs entrelaçats en les cares dels cristalls octaèdrics de MUV-10(Ca) i una relació Ti:Cu pròxima a 1:4 per a la mostra tres 5 dies d'intercanvi. L'anàlisi estructural per raigs X de pols va confirmar la formació d'una nova fase isoestructural a HKUST que es va denominar MUV-102(Cu). Els canvis en funció del temps d'intercanvi van ser seguits per difracció de raigs X de pols, anàlisis termogravimètric i adsorció de N₂. Aquestos resultats van evidenciar una major velocitat de transformació en MUV-102(Cu) que en MUV-101(Co); només un dia va ser suficient per a aconseguir la transformació completa. La composició metàl·lica final de MUV-102(Cu) va implicar la formació de nodes mixtos format per un clúster heterometàlic de TiCu compensat per les càrregues del lligant O₂⁻, [TiCu(CO₂)₂(O)(H₂O)], i per 2,5 unitats homometàliques de Cu₂, [Cu₂(CO₂)₂(H₂O)₂]. La presència de nodes heterometàlics va ser corroborada per l'absorció de raigs X i els mesuraments de ressonància paramagnètica electrònica. Aquest últim compost, el MUV-102(Cu), juntament amb el MUV-101(Zn) van confirmar la capacitat del MUV-10 per a produir MOFs no accessibles per síntesi directa a través de transformacions topològiques induïdes pel node bimetàl·lic.

